CHALMERS
UNIVERSITY OF TECHNOLOGY

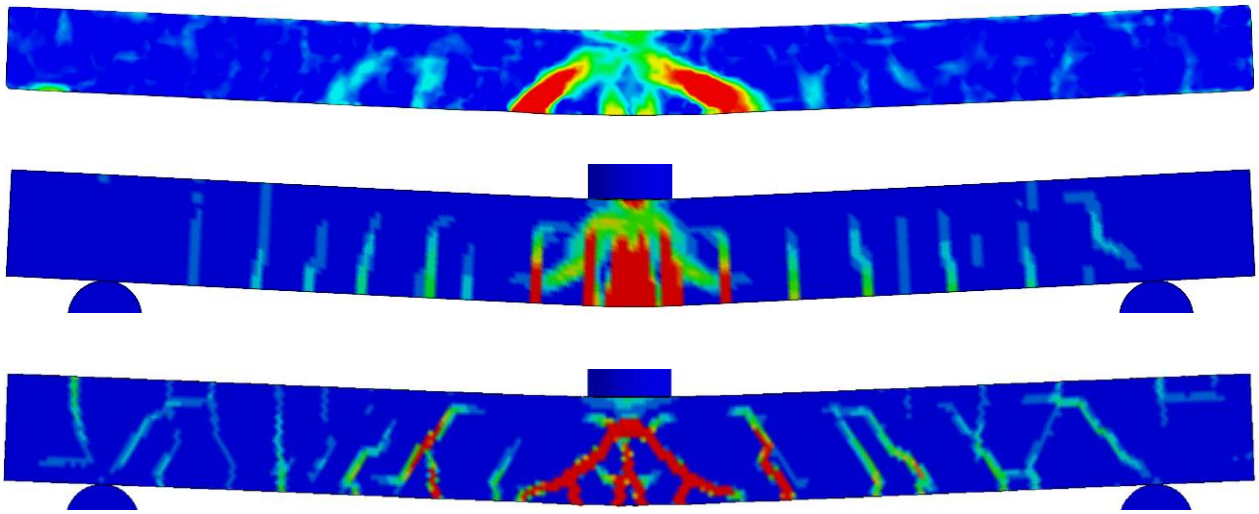

Concrete Beams Subjected to Drop-Weight Impact and Static Load

Structural Behavior and Plastic Rotational Capacity from Experiments and Finite Element Analysis

Master's Thesis in the Master's Programme Structural Engineering and Building Technology

FABIO LOZANO MENDOZA
JOSEF MAKDESI APHRAM

Architecture and Civil Engineering
Division of Structural Engineering
Concrete Structures
CHALMERS UNIVERSITY OF TECHNOLOGY
Gothenburg, Sweden 2017
Master's Thesis BOMX02-17-21

MASTER'S THESIS BOMX02-17-21

Concrete Beams Subjected to Drop-Weight Impact and Static Load

Structural Behavior and Plastic Rotational Capacity from Experiments and Finite Element Analysis

Master's Thesis in the Master's Programme Structural Engineering and Building Technology

FABIO LOZANO MENDOZA
JOSEF MAKDESI APHRAM

Architecture and Civil Engineering
Division of Structural Engineering
Concrete Structures
CHALMERS UNIVERSITY OF TECHNOLOGY

Gothenburg, Sweden 2017

Concrete Beams Subjected to Drop-Weight Impact and Static Load
Structural Behavior and Plastic Rotational Capacity from Experiments and Finite Element Analysis
FABIO LOZANO MENDOZA
JOSEF MAKDESI APHRAM

Master's Thesis BOMX02-17-21
ISSN 1652-8557
Architecture and Civil Engineering
Division of Structural Engineering
Concrete Structures
Chalmers University of Technology
SE-412 96 Gothenburg
Sweden
Telephone: +46 (0)31-772 1000

Cover:
Crack pattern of beam B-06 due to an impact from a height of 5 m determined through DIC analysis at the time of maximum deflection, compared to the strain field obtained from LS-DYNA models with hexahedron and tetrahedron elements, respectively.

Chalmers Reproservice
Gothenburg, Sweden 2017

Concrete Beams Subjected to Drop-Weight Impact and Static Load
Structural Behavior and Plastic Rotational Capacity from Experiments and Finite Element Analysis
Master's Thesis in the Master's Programme Structural Engineering and Building Technology
FABIO LOZANO MENDOZA
JOSEF MAKDESI APHRAM
Architecture and Civil Engineering
Division of Structural Engineering
Concrete Structures
Chalmers University of Technology

ABSTRACT

The behavior of simply supported concrete beams subjected to impact loading was evaluated through an experimental study consisting of a drop-weight falling on the specimens from different heights. Static tests were subsequently performed on the impact-damaged specimens in order to examine the post-impact behavior. Undamaged beams were also tested under static loading to obtain a basis of comparison. All tests were recorded using high- and normal-speed cameras. The footages were afterwards processed through digital image correlation (DIC).

The rotational capacity and cracking distribution on both undamaged and damaged beams were studied based on the experimental results. The beams subjected to low impact energy exhibited similar behavior during the subsequent static testing compared to undamaged specimens. On the other hand, an increase of the post-impact rotation capacity was observed in the specimens previously subjected to a larger impact energy.

The test results were compared with predictions based on different numerical models, including a 2DOF model and non-linear finite element analysis in LS-DYNA with hexahedron and tetrahedron solid elements using concrete material model CDPM2. The 2DOF model and the hexahedron LS-DYNA model tended to overestimate the deflection of the beam, although the results were still reasonable. It was observed that the hexahedron LS-DYNA model was not able to properly describe inclined cracking; however, signs of inclined cracking could still be seen in the form of cracked regions. The tetrahedron LS-DYNA model, on the other hand, predicted rather accurately the maximum deflection and the cracking distribution on the beam surface; however, an overly stiff response and high sensitivity to input parameters was detected in this model.

In general, rather good correspondence was found between experimental results and the results from the numerical models, and the general behavior of the beams under impact loading was fairly well described by the numerical models.

Keywords: Plastic rotational capacity, reinforced concrete, simply supported beams, impact loading, static loading, CDPM2, Digital Image Correlation, DIC, two-degree-of-freedom, 2DOF, non-linear finite element analysis, FEA, LS-DYNA

Betongbalkar Utsatta för Fallviktsförsök och Påföljande Statisk Belastning
Strutkurrespons och Plastisk Rotationskapacitet från Experimentell Data och Analyser inom Finita Elementmetoden
Examensarbete i Structural Engineering and Building Technology
FABIO LOZANO MENDOZA
JOSEF MAKDESI APHRAM
Arkitektur och samhällsbyggnadsteknik
Avdelningen för Konstruktionsteknik
Betongbyggnad
Chalmers Tekniska Högskola

SAMMANFATTNING

Responsen har undersökts av fritt upplagda och armerade betongbalkar utsatta för fallviktsförsök utifrån olika fallhöjder. Statiska tester har även utförts på dessa balkar i syfte att undersöka hur stöten inverkar på strukturresponsen. Dessutom utfördes det statiska tester på balkar som var oskadade i syfte att jämföra skillnader i responsen. Experimenten var inspelade med höghastighets- och normalhastighetskameror och analyserade med digital image correlation (DIC).

Rotationskapaciteten och sprickfördelningen av skadade balkar utifrån experimentella försök visade att prover utsatta för en svag stöt hade en liknande statisk strukturrespons som oskadade balkar. Däremot visade det sig att prover utsatta för en stark stöt har en högre plastisk rotationskapacitet efter att stöten har skett.

Vidare utfördes jämförelser mellan testförsök och olika numeriska metoder, såsom 2DOF och finita elementmetodsberäkningar gjorda i LS-DYNA med kubiska- och tetraederelement baserade på materialmodell CDPM2. 2DOF och LS-DYNA beräkningar baserade på kubiska element visade sig överskatta den maximala nedböjningen. Dessutom observerades det att LS-DYNA vid användande av kubiska element, var oförmögen att beskriva lutningen av sprickbildningen iakttagna från experiment. Sprickbildningen beskrevs istället som spruckna regioner. LS-DYNA modellen bestående av tetraederelement kunde däremot i hög grad skildra sprickbildning och maximal nedböjning, dock konstaterades det att den hade en styvare respons än experimentella resultat och även en hög känslighet för vald indata.

I allmänhet kunde det dock konstateras att det fanns en hög korrelationsgrad mellan experimentella resultat och numeriska metoder och att förutsägelser av fallviktsförsök enligt numeriska beräkningsmetoder var acceptabla.

Nyckelord: Plastisk rotationskapacitiet, armerad betong, fritt upplagda balkar, stötbelastning, statisk belastning, CDPM2, Digital Image Correlation, DIC, tvåfrihetsgradssystem, 2DOF, olinjär finita elementmetodsanalys, FEM, LS-DYNA

Contents

PREFACE

The behavior of simply supported reinforced concrete beams subjected to an impact load and subsequent static loading, with emphasis on plastic rotational capacity, has been investigated in this Master's thesis. Several experiments were performed under different loading conditions; furthermore, the experiments were also replicated using non-linear finite element analysis and simpler numerical methods.

The project was developed from January to June 2017 and experiments were carried out in February 2017. The thesis is part of an ongoing research project financed by the Swedish Civil Contingencies Agency (MSB), and is a collaboration between the Structural Engineering Division at Chalmers University of Technology, Norconsult, and RISE (The Swedish Research Institute). The project was supervised by Morgan Johansson and examined by Joosef Leppänen.

We would like to express our deepest gratitude to Morgan Johansson for his insightful supervision and unrelenting guidance throughout the course of the thesis. We would also like to thank Joosef Leppänen for his support and encouragement throughout the entire project. Additionally, we thank Mathias Flansbjer for his help regarding the recording of the experiments and processing of the information through DIC, and Sebastian Almfeldt for his supervision during the experiments.

Lastly, we would like to acknowledge our fruitful and wonderful time working together throughout the years spent in the Master's programme Structural Engineering and Building Technology; our efforts have culminated into a Master's thesis which we are very proud of.

NOMENCLATURE

Abbreviations

2DOF	Two degrees of freedom
SDOF	Single degree of freedom
DIC	Digital image correlation
DIF	Dynamic increase factor
EC	Eurocode
EFC	Softening parameter of compressive damage, ε_{fc}, in CDPM2
FE	Finite element
FEA	Finite element analysis
FEM	Finite element model
IP	Integration points
QM	Hourglass control parameter in CDPM2
RC	Reinforced concrete

Roman upper case letters

A	Area
E	Modulus of elasticity
E_c	Compressive modulus of elasticity of concrete
E_{cm}	Compressive modulus of elasticity of concrete; mean value
E_k	Kinetic energy
E_s	Modulus of elasticity of reinforcing steel;
E_{sm}	Modulus of elasticity of reinforcing steel; mean value
E_t	Tangent modulus of reinforcing steel
F	External force
F_k	Characteristic pressure load
I	Impulse, moment of inertia
I_k	Characteristic impulse
L	Total length of beam member
M	Bending moment
R	Internal resistance, radius of curvature
R_m	Maximum internal resisting force
W	Work
W_e	External Work
W_i	Internal Work

Roman lower case letters

a	Acceleration, coordinate along beam main axis
b	Width of beam cross-section
c	Damping coefficient

d	Distance to center of bottom reinforcement layer; measured from top edge
d'	Distance to center of top reinforcement layer; measured from top edge
e	Eccentricity parameter
f_{bc}	Equibiaxial compressive strength of concrete
f_c	Compressive cylinder strength of concrete
f_{cm}	Compressive cylinder strength of concrete; mean value
f_{ct}	Tensile strength of concrete
$f_{ct,fl}$	Flexural tensile strength of concrete
$f_{ct,sp}$	Splitting tensile strength of concrete
$f_{0.2}$	0.2% proof stress of reinforcing steel
f_t	Tensile strength of reinforcing steel
f_{tk}	Tensile strength; characteristic value
f_y	Yield strength of reinforcing steel
f_{yd}	Yield strength of reinforcing steel; design value
f_{yk}	Yield strength of reinforcing steel; characteristic value
h	Height of beam cross section, drop-height
h_{BW}	Crack band width
k	Linear elastic stiffness
l	Distance along beam
l_0	Distance from zero moment section to point of maximum moment
l_{el}	Element size
l_p	Equivalent plastic hinge length
l_y	Length of yielding region
m	Mass
n_{el}	Number of elements
p	Momentum of a particle
t	Time
t_{max}	Time when maximum deflection occurs
u	Deflection or deformation
u_{el}	Elastic deflection or deformation
u_{pl}	Plastic deflection or deformation
$u_{fail,s}$	Deflection or deformation at which steel rupture occurs
u_{max}	Maximum deflection during dynamic response
u_s	System coordinate
v	Velocity
w	Crack width
w_f	Ultimate crack width
x	Distance to neutral axis from top edge

Greek letters

α_R	Stress block factor for average stress
β_R	Stress block factor for resultant location
Δt	Time increment

δ	Displacement
$\dot{\varepsilon}$	Rate of strain
ε_c	Concrete strain
ε_{cc}	Concrete strain; compression
ε_{cu}	Ultimate concrete strain; compression
ε_{fc}	Softening parameter of compressive damage in CDPM2
ε_s	Reinforcing steel strain
ε_{su}	Ultimate reinforcing steel strain
φ	Curvature
κ	Transformation factor
ν	Poisson's ratio
ω	Angular eigenfequency
ω_b	Balanced mechanical reinforcement ratio
ω_s	Mechanical ratio of tensile reinforcement
ω'_s	Mechanical ratio of compression reinforcement
ω_v	Mechanical ratio of shear reinforcement
ρ'_w	Ratio of the volume of confining reinforcement
σ	Stress
θ	Rotation
θ_{pl}	Plastic rotation
$\theta_{pl,x\%}$	Plastic rotation at a given load level
$\theta_{pl,imp}$	Plastic rotation due to impact

Index

0	Initial
1	Body 1, drop-weight
2	Body 2, beam
c	Concrete
cube	Cubic strength of concrete
d	Design
f	Field
I	State I
II	State II
imp	Impact
k	Characteristic
m	Mean value
s	Reinforcing steel
sup	Support
u	Ultimate
y	Yield
el	Elastic
pl	Plastic

1 Introduction

1.1 Background

A high resilience is demanded of structures where the risk of impulse loading has to be considered. Examples of impulse loading can be explosions or impact loads from collisions. Structures designed to withstand such loads are commonly built using reinforced concrete, and a large plastic deformation capacity provided by key structural elements is essential in order to absorb energy from such actions. An impulse-loaded structure may exhibit a response that differs much from that of the static case, and consequently can give rise to different failure modes. It is therefore important to have a thorough understanding of the behavior of impulse-loaded structures, and how their response can be accurately predicted.

This thesis project is intended to support the ongoing research in the field of impulse-loaded structures at the Structural Engineering Division at Chalmers University of Technology in collaboration with Norconsult and RISE. It also intends to build upon the knowledge and conclusions gathered in previous Master's thesis projects carried out at Chalmers, such as (Lovén and Svavarsdóttir, 2016).

1.2 Aim

The general aim of this project is to provide a better understanding of reinforced concrete structures subjected to impulse loading. During the thesis work, the impulse load is represented by a drop-weight impact, since such a scenario can easily be replicated in a laboratory. A strong focus is placed on plastic deformation capacity of impulse-loaded structures, and specifically the residual plastic capacity after the impact loading.

A series of tests is carried out in order to determine the plastic deformation capacity of concrete beams under different loading conditions. The accuracy of different methods described in the literature to predict the plastic deformation capacity is also studied.

Furthermore, the thesis work aims to predict the response of structures subjected to impact loading by means of non-linear finite element analysis (FEA) in the software package LS-DYNA, where suggestions from (Lovén and Svavarsdóttir, 2016) are considered in order to further improve the reliability of the FE simulations. The results from the finite element analyses are compared to observations from the drop-weight impact experiments, and the models are modified accordingly in order to more accurately describe the response of the structure.

A simplified model based on a two-degree-of-freedom system (2DOF) is also implemented. The objective is to study how effectively such a simplified tool could be used to predict the behavior of the test specimens. The model is formulated similarly as done in previous thesis works at Chalmers. Additionally, a brief investigation of the time-dependent mass participation is performed.

Moreover, parametric studies are carried out for the FE models in order to investigate the influence of different input data regarding modelling techniques, material properties, and loading conditions on the behavior of the beam, which may serve as a basis for future studies and analyses.

1.3 Method

Initially, a literature study was performed in order to deepen the knowledge regarding structural dynamics and the response of impulse-loaded structures. A significant part of the literature review was focused on plastic deformation capacity of concrete beams, as an appropriate understanding of the definition of plastic capacity was considered essential for the evaluation of the experimental results. Furthermore, a description of the influence of the properties of reinforcing steel and concrete on the rotational capacity was made.

A preliminary static test was carried out on an old test specimen, which was a simply-supported reinforced concrete beam with a free span of 1.0 m, which had been previously subjected to impact loading by a drop-weight. The old beam was tested under deformation-controlled static loading in order to assess the remaining plastic rotation capacity. Based on the residual capacity, suitable loading conditions – in terms of drop-height – were determined for further drop-weight impact tests applied to newly-cast concrete specimens with same geometry and similar properties as the old specimen. Additionally, the material properties of the newly-cast concrete and reinforcement bars were determined through a series of tests.

Different loading conditions were applied on the new specimens, namely: static loading only, dynamic loading with a high impact velocity, and dynamic loading with a low impact velocity. In a later stage, the beams tested under impact loading were subjected to a deformation-controlled static load so as to compare the residual plastic rotation capacity with the capacity of the beams loaded with static load only. During the experiments, a high-speed camera was used to capture the development and propagation of cracks and deformations. Based on the information collected, the strain field, deflection, and velocity of the beams (as well as the displacement and velocity of the drop-weight) could be calculated by using digital image correlation (DIC) with the aid of the software GOM Correlate. The observed plastic rotational capacity was compared to the capacity predicted by existing theoretical models.

A simplified 2DOF system was used in order to predict the dynamic response. The system of dynamic equations of motion was solved by using the Central Difference Method (CDM). Transformation factors to transform the beam and the drop-weight into a mass-spring system was also studied.

Furthermore, finite element models were created in LS-DYNA using 3D solid elements and material model CDPM2 to model the concrete material. Initially, continuous hexahedron elements and full interaction between reinforcement bars and surrounding concrete was considered. Subsequently, tetrahedron elements were adopted, as suggested by Lovén and Svavarsdóttir (2016), in an attempt to better describe inclined cracking. The results were compared with the 2DOF analyses and the experimental observations, as well as with the results obtained by Lovén and Svavarsdóttir (2016). Additionally, different modelling approaches were investigated, such as scaling of the fictitious hourglass forces applied on hexahedron elements, and implementing different element types to model the reinforcement bars.

After the LS-DYNA models had been properly calibrated, a study of the influence of various parameters on the behavior of the beam was carried out. Such parameters include, among others, impact velocity, different drop-heights, and position of the point of impact. The results contributed to formulate suggestions for possible future drop-weight experiments.

1.4 Limitations

This project only treated simply supported normal strength concrete beams with longitudinal reinforcement. The beams were not provided with transversal reinforcement as bending failure was initially expected. The beams were subjected to concentrated impact load at midspan. The high-speed camera used to record the experiments features a frame-rate of 5000 fps.

Two different groups of specimens were cast out of two different concrete batches, albeit with the same proportions. The properties of concrete regarding tensile and compressive strength were determined for both batches, whereas a wedge-splitting test was performed only for one of the batches in order to estimate the fracture energy.

Finite element models were created in LS-DYNA using 3D continuum solid elements. The chosen material model was CDPM2, developed by Peter Grassl in collaboration with Chalmers University of Technology, as described in (Grassl, Xenos, *et al.*, 2013). The reinforcement bars were modelled as fully embedded in the concrete solids.

The damping coefficient was assumed to be zero for both the beam and the drop-weight in the 2DOF system and in the FE models, as it was considered to have a negligible effect for short duration loads. Furthermore, effects due to strain-rate were not considered either in the 2DOF system or in the FEA in LS-DYNA.

1.5 Thesis Outline

This thesis consists of three interconnected parts. The first part, which comprises Chapters 2- 6, begins with a description of relevant knowledge and theories. The second part consists of Chapters 7 - 9, and provides with a description of the experiments performed and conclusions gathered from the experimental results. The last part consists of Chapters 10 - 11, where basic theory related to FE modelling is initially described; subsequently, the results from FE analyses are presented and compared with experimental results in order to investigate the accuracy of the models and draw conclusions. Finally, a brief discussion regarding all the content of the thesis is presented in the last chapter.

Chapter 2: Basic general concepts related to the structural response of materials are described in this chapter. Furthermore, material properties of reinforcing steel and concrete, as well as their behavior under loading, are detailed.

Chapter 3: Fundamentals of dynamics theory, essential to the understanding of impulse loaded structures, are presented here.

Chapter 4: Here, formulation of discrete models such as SDOF and 2DOF are described. Furthermore, the procedure for the transformation of reinforced concrete beams subjected to impact loading into a equivalent 2DOF model is also detailed.

Chapter 5: A literature study is conducted in this chapter which covers basic theory of plastic rotational capacity as well as methods to predict plastic rotational capacity of reinforced concrete beams.

Chapter 6: Various factors which influence rotational capacity of concrete beams are covered here. The residual capacity of concrete beams after impulse loading is also briefly discussed.

Chapter 7: The experimental determination of the properties of the materials used, as well as the procedure used for the various experiments, are detailed here.

Chapter 8: Predictions of experimental outcome in terms of load capacity, dynamic response, and plastic rotational capacity of the investigated beams are presented in this chapter.

Chapter 9: Presentation and comparisons of experimental results. Furthermore, validation of preliminary predictions with respect to experimental results are made here.

Chapter 10: This chapter describes the basic concepts and theory pertinent to FE modelling. Moreover, the modelling procedure adopted for subsequent FE analyses is also presented here.

Chapter 11: The results of the FE analyses are presented and compared to experimental results in order to verify their validity. Furthermore, sensitivity studies are also performed here to discern how various parameters influence the outcome of FE results. Lastly, parametric studies in terms of varying loading conditions or material properties are made in order to gain further understanding of impact loaded structures.

Chapter 12: A general discussion regarding results gathered throughout the thesis is presented here.

Chapter 13: Concluding remarks and possibilities for future topics of study are presented here.

2 Materials and Structural Response

2.1 Introduction

The beam specimens tested during the development of this project were produced out of concrete reinforced with steel bars. Basic knowledge regarding the properties of these materials and their behavior under loading is essential to facilitate the understanding of the theoretical discussions treated in subsequent chapters. Although previous knowledge of the fundamentals of reinforced concrete is expected, a general description is presented in this chapter.

Initially, the typical response functions usually assumed in design and analysis of structures are studied. Thereafter, the properties of reinforcing steel and concrete, as isolated materials, are briefly described. Finally, the response of reinforced concrete structures is treated.

2.2 Structural Response

2.2.1 Overview

When a load is applied to a given element, it causes an internal force in the structure. Such an internal force tends to restore the element to its undeformed position, provided that the material is still in the elastic range. The resistance functions for actual structural elements might assume a variety of forms, depending on material properties, boundary conditions, and type of loading. In order to simplify analysis, these resistance functions are commonly idealized. Three basic responses are often used in common practice, namely: linear elastic response, plastic response, and elasto-plastic response.

2.2.2 Linear elastic response

In the elastic range, the resistance, R, and the deformation, u, are related by

$$R(u) = k \cdot u \tag{2.1}$$

where k correspond to the stiffness of the structure [N/m]. Figure 2.1 illustrates the reaction force as a function of deformation for a linear elastic material.

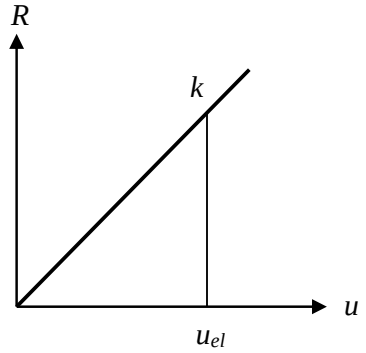

Figure 2.1 Relationship between internal resistance and deformation for a linear elastic material.

2.2.3 Plastic response

An ideally plastic material will not exhibit any deformation if the load applied is less than the material capacity, as shown in Figure 2.2. On the other hand, if the external load reaches the maximum internal resistance, R_m, the material will deform indefinitely until the load is removed. Moreover, the resistance force cannot exceed R_m of the material.

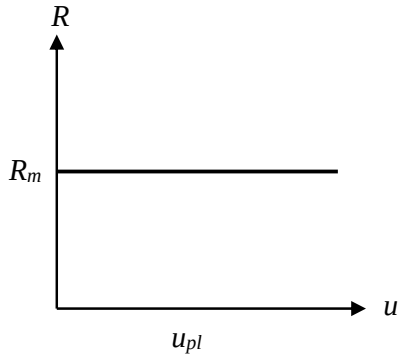

Figure 2.2 Relationship between internal resistance and deformation for a perfectly plastic material.

The relationship between R and u is given by

$$R(u) = \begin{cases} F & \text{if} \quad u = 0 \\ R_m & \text{if} \quad u > 0 \end{cases} \tag{2.2}$$

where F is an external force with a magnitude less than R_m.

2.2.4 Elasto-plastic response

As shown in Figure 2.3, the resistance of an elasto-plastic material can be described with a bi-linear function in which the material exhibits a linear behavior until the limit for elastic response, u_{el}, is reached. From that point on, the material undergoes plastic deformation, u_{pl}, and the resistance force cannot exceed the capacity of the material.

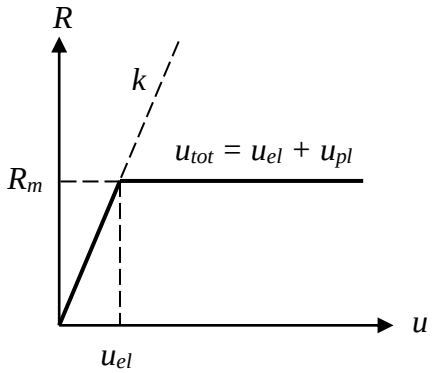

Figure 2.3 Relationship between internal resistance and deformation for an elasto-plastic material.

A elasto-plastic response can be described mathematically by

$$R(u) = \begin{cases} k \cdot u & \text{if} \quad u \leq u_{el} \\ R_m & \text{if} \quad u > u_{el} \end{cases} \tag{2.3}$$

where the elastic limit can be determined as

$$u_{el} = \frac{R_m}{k} \tag{2.4}$$

2.3 Reinforcing Steel

2.3.1 Introduction

A brief description of the properties of reinforcing steel is presented in this section. The information discussed in this section is mainly based on (Engström, 2001).

The reinforcing steel commonly used in modern concrete structures is classified according to the following parameters:

- grade
- ductility class
- size
- surface properties
- weldability

The strength and deformation properties are commonly defined from the parameters in Table 2.1.

Table 2.1 Common reinforcing steel parameters.

Parameter	Description
f_{yk}	Characteristic yield strength
f_{tk}	Characteristic tensile strength
$(f_t/f_y)_k$	Characteristic ratio of tensile strength to yield strength
ε_{suk}	Characteristic ultimate strain
E_{sm}	Mean value of modulus of elasticity

The ductility, which is the ability of the steel to undergo large deformation under tensile force, is of special interest with regard to plastic deformation capacity. The ductility class is defined according to the ultimate strain and the ratio of tensile strength to yield strength. According to the description provided in Annex C in Eurocode 2 (CEN, 2004), reinforcement bars can be classified into three different categories, as summarized in Table 2.2.

Table 2.2 Classification of steel regarding ductility properties according to Eurocode 2 (CEN, 2004).

Property	Class		
	A	B	C
Characteristic yield strength, f_{yk} or $f_{0.2k}$ [MPa]	400 to 600		
Minimum value of $(f_t/f_y)_k$	≥ 1.05	≥ 1.08	≥ 1.15 & < 1.35
Characteristic strain at maximum force, ε_{suk} [%]	≥ 2.5	≥ 5.0	≥ 7.5

2.3.2 Hot-rolled and cold-worked steel

Depending on the production method, reinforcing steel is commonly classified into two categories: *hot-rolled* steel and *cold-worked* steel. The difference can easily be recognized by the shape of the stress-strain diagram for each type, as illustrated in Figure 2.4. Hot-rolled steel usually exhibits a evident yield stress, followed by a plastic plateau, and subsequently by an increase in stress due to strain hardening effect. The ratio of tensile strength to yield strength and the ultimate strain are usually high. The characteristic yield stress f_{yk} corresponds to the lower 5%-fractile of the upper yield stress.

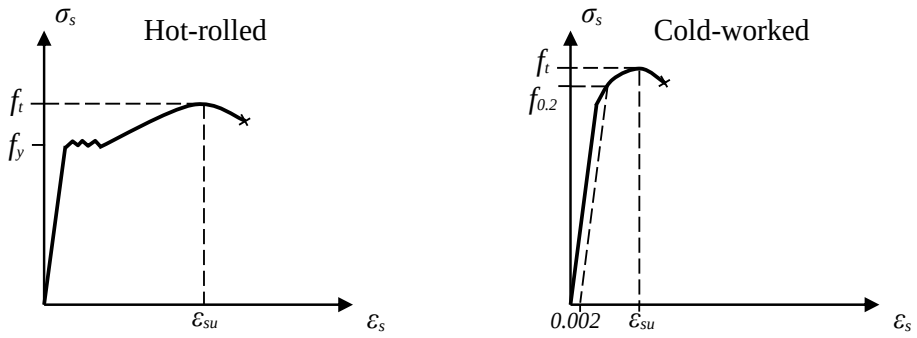

Figure 2.4 Stress-strain diagram of hot-rolled and cold-worked steel, modified from (CEN, 2004).

On the other hand, it is not possible to clearly identify the yield stress for cold-worked steel from the stress-strain diagram. Instead, a value of stress, called *proof stress* and corresponding to the stress that produces a remaining strain of 0.2 %, is normally used in design. The characteristic proof stress $f_{0.2k}$ corresponds to the lower 5 %-fractile of the proof stress. The strain hardening and plastic deformation capacity of cold-worked steel are relatively small, and no plastic plateau can be distinguished in the stress-strain diagram.

2.4 Concrete

2.4.1 Introduction

Concrete exhibits a different stress-strain relationship when subjected to uniaxial tension compared to uniaxial compression loading; furthermore, the tensile strength of concrete, f_{ct}, is significantly lower than its compressive counterpart, f_c, see Figure 2.5. Moreover, the ultimate concrete strain, ε_{cu}, after reaching maximum compressive strength is much larger than the ultimate strain achieved for tensile stress. In other words, concrete shows a more brittle failure when subjected to tensile stresses.

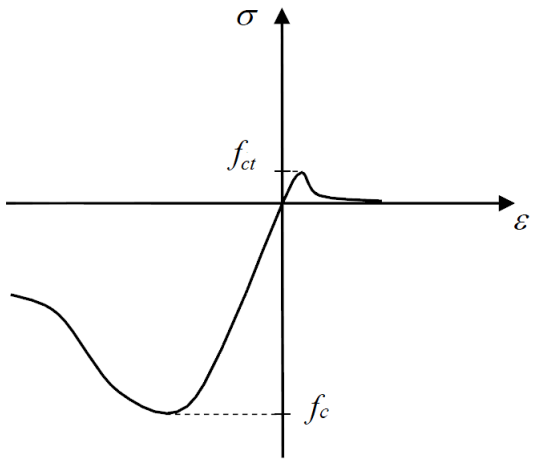

Figure 2.5 Schematic stress-strain relationship of concrete under uniaxial compression and tension (Lovén and Svavarsdóttir, 2016).

2.4.2 Properties in compression

Since concrete is used mostly in compression, its response and stress-strain relationship under compressive loading is of major interest. As a matter of fact, the most commonly tested parameter of concrete is its compressive strength, from which a general overview of various concrete properties can be estimated (Burström, 2001). Compressive strength at 28 days is generally used to characterize the concrete class, and therefore, the determination of the strength of concrete is usually performed 28 days after casting and curing under proper conditions. Concrete strength gradually grows with time, and the 28-day strength corresponds to roughly 80 % of the strength after a year, from which little increase is expected (Martin and Purkiss, 2006).

The stress-strain relationship of concrete subjected to compression loading is non-linear. However, for relatively low stresses, the response is assumed to be linear and is defined by the modulus of elasticity, E_c. A larger compressive strength results in a larger value of E_c. As shown in Figure 2.6, the compressive strain at peak load increases with increased concrete class; moreover, ductile response after reaching peak strength decreases with increased compressive strength.

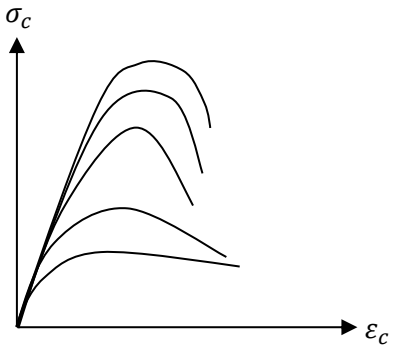

Figure 2.6 Schematic overview of how concrete strain at peak load varies for different compressive strengths, modified from (Engström, 2001).

Eurocode 2 (CEN, 2004) proposes different stress-strain relationships for concrete under uniaxial compression. For non-linear structural analysis, the relation illustrated in Figure 2.7 is recommended.

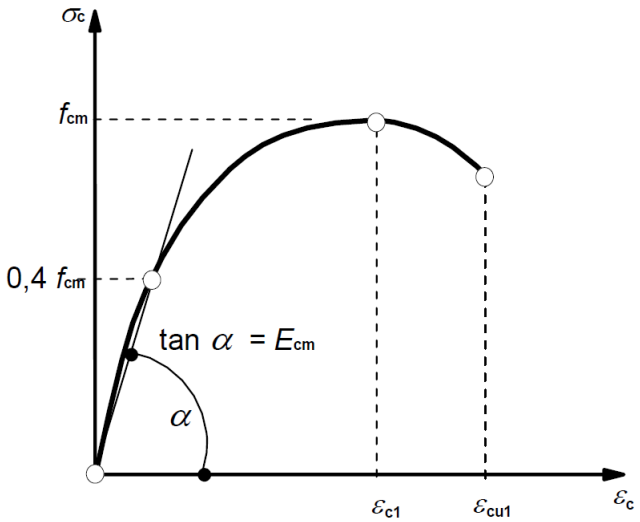

Figure 2.7 Schematic stress-strain relationship for non-linear structural analysis of concrete. The parameter ε_{c1} is the strain at peak stress, ε_{cu1} corresponds to the ultimate compressive strain, f_{cm} is the mean value of concrete compressive strength, and E_{cm} is the mean value of the elasticity modulus (CEN, 2004).

The mean modulus of elasticity, E_{cm}, in Figure 2.7 is determined by the secant modulus between the origin and $\sigma_c = 0.4 f_{cm}$. However, it can also be calculated approximately based on the mean compressive strength determined from tests as

$$E_{cm} = 22 \left(\frac{f_{cm}}{10} \right)^{0.3} \quad \text{[GPa]} \tag{2.5}$$

where f_{cm} is given in [MPa].

Simplified compressive stress-strain curves can also be used for design and verification of capacity. The stress-strain relationship can be represented by a parabolic curve until peak compressive strength has been reached, followed by a constant value of stress until ultimate concrete strain. Additionally, an even more simplified, albeit more conservative, bi-linear model can be adopted as shown in Figure 2.8.

The values of ultimate strain, $\varepsilon_{cu(1-3)}$, for the relationships in Figures (2.7) and (2.8) can be assumed equal to 3.5 ‰ for concrete classes from C12/15 to C50/60 (CEN, 2004). Values of peak strain, $\varepsilon_{c(1-3)}$, differ for each model and has to be chosen depending on concrete class and the relationship adopted.

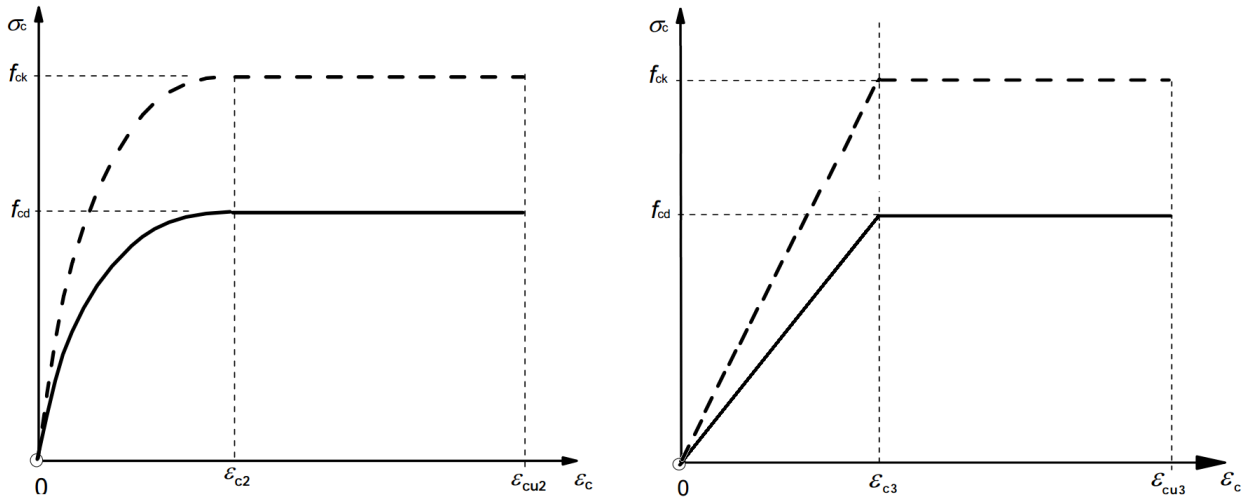

Figure 2.8 Parabola-rectangle (left) and bi-linear (right) stress-strain relationships that may be used in design and verification of load-carrying capacity (CEN, 2004).

2.4.3 Determination of concrete strength

In order to determine the characteristic strength of concrete, different tests can be performed either on cylinder or cubic specimens. The compressive stress can be estimated by following the guidelines in (CEN, 2009a). Figure 2.9a shows a schematic representation of the test setup with cube specimens. Due to restraining effects along the boundaries of cubic testing, a tri-axial stress state is developed, which produces higher values of strength in cubic specimens when compared to slender cylindrical specimens, (Domone and Illston, 2010).

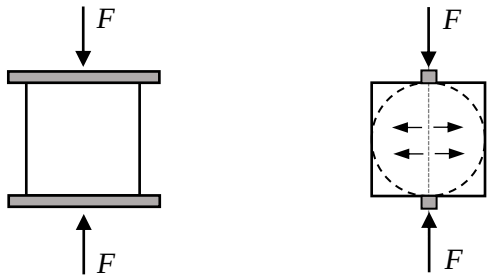

(a) Compressive test. *(b) Tensile test by splitting.*

Figure 2.9 Concrete strength tests on cube specimens.

The mean compressive cylinder strength, f_{cm}, can then be determined from the the mean compressive cube strength, $f_{cm,cube}$, as

$$f_{cm} = 0.8 f_{cm,cube} \tag{2.6}$$

Regarding the tensile strength, it is more difficult to adopt a uniaxial tensile stress state for concrete because of its brittle behavior (Domone and Illston, 2010). However, splitting tests can be adopted as an

indirect test of the tensile strength of concrete (CEN, 2009b), as depicted in Figure 2.9b. An approximate value of the axial tensile strength, f_{ct}, can be calculated from the splitting tensile strength, $f_{ct,sp}$, as

$$f_{ct} = 0.9 f_{ct,sp} \tag{2.7}$$

It is also possible to theoretically determine the tensile strength based on the characteristic compressive strength, as given by

$$f_{ct} = 0.30 f_{ck}^{2/3} \quad \text{for concrete class} \quad \leq \text{C50/60} \tag{2.8}$$

Finally, the relation between the flexural tensile strength, $f_{ct,fl}$, and the axial tensile strength can be estimated as

$$\begin{aligned} &f_{ct,fl} = k \cdot f_{ctm} \\ &\text{where} \quad k = 0.6 + \frac{0.4}{h^{0.25}} \end{aligned} \tag{2.9}$$

2.5 Reinforced Concrete

2.5.1 Definition

Reinforced concrete is a composite material which combines the high compressive strength of concrete together with the high tensile strength and considerably higher ductility of steel. The reinforcing steel, usually in the form of round steel rods with a coarse surface pattern, is embedded in the concrete core in locations where large tensile stresses are expected. This combination makes it possible to use reinforced concrete in a wide spectrum of structures.

A simple case of a reinforced concrete member is a simply supported concrete beam. The response of such beam subjected to a point load goes through different stages which depend to great extent on the properties of the materials.

2.5.2 Structural response of reinforced concrete beams

Consider a simply supported reinforced concrete beam subjected to a concentrated load at midspan. As the load increases, the response of the beam reaches different thresholds until attaining maximum capacity. A typical load-deformation curve for such a case is presented in Figure 2.10.

In *state I*, the section is uncracked and both steel and concrete exhibit a linear-elastic response. When cracking initiates, the response shows a drastic change since the stiffness of cracked regions is smaller than that of uncracked ones. The stiffness in *state II* governs the behavior of cracked regions, and the reinforcement steel has a large influence on the structural response. The theoretical model used for calculations in state II assumes that the concrete and the steel both behave linearly.

In a fully cracked region, the uncracked sections in between flexural cracks contribute to the average stiffness of the cracked region; as a consequence, the average steel strain in such regions is smaller than the steel strain at the flexural cracks. This phenomenon, known as *tension stiffening*, is explained due to the transference of tensile stresses from the reinforcement bars to the surrounding concrete by bond

stresses at the interface (Engström, 2015). This implies that calculating the stiffness of a cracked member using a model in state II would result in underestimation of the real stiffness of the member. It should be noticed, however, that the effects of tension stiffening decrease as the acting load continues to grow with respect to the cracking load.

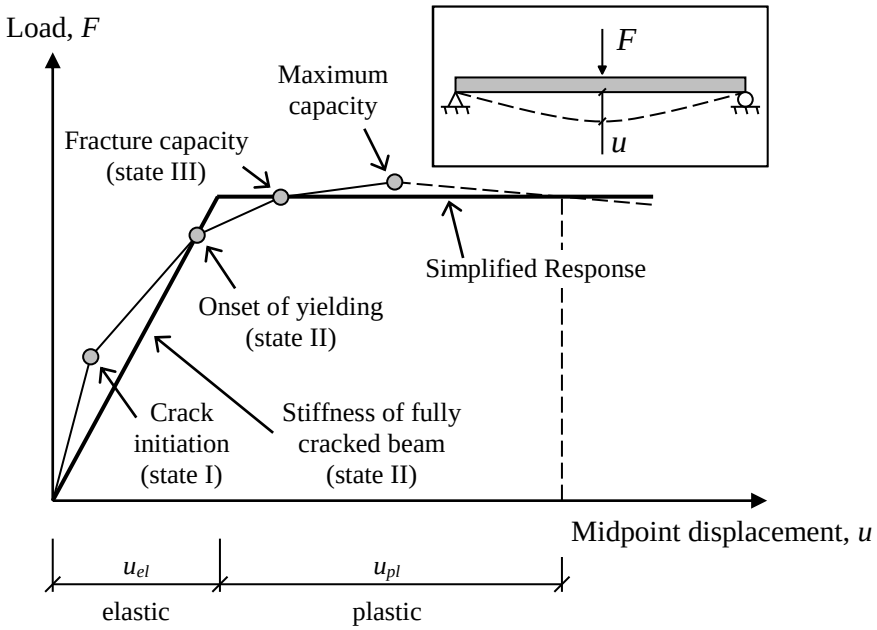

Figure 2.10 Response of a simply supported concrete beam subjected to a concentrated load at midspan, modified from (Johansson and Laine, 2012).

After yielding in the reinforcement bars at a critical section has initiated, the response of the element should be analyzed in *state III*, so that non-linear properties of concrete and steel (or both) can be considered. The external load can still be increased past the onset of yielding until the *ultimate limit state* (ULS) is reached.

However, the structural response of the beam can be simplified to a bi-linear elasto-plastic relationship, as shown in Figure 2.10. The beam is assumed to be fully cracked from the start of loading, and the response is dependent on the stiffness in state II until the load capacity is reached. From that point on, the beam exhibits an ideally plastic deformation.

3 Fundamentals of Dynamics

3.1 Basic Dynamics Theory

3.1.1 Work and kinetic energy

One method to transfer energy into a system is to exert a certain amount of work on it. The work, W, exerted on a particle when an external constant force, F, causes a displacement of magnitude δ along a straight line is defined according to the expression below:

$$W = F \cdot \delta \cdot cos(\theta) \tag{3.1}$$

The angle θ is the angle between the force and the direction of the displacement. When the external force varies along the $x-$axis, the work can be determined as

$$W = \int_0^{\delta} F(x)dx \tag{3.2}$$

The kinetic energy of a particle of mass m moving at a velocity v is calculated by

$$E_k = \frac{1}{2}mv^2 \tag{3.3}$$

The external work done by the external force can also be defined as the change in kinetic energy

$$W_e = E_{k1} - E_{k0} = \frac{1}{2}mv_1^2 - \frac{1}{2}mv_0^2 \tag{3.4}$$

An external work on a system produces an internal reaction, which is denoted *internal work*. In line with the energy conservation law, the internal work needs to be equivalent in magnitude to the external work to reach static equilibrium, which can be expressed as

$$W_i = W_e \tag{3.5}$$

3.1.2 Momentum and impulse

The linear momentum of a particle of mass m, which travels with a velocity v, can be defined as the product of the mass and the velocity as

$$p = m \cdot v \tag{3.6}$$

The momentum of a particle changes if an external force, F, which may vary with time, is applied on the particle; that is,

$$\Delta p = m \cdot v_1 - m \cdot v_0 = \int_{t_0}^{t_1} F(t)dt \tag{3.7}$$

The expression on the right-hand side in Equation (3.7) is called *Impulse*, and can be expressed by

$$I = \Delta p = \int_{t_0}^{t_1} F(t)dt \tag{3.8}$$

The impulse is therefore described as the change in momentum. If the body is originally at rest before the impulse loading (that is, $v_0 = 0$), the impulse can be defined as

$$I = mv \tag{3.9}$$

By combining Equation (3.3) together with Equation (3.9), an expression for kinetic energy in terms of impulse can be found as

$$E_k = \frac{I^2}{2m} \tag{3.10}$$

Two extreme cases of impulse loading are presented in Figure 3.1. A *characteristic impulse*, I_k, is defined by a force of infinite magnitude acting during an infinitesimal time, as depicted in Figure 3.1a. The opposite end of the spectrum corresponds to the *characteristic pressure load*, caused by a load F_k acting for an infinite duration, as illustrated in Figure 3.1b.

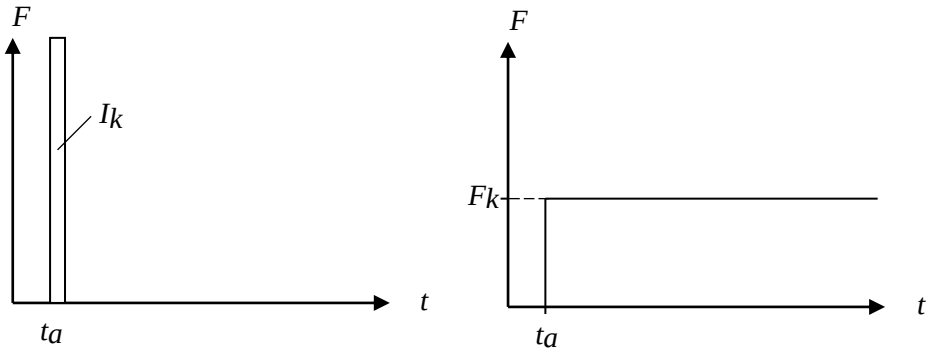

(a) Characteristic impulse load. *(b) Characteristic pressure load.*

Figure 3.1 Extreme cases of impulse loading.

In general, a given impulse exerted on a system is defined by a formulation placed between a characteristic impulse load and a characteristic pressure load. The duration of load application, be it relatively long or short, is heavily dependent on the properties of the dynamically loaded structure. For the remainder of the thesis work, the response of a structural system subjected to a characteristic impulse load, I_k, is adopted, since the dynamic loading by a drop-weight impact is assumed to act within a relatively short duration.

3.1.3 Impact theory

In order to describe an impact event, a classical collision model can be used. During a collision, two bodies which have come close to each other, interact by means of a force. This force may vary in time

and have a complex nature; however, it is internal. Therefore, the two bodies form an isolated system and the momentum of the system must be preserved.

The kinetic energy, on the other hand, may or may not be conserved depending on the nature of the collision. Two different scenarios are commonly found in literature; for the first case, the collision is considered *elastic*, whereas the latter represents a *plastic* collision.

Consider the system in Figure 3.2. The right-moving body with mass m_1 has an initial velocity $v_{m1} = v_0$, while the body of mass m_2 is at rest, that is, $v_{m2} = 0$.

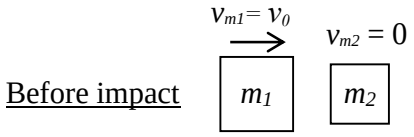

Figure 3.2 Two bodies before impact.

The kinetic energy and momentum for the first body before impact occurs can be calculated by using Equations (3.3) and (3.6), respectively, as

$$E_{k,0} = \frac{m_1 v_0^2}{2} \tag{3.11}$$

$$p_0 = m_1 v_0 \tag{3.12}$$

If the collision is perfectly elastic, the bodies will have two different velocities after impact. However, if the collision is perfectly plastic, the two bodies will move together at the same velocity, see Figure 3.3.

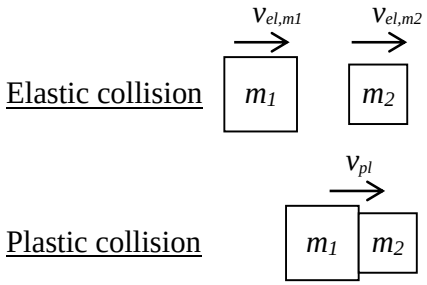

Figure 3.3 Representation of elastic and plastic collision.

The final velocities after an ideally elastic collision can be determined as

$$v_{el,m1} = \frac{m_1 - m_2}{m_1 + m_2} v_0 \tag{3.13}$$

$$v_{el,m2} = \frac{2m_1}{m_1 + m_2} v_0 \tag{3.14}$$

The resultant kinetic energy for both bodies after an elastic collision can be computed by means of Equation (3.15) and Equation (3.16). For this case, both the total kinetic energy and the total momentum of the system have the same magnitude before and after collision.

$$E_{k,m1} = \frac{m_1 v_{el,m1}^2}{2} = \frac{m_1}{2}\left[\frac{m_1 - m_2}{m_1 + m_2}\right]^2 v_0^2 = \left[\frac{m_1 - m_2}{m_1 + m_2}\right]^2 E_{k,0} \tag{3.15}$$

$$E_{k,m2} = \frac{m_2 v_{el,m2}^2}{2} = \frac{m_2}{2}\left[\frac{2m_1}{m_1 + m_2}\right]^2 v_0^2 = \frac{4m_1 m_2}{(m_1 + m_2)^2} E_{k,0} \tag{3.16}$$

During a plastic collision, the total kinetic energy of the system does not remain the same before and after collision. After colliding head-on, the two bodies move together with a velocity v_{pl}, which can be calculated as

$$v_{pl} = \frac{m_1}{m_1 + m_2} v_0 \tag{3.17}$$

Therefore, the resultant total kinetic energy after impact is given by the expression below

$$E_{k,pl,tot} = \frac{(m_1 + m_2) v_{pl}^2}{2} = \frac{m_1 + m_2}{2}\left[\frac{m_1}{m_1 + m_2}\right]^2 v_0^2 = \frac{m_1}{m_1 + m_2} E_{k,0} \tag{3.18}$$

3.2 Impulse Loading and Energy

3.2.1 General description

A structure subjected to external work due to an impulse load exhibits an internal response which results in an internal work, see Figure 3.4. Energy equilibrium, $W_i = W_e$, determines the total deformation of the structure due to impulse loading.

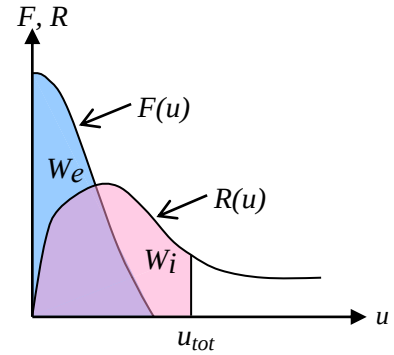

Figure 3.4 Schematic representation of energy equilibrium between external work, W_e, and internal work, W_i, for a given structure.

3.2.2 External energy

Based on the concept of a characteristic impulse load, the external work exerted on a dynamically loaded structure can now be expressed as

$$W_e = E_k = \frac{I_k^2}{2m} \tag{3.19}$$

3.2.3 Internal energy based on linear elastic response

The linear elastic response of a structure was previously defined in Section 2.2.2. The relationship between internal force and deformation is shown again below:

$$R(u_{el}) = k \cdot u_{el} \tag{3.20}$$

where u_{el} is the elastic deformation. Additionally, Figure 3.5 shows schematically the internal work in a structure that deforms with a linear elastic response when subjected to an external work.

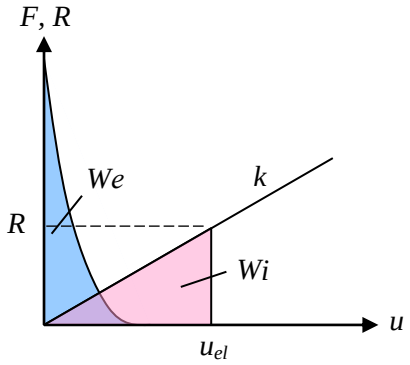

Figure 3.5 Energy equilibrium between external work, W_e, and internal work, W_i, for a system with elastic response.

The internal work of a structure which exhibits a linear elastic response can then be defined as

$$W_i = \frac{R(u) \cdot u_{el}}{2} = \frac{k \cdot u_{el}^2}{2} \tag{3.21}$$

By combining Equations (3.5), (3.19), and (3.21), the following expression to determine the elastic deformation is derived:

$$u_{el} = \frac{I_k}{m\omega} \tag{3.22}$$

where ω corresponds to the angular eigenfrequency of the system, and can be calculated as

$$\omega = \sqrt{k/m} \tag{3.23}$$

3.2.4 Internal energy based on plastic response

A structure which exhibits an ideally plastic response does not deform unless the force exerted on it exceeds its internal resistance. Once this condition is met, the structure starts to deform with a constant internal resistance, as previously explained in Section 2.2.3. Therefore,

$$W_i = R(u_{pl}) \cdot u_{pl} = R_m \cdot u_{pl} \tag{3.24}$$

where u_{pl} is the plastic deformation which the structure undergoes due to impulse loading.

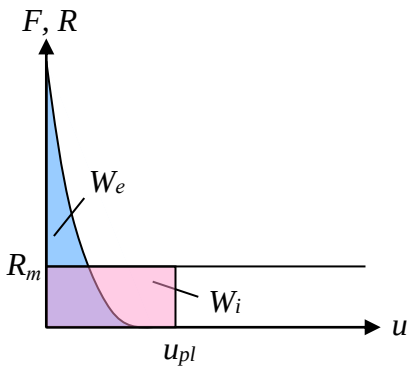

Figure 3.6 Energy equilibrium between external work, W_e, and internal work, W_i, for a system with ideal plastic response.

Combining Equations (3.5), (3.19) and (3.24) the following expression is obtained:

$$u_{pl} = \frac{I_k^2}{2mR_m} \tag{3.25}$$

The internal work of a structure which deforms with an ideally plastic response when subjected to external work is shown in Figure 3.6.

3.2.5 Internal energy based on elasto-plastic response

The internal work generated in a structure with an elasto-plastic response by an external work is shown schematically in Figure 3.7.

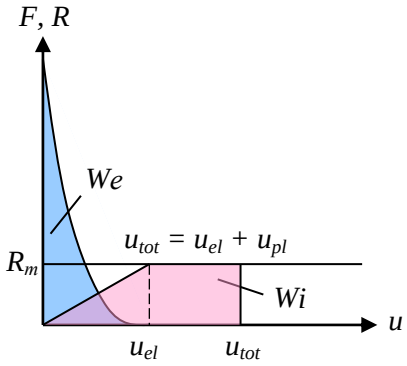

Figure 3.7 Energy equilibrium between external work, W_e, and internal work, W_i, for a system with elasto-plastic response.

The total internal work produced in the structure is given by

$$W_i = \frac{R_m}{2}(u_{el} + 2u_{pl}) \tag{3.26}$$

The parameter u_{el} corresponds to the limit for the elastic response of the structure and it is expressed as

$$u_{el} = \frac{R_m}{k} \tag{3.27}$$

Based on Equations (3.5), (3.19) and (3.26), the plastic part of the elasto-plastic deformation can be defined as

$$u_{pl} = \frac{I_k^2}{2mR_m} - \frac{u_{el}}{2} \tag{3.28}$$

3.3 Strain Rate Effect

The properties of concrete and reinforcing steel are dependent on the rate of strain, $\dot{\varepsilon}$, to which they are subjected. Therefore, the response of a reinforced concrete member may differ if the rate of strain varies drastically compared to a static load case. See Figure 3.8 for various strain rates due to different loading conditions.

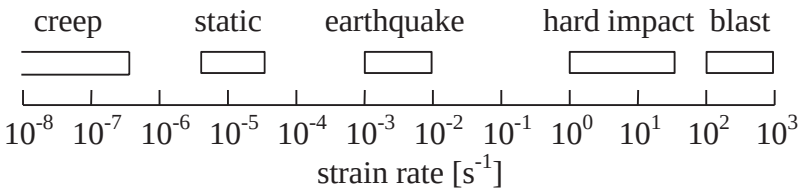

Figure 3.8 Intervals of strain rates for given loading scenarios (Johansson, 2000).

In general, the structural response in terms of strength and modulus of elasticity is amplified with increasing rate of strain. This has been documented to occur for both reinforcing steel and concrete; an example of such a phenomena is presented in Figure 3.9. The relative increase of a parameter with respect to its static counterpart is commonly referred to as the dynamic increase factor, *DIF*, and can be expressed as

$$F_{dyn} = F_{static} \cdot DIF \tag{3.29}$$

This topic has been treated to a greater extent in publications such as (Johansson, 2000).

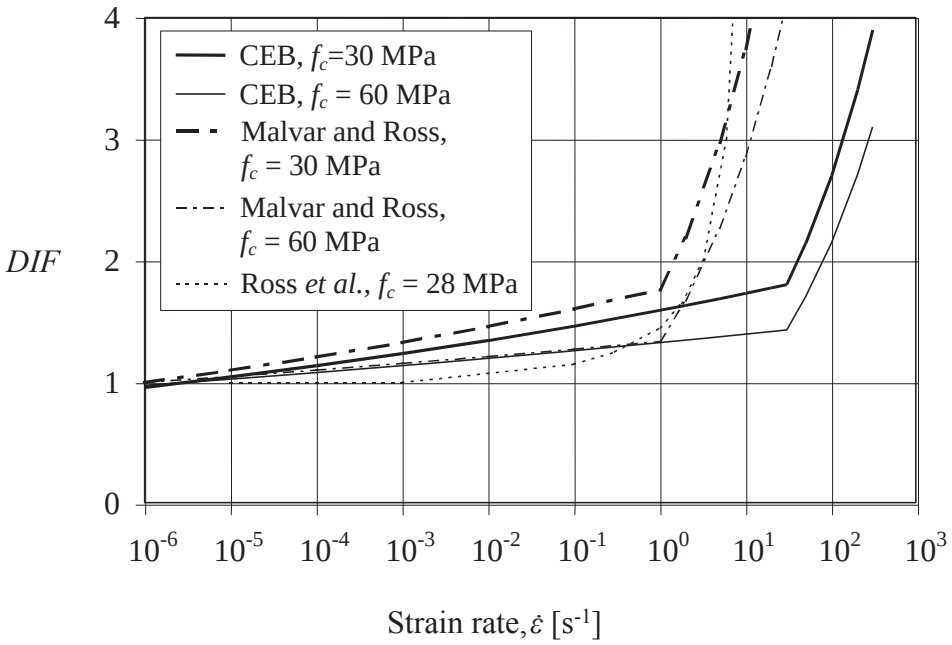

Figure 3.9 Strain rate and its influence on compressive strength of concrete, modified from (Johansson, 2000).

4 Discrete Model for Dynamic Analysis

4.1 Introduction

This chapter presents a simplified model to predict the behavior of a beam subjected to an impact caused by a falling drop-weight. The model consists of a two-degree-of-freedom (2DOF) spring-mass system, whereby the beam is simplified into a rigid body with an equivalent lumped mass and a given internal resistance. Likewise, the drop-weight is represented as a rigid body and the contact between the beam and the drop-weight is modelled as a spring element with certain stiffness properties.

Studying the beam and the drop-weight as a 2DOF system implies that only the fundamental eigenfrequency of both elements is considered, although there exists an infinite number of eigenfrequencies in reality. Furthermore, the damping present in the system is omitted in future calculations with the 2DOF model. Further simplifications are adopted in the formulation of the 2DOF system, which are described in the content of this chapter. It is understood that such assumptions introduce errors to the solution; however, it is assumed that the effects of the simplifications can be disregarded.

In order to treat the system with a beam and a drop-weight as a simplified 2DOF system, an understanding of basic concepts is needed. To that end, a description of a single-degree-of-freedom (SDOF) system is initially provided. Thereafter, the theoretical procedure to transform both the beam and the drop-weight into equivalent SDOF systems is explained, where dimensionless transformation factors are introduced. Finally, both SDOF systems are extended and coupled into a 2DOF system. Furthermore, a numerical method to solve the equation of motion is presented.

4.2 Equation of Motion for a SDOF System

The theoretical description of a SDOF system and the formulation of the equation of motion is based mainly on (Craig and Kurdila, 2006). In order to obtain an equation which represents the behavior of a vibrating body, Newton's Second Law can be applied:

$$\sum F_x = ma_x \tag{4.1}$$

where m corresponds to the mass of the body, and a_x to the acceleration of such mass in the x direction. Mathematically, the acceleration is equivalent to the second time derivative of the displacement; that is, $a_x = \ddot{u}$. In a similar manner, the velocity is given as the first time derivative of the displacement, $v_x = \dot{u}$.

Consider the free body diagram of the system in Figure 4.1. The body is assumed to be attached to a linear spring with spring constant k, and to a damper. The force $F(t)$ represents an external force acting on the body, whereas F_k and F_c represent the spring force and the damping force, respectively. Note that the displacement, u, is taken as positive when moving to the right.

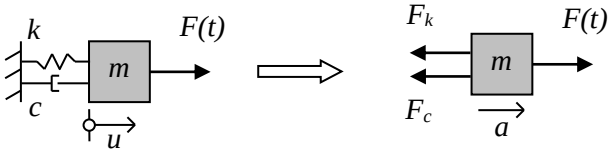

(a) SDOF system. *(b) Free-body diagram.*

Figure 4.1 Free-body diagram of a SDOF system.

The spring-type element allows the system to store potential energy. Let the force in the spring relate linearly to its deformation, so that

$$F_k = ku \tag{4.2}$$

On the other hand, the damper represents the mechanism by which the energy is dissipated from a vibrating structure. Damping is usually defined as a linear function of the velocity, see Equation (4.3). However, it should be noticed that damping is a complex phenomenon and there are several mathematical methods to describe it.

$$F_c = c\dot{u} \tag{4.3}$$

For a displacement of the mass to the right, the spring is subjected to a tension force. Dynamic equilibrium according to Equation (4.1) gives

$$F(t) - F_k - F_s = ma_x \tag{4.4}$$

By inserting Equation (4.2) and Equation (4.3) into Equation (4.4) and rearranging, the following expression for a vibrating mass is obtained:

$$m\ddot{u} + c\dot{u} + ku = F(t), \tag{4.5}$$

which is the expression describing the *equation of motion* for a single-degree-of-freedom (SDOF) system.

4.3 Transformation of Structural Members to Equivalent SDOF Systems

4.3.1 General description

Both the beam and the drop-weight can be simplified into a SDOF system, which may be subjected to a time-dependent load $F(t)$, consisting of a mass m, a resistance $R(u)$, and a damper with damping coefficient c. The external force exerted on the SDOF system is balanced by the internal forces which are composed of a viscous damping force, $R_{dyn}(\dot{u})$, and a static force, $R_{sta}(u)$. However, for the purpose of this thesis work, the damping force is neglected as the loading duration is relatively short, as shown in Figure 4.2. Besides, the maximum displacement of a system subjected to an impulse load is of interest in this thesis work, and disregarding the damping force leads to a more conservative estimation.

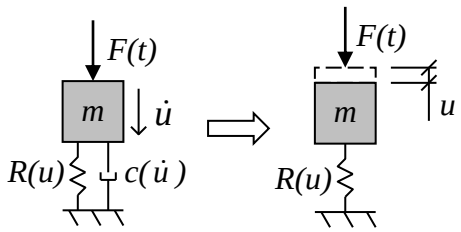

Figure 4.2 Simplified SDOF model adopted. The viscous damping force is neglected.

4.3.2 Modelling of a beam into an equivalent SDOF system

A beam which is assumed to behave linear-elastically exhibits a certain deformed shape which depends on the type of loading and the boundary conditions. A linear elastic response results in constant proportions of the deformed shape, regardless of the magnitude of the load applied, as illustrated in Figure 4.3 for a concentrated load at midspan. Thus, it is possible to describe the deflection along the length of such a beam by only analyzing one system coordinate of the beam, denoted u_s, in a SDOF model (Johansson and Laine, 2012). The system coordinate is commonly chosen so that it corresponds to the point where maximum deflection is expected or at the midspan of the beam. A similar reasoning can be drawn for beams assumed to deform with an ideal plastic response.

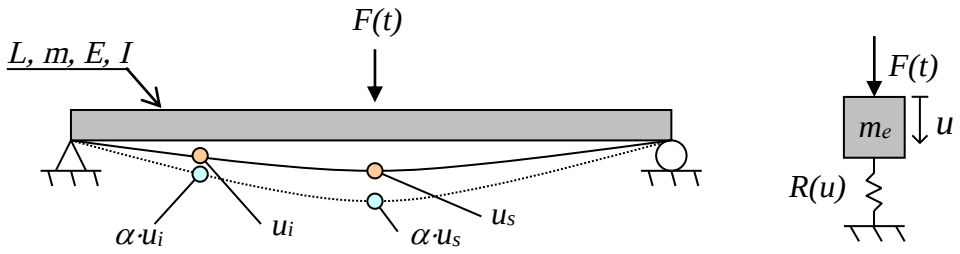

Figure 4.3 Beam subjected to a concentrated load and an equivalent SDOF system. The deformed shape scales linearly with α since the beam is assumed to behave linear-elastically.

In order to convert the real beam in Figure 4.3 into the equivalent SDOF system, the real parameters of mass, stiffness, and external load are multiplied by dimensionless transformation factors, κ, (Biggs, 1964). The equation of motion for the equivalent SDOF described in Equation (4.5) becomes

$$\kappa_m m\ddot{u} + \kappa_k k u = \kappa_F F(t) \tag{4.6}$$

A more general expression can be derived considering the internal resistance, $R(u)$, as

$$\kappa_m m\ddot{u} + \kappa_k R(u) = \kappa_F F(t) \tag{4.7}$$

The transformation factors κ_m, κ_k and κ_F are used to modify the mass, the stiffness, and the external load, respectively. These transformation factors are based on the conservation of energy of the system

and are dependent on the type of load applied to the structure, the assumed deformed shape, and the system point adopted. A complete description of the derivation of the κ factors can be found in (Biggs, 1964) and (Johansson and Laine, 2012).

For the purpose of this thesis work, only the transformation factors pertaining to a simply supported beam subjected to a point load at midspan and to a system point located at midspan (position of maximum deflection) are presented.

In order to preserve the kinetic energy after transformation, the mass transformation factor of the system should be defined as

$$\kappa_m = \frac{1}{L u_s^2} \int_0^L u(x)^2 dx \tag{4.8}$$

Equation (4.8) implies that the mass transformation factor is directly dependent of the deformed shape of the beam. The respective values for linear elastic deformation and plastic deformation are given in Table 4.1.

Likewise, the transformation factor for the external load can be derived considering conservation of the external energy, as

$$\kappa_f = \frac{1}{F u_s} \int_0^L q(x) u(x) dx \tag{4.9}$$

For the case when the external load, $q(x)$, corresponds to a point load, F, Equation (4.9) leads to a value of κ_f equal to the unit, regardless of the deformed shape of the beam.

Finally, the expressions to calculate the stiffness transformation factor are obtained by considering the conservation of internal energy. For a linear elastic response, the following equation should be used:

$$\kappa_{k,el} = \frac{1}{F u_s} \int_0^L M(x) \frac{\mathrm{d}^2 u}{\mathrm{d}x^2} dx \tag{4.10}$$

where $M(x)$ is the sectional moment along the length of the beam. On the other hand, if an ideal plastic response is adopted, the stiffness transformation factor is calculated as

$$\kappa_{k,pl} = \frac{1}{R_m u_s} \int_0^L M(x) \frac{\mathrm{d}^2 u}{\mathrm{d}x^2} dx \tag{4.11}$$

As discussed previously, the external work applied on the structure must be in equilibrium with the internal work. This statement ultimately indicates that the transformation factors derived based on conservation of internal energy and external energy are equal:

$$\kappa_F = \kappa_k \tag{4.12}$$

Dividing Equation (4.7) by the load transformation factor, κ_f, yields

$$\kappa_{mF} m\ddot{u} + R(u) = F(t) \tag{4.13}$$

Here, the factor κ_{mF} has been introduced, which can be defined as

$$\kappa_{mF} = \frac{\kappa_m}{\kappa_F} \tag{4.14}$$

The transformation factors for a simply supported beam loaded by a point load at midspan are summarized in Table 4.1.

Table 4.1 Transformation factors for a simply supported beam subjected to a concentrated load for different material responses (Johansson and Laine, 2012).

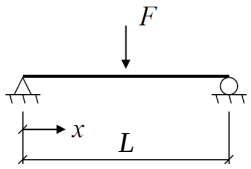

Material response	κ_m	κ_F	κ_k	κ_{mF}
Elastic	0.486	1.00	1.00	0.486
Plastic	0.333	1.00	1.00	0.333

4.3.3 Modelling of drop-weight into an equivalent SDOF system

Similarly to the procedure followed in Section 4.3.2 for a beam, transformation factors can be included in the equation describing the motion of the falling drop-weight impacting a surface in order to obtain an equivalent SDOF system. The drop-weight is assumed to undergo axial deformation only; hence, the determination of the transformation factors is performed under the assumption that the drop-weight can be represented as a bar.

The equivalent SDOF system is shown in Figure 4.4. When the drop-weight impacts a surface, be it rigid or not, a distributed load $q(x,t)$ arises along the length of the drop-weight, which results in a displacement field that reaches a maximum displacement value at the base of the bar, where the impact occurred. Therefore, the system point, u_s, is chosen so that it coincides with the location where maximum displacement occurs, at the base of the falling drop-weight.

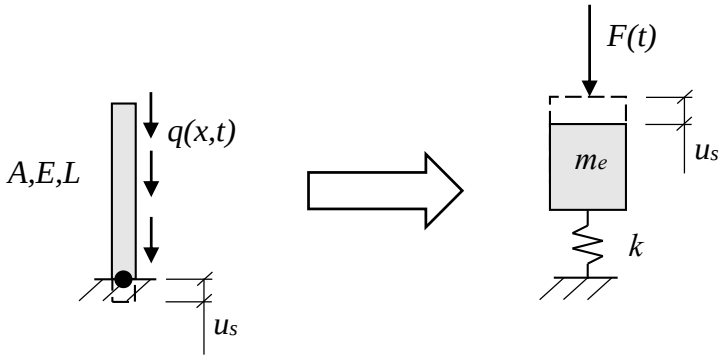

Figure 4.4 Bar falling onto a rigid surface modelled into an equivalent SDOF system, modified from (Lovén and Svavarsdóttir, 2016).

A complete description of the determination of the transformations factors for a bar impacting a rigid surface can be found in (Lovén and Svavarsdóttir, 2016). A summary of such factors is provided in Table 4.2, where two extremes of displacement shapes are presented.

Table 4.2 Transformation factors of a fixed-end bar (Lovén and Svavarsdóttir, 2016).

Displacement shape	κ_m	κ_F	κ_k	κ_{mF}
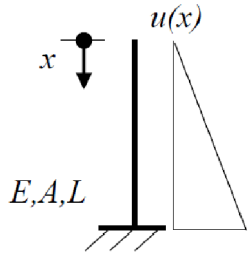	0.333	0.50	0.50	0.667
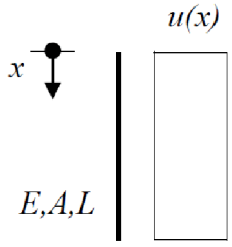	1.00	1.00	1.00	1.00

The first case in Table 4.2 (top picture) is based upon the assumption that both the elastic and plastic deformation shapes of the bar are triangular, due to the fact that one end of the falling bar is considered as fixed. This fixation is made in order to simulate an impact against a very stiff surface.

In the second case (bottom picture), transformation factors are derived based on the assumption that the bar behaves rigidly. The displacement field is constant throughout the length of the drop-weight, as the bar is regarded as very stiff in comparison to the impacted surface.

However, in reality, the behavior of the falling drop-weight is somewhere in between the two extreme cases presented in Table 4.2. As explained in (Lovén and Svavarsdóttir, 2016), since the stiffness of the drop-weight is much larger than that of the beam, the transformation factors of a rigid bar are considered more suitable to model the response. Therefore, a proper representation of the behavior of the drop-weight can be achieved by assuming:

$$\kappa_m = \kappa_F = \kappa_k = 1 \tag{4.15}$$

4.4 2DOF Systems

4.4.1 General description

Equivalent SDOF systems have been established for both the beam and the drop-weight in Section 4.3. This was done by transforming the structural elements into rigid bodies with equivalent mass, $\kappa_m m$, and equivalent stiffness properties, $\kappa_k k$, which undergo deformation due to an equivalent variable force, $\kappa_F F(t)$. In this section, the coupling of the two equivalent SDOF systems into an equivalent 2DOF system, as described in Figure 4.5, is treated. In order to do so, the equation of motion of a 2DOF system is firstly established; thereafter, the equivalent 2DOF model is introduced by adopting the transformation factors derived earlier.

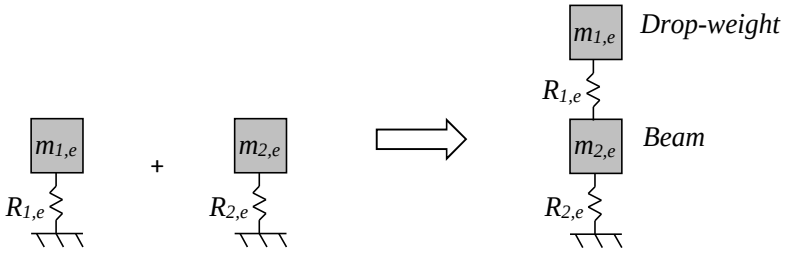

Figure 4.5 Equivalent SDOF systems coupled together into an equivalent 2DOF system.

Observe that the subscript "1" is used henceforth to refer to the body corresponding to the drop-weight, while number "2" is used to name the equivalent body corresponding to the beam.

4.4.2 Equation of motion of 2DOF systems

In order to establish the system of equations which describes a 2DOF system, a free-body diagram representing the forces acting on the bodies should be drawn, as shown in Figure 4.6.

Consider dynamic equilibrium of each body according to Newton's Second Law:

$$\begin{aligned} \sum F_1 &= m_1 \cdot a_1 \\ \sum F_2 &= m_2 \cdot a_2 \end{aligned} \tag{4.16}$$

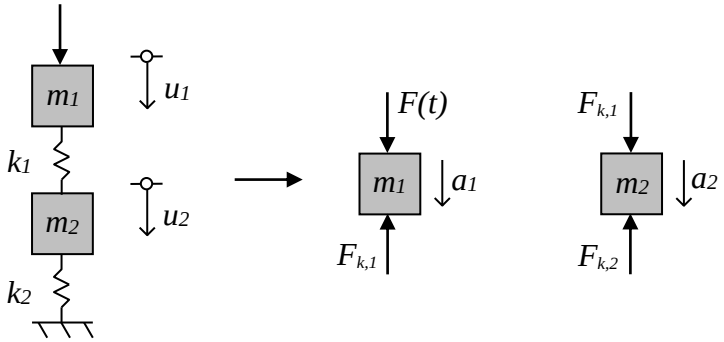

Figure 4.6 Free-body diagram of a 2DOF system.

Force equilibrium of the two free bodies yields

$$\begin{aligned} F(t) - F_{k,1} &= m_1 \ddot{u_1} \\ F_{k,1} - F_{k,2} &= m_2 \ddot{u_2} \end{aligned} \tag{4.17}$$

Introducing the constitutive relations for the springs given by Equation (4.2) results in the following set of equations of motion:

$$\begin{aligned} m_1 \ddot{u_1} + k_1(u_1 - u_2) &= F(t) \\ m_2 \ddot{u_2} + k_2 u_2 - k_1(u_1 - u_2) &= 0 \end{aligned} \tag{4.18}$$

which can also can be expressed in matrix form as

$$\begin{bmatrix} m_1 & 0 \\ 0 & m_2 \end{bmatrix} \begin{bmatrix} \ddot{u_1} \\ \ddot{u_2} \end{bmatrix} + \begin{bmatrix} k_1 & -k_1 \\ -k_1 & k_1 + k_2 \end{bmatrix} \begin{bmatrix} u_1 \\ u_2 \end{bmatrix} = \begin{bmatrix} F(t) \\ 0 \end{bmatrix} \tag{4.19}$$

By expressing Equation (4.19) in symbolic matrix notation, the following equation of motion is obtained for a 2DOF system:

$$\mathbf{M\ddot{u} + Ku = F}(t) \tag{4.20}$$

4.4.3 Equivalent 2DOF system

An equivalent 2DOF system is established by adopting the transformation factors summarized in Sections 4.3.2 and 4.3.3 into Equation (4.19). Additionally, no force $F(t)$ is considered to act on the bodies (the gravitational force is disregarded); instead, the impact load is introduced to the system as initial velocity of body 1, corresponding to the drop-weight. A solution to the system of equation can be obtained by means of numerical methods, such as the Central Difference Method described in Section 4.5.

For a linear elastic response, the equation below is obtained:

$$\begin{bmatrix} \kappa_{mF,1} m_1 & 0 \\ 0 & \kappa_{mF,2} m_2 \end{bmatrix} \begin{bmatrix} \ddot{u_1} \\ \ddot{u_2} \end{bmatrix} + \begin{bmatrix} k_1 & -k_1 \\ -k_1 & k_1 + k_2 \end{bmatrix} \begin{bmatrix} u_1 \\ u_2 \end{bmatrix} = \begin{bmatrix} 0 \\ 0 \end{bmatrix} \tag{4.21}$$

If an elasto-plastic response is assumed, Equation (4.21) is instead expressed in terms of the internal resistance as

$$\begin{bmatrix} \kappa_{mF,1} m_1 & 0 \\ 0 & \kappa_{mF,2} m_2 \end{bmatrix} \begin{bmatrix} \ddot{u}_1 \\ \ddot{u}_2 \end{bmatrix} + \begin{bmatrix} R_1 & -R_1 \\ -R_1 & R_1 + R_2 \end{bmatrix} = \begin{bmatrix} 0 \\ 0 \end{bmatrix} \tag{4.22}$$

where the elasto-plastic resistance of each member can be described accordingly as

$$R_i = \begin{cases} k_i \cdot u & if \quad u_i \leq u_{el,i} \\ R_{m,i} & if \quad u_i > u_{el,i} \end{cases} \tag{4.23}$$

However, when modelling the interaction between the drop-weight and the beam with a spring-type element, an additional condition has to be considered, specifically when the drop-weight displaces upwards after the collision. In such a case, when the spring between the drop-weight and the beam is subjected to tension force, the stiffness is set to zero; therefore,

$$R_1 = \begin{cases} k_1 \cdot u & if \quad u_1 \leq u_{el,1} \\ R_{m,1} & if \quad u_1 > u_{el,1} \\ 0 & if \quad u_1 \leq 0 \end{cases} \tag{4.24}$$

The internal resistance of the drop-weight, $R_{m,1}$, can be derived from the strength of the material and the impact area as

$$R_{m,1} = f \cdot A_{imp} \tag{4.25}$$

Here, the value of strength, f, depends on both the resistance of the steel rod and the local behavior of the concrete in the impact area. This implies that the internal resistance of the drop-weight can have a value within a significantly large interval given by

$$f_{cm} \cdot A_{imp} \leq R_{m,1} \leq f_{ym} \cdot A_{imp} \tag{4.26}$$

where the lower limit corresponds to local concrete crushing, and the upper limit to yielding of steel. The lower limit due to concrete crushing increases due to strain rate effects as well as through local confinement of the impacted concrete provided by surrounding concrete and the drop-weight.

A study of the influence of $R_{m,1}$ on the 2DOF system was performed in (Lovén and Svavarsdóttir, 2016). Different values were considered and compared to results from finite element analyses of the impact-loaded beam. It was concluded that a value $R_{m,1} = 50\,\text{kN}$ yields reasonable results.

On the other hand, the maximum internal resistance for the beam, $R_{m,2}$, is determined from the maximum moment at ultimate limit state. For a beam subjected to a point load at midspan, the maximum moment along the beam can be related to the external load as

$$M_u = \frac{F \cdot L}{4} \tag{4.27}$$

Setting $F = R_{m,2}$, the maximum internal plastic resistance can then be derived from Equation (4.27):

$$R_{m,2} = \frac{4 \cdot M_u}{L} \tag{4.28}$$

The beam is also statically loaded by its self-weight. This means that the internal resistance is slightly lower than the value calculated according to Equation (4.28). To account for the self-weight, $R_{m,2}$ should be reduced by subtracting the equivalent static load, R_{stat}, pertaining to a beam subjected to a uniformly distributed load, as depicted schematically in Figure 4.7.

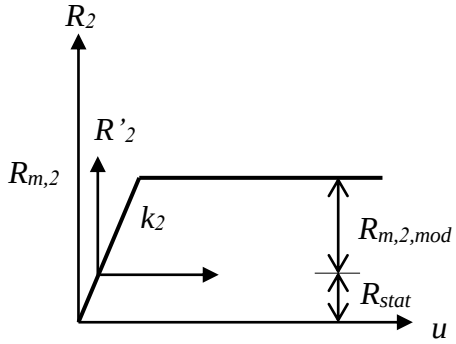

Figure 4.7 Internal resistance of the beam, modified from (Johansson and Laine, 2012).

If g_{beam} corresponds to the self-weight of the beam [N/m], the modified maximum internal resistance of the beam can finally be expressed as

$$R_{m,2,mod} = R_{m,2} - R_{stat} = \frac{4 \cdot M_u}{L} - \frac{g_{beam} \cdot L}{2} \tag{4.29}$$

4.5 Central Difference Method

4.5.1 Introduction

The Central Difference Method (CDM) is an explicit direct integration method which can be used to determine an approximate solution to a second-order differential equation, such as Equation (4.20). The solution is calculated stepwise for a given time step Δt, where $\mathbf{u}_n$ represents the displacement field at a certain time t_n. Furthermore, the discretized field $\mathbf{u}_{n+1}$ are expressed in terms of the of previous fields $\mathbf{u}_n$ and $\mathbf{u}_{n-1}$.

The CDM is conditionally stable, and results in a stable solution provided that certain conditions are fulfilled. Should such conditions not be met, the solutions obtained with the method are unstable and the error will increase without bound.

4.5.2 Numerical formulation

The method is based on a straightforward definition of the first derivative as a simple finite difference approximation:

$$\dot{\mathbf{u}}_n \approx \frac{\mathbf{u}_{n+1} - \mathbf{u}_{n-1}}{2 \cdot \Delta t} \tag{4.30}$$

Likewise, the second order derivative is approximated as the difference of the first-order forward and backward finite differences:

$$\begin{aligned}\ddot{\mathbf{u}}_n &\approx \frac{\dot{\mathbf{u}}_{n+1/2} - \dot{\mathbf{u}}_{n-1/2}}{\Delta t} \\ &\approx \frac{(\mathbf{u}_{n+1} - \mathbf{u}_n)/\Delta t - (\mathbf{u}_n - \mathbf{u}_{n-1})/\Delta t}{\Delta t} = \frac{\mathbf{u}_{n+1} - 2\mathbf{u}_n + \mathbf{u}_{n-1}}{\Delta t^2}\end{aligned} \tag{4.31}$$

Inserting Equation (4.30) and Equation (4.31) into the governing equation of motion at a time step n produces

$$(\mathbf{M}/\Delta t^2)\mathbf{u}_{n+1} + (\mathbf{K} - 2\mathbf{M}/\Delta t^2)\mathbf{u}_n + (\mathbf{M}/\Delta t^2)\mathbf{u}_{n-1} = \mathbf{F}(t_n) \tag{4.32}$$

Equation (4.32) can be solved for $\mathbf{u}_{n+1}$ by introducing the initial conditions as $\mathbf{u}(0) = \mathbf{u}_0$, $\dot{\mathbf{u}}(0) = \dot{\mathbf{u}}_0$, and $\mathbf{F}(0) = \mathbf{F}_0$, for an initial value of $n = 0$.

It can be noticed that the first iteration requires the displacement field for a time step previous to $n = 0$, that is, $\mathbf{u}_{-1}$. This field can be approximated by means of Taylor series as

$$\mathbf{u}_{-1} \approx \mathbf{u}_0 - \Delta t \cdot \dot{\mathbf{u}}_0 + (\Delta t^2/2)\ddot{\mathbf{u}}_0 \tag{4.33}$$

Additionally, the second derivative of the displacement for $n = 0$ can be determined from the original equation of motion as

$$\ddot{\mathbf{u}}_0 = \mathbf{M}^{-1}(\mathbf{F}_0 - \mathbf{K}\mathbf{u}_0) \tag{4.34}$$

4.5.3 Stability

As stated in Section 4.5.1, the CDM is a conditionally stable algorithm and the method is stable only if the chosen time step Δt is less than

$$\Delta t_{crit} = \frac{2}{\omega_{max}} = \frac{T_n}{\pi}. \tag{4.35}$$

Here, ω_{max} is the highest eigenfrequency determined from $\det(\mathbf{K} - \omega^2\mathbf{M}) = 0$. Therefore, T_n corresponds to the smallest period.

Selecting a time step which is smaller than the critical value Δt_{crit} guarantees that the wave information does not propagate across more than one element per time step. Moreover, when a high level of accuracy is needed, a significantly smaller time step might be required. According to (Johansson and Laine, 2012), a suitable time step is dependent on the loading conditions and the response time of the system; although a time step less than one percent of the load duration usually suffices:

$$\Delta t \leq \begin{cases} \Delta t_{crit} \\ \frac{t_l}{100} \end{cases} \tag{4.36}$$

where t_l is the duration of the load.

5 Plastic Rotational Capacity

5.1 Introduction

A large plastic rotational capacity is associated with a more ductile behavior of a given structural element, and is a desirable property since large deformations near ultimate load can serve as a warning when structures subjected to static loading are close to failure. Moreover, the rotational capacity of a reinforced concrete element allows for moment redistribution in statically indeterminate structures, which results in an increased load carrying capacity. Furthermore, a large plastic rotational capacity is also a sought-after property in structures subjected to impulse loads, since it is proportionally related to the capacity to absorb energy.

Provided that a reinforced concrete structure is ductile enough, yielding of reinforcement causes plastic hinges to form with an increased load. It is common in engineering practice to assume such hinges to be concentrated to certain sections, as can be seen in Figure 5.1a for a simply supported beam. The need of plastic rotation is then usually defined as the rotation of such concentrated hinges from the onset of yielding until a failure mechanism is reached.

However, in reality plastic rotation of a structure is the result of plastic deformation along a plastic region, as represented schematically in Figure 5.1b. Furthermore, plastic rotation is a complex phenomenon that depends on several factors, such as the properties of steel reinforcement, amount of reinforcement, loading conditions, cracking and tension stiffening, among others. Due to the number of factors and conditions affecting rotation capacity, experimental results have shown a large variation of the measured values of plastic rotation. This has led researchers to develop several different methods to predict the plastic behavior of concrete beams, which are covered in later sections of this chapter.

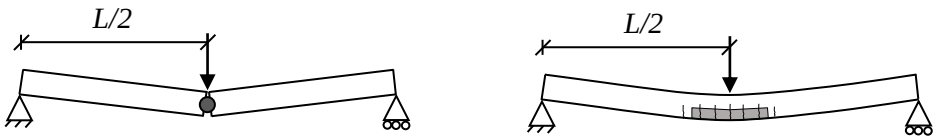

(a) Assumption of concentrated hinge. *(b) Real distribution of plastic hinge.*

Figure 5.1 Representation of a plastic hinge.

In order to define plastic rotational capacity, an understanding of the relationship between curvature and rotation is needed. Initially, the definition of these concepts is given. Subsequently, different methods found in the literature to predict the plastic rotation capacity are presented.

5.2 Curvature

5.2.1 Definition

Consider a certain reinforced concrete element of infinitesimal length, *da*, subjected to a bending moment, M, as shown in Figure 5.2. Based on the assumption that plane sections remain plane, the radius of curvature, denoted R, is measured with respect to the distance to the neutral axis, x, of the concrete

section. The curvature of the element, φ, measured between the two ends of the element, can be given as da/R.

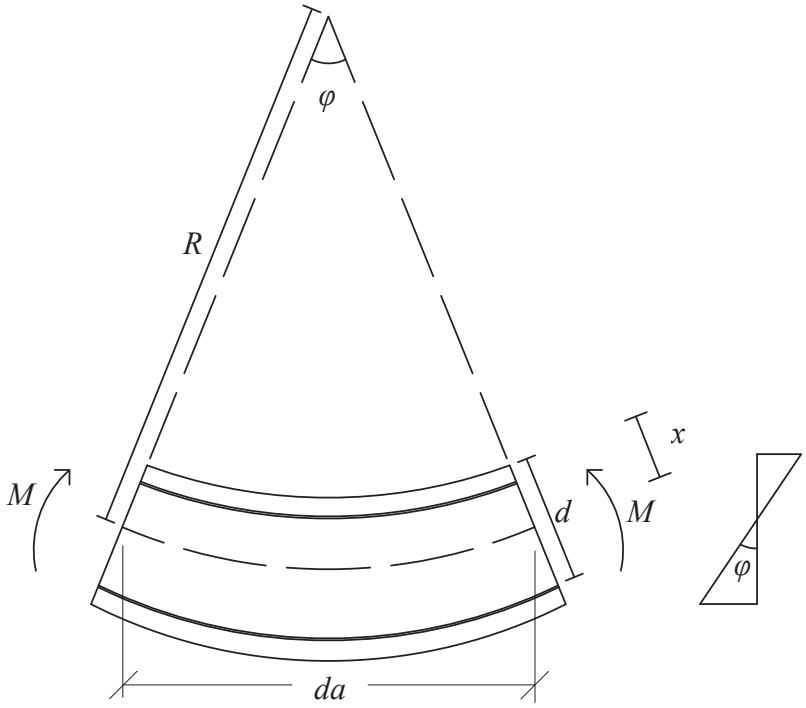

Figure 5.2 Definition of curvature of a reinforced concrete element of length da subjected to a bending moment, modified from (Park and Paulay, 1975).

It is observed in Figure 5.2 that the curvature of the infinitesimal element corresponds to its strain gradient (Park and Paulay, 1975). By assuming a unit length, $da = 1$, the curvature of the element can therefore be defined as

$$\varphi = \frac{1}{R} = \frac{\varepsilon_c}{x} = \frac{\varepsilon_s}{d - x} \tag{5.1}$$

where d is the distance from the compressed edge to the center of gravity of the tensile reinforcement; and ε_c and ε_s correspond to the concrete strain at the compressed edge and the strain in the tensile reinforcement, respectively.

5.2.2 Curvature of a cracked element

If a member is cracked, the stiffness can no longer be considered constant along its length. The position of the neutral axis is influenced by the location and size of the cracks, as shown schematically in Figure 5.3. Consequently, a shift of the neutral axis due to cracking results in a larger curvature. However, due to *tension stiffening*, the average steel strain in cracked regions is smaller than the steel strain at the flexural cracks. This implies that calculating the stiffness of a cracked member using a model in state II would lead to underestimation of the real stiffness of the member.

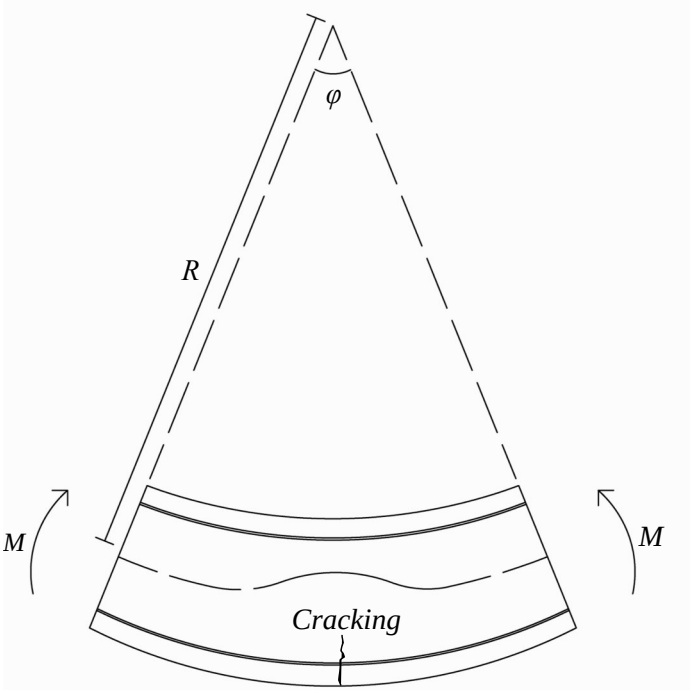

Figure 5.3 Shift of neutral axis due to the presence of cracking, modified from (Park and Paulay, 1975).

5.3 Plastic Rotation

5.3.1 Relationship between rotation and curvature

The change in rotation from one section, a_1, to another section, a_2, is calculated by the integration of the curvature between the sections as

$$\theta_{12} = \int_{a_1}^{a_2} \frac{1}{R}(a)da = \int_{a_1}^{a_2} \varphi(a)da \tag{5.2}$$

Equation (5.2) may be applied to a member where the moment-curvature relationship of said member is known, and where the moment distribution along its length is also known (Park and Paulay, 1975).

5.3.2 Theoretical plastic rotation capacity

Various definitions of plastic rotation capacity have been suggested by different authors as the understanding of the plastic hinge phenomenon developed (CEB-FIP, 1998). Understanding the differences in the various definitions of plastic rotation is essential when comparing research results, considering that the measured rotations can vary significantly due to the different definitions adopted.

Model Code 90 (CEB-FIP, 1991) defines the plastic rotation capacity as the difference between the total rotation at failure, θ_{tot}, and the elastic rotation, $\theta_{el,tot}$. Therefore, the plastic rotation capacity represents the additional curvature which takes place from the onset of yielding to *failure* of the member. Then, the definition of failure becomes important, as the chosen criteria for structural failure affect the calculation of the plastic rotation capacity. In general terms, two different failure modes should be considered, namely: *concrete failure* and *steel failure*. In the former, concrete crushing occurs when the ultimate

strain of concrete, ε_{cu}, is reached at the compressed edge; while in the latter, the ultimate reinforcing steel strain, ε_{su}, is reached before the total capacity of the concrete has been utilized and one or more reinforcement bars rupture.

Consider Figure 5.4. The total rotation, θ_{tot}, is equal to the integration of the curvature at failure along the beam length; while the total elastic rotation, $\theta_{el,tot}$, is equal to the rotation at a load causing yielding of the reinforcement at a point of maximum moment. On the other hand, the total plastic rotation, $\theta_{pl,tot}$ – represented as the shaded area in the curvature diagram in Figure 5.4 – can be determined based on Equation (5.2) as

$$\theta_{pl,tot} = \theta_{tot} - \theta_{el,tot} = \int_L \left[\varphi(a) - \varphi_y(a)\right] da \tag{5.3}$$

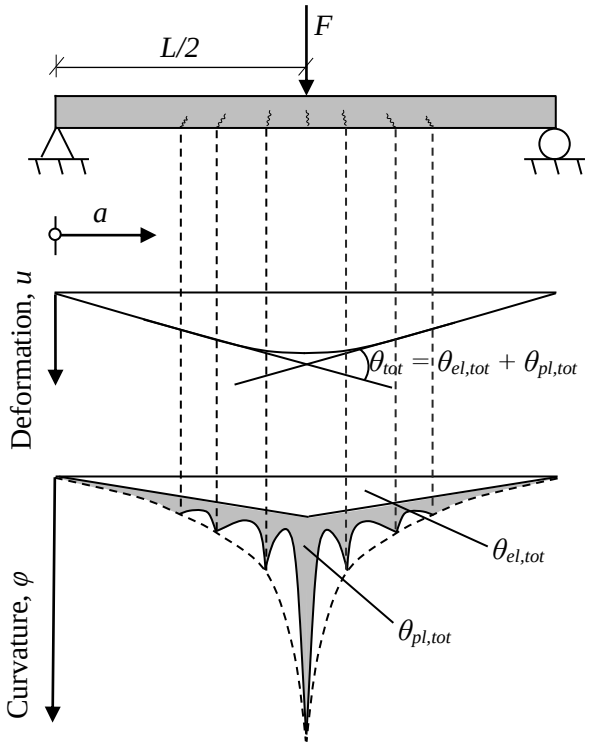

Figure 5.4 Schematic illustration of plastic rotation.

Each of the peaks of curvature in Figure 5.4 corresponds to a crack location. According to Latte (1999), a calculation model that takes into account the increase of curvature at each crack location is denoted a *discrete crack model* [1]. The moment-curvature is established for the cracked cross sections; in addition, the curvature for the uncracked elements between the cracks are reduced due to tension stiffening effect, which is commonly considered through local bond-slip relations.

[1]The different calculation models to evaluate rotation capacity described by Latte (1999) should not be confused with the crack approaches adopted in finite element modelling of cracks in concrete structures. For a detailed definition of the crack approaches used in FEA refer to (Johansson, 2000).

However, it is possible to smear out the crack opening over an equivalent region, which is normally based on the mean crack distance. The *smeared-crack model*, therefore, allows to determine an average moment-curvature relationship which is valid between two cracks. The rotations are then calculated by integrating the average curvature along the length of the beam.

Simpler approaches assume that the plastic curvature occurs in a localized area denoted plastic length, l_y, in which the tensile reinforcement strain is larger than the yield strain. Figure 5.5 shows schematically how the curvature may vary along the length of a simply supported beam for two different definitions of plastic rotation. In Figure 5.5a the elastic curvature varies linearly along l_y; while in Figure 5.5b the elastic curvature is assumed to remain constant along l_y.

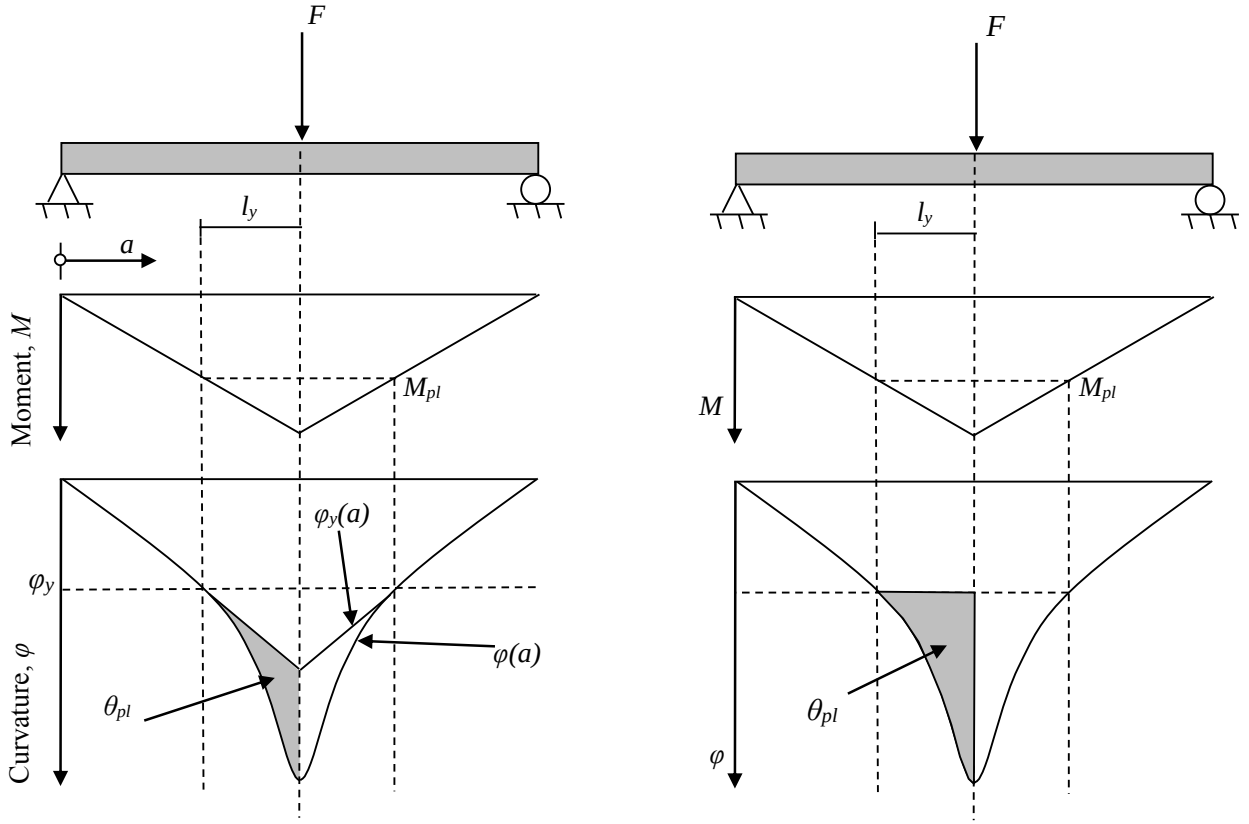

(a) Model with variable elastic curvature along l_y. *(b) Model with constant elastic curvature along l_y.*

Figure 5.5 Schematic representation of different simplified models to determine plastic rotation capacity, modified from (CEB-FIP, 1998).

Based on Figure 5.5, the plastic rotation at *one side* of the critical section can be calculated as the integral of the difference between the curvature at failure and the elastic curvature along the plastic length, l_y, (Park and Paulay, 1975). This relationship can be represented as

$$\theta_{pl} = \int_{l_y} \left[\varphi(a) - \varphi_y(a)\right] da \tag{5.4}$$

For the case when a simply supported beam is subjected to a concentrated load applied at midspan, the rotation at one side of the critical section corresponds to the rotation at the support, as shown in Figure 5.6. Based on this definition, θ_{pl} is considered equivalent to the plastic rotation at one of the supports, unless stated otherwise.

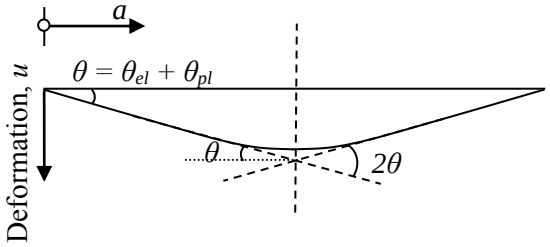

Figure 5.6 Equivalence between plastic hinge rotation and support rotation for a simply supported beam subjected to a point load at midspan.

The elastic curvature, $\varphi_y(a)$, is described by

$$\varphi_y(a) = \frac{\varepsilon_{cy}}{x(a)} = \frac{\varepsilon_{sy}}{d - x(a)} \tag{5.5}$$

Here, ε_{cy} is the compressive concrete strain when the reinforcement starts to yield, ε_{sy} is the yield strain of the tensile reinforcement, and $x(a)$ is the depth of the compressive zone along l_y. Similarly, the ultimate curvature is given as

$$\varphi_u = \frac{\varepsilon_{cu}}{x_u} = \frac{\varepsilon_s}{d - x_u} \tag{5.6}$$

where ε_{cu} corresponds to the ultimate concrete strain at the compressed edge, and x_u to the height of the neutral axis in ultimate limit state. The plastic curvature, $\varphi_{pl}(a)$, can then be expressed in terms of the strains of the reinforcement as

$$\varphi_{pl}(a) = \varphi(a) - \varphi_y(a) = \frac{\varepsilon_s(a) - \varepsilon_{sy}}{d - x(a)} \tag{5.7}$$

Here, the reinforcing steel strain, $\varepsilon_s(a)$, corresponds to the average steel strain (CEB-FIP, 1991). Combining Equation (5.7) with Equation (5.4), the following expression for plastic rotation in terms of steel strain can be defined:

$$\theta_{pl} = \int_{l_y} \frac{\varepsilon_s(a) - \varepsilon_{sy}}{d - x(a)} da \tag{5.8}$$

It should be noted that Equation (5.8), adopted by Model Code 90, describes a model in which the position of the neutral axis varies continuously from the position at which yielding takes place until the point of maximum curvature; as a result, the elastic curvature also varies in the yielding domain. However, the

height of the compressive zone at yielding (and at any instance after yielding) can be approximated as the height of the compressive zone at failure as $x_y \approx x_u$. This implies that φ_y is expressed independently of a along l_y. Equation (5.8) can be rewritten as

$$\theta_{pl} = \int_{l_y} \left[\varphi(a) - \varphi_y\right] da = \int_{l_y} \frac{\varepsilon_s(a) - \varepsilon_{sy}}{d - x_u} da \tag{5.9}$$

One of the major difficulties to apply the theoretical expressions in Equations (5.8) and (5.9) lies in the definition of the criteria at which yielding and failure are assumed to occur; along with the estimation of the plastic zone, l_y, which depends on several factors, such as the influence of shear force, the presence of inclined shear cracks, and the bond relationship between concrete and steel. Another important factor is the definition of the ultimate strain of concrete, ε_{cu}.

5.3.3 Equivalent plastic hinge length

An approximation of the resulting plastic rotation, θ_{pl}, can be made by assuming a constant plastic curvature, $\varphi_{pl} = \varphi_u - \varphi_y$, over an *equivalent plastic hinge length*, l_p. The equivalent plastic rotation capacity is given by

$$\theta_{pl} = (\varphi_u - \varphi_y) l_p = \varphi_p l_p \tag{5.10}$$

where φ_u and φ_y correspond to the curvature at ultimate load and at yielding, respectively. The relationship described in Equation (5.10) is also depicted in Figure 5.7. Park and Paulay (1975) state that a common approach is to first approximate the equivalent plastic hinge length, l_p, and subsequently calculate the plastic rotation capacity. Some empirical methods to determine l_p proposed by different authors are described in Section 5.4.5.

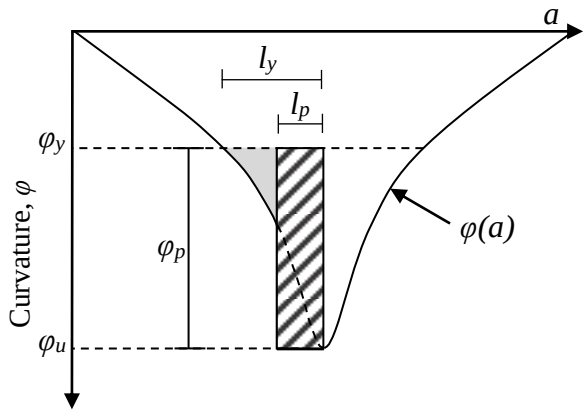

Figure 5.7 Concept of equivalent plastic hinge length. Constant plastic curvature is assumed along the equivalent length, l_p. The area provided by l_p and φ_p should correspond to the total plastic rotation given by the shaded area under $\varphi(a)$ along l_y.

5.3.4 Definition of plastic rotation from test results

Consider a simply supported concrete beam subjected to a concentrated load during a static loading test. When the reinforcement bars begin to yield, a plastic hinge is formed at the location of maximum moment. From this point, the deformation increases significantly for a small increment of the load until the ultimate load is reached. However, in deformation-controlled tests, the deformation can still be increased further if the load applied on the beam is gradually reduced accordingly with the remaining capacity of the beam. Figure 5.8 shows schematically this type of response.

Based on the load-displacement (or moment-curvature) relation for static loading obtained from deformation-controlled tests, the rotation capacity can be defined as the non-elastic rotation, $\theta_{pl,x\%}$. Such rotation capacity is expressed in terms of the deformation required to reach a certain percentage of the maximum load along the descending branch of the load-displacement curve. This definition is illustrated for $\theta_{pl,95\%}$ in Figure 5.8 as an example.

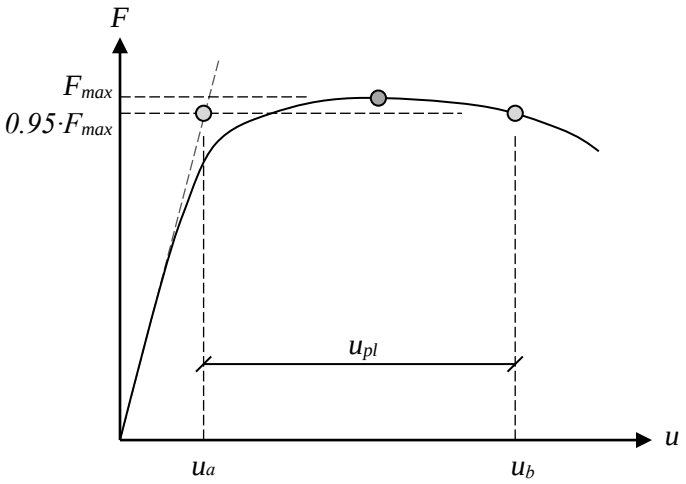

Figure 5.8 Rotation capacity defined at 95 % of the ultimate load.

The parameters u_a and u_b in Figure 5.8 and Figure 5.9 correspond to the total deformation at a load $(x\%/100) \cdot F_{max}$ on the descending branch of the load-displacement curve, and the elastic deformation at the chosen load level, respectively.

Let L_e be defined as the length from the support to the plastic hinge, which for a simply supported beam loaded at midspan corresponds to half the span, as shown in Figure 5.9. The plastic rotation capacity – given as the rotation at the support – can therefore be determined as

$$\theta_{pl,x\%} = \frac{(u_{b,x\%} - u_{a,x\%})}{L_e} = \frac{u_{pl,\%}}{L_e} \tag{5.11}$$

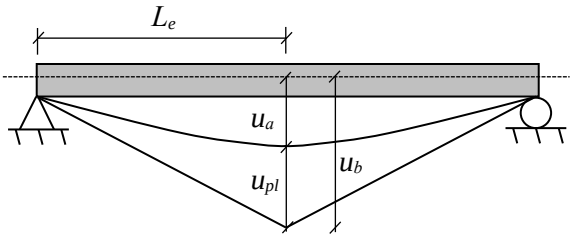

Figure 5.9 Representation of elastic and plastic deformation measured from experiments.

5.4 Different Methods to Predict Plastic Rotation Capacity

5.4.1 Overview

A brief description of different methods to estimate the plastic rotational capacity of reinforced concrete beams is presented in this section.

Initially, the methodology suggested in Eurocode 2 (CEN, 2004) to estimate the available rotational capacity is described. Additionally, the methods proposed in *Betonghandboken* (1980) and *Bk 25* are presented, according to the information provided in (Johansson and Laine, 2012).

Finally, various empirical expressions available in the literature for determining the equivalent plastic hinge length, l_p, and the maximum concrete strain, ε_u, at ultimate curvature are treated. These expressions are mainly based on static tests on simply supported concrete beams subjected to concentrated loading at midspan. The calculated values of l_p could afterwards be used in Equation (5.10) to determine the plastic rotation capacity.

5.4.2 Rotation capacity according to Eurocode 2

5.4.2.1 Definition

The definition of plastic rotational capacity, $\theta_{pl,d}$, provided by Eurocode 2 (CEN, 2004) has been formulated for rotation over an inner support in a continuous beam, as illustrated in Figure 5.10, where the length of rotation is assumed to occur over a length equal to 1.2 times the depth of the support section.

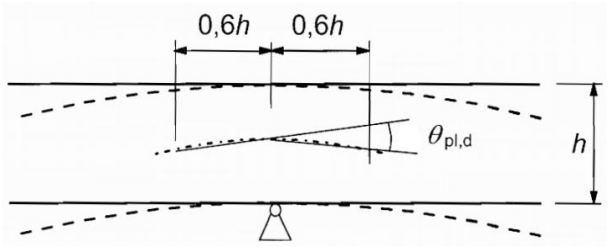

Figure 5.10 Plastic rotational capacity according to Eurocode 2 (CEN, 2004).

An equivalence between the definition by Eurocode 2 and the experimental conditions in this project is needed. According to Latte (1999), the inner support rotation in a continuous beam is approximately equal to the rotation at midspan of an equivalent simply supported beam subjected to a concentrated

load, with a length corresponding to the distance between zero moments over the support. Figure 5.11 provides with a graphical description of such assumption.

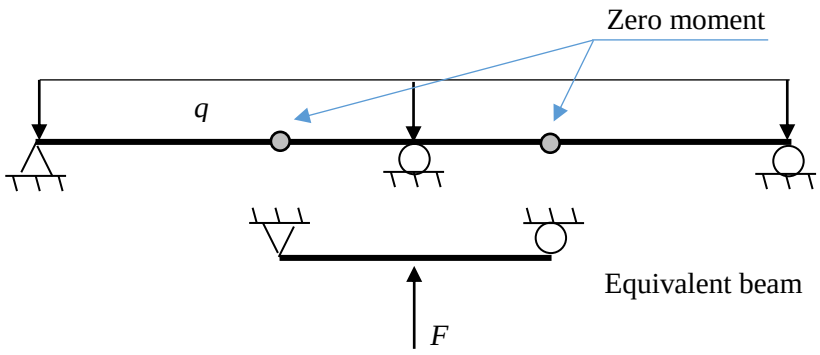

Figure 5.11 Equivalence between a continuous beam and a simply supported beam.

Furthermore, the rotation defined in Figure 5.10 corresponds to the summation of the rotation on both sides of the studied critical section – that is, the *total rotation* – as given by Equation (5.3); while the expressions for plastic rotation given by Equations (5.4) and (5.10) are defined for only one side of the critical section. Hence, by calculating the rotation at midspan of a simply supported beam assuming that the conditions at the point of load application are equivalent to an inner support, the value of $\theta_{pl,d}$ according to Eurocode 2 corresponds to *twice* the size of the rotation at the support, see Figure 5.12.

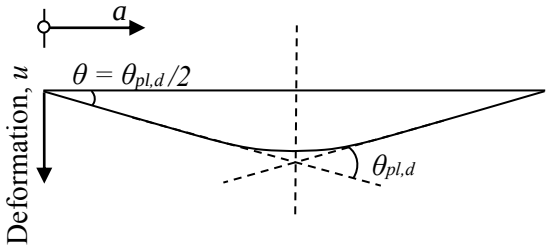

Figure 5.12 Equivalence between plastic rotation capacity, $\theta_{pl,d}$, as defined by Eurocode 2 and support rotation.

5.4.2.2 Rotational capacity

By a simplified procedure, Eurocode 2 relates the ratio x_u/d to the plastic rotational capacity depending on the concrete class and the reinforcement steel class. The relationship between the ratio x_u/d and $\theta_{pl,d}$ is shown in Figure 5.13. The noticeable difference between rotational capacities for different reinforcement classes is due to different ductility properties, as Class C steel exhibits a more ductile behavior and therefore provides for a larger rotational capacity.

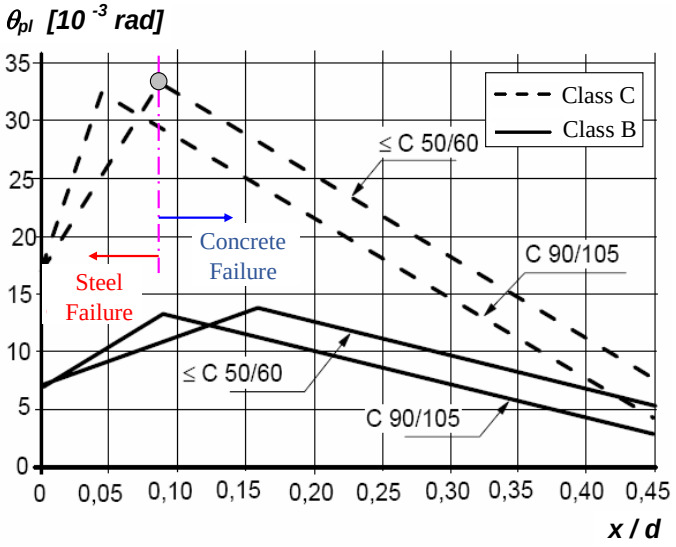

Figure 5.13 Allowable rotation of reinforced concrete sections for different concrete classes, and Class B and C steel reinforcement. Valid for shear slenderness λ=3. Modified from (CEN, 2004).

The position along a given curve in Figure 5.13 with respect to its peak signals the failure mode to be expected, either due to crushing of concrete or to rupture of reinforcement. In the region where steel failure is critical, the rotation capacity is directly governed by the ductility of the steel; in this case, the strain capacity of the reinforcement bars is fully utilized. An increasing ratio of x_u/d leads to a larger deformation capacity.

Contrarily, failure due to concrete crushing occurs on the other side of the peak. In this case, the height of the compressive zone in relation to the internal lever arm is relatively large; crushing of concrete at the compressed edge will therefore occur for values of steel strain lower than the strain capacity at rupture of the reinforcement. In this interval, larger values of x_u/d result in reduced deformation capacity.

It should be highlighted that the chart in Figure 5.13 is only applicable to shear slenderness $\lambda = 3$; where shear slenderness is defined as

$$\lambda = \frac{l_0}{d} \tag{5.12}$$

Here, l_0 is the distance from the zero moment section to the point of maximum moment after redistribution. For different values of shear slenderness, $\theta_{pl,d}$ is modified by a factor k_λ in the following way:

$$\theta^*_{pl,d} = k_\lambda \theta_{pl,d} \tag{5.13}$$

where k_λ is defined as

$$k_\lambda = \sqrt{\frac{\lambda}{3}} \tag{5.14}$$

Furthermore, the ratio of x_u/d should be limited to

$x_u/d \leq 0.45$ for classes less or equal to C50/60

$x_u/d \leq 0.35$ for classes higher or equal to C55/67

5.4.3 Betonghandbok-Konstruktion 1980 (ABC method)

Betonghandboken (1980) provides an empirical equation to calculate the plastic rotation capacity on one side of the critical section of a reinforced concrete beam (Johansson and Laine, 2012). Such rotation capacity corresponds to the rotation at a load level equivalent to 95 % of the maximum load, similarly to the case presented in Figure 5.8, and can be determined as

$$\theta_{pl,95\%} = A \cdot B \cdot C \cdot 10^{-3} \tag{5.15}$$

The formulation of Equation (5.15) was introduced in (Öberg, 1980) based on the results collected from a series of experiments on reinforced concrete beams subjected to concentrated loads for the conditions described in Figure 5.14.

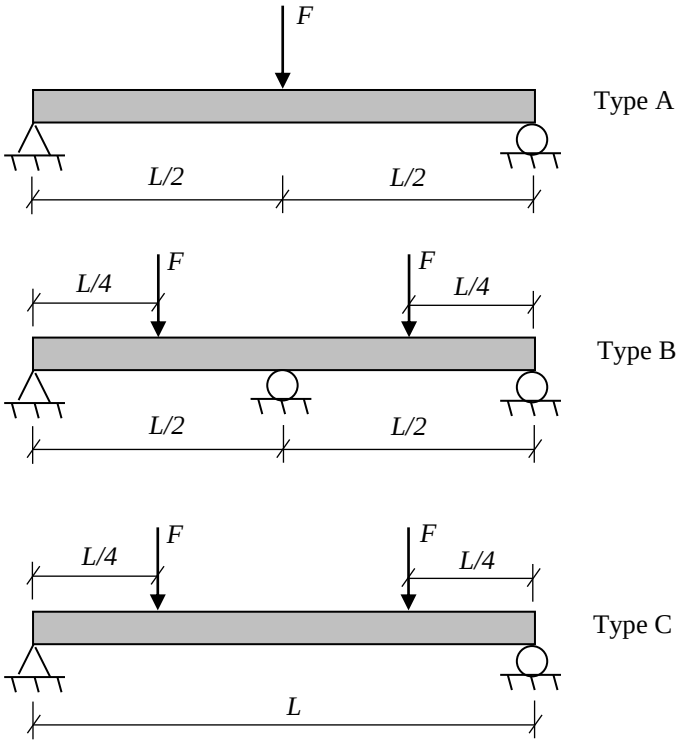

Figure 5.14 Different types of specimen in (Öberg, 1980).

The factor A takes into account the amount of tensile and compression reinforcement as well as the amount of transverse reinforcement. When the strength values are taken from the *Swedish Concrete Code*, A can determined as

$$A = 1 + 0.6\omega_v + 1.7\omega_s' - 1.4\frac{\omega_s}{\omega_b} \tag{5.16}$$

The parameters ω_s, ω'_s, and ω_v correspond to the mechanical ratio of tensile reinforcement, the mechanical ratio of compression reinforcement, and the mechanical ratio of shear reinforcement, respectively, and can be determined according to the following equations:

$$\omega_s = \frac{A_s}{bd} \cdot \frac{f_y}{f_c} \tag{5.17}$$

$$\omega'_s = \frac{A'_s}{bd} \cdot \frac{f_y}{f_c} \tag{5.18}$$

$$\omega_v = \frac{A_v}{bs} \cdot \frac{f_y}{f_{ct}} \tag{5.19}$$

The balanced mechanical reinforcement ratio, ω_b, can be estimated from Equation (5.20) by letting $\varepsilon_{cu} = 3.5\,‰$ and $\varepsilon_{sy} = f_y/E_s$.

$$\omega_b = \frac{0.8\varepsilon_{cu}}{\varepsilon_{cu} + \varepsilon_{sy}} \tag{5.20}$$

However, when measured values of material strength are used in the calculation, the following equation may be used:

$$\begin{aligned} &A = 1 + 1.3\omega_v + 3\omega'_s - 5\omega_s \\ &\text{but, } 0.05 \leq A \leq 2.30 \end{aligned} \tag{5.21}$$

The parameter B considers the shape of the stress-strain curve of the reinforcement steel and varies depending on the type and grade of steel. The values of B can be obtained from Table 5.1. Note that the nomenclature used in Table 5.1 to classify the reinforcing steel corresponds to an outdated classification according to the Swedish standards.

Table 5.1 Values for factor B.

Steel type	B	Max $A \cdot B$
Ks 60, Ks 40, Ss 26, Ss 26S	1.0	1.7
Ks 60S, Ks 40S [1]	0.8	1.1
Cold-worked steel with $\varepsilon_{su} \geq 3\,\%$ and $f_{su}/f_{0.2} \geq 1.1$	$0.6\left(1 - 0.7\varepsilon_p/\varepsilon_{su}\right)$	5

[1] Use values for Ks 60 and Ks 40 if $\varepsilon_{su} \geq 8\,\%$ and $f_{su}/f_{0.2} \geq 1.4$.

The factor C takes into account the position of the plastic hinge in the structure, as well as the type of load. The expressions to determine C for a uniformly distributed load, and a plastic hinge located either over the support or along the span, are given by

$$C_{sup} = 10 \cdot l_{0,sup}/d \tag{5.22}$$

$$C_{field} = 7 \cdot l_{0,field}/d \tag{5.23}$$

The definition of $l_{0,sup}$ and $l_{0,field}$ is shown in Figure 5.15.

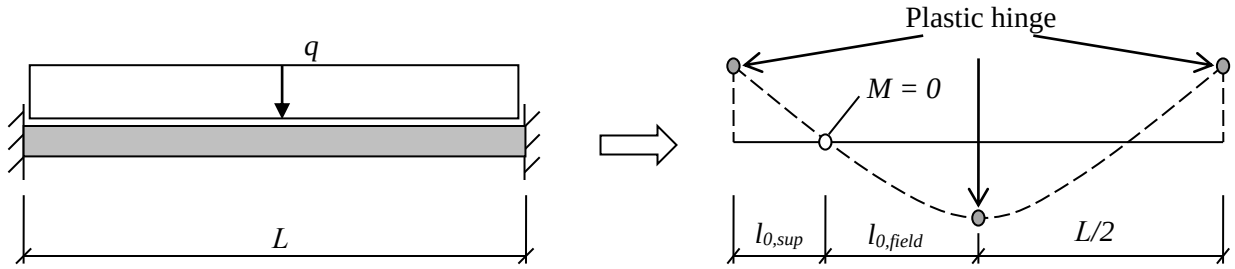

Figure 5.15 Definition of $l_{0,sup}$ and $l_{0,field}$ depending on the moment diagram.

5.4.4 Bk 25

According to Johansson and Laine (2012), the Swedish Fortifications Agency provides in *Bk 25* a method to estimate the rotational capacity of an impulse-loaded reinforced concrete beam. The beam is assumed to be subjected to a distributed load with geometry notation as shown in Figure 5.16.

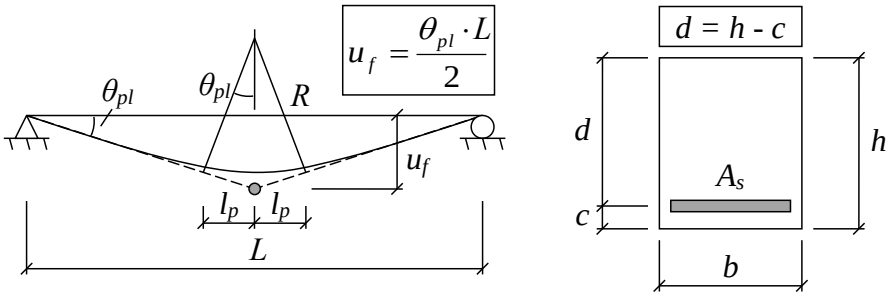

Figure 5.16 Geometry definition of a simply supported beam, modified from (Johansson and Laine, 2012).

The equivalent plastic hinge, l_p, for which a constant curvature is assumed, can be calculated as

$$l_p = 0.5d + 0.15L \tag{5.24}$$

The plastic rotational capacity, θ_{pl}, is directly proportional to l_p as

$$\theta_{pl} = \frac{l_p}{R} \tag{5.25}$$

Hence, the total deformation at midspan due to the plastic hinge is given by

$$u_f = \frac{\theta_{pl} L}{2} \tag{5.26}$$

The curvature of a cross-section at ultimate moment has previously been defined in Equation (5.1) as

$$\varphi_u = \frac{1}{R} = \frac{\varepsilon_{cu}}{x} = \frac{\varepsilon_s}{d - x} \tag{5.27}$$

Note that ε_s is the average steel strain over the equivalent plastic length and ε_{cu} is the value of ultimate concrete strain.

Consider a concrete beam provided with a bottom layer of reinforcement. Figure 5.17 shows the assumed distribution of strain and stress over the cross section at ultimate moment.

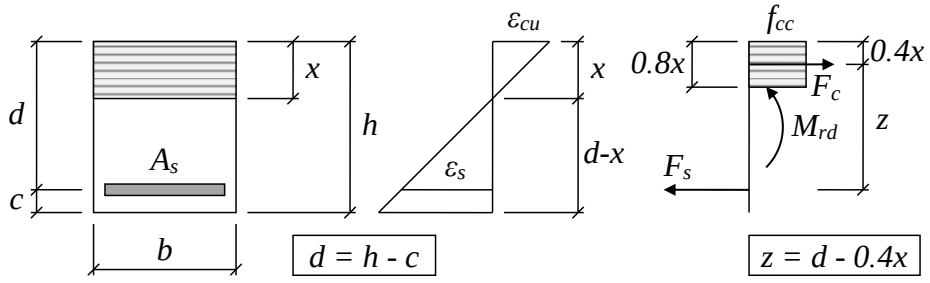

Figure 5.17 Geometry definition of a cross-section subjected to an ultimate moment, modified from (Johansson and Laine, 2012).

By the assumption that tensile reinforcement yields, horizontal equilibrium in Figure 5.17 produces

$$0.8b \cdot x \cdot f_c = A_s \cdot f_y \tag{5.28}$$

Equation (5.28) can be solved for the height of the compressive block, x. By introducing the reinforcement ratio parameter, ρ_s, which is defined as

$$\rho_s = \frac{A_s}{bd}, \tag{5.29}$$

and considering mechanical reinforcement ratio for tensile reinforcement, ω_s, previously given as

$$\omega_s = \frac{A_s}{bd} \cdot \frac{f_y}{f_c}; \tag{5.30}$$

the compressive height, x, can therefore be expressed from Equation (5.28) as

$$x = \frac{\rho d}{0.8} \cdot \frac{f_y}{f_c} = \frac{\omega_s d}{0.8} \tag{5.31}$$

The distance d needs to be calculated to the gravity center of the tensile reinforcement if multiple layers are present. The change of failure mode from steel rupture to concrete crushing can be stated for a

cross-section containing only tensile reinforcement in terms of a critical mechanical reinforcement ratio as

$$\omega_{s,crit} = \frac{0.8 \cdot \varepsilon_{cu}}{\varepsilon_{cu} + \varepsilon_{su}} \tag{5.32}$$

If $\omega_s > \omega_{s,crit}$, the concrete beam is theoretically expected to fail due to concrete crushing. The following expression is obtained when it is assumed that concrete crushing is the decisive failure mode when combining equations (5.24), (5.25), and (5.28):

$$\theta_{pl,f} = \frac{l_p}{R} = \frac{0.8 \cdot \varepsilon_{cu}}{\omega_s \cdot d}(0.5d + 0.15L) = \frac{0.4 \cdot \varepsilon_{cu}}{\omega_s}\left(1 + 0.3\frac{L}{d}\right) \tag{5.33}$$

If rupture of the reinforcing steel is the decisive failure mode, then

$$\theta_{pl,f} = \frac{l_p}{R} = \frac{0.8 \cdot \varepsilon_{su}}{d(0.8 - \omega_s)}(0.5d + 0.15L) = \frac{0.4 \cdot \varepsilon_{su}}{(0.8 - \omega_s)}\left(1 + 0.3\frac{L}{d}\right) \tag{5.34}$$

The subscript f in Equations (5.33) and (5.34) stands for *field*, as the plastic hinge is assumed to take place along the span of a simply supported beam.

For continuous beams, the rotation capacity at the plastic hinge in the field can be determined as described before for simply supported beams. However, the definition of plastic hinge length differs for a plastic hinge located over the support. Instead of using Equation (5.24), the plastic hinge length over the support can be calculated as

$$l_p = 0.5d + 0.1l_0 \tag{5.35}$$

where l_0 is the distance from the zero moment section to the point of maximum moment. If M_s and M_f are the moment over the support and maximum moment in the field, respectively, then l_0 can be estimated as

$$l_0 = \frac{M_s}{V_s} \tag{5.36}$$

Therefore, when concrete crushing is the decisive failure mode, the rotational capacity over the support is given by

$$\theta_{pl,s} = \frac{l_p}{R} = \frac{0.8 \cdot \varepsilon_{cu}}{\omega_s \cdot d}(0.5d + 0.1l_0) = \frac{0.4 \cdot \varepsilon_{cu}}{\omega_s}\left(1 + 0.2\frac{l_0}{d}\right) \tag{5.37}$$

When rupture of the reinforcing steel is the governing failure mode, then

$$\theta_{pl,s} = \frac{l_p}{R} = \frac{0.8 \cdot \varepsilon_{su}}{d(0.8 - \omega_s)}(0.5d + 0.1l_0) = \frac{0.4 \cdot \varepsilon_{su}}{(0.8 - \omega_s)}\left(1 + 0.2\frac{l_0}{d}\right) \tag{5.38}$$

5.4.5 Plastic rotation capacity based on equivalent plastic hinge length

5.4.5.1 Mattock

Mattock (1965) investigated the rotational capacity of hinging regions in reinforced concrete members, as it occurs at an inner support in a continuous beam. In order to simulate the conditions at a section adjacent to a support in a continuous beam, a number of single-span beams were subjected to a concentrated load at midspan. The thirty-seven tested beams possessed different properties regarding concrete strength, reinforcement amount, and geometry.

The information collected from the tests indicates that the distribution of plasticity from the section of maximum moment depends mainly on the ratio l_0/d, and on the degree of longitudinal reinforcement in the cross section. For a simply supported beam subjected to a point load at midspan, l_0 is given by

$$l_0 = \frac{L}{2} \tag{5.39}$$

Based on this information, a method to estimate the rotational capacity of a hinging region was proposed. An expression to approximate the equivalent plastic hinge was presented as

$$l_p = 0.5d + 0.5d\left(1.14\sqrt{\frac{l_0}{d}} - 1\right) \cdot \left(1 - \frac{\omega_s - \omega'_s}{\omega_b} \cdot \sqrt{\frac{d}{412}}\right) \tag{5.40}$$

where l_0 and d should be given in millimeter [mm]. The parameters ω_s and ω'_s can be calculated according to Equations (5.17) and (5.18), while the mechanical ratio of balanced reinforcement, ω_b, is given by Equation (5.20).

Mattock showed that the maximum concrete strain was inversely proportional to the distance between the points of maximum and zero moments. For similar conditions as in his experiments, Mattock proposed that the maximum concrete compressive strain be calculated as

$$\varepsilon_{cu} = 0.003 + \frac{12.7}{l_0} \tag{5.41}$$

where l_0 is given in millimeter [mm]. The original expressions in imperial units as given in (Mattock, 1965) can be found in Appendix A.

It should be highlighted that all specimens in (Mattock, 1965) were provided with stirrups with different values of spacing. Moreover, Mattock warns that Equation (5.41) is not dimensionally consistent, and that the equation should be further refined. If not confining reinforcement is present in the cross section, Equation (5.41) is reduced to the lower limit, $\varepsilon_{cu} = 3\,‰$.

5.4.5.2 Corley

Based on a series of experiments on simply supported beams of different dimensions loaded with a concentrated load at midspan, Corley (1966) proposed an equation to determine the equivalent plastic hinge length and the maximum concrete strain as

$$l_p = 0.5d + 1.008\sqrt{d}\left(\frac{l_0}{d}\right) \tag{5.42}$$

$$\varepsilon_{cu} = 0.003 + 0.02\left(\frac{b}{l_0}\right) + \left(\frac{\rho'_w \cdot f_y}{137.9}\right)^2 \tag{5.43}$$

where l_0 and d should be given in millimeter [mm] and f_y in megapascal [MPa]. The original expressions, which have been converted into SI-units, are provided in Appendix A. The parameter ρ'_w is defined as the ratio of the volume of confining reinforcement (one stirrup plus longitudinal compressive reinforcement) to the volume of the concrete core (area enclosed by one stirrup multiplied by the stirrup spacing), while b corresponds to the width of the beam. Equation (5.43) represents the ultimate concrete strain under the conditions of confinement and binding described in (Corley, 1966), in which all specimens were provided with transversal reinforcement. For small amount of confining reinforcement and for constant moment, Corley recommends using a value $\varepsilon_{cu} = 3\,‰$, which is equivalent to the value used for ultimate strength calculations in the ACI Building Code (1963).

5.4.5.3 Mattock's discussion on Corley's work

As described in (Corley, 1967), Mattock suggested a simpler version of Equations (5.42) and (5.43) as

$$l_p = 0.5d + 0.05l_0 \tag{5.44}$$

$$\varepsilon_{cu} = 0.003 + 0.02\left(\frac{b}{l_0}\right) + 0.2\rho'_w \tag{5.45}$$

The value of ε_{cu} determined with Equation (5.45) would become more conservative for high values of ρ'_w. Mattock disregarded the spalling of concrete at high strains and adopted the compressive stress block parameters for concrete provided by ACI Building Code (1963).

Mattock discussed that Corley (1966) based the strength calculations on the yield strength of reinforcement, disregarding the increase in strength due to strain hardening effects. However, the position of the neutral axis at failure, x_u, calculated based on the yield strength of reinforcement is closer to the compressive edge than the actual position in a beam in which strain hardening of reinforcement is occurring, as the tensile reinforcement develops a larger force for the latter condition. Therefore, an underestimation of the value x_u will lead to an overestimation of ultimate curvature, as curvature and rotation are inversely proportional.

Considering that the steel may be in the strain hardening stage at large ultimate curvatures; the increase in tensile force due to this phenomenon should be factored in during the calculation of the neutral axis depth. Mattock proposed using Equation (5.46) to calculate a modified value of neutral axis depth, x'_u, to account for strain hardening effect when x_u is determined based on yield strength of the reinforcement.

$$x'_u = \frac{x_u}{0.5 + \omega_s - \omega'_s} \tag{5.46}$$

The ultimate curvature could then be calculated by inserting Equation (5.46) into Equation (5.6) as

$$\varphi_u = \frac{\varepsilon_{cu}}{x'_u} \tag{5.47}$$

5.4.5.4 Sawyer

Equation (5.48) was proposed by Sawyer in 1964 (Park and Paulay, 1975) to determine the equivalent plastic hinge length based on the assumptions that the maximum moment in the member corresponds to the ultimate moment, M_u; that the ratio between the yielding moment and the ultimate moment is equal to 0.85; and that the yielding region is extended $d/4$ past the section in witch the bending moment equals the yielding moment.

$$l_p = 0.25d + 0.075l_0 \tag{5.48}$$

6 Influences on Plastic Rotational Capacity

6.1 Introduction

This chapter explores the effects of different material and geometrical parameters – including, among others, ductility of reinforcing steel, concrete strength, bond strength, and cross-sectional size – on the plastic rotation capacity of reinforced concrete beams. The information is presented as a brief description of different results obtained in different research works.

Additionally, the influence of the loading conditions on the rotational capacity is treated. The chapter ends with a discussion on the residual load-carrying and deformation capacity of dynamically loaded reinforced concrete beams made out of both normal strength concrete and high strength concrete.

6.2 Influence of Reinforcement Properties

6.2.1 Ductility

The influence of the properties of reinforcing steel in the plastic rotation capacity of reinforced concrete beams has been proved to be significant (Latte, 1999). The choice of steel type can play an important role regarding the magnitude of the curvature at failure as well as the extension of the plastic hinge length.

The ductility of the reinforcement bars, therefore, can serve as a good indication of the rotational capacity, especially if the member fails due to rupture of the reinforcement. According to CEB Bulletin No. 242 (CEB-FIP, 1998), the ductility can be described by two parameters; namely: ratio of tensile strength to yield stress, f_t/f_y; and ultimate steel strain, ε_{su}. Both parameters are important when determining the performance of the reinforcement bars in relation to the plastic rotational capacity of the structure.

Consider Figure 6.1, which is valid for a single-span beam failing due to steel rupture. Two important observations can be made. First, the length of the plastic region decreases with decreasing f_t/f_y – hence, with increasing values of yield stress – if constant values of ultimate strength, f_t, and ultimate strain, ε_{su}, are assumed, as shown in Figure 6.1a. Contrarily, the maximum curvature at failure and ultimate moment are almost independent of the ratio f_t/f_y.

Furthermore, as stated in CEB Bulletin No. 242 (CEB-FIP, 1998), the ratio of the mean steel strain to the steel strain at a crack location, $\varepsilon_{sm}/\varepsilon_{sr}$, decreases with a reduction in f_t/f_y due to a decrease in the penetration of yielding in the vicinity of the crack. These effects, therefore, contribute to the reduction in plastic rotational capacity if the ratio f_t/f_y decreases.

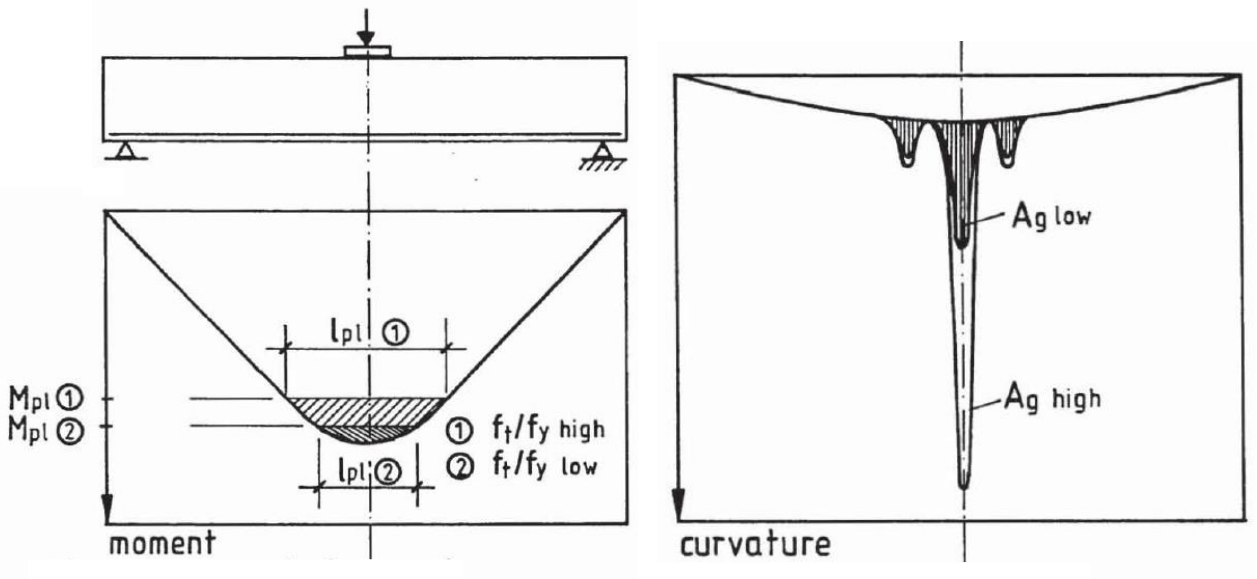

(a) Moment diagram, ε_{su} and f_t constant.

(b) Curvature diagram, f_t/f_y constant. The parameter A_g corresponds to the ultimate steel strain, ε_{su}.

Figure 6.1 Influence of ductility on the length of the plastic hinge and ultimate curvature given the same ratio of reinforcement, modified from (Langer and Eligehausen, 1987).

On the other hand, when f_t/f_y is kept constant, the length of the plastic hinge length is observed to be constant for different values of ε_{su}. However, the ultimate curvature does exhibit an increase for a larger value of ε_{su}, resulting in an increase in plastic rotational capacity, as illustrated in Figure 6.1b.

However, the influence of both parameters is dependant on the amount of reinforcement steel. For lower reinforcement ratios, where rupture of steel is the failure mechanism, both parameters have a direct influence. For larger reinforcement amounts which lead to concrete crushing the length of the plastic hinge, and hence the plastic rotational capacity, increases with an increasing ratio f_t/f_y. However, ε_{su} is not as relevant since it is not fully utilized in this case; although it is important for the definition of the transition point between the two failure modes.

It should be noticed, however, that the influence of both parameters is difficult to separate. In CEB Bulletin No. 242 (CEB-FIP, 1998) a new parameter to judge the effect of steel ductility on deformation capacity, which combines f_t/f_y and ε_{su}, has been introduced. The new parameter, denoted p, was determined through an extensive numerical analysis considering a reference beam tested during an experimental study conducted in Turin (Bosco and Debernardi, 1992). The properties of the reference beams are: cross section 30×60 cm, span length 6 m, 2 longitudinal reinforcement bars $\phi 12$, and $x/d = 10$ at failure. The numerical analysis showed that for cold-worked steel the plastic rotation is proportional to the parameter p as

$$\theta_{pl} = 1.3 \cdot p = 1.3 \cdot \varepsilon_{su}{}^{0.73} \cdot \left(\frac{f_t}{f_y} - 1 \right)^{0.92} \tag{6.1}$$

which only depends on steel characteristics. According to Equation (6.1), two beams reinforced with different steel types, but otherwise identical properties, will exhibit a plastic rotation capacity proportional to the parameter p.

6.2.2 Hot-worked and cold-worked steel

The influence of heat-treated and cold-worked steel has been briefly described in CEB Bulletin No. 242 (CEB-FIP, 1998). As discussed in Section 2.3, the ratio f_t/f_y and the ultimate strain, ε_{su}, exhibit larger values for heat-treated bars, which ultimately favors the plastic rotational capacity if hot-worked steel is used to reinforce a given concrete beam. Furthermore, hot-treated reinforcing steel can be expected to have larger plastic rotational capacity than cold-worked steel given same ratio f_t/f_y and ε_{su}. One of the main reason for this phenomenon is the plastic plateau present in the stress-strain relationship of hot-rolled steel, as illustrated in Figure 2.4.

CEB Bulletin No. 242 introduces the parameter ε_{sh}, which is equivalent to the length (unitless) of the plastic plateau in the stress-strain diagram, to take into account the increment of rotation capacity due to the post-yielding plastic plateau. The effects of ε_{sh} can be considered when calculating p as

$$p = \left(\varepsilon_{su} + 3\varepsilon_{sh}\right)^{0.75} \cdot \left(\frac{f_t}{f_y} - 1\right)^{0.9} \tag{6.2}$$

The characteristics of the stress-strain relationship in the post-yield range, which depend on the steel type, also have a significant influence on the deformation capacity of concrete beams. This can be explained considering the ratio between the mean steel strain and the steel strain in the crack, $\varepsilon_{sm}/\varepsilon_{sr}$. For a tension specimen reinforced with low ductility cold-worked steel, the ratio of average strain to strain in the crack shows a small value at failure, whereas for specimens reinforced with high-ductility heat-treated steel, the ratio $\varepsilon_{sm}/\varepsilon_{sr}$ decreases to a value similar to that observed for specimens reinforced with cold-worked steel, but increases gradually in the hardening range.

6.3 Concrete Influence on Rotational Capacity

6.3.1 Concrete strength

In (Fransson, 1997) and (Magnusson, 2007) a discussion of the effect of concrete compressive strength, f_c, on rotation capacity can be found. The authors concluded that the rotational capacity is almost independent of the concrete strength provided that the mechanical reinforcement ratio, ω_s, is constant. This behavior can be explained by the fact that the distance to the neutral axis from the compressed edge decreases as the concrete strength is increased, and therefore increases the internal lever arm, which effectively compensates for the more brittle nature of higher strength concrete. On the other hand, the plastic rotation is significantly influenced by the variation of ω_s in such a way that the maximum deformation increases for decreasing values of ω_s.

However, the compensating effect of increased lever arm in high strength concrete beams is assumed to be beneficial only when concrete crushing is the limiting factor. High strength concrete when reinforcement rupture is limiting would provide with a detrimental effect to the plastic rotational capacity, since the height of the compressive zone would decrease, resulting in an increase of tensile steel strain.

Lopez and Bernardo (2003) studied the influence of concrete strength on plastic rotation capacity on two groups of concrete beams with the same dimensions and mean tensile reinforcement ratios, ρ_s, of 2.13 % and 2.78 %, respectively. Two values of concrete strength were considered for each group; namely, 64 MPa and 84 MPa. The beams had a free span of 2.8 m and were subjected to two point loads applied approximately at the third-points. It was observed that the plastic rotation tended to increase with increasing concrete strength for the same percentage of reinforcement. Observe that a larger value of f_c results in a smaller value of ω_s if ρ_s is kept constant. Additionally, the authors reported a reduction in the rotational capacity for increasing longitudinal reinforcement amount and constant concrete strength. It should be noted that in (Lopez and Bernardo, 2003) it is not stated whether the section is limited by concrete crushing or steel rupture. However, the ratio x/d at ultimate limit state for a beam section with $\rho_s = 2.13\,\%$ (calculated according to the mechanical and geometrical properties of the specimens provided in (Lopez and Bernardo, 2003)) takes an approximate value of 0.19, which, by correlation with Figure 5.13, indicates that concrete crushing was the dominant failure mode.

6.3.2 Ultimate strain and compression zone confinement

The ultimate concrete strain, ε_{cu}, and strain at maximum stress, ε_{c2}, in Figure 2.8 also have an influence on the rotational capacity of a structure. As described in (Plem, 1981), the values $\varepsilon_{c2} = 2\,‰$ and $\varepsilon_{cu} = 3.5\,‰$, which are currently recommended by Eurocode 2 (CEN, 2004), are chosen rather conservatively. Even though the chosen ε_{c2} and ε_{cu} have little influence when calculating the ultimate moment, their importance is more profound regarding plastic rotational capacity for the case when the element fails due to concrete crushing. Indeed, a larger value of ε_{cu} would represent an increase in ultimate curvature, φ_u, and consequently in the rotation capacity, when failure is reached due to concrete crushing. Furthermore, the parameter ε_{cu} is important to determine the transition point between steel rupture and concrete failure.

The behavior of the concrete in compression is significantly influenced by confinement action. Confinement is normally introduced by stirrups enclosing the concrete in compression. Uni-axial compression tests show that the use of stirrups affect minimally the compressive strength, but influences significantly the ultimate concrete strain, ε_{cu} (CEB-FIP, 1998).

In CEB Bulletin No. 242, it is stated that providing confinement is a very effective strategy to increase the plastic rotational capacity when concrete compression governs the failure of the member. Furthermore, decreasing the spacing between stirrups would enhance the confining action and, therefore, increase the plastic deformation capacity. On the opposite end, little improvement of the rotational capacity can be expected if stirrups are placed in an element where rupture of the tensile steel is the dominant failure mode.

6.3.3 Influence of bond strength

Among all factors which influence rotational capacity, the bond behavior between the reinforcement and the concrete is one of the most complex, since it is itself dependent on a broad range of parameters, both of the materials and the member geometry, which are linked together. Additionally, the large scatter of combined actions which can be observed in bond tests makes it difficult to draw direct conclusions regarding the influence of each individual parameter (Latte, 1999). However, it has been experimentally found that a strong bond between steel and concrete results in an increase of tension stiffening, leading to a reduction of crack width, and thus a decrease in rotation capacity (CEB-FIP, 1998).

The effect of bond between reinforcement bars and concrete on plastic rotation is illustrated in Figure 6.2, according to simulations performed by Langer and Eligehausen (1987). A significant decrease of plastic rotational capacity can be observed when perfect bond is considered in the simulations in comparison with the rotational capacity obtained when no bond is assumed. Considering this fact, concrete elements reinforced with ribbed bars will exhibit a different performance compared to a member reinforced with plain bars, even if the ductility of both types of bars is the same.

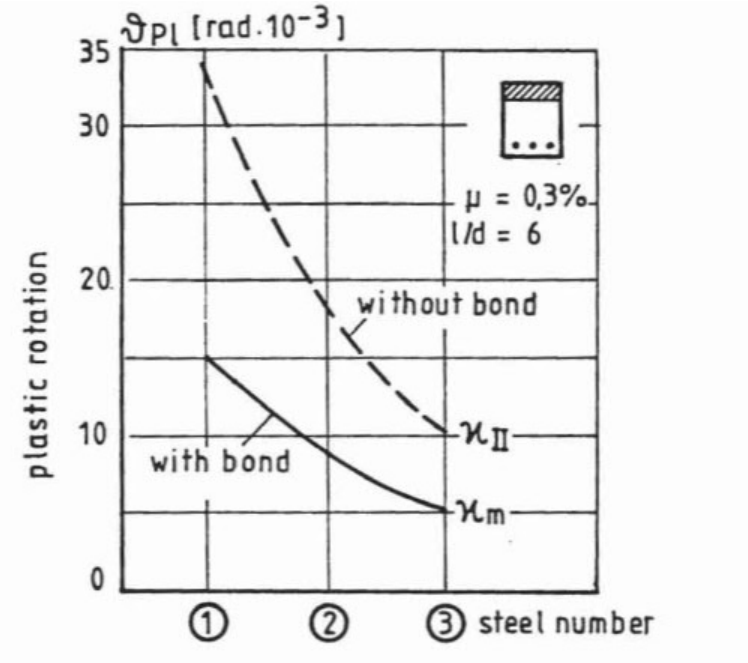

Figure 6.2 Bond influence on the plastic rotational capacity (Langer and Eligehausen, 1987).

Similar results are also reported in (CEB-FIP, 1998) from investigations carried out in 1990 in the University of Pavia. In this research, a comparison of the plastic rotational capacity of one-way slab specimens subjected to two different loading conditions (three-point loading and five-point loading) and reinforced with reinforcement bars with different ductility and surface properties (plain and ribbed reinforcement meshes) was performed. It was found that the plastic deformation capacity of the slabs containing the plain reinforcement was higher due to an increased transmission length in case of low bond, meaning that more steel would yield in the vicinity of the crack before full interaction between concrete and reinforcement was reached.

However, it should be observed that the crack distance and number of cracks that develop in the plastic hinge region, which are directly influenced by the bond strength, also affect notably the rotation capacity of the member.

6.4 Influence of Size

A summary of various investigations regarding the effects of beam depth and its influence on rotation capacity has been performed in (Fransson, 1997). The author explains that Bosco and Debernardi (1992) carried out a series of experiments on 44 simply supported reinforced concrete beams with heights 0.2 m, 0.4 m, and 0.6 m, which were subjected to a concentrated load acting at the midspan position. The amount of reinforcement was varied between $\rho_s = 0.13\,\%$ and $\rho_s = 1.7\,\%$; while the beam slenderness, $L/h = 10$, and the ratio of effective depth to total depth, $d/h = 0.9$, were kept constant. It was concluded from the experimental tests that the plastic rotation capacity decreases as the beam height increases, as illustrated in Figure 6.3 for different specimens with $\rho_s = 1.13\,\%$.

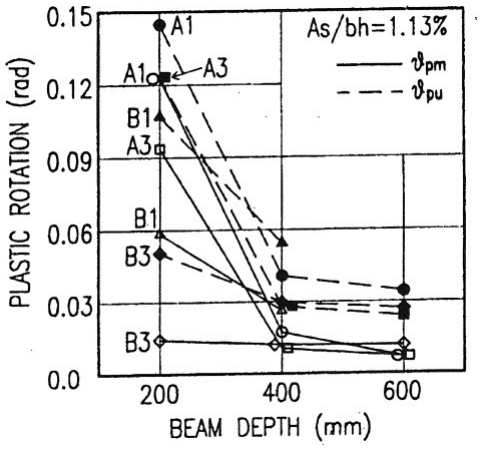

Figure 6.3 Experimental plastic rotation vs beam depth in Bosco and Debernardi's research (Fransson, 1997). The dashed lines refer to ultimate rotation, while the solid lines correspond to values at maximum moment.

Bigaj and Walraven (1993) found a similar relation for members that fail due to rupture of the steel reinforcement bars as well as for members failing due to crushing of concrete. The beams were made out of normal strength concrete, with reinforcement ratios ranging from 0.28 % to 1.12 %. They observed that beams with smaller section height show a much higher plastic rotation capacity than members with the same characteristic but larger dimensions.

Carpinteri *et al.* (2009) described a numerical algorithm based on non-linear fracture mechanics models to investigate the effect of the mechanical and geometrical parameters on the rotational capacity of RC beams. The authors made an extensive comparison with the experimental results for the beams tested by Bosco and Debernardi (1992) and with the methodology presented in Eurocode 2, as described in Section 5.4.2. They concluded that, regardless of the reinforcement ratio, the behavior of the beam becomes more brittle as the beam height increases. It was observed that beams with a 0.2 m depth have rotational capacity greater than that suggested by Eurocode 2; while for beam depths 0.6 m, and 0.8 m the guidelines provided by Eurocode 2 appear to overestimate the rotational capacity. However, it is worth highlighting that Carpinteri *et al.* (2009) used the reference curve for steel class C and concrete class less than or equal to 50 MPa provided by Eurocode 2 (see Figure 5.13) as the basis of comparison, without apparent consideration of the shear slenderness, λ.

6.5 Influence of Load Application

6.5.1 Introduction

Different studies have shown that the type of loading has a significant effect on the plastic rotation capacity and on the length of the plastic hinge. Three different loading situations are commonly discussed in research papers, as shown in Figure 6.4; namely: (a) concentrated load at midspan or three-point loading, which is equivalent to a linear moment distribution; (b) four-point loading, constant moment between two loads; and (c) uniformly distributed loading, which exhibits a nonlinear moment distribution.

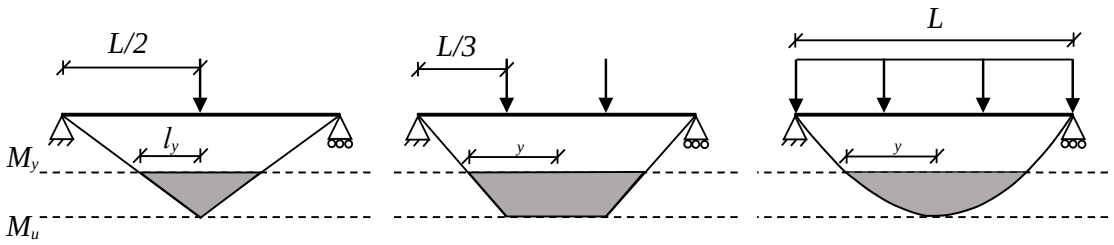

(a) Three-point loading. *(b) Four-point loading.* *(c) Uniform load.*

Figure 6.4 Moment diagram along a simply supported beam for three different static load cases.

The shape of the moment diagram and the length of the yielding region, l_y, as shown in Figure 6.4, provides a good explanation for the different values of available plastic rotation. For the same reinforcement amount, the yielding length in a beam subjected to concentrated load is less than the yielding length of a beam under four-point or uniformly distributed loading, and therefore exhibits a smaller rotation. On the other hand, beams subjected to uniform load and four-point loading show a considerable increase of plastic hinge length and, therefore, an increased rotational capacity of such loaded structures can be expected.

6.5.2 Loading conditions and reinforcement ratio

The influence of loading conditions on beams with same reinforcement ratio was investigated in (Kheyroddin and Naderpour, 2007). A series of numerical analyses on 15 simply supported beams with different amount of tension reinforcement were performed for the three different load conditions presented in Figure 6.4. For a constant amount of reinforcement with mechanical reinforcement ratio $\omega \leq 0.38$, and similar geometry, the largest available plastic hinge rotation was observed for beams under uniformly distributed load. The plastic rotation decreased as the loading type was changed to four-point loading, and showed a minimum value for a concentrated load applied at midspan.

However, it was also found that for values of $\omega \geq 0.38$, the plastic rotation capacity for four-point loaded beams was slightly smaller than the corresponding values obtained for beams loaded with a concentrated load at midspan. Similar results were obtained by Ko *et al.* (2001), who conducted tests on 36 simply supported high-strength concrete beams with different values of compressive strength, different reinforcement ratios, and two different loading types. Experiments showed that the ductility tends to be larger for the beams subjected to concentrated load than for those under four-point load for specimens with $\omega \geq 0.54$.

Kheyroddin and Naderpour (2007) discuss that comparable conclusions were drawn by Bosco and

Debernardi (1992), where the plastic hinge rotation of lightly reinforced beams subjected to three concentrated loads applied symmetrically with respect to midspan was higher than that of beams subjected to a concentrated load at midspan, while the plastic rotation tended to be higher for midspan-loaded beams for heavy reinforcement ratios.

It is concluded in (Kheyroddin and Naderpour, 2007) that the plastic rotation under four-point loading is dependent on the length of constant moment zone – that is, the distance between the two loads – and the localization of the plastic zone and the crushing of concrete, which takes place within a narrow area. The variation of curvature along half the span of a beam with $\omega = 0.412$ subjected to different types of loading is presented in Figure 6.5. Even though the yielding length for the case with four-point loading is larger than for the other two load cases, the localization of the plastic zone and the crushing of concrete lead to smaller values of θ_p for beams under four-point loading compared to the plastic capacity of beams subjected to concentrated loads.

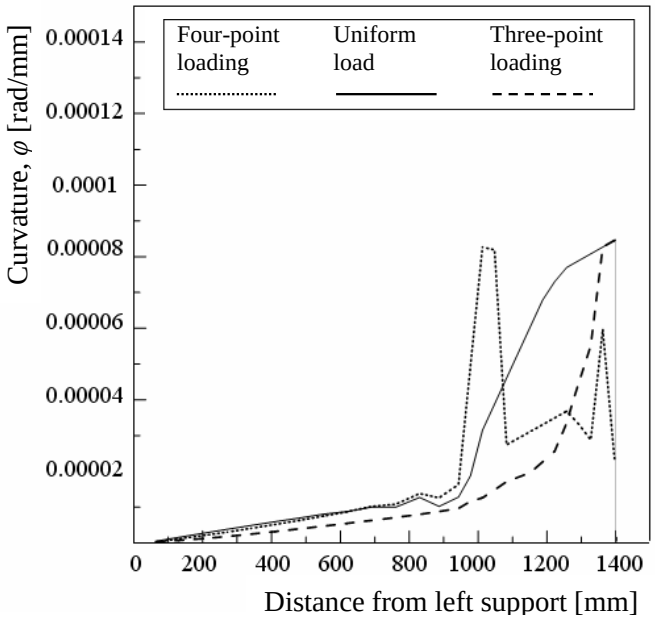

Figure 6.5 Effect of loading type on curvature of beams with $\omega = 0.412$, modified from (Kheyroddin and Naderpour, 2007).

6.5.3 Static and dynamic loading

A reinforced concrete beam which is subjected to a time-dependent load generally exhibits a stiffer response with increased loading rate (Costovos *et al.*, 2010). The stiffer response due to impulse loading can be explained due strain rate effect, as described in Section 3.3, which lead to a higher yield stress of reinforcement steel and higher concrete strength.

Investigations carried out by Miyamoto *et al.* (2008) show that with an increased loading rate also comes a higher maximum load which the structure can endure, albeit with a reduction in its deformability, see Figure 6.6. Furthermore, it was concluded that the total energy absorption, defined as the area under the load vs mid-span deflection curve also increased with increased loading rate.

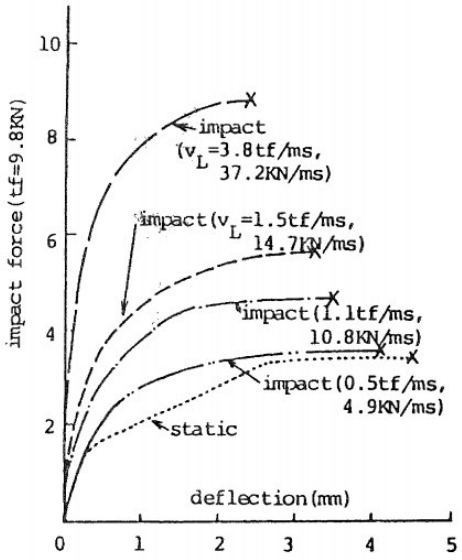

Figure 6.6 Impact force vs midspan deflection for different loading rates (Miyamoto et al., 2008).

Similar results were found in (Adhikary *et al.*, 2012), where a series of tests on simply supported RC beams with 150 mm × 250 mm cross section and 1400 mm free span subjected to varying rates of concentrated loading were conducted. The amount of tensile reinforcement in all specimens was $\rho_s = 2.4\,\%$, while only part of the test samples were provided with shear reinforcement. Due to the lack of transverse reinforcement, the theoretical failure mode under static loading for some specimens was shear failure. Four different rates of loading were tested, namely: static, low (1 s), medium (100 ms), and high (20 ms). For beams designed to fail in bending, it was observed that the load resistance increased by 7 %, 11 % and 15 % for low, medium, and high loading rates, respectively, compared to the static case. Conclusions were similar to what was reported in (Miyamoto *et al.*, 2008) in that beams subjected to an increased load rate exhibit higher energy absorption but at a cost of the deformability of the structure. Additionally, it was found that transverse reinforcement had a significant contribution by confining the core concrete; therefore, specimens having more transverse reinforcements were capable to absorb more energy.

6.6 Residual Capacity in Dynamically Loaded RC Beams

6.6.1 Introduction

Various experiments have been conducted to assess the residual capacity of concrete beams after the application of an impact load. However, such studies mainly focus on determining the influence of the impact loading on the peak load capacity and stiffness of the beam, rather than on the remaining plastic rotation capacity. Some of these research works are discussed in this section, including the conclusions made by the respective authors regarding ultimate load capacity and stiffness.

6.6.2 Residual capacity on normal strength concrete

Adhikary *et al.* (2015) conducted a series of experiments similar to the experiments carried out in this thesis work. Several reinforced concrete beams were tested under free-falling impact loading from various

drop heights ranging from 0.15 m to 1.20 m. Such beams were subsequently subjected to static loading in order to study the residual response. The behavior of the impact-damaged beams were compared to the behavior of undamaged beams subjected to static loading only.

However, only one test for a given type of specimens and at a certain drop-height was carried out, whereas in the present studies different tests for the same conditions are conducted.

It was observed that, for low impact energy, the post-impact behavior of the beams show virtually the same stiffness and slightly decreased load resistance as compared to the behavior of undamaged beams. However, as the drop-height increased, the residual stiffness and the load resistance of the statically loaded beams decreased notably, see Figure 6.7. This behavior was noticed for both shear failure as well as for flexural failure. The reduction in stiffness and load capacity can be explained due to the appearance of several flexural and shear cracks and the decrease in the cross-sectional area due to crushing of top concrete at impact.

Additionally, for beams with identical conditions, but with a higher amount of transverse reinforcement, the degradation on stiffness and resistance was significantly less pronounced. Figure 6.7 illustrates the load-midspan deflection curves for two different beam types with the same geometry with and without transverse reinforcement tested by (Adhikary *et al.*, 2015), where a better performance due to higher amount of shear reinforcement can be observed after impact.

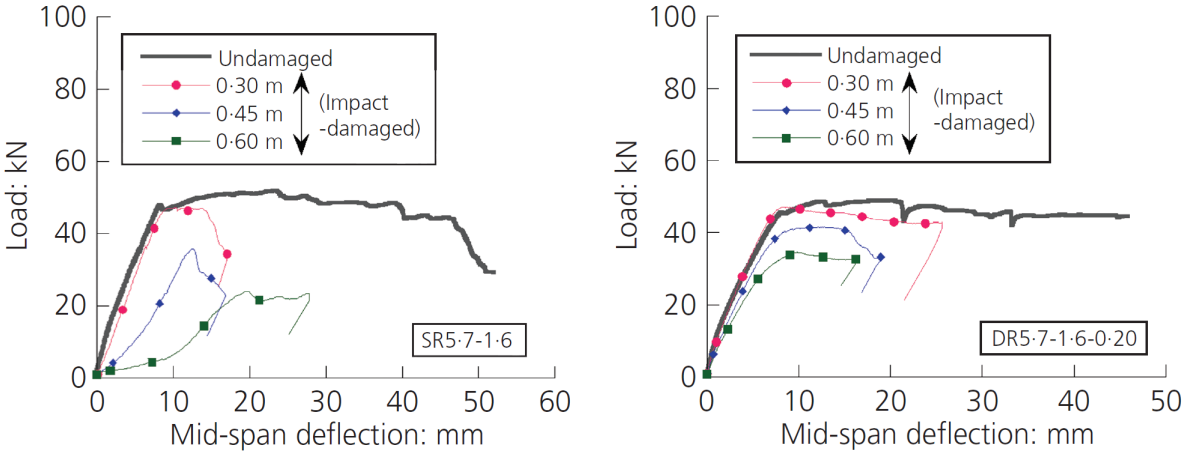

(a) Specimens without stirrups. *(b) Specimens with stirrups.*

Figure 6.7 Static load against mid-span deflection of undamaged and impact-damaged beams for various drop heights (Adhikary et al., 2015).

Comparing the maximum displacement for undamaged beams loaded statically to failure with the maximum displacement of beams previously subjected to a drop-weight impact in Figure 6.7 evidences that a portion of the plastic deformation capacity is exhausted during impact loading. A clear relationship between the residual peak strength and the drop height can also be observed.

An interesting observation was the change of failure mode for one group of specimens with the same amount of reinforcement and same geometry after being subjected to impact loading, as shown in

Figure 6.8. The undamaged specimen exhibited a shear failure mode and a low deformation capacity. However, the impact-damaged beams failed in bending and the measured values of ultimate midspan deflection was significantly larger. Additionally, the stiffness and load capacity of the specimens did not show a significant reduction due to impact loading. Possible explanation for the change in failure mode is the formation of flexural cracks during impact and the similarity in shear and moment capacity ($V_d = 67.8\,\text{kN}$ and $M_d = 70.4\,\text{kN}$) for this group of specimens, which implies that a small reduction in moment capacity makes bending the dominant action.

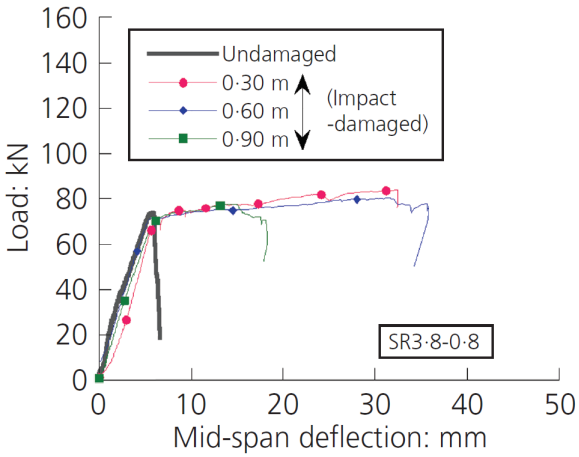

Figure 6.8 Change in failure mode after impact loading (Adhikary et al., 2015).

6.6.3 Residual capacity on high strength concrete

Some authors have focused their effort into studying the post-impact capacity of beams made out of high-strength concrete. Magnusson (2007), for instance, investigated the residual strength of reinforced concrete beams with 140 MPa and 200 MPa compressive strength, with and without steel fibers. The beams were subjected to air-blast loading. It was noticed that the residual load carrying capacity tended to reach the descending branch of the load-deflection curve of the statically tested undamaged beams, albeit with a decreased stiffness, see Figure 6.9. Additionally, the results showed that the reduction of the load-carrying capacity was smaller for fiber-reinforced concrete beams.

Fujikake *et al.* (2006) tested a number of simply-supported beams with an I-shaped cross section made out of Reactive Powder Concrete (RPC) under drop-weight impact. RPC, reinforced with short steel fibers, is characterized by an ultra-high strength of over 200 MPa and high fracture toughness. The I beams had a cross section 200 mm high and 150 mm wide, and a free span of 1200 mm long. The reinforcement ratio was $\rho_s = 2.6\,\%$. Even though the beams were not provided with shear reinforcement, all specimens were observed to fail under bending mechanism. Some beams were loaded statically only, though the loading was finished when the midspan deflection reached 40 mm. The rest of the specimens were subjected to a drop hammer impact and subsequently brought to failure under a deformation-controlled static load applied at midspan. Figure 6.10 illustrates the load-deformation curves of two specimens subjected to hammer impact from two different heights. The results showed that the residual load-midspan deflection curve tended to meet the curve obtained for an equivalent virgin specimen under static loading, and not visible reduction of stiffness was observed. This suggests that the damage due to impact loading on

RPC beams can be directly related to maximum deformation response at impact. Then, the maximum deformation can be used as an index for evaluating the overall flexural damage.

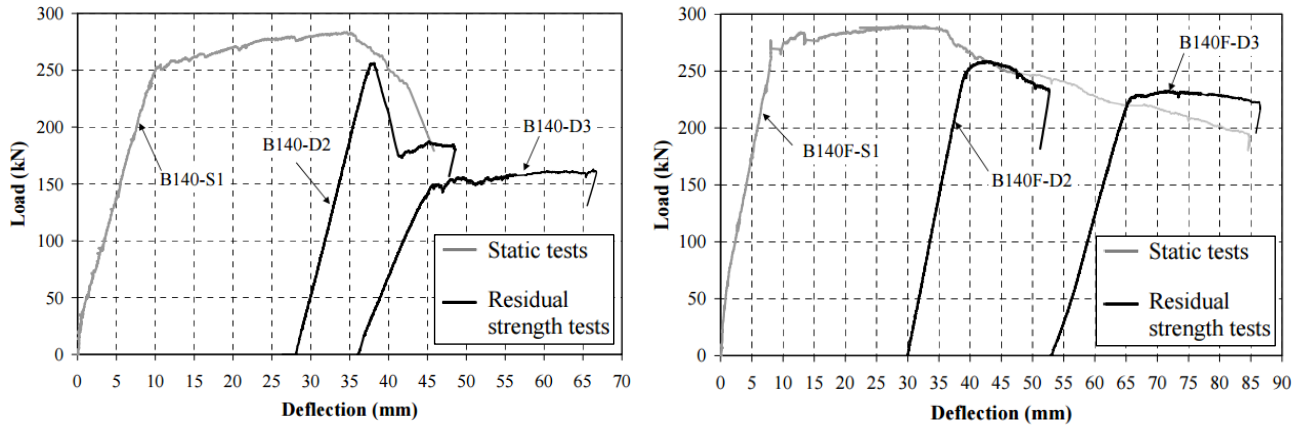

(a) Specimens without fibers. *(b) Specimens with fibers.*

Figure 6.9 Static and residual tests on 140 MPa concrete beams without (B140) and with (B140F) steel fibers (Magnusson, 2007).

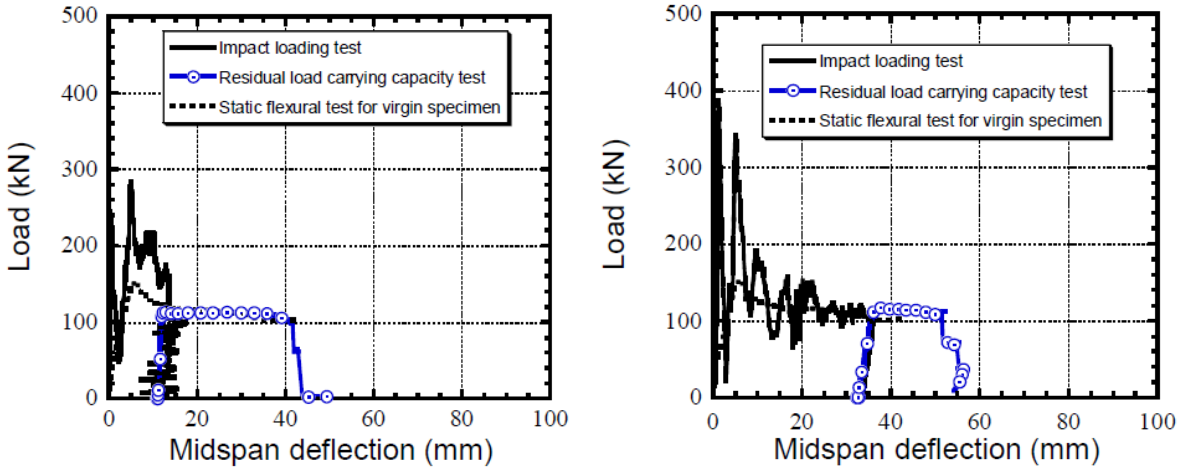

(a) Drop height = 0.8 m. *(b) Drop height = 1.6 m.*

Figure 6.10 Load-midspan relations obtained in impact loading test and post-impact load carrying capacity test of RPC I-beams. Comparison with static flexural tests on undamaged specimens (Fujikake et al., 2006).

Yoo *et al.* (2017) also carried out a series of drop tests on simply supported Ultra-High Performance concrete (UHPC) beams. The impact load was applied at midspan by dropping a hammer with a mass of 510 kg from two different drop heights of 0.9 and 1.15 m. The specimens were classified in three series: specimens without fibers, specimens with smooth steel fibers, and specimens with twisted steel fibers. In accordance with the findings described in (Fujikake *et al.*, 2006), it was noticed that the drop-weight impact did not cause a significant change in the stiffness of the statically reloaded beams,

and the overall flexural damage corresponded only to a right-shift in the moment-curvature relationship. The authors concluded that the residual capacity of UHPC beams can be simply estimated if the static flexural response and the maximum deflection due to impact are known, without performing residual tests. In that sense, the residual capacity could be estimated by finding the value of moment (or load) on the static moment-curvature (or load-deflection) relation which corresponds to the maximum curvature (or maximum deflection) due to impact loading.

Yoo *et al.* (2017) found that beams with steel fiber exhibited a much higher residual stiffness and residual load capacity than those without fibers. In contrast, fiber-reinforced beams showed a significantly lower residual deformation capacity - defined as the curvature corresponding to rupture of a reinforcement bar - than the beams without fibers, see Figure 6.11. This behavior can be explained due to the crack localization phenomenon observed in UHPC beams with steel fibers; that is, only one or two cracks, where the fibers have been pulled out, opened up considerably more than the others; therefore, the deformation in the steel bars is localized at the point of crack localization. Conversely, the beams without steel fibers experienced several cracks with large opening and thus the steel strain was dispersed along the length of the beam rather than being localized. This observation differs with the results from static tests on *undamaged* fiber-reinforced concrete beams reported in (Magnusson, 2007), where it is stated that the ductility increases notably for beams reinforced with steel fibers.

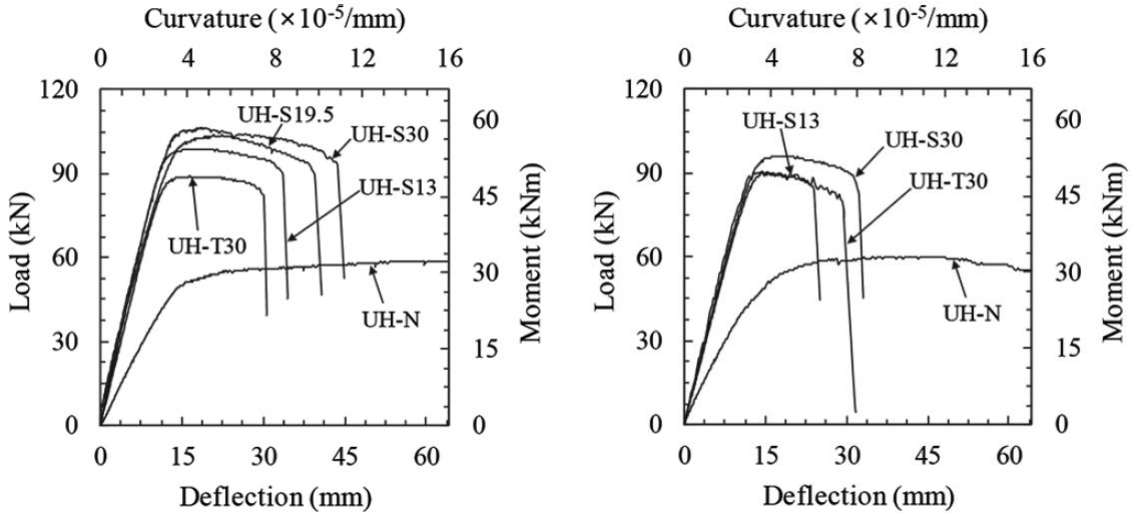

(a) Drop height = 0.9 m. *(b) Drop height = 1.15 m.*

Figure 6.11 Comparison of load-deflection relations after impact damage for specimens without fiber (UH-N), specimens with smooth steel fiber (UH-SX), and specimens with twisted steel fibers (UH-TX) (Yoo et al., 2017).

A comparison of the response of specimens with smooth steel fibers before and after impact loading for two different drop-heights is shown in Figure 6.12, as described in (Yoo *et al.*, 2017). It can be seen that the initial stiffness of the UHPC beams was virtually not affected by the impact damage. Moreover, the residual moment-curvature relationships display a similar response to those of the undamaged specimens. The authors attribute this results to the fiber bridging capacity after cracking provided by the steel fibers, which leads to a strain-hardening response.

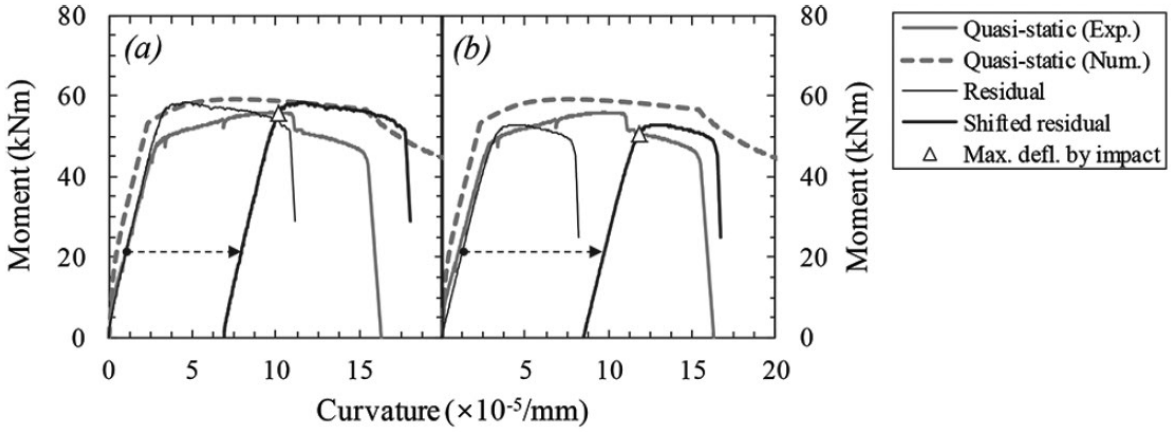

Figure 6.12 Comparison of moment-curvature curves before and after impact damage for specimens with smooth steel fibers (Yoo et al., 2017). (a) Drop height = 0.9 m (b) Drop height = 1.15 m.

7 Experimental Procedure

7.1 General Description

A total of 18 reinforced concrete beams were cast and tested under different loading conditions in order to, among others, study the impact behavior of the specimens and determine how plastic rotational capacity is influenced by impact loading. The concrete specimens were equally divided into three series of six beams each, namely: Series-1, Series-2, and Series-3. Each series was subjected to a certain loading condition and testing procedure.

The specimens of Series-1 were initially tested dynamically by releasing a drop-weight of 10.1 kg from a height $h = 2.5$ m. The specimens of Series-2 were also tested dynamically by releasing the same drop-weight from a height $h = 5.0$ m. Thereafter, the dynamically loaded test specimens of Series-1 and Series-2 were tested statically under three-point loading in order to determine the residual plastic rotational capacity. The specimens of Series-3 were only subjected to static loading by means of three-point loading in order to determine the plastic rotational capacity of undamaged beams.

All tests were recorded using a camera positioned in front of the test specimens. During the impact-loading tests, a high-speed camera which is able to record at a frame-rate of 5000 fps was used. On the other hand, a set of cameras with a frame-rate of 0.5 fps was used during the static trials of undamaged and damaged beams in order to decrease the amount of data stored. The information recorded was subsequently processed using digital image correlation (DIC).

7.2 Test Specimens

7.2.1 Geometry of the specimens

As shown in Figure 7.1, the beams have a cross-sectional area of 100×100 mm and a total length of 1180 mm. The specimens were provided with four longitudinal reinforcement ribbed bars with a nominal diameter of 6.0 mm and steel class K500C-T. No transversal reinforcement was used.

The distance from the center of the bars to the concrete surface was 20 mm. However, no reinforcement bar spacers were used during assembling or casting of the beams to keep the bars in place as the length was considered relatively short. As a result, deviations with respect to the nominal distance of 20 mm may have occurred in some of the specimens, this is addressed further in Section 9.6

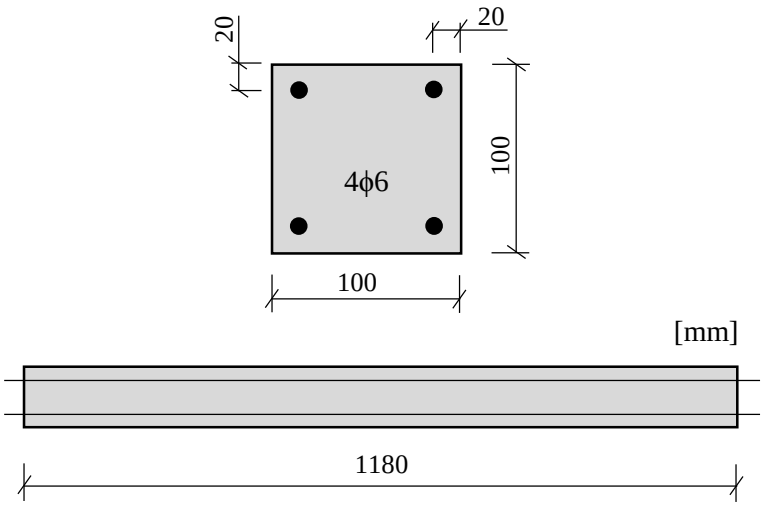

Figure 7.1 Geometry of the concrete beams.

7.2.2 Beam classification

The reinforced concrete beams were cast from two concrete batches of the same proportions. The casting procedure was completed during one day under similar conditions. The specimens were kept in their molds and covered with a plastic foil during 30 days for curing. Nine beams were produced out of each batch. The beams made out of batch number 1 were labeled from number B-01 to B-09. Likewise, beams made from batch 2 were labeled from number B-10 to B-18.

Beams of each batch were equally distributed within the different testing series so that each of the series was formed by three beams from batch 1 and three beams from batch 2. Table 7.1 shows how the beams were arranged according to the different experiments.

Table 7.1 Classification of beams.

Specimen	Batch	Series	Experiment
B-01, B-02, B-03	1	1	Drop-height $h = 2.5$ m
B-04, B-05, B-06	1	2	Drop-height $h = 5.0$ m
B-07, B-08, B-09	1	3	Static testing only
B-10, B-11, B-12	2	1	Drop-height $h = 2.5$ m
B-13, B-14, B-15	2	2	Drop-height $h = 5.0$ m
B-16, B-17, B-18	2	3	Static testing only

7.3 Material Properties

7.3.1 Concrete proportions

The concrete specimens were cast from two batches, which were prepared by following the same recipe, as shown in Table 7.2, with a target mean compressive strength $f_{cm,target} = 38$ MPa corresponding to concrete class C30/37. The amount of water in the recipe was adjusted according to the water content in the aggregates. To that end, the water content in both the fine and coarse material was previously

determined, as listed in Table 7.3.

Table 7.2 Concrete recipe proportions, water to cement ratio of mixture corresponds to w/c = 0.55.

Material	Description	[kg/m^3]
Cement	CEM II/A-LL 42.5 R	335
Limestone filler	Limus 40 (Nordkalk)	160
Sand	Sköllunga sand (Ucklum)	747.3
Aggregate 4-8 mm	Crushed	268.9
Aggregate 8-16 mm	Crushed	717.1
Superplasticiser	MasterGlenium 51/18 (BASF)	5.36
Water	– – –	184.3

Table 7.3 Water content in aggregates.

Material	Water content [%]
Sand	6.61
Aggregate 4-8 mm	1.17
Aggregate 8-16 mm	0.54

7.3.2 Concrete properties

In order to determine the compressive and tensile strength of the hardened concrete of each batch, testing was performed in accordance with (CEN, 2009a) and (CEN, 2009b) at 28 days and at 36 days after casting (the latter corresponding to the last day of static tests). Six cubic specimens with nominal dimension of 150 mm were cast from each batch. For each batch, three cubic specimens were tested for compressive strength, while the other three were tested for splitting tensile strength. The average strength properties are presented in Table 7.4. The results for all individual cubic specimens are provided in Table B.1 of Appendix B.1.

In order to determine the fracture energy, a wedge splitting test was performed on three cubic specimens with nominal size of 150 mm cast from batch 2. The procedure was carried out in accordance with the guidelines described in (Löfgren *et al.*, 1981). The horizontal splitting force, F_{sp}, was calculated from the vertically applied force, whereas the *crack mouth opening displacement* (CMOD) was measured by a clip gauge at the same level at which the splitting force was applied to the specimen. The relationship between the horizontal splitting force and CMOD could therefore be established, and the fracture energy was calculated as the total area below the obtained curves. The average fracture energy, G_f, is shown in Table 7.4. The F_{sp} vs CMOD curves, as well as the calculated fracture energy, can be seen in Appendix B.2 for each specimen.

Table 7.4 Average values of concrete properties determined experimentally. Observe that the fracture energy was only determined from batch 2.

Property	Description	Batch 1	Batch 2	Average
$f_{cm,cube,28}$	Mean compressive cube strength after 28 days	48.7 MPa	52.6 MPa	50.6 MPa
$f_{cm,cube,36}$	Mean compressive cube strength after 36 days	50.3 MPa	55.2 MPa	52.7 MPa
$f_{ctm,sp,28}$	Mean splitting tensile strength after 28 days	3.6 MPa	4.0 MPa	3.8 MPa
$f_{ctm,sp,36}$	Mean splitting tensile strength after 36 days	3.9 MPa	4.3 MPa	4.1 MPa
$G_{f,36}$	Fracture energy after 36 days	– – –	132 Nm/m^2	132 Nm/m^2

Table 7.5 shows a summary of equivalent values of cylinder concrete strength which were determined from the material tests results by using Equations (2.5), (2.6), and (2.7). Observe that the values of mean compressive strength presented in Table 7.5 correspond rather well with the target mean compressive strength, $f_{cm,target} = 38$ MPa.

Table 7.5 Calculated values of cylinder concrete properties.

Property	Description	Average
$f_{cm,28}$	Mean compressive strength after 28 days	40.5 MPa
$f_{cm,36}$	Mean compressive strength after 36 days	42.2 MPa
$f_{ctm,28}$	Mean tensile strength after 28 days	3.4 MPa
$f_{ctm,36}$	Mean tensile strength after 36 days	3.7 MPa
$E_{cm,28}$	Modulus of elasticity after 28 days	33.5 GPa
$E_{cm,36}$	Modulus of elasticity after 36 days	33.9 GPa

7.3.3 Steel properties

Tensile testing was also performed on the steel bars used to reinforce the concrete beams. Seven samples of reinforcement bars were tested under tensile stress in a universal testing machine in order to get accurate values of strength properties, where values of load vs deformation were recorded until failure. This information was used to determine the yield stress, the ultimate tensile strength, and the ultimate steel strain, by converting the values of load and deformation into values of stress and strain using a nominal diameter of 6.0 mm and a reference length of 200 mm. However, in order to accurately determine the modulus of elasticity, an extensometer was used to directly record values of strain until a point short after the onset of yielding. The average values of the steel properties are shown in Table 7.6

Table 7.6 Mechanical properties of the reinforcing steel, mean values.

Property	Description	Value
f_t	Ultimate tensile strength	686 MPa
$f_{0.2}$	Proof stress	575 MPa
E_{sm}	Modulus of elasticity	196 GPa
ε_{sy}	Yield strain	2.93 ‰
ε_{su}	Ultimate strain	10.8 %

Results for all tested reinforcement samples are given in Appendix B.3, including stress-strain curves. It should be remarked that no distinct yield strength was observed and that the reinforcement bars exhibited a behavior similar to cold-worked steel. For that reason, a value of yield strength is not shown in Table 7.6; instead, the mean *proof stress* – the stress that produces a residual strain of 0.2 % – is given. However, the notation f_y and the name *yield stress* are used to refer to the experimental proof stress henceforth.

Additionally, the mean yield strength was observed to be approximately 15 % larger than the average value expected for reinforcement class K500C-T, which is 500 MPa. This could indicate that the plastic deformation corresponding to a yield plateau has been exhausted during the manufacturing process and, therefore, the plastic region of the steel-strain curve shows only the increase of strength due to strain hardening effect.

7.4 Impact Loading Tests

7.4.1 Test conditions

The impact loading tests took place 34 days after casting of the specimens. All specimens were simply supported on rollers near the ends, allowing for a clear span of 1000 mm; therefore, the beams could rotate freely and translate sideways and in the upwards direction. Figure 7.2 provides with a schematic representation of the test setup.

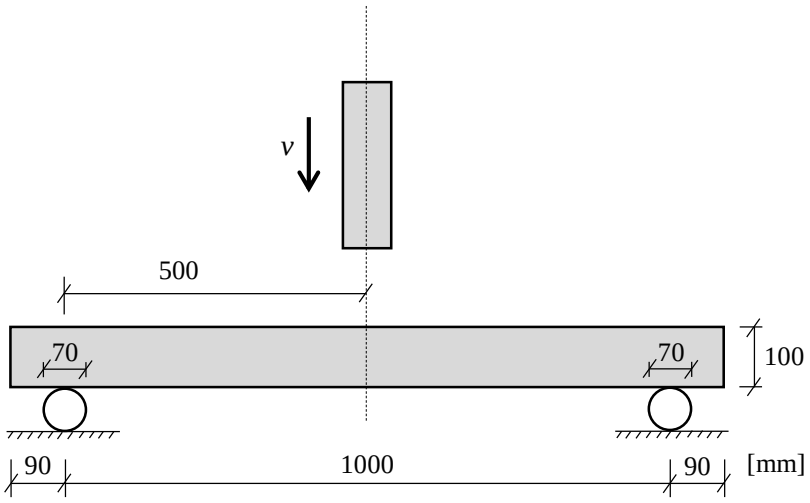

Figure 7.2 Beam dimensions and boundary conditions.

A drop-weight with a mass of 10.1 kg was dropped freely onto the top surface of the beam at midspan and from two different heights. The drop-weight corresponds to a cylindrical steel rod with a rounded tip. The dimensions are shown in Figure 7.3. The cylinder is not entirely solid, as a hole is present in order to accommodate an accelerometer and a sensor. However, such devices were not used during the experiments. Instead, by painting a high contrast black and white speck pattern, the position and the change over time for both the drop-weight and the impacted beams could be determined by means of digital image correlation (DIC). Figure 7.4 shows a real beam specimen together with the drop-weight.

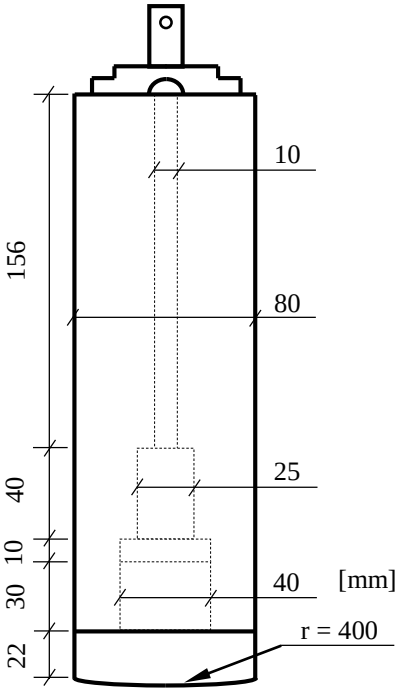

Figure 7.3 Dimensions of the drop weight, modified from (Lovén and Svavarsdóttir, 2016).

Figure 7.4 Setup for impact loading tests. Note the back and white speck pattern painted on the beam surface and the drop-weight.

The test specimen was installed below a metal frame consisting of three long slender rods, which fulfilled the purpose of controlling and directing the free fall of the drop-weight. Special attention was put in placing the beam properly so that the drop-weight hit the center. At the top of the metal cage, a simple truss system allowed to hoist the drop-weight up to the desired position. Once in position, the cylinder could be released by pulling on a lever.

A high-speed camera, which was able to record at a frame-rate of 5000 fps, was placed directly in front of the beam so as to capture the beam behavior during the impact event. The image resolution of the recording was 1024×304. Additionally, a lamp was positioned in front of the beam in order to enhance the lighting conditions. Figure 7.5 shows the setup adopted in order to record the impact tests. The camera was activated manually a short time before the drop-weight was released.

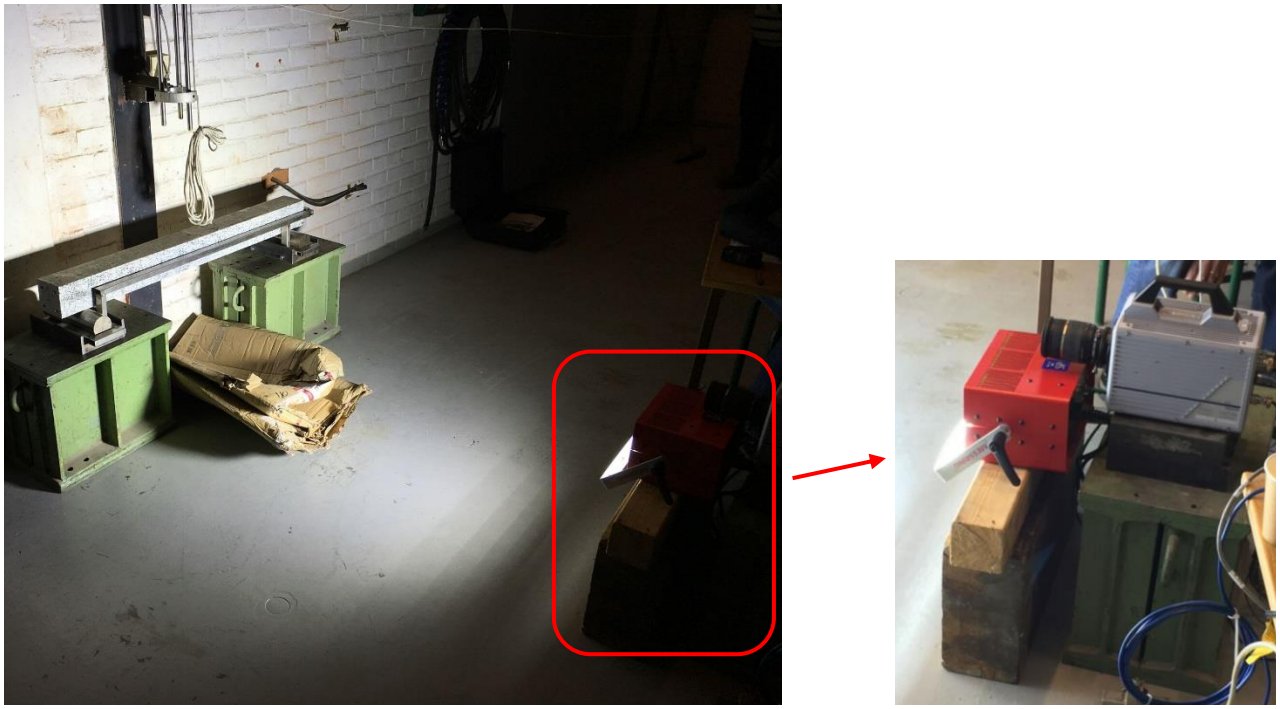

Figure 7.5 Setup for recording of the impact loading tests.

The cardboard placed below the specimen in Figure 7.5 served the purpose of preventing the drop-weight from hitting the floor after impacting the concrete beam. Additionally, Figure 7.5 shows the metal frame used to position correctly the specimen in relation with the roller supports. This frame was carefully removed after mounting the beam on the supports, before the impact test.

7.4.2 Determination of drop-height

The specimens of Series-1 and Series-2 were subjected to different impact energies, defined by different drop-heights. The drop-heights adopted in this study are 2.5 m and 5.0 m, which, by neglecting air resistance and friction, lead to theoretical values of impact velocity equal to 7.0 m/s and 9.9 m/s, and values of impact energy equal to 248 J and 495 J, respectively.

The drop-heights for both Series-1 and Series-2 were chosen by means of a preliminary analysis. The intention was to choose two different drop-heights which allowed the test specimens to have sufficient residual deformation capacity in order to properly study the post-impact behavior of the beams. Firstly, a pre-test consisting of a three-point static experiment was carried out on an impact-damaged specimen with equal geometry and similar material properties in order to determine the residual plastic deformation capacity. The pre-test specimen had previously been subjected to an impact, as described in (Lovén and

Svavarsdóttir, 2016), with the same drop-weight shown in Figure 7.3 but from a height of 3.5 m. The results of the pre-test were compared with the load-deformation curves determined under static loading for the undamaged beams with similar properties (Lovén and Svavarsdóttir, 2016). Further information regarding the pre-tests can be found in Appendix D.

The residual plastic deformation measured on the pre-test beam indicates that an impact from a height of 3.5 m does not exhaust the entire plastic deformation capacity of the concrete beam; moreover, there appears to be sufficient remaining deformation capacity which can allow to study the post-impact behavior. Therefore, it was decided to set the maximum drop-height to 5.0 m for the experiments on specimens of Series-2.

The second value of drop height was decided so that the ratio between the values of height and the ratio between the values of plastic deformation are both approximately equal to 2. In order to estimate the plastic deformation, the simplified 2DOF model was used. Further discussion regarding results from the 2DOF system is provided in Section 8.4. Finally, a drop-height of 2.5 m was chosen for the specimens of Series-1.

7.5 Static Tests

The static tests were performed in order to determine the load-carrying and deformation capacity of the undamaged beams, and to measure the residual deformation capacity of the beams previously subjected to impact loading. The experiments on beams from batch 1 were conducted 35 days after casting, while the beams from batch 2 were tested 36 days after casting.

The deformation-controlled static tests were carried out using a uniaxial compression/tension hydraulic jack. The beams were supported over a length of 1000 mm, with identical boundary condition as in the impact tests. Figure 7.6 shows a specimen at the beginning of a static test.

The load was applied at midspan with a deformation rate of 2 mm/min until a deformation of 10 mm was reached. From that point, the loading rate was increased gradually over a span of 40 s until a final loading rate of 10 mm/min was reached. The static tests were terminated when either rupture of one of the reinforcement bars took place or when the applied load corresponded to approximately 70 % of the maximum load capacity for a given specimen. The applied load and the midspan deflection were measured simultaneously using a load cell and a displacement sensor, respectively.

The static tests were recorded by using a pair of cameras which pointed at the beam center from different angles with regard to an imaginary line perpendicular to the main beam axis and which intersects the beam at midspan. These cameras recorded at a rate of 0.5 fps. A lower frame-rate (compared to the camera used to record the impact loading tests) allowed to reduce the amount of data collected during the experiments and also to increase the resolution of the recording. Additionally, a lamp was placed behind the cameras to improve the lighting conditions. The setup for the experiments can be seen in Figure 7.7.

Figure 7.6 Setup for static tests.

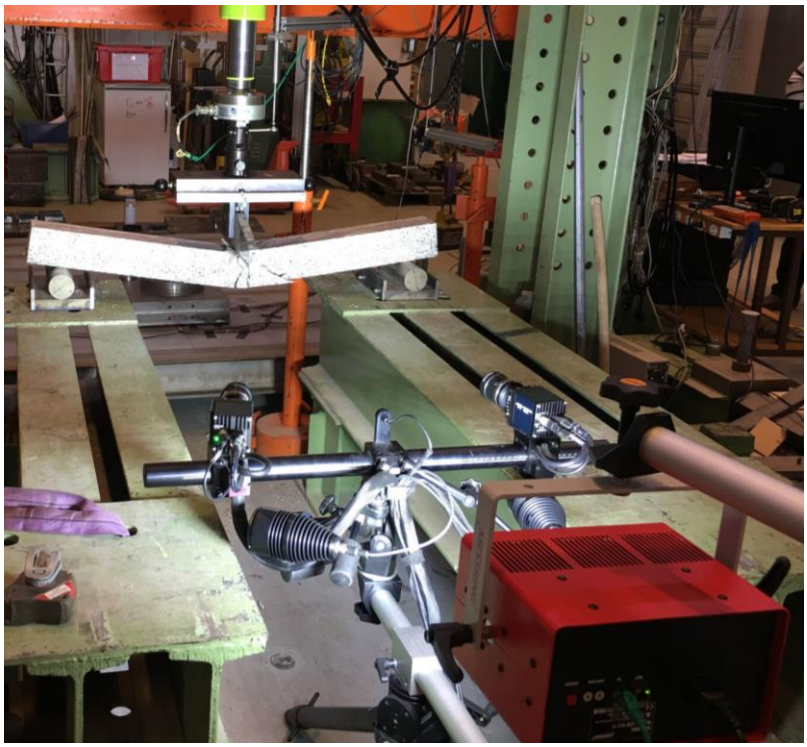

Figure 7.7 Setup for recording of the static tests.

7.6 Digital Image Correlation

The data recorded with the cameras during both impact loading and static tests was processed using a method called digital image correlation (DIC), which is an optical, non-contact method that allows to register changes in 2D and 3D digital image series by tracking the movement between pixels. A stochastic pattern is required on the surface (or volume) of interest to describe discrete image areas. DIC can be used to measure deformation, displacement, and strain; and it is a convenient alternative to traditional methods, such as strain gauges and extensometers. The equipment needed to record the tests was provided by RISE (Research Institutes of Sweden).

The free version of the software package GOM Correlate 2016[1] was used to perform the DIC analysis. Information of interest for the development of this project which can be obtained from GOM Correlate after processing the data recorded by the cameras includes velocity and displacement of the beam midpoint and the drop-weight, strain field on the surface of the beam, and the deformed shape of the beam over time.

[1] Revision 100682

8 Predictions

8.1 Introduction

This chapter presents a brief description of the procedure followed to calculate the theoretical response of the concrete beam for both static and impact loading according to the theory discussed in previous chapters. The theoretical predictions are to be compared with the experimental results and the results from the finite element analyses in later chapters.

The geometry of the beam and the drop-weight are described in Section 7.2; while the boundary and loading conditions are explained in Section 7.4.

Initially, the static load capacity of the reinforced concrete beam is calculated at ultimate limit state. Furthermore, the load at cracking and yielding, as well as the theoretical load-deflection curve under static loading, are determined.

Additionally, the plastic rotational capacity is estimated according to the different methods presented in Section 5.4. The software Mathcad 15.0 was used to make the calculations; which are presented in detail in Appendix I.

Finally, the response of the beam during the impact event is studied based on a simplified 2DOF model, as described in Chapter 4. An approximate solution of the 2DOF system was obtained by means of the Central Difference Method (CDM). The computations were performed with the software MATLAB R2015b. The script can be found in Appendix J.

8.2 Load Capacity

8.2.1 Ultimate Limit State

In the ultimate limit state it is assumed that the ultimate concrete strain, $\varepsilon_{cu} = 3.5\,‰$, is reached. The stress distribution in the compressive zone follows the idealized parabolic-rectangular stress-strain relationship for concrete described in Section 2.4. Likewise, complete interaction between the reinforcing steel and concrete, as well as linear strain distribution, is assumed. Figure 8.1 illustrates the cross-sectional strain and stress distribution at failure.

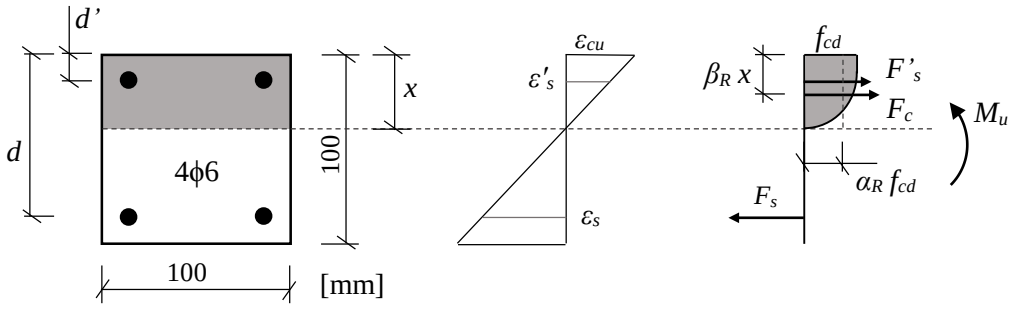

Figure 8.1 Parabolic-rectangular stress distribution and linear strain distribution across the cross section.

Assuming that the neutral axis is located below the center of gravity of the top layer of reinforcement, the equilibrium conditions at ultimate limit state can be expressed as

$$\alpha_R \cdot f_{cd} \cdot b \cdot x + \sigma'_s \cdot A'_s = \sigma_s \cdot A_s \tag{8.1}$$

$$M_u = \alpha_R \cdot f_{cd} \cdot b \cdot x(d - \beta_R \cdot x) + \sigma'_s \cdot A'_s(d - d') \tag{8.2}$$

where α_R and β_R correspond to the stress block factors for average stress and resultant location, respectively. For the case when the ultimate strain of concrete $\varepsilon_{cu} = 3.5\,‰$ is reached, the stress block factors take the values:

$$\begin{aligned} \alpha_R &= 0.81 \\ \beta_R &= 0.42 \end{aligned} \tag{8.3}$$

The magnitude of the corresponding steel strain reached in the ultimate state can be calculated from the strain distribution as

$$\varepsilon_s = \frac{d - x}{x} \cdot \varepsilon_{cu} \tag{8.4}$$

$$\varepsilon'_s = \frac{x - d'}{x} \cdot \varepsilon_{cu} \tag{8.5}$$

The steel stress in each layer of reinforcement depends on the actual stress-strain relationship for the reinforcing steel. When a bi-linear curve with a inclined top branch is adopted to represent the stress-strain relationship, the steel stress can be determined as

$$\sigma_s = \begin{cases} E_{sm} \cdot \varepsilon_s & if \quad \varepsilon_s \leq \varepsilon_{sy} \\ f_{yd} + p_1(f_{td} - f_{yd}) & if \quad \varepsilon_s > \varepsilon_{sy} \end{cases} \tag{8.6}$$

where

$$p_1 = \frac{\varepsilon_s - \varepsilon_{sy}}{\varepsilon_{su} - \varepsilon_{sy}} \tag{8.7}$$

Note that Equations (8.6) and (8.7) are applicable for both the top and bottom layer reinforcement. In order to obtain a prediction of the behavior of the material closer to reality, the partial safety factors γ_c and γ_s normally used in design were set to 1.0, and the design values of strength were set equal to the mean values of strength in the calculations as

$$\begin{aligned} f_{cd} &= f_{cm} \\ f_{yd} &= f_{ym} \end{aligned} \tag{8.8}$$

The complete procedure to determine the load capacity is detailed in Appendix I. Initially, the load capacity was determined considering both layers of steel. It was found that the top reinforcement is subjected to low *tensile* stress. However, since the expressions to determine plastic rotational capacity are either based on cross sections with only bottom reinforcement or cross-section with top reinforcement under *compressive* stress, it was decided to disregard the contribution of the top layer during the calculation of plastic rotational capacity. That means that the values of load capacity calculated only by considering the bottom reinforcement are also needed.

Furthermore, two different values of yield stress were considered in the calculations. First, the proof stress, as determined in Section 7.3, provides with the design load capacity for the concrete beam. Additionally, a theoretical upper value of load capacity was determined by setting the yield stress equal to the ultimate stress, f_t. Table 8.1 shows the calculated values of ultimate moment and point load for different conditions.

Table 8.1 Moment and external force in the Ultimate Limit State for different values of yield stress.

f_{yd} [MPa]	Layers of reinforcement considered	M_u [kNm]	F_u [kN]
575	Top and bottom	2.7	10.7
	Bottom only	2.6	10.3
686	Top and bottom	3.0	12.1
	Bottom only	2.9	11.7

8.2.2 Cracking and yielding

The external moment which is acting on the section when cracking occurs can be calculated based on the mean flexural tensile concrete strength and the moment of inertia for state I as

$$M_{cr} = \frac{f_{ct,fl} \cdot I_I}{h/2} \tag{8.9}$$

To determine the yielding moment, it is assumed that the stress distribution in the compressive zone corresponds to the idealized parabolic-rectangular stress-strain relationship described in Section 2.4. At the onset of yielding, the steel strain ε_{sy} is known, while the concrete strain at the compressive edge is unknown; that is, $\varepsilon_{cc} < \varepsilon_{cu}$. Moreover, since the stress block factors α_R and β_R are dependent on ε_{cc}, they have unknown values different to those given by Equation (8.3). In order to calculate the cross-sectional forces, an iterative procedure must be followed. Initially, a tentative position of neutral axis, x_y, is assumed. Then, the strain in the compressive edge and in the top layer of reinforcement can be determined as

$$\varepsilon_{cc.y} = \frac{x_y}{d - x_y} \cdot \varepsilon_{sy} \tag{8.10}$$

$$\varepsilon'_{sy} = \frac{d' - x_y}{d - x_y} \cdot \varepsilon_{sy} \tag{8.11}$$

The corresponding stress block factors are consequently calculated for that strain distribution. Finally, the condition of horizontal equilibrium is verified. This procedure is repeated with a new assumption of x_y until the condition of horizontal equilibrium is fulfilled.

The calculated values of moment and external concentrated force for both the beginning of cracking and the onset of yielding are shown in Table 8.2. The variation of these values depending on whether or not the top layer of reinforcement is considered is negligible; therefore, no distinction regarding the layers of reinforcement is made.

Table 8.2 Moment and external force at the onset of cracking and yielding.

f_{yd} [MPa]	State	M_{cr} or M_y [kNm]	F_{cr} or F_y [kN]
575	Onset of cracking	0.9	3.4
	Onset of yielding	2.4	9.5
686	Onset of cracking	0.6	2.5
	Onset of yielding	2.8	11.3

8.2.3 Theoretical load-deflection curve

In order to create a theoretical load-deflection curve, the stiffness for the different states should be calculated. Equation (8.12) can be used to determine the equivalent stiffness for both state I and state II by setting $I = I_I$ or $I = I_{II}$, respectively. Note that Equation (8.12) is only valid for the midspan deflection of a simply supported beam with linear elastic material properties subjected to a point load at midspan.

$$k = \frac{48 E_{cm} I}{L^3} \tag{8.12}$$

Provided that the top layer of reinforcement is subjected to compressive stress, the second moment of area for a state II response can be calculated according to

$$I_{II} = b \cdot \frac{x_{II}^3}{3} + (\alpha - 1) \cdot A_s'(x_{II} - d')^2 + \alpha \cdot A_s(d - x_{II})^2 \tag{8.13}$$

where the position of the neutral axis must be determined by considering area balance as

$$b \cdot \frac{x_{II}^2}{2} + (\alpha - 1) \cdot A_s'(x_{II} - d') = \alpha \cdot A_s(d - x_{II}) \tag{8.14}$$

If equilibrium cannot be found under the assumption of compressive stress in the top bars, then Equations (8.13) and (8.14) can be modified accordingly to consider tension in the top bars.

The stiffness of the transformed section in state I is used up to initiation of cracking. Thereafter, it is assumed that the beam deflects linearly until the ultimate load is reached. The beam is assumed to behave plastically from that point on. However, the slope of the linear load-deflection curve between cracking and ultimate load is unknown. In order to determine an equivalent stiffness for that interval, the

midpoint deflection when peak load is reached can be estimated by assuming that the structure deflects with a stiffness equivalent to a response in state II from the undeformed position. Once the coordinates of this point have been found, a straight line can be drawn from the onset of cracking to ultimate load. Figure 8.2 shows the theoretical load-deflection curve for different values of yield stress.

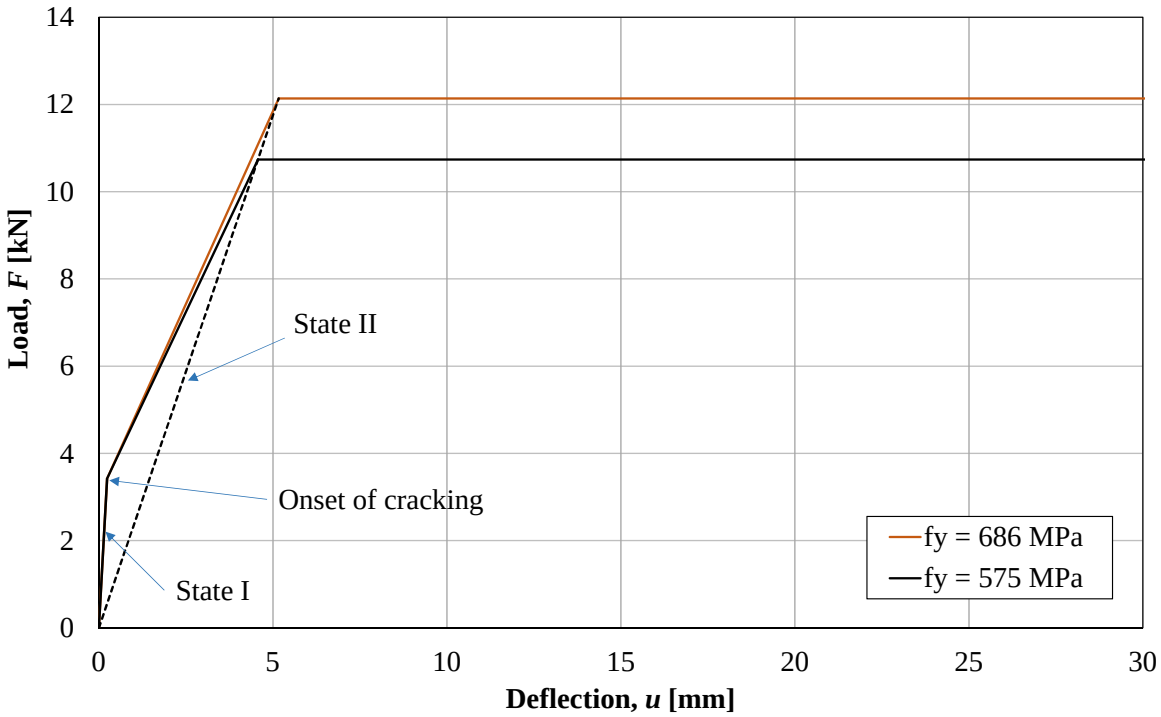

Figure 8.2 Theoretical load vs deflection curve for different values of yield stress when the top layer of reinforcement is taken into account.

8.3 Rotational Capacity

8.3.1 General description

Most of the different methodologies to calculate the rotational capacity discussed in Chapter 5 are based on a cross section with top reinforcement subjected to compressive stress; however, as described in Section 8.2.1, the top reinforcement in the specimen beam has been proved to be subjected to low tensile stress. For this reason, the contribution of the top reinforcement was disregarded when predicting the rotational capacity of the concrete beam.

Common input parameters for all equations are the distance from the point of maximum moment to the zero moment region, l_0; and the effective cross-section height, d. The former is equal to half the span of the beam, $l_0 = L/2 = 0.5$ m; the latter corresponds to the distance from the top edge to the bottom layer of steel (the top layer is disregarded), $d = 80$ mm.

8.3.2 Rotational capacity according to Eurocode 2

The position of the neutral axis at failure and the effective depth of the section are $x_u = 9.9$ mm and $d = 80$ mm, respectively; therefore, $x_u/d = 0.124$. From Figure 5.13, the corresponding total plastic

rotational capacity is $\theta_{pl,tot} = 31$ mrad. This value should be corrected considering the shear slenderness $\lambda = l_0/d = 6.25$ as

$$\begin{aligned} \kappa &= \sqrt{\lambda/3} = 1.44 \\ \theta_{pl,tot,EC} &= \kappa \cdot \theta_{pl,tot} = 45\,\text{mrad} \end{aligned} \tag{8.15}$$

The plastic rotational capacity at *one side* of the critical section (equivalent to the rotation at one of the supports) can be determined as

$$\theta_{pl,EC} = \frac{\theta_{pl,tot,EC}}{2} = 22\,\text{mrad} \tag{8.16}$$

The corresponding plastic deformation is given by

$$u_{pl,EC} = \frac{\theta_{pl,EC} \cdot L}{2} = 11.2\,\text{mm} \tag{8.17}$$

8.3.3 Betonghandbok-Konstruktion (ABC method)

Initially, the factors A, B, and C should be determined. Equation (5.21) is used given that the strength of the materials was measured in the laboratory. For the calculation of A, the parameters ω_v and ω_c were both set equal to zero since the specimen beams were not provided with shear reinforcement, which in turn would hinder the ability of the top bars to provide confinement of the concrete. Additionally, the top bars are acting in tension. The tensile mechanical reinforcement ratio, ω_s, was determined by considering only the bottom layer of reinforcement.

As for the factor B, the maximum allowable value was adopted, as pertaining to high ductility steel. Even though the steel classification shown in Table 5.1 is currently outdated, it was assumed that the modern steel type C provides sufficient ductility, equivalent to the ductility provided by steel class Ks 60.

Considering that the plastic hinge length is located at midspan, Equation (5.23) can be used to calculate the factor C. The plastic rotational capacity and the corresponding plastic deformation according to *Betonghandboken* method are shown below:

$$\theta_{pl,95,ABC} = A \cdot B \cdot C \cdot 10^{-3} = 0.52 \cdot 1.0 \cdot 43.8 \cdot 10^{-3} = 23\,\text{mrad} \tag{8.18}$$

$$u_{pl,95,ABC} = \frac{\theta_{pl,95,ABC} \cdot L}{2} = 11.3\,\text{mm} \tag{8.19}$$

8.3.4 Bk 25

The derivation of the equation to calculate the rotation capacity according to Bk 25 as described in Section 5.4.4 is based on a cross section without top reinforcement. The first step to determine the plastic rotational capacity is to identify the dominant failure mode. Since the tensile mechanical reinforcement ratio is proven to be larger than the critical mechanical reinforcement ratio, $\omega_{s,crit}$, it is concluded that concrete crushing is the governing failure mode.

According to (Latte, 1999), the rotation a midspan for a three-point bending test could be considered equivalent to the rotation over an inner support in a continuous beams. Following this reasoning, the plastic hinge length at midspan for a beam loaded with a point load can be determined as the plastic hinge length at an inner support in a continuous beam. Therefore, Equation (5.35) is used here:

$$l_p = 0.5d + 0.1l_0 = 0.5 \cdot 80\,\text{mm} + 0.1 \cdot 500\,\text{mm} = 90\,\text{mm} \tag{8.20}$$

This value of plastic hinge length is comparable with the equivalent plastic hinge lengths calculated with other methods, as shown in Table 8.4. The rotational capacity can be calculated according to Equation (5.37).

$$\theta_{pl,Bk25,s} = 33\,\text{mrad} \tag{8.21}$$

The plastic hinge length according to Bk 25 derived for a plastic hinge located in the field is calculated for the sake of comparison by using Equation (5.24):

$$l_p = 0.5d + 0.15L = 0.5 \cdot 80\,\text{mm} + 0.15 \cdot 1000\,\text{mm} = 190\,\text{mm} \tag{8.22}$$

Subsequently, the corresponding value of rotational capacity is determined by means of Equation (5.33) as

$$\theta_{pl,Bk25,f} = 69\,\text{mrad} \tag{8.23}$$

Note that the $\theta_{pl,Bk25,f}$ is more than twice as large as $\theta_{pl,Bk25,s}$; as well as much larger than the plastic rotational capacity calculated according to the methodologies proposed in Eurocode 2 and *Betonghandboken*. This could be due to the fact that the derivation of the expressions to calculate the plastic hinge length in the Bk 25 method are based on a concrete beam subjected to a uniformly distributed load; therefore, the rotational capacity on the field determined for a uniformly distributed load is expected to be larger than the corresponding capacity for an external concentrated load.

8.3.5 Methods based on equivalent plastic hinge length

The first step to estimate the plastic rotational capacity consists in calculating the equivalent plastic hinge length according to the empirical equations presented in Section 5.4.

Secondly, the plastic curvature should be determined. The curvature at failure, φ_u, is initially calculated for $\varepsilon_{cu} = 3.5\,‰$, as described in Section 8.2.2, even though some methods suggest calculating a different value of ultimate concrete strain. The purpose of assuming $\varepsilon_{cu} = 3.5\,‰$ is to use a similar cross-sectional strain distribution for the sake of comparison. Similarly, the curvature at yielding, φ_y, is determined from the results in Section 8.2.1. Table 8.3 summarizes such calculations.

Table 8.3 Determination of curvature.

State	x [mm]	ε_s [%]	d [mm]	φ [m^{-1}]
ULS	9.9	2.478	80	0.354
Yielding	19.4	0.293	80	0.048

Therefore, the plastic curvature is given by

$$\varphi_{pl} = \varphi_u - \varphi_y = 0.354\,\mathrm{m}^{-1} - 0.048\,\mathrm{m}^{-1} = 0.305\,\mathrm{m}^{-1} \tag{8.24}$$

The plastic rotation capacity is estimated according to Equation (5.10). The values of plastic rotational capacity for the different methods and the corresponding plastic deformation are shown in Table 8.4.

Table 8.4 Equivalent plastic hinge length and plastic rotational capacity according to different methods.

Method	l_p [mm]	θ_{pl} [mrad]	u_{pl} [mm]
Mattock	107	32	16.1
Corley	96	29	14.5
Mattock's discussion on Corley's work	65	20	9.8
Sawyer	58	18	8.8

8.4 Dynamic Response According to 2DOF System

8.4.1 Overview

The setup of the 2DOF model according to the particular conditions of this project are discussed in this section. Henceforth the subscripts 1 and 2 are used to represent the drop-weight and the beam, respectively.

The response of both the drop-weight and the beam was modelled by a bi-linear elasto-plastic function, as described in Section 2.2.3; that is, the material exhibits a linear behavior defined by an elastic stiffness, k, until the limit for elastic response is reached. From that point on, the material undergoes plastic deformation and the resistance force cannot further increase above the capacity of the material.

Two different values of internal resistance were considered. Initially, the resistance was calculated based on the moment capacity obtained with the average yield stress measured in the laboratory, $f_{ym} = 575\,\mathrm{MPa}$. Additionally, a theoretical upper value of resistance was determined by assuming that the yield stress is equal to the ultimate steel stress, $f_{ym} = 686\,\mathrm{MPa}$. The contribution of both top and bottom layer of reinforcement was considered, see Table 8.1 for the adopted load capacities.

The impact load is introduced as initial velocity of body 1, namely $v_0 = 7.0\,\mathrm{m/s}$ and $v_0 = 9.9\,\mathrm{m/s}$; which in turn depends on the drop-height; that is, 2.5 m and 5.0 m respectively.

8.4.2 Maximum internal resistance

As described in Section 4.4, the internal resistance for the drop-weight, $R_{m,1}$, can be derived from the strength of the material and the impact area as

$$R_{m,1} = f \cdot A_{imp} \tag{8.25}$$

Based on the work in (Lovén and Svavarsdóttir, 2016), the internal resistance of the drop-weight was chosen as

$$R_{m,1} = 50\,\text{kN} \tag{8.26}$$

By choosing $R_{m,1} = 50\,\text{kN}$, the impact between the drop-weight and the beam is close to a plastic impact.

The maximum internal resistance for the beam, $R_{m,2}$, can be determined from the maximum moment at ultimate limit state, as calculated in Section 8.2.1, by using Equation (4.28) as

$$R_{m,2} = \frac{4 \cdot M_u}{L} \tag{8.27}$$

However, the beam is also statically loaded by its self-weight. To account for the self-weight, $R_{m,2}$ should be reduced by subtracting the equivalent static load pertaining to a beam subjected to a uniformly distributed load according to Equation (4.29) as

$$R_{m,2,mod} = \frac{4 \cdot M_u}{L} - \frac{g_{beam} \cdot L}{2} \tag{8.28}$$

A summary of the values of internal resistance for the drop-weight and the beams is provided in Table 8.5.

8.4.3 Stiffness

The stiffness of the drop-weight can determined as

$$k_1 = \frac{E_{sm} \cdot A_{drop}}{L_{drop}} \tag{8.29}$$

On the other hand, the stiffness of the beam in the elastic range is assumed to be equivalent to the stiffness in state II, that is

$$k_2 = k_{II} = \frac{48 E_{cm} I_{II}}{L^3} \tag{8.30}$$

The calculated values of stiffness are listed in Table 8.5.

Table 8.5 Internal resistance and elastic stiffness for the bodies in the 2DOF model.

Body	f_{yd} [MPa]	$R_{m,i}$ [kN]	$R_{m,i,mod}$ [kN]	k_i [MN/m]
Drop-weight, 1	- - -	50	- - -	$3.9 \cdot 10^3$
Beam, 2	575 686	10.7 12.1	10.6 12.0	2.4 2.4

8.4.4 Transformation factors

Considering that the drop-weight exhibits a much more rigid behavior than the beam, it is assumed that the response of the drop-weight is closer to the behavior of a rigid body than to that of an elastic body. Therefore, the transformation factors derived for plastic deformation have been adopted to model the response of the steel rod in the 2DOF system.

$$\begin{aligned} &\kappa_{m,1} = \kappa_{F,1} = \kappa_{k,1} = 1 \\ &\kappa_{mF,1} = 1 \end{aligned} \tag{8.31}$$

As for the beam, when an elasto-plastic response of the material is assumed, the combined transformation factor, $\kappa_{mF,2}$, depends on both the elastic and plastic parts; therefore, a proper value for $\kappa_{mF,2}$ would lie between the values for ideal plastic and elastic response presented in Table 4.1. However, in (Andersson and Antonsson, 2015) a comparison between a 2DOF system and a beam model in the software ADINA was made. For the conditions in that experiment, it was found that the response of the beam in the FE model was closer to the fully plastic condition. Based on these results, the transformation factors for a fully plastic beam were assumed in this thesis work, so that

$$\begin{aligned} &\kappa_{m,2} = 0.333 \\ &\kappa_{F,2} = \kappa_{k,2} = 1 \\ &\kappa_{mF,2} = 0.333 \end{aligned} \tag{8.32}$$

The value for $\kappa_{mF,2}$ in Equation (8.32) is kept constant for the entire duration of the 2DOF analysis, which is equivalent to the assumption that the beam undergoes plastic deformation and exhibits a triangular deformed shape, as shown in Figure 8.3, from the beginning of loading. It should be highlighted that the assumption of plastic deformation is only for the calculation of the transformation factors, as an elasto-plastic response is considered for the determination of deformations, stiffness, and internal resistance of the beam, as explained previously.

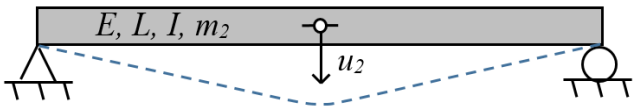

Figure 8.3 Assumed triangular shape of the beam pertaining to plastic response for calculation of transformation factors.

8.4.5 Results from the 2DOF model

The 2DOF analysis was performed for four different conditions regarding drop-height and internal plastic resistance of the beam. A summary of the results is shown in Table 8.6. Observe that the ratio between the plastic deformation for a drop-height of 5.0 m and the plastic deformation for a drop-height of 2.5 m is approximately equal to 2.2 for both values of yield stress, which in turn is close to 2, as originally intended when selecting the drop-heights.

Table 8.6 Deformation according to 2DOF system.

Series	Drop height [m]	Impact velocity [m/s]	$R_{m,2,mod}$ [kN]	u_{max} [mm]	u_{pl} [mm]	$u_{max,5.0}/u_{max,2.5}$ [-]	$u_{pl,5.0}/u_{pl,2.5}$ [-]
1	2.5	7.0	10.6 12.0	15.1 13.9	10.6 8.8	- - - - - -	- - - - - -
2	5.0	9.9	10.6 12.0	27.9 25.2	23.4 20.1	1.8 1.8	2.2 2.3

The deflection over time of the beam midpoint according to the 2DOF model is depicted in Figure 8.4. More results regarding the dynamic response can be found in Appendix E.

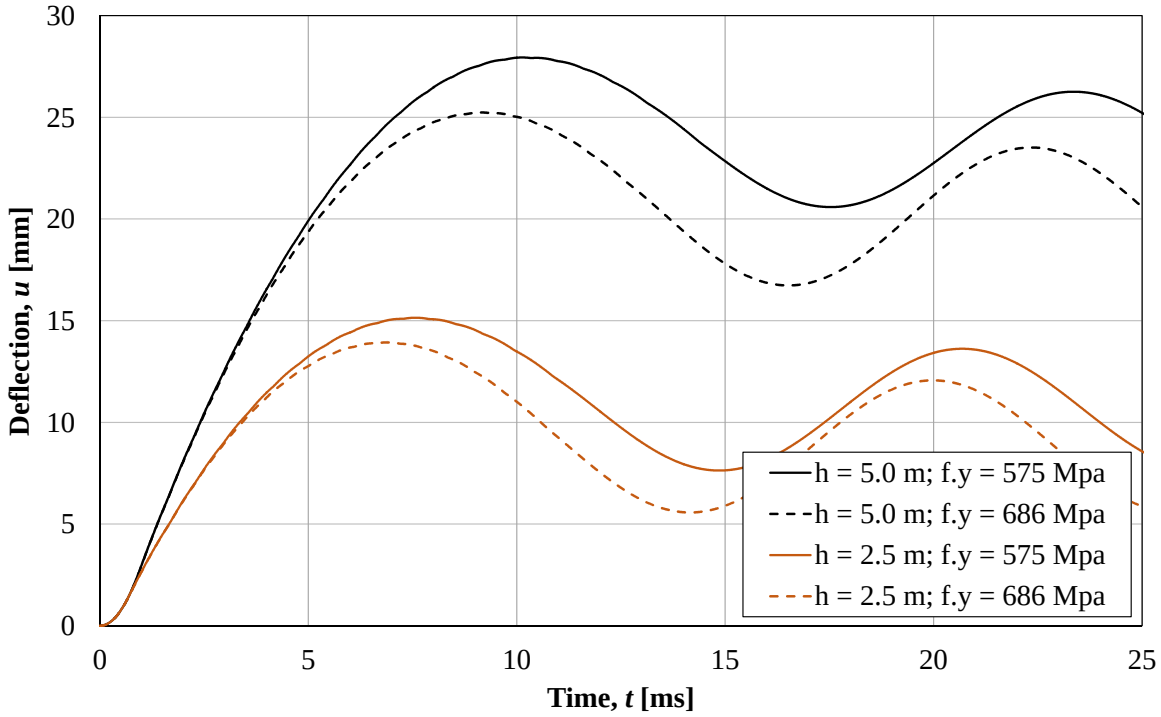

Figure 8.4 Deflection vs time curve for body 2 according to simplified 2DOF model.

9 Experimental Results

9.1 Impact Loading Tests

9.1.1 Overview

The experimental procedure started with the dynamic testing of Series-1 and Series-2 from the predetermined drop-heights $h = 2.5\,\text{m}$, and $h = 5.0\,\text{m}$, respectively. This section presents results gathered from the high-speed camera footages recorded during the impact events and subsequent digital image correlation (DIC) analyses performed on the program GOM Correlate. The information treated in this section covers, among others, the strain field of the beam specimens due to impact, beam midpoint deflection over time, as well as the variation of the deflected shape of the beam over time.

9.1.2 Methodology

The DIC analysis was performed using GOM Correlate, as introduced in Section 7.6, where a *surface component* was created over the recorded face of the specimen of interest in order to determine some of the key parameters. After several trials, it was decided to construct the surface component using a facet size of 21 pixels, point distance of 5 pixels, and *high accuracy* computation, as this setup was found to yield interpretable results. Key parameters could thereafter be derived from the constructed surface component, such as the major strain field, midpoint deflection, deformed beam shape, and displacement of the beam over the supports.

The *major strain* field can be requested directly from the surface component. In order to determine beam midpoint deflection and velocity, a *surface point* was created below the impact region close to the center of the beam and associated with the surface component. Information regarding displacement and velocity can be requested from such a point. Additionally, a *single section* was defined along a longitudinal axis positioned on the geometrical center of the beam. The deformed shape of the beam for different times can be determined from this section.

Finally, a *facet point component* was created on the drop-weight in order to determine velocity of the drop-weight over time.

9.1.3 Midpoint deflection over time: Series-1

The deflection of the midpoint over time for dynamically loaded beams of Series-1 (drop-height $h = 2.5\,\text{m}$) is shown in Figure 9.1. Based on this information, an average, maximum and minimum value were calculated for each time step. The average deflection curve is presented in Figure 9.2, the envelopes in the same figure mark the maximum and minimum recorded deflection over time for all beams in Series-1.

As seen in Figure 9.2, the average deflection curve remains centered with respect to the outer envelopes for the presented duration. The scatter of the results appears to be minor before maximum deflection is reached. From that point onward, the deviation of the outer envelopes remains approximately constant.

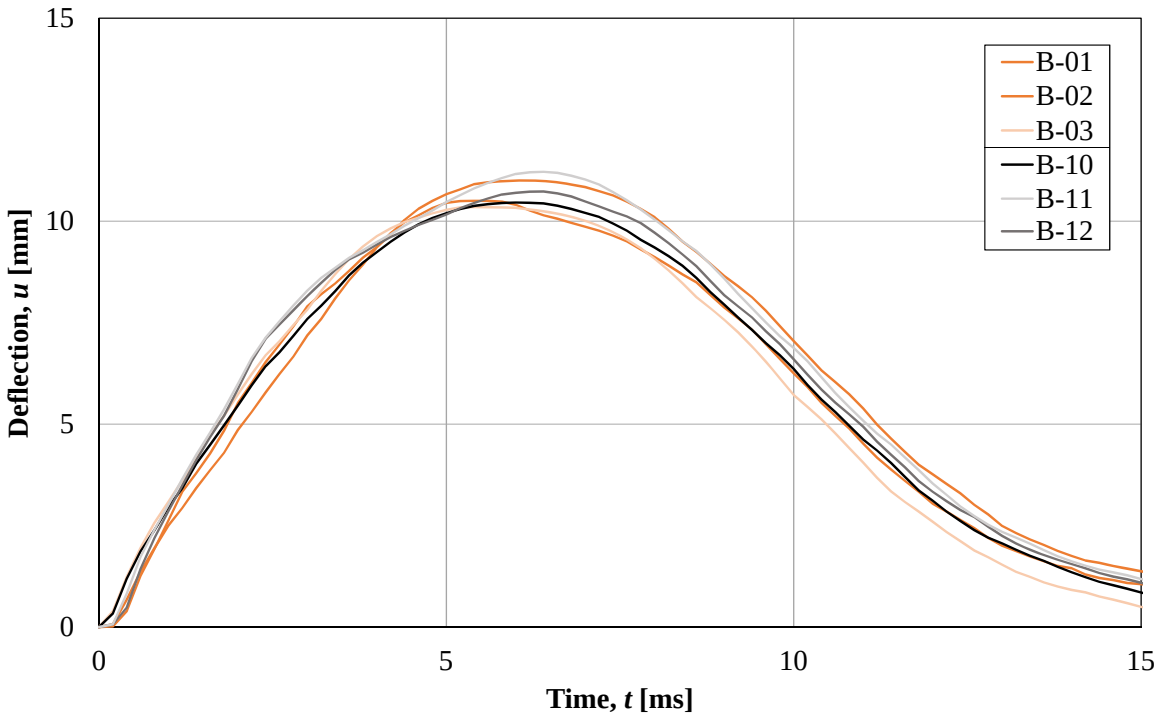

Figure 9.1 *Deflection of midpoint over time for Series-1, drop-height of h = 2.5 m, from DIC analysis. Beams from the first batch are listed in the upper part of the legend box, while beams from the second batch are listed in the lower part.*

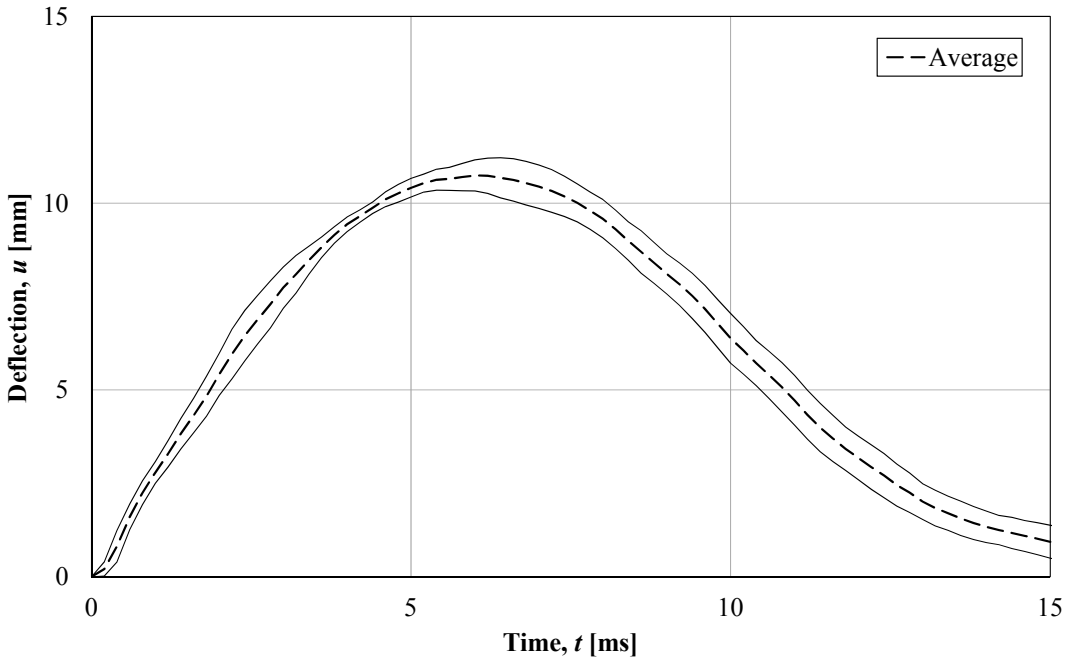

Figure 9.2 *Deflection of midpoint over time from DIC analysis. Outer envelopes and average values for all beams of Series-1. Drop-height of h = 2.5 m.*

Table 9.1 presents key parameters collected from DIC analysis, where the recorded impact velocity is given as v_0, and maximum deflection during dynamic response is given as u_{max}. Plastic deformation due to impact is given as u_{pl}. The parameter u_{pl} was determined based on the results from subsequent DIC analysis of the respective static trials; a schematic procedure to determine u_{pl} is shown in Appendix F.3.

Table 9.1 Key parameters collected from DIC analysis for Series-1, together with preliminary estimations with the 2DOF model.

Batch	Beam-ID	v_0 [m/s]	u_{max} [mm]	u_{pl} [mm]
1	B-01	6.9	10.5	4.1
	B-02	6.9	11.0	5.0
	B-03	6.9	10.4	4.7
	Average	**6.9**	**10.6**	**4.6**
2	B-10	6.9	10.5	5.1
	B-11	6.9	11.2	4.3
	B-12	6.9	10.7	4.7
	Average	**6.9**	**10.8**	**4.7**
1 & 2	**Average all**	**6.9**	**10.7**	**4.7**

(a) Experimental results.

h	f_y [MPa]	v_0 [m/s]	u_{max} [mm]	u_{pl} [mm]
2.5 m	575	7.0	15.1	10.6
	686		13.9	8.8

(b) 2DOF predictions.

Preliminarily, an overestimation by the 2DOF model is noticed when comparing average values of u_{max} and u_{pl} from experimental results in Table 9.1a with predictions made with the 2DOF model in Table 9.1b; this topic is addressed further in Section 9.6.3.

The recorded values of velocity have essentially equal magnitude in all cases presented in Table 9.1a. However, the average recorded value is slightly smaller than the theoretical value calculated in Table 9.1b. This can be due to the effect of air resistance and possible deviations in the drop-height during the experiments. The theoretical value is, nonetheless, still considered sufficiently close to the experimental values.

Ultimately, when comparing results presented in Figure 9.1 together with results given in Table 9.1a, no definitive conclusions can be drawn regarding whether beams from a certain batch behave differently than the beams from the other. Furthermore, while differences between individual beams are noticed, such differences are regarded as relatively small when comparing them to the set of test data gathered for Series-1. Consequently, the average curve presented in Figure 9.2 is considered to represent a characteristic response of the impact behavior for the beams of Series-1.

9.1.4 Midpoint deflection over time: Series-2

Figure 9.3 presents the recorded midpoint deflection over time for Series-2, drop-height of $h = 5.0$ m. Average values over time are shown in Figure 9.4, and key results are presented in Table 9.2.

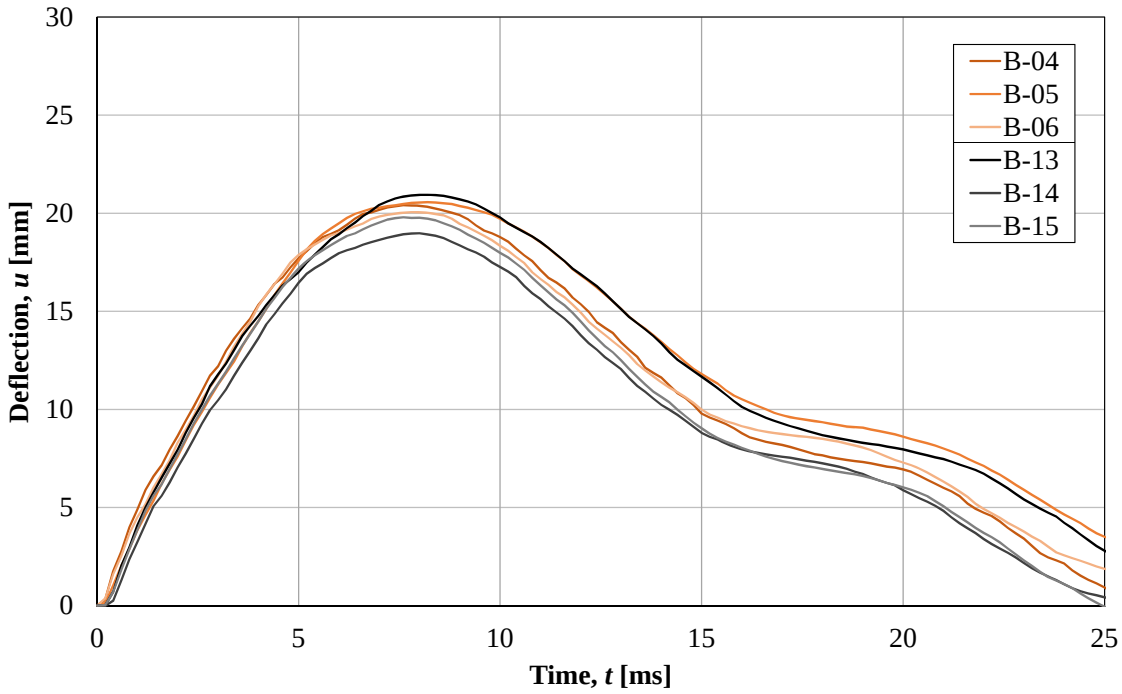

Figure 9.3 Displacement of midpoint over time for Series-2, drop-height of h = 5.0 m, from DIC analysis. Beams from the first batch are listed in the upper part of the legend box, while beams from the second batch are listed in the lower part.

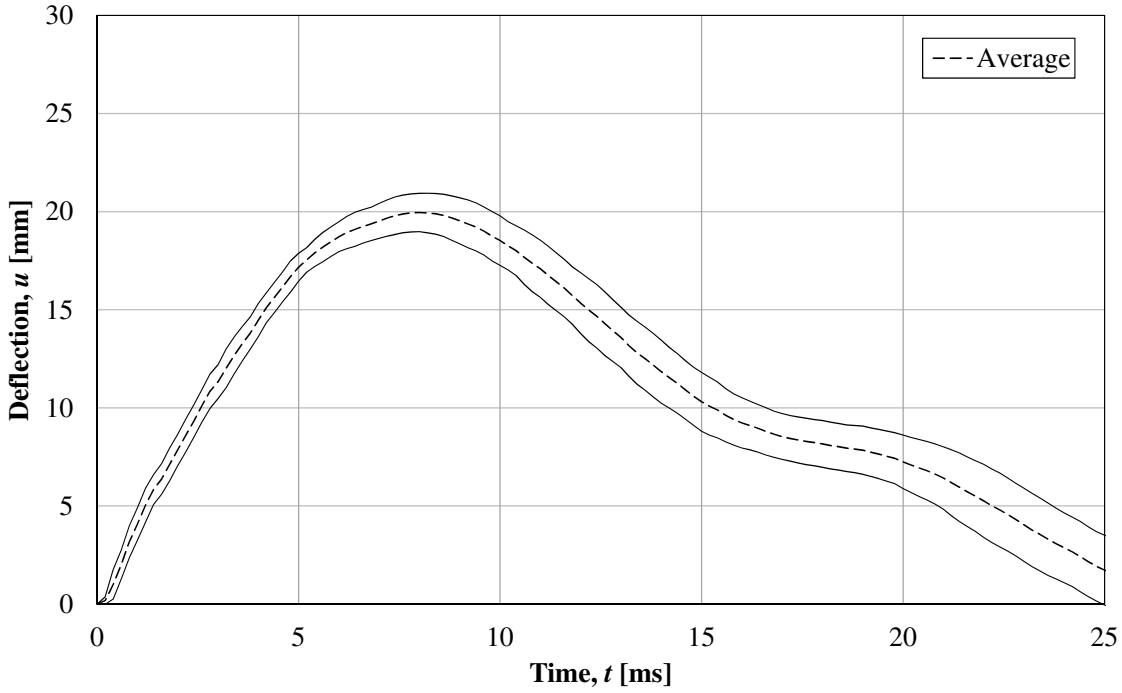

Figure 9.4 Displacement of midpoint over time from DIC analysis. Outer envelopes and average values for all beams of Series-2. Drop-height of h = 5.0 m.

Table 9.2 Key parameters collected from DIC analysis for Series-2, together with preliminary estimations with the 2DOF model.

Batch	Beam-ID	v_0 [m/s]	u_{max} [mm]	u_{pl} [mm]
1	B-04	9.8	20.4	13.0
	B-05	9.8	20.6	12.8
	B-06	9.8	20.0	12.7
	Average	**9.8**	**20.3**	**12.8**
2	B-13	9.7	20.9	13.3
	B-14	9.8	19.0	11.7
	B-15	9.8	19.8	11.7
	Average	**9.8**	**19.9**	**12.2**
1 & 2	**Average all**	**9.8**	**20.1**	**12.5**

(a) Experimental results.

h	f_y [MPa]	v_0 [m/s]	u_{max} [mm]	u_{pl} [mm]
5.0 m	575	9.9	27.9	23.4
	686		25.2	20.1

(b) 2DOF predictions.

The scatter of the data is observed to be fairly symmetrical with respect to the average curve; although the deviation appears to increase somewhat as time progresses. Similar conclusions regarding differences in the behavior depending on the batch can be drawn as previously done for Series-1; that is, no significant distinction between batches can be observed for the impact response, and therefore the average values between all beams are assumed as representative of the dynamic response.

Once more, the recorded value of impact velocity is slightly smaller than the theoretical value, as seen when comparing predicted values in Table 9.2b together with average values gathered from DIC analysis in Table 9.2a. Furthermore, it is noticed that the 2DOF model overpredicts the deflection of the beam. A summary of experimental average values compared with 2DOF predictions is presented in Table 9.3.

As observed in Table 9.3, the maximum deflection increases for an increased drop-height. Moreover, when comparing experimental results between drop-heights in Table 9.3a, it is noticed that the elastic deflection increases for a higher drop-height, and could be an indication of strain rate effects, since the beams have an extended linear-elastic behavior range for a larger impact energy. No consideration of strain rate effects were taken into account in the 2DOF model, which produces the same elastic deformation regardless of drop-height, as can be seen in Table 9.3b. Further verification of the results from the 2DOF model is carried out in Section 9.6.

Table 9.3 Summary of average experimental values compared to 2DOF predictions.

Series	h [m]	u_{max} [mm]	u_{pl} [mm]	u_{el} [mm]	$u_{max,5.0}$ / $u_{max,2.5}$ [-]	$u_{pl,5.0}$ / $u_{pl,2.5}$ [-]	$u_{el,5.0}$ / $u_{el,2.5}$ [-]
1	2.5	10.7	4.7	6.0	1.9	2.7	1.3
2	5.0	22.1	12.5	7.6			

(a) Experimental results; average values

f_y [MPa]	h [m]	u_{max} [mm]	u_{pl} [mm]	u_{el} [mm]	$u_{max,5.0}$ / $u_{max,2.5}$ [-]	$u_{pl,5.0}$ / $u_{pl,2.5}$ [-]	$u_{el,5.0}$ / $u_{el,2.5}$ [-]
575	2.5	15.1	10.6	4.5	1.8	2.2	1
	5.0	27.9	23.4				
686	2.5	13.9	8.8	5.1	1.8	2.3	1
	5.0	25.2	20.1				

(b) 2DOF predictions

9.1.5 Strain field due to impact loading

The strain field was determined through the surface component established in GOM Correlate for each beam. *Major strain* is the requested output parameter, which is displayed against the reference stage (before impact). As previously mentioned in Section 7.4, the dynamic response of the impacted beams was filmed using a high-speed camera recording at a frame-rate of 5000 fps, where the entire length of each beam was recorded in order to capture any possible asymmetric response of the dynamically loaded beams. A consequence of recording the whole beam was a reduction in the level of detailing when outlining cracks in the strain field; as only main cracked regions could be reliably determined using DIC analysis.

Before analyzing the cracking pattern obtained from DIC analysis, a comparison between DIC results from the thesis work by Lovén and Svavarsdóttir (2016) and the results from this project was carried out in order to gain insight regarding the quality of the cracking pattern obtained, to identify to what extent the information can be used, and to draw conclusions regarding similarities between recording half the beam and recording the entire beam. It should be noted that the impact tests described in (Lovén and Svavarsdóttir, 2016) were performed by using the same recording equipment and adopting the same frame-rate and resolution, but only half of the beam was recorded. Furthermore, while the geometry of the beam specimens and drop-weight is identical and the material properties are similar, there is a difference in the drop-height; which was set to $h = 5.5$ m in (Lovén and Svavarsdóttir, 2016) whereas the maximum drop-height adopted in this project is $h = 5.0$ m.

Beam B-06 was selected as a reference beam for $h = 5.0$ m based on the deflection of the midpoint over time, as it can be seen in Figure 9.3 that the response of B-06 resembles the average curve the closest. The reference beam in (Lovén and Svavarsdóttir, 2016) corresponds to beam RPC2, hereby referred to as

DIC-2016. The comparison is shown in Table 9.4.

Table 9.4 Comparison of strain fields for the characteristic beam from (Lovén and Svavarsdóttir, 2016) together with B-06 from this thesis work. Note that the impact height for DIC-2016 is $h = 5.5\,m$, whereas B-06 was impacted from a drop-height of $h = 5.0\,m$.

Time [ms]	DIC-2016	B-06
0.2		
0.4	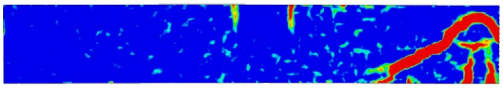	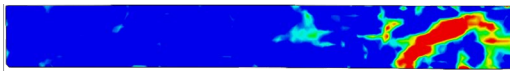
0.6	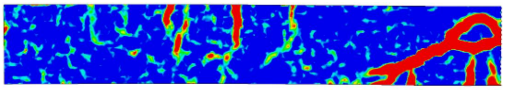	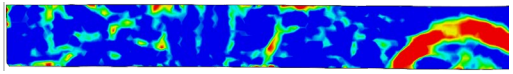
0.8	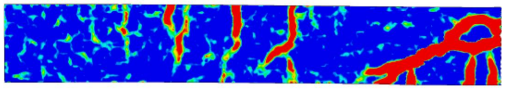	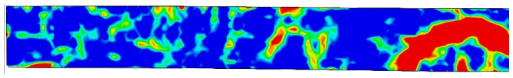
1.0	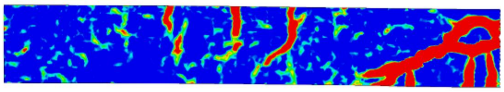	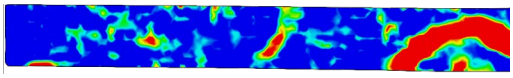
2.0	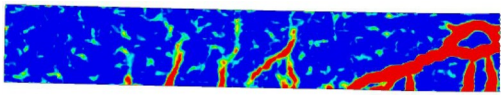	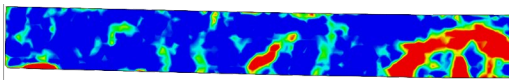
4.0	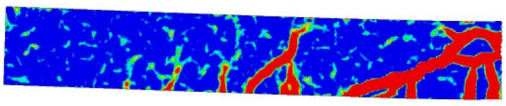	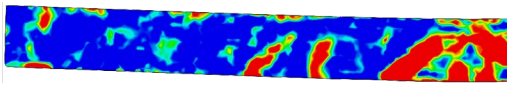
Principal strain [%]		

In Table 9.4 it is noticed that the strain field for beam B-06 is visibly coarser compared to DIC-2016. While it is possible to outline the major crack regions, difficulty lies in identifying precise cracking patterns, especially so if the location of the minor cracks are desired.

However, despite differences in drop-height, similarities can still be seen between the two alternatives. For instance, the major cracks occurring at midspan have similar outlines for both beams, albeit with less level of detail for B-06. Furthermore, indications of minor cracks occurring soon after impact at the top edge can be detected, which then turn into minor cracks occurring at the bottom edge. However, due to low resolution and the presence of noise in the measurements, there exists a risk of misinterpreting results as far as the occurrence of minor cracks is concerned.

Based on the comparison made in Table 9.4, the lower limit of the colorscale when displaying the principal strain with GOM Correlate was chosen to be the same value of 0.5 %; however, the upper limit was set to 5 % so that lower values are damped out in order to facilitate a more reliable reading of minor cracking. Using the adopted limits, the strain field at the time of maximum deflection is presented

in Tables 9.5 and 9.6 for Series-1 and Series-2, respectively. For further information concerning the dynamic response, refer to Appendix F.6, where the strain field of each beam is presented at certain times until the time of maximum deflection.

Table 9.5 Strain field for beams of Series-1 at the time of maximum deflection.

Deflection / Time	Strain field at maximum deflection due to impact loading
Beam B-01 $u = 10.5$ mm $t = 5.6$ ms **Beam B-02** $u = 11.0$ mm $t = 6.0$ ms **Beam B-03** $u = 10.4$ mm $t = 5.4$ ms **Beam B-10** $u = 10.5$ mm $t = 6.0$ ms **Beam B-11** $u = 11.2$ mm $t = 6.4$ ms **Beam B-12** $u = 10.7$ mm $t = 6.4$ ms	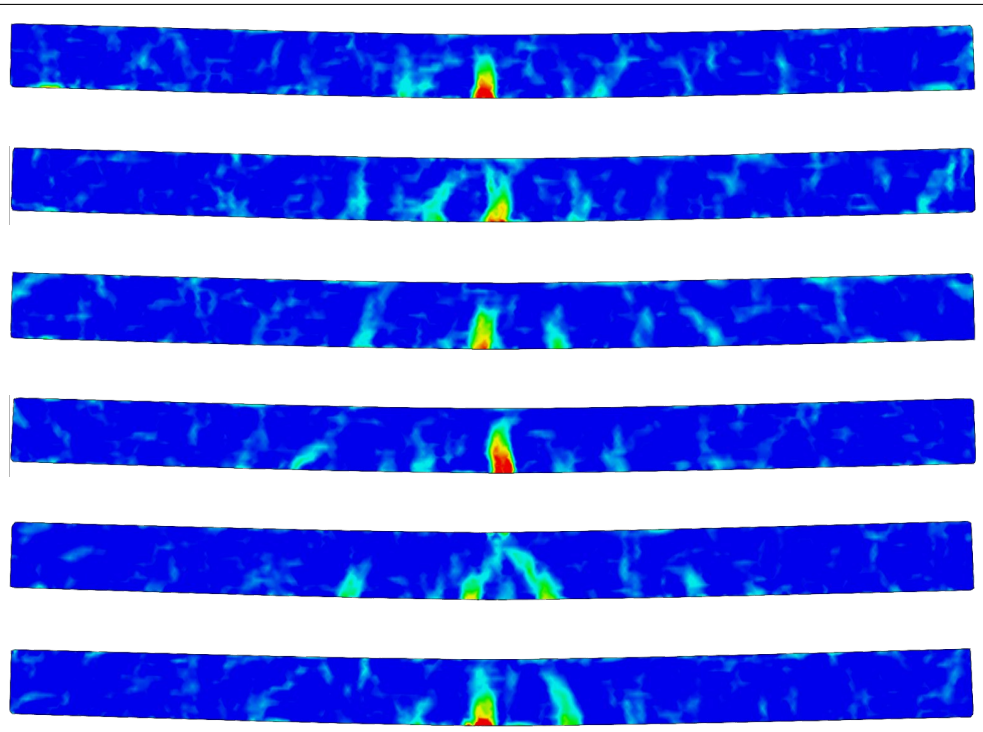
Principal Strain [%]	

Most beams of Series-1 exhibit a similar strain field at the time of maximum deflection in that a major bending crack is found at the bottom edge at midspan, below the impact region, for most beams. A significant exception to this is the response of B-11, for which a more distributed cracking at the bottom at midspan is observed. Coincidentally, B-11 is also the beam which exhibits the largest deflection and the longest duration to maximum deflection.

Additionally, indications of cracking at the bottom edge can be seen along the span further away from midspan for all specimens of Series-1. In general terms, and as far as the available information permits, it can be stated that the strain field shows a relatively good degree of symmetry, where indications of equivalent cracks can be found at both sides of the major bending crack at midspan.

Stronger indications of cracking can be measured for beams of Series-2, as can be seen in Table 9.6, due to the higher external energy exerted by the drop-weight impact. Similarly to Series-1, an important flexural crack can usually be distinguished at the bottom edge at midspan, although the magnitude of the

strains varies significantly. This flexural crack is more pronounced in B-05 and B-14, while only the outline of a distributed cracked region is observed at the same location in B-04 and B-06.

Furthermore, more pronounced inclined shear cracks below the impact region are found for beams of Series-2 compared to Series-1. It is also noted that the dynamic strain field exhibits in general a less symmetrical pattern for beams of Series-2.

An important observation is the occurrence of an inclined shear crack originating in the web at a certain distance from the midpoint in beams B-13 and B-15, though the length and width of such a crack are visibly larger for B-13. The slope of the inclined cracks at midspan appear to be steeper and the extension of the cracked area below the impact zone seems to be shorter for these two beams compared to the other specimens. This phenomenon could indicate that the presence of an important shear crack at a distance away from midspan influences and limits the spread of cracking at midspan during impact loading.

No reasonable relationship between the cracking pattern in Table 9.6 and the maximum displacement can be found. B-13, for instance, exhibits the largest maximum deflection, while B-15 which shows a fairly similar cracking response, showed the second smallest maximum deflection.

Table 9.6 Strain field for beams of Series-2 at the time of maximum deflection.

Deflection / Time	Strain field at maximum deflection due to impact loading
Beam B-04 $u = 20.4$ mm $t = 7.6$ ms	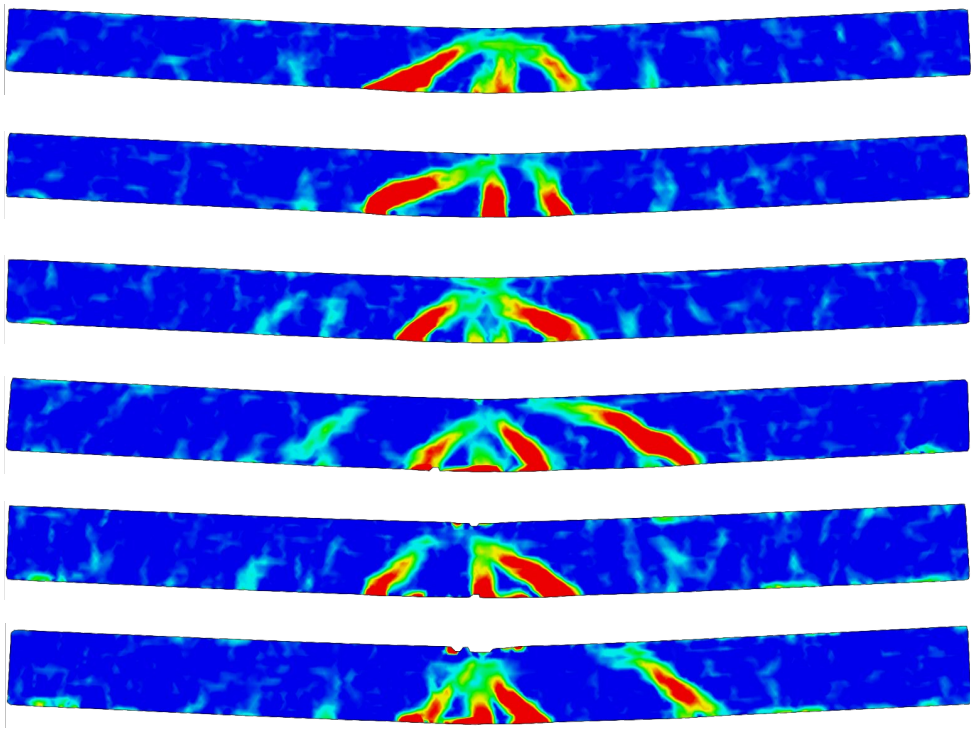
Beam B-05 $u = 20.6$ mm $t = 8.2$ ms	
Beam B-06 $u = 20.0$ mm $t = 7.8$ ms	
Beam B-13 $u = 20.9$ mm $t = 8.2$ ms	
Beam B-14 $u = 19.0$ mm $t = 8.0$ ms	
Beam B-15 $u = 19.8$ mm $t = 7.6$ ms	
Principal Strain [%]	

9.1.6 Deformed shape of the beam

Studying the variation of the deformed shape of the beam over time after impact loading is also of interest. This information can be collected from the DIC analysis by creating a *single section* along the longitudinal center line of a given specimen in GOM Correlate. Due to the large amount of information collected for just one single specimen, it was decided to choose one reference beam for each drop-height (instead of calculating average values from the results for all beams). The reference beams, which should exhibit a response the closest to the average values, were selected according to the midpoint deflection-time data. Beams B-06 and B-12 were chosen as representative for drop-heights $h = 5.0\,\text{m}$ and $h = 2.5\,\text{m}$, respectively. The deformed shape of B-06 is detailed in this subsection, whereas information regarding B-12 is presented in Appendix F.2.

Figure 9.5 shows the deformed shape of beam B-06 during the first 2 milliseconds after impact. It can clearly be seen that only a small portion of the beams deflects a short time after impact. In fact, at $t = 0.2\,\text{ms}$, about 300 mm of the beam show signs of deflection. The rest of the beam serves as a restraint for the deflected inner portion, and the beam behaves in a similar manner as a double-fixed beam with a shorter span. The negative curvature arising in the transition between active portion and the inactive portion leads to cracking at the top side of the beam.

A change of curvature close to the impact region is also visible. This sudden change corresponds with the inclined shear crack present in the impact region.

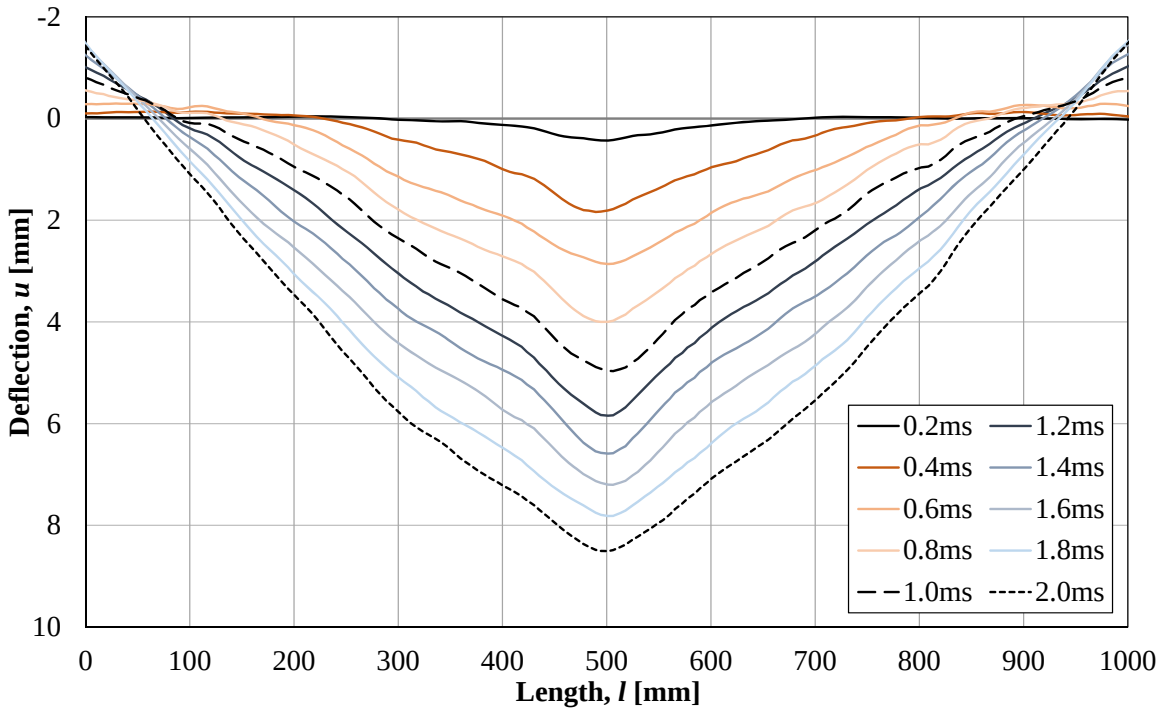

Figure 9.5 Deformed shape of beam B-06 at different times after impact. B-06 is assumed to be representative of the behavior of beams subjected to 5.0 m drop-weight impact.

The relative deflection of B-06 is illustrated in Figure 9.6. The information was adjusted correspondingly to negate any deflection over the support, while maintaining the difference in deflection between the

support and any other point along the span. Moreover, all values of deflection were normalized in relation to the corresponding maximum deflection at all times considered.

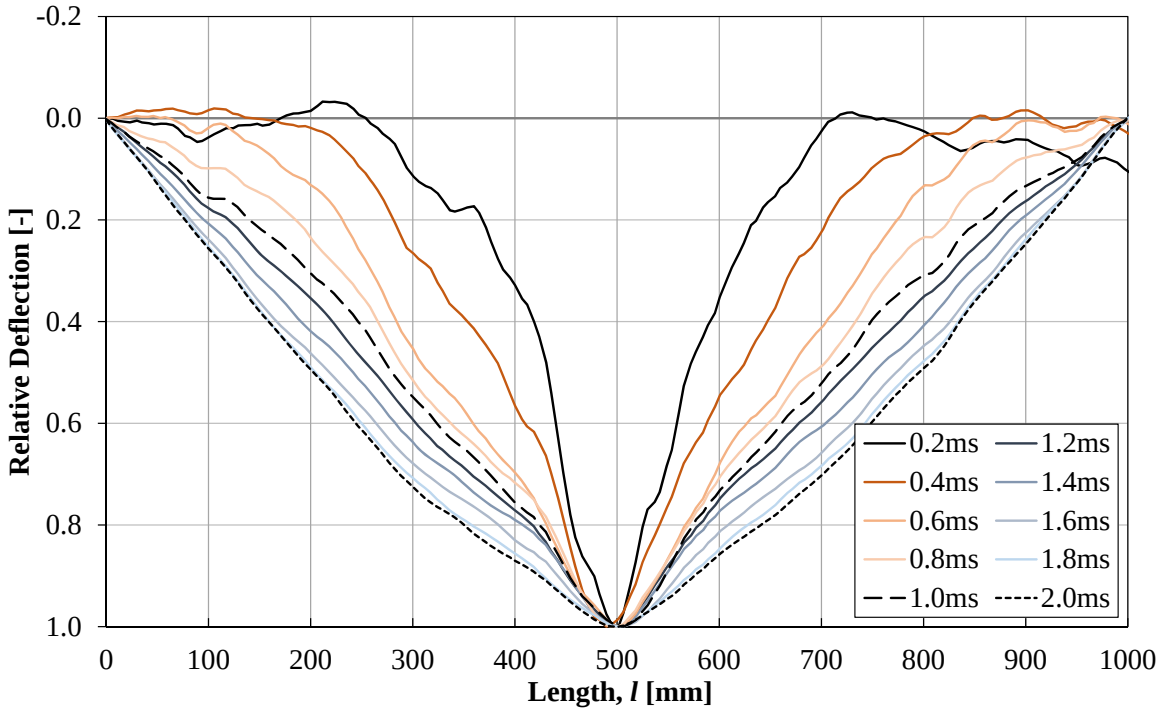

Figure 9.6 Relative deformed shape of beam B-06 at different times after impact. B-06 is assumed to be representative of the behavior of beams subjected to 5.0 m drop-weight impact.

Figure 9.6 shows that the beam adopts a triangular deformed shape only after approximately 2.0 ms have elapsed. This behavior is in conflict with the assumption of a deformed triangular shape adopted in Section 4.3.2 for the determination of transformation factors for a beam element when ideal plastic response is adopted.

9.1.7 Conclusions

No significant difference can be detected regarding the dynamic response between specimens from different batches, regardless of the drop-height. As a consequence, the average midpoint deflection-time curves are considered to represent a characteristic response for both Series-1 and Series-2, respectively. Furthermore, it was noticed that the initial predictions made by the 2DOF model seem to overestimate the resulting deflection, this topic is addressed further in Section 9.6.3.

Comparison of the strain fields due to the impact event between the results from (Lovén and Svavarsdóttir, 2016) and the results gathered in this project indicates that recording the entire beam while maintaining the same frame rate and resolution results in a loss of information. As a consequence, detailing the initiation and location of cracks becomes difficult and especially so for minor cracks, as random noise in the strain field may be misinterpreted as minor cracks. It is possible, however, to detect cracked regions corresponding to major cracks.

The analysis of the strain field due to impact loading for beams of Series-1 at the time of maximum

deflection indicates that the major cracks which form at midspan are of a flexural nature and tend to spread following a vertical path; whereas a stronger presence of inclined shear cracks below the impact zone is noticed for Series-2. Furthermore, indications of web shear cracks have also been noted for some specimens of Series-2.

When studying the deformed shape over time for B-06, it was observed that only a portion of the beam deflects shortly after the impact event. Eventually, the entire beam becomes active in the dynamic response, as the beam shows a triangular shape corresponding to plastic response at $t = 2.0$ ms. Moreover, good correspondence between the cracking pattern for the reference beam in (Lovén and Svavarsdóttir, 2016) and the deformed shape was found, such as crack occurrence at the top edge shortly after impact in the region of transition between active and inactive portions, and indications of inclined cracking at the impact region.

9.2 Static Tests

9.2.1 General introduction

After the impact loading tests were carried out, the damaged beams of Series-1 and Series-2 were brought to failure by means of deformation-controlled static three-point loading. The undamaged beams of Series-3 were also loaded to failure by the same procedure, and would serve as a reference to determine residual rotational capacity for the previously damaged beams of Series-1 and Series-2.

This section presents results from the static testing. The behavior of the beams from each series is studied with respect to each other and in between batches in terms of load-deflection data. Thereafter, the rotational capacity of all beams is determined and presented. The calculations of plastic rotation at a given load percentage $\theta_{pl,x\%}$ is performed in accordance to what has been previously described in Section 5.3.4 and is schematically shown in Appendix F.3.2.

9.2.2 Load-deflection results: Series-3

Figure 9.7 presents load-deflection curves for beams of Series-3, where a comparison between the two batches is made. Additionally, Figure 9.8 presents the average load at a given deflection together with the maximum and minimum values registered among all specimens in Series-3. Important values gathered and calculated are also presented in Table 9.7. For full overview of key parameters, refer to Appendix F.4.3.

The beams of the first batch in Figure 9.7 exhibit a response which is closer to the average curve and are overall better distributed, while beams of the second batch show a more erratic response between beams after ultimate load has been reached. Noticeably so for beams B-16 and B-17, for which signs of extensive concrete crushing can be observed, marked by a steep drop at the point of ultimate load. This generally results in a lower rotational capacity $\theta_{pl,x\%}$ for a load level of 95 % of the peak load (and lower), as can be seen for beams B-16 and B-17 in Table 9.7. However, the response of the beams of the second batch approach the average curve from both sides; hence, no consistent pattern between batches can be noted.

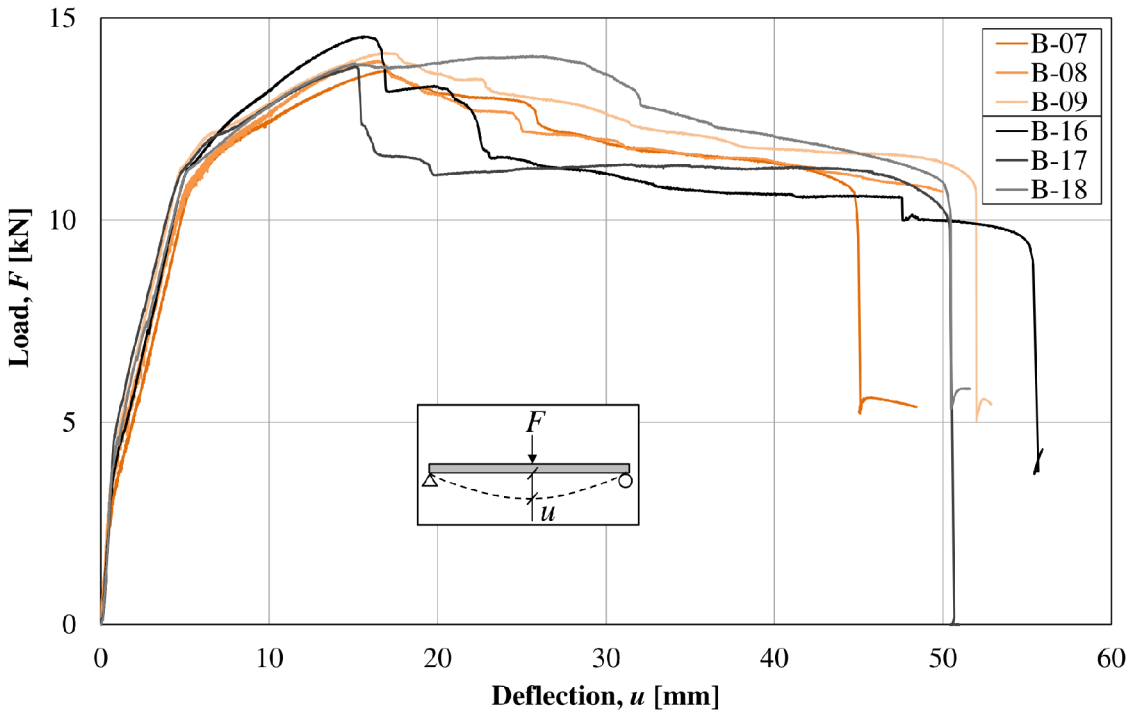

Figure 9.7 *Load vs deflection for beams of Series-3 (undamaged beams). Beams from the first batch are listed in the upper part of the legend box, while beams from the second batch are listed in the lower part.*

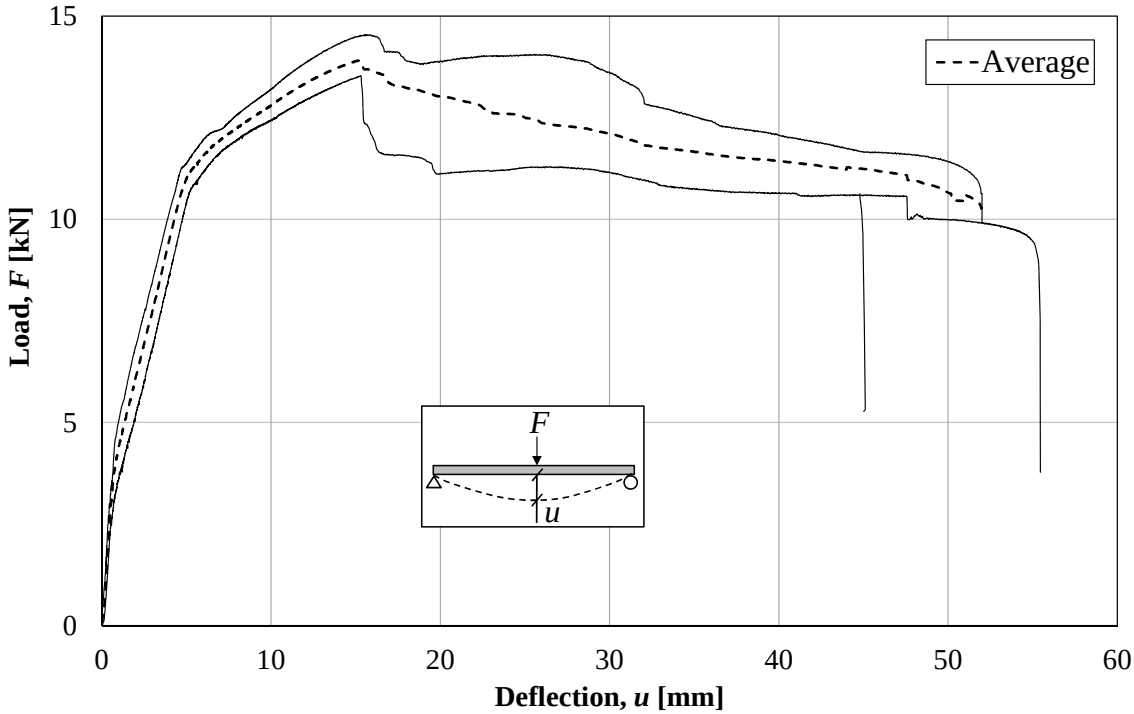

Figure 9.8 *Outer envelopes and average values of load-deflection curves for beams of Series-3.*

Table 9.7 Average key parameters gathered and calculated based on load-deflection plots for Series-3. Stiffness parameter, k, has been determined as a state II stiffness.

Beam-ID	$u_{fail,s}$ [mm]	k [kN/mm]	$F_{100\%}$ [kN]	$\theta_{pl,100\%}$ [mrad]	$\theta_{pl,95\%}$ [mrad]	$\theta_{pl,90\%}$ [mrad]	$\theta_{pl,80\%}$ [mrad]
B-07	48.4	2.0	13.7	20.5	34.1	40.4	77.1
B-08	-	2.2	13.9	20.0	25.7	37.8	77.9
B-09	52.9	2.4	14.1	22.1	34.4	48.3	92.1
Average	**50.7**	**2.2**	**13.9**	**20.9**	**31.4**	**42.2**	**82.3**
B-16	55.9	2.2	14.5	18.2	21.3	30.1	35.7
B-17	51.0	2.4	13.8	18.9	19.9	20.6	85.1
B-18	51.6	2.2	14.1	38.4	49.8	56.1	86.6
Average	**52.8**	**2.3**	**14.1**	**25.2**	**30.3**	**35.6**	**69.1**
Average all beams	**51.6**	**2.2**	**14.0**	**23.0**	**30.9**	**38.9**	**75.7**

9.2.3 Load-deflection results: Series-1

Figure 9.9 shows load-deflection plots from static tests for beams of Series-1. Key values gathered and calculated from the results of the static testing are presented in Table 9.8. For more extensive results regarding key parameters, refer to Appendix F.4.1.

According to information in Figure 9.9, the beams deformed elastically until the onset of yielding. From that point on, there is a gradual increase of the load capacity which corresponds to a response in state III. This is more noticeable for some specimens, such as B-03, B-10 and B-12. Thereafter, the load required to further deform the beam decreases until steel rupture is reached. Some specimens show a sudden drop of load capacity after peak load; for instance, B-02 and B-03.

Similarly to what has been deduced in Section 9.1.3, a scatter of results can be noticed between beams in Figure 9.9; however, no definitive conclusion can be drawn regarding whether the response of the beams from one batch differs from the other. This is further strengthened by the results presented in Table 9.8. The static response of the beams from Series-1 are therefore regarded to behave independently of the concrete batch they were cast from.

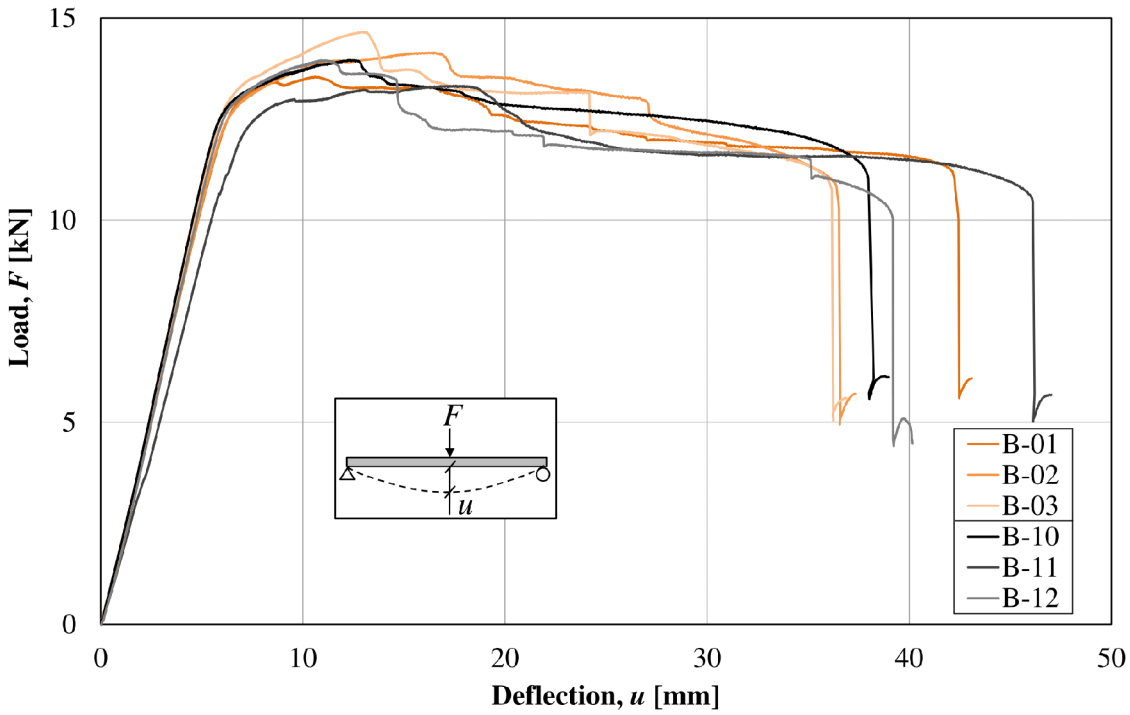

Figure 9.9 *Load vs deflection for beams of Series-1. The beams had previously been subjected to a 2.5 m drop-weight impact. Beams from the first batch are listed in the upper part of the legend box, while beams from the second batch are listed in the lower part.*

Table 9.8 *Key parameters recorded and calculated for Series-1. The recorded deflection at which a reinforcement bar ruptures is denoted $u_{fail,s}$; the linear elastic material stiffness is given by k; and the permanent plastic rotation caused by impact is referred to as $\theta_{pl,imp}$.*

Beam-ID	$u_{fail,s}$ [mm]	k [kN/mm]	$F_{100\%}$ [kN]	$\theta_{pl,imp}$ [mrad]	$\theta_{pl,100\%}$ [mrad]	$\theta_{pl,95\%}$ [mrad]	$\theta_{pl,90\%}$ [mrad]	$\theta_{pl,80\%}$ [mrad]
B-01	43.1	2.1	13.6	8.2	8.2	25.3	39.2	-
B-02	-	2.1	14.1	10.0	19.5	29.0	42.2	59.7
B-03	36.9	2.3	14.7	9.4	12.9	15.3	26.0	-
Average	**40**	**2.2**	**14.1**	**9.2**	**13.6**	**23.2**	**35.8**	**59.7**
B-10	39.0	2.2	14.0	10.2	12.0	21.1	44.1	-
B-11	47.0	1.9	13.3	8.6	20.8	26.9	34.0	80.2
B-12	40.2	2.2	14.0	9.4	8.8	17.0	19.7	59.8
Average	**41.2**	**2.1**	**13.8**	**9.4**	**13.8**	**21.6**	**32.6**	**70.0**
Average all beams	**40.6**	**2.1**	**13.9**	**9.3**	**13.7**	**22.4**	**34.2**	**66.6**

9.2.4 Load-deflection results: Series-2

Figure 9.10 presents load-deflection graphs gathered from three-point static loading for beams of Series-2. Table 9.9 presents a summary of important values for each batch gathered from the load-deflection plots, refer to Appendix F.4.2 for more extensive results regarding the presented key parameters.

Most of the beams in Series-2 show a similar response, where a linear deformation is observed until yielding load is reached. From that point on, the load required to deform the specimens decreases slightly. This behavior resembles the elasto-plastic response described in Section 2.2.4, where a plateau can clearly be distinguished after maximum peak load has been reached. Beam B-15, however, shows a sudden drop in the load capacity when the midpoint deformation is approximately 30 mm.

A remarkable exception to the description in the previous paragraph is beam B-13, which is observed to fail abruptly at a significantly low load level. It was concluded that the beam developed a shear failure mechanism which gave rise to the brittle failure. Since beam B-13 exhibited a different failure mode, it was excluded when calculating average values for the key parameters presented in Table 9.9. Ultimately, no definitive distinction can be made between batches for statically loaded beams of Series-2.

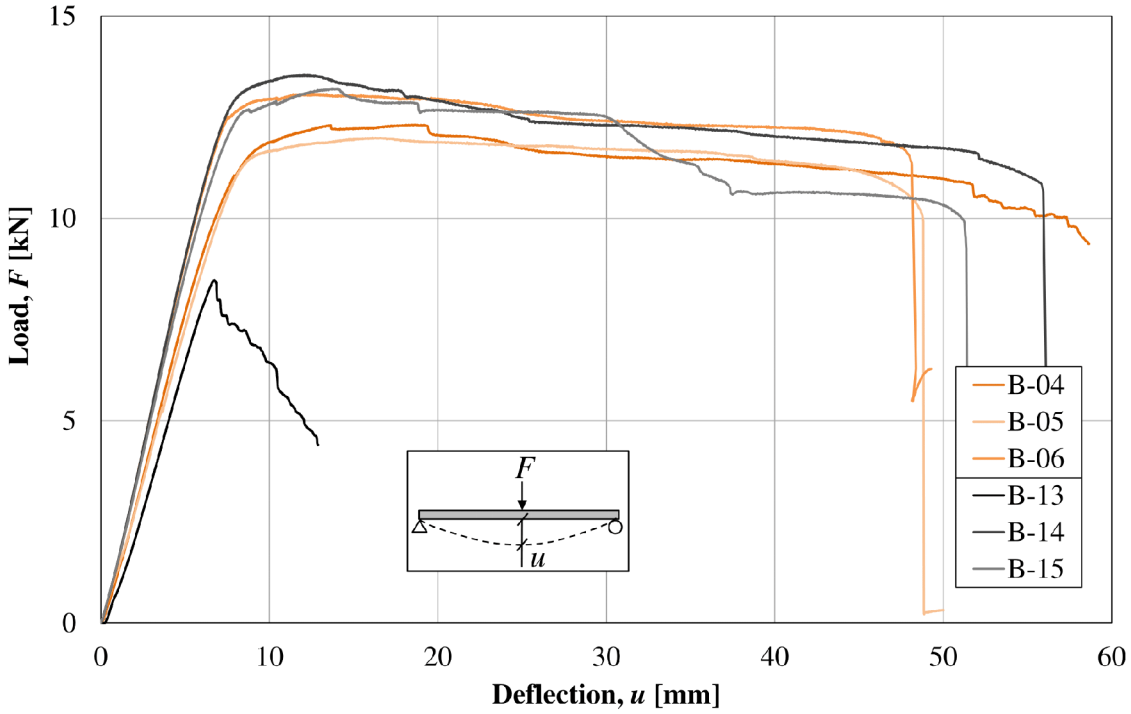

Figure 9.10 *Load vs deflection for beams of Series-2. The beams had previously been subjected to a 5.0 m drop-weight impact. Beams from the first batch are listed in the upper part of the legend box, while beams from the second batch are listed in the lower part. Failure due to shear was noted in B-13.*

Table 9.9 Key parameters recorded and calculated for Series-2. The recorded deflection at which a reinforcement bar ruptures is denoted $u_{fail,s}$; the linear elastic material stiffness is given by k; and the permanent plastic rotation caused by impact is referred to as $\theta_{pl,imp}$.

Beam-ID	$u_{fail,s}$ [mm]	k [kN/mm]	$F_{100\%}$ [kN]	$\theta_{pl,imp}$ [mrad]	$\theta_{pl,100\%}$ [mrad]	$\theta_{pl,95\%}$ [mrad]	$\theta_{pl,90\%}$ [mrad]	$\theta_{pl,80\%}$ [mrad]
B-04	-	1.6	12.3	26.0	22.1	37.5	81.1	102.7
B-05	50.0	1.5	12.0	25.6	15.8	65.3	79.5	-
B-06	49.3	1.8	13.1	25.4	11.2	44.8	81.7	-
Average	**49.7**	**1.6**	**12.5**	**25.7**	**16.4**	**49.2**	**80.8**	**102.7**
B-13[1]	12.9	1.4	8.5	26.6	0.7	6.9	7.5	8.5
B-14	56.6	1.8	13.5	23.4	9.1	26.6	58.6	99.6
B-15	52.3	1.7	13.2	23.4	12.1	44.6	50.2	79.5
Average	**54.5**	**1.8**	**13.4**	**24.5**	**10.6**	**35.6**	**54.4**	**89.5**
Average all beams	**56.5**	**1.7**	**12.8**	**25.1**	**14.1**	**43.8**	**70.2**	**93.9**

[1] The beam developed a shear failure mechanism; it is not factored in the calculations of average values.

9.2.5 Conclusions

In general, no significant difference is observed between specimens of the same series cast from different batches, although specimens of the first batch for Series-3 were somewhat better distributed with respect to the average curve than the beams of the second batch. However, it is concluded that the structural response of the beams of a given series is fairly well represented by the average values calculated from the results of the beams of said series.

It is noted that a steep drop due to excessive concrete crushing can lead to reduced rotational capacities at a given load percentage; however, such beams do not necessarily deflect less before reaching steel rupture despite small rotational capacities at, for instance, $\theta_{pl,80\%}$. This observation can be seen to happen for B-16 in Table 9.7.

An important observation for Series-2 is that such beams exhibit, on average, steel rupture (that is, higher values of $u_{fail,s}$) at a later stage than the undamaged reference beams. The difference between testing Series-2 and Series-3 increases when considering permanent deflection due to impact for Series-2; this topic is addressed further in Section 9.3.

9.3 Comparison of Static Response of Impact-loaded Beams and Undamaged Beams

9.3.1 Introduction

In this section, the residual static response of previously dynamically loaded beams is compared with the static response of the undamaged beams of Series-3. The response of the undamaged beams is represented by the average load-deformation curve and the outer envelopes, and the comparisons of load-deflection curves are made batch-by-batch for the sake of clarity and interpretable results. Furthermore, the curves have been adjusted in order to account for the plastic deformation due to impact by shifting the curves of damaged beams accordingly.

9.3.2 Comparison of Series-1 and Series-3

Figure 9.11 presents the adjusted load-deflection curves of Series-1, batch 1, together with the average values and outer envelopes gathered from Series-3. Similarly, results are also shown for batch 2 in Figure 9.12.

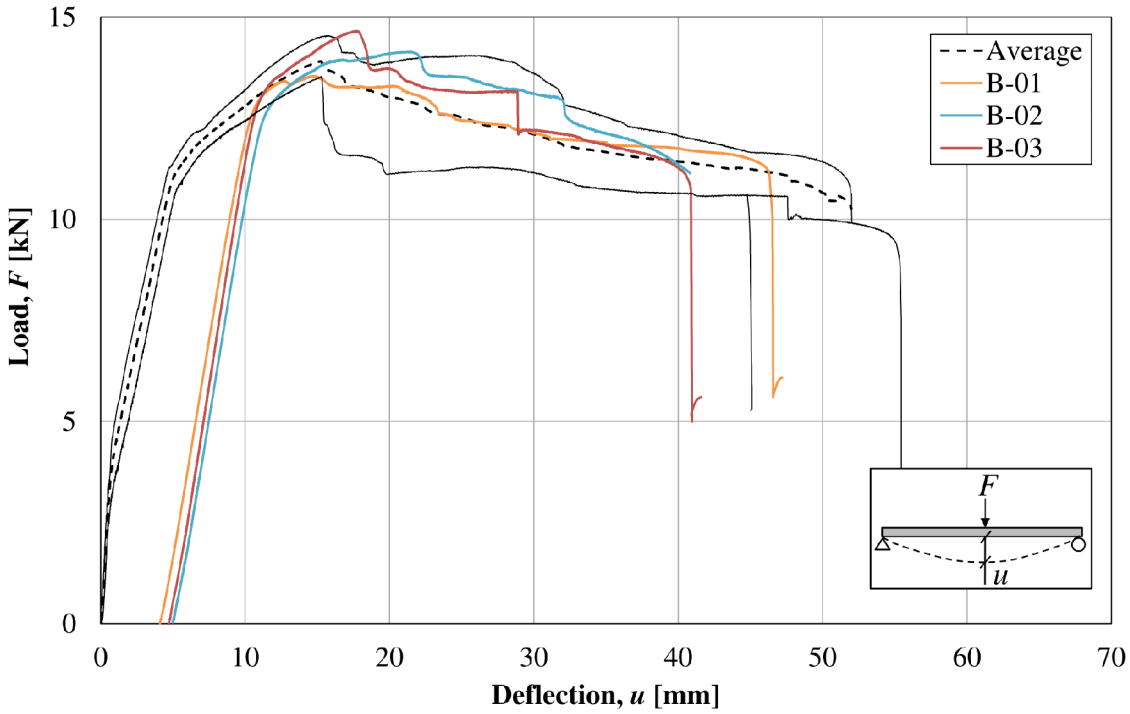

Figure 9.11 Comparison of load-deflection curves of Series-1, batch 1, with average curve of Series-3. Curves of Series-1 have been adjusted to consider plastic deformation due to impact.

The linear-elastic response of Series-1 shows similar stiffness compared to the response of the undamaged beams from the initiation of cracking to the onset of yielding, which can be further verified when comparing values presented in Tables 9.7 and 9.8. Generally, the dynamically loaded beams exhibit a linear-elastic response until the load-deflection curve reaches the average curve of undamaged beams; at this point, non-linear behavior resumes with a response which is within the boundaries of the outer

envelopes of the undamaged beams. The load increases until reaching ultimate load, where it can be observed that the ultimate load capacity of the specimens has not been affected greatly due to impact loading. As a matter of fact, the information stated in Tables 9.7 and 9.8 shows that the average maximum load is, in practical terms, equal for impact-damaged and undamaged beams.

Visually, it can be seen that the deflection at which steel rupture takes place is on average lower for beams of Series-1, even when factoring in permanent plastic deformation due to impact. This indicates that rotational capacities at low load levels, such as $\theta_{pl.80\%}$, may not be registered, something which can be noted for some specimens when examining Table 9.8.

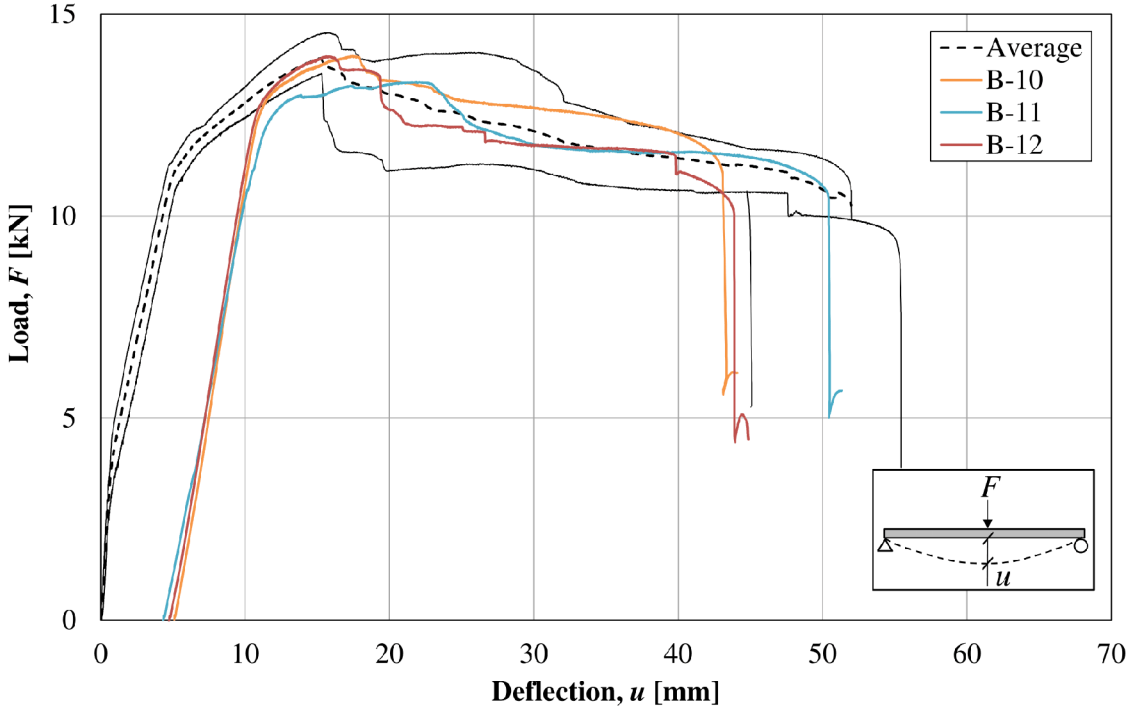

Figure 9.12 Comparison of load-deflection curves of Series-1, batch 2, with average curve of Series-3. Curves of Series-1 have been adjusted to consider plastic deformation due to impact.

9.3.3 Comparison of Series-2 and Series-3

Comparison of load-deflection curves between Series-2 and Series-3 with adjusted deflection due to plastic deformation is presented in Figure 9.13 for specimens of batch 1, and in Figure 9.14 for beams of batch 2.

The linear-elastic response of impacted beams in Series-2 is less stiff on average, which can be verified by key values presented in Tables 9.7 and 9.9. This behavior can be related to the fact that the cross-sectional area of the beams has decreased due to deterioration of the concrete after impact loading.

Similarly to what was noted when comparing Series-1 and Series-3, the linear elastic response of the beams of Series-2 continues until meeting the descending branch of the average curve for undamaged beams. Notice that, due to plastic deformation from impact loading, the load-deformation curves for damaged beams meet the curve for the undamaged specimens after ultimate load has been reached.

Moreover, the static load capacity of the damaged specimens of Series-2 has been reduced approximately 9 % on average due to impact loading. Additionally, large deflections are registered for practically constant values of load until steel rupture occurs for most specimens, as opposed to the gradual reduction of load capacity after peak load for specimens of Series-1 and Series-3.

Two important observations can be discussed. Firstly, the deflection at which steel rupture takes places, $u_{fail,s}$, is larger for all impact-damaged specimens – apart from B-13 – than for undamaged specimens. This indicates that the beams subjected to a drop-weight impact from $h = 5.0$ m can be expected to have a plastic rotational capacity, after considering the plastic deformation due to drop-weight impact, that supersedes that of the undamaged beams.

Secondly, the decrease of the load required to deform the beam after peak load appears to be less pronounced for beams of Series-2 than for undamaged specimens. As discussed in Section 9.2.4, the beams of Series-2 exhibit a behavior similar to elasto-plastic response.

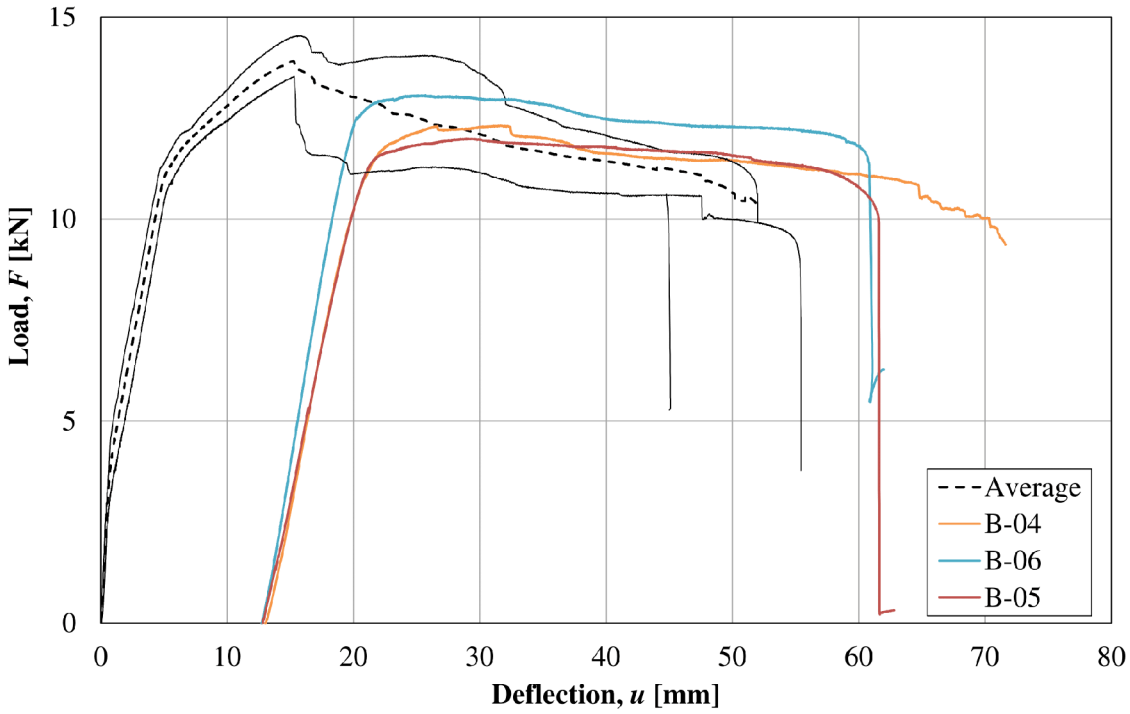

Figure 9.13 *Comparison of load-deflection curves of Series-2, batch 1, with average curve of Series-3. Curves of Series-2 have been adjusted to consider plastic deformation due to impact.*

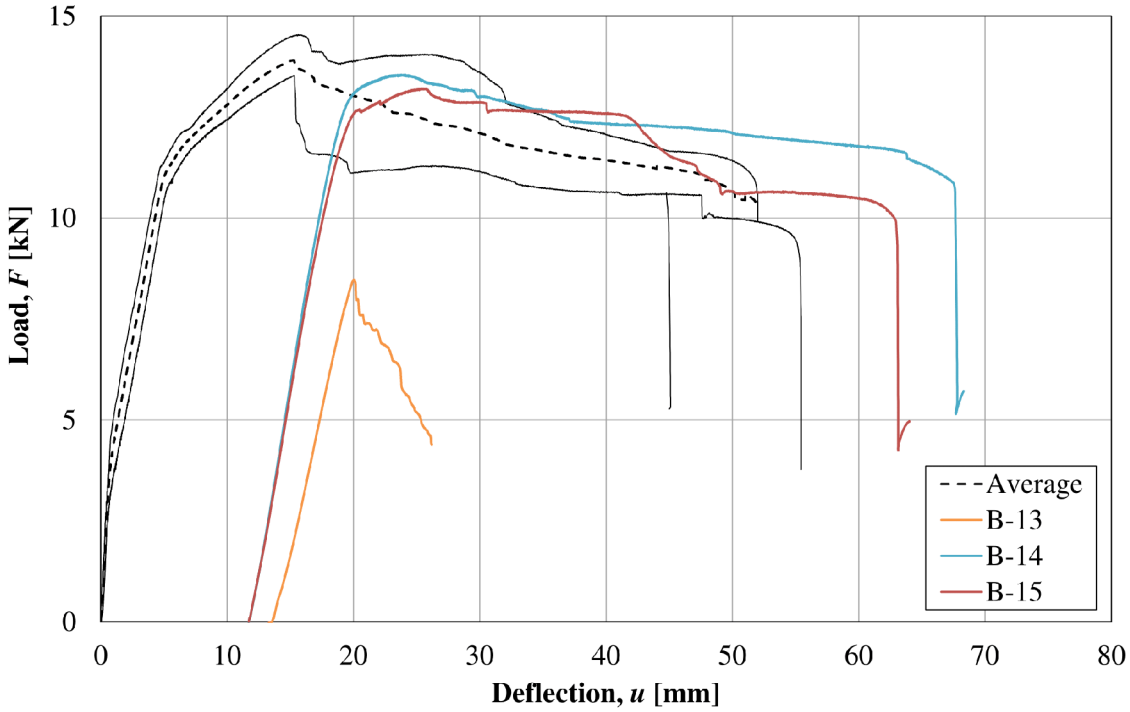

Figure 9.14 Comparison of load-deflection curves of Series-2, batch 2, with average curve of Series-3. Curves of Series-2 have been adjusted to consider plastic deformation due to impact.

9.3.4 Conclusions

The linear elastic stiffness exhibited by specimens of Series-1 corresponds fairly well with measured stiffness values gathered for Series-3, whereas the stiffness of beams of Series-2 was approximately 20 % lower. A possible reason to this phenomenon could be the loss of material and consequently reduction in cross-sectional area caused by impact loading; another contributing factor could be that the concrete close to the impact region was subjected to significantly large compressive strains, which might result in the reduction of the concrete secant modulus when loading the impacted beams statically.

Trends regarding ultimate load, $F_{100\%}$, showed that specimens of Series-2 exhibited a 9 % reduction of static load capacity compared to Series-3, while beams of Series-1 showed similar average values of load capacity in relation to Series-3.

The beams of Series-2 are able to deform further before reaching failure of the reinforcement bars than the undamaged specimens of Series-3.

9.4 Plastic Rotational Capacity

9.4.1 Introduction

This section details the measured plastic rotational capacity of both the undamaged and impact-damaged beams after static loading, where the permanent plastic rotation caused by impact loading, $\theta_{pl,imp}$, is also taken into account. Refer to Section 5.3.4 for information regarding the method used to calculate rotational capacity at a given load percentage, $\theta_{pl,x\%}$. Thereafter, the measured values of rotational capacity are compared to the rotational capacity predicted by the different methods described in Section 5.4.

9.4.2 Results

Figure 9.15 provides with a summary of average values of rotational capacity at a given percentage, $\theta_{pl,x\%}$, per batch for all series. Furthermore, average values of $\theta_{pl,x\%}$ per series are presented in Figure 9.16. Refer to Appendix F.5.1 for complete information regarding $\theta_{pl,x\%}$ for all beams.

It is noted in Figure 9.15 that no typical pattern can be distinguished when comparing values of $\theta_{pl,x\%}$ between batches for a given series. Therefore, the average values presented in Figure 9.16, where the results for the two batches are combined, are regarded as representative for the response of a given load series.

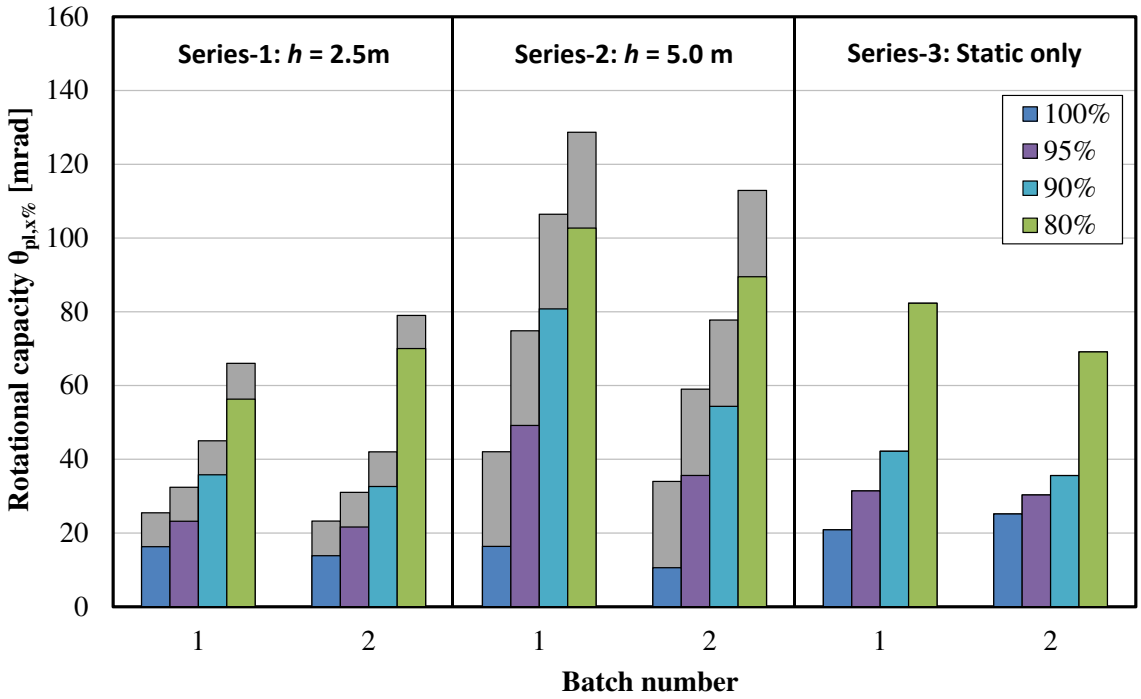

Figure 9.15 Plastic rotational capacity with respect to a given load percentage, average values for specimens within a batch and testing series. The upper value indicated by the gray bar for Series-1 and Series-2 accounts for the permanent plastic rotation due to impact, $\theta_{pl,imp}$.

9.4.2.1 Comparison of Series-1 with Series-3

When comparing values of $\theta_{pl,100\%}$ in Figure 9.16, it is observed that Series-1 exhibit similar values for all load levels compared to Series-3. This indicates that the impact-loaded beams tend to conserve the total rotational capacity available for undamaged specimens.

As stated in Section 9.3.2, the response of the specimens of Series-1 conforms to the undamaged response when the load-deformation curves meet. The results indicate that the residual rotational capacity of beams subjected to a drop impact from $h = 2.5$ m can be determined by subtracting the permanent rotation due to impact from the total rotational capacity at a given load level of undamaged specimens.

However, only three out of six beams registered values for $\theta_{pl,80\%}$ before steel rupture occurs, while all beams in Series-3 reached a load level of 80 % after peak load. The smaller sample size regarding $\theta_{pl,80\%}$

in Series-1 indicates that the dynamic loading might influence the total ductility of impact loaded beams.

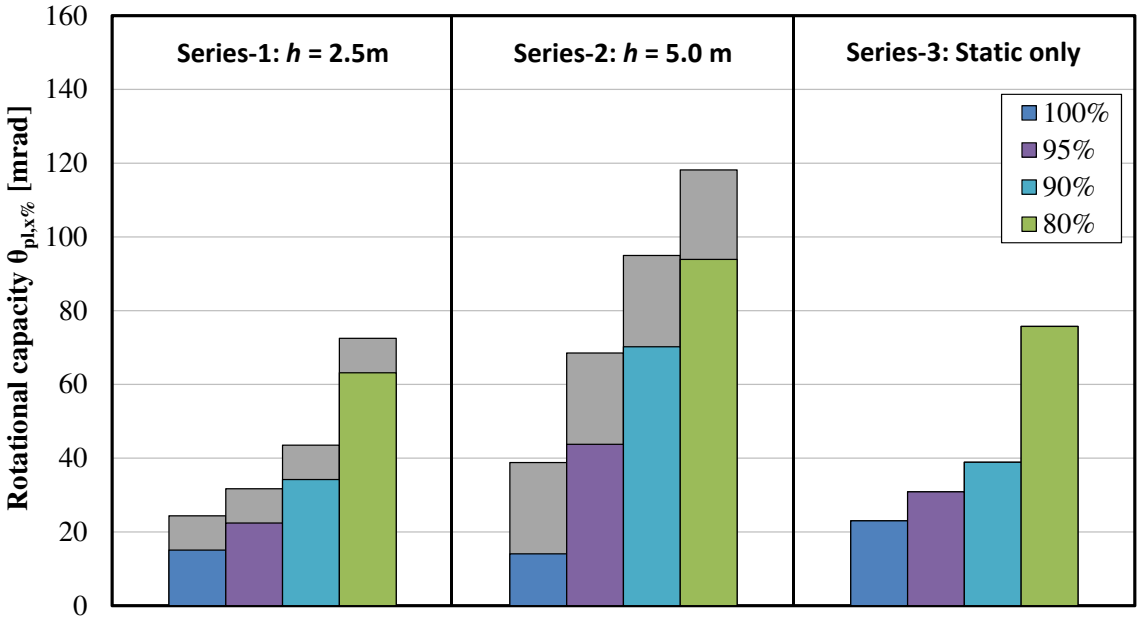

Figure 9.16 Plastic rotational capacity with respect to a given load percentage, average values for all specimen within a testing series. The upper value indicated by the gray bar for Series-1 and Series-2 accounts for the permanent plastic rotation due to impact, $\theta_{pl,imp}$.

9.4.2.2 Comparison of Series-2 with Series-3

The difference in values of $\theta_{pl,x\%}$ becomes more significant between Series-2 and Series-3, as specimens of Series-2 possess an increased rotational capacity compared to undamaged specimens. This phenomenon is related to the structural response described in Section 9.3.3. The impact-damaged beams deform linear-elastically until they reach the load-deformation curve of the undamaged specimen. From that point on, the response reaches a plateau and the load capacity start to decrease at a slow rate, resulting in larger measurements of deflection, particularly so for load levels lower than peak load.

Therefore, the impact event seems to trigger a response which enables the beams of Series-2 to plastically deform beyond their undamaged counterparts. A possible explanation could be related to the more extended cracking pattern which arises due to dynamic loading, which would allow for a longer portion of reinforcement steel to yield. This is further studied in Section 9.5. It should be noted that only for three out of five beams that failed in bending it was possible to determine values of $\theta_{pl,80\%}$ before rupture of steel occurred; while one of the beams failed in an abrupt and brittle shear failure. This implies that $\theta_{pl,80\%}$ may not be a reliably measurement for impact-loaded beams, as only few specimens would reach that level.

9.4.3 Internal work

The plastic rotational capacity of a given concrete beam is related to its capacity to absorb energy when subjected to a certain load. For this reason, it is of interest to determine the internal work in the specimens

for different load levels, and compare such values to their respective rotational capacity. The internal work can be calculated as the area below the curve if the load-deformation relationship of the structure due to an external load is known. This procedure was briefly introduced in Section 3.2, though the internal work in impulse loaded structures was treated there. The total internal work, $W_{i,tot}$, determined for all beams, as well as the accumulated internal work, $W_{i,x\%}$, for different load levels on the descending branch of the load-deformation relationship, are presented in Appendix F.5.2. Observe that the internal work was determined for static loading for all specimens.

Furthermore, a comparison of $W_{i,x\%}$ to $\theta_{pl,x\%}$ is also made by introducing the ratio $W_{i,x\%}/\theta_{pl,x\%}$ for given load levels for all specimens; the average results for all series are presented in Figure 9.17. It can be observed that the proportion of internal work to rotational capacity decreases for lower load levels (after peak load has been reached) for all series. This indicates that, even though the rotational capacity of the specimens is larger for lower levels, the capacity to absorb energy in relation to the rotation capacity decreases.

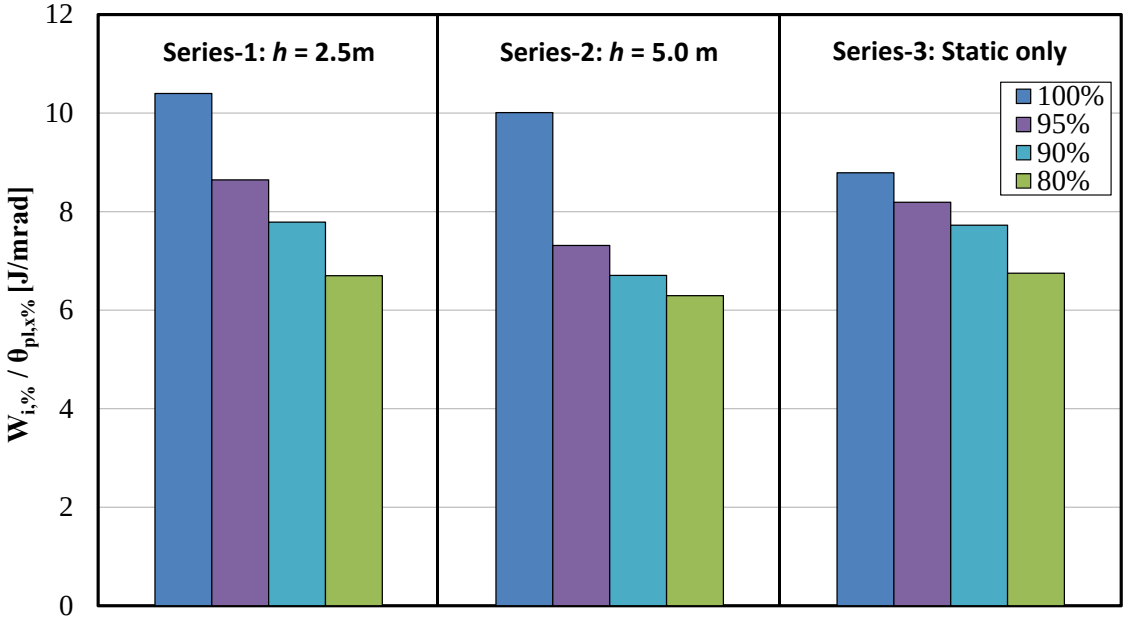

Figure 9.17 Average values of the ratio $W_{i,x\%}/\theta_{pl,x\%}$ for all series at a given load level. Plastic rotation due to impact, $\theta_{pl,dyn}$, is not taken into account.

The calculated ratios for Series-1 and Series-3 show similar values, apart from the values for maximum load. The difference for 100 % is due to the fact that the specimens of Series-1 deform with a stiffness equivalent to stiffness in state II from the beginning of loading. However, as the static loading progresses and the response of Series-1 conforms to the response of the undamaged specimens, the influence of the differences in deformation in the elastic range becomes less relevant. Thereafter, the difference in values of $W_{i,x\%}/\theta_{pl,x\%}$ between the two testing series diminishes for subsequent load levels. This indicates that a comparison of the deformation capacity between specimens of Series-1 and Series-3 based solely on the plastic rotational capacity, $\theta_{pl,x\%}$, is consistent and acceptable.

However, the results in Figure 9.17 point to significant differences between Series-2 and Series-3. Except

for a load level of 100%, the ratio $W_{i,x\%}/\theta_{pl,x\%}$ is consistently lower for Series-2, which indicates that comparisons made for plastic rotational capacity between these two series may not result in a proper assessment in terms of internal work. Moreover, it seems that the method used to determine rotational capacity $\theta_{pl,x\%}$ for Series-2 yields an excessively large value for load levels of 95 % and less.

A new methodology for calculation of the rotational capacity from experimental results where the maximum load level (used as a basis to calculate different load levels) corresponds to the average load capacity of undamaged specimens, as described schematically in Figure 9.18, might give a better description of the deformation capacity of the specimens of Series-2. In that sense, the blue column in Figure 9.17 for Series-2, for instance, would not correspond to 100 %, but to a lower percentage of the average maximum load measured in undamaged specimens, considering that the load capacity of the beams of Series-2 is lower than that of undamaged specimens. This approach could be more reliable, since, even though specimens of Series-2 can deform to a larger extent, the load needed to exert such deformation is lower compared to the undamaged specimens.

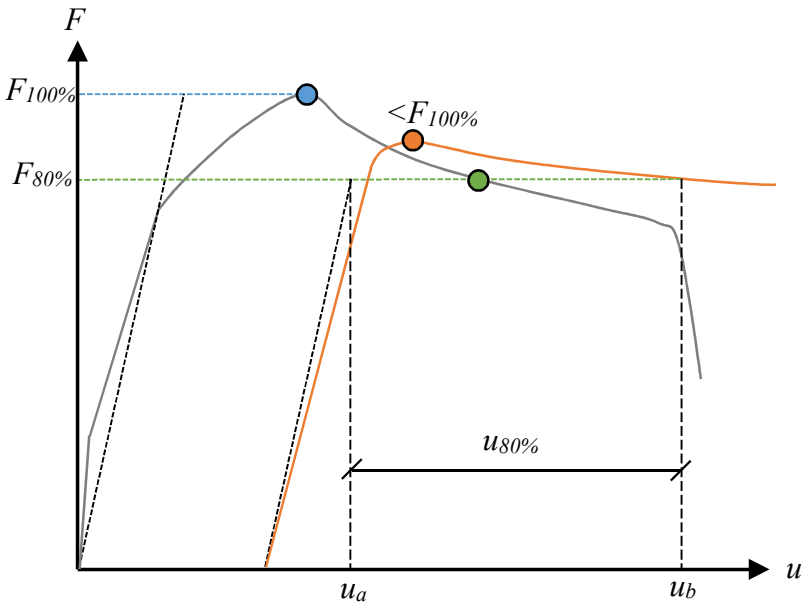

Figure 9.18 Schematic illustration of an alternative method for determining the deformation of impact-damaged beams at a given load level based on the average response of undamaged beams. The linear elastic stiffness used to determine the plastic deformation is based on the state II stiffness of the average undamaged response.

9.4.4 Conclusions

Comparison of Series-1 beams against undamaged beams indicates that the plastic rotational capacity is conserved for such impact scenario. Therefore, the residual rotational capacity can be determined by deducting permanent plastic rotation due to impact from the rotational capacity available for undamaged specimens. However, the rotational capacity was observed to increase when comparing Series-2 against undamaged beams. The impact scenario seems to trigger a response that allows for damaged beams to rotate to a greater extent than their undamaged counterparts.

In the assessment of $W_{i,x\%}/\theta_{pl,x\%}$, it was concluded that measurements of rotational capacity between Series-1 and Series-3 provided with a fair comparison in terms of internal work generated between the two testing series for load levels below 100%. However, rotational capacities between Series-2 and Series-3 may not result in accurate comparisons in terms of internal work, since the response in terms of load capacity and behavior differs.

9.5 DIC Analysis of Static Tests

9.5.1 Overview

The cracking pattern observed during static loading of the specimens is discussed in this section. The principal strain field has been determined on GOM Correlate 2016 by adopting a facet size of 10 pixels, a point distance of 15 pixels, and a *standard* computation method.

A summary of the cracking pattern for all specimens is presented at a load level equivalent to 95 % of the peak load, $F_{95\%}$, after peak load has been reached. It was decided to display the crack pattern at this load level as it was found that generally no new cracks were formed beyond this stage; instead, the already existing cracks would continue growing in size. Refer to Appendix F.6 for complete information concerning the strain field of all beams, and to Appendix F.7 for details regarding the structural response and crack pattern at given load levels for certain beams.

9.5.2 Crack patterns of Series-3

The cracking pattern for beams of Series-3 is presented in Table 9.10 as reference for comparison with the strain field obtained for impact-damaged beams. Vertical flexural cracks and inclined flexural shear cracks can be observed along the span for all specimens. The extension of the cracking region and the numbers of cracks seem to be consistent among most specimens.

Table 9.10 Strain field for beams of Series-3 during static loading at a load level of 95 % of the maximum load, $F_{95\%}$, after maximum load has been reached.

Deflection/Load	Strain field due to static loading
B-07 $u_{95\%} = 29.4$ mm $F_{95\%} = 12.4$ kN B-08 $u_{95\%} = 19.0$ mm $F_{95\%} = 13.2$ kN B-09 $u_{95\%} = 22.8$ mm $F_{95\%} = 13.4$ kN B-16 $u_{95\%} = 16.8$ mm $F_{95\%} = 13.8$ kN B-17 $u_{95\%} = 15.4$ mm $F_{95\%} = 13.1$ kN B-18 $u_{95\%} = 31.1$ mm $F_{95\%} = 13.4$ kN	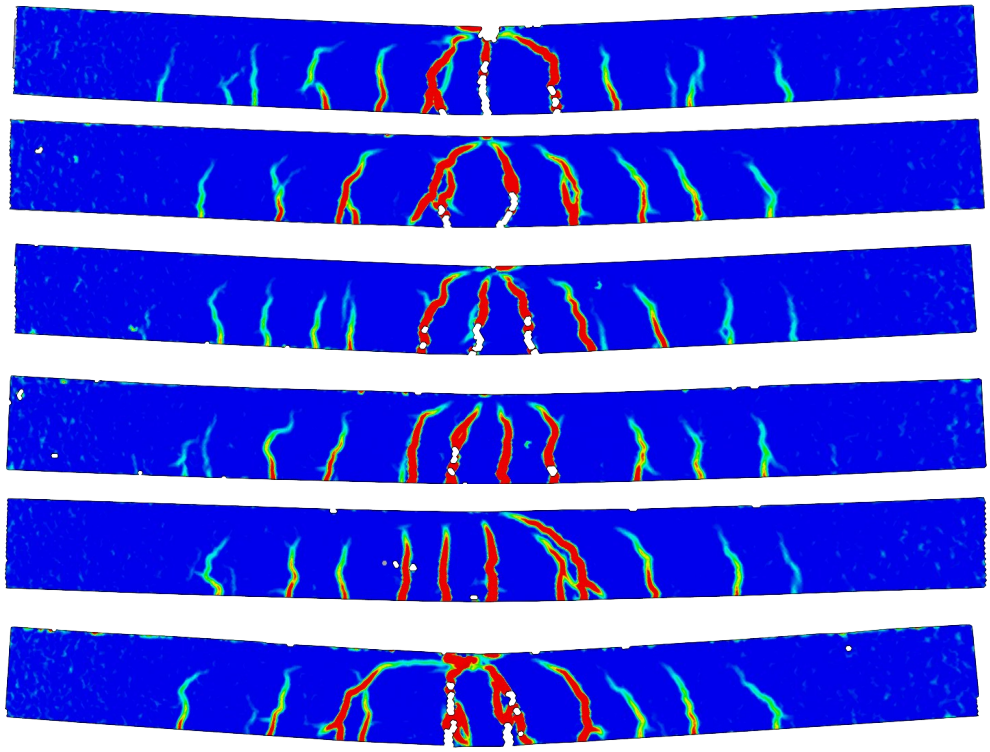
Principal strain [%]	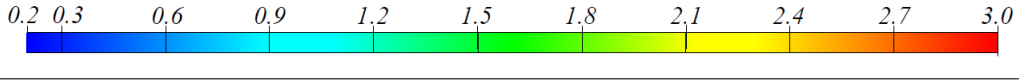

9.5.3 Crack patterns of Series-1

Table 9.11 shows the cracking pattern for specimens subjected to an impact from a drop-height equal to $h = 2.5$ m. In contrast to specimens of Series-3, some beams of Series-1 exhibit inclined cracking in the area close to the point of load application. Moreover, the cracks in the region between midspan and the support show a larger rotation than observed for undamaged specimens. The emerging crack pattern is mostly the result of cracks reopening; these cracks had previously been initiated by the drop-weight impact event, this is covered further in Appendix F.7. This indicates that the previous damage due to impact loading governs to some extent the cracking response of the beams when loaded statically. However, some specimens, such as B-03 and B-10, still show vertical flexural cracks in the midspan region, in a similar way to the cracking pattern observed for undamaged beams in Table 9.10.

Table 9.11 Strain field for beams of Series-1 during static loading at a load level of 95 % of the maximum load, $F_{95\%}$, after maximum load has been reached.

Deflection/Load	Strain field due to static loading
B-01 $u_{95\%} = 12.2$ mm $F_{95\%} = 12.9$ kN	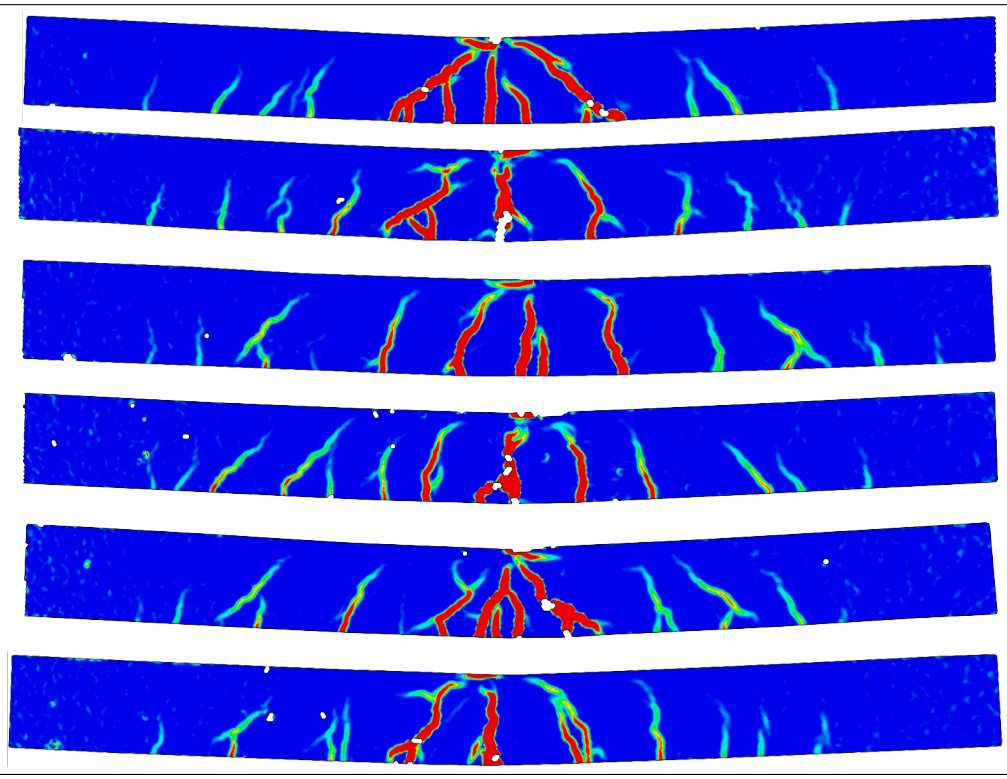
B-02 $u_{95\%} = 20.9$ mm $F_{95\%} = 13.4$ kN	
B-03 $u_{95\%} = 13.8$ mm $F_{95\%} = 13.9$ kN	
B-10 $u_{95\%} = 16.6$ mm $F_{95\%} = 13.3$ kN	
B-11 $u_{95\%} = 20.3$ mm $F_{95\%} = 12.7$ kN	
B-12 $u_{95\%} = 14.7$ mm $F_{95\%} = 13.3$ kN	
Principal strain [%]	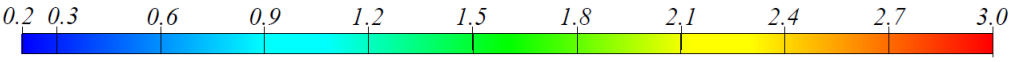

9.5.4 Crack patterns of Series-2

The beams of Series-2 show a markedly different cracking pattern compared to the undamaged specimens. Inclined cracks are more prominent in the midspan region, as shown in Table 9.12. Moreover, by visual inspection, it appears that the total number of cracks is less than what can be seen for undamaged beams. As was found for Series-1 beams, the crack pattern developed at $F_{95\%}$ is largely due to pre-existing cracks initiated during the impact event which reopened during the static tests.

Important shear cracks are visible for specimens B-13 and B-15. For B-13, this shear crack limited the extension of cracking at midspan and reduced the load capacity considerably. As described in Appendix F.7, the shear crack in B-13 became the most critical with increased load levels, whereas the propagation of the shear crack in B-15 halted as cracks close to the center became critical instead.

Table 9.12 Strain field for beams of Series-2 during static loading at a load level of 95 % of the maximum load, $F_{95\%}$, after maximum load has been reached.

Deflection/Load	Strain field due to static loading
B-04 $u_{95\%} = 26.0$ mm $F_{95\%} = 11.7$ kN	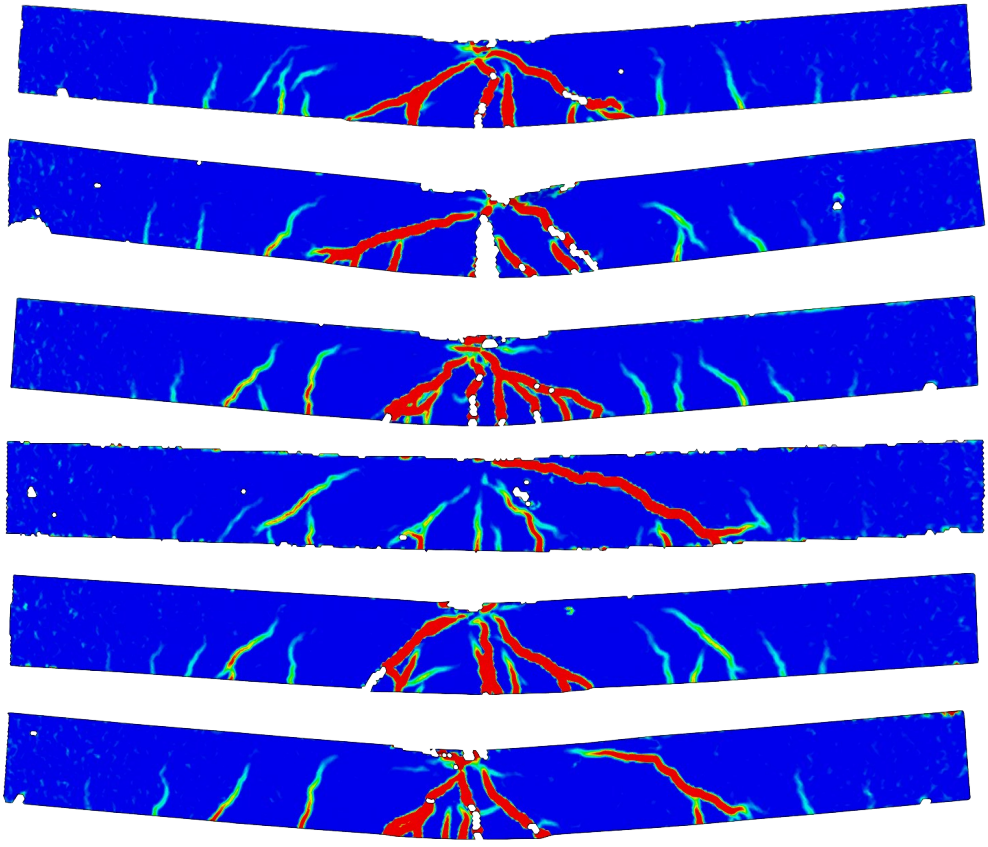
B-05 $u_{95\%} = 40.5$ mm $F_{95\%} = 11.4$ kN	
B-06 $u_{95\%} = 29.4$ mm $F_{95\%} = 12.4$ kN	
B-13 $u_{95\%} = 6.9$ mm $F_{95\%} = 8.1$ kN	
B-14 $u_{95\%} = 20.4$ mm $F_{95\%} = 12.9$ kN	
B-15 $u_{95\%} = 29.6$ mm $F_{95\%} = 12.5$ kN	
Principal strain [%]	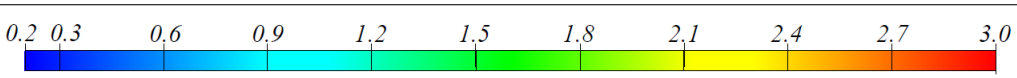

9.5.5 Major cracking pattern

Important differences were noticed regarding the crack distribution at $F_{95\%}$ obtained through DIC analysis in specimens of Series-2 compared with beams of Series-1 and Series-3. Therefore, certain beams were selected from all test series to highlight differences found in crack patterns between series. In Table 9.13, the crack pattern after static testing can be seen for the chosen beams. The cracks which can be visually detected are assumed to be major cracks; and the reinforcing steel is most likely to yield to a higher extent in the close proximity of these observable cracks. Refer to Appendix F.8 for photos of all beams after static loading.

The cracks present in the beams of Series-1 and Series-3 exhibit a pattern which is similar to flexural cracks, and are localized in the midspan region. As mentioned in Section 9.5.3, minimal signs of new crack initiation due to static loading were observed, instead cracks due to impact loading reopened during the static experiments. These results suggest that the cracks caused by an impact from $h = 2.5$ m tend to distribute in a similar manner to the undamaged cracking response. This is also in agreement with the observations regarding the load-deformation curves described in Section 9.3.2; that is, beams of Series-1 and Series-3 appear to converge to a common response.

When studying the cracks present in Series-2 beams, the differences become more apparent. More major cracks can be observed and these are distributed over a larger zone across the midspan region; moreover, most cracks have propagated with a pronounced inclination. As stated in Section 9.5.4, no new crack initiation took place due to static loading, instead reopening of already present cracks generated due to impact loading was observed in the DIC analysis; this indicates that the crack initiation due to an impact from $h = 5.0$ m differs from the static cracking response of undamaged specimens. Furthermore, the longer length along which the cracks are distributed is most likely the main reason as to why larger plastic rotations are observed for Series-2 compared to Series-3 and Series-1, as this would allow for more sections of reinforcement to yield, effectively increasing the plastic hinge length.

An attempt to produce DIC results indicating the presence of major cracks at $F_{95\%}$ was made, as presented in Table 9.14 for the same selected beams listed in Table 9.13. Here, the upper limit of the colorscale has been adjusted to 20 % instead of the previous limit of 3 %, as doing so hides the presence of minor cracks in the principal strain field. These DIC results are similar to the photos taken of the specimens after static testing shown in Table 9.13. The strain field for all beams are presented in Appendix F.7.5.

Table 9.13 Photographs of selected beams displaying the cracks present after static testing was performed.

Series	Beam-ID	Crack pattern at the end of the static test
3	B-07	
	B-09	
	B-16	
1	B-02	
	B-03	
	B-10	
2	B-05	
	B-06	
	B-14	

Table 9.14 Strain field for selected beams during static loading at a load level of 95 % of the maximum load, $F_{95\%}$, after maximum load has been reached. The upper limit of the colorscale has been adjusted to enhance the presence of major cracks.

Series	Beam-ID	Strain field due to static loading
3	B-07	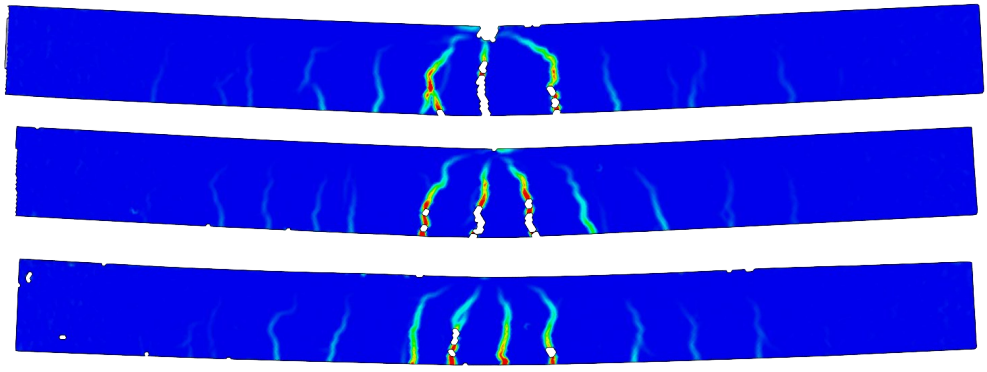
	B-09	
	B-16	
1	B-02	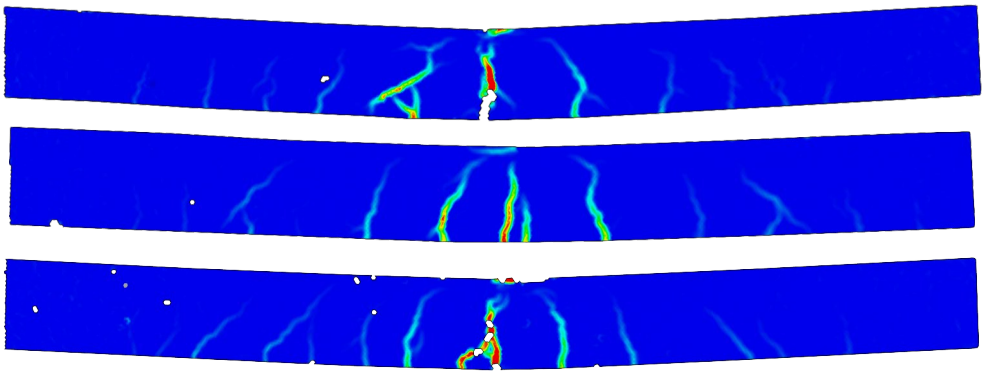
	B-03	
	B-10	
2	B-05	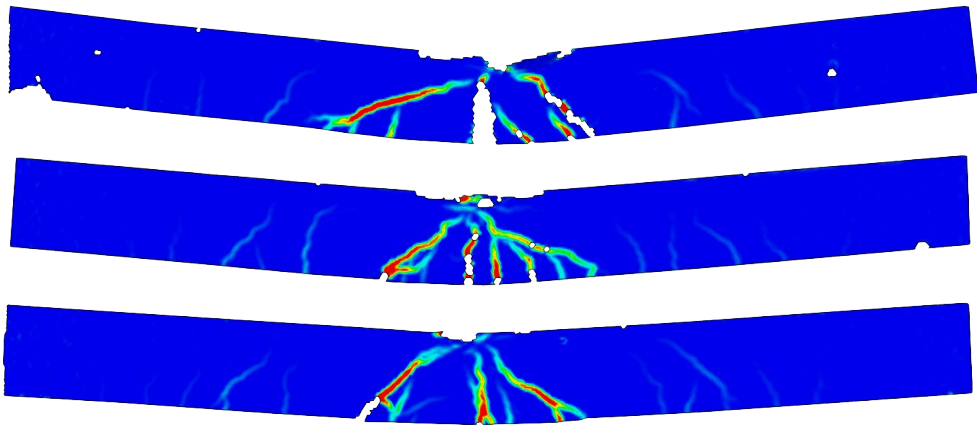
	B-06	
	B-14	
Principal strain [%]		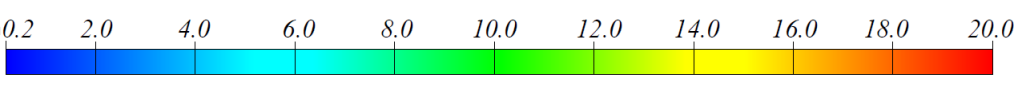

9.6 Verification of Predictions

9.6.1 Overview

In this section, the response of the reinforced concrete beams as observed during both the impact-loading and static experiments is compared with the predictions presented in Chapter 8. The objective is to evaluate the accuracy and suitability of the different theoretical methods discussed previously.

9.6.2 Predicted load-deflection curve and load capacity

Figure 9.19 presents the average load-deflection curves obtained from static experiments of undamaged beams of Series-3, together with the theoretical load-deflection curves determined for two different values of yield stress, namely: the mean measured value, $f_y = 575\,\text{MPa}$, and adopting a value of yield stress equal to the ultimate tensile stress, $f_y = f_t = 686\,\text{MPa}$.

Good correspondence concerning the cracking load and the stiffness in state I is observed in Figure 9.19, although with slight deviations from experimental curves. The experimental stiffness of the response between cracking initiation and the onset of yielding is also accurately represented. However, the two theoretical alternatives show an underestimation of the ultimate load. The overall non-linear response after peak load is predicted to a good extent by the design curve determined using $f_y = 686\,\text{MPa}$, whereas the assumed elasto-plastic response for $f_y = 575\,\text{MPa}$ is deemed to be too conservative from visual inspection.

A possible explanation for the underestimation of the load carrying capacity of the beams could be deviations in the position of reinforcement bars assumed during calculations. As explained in Section 7.2.1, there existed a possibility that the bars were displaced from their intended position during casting of concrete. For that reason, after the impact-loading and static tests were completed, the specimens were sawed in order to measure the correct position of the reinforcement bars.

The cut was performed as close as possible to midspan, where the largest deviation was expected. Some specimens had been damaged considerably after the static tests and, therefore, were disregarded. The average distance measured in the laboratory for both the top and the bottom layer is presented in Figure 9.20. Further information for all specimens can be found in Appendix C. It can be noticed that the top bars were lowered in average by 2 mm, while the bottom bars were displaced downwards 3 mm in average.

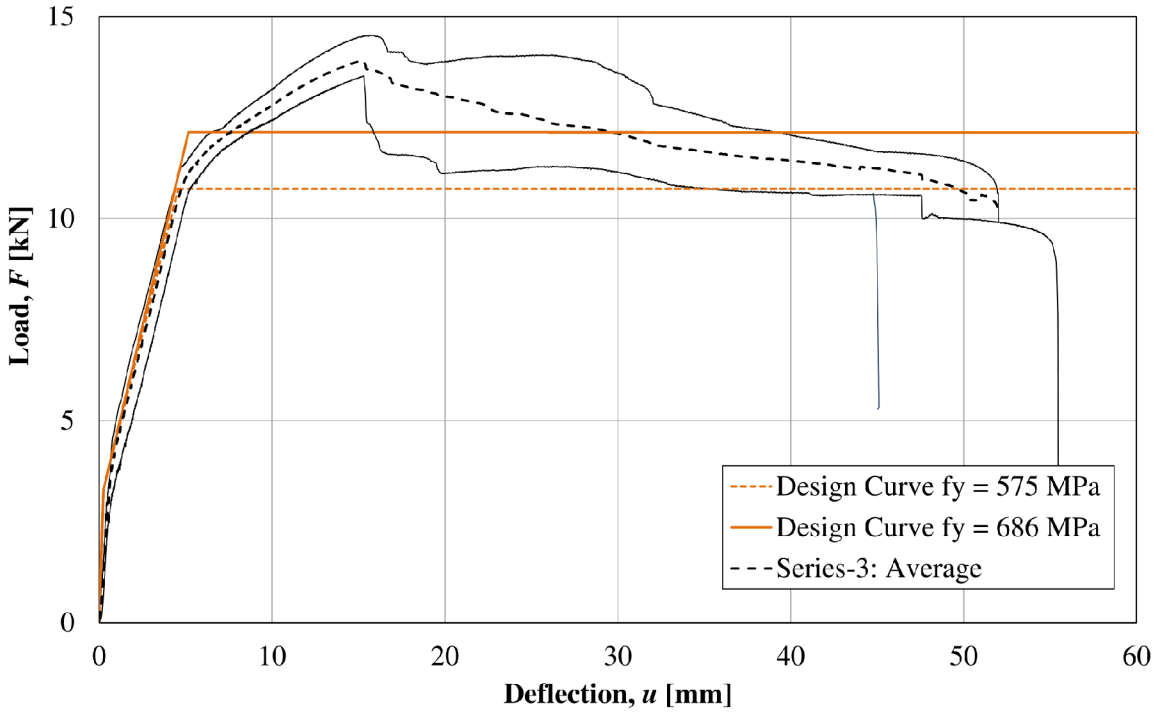

Figure 9.19 *Theoretical load-deformation curves for different values of yield stress against experimental load-deformation curve.*

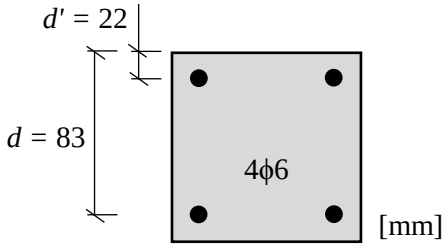

Figure 9.20 *Average values of measured distances from the center of the bars to the concrete surface. Nominal values for d and d′ correspond to 20 mm and 80 mm respectively.*

New calculations were performed considering the real position of the reinforcing steel, following the same methodology as explained in Section 8.2. Table 9.15 shows the calculated value of load capacity for the nominal and adjusted position of the bars. An increase of around 6 % can be observed. However, as can be seen in Table 9.15, the calculations still lead to an underprediction of the load capacity.

Table 9.15 Moment and external force at Ultimate Limit State for different positions of the reinforcement bars; compared with experimental average values gathered from Series-3.

f_{yd} [MPa]	Position	M_u [kN m]	F_u [kN]
575	Nominal	2.7	10.7
	Adjusted	2.8	11.3
686	Nominal	3.0	12.1
	Adjusted	3.2	12.8

(a) Calculated load and moment capacities.

M_u [kN m]	F_u [kN]
3.5	14.0

(b) Experimental static load capacity from Series-3.

9.6.3 Dynamic behavior according to 2DOF model

The experimental dynamic response of the specimens gathered through DIC analysis is presented in terms of deflection at midspan over time in Figure 9.21 together with the predictions made by the 2DOF model, using $f_y = 575$ MPa or $f_y = 686$ MPa, for the two drop-heights. Here, the 2DOF response is based on the nominal position of the reinforcement bars; furthermore, the internal resistance of the beam in the 2DOF model has been simplified to a bi-linear response by adopting state-II stiffness from the moment of load application to ultimate load, as previously explained in Section 8.4. Key parameters are presented in Table 9.16.

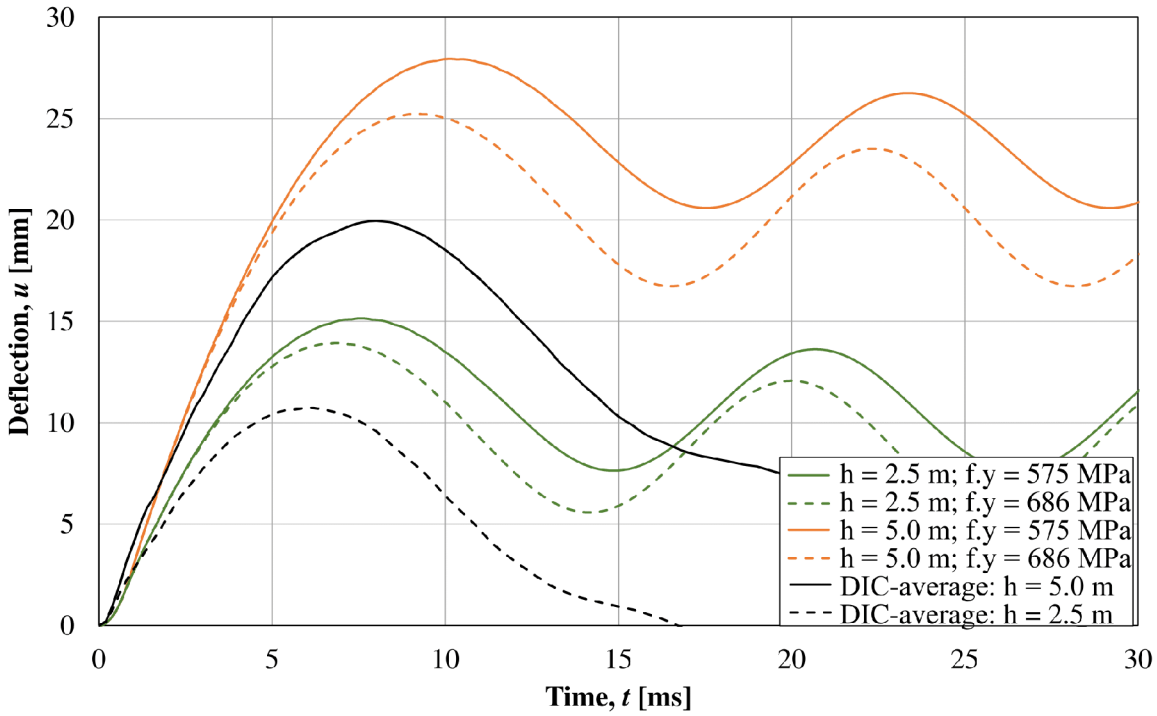

Figure 9.21 Dynamic response according to the 2DOF model due to impact from h = 2.5 m and h = 5.0 m, together with experimental average values gathered from DIC analysis for the two drop-heights.

Table 9.16 Comparison of values of maximum deflection due to impact-loading calculated with a 2DOF model with the experimental results obtained through DIC analysis.

Results	DIC Series-1	f_y 575 MPa	f_y 686 MPa
u_{max} [mm]	10.7	15.1	13.9
Relative error to DIC	-	42 %	30 %

(a) Drop-height, $h = 2.5$ m

Results	DIC Series-2	f_y 575 MPa	f_y 686 MPa
u_{max} [mm]	20.1	27.9	25.2
Relative error to DIC	-	39 %	26 %

(b) Drop-height, $h = 5.0$ m

The dynamic response predicted by the 2DOF model consistently overestimates the maximum deflection for both drop-heights. This is inherently related to the underprediction of load capacity shown in Table 9.15. As a result, the internal resistance for the beam in the 2DOF model is lower than in reality, and therefore overprediction of deflection is to be expected. Furthermore, strain rate effects have not been considered when predicting deflection over time with the 2DOF models. These effects would dynamically enhance properties such as stiffness and strength of concrete as well as reinforcing steel, which would affect the internal resistance function and result in reduction of the deflection estimated by the 2DOF system.

The 2DOF model based on $f_y = 686$ MPa shows a higher correspondence to average experimental measurements from DIC analysis. This can be coupled to its internal resistance function, as a higher load capacity is obtained for $f_y = 686$ MPa than for $f_y = 575$ MPa. Considering that the impact event is identical and that the stiffness in the two prediction models is essentially the same, it can be concluded that a higher theoretical load capacity would ultimately result in lower estimated values of deflection.

2DOF analyses were also performed where the calculation of the internal resistance of the beam was based on the measured average distances to reinforcement bars in Figure 9.20. A comparison of the maximum midpoint deflection between analyses with the nominal position and the adjusted position for $f_y = 575$ MPa and $f_y = 686$ MPa is presented in Table 9.17.

While a higher correspondence is found when using adjusted positions, the change is rather small. However, the results indicate that if a good prediction of the load carrying capacity under static loading is achieved, and such capacity is used as internal resistance of the beam in an equivalent 2DOF system, a good prediction of the dynamic behavior could be possible.

Another important factor that could influence significantly the predictions obtained with the 2DOF model corresponds to the assumptions adopted when choosing transformation factors to transform the beam into an equivalent spring-mass system. In Section 4.3.2 it is stated that the mass transformation factor, κ_m, depends on the deformed shape of the beam, and two values were derived for different responses, as presented in Table 4.1. During calculations with the 2DOF system, it was assumed that the beam undergoes plastic deformation and takes a triangular deformed shape from the beginning of loading. However, as described in Section 9.1.6, only a portion of the beam reacts shortly after impact, and only after approximately 2 ms does the beam exhibit a triangular shape. These results show that mass participation increases gradually after impact, and low values of mass are to be expected at the beginning

of the response. In that sense, assuming a constant mass transformation factor during the entire event could lead to incorrect prediction of the response.

Table 9.17 Deformation according to 2DOF system considering the adjusted position of the reinforcement bars.

Drop-height [m]	f_y [MPa]	Rebar Position	u_{max} [mm]
2.5	575	Nominal	15.1
		Adjusted	14.4
	686	Nominal	13.9
		Adjusted	13.3
5.0	575	Nominal	27.9
		Adjusted	26.5
	686	Nominal	25.2
		Adjusted	24.0

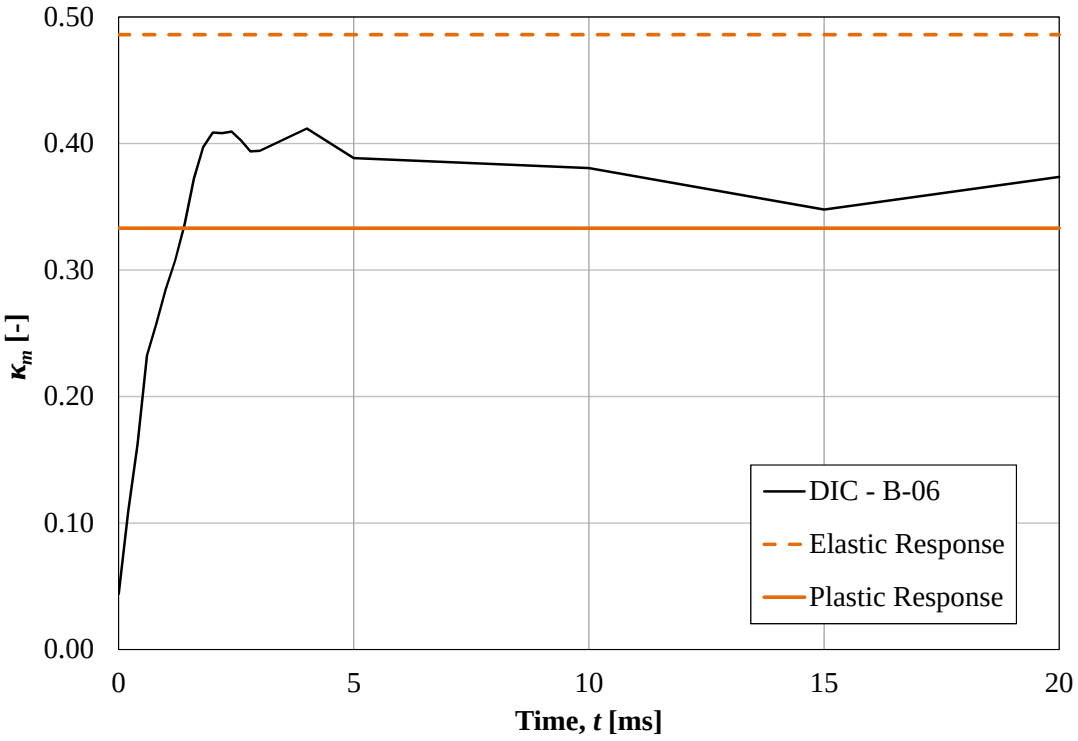

Figure 9.22 Variation of κ_m over time for a beam specimen subjected to an impact from a 5.0 m drop-height. Comparison of theoretical values according to elastic and plastic response with experimental values for B-06.

In order to determine real values of mass transformation factors, experimental data obtained for B-06 from DIC analysis were used in Equation (4.8). The results are shown in Figure 9.22. It can be observed that the mass participation at the moment of impact is much lower than the assumed value for plastic response, $\kappa_m = 0.333$, and it increases until reaching a value close to 0.4 at approximately $t = 2$ ms. Thereafter, it is noticed that the response of the beam lies somewhere in between ideal plastic and ideal elastic response, though it seems to be closer to a plastic response. Therefore, introducing a function for κ_m variable on time in the 2DOF model might lead to better predictions of the dynamic response, and could be an important suggestion for future work.

Ultimately, the 2DOF model with an internal resistance function based on nominal positions of reinforcement bars and with $f_y = f_t = 686$ MPa was chosen as a base model. This base model would serve for further comparisons with results from FE analyses performed in LS-DYNA (which are also based on nominal distances), as detailed in Chapter 10. Furthermore, the effects of the adjusted position of reinforcement bars in a LS-DYNA model are studied in Section 11.8.2.

9.6.4 Predicted rotational capacity

Figure 9.23 presents the calculated rotational capacity according to the methods presented in Section 5.4 in comparison with the average values of rotational capacity, $\theta_{pl,x\%}$, for different load levels determined for undamaged beams of Series-3, as previously presented in Figure 9.16. The rotation capacity according to the ABC method corresponds to $\theta_{pl,95\%}$, whereas the remaining methods should yield a value of rotational capacity equivalent to $\theta_{pl,100\%}$.

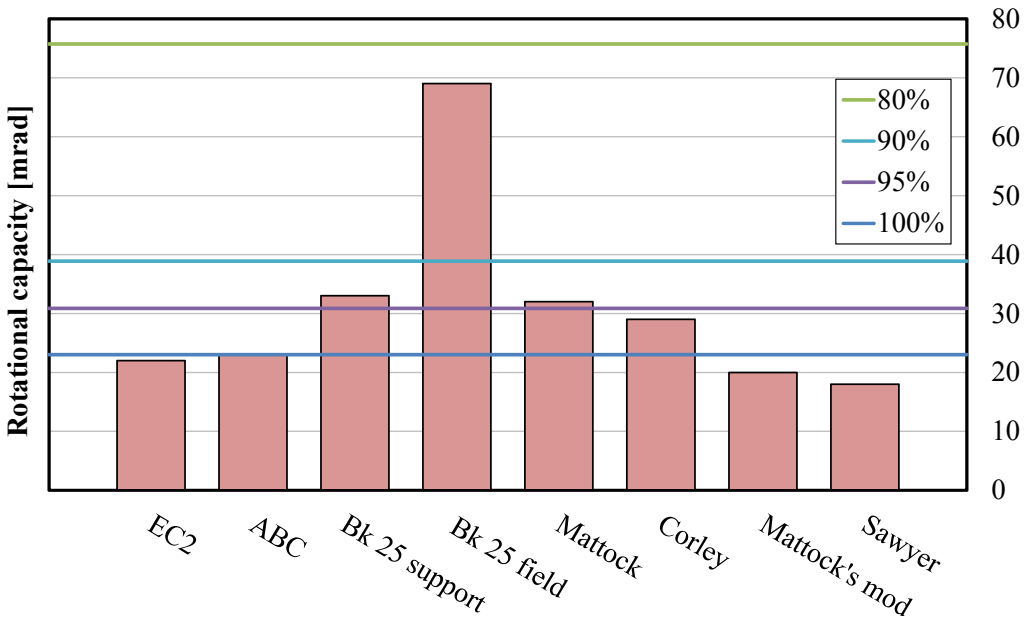

Figure 9.23 Comparison of predicted plastic rotational capacity according to different theoretical and empirical methods with average plastic rotational capacity from Series-3.

Predictions according to the guidelines in Eurocode 2 (CEN, 2004) show high correspondence with experimental values of $\theta_{pl,100\%}$ measured for undamaged beams of Series-3. Moreover, the rotational

capacity calculated according to Sawyer's and Modified Corley's methods is less but close to the experimental $\theta_{pl,100\%}$, meaning that the predictions become conservative. The results according to the ABC method are also conservative, as they are closer to the experimental $\theta_{pl,100\%}$ rather than $\theta_{pl,95\%}$, as intended by its theoretical formulation. Mattock and Corley methods, on the other hand, give results closer to $\theta_{pl,95\%}$.

Two different results are presented for the Bk 25 method in Figure 9.23. When the rotational capacity is calculated assuming that the plastic hinge under a concentrated load is equivalent to the conditions at an inner support in a continuous beam, a value close to $\theta_{pl,95\%}$ is obtained. This result can be considered as reasonable compared with the experimental values. On the other hand, when using the Bk 25 equation for a plastic hinge located in the field of a continuous beam to determine the rotational capacity for a concentrated loading in a simply supported beam, the obtained value seems to be unreasonable large, as it is close to experimental $\theta_{pl,80\%}$. It should be highlighted that the Bk 25 method was developed for impulse-loaded structures, so a higher value of rotational capacity is expected compared with the other methods, which were formulated for estimation of rotational capacity of structures subjected to static loading. Yet, the results indicate that using the Bk 25 equations as formulated for an inner support in a continuous beam might be more appropriate for the experimental conditions in this thesis work.

In general, the results show that the decision of disregarding the top layer of reinforcement, which was proven to be subjected to a low tensile force instead of compressive force, leads to acceptable predictions. Besides, these methods (apart from Bk 25) were originally meant to be used during design of the reinforced concrete beams under static loading, and therefore, conservative values should be expected. In that sense – apart from Corley and Mattock methods, which show an overestimation – most methods seem to provide with reasonable values of rotational capacity. Bk 25 (support), also seems to be reasonable for impacted-loaded beams.

10 Finite Element Model - Theory

10.1 Introduction

This chapter provides with a general description of the procedure followed in order to replicate the impact-loading experiments using non-linear finite element analysis (FEA). The content of the chapter includes the element types, material models, interaction between elements, and other parameters related to finite element modelling of the experiments.

The models were created in the software package LS-DYNA developed by the Livermore Software Technology Corporation (LSTC) in 1976, which has been continuously developed ever since. The software can be used for, among others, simulation of high-speed, short-duration events.

Two different models were created to replicate the experiments. The only difference between the two models is the solid element type used to model the concrete material, and some input data related to the element type used.

The creation of the models and the preparation of input data was done specifically with the program LS-PrePost[1]. The same program was also used for post-processing of the results. The analysis itself was performed using a licensed version of a LS-DYNA solver[2].

The solution method used by default by LS-DYNA is of an explicit nature. That implies that the equation of motion is solved based on the displacement in previous time steps. A sufficiently small time step is required in order to obtain acceptable results.

The material models and element types were chosen based to great extent on experience gained in previous Master's thesis projects within the Structural Engineering Division at Chalmers. Furthermore, the decisions regarding modelling techniques were based on information provided in LS-DYNA Keyword User's Manual (LSTC, 2015) and LS-DYNA Theory Manual (LSTC, 2006).

LS-DYNA does not have a default unit system. The user must provide all the values in a consistent system, which usually depends on in which units the results are desired. The system adopted during this project are shown in Table 10.1.

Table 10.1 Consistent system of units.

Property	Mass	Length	Time	Force	Stress	Energy
Unit	g	mm	ms	N	MPa	N mm

10.2 Model Geometry

The global geometry of the specimens should be defined before creating a mesh and assigning material properties to the model. LS-DYNA allows to replicate the real geometry of the specimens fairly accurately.

[1] LS-PrePost 4.2 X64 release version 2016

[2] Redhat 5.9 (release 9.0.01. Linux, double precision)

Four main parts (or sets of parts) were created, including the concrete beam, the reinforcement bars, the drop-weight, and the roller supports. Figure 10.1 shows an isometric view of the setup of the model in LS-DYNA.

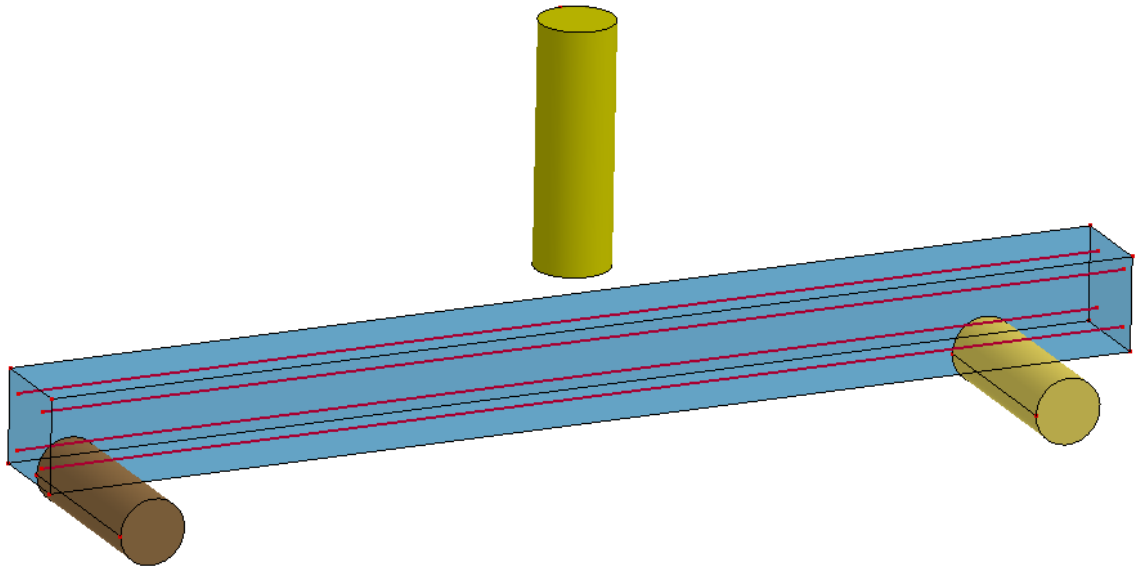

Figure 10.1 LS-DYNA model geometry.

The beam was modelled as a solid box, while the roller supports were created as solid cylinders. The drop-weight was also modelled as a solid cylinder, but with a curved surface on the side that hits the beam. However, the hole present in the drop-weight, as explained in Section 7.4, was not included in the model, as the element size required to create a suitable mesh in the drop-weight would need to be too small due to the dimensions of the hole. The mass density of the drop-weight was adjusted accordingly in order to maintain the correct weight.

10.3 Element Types and Properties

Two different types of solid elements were used to model the concrete beam, namely, *hexahedron* and *tetrahedron* elements. For the hexahedron solids, underintegrated constant stress elements of equal sides were used, as depicted in Figure 10.2. This element corresponds to Solid Type 1 in LS-DYNA and is the default element. The hexahedron mesh can be generated by using the in-built meshing tool in LS-DYNA, *Solid Mesher*. Provided some conditions, the standard solid element is capable of producing accurate results while being relatively efficient with regards to computation time. The roller supports and the drop-weight were modelled using only this element type.

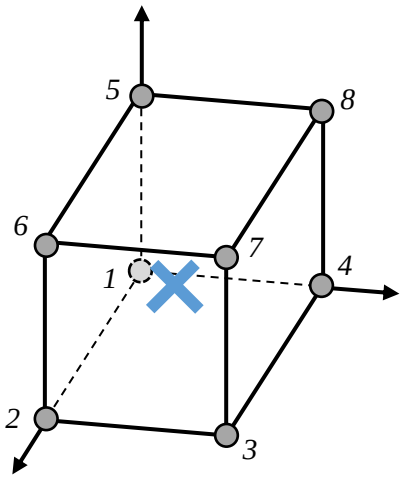

Figure 10.2 8-node hexahedron element with one integration point.

The other solid element considered in this project is the four-node tetrahedron element with one integration point, as shown in Figure 10.3. This element corresponds to Solid Type 10 in LS-DYNA. The tetrahedron elements are generated by using *Tetrahedron Mesher* which is a meshing tool provided in LS-DYNA. A merge tolerance must be introduced; for this project, the default value 0.001 was chosen. Additionally, LS-DYNA provides two optional methods, *Method 1* or *Method 2*, in order to remesh the surface of the geometry after creating a trial mesh. Finally, three methods – *Method 1*, *Method 2* or *Method 3* – must be chosen in order to create a definite mesh. The meshing procedure was performed using a *Method 2* skin remesh; thereafter, the final tetrahedron mesh was generated by using *Method 3*. It should be noted that not all sides of the individual tetrahedron elements correspond to the input value of edge size, as the length of some sides deviates from the input parameter due to the geometry of the tetrahedron element when the meshing tool adapts the local geometry to the global geometry of the structure.

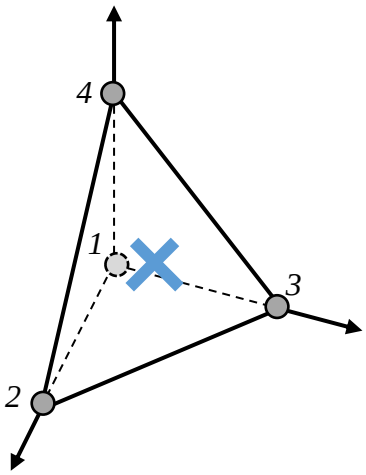

Figure 10.3 4-node tetrahedron element with one integration point.

The reinforcement bars were modelled in a discrete manner using beam elements, specifically the Hughes-Liu formulation, with circular cross-section. This beam element is based on a degenerated eight-node solid element, which makes it compatible with hexahedron elements. The formulation is robust and computationally efficient (LSTC, 2006). The integration could be evaluated with one integration point along the axis and multiple points in the cross section. Different integration schemes are available by default, such as 2x2 Gauss quadrature and 3x3 Gauss quadrature. However, to create the base model in this project, only one integration point in the cross-section was initially considered; therefore, only the axial stress on the bars are computed.

10.3.1 Hourglass control and volumetric locking

Since the chosen hexahedron elements are provided with only one integration point, there is a risk to obtain spurious zero-energy modes, also called *hourglass modes*. Such modes, which are different to modes corresponding to rigid body motion, create zero strain energy. Figure 10.4 illustrates two possible hourglass modes, though a total of twelve modes exist.

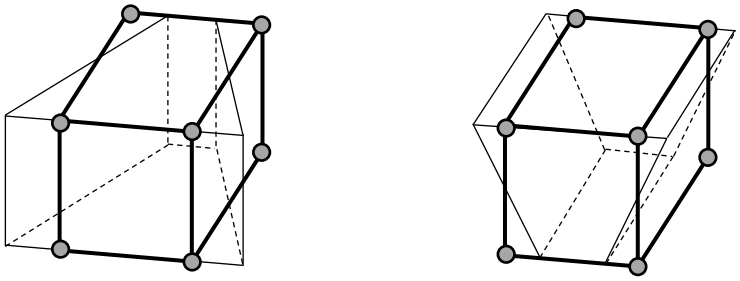

Figure 10.4 Examples of hourglass modes of a hexahedron element with one integration point.

An hourglass control can be included in the model in order to avoid spurious zero-energy modes. This control introduces fictitious forces within the element to prevent excessive hourglass deformation. This method is more cost-effective than using fully integrated hexahedron elements, which may also give rise to locking effects. There are several types of hourglass control available in LS-DYNA. Type 6 was chosen for this project. It is formulated as a stiffness type stabilization based on elastic constants and an assumed strain field, and is only available for 2D and 3D solid elements (LSTC, 2006).

An important parameter which can be defined by the user is the Hourglass Coefficient, QM, which scales proportionally to the hourglass force. A value of QM = 1.0 is recommended for elastic materials if a coarse mesh is used. For non-linear models, a smaller value of QM, usually in the interval from 0.001 to 0.01, is suggested. The default value is QM = 0.1.

As stated before, the roller supports and the drop-weight were all modelled using Type 1 hexahedron elements. Since the deformations of these parts were expected to remain relatively small, it was not considered necessary to use hourglass control for these parts (Lovén and Svavarsdóttir, 2016).

As for tetrahedron elements, while the theoretical formulation for this type of element is in line with the formulation for one point hexahedron element, there are no spurious zero-energy modes for this type of elements, and therefore hourglass control is not needed. However, this type of element may exhibit a stiff response due to volumetric locking effects (Erhart, 2011).

10.4 Interaction Between Elements and Boundary Conditions

To model the interaction between the beam and the drop-weight, and between the beam and the roller supports, a contact algorithm called Contact_Automatic_Surface_to_Surface was used. This command allows for compression loads to be transferred from the slave surface to the master surface without constraining elements. With this setup, the beam is able to bounce upwards from the supports when needed.

The bottom nodes of the supports were fully restrained in the z-direction as shown in Figure 10.5. Moreover, additional restraint in both x- and y-direction was included in some side nodes to avoid undesired unreasonable displacements during the analysis.

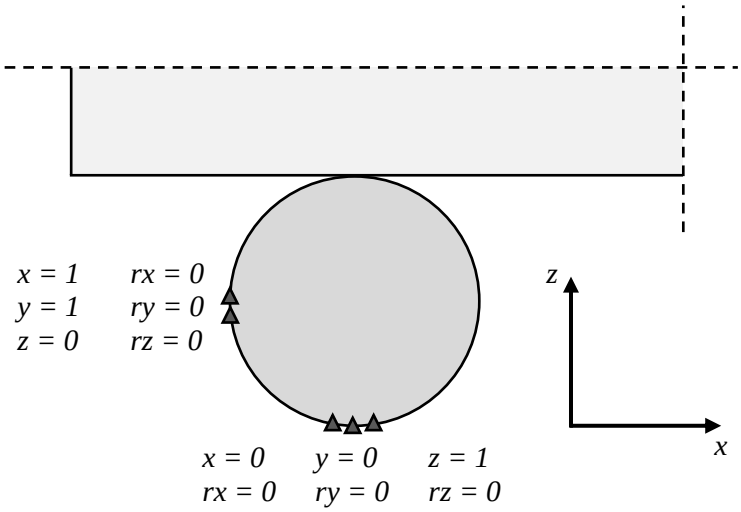

Figure 10.5 Degree of restraint in roller supports.

10.5 Material Models

10.5.1 Material model for concrete

Material Type 273 was used to model the concrete. This material model is called Mat_CDPM in LS-DYNA, which stands for Concrete Damage Plastic Model. The current version – referred to as CDPM2 by its authors – was developed by Grassl, Xenos, *et al.* (2013) as an extension to the damage plasticity model CDPM presented by Grassl and Jirasek (2006).

CDPM2 is only available for solid elements. Several parameters can be defined by the user, although most of them have default values based on experimental observations. The model is intended to describe the failure of concrete structures subjected to multiaxial dynamic loading and was formulated as a damage-plasticity constitutive model. The plasticity part of the model is based on the effective stress, which is independent of damage. On the other hand, the damage model is based on plastic and elastic strain measures.

The initiation of tensile damage takes place when the maximum equivalent strain of the material reaches a threshold value, $\varepsilon_0 = f_{ct}/E_c$. The model offers three different types of softening law to describe tensile

damage; namely: linear, bi-linear, and exponential damage type. In the present study, bi-linear softening was adopted. The stress-crack width relationship for bi-linear damage is illustrated in Figure 10.6.

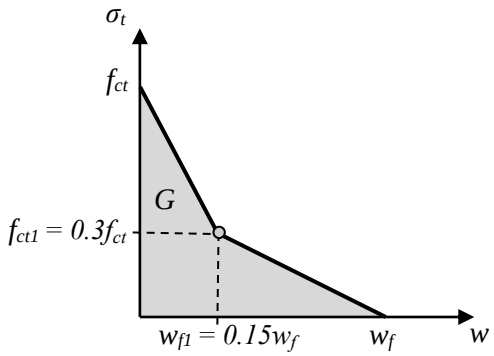

Figure 10.6 Bi-linear tensile damage as defined for CDPM2.

Two additional parameters, f_{ct1} and w_{f1}, are needed for bi-linear softening. The default values included in the material model are calculated according to

$$\begin{aligned} f_{ct1} &= 0.3 f_{ct} \\ w_{cf1} &= 0.15 w_f \end{aligned} \tag{10.1}$$

The parameter w_f represents the ultimate crack width; that is, the crack width at which no further transfer of tensile stress between two elements of concrete on each side of the crack is possible. The parameter w_f can be calculated from the fracture energy and the tensile concrete strength as

$$w_f = \frac{4.444 G_f}{f_{ct}} \tag{10.2}$$

A given input value of crack width, w, is converted into strain, ε, by assuming a certain length along which the cracks are assumed to spread. This length is termed *crack band width*, h_{BW}. In the material model CDPM2, the crack band width is considered to be equivalent to the element size, l_{el}. The parameter l_{el} is mesh-dependent and corresponds to the length of one finite element for cubic hexahedron elements. However, when tetrahedron elements are used, l_{el} is calculated in proportion to the volume of the element. Equation (10.3) is used to determine the strain for given values of crack width and crack band width.

$$\varepsilon = \frac{w}{h_{BW}} \tag{10.3}$$

If tetrahedron elements are used to create the mesh, it is recommended in (Grassl, 2016) to use a modified value of ultimate crack width equal to $0.56 w_f$ to account for the overestimation of fracture energy for tetrahedron elements, which is a result of the method used by LS-DYNA to calculate the element size l_{el} for these elements.

Another input parameter to CDPM2 is the eccentricity parameter, e. This parameter is used to control the shape of the deviatoric section of the yield surface and can be calculated according to

$$e = \frac{1+\varepsilon}{2-\varepsilon}, \quad \text{where} \quad \varepsilon = \frac{f_{ct}(f_{bc}^2 - f_c^2)}{f_{bc}(f_c^2 - f_{ct}^2)} \tag{10.4}$$

The variable f_{bc} corresponds to the strength in equibiaxial compression, and can be approximated as $f_{bc} = 1.16 f_c$.

The evolution of compressive damage is based on an exponential stress-inelastic strain function, as depicted in Figure 10.7. The inclination of such softening curve is controlled by the parameter ε_{fc}, henceforth named *compressive softening parameter*. The smaller ε_{fc} is, the more brittle the nature of the failure is. The default value is set to $\varepsilon_{fc} = 1 \cdot 10^{-4}$.

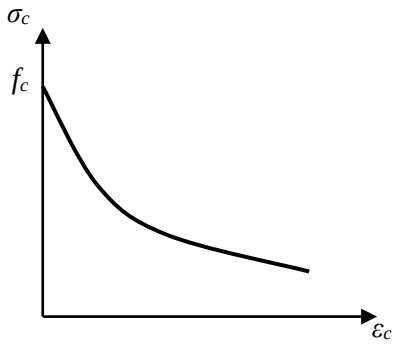

Figure 10.7 Compressive damage as defined for CPDM2.

The user-defined input parameters used to model the concrete material are shown in Table 10.2. Such parameters were adjusted according to the material properties and the experimental conditions described in Chapter 7. Note that the hardening parameter, HP, was set equal to 0.01, which is the value recommended for analyses without consideration of strain rate effect. Other model parameters which are not shown were set to their default values.

Table 10.2 Input parameters for CDPM2.

Notation in LS-DYNA	Description	Value
RO	Density, ρ_c	$2425\,\mathrm{kg/m^3}$
E	Elasticity modulus, E_c	$33.9 \cdot 10^3$MPa
PR	Poisson's ratio, ν_c	0.2
ECC	Eccentricity parameter, e	0.52
FT	Concrete tensile strength, f_{ct}	3.7 MPa
FC	Concrete compressive strength, f_c	42.2 MPa
HP	Hardening parameter	0.01
STRFLG	Strain rate flag	0: No strain rate

10.5.2 Material model for reinforcing steel

The reinforcing steel was modelled using Material Type 3, which is called Mat_Plastic_Kinematic. This material model is computationally efficient and is suitable to model isotropic and hardening plasticity for beam, shell and solid elements (LSTC, 2015). The stress-strain relationship depicted in Figure 10.8 illustrates the elasto-plastic behavior of the material.

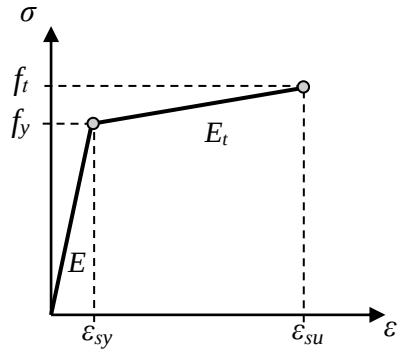

Figure 10.8 Elastic-plastic behavior as defined for Mat_Plastic_Kinematic.

Mat_Plastic_Kinematic is also able to consider strain rate effect; however, such option was not enabled for this study. The input parameters listed in Table 10.3 were selected in accordance with the material properties determined experimentally for the steel bars, as described in Chapter 7. Observe that the tangent modulus, E_t, is calculated as

$$E_t = \frac{f_t - f_y}{\varepsilon_{su} - \varepsilon_{sy}} \tag{10.5}$$

Table 10.3 Input parameters for Mat_Plastic_Kinematic.

Notation in LS-DYNA	Description	Value
RO	Mass density, ρ_s	$7800\,\mathrm{kg/m^3}$
E	Elasticity modulus, E_s	$196 \cdot 10^3$MPa
PR	Poisson's ratio, ν_S	0.30
SIGY	Yield stress, f_y	575 MPa
ETAN	Tangent Modulus, E_t	1056 MPa

10.5.3 Material model for drop-weight and supports

The drop-weight and the roller supports were modelled using Material Type 1: Mat_Elastic in order to reduce computational costs, since limited plastic deformation was assumed to occur for the supports and drop-weight. This material model is designed to exhibit a simple isotropic elastic behavior and is suitable for beam, shell and solid elements. The input parameters are shown in Table 10.4. Since the drop-weight was modelled as a solid object, without consideration of the cavity described in Section 7.4, the value of ρ_s was adjusted accordingly in order to compensate for the difference in volume.

Table 10.4 Input parameters for Mat_Elastic.

Notation in LS-DYNA	Description	Value
RO	Mass density, ρ_s	$7829\,\mathrm{kg/m^3}$
E	Elasticity modulus, E_s	$200 \cdot 10^3$MPa
PR	Poisson's ratio, ν_S	0.30

10.6 Interaction Between Reinforcement and Concrete

The reinforcement bars were assumed to be fully embedded in the concrete core. This response can be achieved by defining the constraint type Constrained_Beam_in_Solid. This command constrains beam or truss elements (slave components) to move along with solid elements (master elements). The meshes for both materials can be created separately and then superimposed, and the displacement between the nodes are automatically constrained to zero. When using this keyword, it is not necessary to align the nodes of the beam elements to the nodes of the solid element.

10.7 Load Application

The dynamic load was introduced to the FE model by assigning an initial velocity to the drop-weight. The values of velocity were chosen to be equal to the average values determined through DIC analysis for both drop-heights. The gravitational force was not considered in the model, since its influence to the behavior of the beam was regarded as negligible. This allows to reduce computational costs.

Besides impact analyses, separate analyses where a static load was applied to the beam were also performed. This load was applied by prescribing velocity on the nodes on the top of the beam at midspan. The velocity was increased gradually from 0 mm/ms to 0.07 mm/ms during the first 100 ms and kept constant thereafter until reaching the desired deformation. The analysis was run for 500 ms, which yields at maximum midspan deflection of 31.5 mm.

10.8 Solution Method and Time Step

The default numerical integration method in LS-DYNA to solve non-linear problems corresponds to an explicit method. Its formulation is a modification to that of the Central Difference Method, whereby the equation of motion is solved based on the displacement in previous time steps. CDPM2 has been adapted to explicit methods; therefore, the default integration method was used in the computations in LS-DYNA. The determination of a proper time step size is essential to obtain reasonable results when using an explicit method, as the the time step must be small enough to be able to capture the wave propagation through all elements. LS-DYNA calculates automatically an appropriate time step by choosing the minimum value from all elements, as

$$\Delta t = \mathrm{TSSFAC} \cdot min\{\Delta t_1, \Delta t_2, ..., \Delta t_{n_{el}}\} \tag{10.6}$$

where n_{el} is the number of elements and TSSFAC corresponds to a scale factor set to a default value of 0.9, which can be reduced in order to improve numerical stability.

For solid elements, the calculation of the time step is based on the length of the element and the sound speed, c, through such an element, and can be expressed as

$$\Delta t_e = \frac{l_e}{c} \tag{10.7}$$

Here, the length of the element depends on the solid element type and is given by

$$\begin{aligned} l_e &= \frac{V_e}{A_{e,max}} && \text{for a hexahedron element} \\ l_e &= \text{minimum height} && \text{for a tetrahedron element} \end{aligned} \tag{10.8}$$

where V_e is the element volume and $A_{e,max}$ is the area of the largest element side.

For materials with a constant bulk modulus, the sound speed depends on the modulus of elasticity, E, Poisson's ratio, ν, and the specific mass density, ρ, as

$$c_{solid} = \sqrt{\frac{E(1-\nu)}{(1+\nu)(1-2\nu)\rho}} \tag{10.9}$$

Equation (10.7) can also be used to determine the critical time step for Hughes-Liu beam elements; however, the wave speed should be calculated as

$$c_{beam} = \sqrt{\frac{E}{\rho}} \tag{10.10}$$

11 Finite Element Model - Results and Comparisons

11.1 Introduction

This chapter covers the results from the non-linear FE modelling procedure adopted and explained in Chapter 10. Two different solid element types were used to model the concrete; namely, hexahedron and tetrahedron elements. Initially, a convergence study of the impact event was performed in order to determine a suitable mesh size for both element types. Subsequently, a verification of the two FE models was performed, where comparisons with results gathered from DIC analysis, and when possible, from the base 2DOF model established in Chapter 4 were carried out.

Further studies of the FE models were performed in order to investigate the sensitivity to various input parameters used in the modelling procedure. These studies were conducted by changing the input value for one parameter of interest at a time.

LS-DYNA was also used to perform static analyses. The purpose was to further study similarities and differences between different element types. Considering that the behavior of beams under static loading is better understood, a static FEA could provide with an appropriate insight about how well the simulation can capture the real behavior of the structure.

Parametric studies were also conducted in order to gather further insight of the dynamic behavior of impacted reinforced concrete beams by altering the loading conditions or material properties of the established FE models.

Lastly, it is important to highlight that the effects of strain rate were not considered during the simulation. Moreover, perfect bond was assumed between the reinforcement bars and the surrounding concrete material.

11.2 Choice of Element Size

A convergence study was performed in order to determine a suitable mesh size for both hexahedron and tetrahedron element types. Such analyses were performed for an impact loading from a drop-height equal to 5.0 m, and were based on the deflection of the beam midpoint over time. Furthermore, besides numerical convergence, a sufficient level of detail is also preferred in order to be able to properly represent the crack pattern.

The different nominal mesh sizes adopted for the convergence study correspond to 20 mm, 10 mm, 5 mm, and 2.5 mm. However, the amount of elements for a given nominal element size differs significantly depending on the element type, as the number of elements is much larger for a tetrahedron mesh. For this reason, a 2.5 mm tetrahedron mesh was not studied since it was assumed that such a mesh would be too computationally demanding due to the large number of elements generated. The resulting meshes for tetrahedron and hexahedron elements with varying input sizes are shown in Appendix G.

The reinforcement bars were modelled according to the nominal geometry, as detailed in Figure 7.1, with an element length equal to the input size of the solid concrete elements.

The deflection over time at midpoint for the models with different mesh types and sizes, as well as the

minimum and maximum envelopes and average values collected from DIC data, are shown in Figure 11.1. Hexahedron and tetrahedron elements are denoted *Hexa* and *Tetra* in Figure 11.1 (as well as in subsequent plots). The numerical values of *02.5*, *05*, *10* and *20* correspond to a given input value of edge size; that is, 2.5 mm, 5 mm, 10 mm and 20 mm, respectively.

An important observation is that it was not possible to perform a successful analysis with the default value of the compressive softening parameter, $\varepsilon_{fc} = 1 \cdot 10^{-4}$, with tetrahedron elements as all the attempts reached convergence problems soon after impact occurred. Therefore, the magnitude of ε_{fc} needed to be increased to $\varepsilon_{fc} = 1 \cdot 10^{-3}$ for the tetrahedron models in order to simulate a more ductile behavior of the concrete material with CDPM2.

Results from the Tetra-20 model were omitted from Figure 11.1 since the analysis was terminated prematurely due to convergence issues in the concrete material model, CDPM2. Furthermore, unrealistic and excessively large local deformations were observed for this model. Additionally, the analysis for the Tetra-05 model also terminates prematurely due to convergence problems; however, this occurs at about 12 ms after impact, and maximum deflection is clearly described by the model.

Additional key parameters from the convergence study are presented in Table 11.1. The relative error for the maximum deflection for each model is calculated with respect to the maximum average experimental midpoint deflection, equivalent to 20 mm. Observe that the number of elements for the tetrahedron mesh is significantly larger for all nominal element sizes.

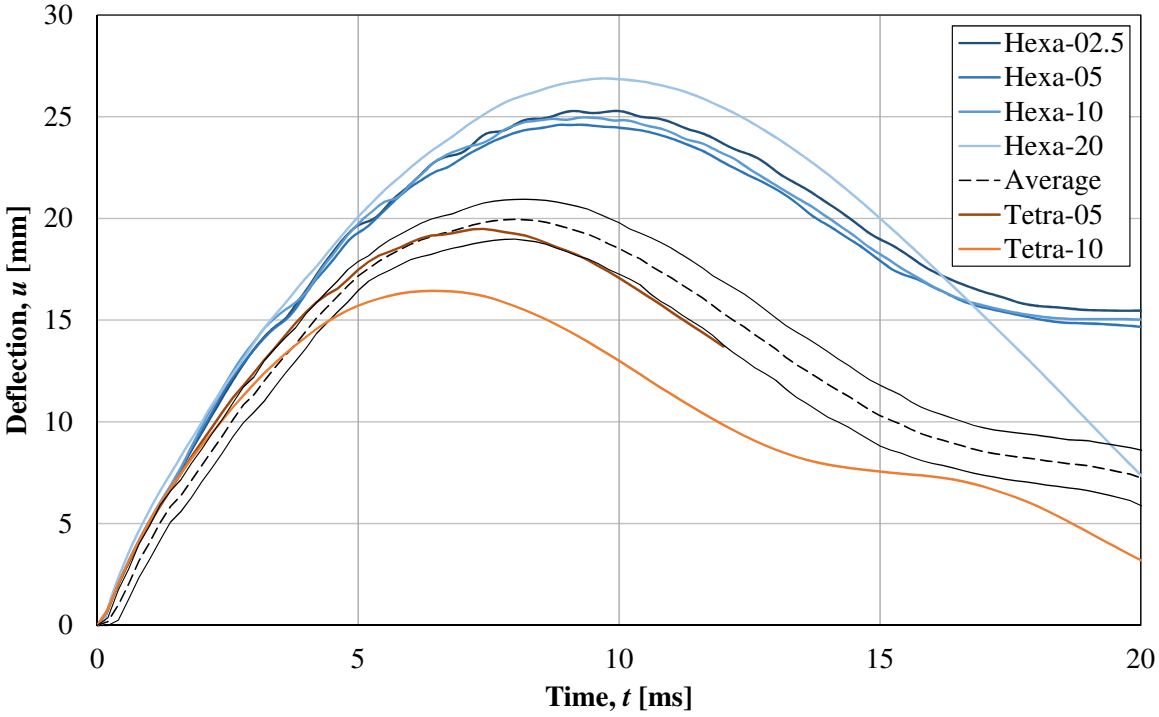

Figure 11.1 Convergence study performed for different mesh sizes using different element types. Midpoint deflection over time due to an impact from a drop-height of 5.0 m is presented.

All models based on hexahedron elements seem to overpredict the maximum deflection. Although, apart from the Hexa-20 model, a rather good correspondence is observed for the different mesh sizes. Based on these results, it was decided to use a 5 mm element size for hexahedron elements, which would also be adequate to represent the crack pattern.

On the other hand, the tetrahedron models yield a smaller maximum deflection compared to the experimental curve. Additionally, a significant difference is observed between the response of the two shown element sizes. Based on the data available, it is not possible to guarantee that the model is converging towards a given value for decreasing element size; however, the results for 5 mm mesh size are fairly close to the experimental curve. For this reason, it was decided to also adopt a size of 5 mm for the tetrahedron mesh.

Table 11.1 Maximum estimated deflection for various mesh sizes and element types, as well as the number of elements generated for each type and size. The relative error of maximum deflection, $u_{max,error}$, is compared with respect to the maximum average deflection, u_{max} = 20 mm, obtained from DIC analysis for an impact from a height h = 5.0 m.

Description	Hexa-20	Hexa-10	Hexa-05	Hexa-02.5	Tetra-20	Tetra-10	Tetra-05
No. concrete elements [$\cdot 10^3$]	2	12	99	755	13	103	896
u_{max} [mm]	26.9	25.0	24.6	25.3	-	16.4	19.5
$u_{max,error}$ [%]	35	25	23	27	-	-18	-2

11.3 Verification

11.3.1 Overview

In order to verify the accuracy of the models at representing the real behavior of the beam, different analyses were carried out to ensure that all models exhibit a similar response to the experimental results. Particularly, three parameters were considered: beam velocity at midpoint, drop-weight velocity, and the displacement over the support. The experimental values were determined by means of DIC analysis, presented in Section 9.1. When possible, results from the 2DOF model were also included in the verification. Only a discussion for the analysis with a drop-height of 5.0 m is presented; however, similar information corresponding to a drop-height of 2.5 m is provided in Appendix H.

11.3.2 Midpoint velocity

The velocity of the beam at the midpoint for a 5.0 m drop-height is shown in Figure 11.2. The two LS-DYNA models show a higher peak value soon after impact and their response is similar until approximately $t = 1.2$ ms. Thereafter, the tetrahedron LS-DYNA curve follows more closely the experimental curve. As a matter of fact, both the tetrahedron and the DIC curve reach a negative value earlier than the 2DOF and the hexahedron curve. Unfortunately, no information beyond 12.8 ms is available for the tetrahedron model due to convergence issues. On the other hand, the hexahedron LS-DYNA curve shows noticeable oscillation from $t = 1.2$ ms until $t = 6.8$ ms, when it meets the 2DOF curve. From that point, the velocity

for both models is fairly similar until approximately $t = 14$ ms.

Another observation is that the experimental curve and both LS-DYNA curves maintain a negative velocity after reaching negative values (between $t = 7.0$ ms and $t = 9.0$ ms), while the 2DOF curve oscillates approximately between -2 m/s and 2 m/s. This response is due to the fact that the boundary conditions of the beam are not fully represented in the 2DOF model. Despite the differences regarding phase and frequency of oscillation, good correlation between the numerical models and the experimental results can be observed.

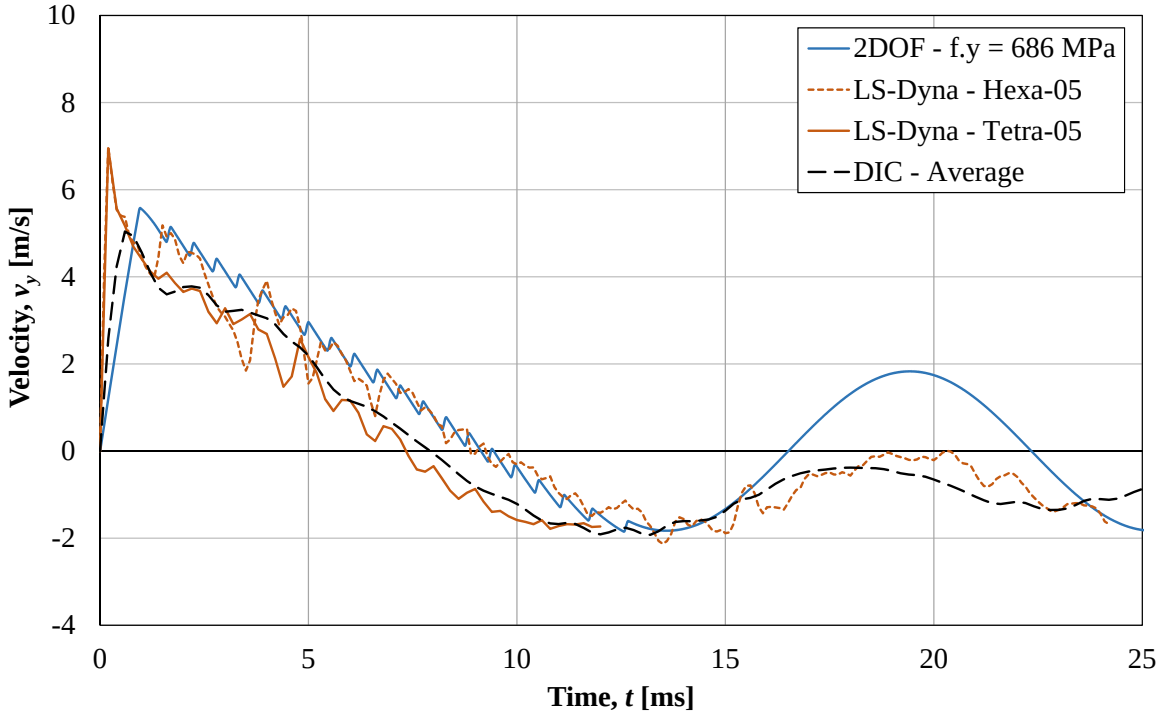

Figure 11.2 Beam midspan velocity vs time for a drop-height h = 5.0 m for all models.

11.3.3 Drop-weight velocity

Another valuable parameter to study is the drop-weight velocity, as it is directly related to the impact phenomenon; that is, the contact between the beam and the drop-weight. The variation of the drop-weight velocity over time is illustrated in Figure 11.3. High correlation is noticed between both LS-DYNA curves and the experimental curve during the first two milliseconds after impact. These curves show a more rapid decrease of velocity than the 2DOF curve. The tetrahedron curve exhibits a better fit to the experimental curve altogether, while the hexahedron curve comes closer to the 2DOF curve at $t = 6.8$ ms. All models eventually converge to a value of approximately -2 m/s.

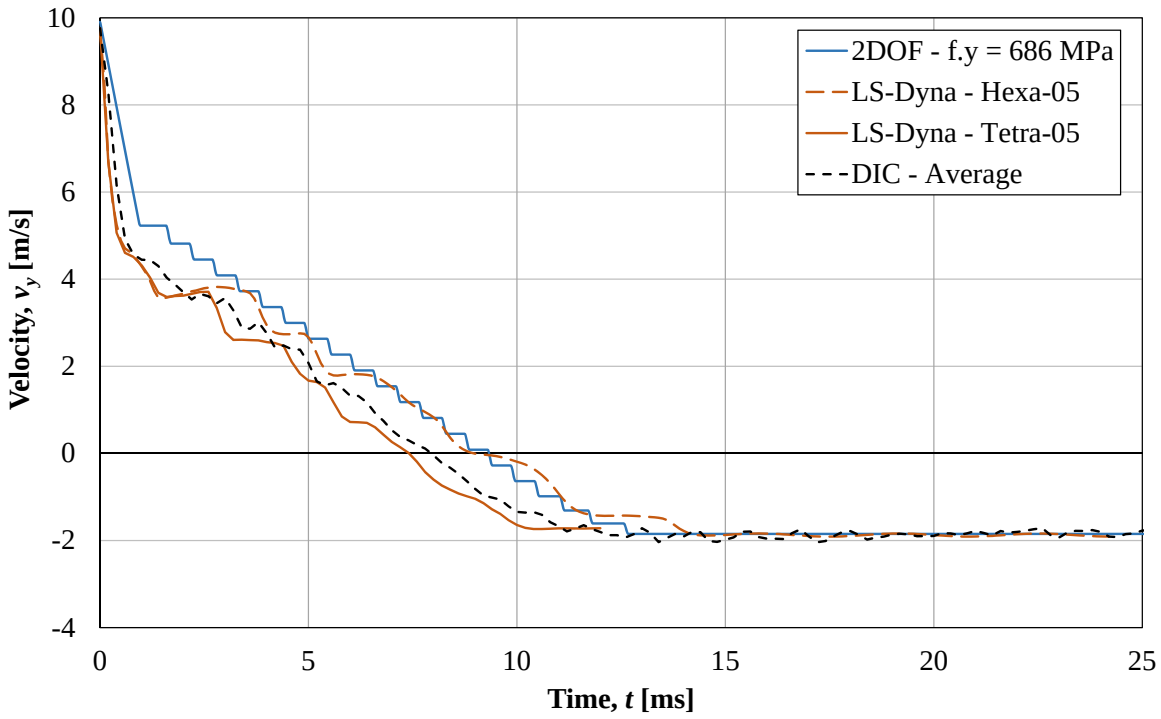

Figure 11.3 Drop-weight velocity vs time for a drop-height h = 5.0 m for all models.

It can also be observed that the rate of decrease for the experimental curve and the 2DOF curve is noticeably similar, albeit with a phase difference of a few milliseconds, until both curves reach the convergence value.

In general, it can be stated that the numerical models are able to describe the drop-weight velocity properly, with the tetrahedron LS-DYNA model producing more accurate results.

11.3.4 Displacement over the support

In (Lovén and Svavarsdóttir, 2016) it is explained that a simply supported beam subjected to a drop impact will show a rapid uplift over the support almost immediately after impact, provided that the uplift is not prevented by the conditions at the support. Such phenomenon was also observed in the laboratory tests during this project. Information regarding the displacement over the support is shown in Figure 11.4. Values larger than zero (equivalent to downward displacement) in the experimental curve are attributed to the noise present in the DIC data.

The hexahedron model is able to accurately represent the uplift in time and magnitude, although its curve shows a slight delayed rebound of the beam compared to the experimental curve. On the other hand, according to the tetrahedron model the beam falls back to the support sooner.

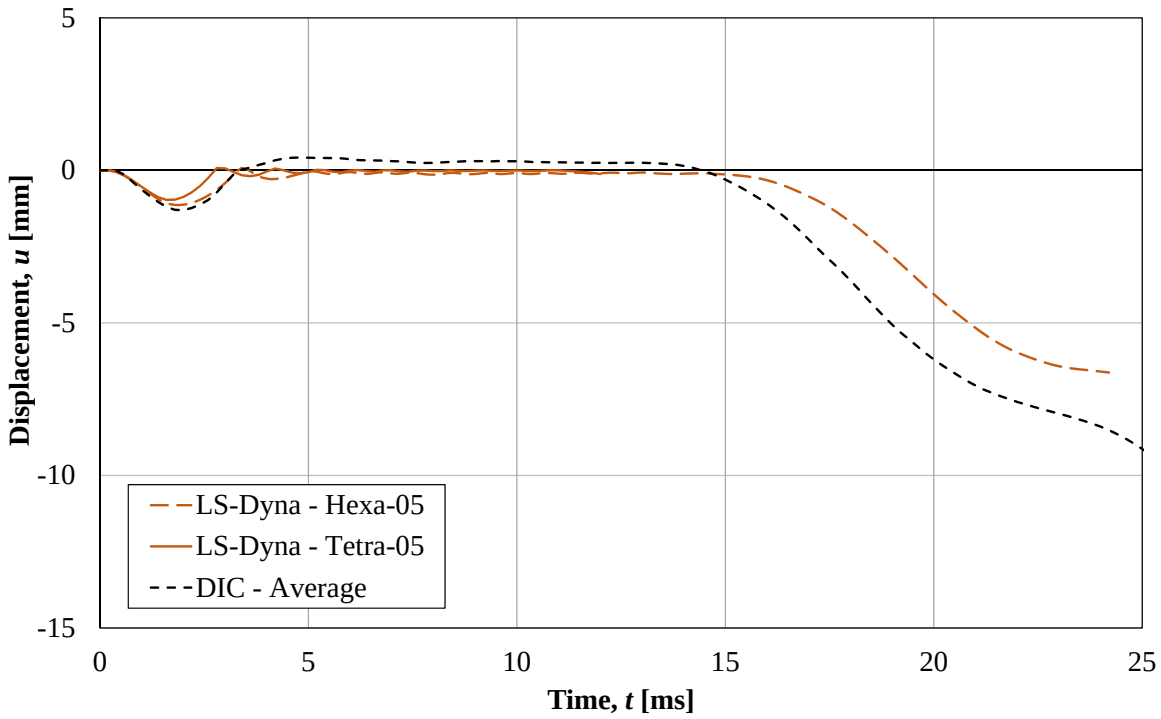

Figure 11.4 Displacement over the support for a drop-height h = 5.0 m for the LS-DYNA models and DIC analysis.

11.4 Drop-weight Impact Analysis

11.4.1 Overview

The deflection of the beam at the midpoint obtained with the LS-DYNA models for different drop-heights, in conjunction with the crack pattern, is discussed in this section. The values of deflection are compared with the experimental results and the results from the 2DOF model.

In order to visualize the crack pattern from the FE analyses, the principal strain field can be requested. The magnitude of the cracking strain differs depending on the element type and size, and can be calculated by introducing $w = w_f$ (or $w = 0.56w_f$ in the models with tetrahedron elements) in Equation (10.3). As previously stated in Section 10.5.1, the crack band width, h_{BW}, is equivalent to the element size l_{el} for hexahedron elements. On the other hand, if tetrahedron elements are used, h_{BW} varies proportionally to the nominal size of the element. Hence, Equation (11.1) was adopted to estimate an equivalent cubic element so that the number of cubic elements equals the number of tetrahedron elements, n_{el}, for a given mesh size. The crack band width and cracking strain for different meshes are summarized in Table 11.2.

$$h_{BW,tetra} = \sqrt[3]{\frac{V_{beam}}{n_{el}}} \tag{11.1}$$

Table 11.2 Crack band width for 5 mm size for hexahedron and tetrahedron meshes and corresponding cracking strain.

Mesh description	h_{BW} [mm]	ε_{crack} [%]
5.0 mm hexahedron mesh	5.0	3.17
5.0 mm tetrahedron mesh	2.4	3.76

11.4.2 Impact from drop-height $h = 5.0$ m

The midpoint deflection over time obtained from the FE analyses, in conjunction with average results gathered from DIC analysis and predictions made by the 2DOF model, are presented in Figure 11.5. Key parameters of the dynamic responses are detailed in Table 11.3; where the maximum recorded deflection, u_{max}, and the time at which maximum deflection occurs, t_{max}, are presented. The principal strain field at certain times after impact, including the time of maximum deflection, are shown in Table 11.4 for the hexahedron LS-DYNA model and in Table 11.5 for the tetrahedron LS-DYNA model.

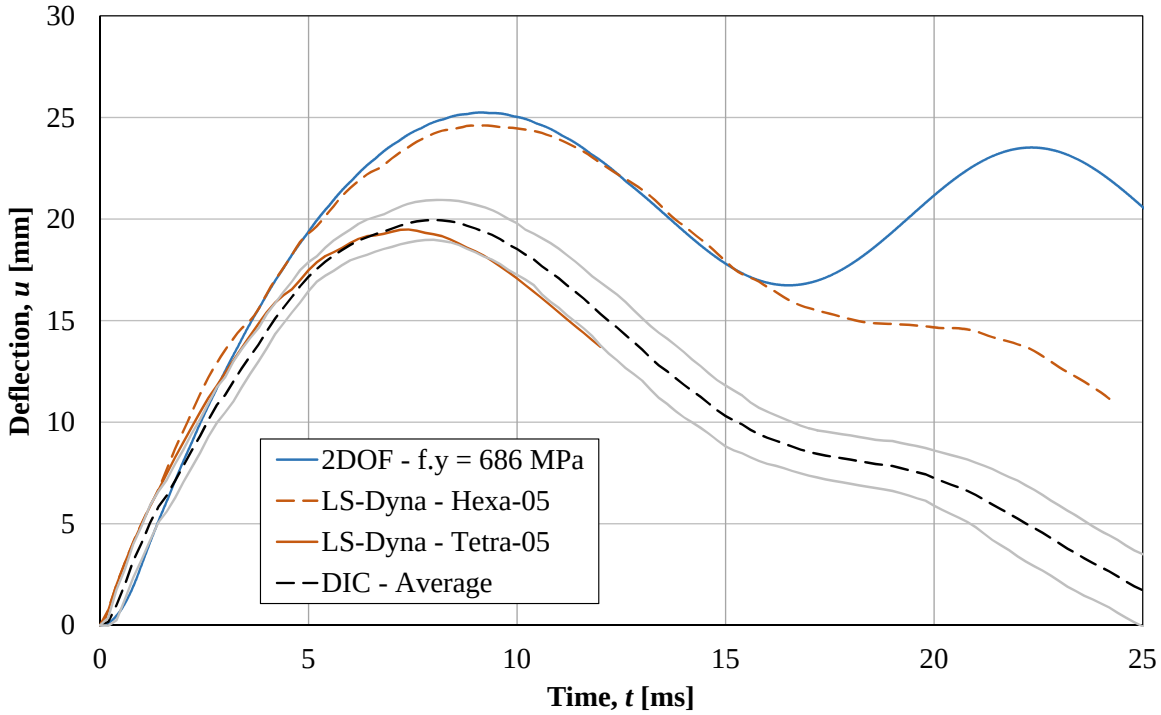

Figure 11.5 Deformation vs time for a drop-height h = 5.0 m for all models.

It should be noted that the FE analysis using tetrahedron element solids terminated prematurely due to convergence issues, as can be seen in Figure 11.5. Nonetheless, for the duration of its run-time a good degree of correspondence to the average values gathered from DIC can be noticed; although the maximum deflection is reached sooner than observed in the laboratory tests.

Table 11.3 *Key parameters for dynamic response due to impact loading, $h = 5.0\,m$. The relative error of maximum deflection, $u_{max,error}$, and time of maximum deflection, $t_{max,error}$, are calculated with respect to the average values gathered from DIC analysis.*

Model	u_{max} [mm]	$u_{max,error}$ [%]	t_{max} [ms]	$t_{max,error}$ [%]
2DOF - $f_y = 686\,MPa$	25.2	26	9.1	14
LS-DYNA Hexa-05	24.6	23	9.2	15
LS-DYNA Tetra-05	19.5	-3	7.4	-8
DIC - Average	20.0	-	8.0	-

Table 11.4 *Strain field for impact-loading analysis of the 5 mm hexahedron LS-DYNA model for 5.0 m drop-height.*

Time	Strain field for impact loading
$t = 0.2\,ms$	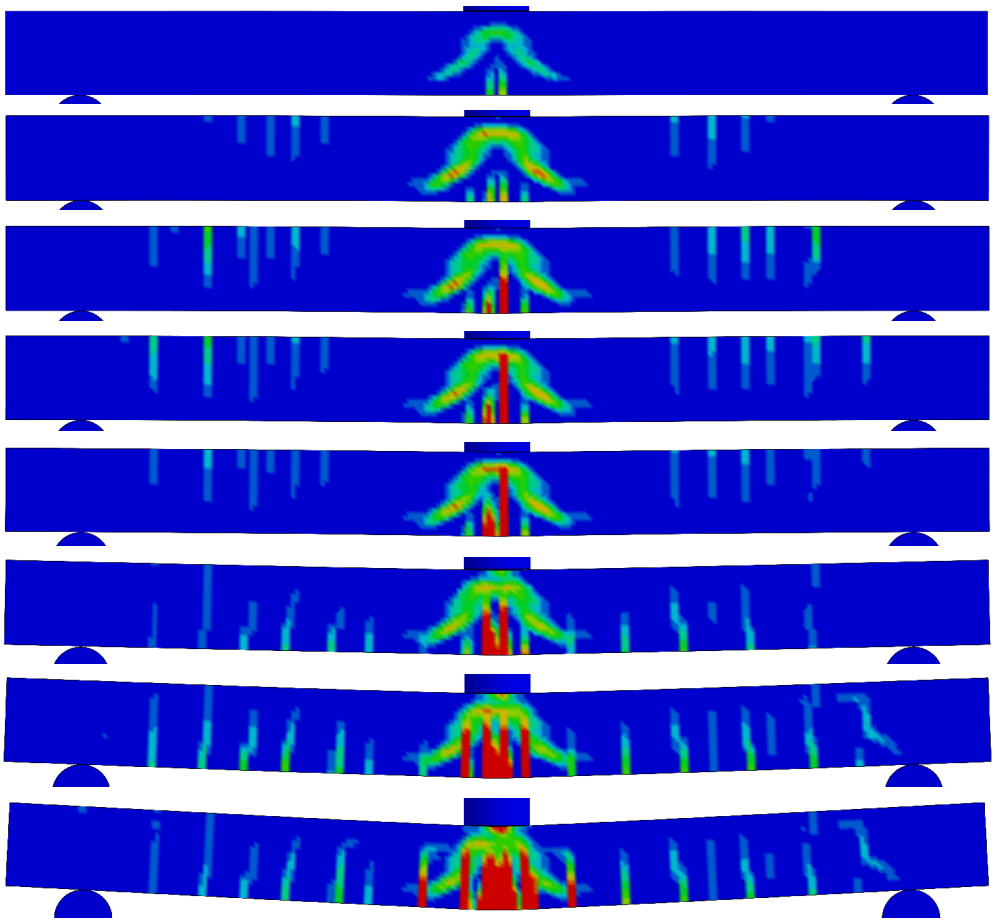
$t = 0.4\,ms$	
$t = 0.6\,ms$	
$t = 0.8\,ms$	
$t = 1.0\,ms$	
$t = 2.0\,ms$	
$t = 4.0\,ms$	
$t = 9.2\,ms$ [1]	
Principal Strain [%]	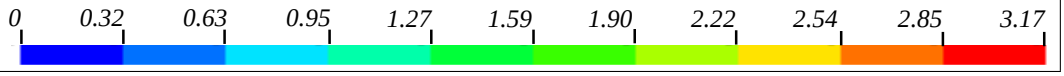

[1] Time at maximum deflection due to impact loading.

The overall dynamic response of the 2DOF model and the hexahedron FE model result in an overprediction by over 20 % in terms of midpoint deflection compared to the DIC results. Moreover, the responses between the two models are similar until approximately $t = 16$ ms, when the deflection according to the 2DOF model begins to increase again.

When analyzing the response of the hexahedron FE model, it is observed that most distinct cracks propagate following a straight vertical path, similar to a purely flexural cracking response, see Table 11.4. While there are indications of inclined cracking underneath the impacted zone, this cracking is described more as a cracked region rather than distinct cracks. This is also true for flexural cracks occurring at the bottom of the beam at midspan. Distinct bending cracks can be distinguished at midspan at times shortly after impact, however they eventually merge together and form a cracked region instead.

Also for the hexahedron model, flexural cracks occur at the top side of the beam at a time $t = 0.4$ ms after impact in a region between the midpoint and the support. These cracks eventually close, as bending cracks are instead formed on the bottom side with a slight inclination. The response, as a whole, appears to be rather symmetric; an exception is a distinct inclined shear crack located over the right support, which can be seen at $t = 4.0$ ms and remains until the time of maximum deflection.

On the other hand, the tetrahedron model in general exhibits a cracking response with a higher degree of inclined shear cracking, see Table 11.5. The inclined cracks which appear below the impact zone are clearly more distinct than for the hexahedron model. These cracks are localized into single element rows, while the same cracking is spread over several rows in the hexahedron model. Other examples of inclined cracking are the cracks occurring at some distance away from midspan at the time of maximum deflection.

An interesting observation is the fact that the inclined cracks in the impact region do not seem to grow significantly in length from approximately $t = 0.6$ ms. Instead, the two bending cracks at the bottom edge in the same region develop further, although they do not merge, as is the case for the hexahedron model.

Furthermore, flexural cracks are also noted in the top edge shortly after impact at approximately one third of the span length from the support. The initiation of top cracking takes place at a similar time as for the hexahedron model. These cracks close with time, as cracking develops at the bottom edge of the beam. In general terms, the strain field of the tetrahedron model at the time of maximum deflection seems to exhibit less symmetry than what was observed for the hexahedron model as the strain distribution becomes more random further away from midspan.

Table 11.5 Strain field for impact-loading analysis of the 5 mm tetrahedron LS-DYNA model for 5.0 m drop-height.

Time	Strain field for impact loading
$t = 0.2$ ms	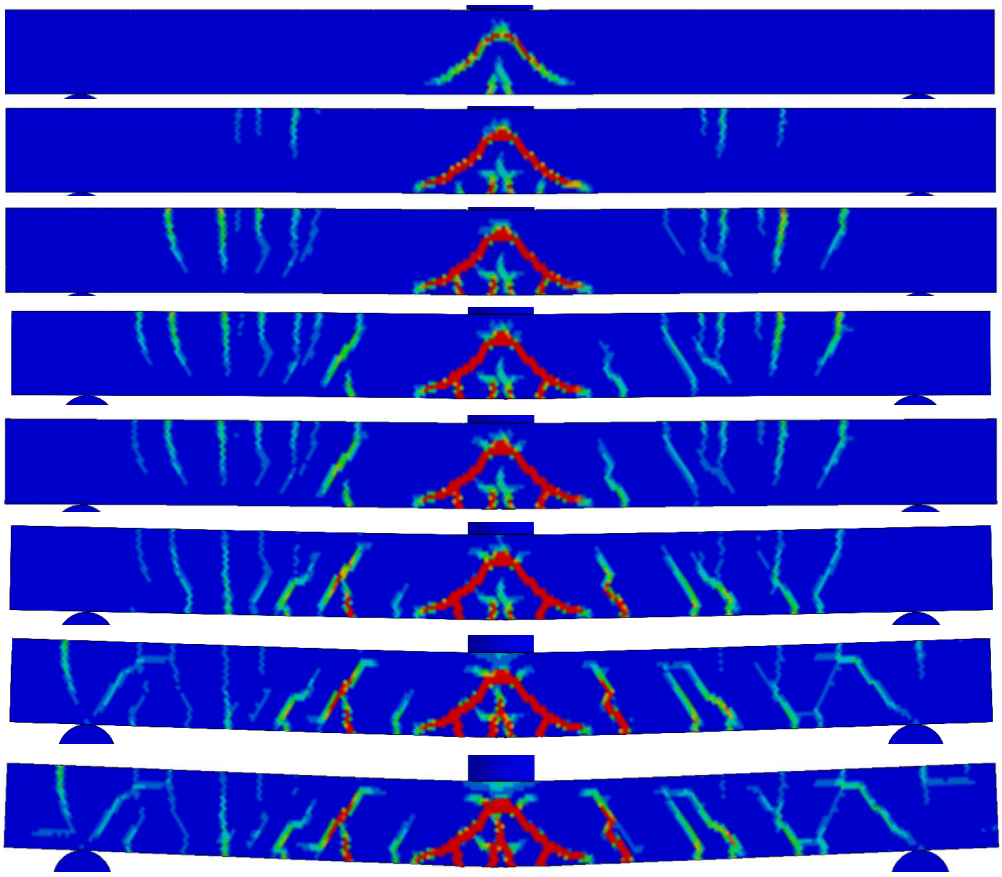
$t = 0.4$ ms	
$t = 0.6$ ms	
$t = 0.8$ ms	
$t = 1.0$ ms	
$t = 2.0$ ms	
$t = 4.0$ ms	
$t = 7.4$ ms [1]	
Principal Strain [%]	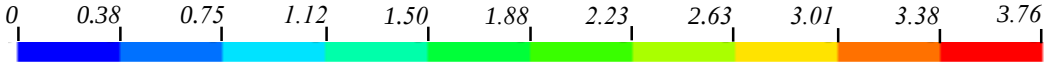

[1] Time at maximum deflection due to impact loading.

Figure 11.6 shows the deformed shape of the left-hand half of the beam for different times, namely: $t = 0.4$ ms, $t = 1.0$ ms, and $t = 2.0$ ms. A comparison between the hexahedron LS-DYNA model, the tetrahedron model, and DIC analysis of B-06 is made. The FE models both show high correspondence to the experimental observations at $t = 0.4$ ms. At that time, only a portion of the beam has been activated due to the impact, and the deformation is localized in the region close to midspan. As a consequence, a negative curvature is seen in the area indicated by the marking *A*. This area corresponds with the top cracks visible in Tables 11.4 and 11.5. Such phenomenon resembles the behavior of a beam with a shorter span fixed at both ends.

A relevant change of curvature can also be observed in the area *B*, which is an indication of the inclined cracking below the impact region. This response is similar for both the hexahedron model and the experimental results. The tetrahedron model, however, exhibits a sharper change of curvature at the

location marked by C, which sees to remain as time progresses, as can be seen at $t = 2.0$ ms indicated by the marking F. This sudden change in curvature can be explained due to the localized inclined crack present in the tetrahedron model.

At $t = 1.0$ ms, the entire beam is participating in the response, and an uplift over the support can be noticed, in accordance with the information in Figure 11.4. The deformed shape of the beam still shows a region with negative curvature (thus, cracks are still present at the top edge of the beam); however, this region has been shifted towards the support, as marked by D.

Finally, at $t = 2.0$ ms, the beam has adopted a deformed shape similar to the triangular shape described for plastic deformation, although a change of curvature is still noticeable at G.

More information concerning the deformed shape of the beams for both FE models can be found in Appendix H.2.

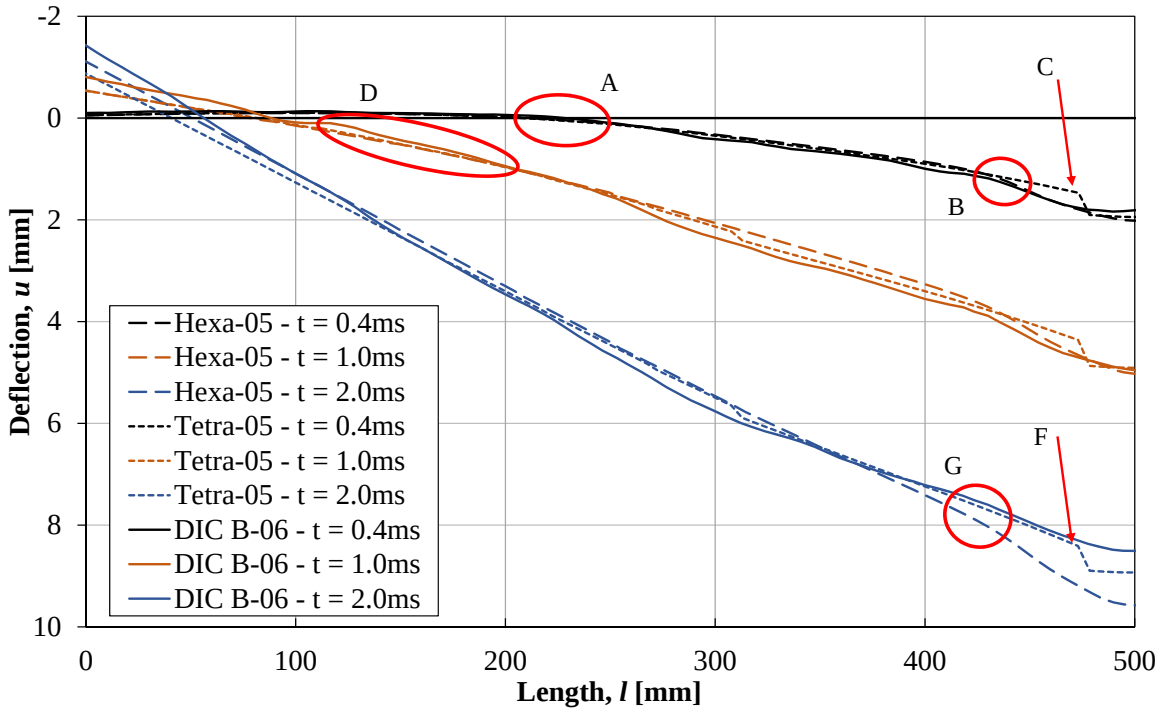

Figure 11.6 Comparison of deformed shape of the beam due to impact loading for h = 5.0 m drop-height for both LS-DYNA models and DIC analysis.

11.4.3 Impact from drop-height $h = 2.5$ m

Figure 11.7 presents the deflection over time due to dynamic loading of the FE models and the 2DOF model together with the average results gathered from experimental testing using DIC for an impact from a drop-height of $h = 2.5$ m. Additional key parameters and measured values are presented in Table 11.6. The principal strain field of the hexahedron model is depicted in Table 11.7 for different times after impact, while the cracking pattern of the tetrahedron model is presented in Table 11.8.

In contrast to the analyses performed for $h = 5.0$ m, no convergence issues was exhibited by the

tetrahedron LS-DYNA model; therefore, the analysis ran for the full duration, as can be seen in Figure 11.7. Both LS-DYNA models predict similar values of midpoint deflection until approximately $t = 4$ ms, from which the responses begin to diverge. Moreover, the dynamic response of the tetrahedron model shows good correspondence to DIC measurements up to the point of maximum deflection and some time afterwards, which can be verified with the values shown in Table 11.6. However, a clear difference in response in terms of deflection and frequency is noted after the time of maximum deflection for the tetrahedron model. This becomes evident at a time close to $t = 10$ ms, from which the degree of correspondence with experimental results decreases as the midpoint deflection according to the tetrahedron model begins to decrease with a rate smaller than the experimental results; this occurrence could point to the fact that the tetrahedron model has a stiffer behavior than the hexahedron model and the experimental results.

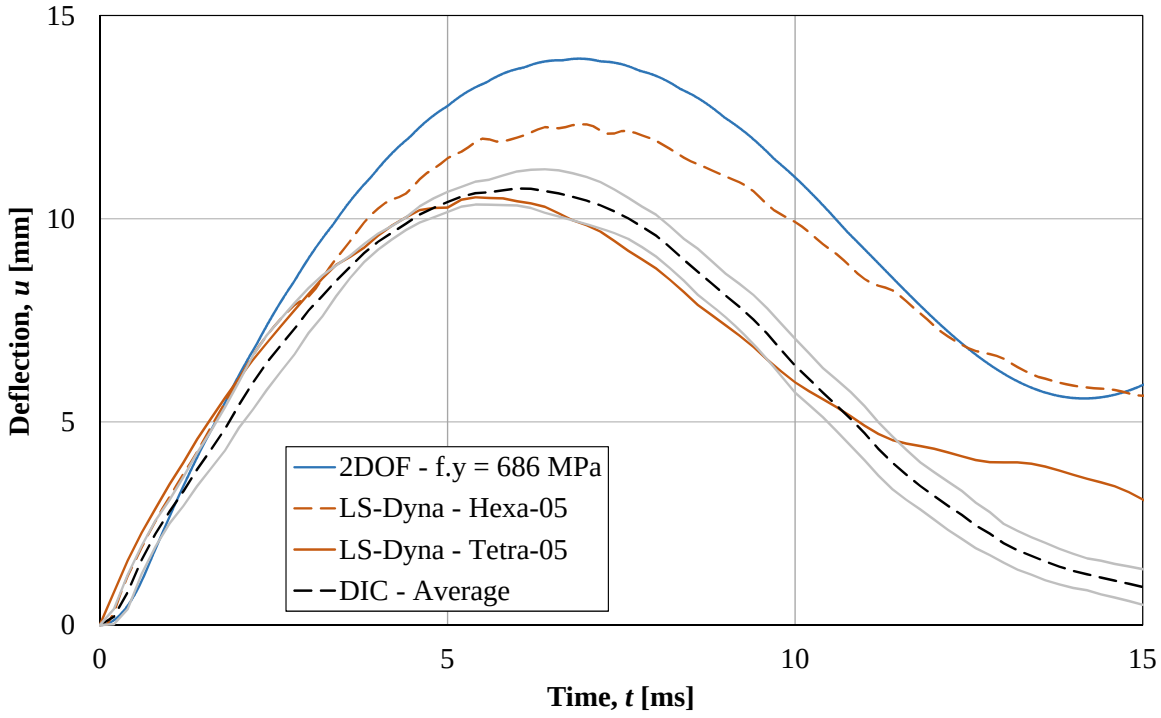

Figure 11.7 Deformation vs time for drop-height h = 2.5 m for all models.

Table 11.6 Key parameters for dynamic response due to impact loading, h = 2.5 m. The relative error of maximum deflection, $u_{max,error}$, and time of maximum deflection, $t_{max,error}$, are calculated with respect to the average values gathered from DIC analysis.

Model	u_{max} [mm]	$u_{max,error}$ [%]	t_{max} [ms]	$t_{max,error}$ [%]
2DOF - $f_y = 686$ MPa	13.9	30	6.9	15
LS-DYNA Hexa-05	12.3	15	6.9	15
LS-DYNA Tetra-05	10.5	-2	5.4	10
DIC - Average	10.7	-	6.0	-

A higher correspondence is found between the hexahedron FE model and DIC measurements for $h = 2.5\,\text{m}$ than for $h = 5.0\,\text{m}$. While an overprediction of the maximum deflection is still observed in Table 11.6, the relative error is smaller than for a $h = 5.0\,\text{m}$ drop. By inspecting key parameters, the 2DOF model, on the contrary, shows less correspondence to average DIC measurements for a $h = 2.5\,\text{m}$ drop than for $h = 5.0\,\text{m}$.

Table 11.7 Strain field for impact-loading analysis of the 5 mm hexahedron LS-DYNA model for $h = 2.5\,\text{m}$ drop-height.

Time	Strain field for impact loading
$t = 0.2\,\text{ms}$	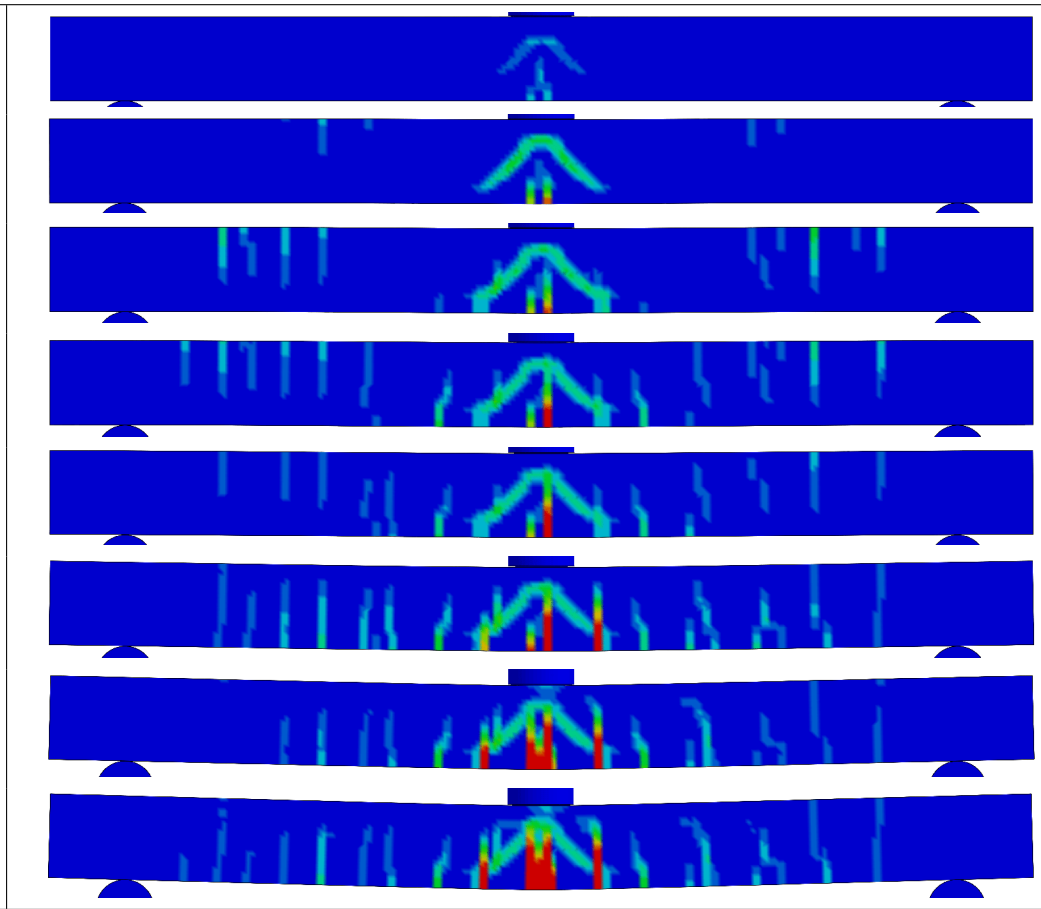
$t = 0.4\,\text{ms}$	
$t = 0.6\,\text{ms}$	
$t = 0.8\,\text{ms}$	
$t = 1.0\,\text{ms}$	
$t = 2.0\,\text{ms}$	
$t = 4.0\,\text{ms}$	
$t = 6.9\,\text{ms}$ [1]	
Principal Strain [%]	0 0.32 0.63 0.95 1.27 1.59 1.90 2.22 2.54 2.85 3.17

[1] Time at maximum deflection due to impact loading.

It is observed in Table 11.7 that the strain field due to impact loading of the hexahedron model for $h = 2.5\,\text{m}$ is similar to that of the model with a $h = 5.0\,\text{m}$ drop in the sense that most of the cracks are represented as straight vertical cracks. Moreover, the inclined cracks appearing underneath the area of impact are yet again described as a cracked region rather than being localized to single element rows. It is, however, noted that the magnitude of the principal strain is smaller for $h = 2.5\,\text{m}$ drop than for $h = 5.0\,\text{m}$. Furthermore, the cracked region is spread across fewer element rows, producing a fairly good

representation of the location of the inclined cracks.

The inclined shear cracks do not reach the bottom edge with the same inclination; instead, they transition into vertical cracks. This can be observed as early as $t = 0.6$ ms. These vertical cracks grow in width and length, until becoming fully open. Additionally, two flexural cracks can be seen to develop at midspan soon after the impact. These two cracks initially localize in individual element rows; although, as time progresses, they eventually form a cracked region, which can be seen at $t = 4.0$ ms and beyond. This behavior was also observed for $h = 5.0$ m; however, the cracked region formed for $h = 2.5$ m appears to be smaller.

Table 11.8 Strain field for impact-loading analysis of the 5 mm tetrahedron LS-DYNA model for h = 2.5 m drop-height.

Time	Strain field for impact loading
$t = 0.2$ ms	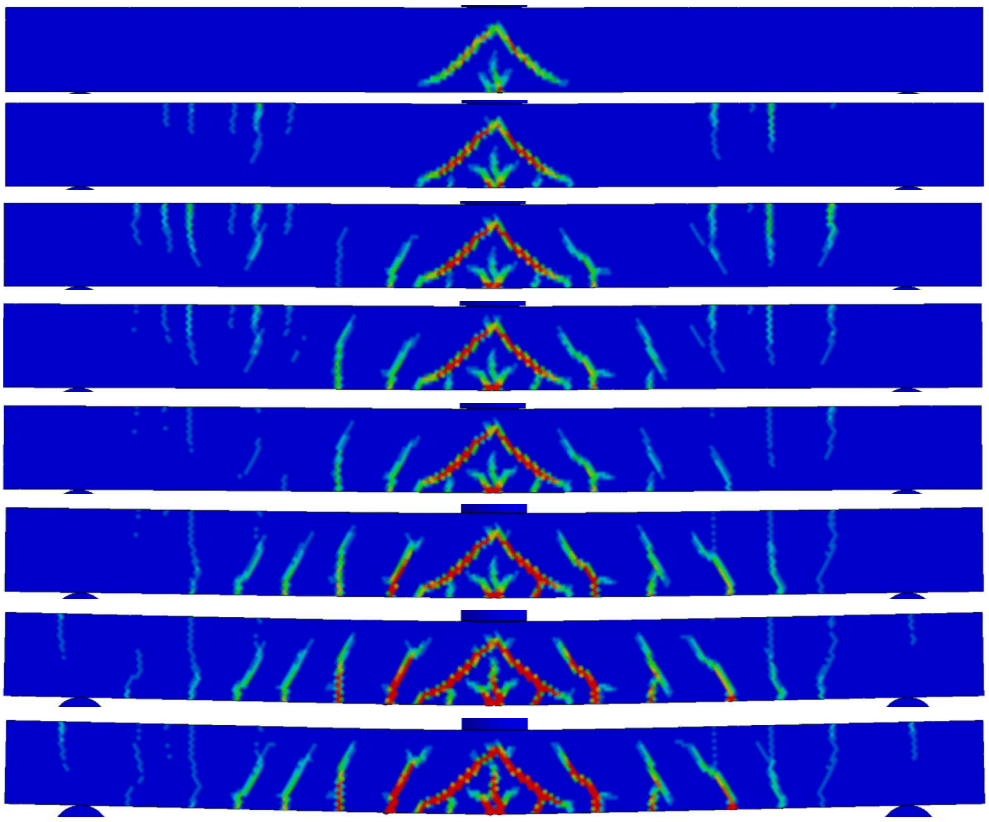
$t = 0.4$ ms	
$t = 0.6$ ms	
$t = 0.8$ ms	
$t = 1.0$ ms	
$t = 2.0$ ms	
$t = 4.0$ ms	
$t = 5.4$ ms [1]	
Principal Strain [%]	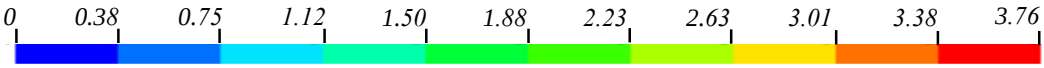

[1] Time at maximum deflection due to impact loading.

Much similar to before, flexural cracking is noted to occur on the top side shortly after impact for the hexahedron model, these cracks eventually close and instead flexural cracks are formed on the bottom edge and propagate with a slight inclination. In general terms, the cracking distribution for the hexahedron model with $h = 2.5$ m is similar to what was found for $h = 5.0$ m, albeit with a seemingly more random pattern.

On the other hand, the strain field predicted by the tetrahedron model is noted to have a more symmetrical response at the time of maximum deflection, compared with the other models, see Table 11.8. The presence of inclined cracking is clearly observed for the response for $h = 2.5$ m. The inclined shear cracks found underneath the impacted area propagate with varying angles and eventually merge with flexural cracks formed at the bottom side at midspan. Further indications of inclined shear cracking can be found away from midspan.

11.4.4 Conclusions

In order to draw conclusions and to highlight differences between the results for the solid element types and the impact cases studied, Table 11.9 presents the strain fields gathered from FE analyses at the time of maximum deflection.

Table 11.9 Strain field at the time when u_{max} occurs for the two drop-height cases. The upper part table presents the strain field for the hexahedron models, while the lower part presents the strain field for the tetrahedron models.

Drop-height	Strain field at point of maximum deflection
$h = 2.5$ m	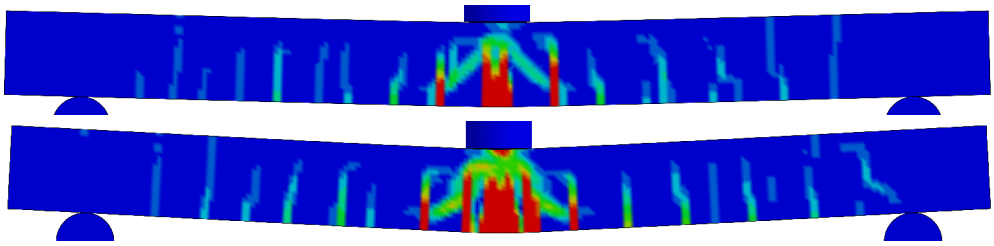
$h = 5.0$ m	
Principal Strain [%]	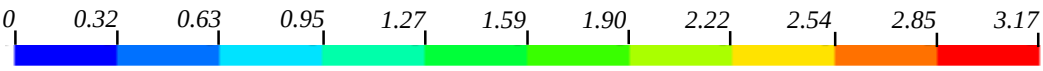
$h = 2.5$ m	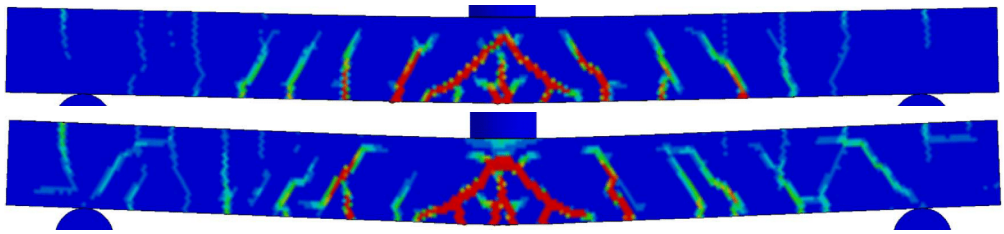
$h = 5.0$ m	
Principal Strain [%]	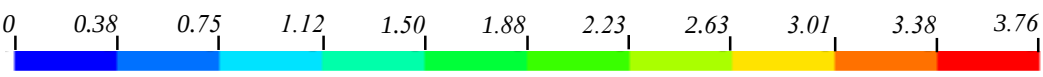

Visual comparison of the strain field of both LS-DYNA models shows that the tetrahedron model exhibits a stronger tendency to describe inclined shear cracking. This is most likely related to the orientation of the elements in the hexahedron model which are defined in an regular pattern of straight vertical and horizontal rows which might lead to crack propagation bias following a vertical path, as suggested in (Lovén and Svavarsdóttir, 2016); while the more irregular pattern generated with tetrahedron elements could facilitate the propagation of inclined cracks.

Perhaps as a consequence of the crack propagation bias, the inclined cracks occurring underneath the impact region are localized to single element rows for the tetrahedron models, whereas the corresponding

cracking obtained with the hexahedron models are described more as cracked regions rather than distinct individual cracks. The same observation holds true regarding the flexural cracking taking place at the bottom edge at midspan, for which the hexahedron models also show a cracked region rather than distinct cracks.

An unusual behavior is noted on the strain field distribution from the tetrahedron model for $h = 5.0\,\text{m}$, in that it shows indications of large strains alongside the top reinforcement on the beam surface. This response is not observed for $h = 2.5\,\text{m}$, nor is it noticed for the hexahedron models, and could serve as an indication that cracking is occurring alongside reinforcement elements due to insufficient anchorage capacity provided by the concrete solids, although this phenomenon was not observed in the laboratory tests.

In general terms, it can be concluded that the ability to represent a realistic cracking pattern is more satisfactory for the tetrahedron models, at least so for the conditions and modelling procedure described in this thesis. This is partly due to the inability of the hexahedron model to capture inclined cracking. This conclusion is further strengthened by the results gathered for the midpoint deflection, which shows a better correspondence to experiments for the tetrahedron models than for the hexahedron ones.

Additionally, the relative error of maximum deflection for the hexahedron model to the average experimental results obtained with DIC analysis diminished for $h = 2.5\,\text{m}$, and could indicate that the capacity of capturing inclined cracking becomes less relevant for the prediction of the midpoint deflection for lower values of impact energy, this topic is further addressed in Section 11.8.3.

The midpoint deflection over time depicted in Figure 11.7 for a $h = 2.5\,\text{m}$ drop-height shows that the tetrahedron model oscillates with a higher frequency than experimental results, and might indicate that the tetrahedron model exhibits an overly stiff response. Results for $h = 5.0\,\text{m}$ drop-height in Figure 11.5 also signal overly stiff response with the tetrahedron model, even though the analysis terminated before reaching completion due to convergence issues. Further investigation on the possibility of overly stiff response with tetrahedron elements is carried out for static analysis in Section 11.7.

11.5 Comparison with DIC Analysis Regarding Crack Pattern

As described in Section 9.1, the strain distribution during impact loading determined from the DIC analysis performed in this thesis does not offer satisfactory level of detail regarding the cracking pattern of the specimens. Hence, it was decided to use the DIC results for the reference beam in (Lovén and Svavarsdóttir, 2016) in order to evaluate how accurately the LS-DYNA models represent the cracking pattern. The DIC results from (Lovén and Svavarsdóttir, 2016) are henceforth denoted DIC-2016.

Table 11.10 shows the comparison between the results from DIC-2016 and the hexahedron model. Fairly good correspondence can be observed. Cracking at the top of the beam along the span can be noticed for both alternatives. Furthermore, the initiation of such cracking occurs at the same time and the cracks continue to open until $t = 1.0\,\text{ms}$. At $t = 2.0\,\text{ms}$, the top cracks have closed, while bending cracks at the bottom edge have distributed along the span. Moreover, the two principal bending cracks located at midspan are clearly visible in the hexahedron model, though as time progresses, the two cracks merge into a cracked region.

However, there are important dissimilarities between the DIC-2016 results and hexahedron LS-DYNA

model results. The major inclined cracks located near the area of impact cannot clearly be represented by the hexahedron model, though a clear tendency to develop such cracks is noticed. This can be attributed to the fact that the hexahedron model seems to have difficulties to represent the real inclination of the cracks. There is an evident dependence on the element type and the direction of the element rows. The cracks appears to be spread over a wider strip, which suggests that gathering the values of strain from the region into a narrower strip, would yield a localized crack. Additionally, such inclined cracks appear to extend further away from the midpoint and have a flatter slope for DIC-2016.

Table 11.10 *Comparison of strain field from DIC-2016 (Lovén and Svavarsdóttir, 2016) with the results for the hexahedron model. Note that the drop-height for DIC-2016 is h = 5.5 m , whereas the impact was modelled from a drop-height of h = 5.0 m in the LS-DYNA analysis.*

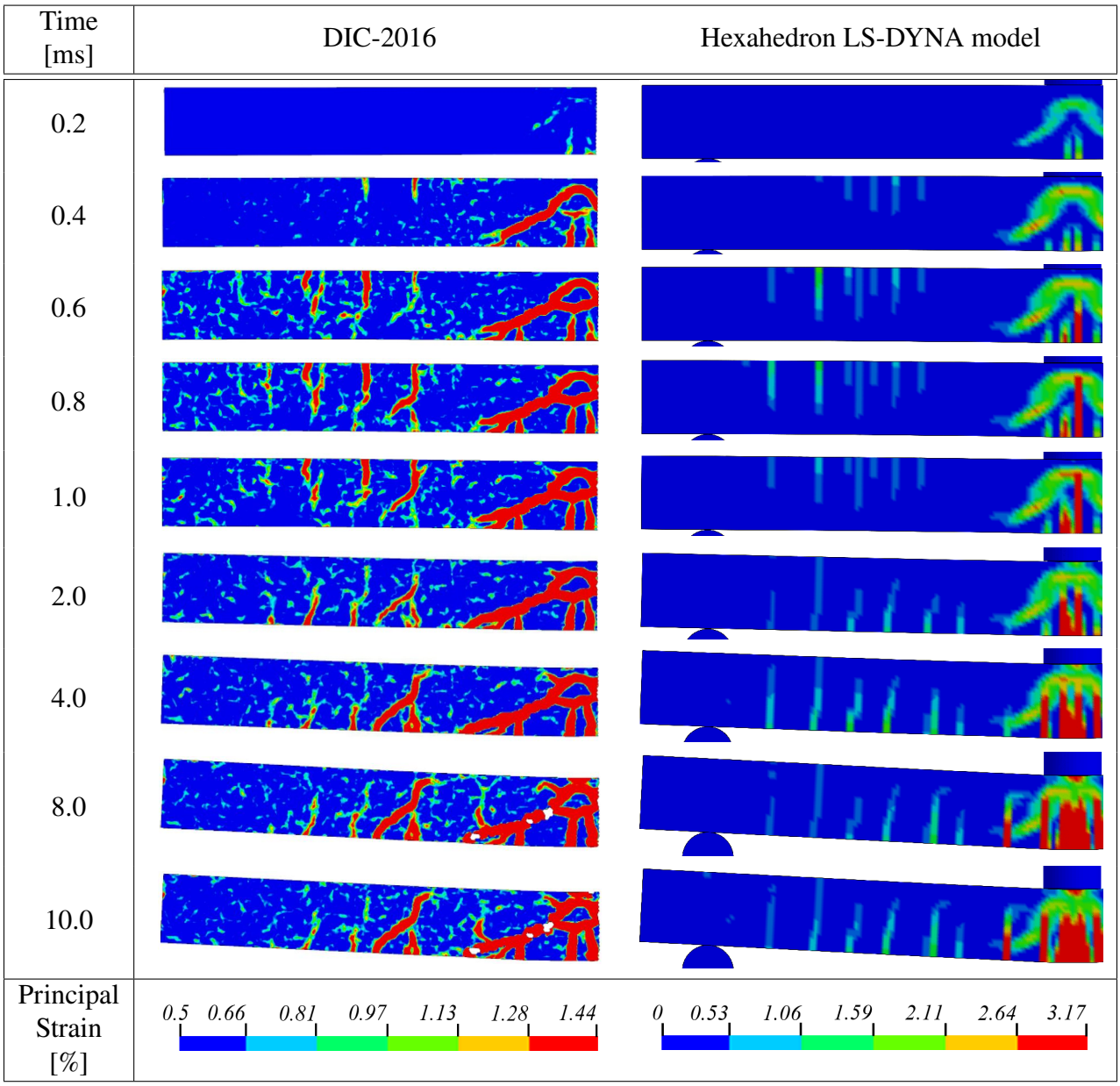

Additionally, new important bending cracks close to the midspan region can be observed at $t = 4.0$ ms in the hexahedron model. By then, the two original cracks at the bottom edge at midspan have merged into a cracked region, while in the DIC-2016 results only two vertical cracks are present at midspan. Thus, it is observed that the damage due to flexural action is more critical for the hexahedron model, which could indicate that the concrete solids have been modelled to be more ductile than in reality. This could be an explanation to the overprediction of the deflection by the hexahedron model, considering that deflection is expected to be larger if bending action is considerably more dominant than shear action.

Table 11.11 Comparison of strain field from DIC-2016 (Lovén and Svavarsdóttir, 2016) with the results for the tetrahedron model. Note that the drop-height from DIC-2016 is h = 5.5 m , whereas the impact was modelled from a drop-height of h = 5.0 m in the LS-DYNA analysis.

Time [ms]	DIC-2016	Tetrahedron LS-DYNA model
0.2		
0.4	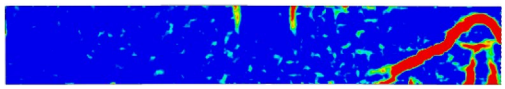	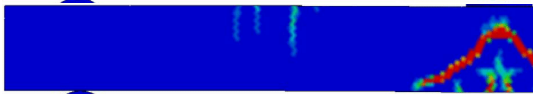
0.6	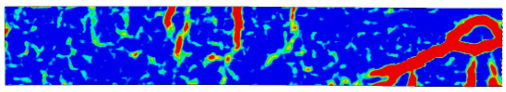	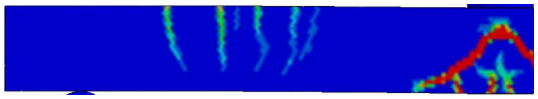
0.8	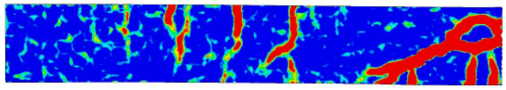	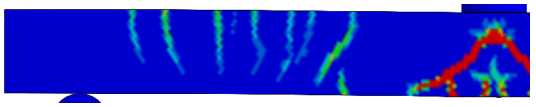
1.0	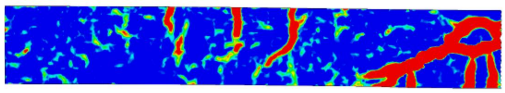	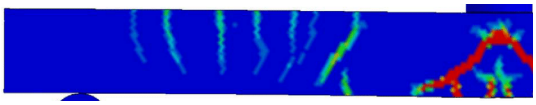
2.0	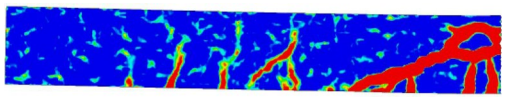	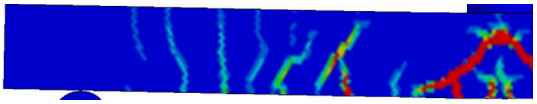
4.0	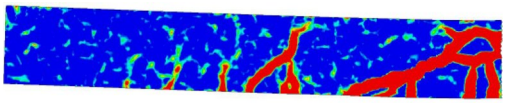	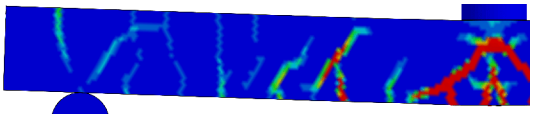
8.0	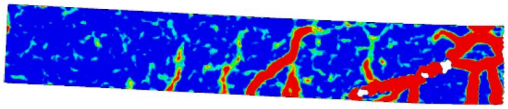	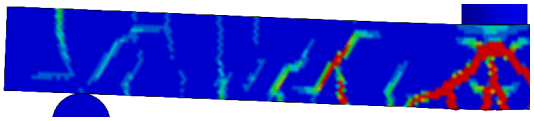
10.0	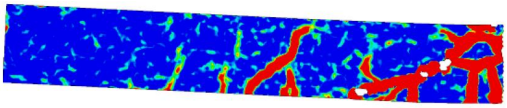	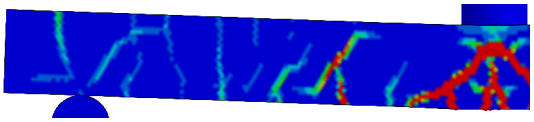
Principal Strain [%]		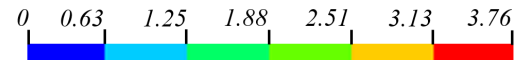

The tetrahedron model, on the other hand, can very well represent the cracking pattern of the beam, as depicted in Table 11.11. This model gives a better prediction of the real inclination of the cracks. The major inclined shear crack close to the impact region is clearly visible in the model, although the real crack seems to extend slightly further from the midspan region. The initiation of cracking at the top of the beam also takes place at the same time. Similarly, the two bending cracks at the bottom edge at midspan are visibly depicted in the LS-DYNA model. Some secondary cracks can also be predicted accurately from the tetrahedron model.

Some noticeable differences related to the cracking pattern correspond to web cracking over the support as well as a flexural crack formed at the top side close to the support from a time $t = 4.0$ ms, which are not observed in the DIC-2016 results.

11.6 Sensitivity Analysis

11.6.1 Overview

During the creation of the LS-DYNA models, different decisions were made regarding input parameters to the FE models. Some of these values were assumed to be equal to the default or recommended values according to the LS-DYNA manual and to the authors of the material models. However, the influence of such parameters is uncertain as it depends on the conditions of a given model. Therefore, a detailed study was carried out in order to analyze the effects of different parameters in the results of the FE simulation. This study serves as a mean of further verification of the LS-DYNA models and to determine possible suggestions for future analyses.

Only parameters concerning modelling procedure were investigated in this section. The experiment conditions regarding geometry, boundary conditions, load application, and basic material properties remained unchanged. Furthermore, for the sake of simplicity, only a drop-height equal to $h = 5.0$ m was considered.

The parameters chosen for the sensitivity analysis include the compressive softening parameter, ϵ_{fc} (or EFC, according to LS-DYNA notations), and the hourglass coefficient, QM.

Furthermore, different beam element types, as well as truss element type, are available in LS-DYNA which could be used to model the reinforcement bars. As discussed in Section 10.3, a beam element with one integration point (1×1) on the cross-section was chosen to represent the bars in the base model. However, in order to investigate the influence of this input parameter, a comparison was also made when modelling the reinforcement bars using 2×2 Gauss integration scheme and also when using truss elements instead of beam elements.

Additionally, the effects of reducing the time step was also evaluated, in accordance with the recommendations in (Lovén and Svavarsdóttir, 2016). The scope of the sensitivity study is summarized in Table 11.12.

Table 11.12 Scope of sensitivity study and studied parameters for both FE models. Underlined values refer to input parameters chosen for respective base models.

Parameter	Hexahedron LS-DYNA model	Tetrahedron LS-DYNA model
QM	0.01 0.1 1.0	Not used
EFC	$1 \cdot 10^{-4}$ $1 \cdot 10^{-3}$	$1 \cdot 10^{-4}$ -
Reinforcement Elements	Beam (1×1 IP) Beam (2×2 IP) Truss	Beam (1×1 IP) Beam (2×2 IP) Truss
Time step factor	0.3 0.6 0.9	0.4 - -

11.6.2 Hourglass coefficient, QM

The hourglass force, that is, the fictitious force needed in order to prevent zero-energy modes in under-integrated hexahedron elements, is proportional to the hourglass coefficient, QM, as described in Section 10.3. The choice of hourglass parameter is expected to have a significant influence on the results. In order to test such influence, different analysis were performed for different values of QM; namely: 1.0, as recommended for elastic materials; 0.1, the default value; and 0.01, as suggested for non-linear material models. The parameter QM is only relevant for hexahedron solid elements, as tetrahedron elements do not develop zero-energy modes and therefore it is not necessary to introduce the hourglass force in the model constructed with tetrahedron elements.

Figure 11.8 shows the deflection of the midpoint over time for different values of hourglass coefficient, compared with the average deflection measured in the laboratory tests. For a reduced value of QM, the maximum deflection is clearly overpredicted. On the other hand, increasing QM to 1.0 reduces the maximum deflection so that the predicted value corresponds rather well with the experimental results, although the curve for QM = 1.0 falls out of phase with the experimental curve after maximum deflection and exhibits a higher frequency, indicating a stiffer response.

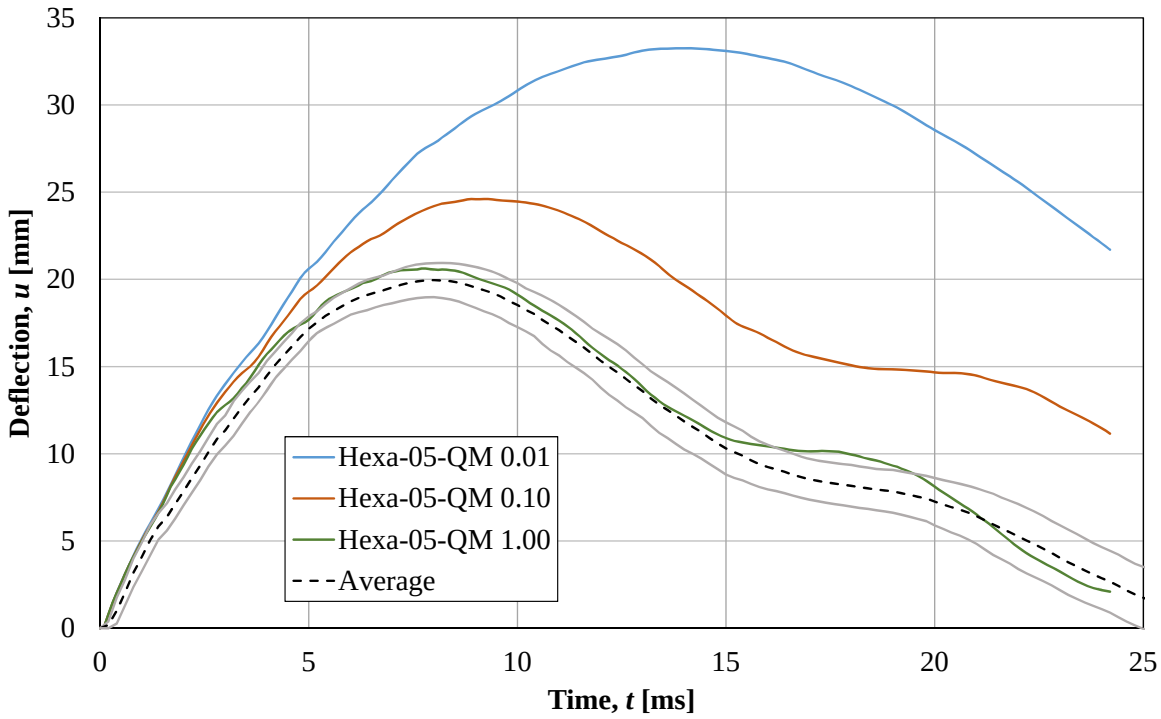

Figure 11.8 Midspan deflection over time for model with 5 mm hexahedron elements for different values of hourglass coefficient, QM.

The deflection-time curves in Figure 11.8 may suggest that using QM = 1.0 produces a better prediction of the experimental results; however, the distribution of strains for an increased value of QM, shown in Table 11.13, does not appear to be consistent with the experiments. The strain field shows even more distributed cracked regions instead of individual cracks for the model with QM = 1.0; furthermore, more cracks are detected along the span, which render the concrete more ductile. The vertical flexural cracks which should take place at the bottom edge at midspan are spread over more than one element row at all times. Additionally, even though there is a tendency for inclined cracking to develop below the impact zone, the cracks are, once more, spread over the midspan region. The magnitude of the strains for QM = 1.0 is smaller than for a model with QM = 0.1, which suggests that gathering the summation of strain into a smaller region could give a similar strain distribution to QM = 0.1. These results indicate that the value of crack band width, assumed equal to the element length by CDPM2, should be larger if QM = 1.0 is used.

According to these results, it appears that choosing the default value of hourglass coefficient, QM = 0.1, gives more accurate results for the conditions of the analyses performed compared to 0.01 and 1.0.

Table 11.13 *Strain field for the 5 mm hexahedron LS-DYNA model for different values of hourglass coefficient.*

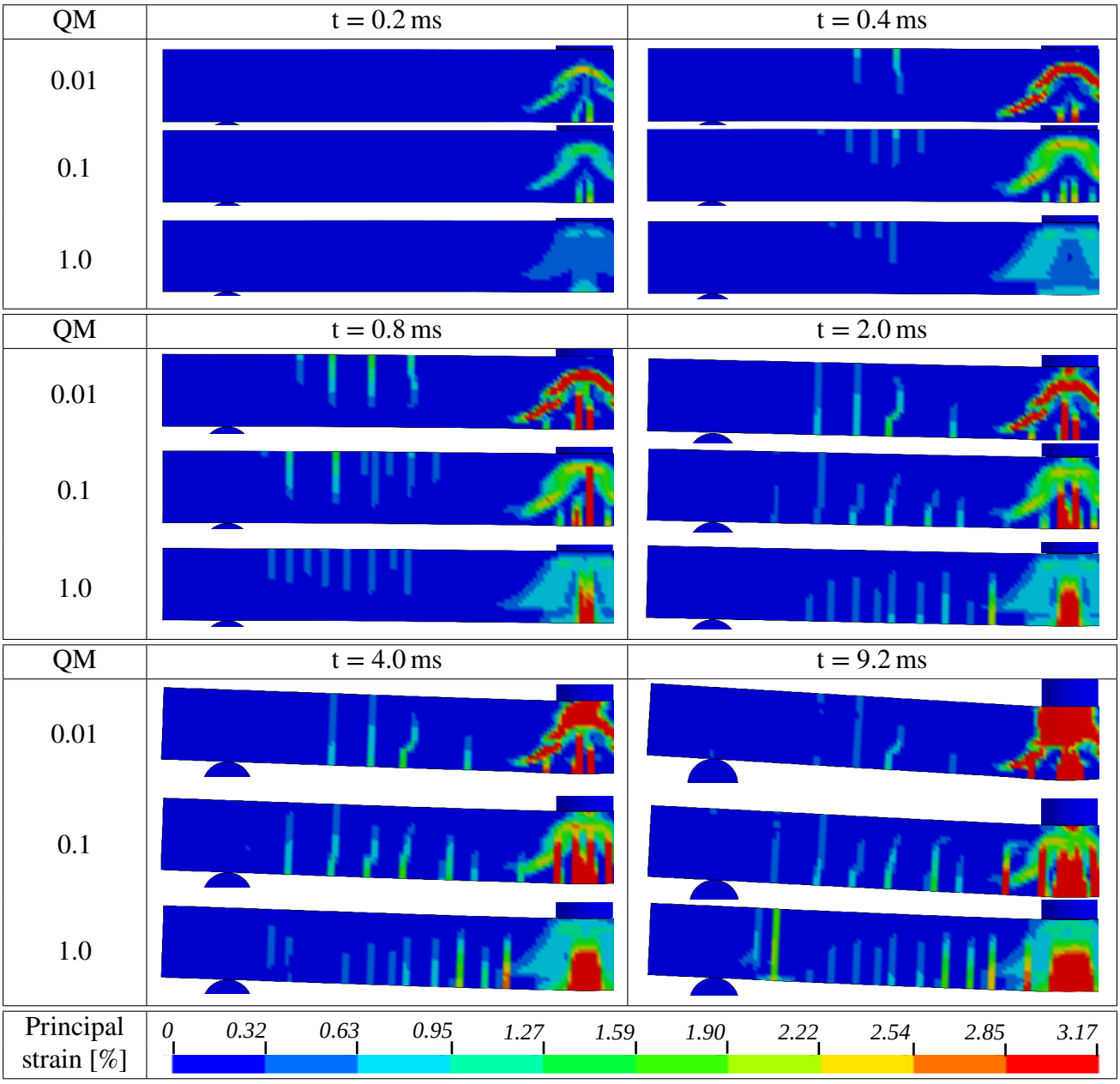

11.6.3 Compressive softening parameter, ε_{fc}

Another interesting study is the verification of the softening parameter in the material model CDPM2, for which a value of $\varepsilon_{fc} = 1 \cdot 10^{-4}$ is set by default in the material model. As described in Section 10.5.1, this parameter controls how ductile the concrete behaves in compression; larger values of ε_{fc} increase the ductility of concrete elements. In Section 11.2 it was explained that ε_{fc} had to be adjusted for the tetrahedron models in order to circumvent convergence problems, while the default value was kept for the hexahedron models. Therefore, since the adopted values of ε_{fc} are different for hexahedron and

tetrahedron elements, an evaluation of the influence of a value of $\varepsilon_{fc} = 1 \cdot 10^{-3}$ in the hexahedron model was performed.

The deformation-time relations can be seen in Figure 11.9. It can be observed that the maximum deflection decreases for an increased value of ε_{fc}, which makes the response closer to the experimental curve.

In Table 11.14, a comparison of the strain fields for different values of ε_{fc} is made. There does not seem to be a significant difference in cracking pattern. However, two additional and longer vertical flexural cracks at the bottom edge can be observed close to the impact region as early as $t = 0.8$ ms for the model with $\varepsilon_{fc} = 1 \cdot 10^{-3}$. These same cracks do appear for the base model, but later, at a time $t = 4.0$ ms.

Furthermore, at $t = 4.0$ ms, a wider bending crack can be observed along the span for the model with $\varepsilon_{fc} = 1 \cdot 10^{-3}$. This crack seems to correlate with the cracks observed in the experimental results and the tetrahedron model, as shown in Table 11.11 from $t = 2.0$ ms. These results indicate that choosing $\varepsilon_{fc} = 1 \cdot 10^{-3}$ for this type of analysis might give a better representation of the dynamic response when using hexahedron elements, though the results are still fairly similar to those obtained with the default value, $\varepsilon_{fc} = 1 \cdot 10^{-4}$.

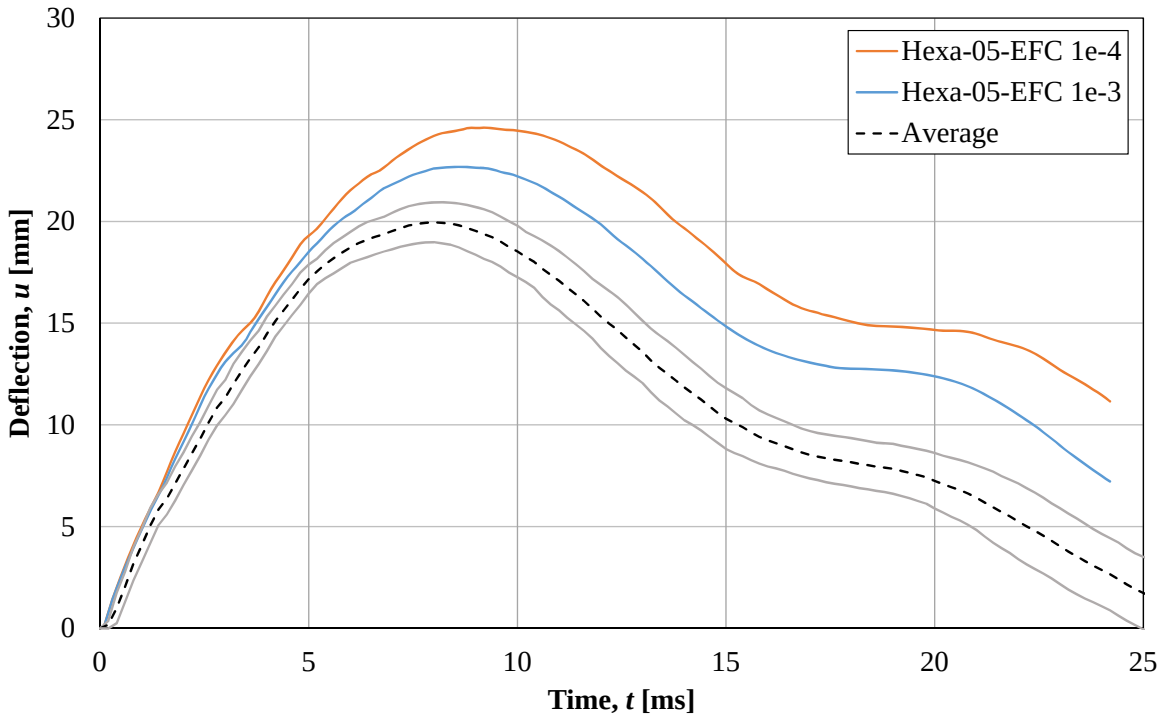

Figure 11.9 Midspan deflection over time for model with 5 mm hexahedron elements for different values of compressive softening parameter, EFC.

Table 11.14 Strain field for the 5 mm hexahedron LS-DYNA model for different values of compressive softening parameter, EFC.

EFC	$t = 0.2$ ms	$t = 0.4$ ms
$1 \cdot 10^{-3}$		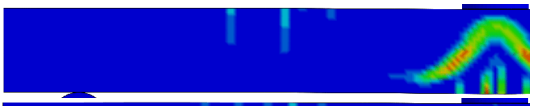
$1 \cdot 10^{-4}$		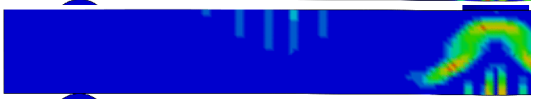
EFC	t = 0.8 ms	t = 2.0 ms
$1 \cdot 10^{-3}$	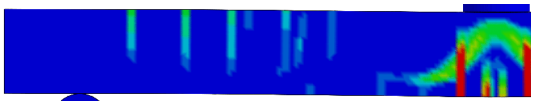	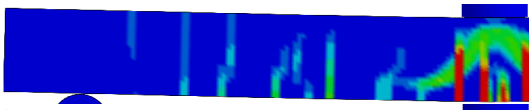
$1 \cdot 10^{-4}$	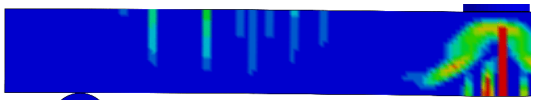	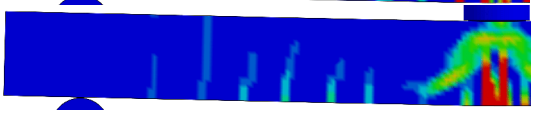
EFC	t = 4.0 ms	t = 9.2 ms
$1 \cdot 10^{-3}$	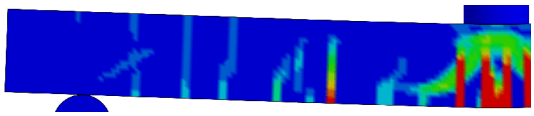	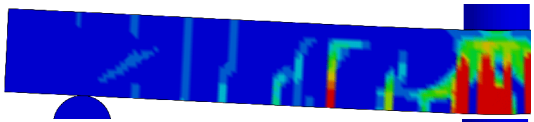
$1 \cdot 10^{-4}$	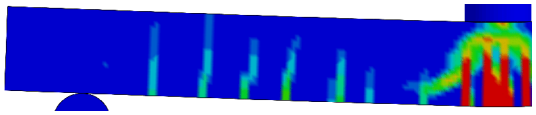	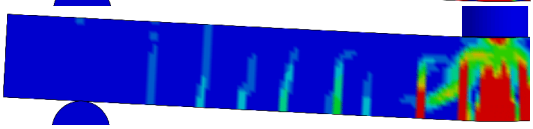
Principal strain [%]	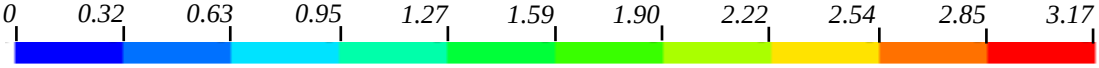	

11.6.4 Element type for modelling the reinforcement bars

Different element types and integration schemes across the cross section are available in LS-DYNA to model beam elements. Due to the cross-sectional size of the reinforcement bars in relation with the beam cross-section, no large variation in the results is expected when choosing the number of integration points (IP). However, a reduction in computational effort is likely for underintegrated beam elements, or truss elements. As explained in Section 10.3, it was decided to use Hughes-Liu beam elements with 1×1 IP to model the reinforcement bars; however, a study of the influence of the integration scheme was performed. Two additional alternatives were considered: truss element, and Hughes-Liu beam element with 2x2 Gauss IP, which is the default option in LS-DYNA.

Figure 11.10 shows the deflection over time of the midpoint for the hexahedron LS-DYNA model for different element types, whereas Table 11.15 shows the cracking pattern for all three models. Only a minor difference can be observed, though the results show that the model with truss elements is closer to the base model with 1×1 IP beam elements.

It can be concluded that the choice of the element type to model the reinforcement bars has a negligible influence in terms of cracking distribution and deflection over time for the hexahedron model.

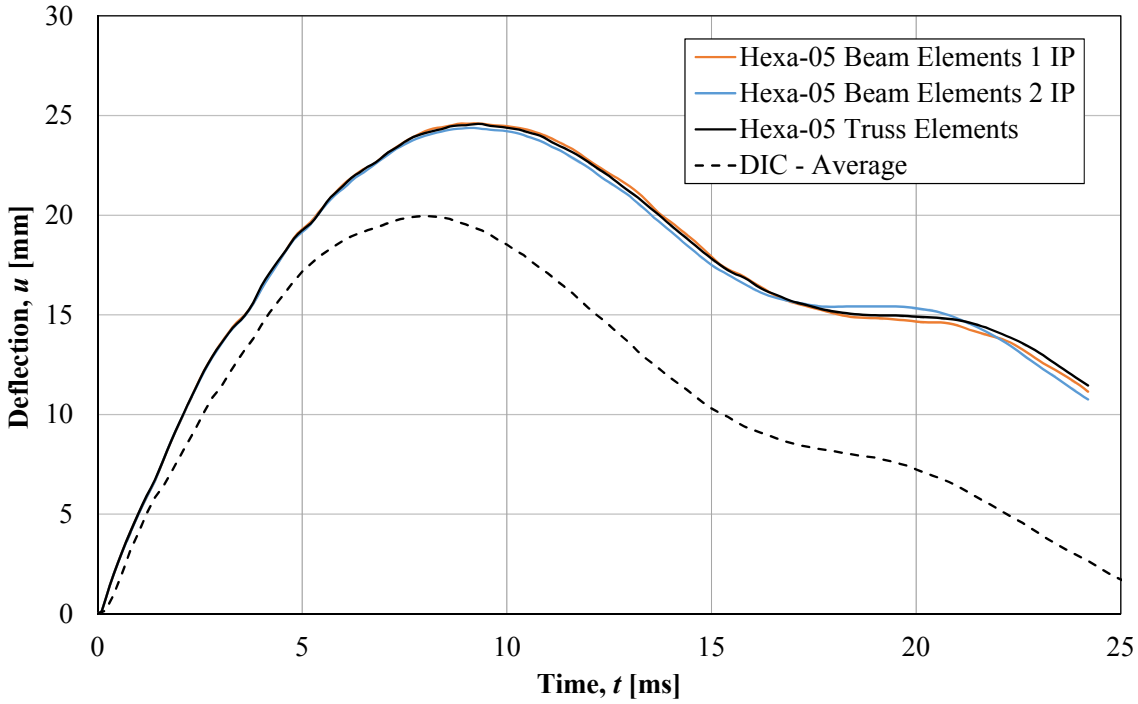

Figure 11.10 *Midspan deflection over time for model with 5 mm hexahedron elements for different modelling techniques of reinforcement bars. "1 IP" corresponds to* 1×1 *integration point, while "2 IP" corresponds to* 2×2 *Gauss integration scheme.*

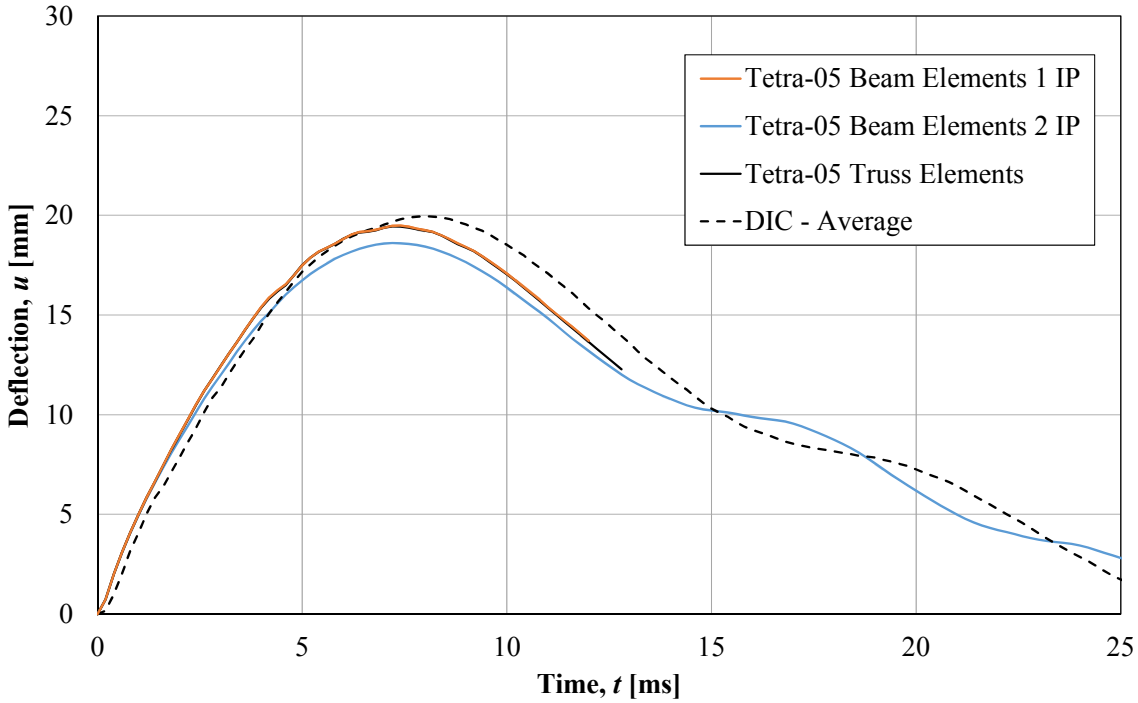

Figure 11.11 *Midspan deflection over time for model with 5 mm tetrahedron elements for different modelling techniques of reinforcement bars.*

Table 11.15 *Strain field for the 5 mm hexahedron LS-DYNA model for different modelling techniques of reinforcement bars.*

IP	t = 0.4 ms	t = 2.0 ms
1 × 1		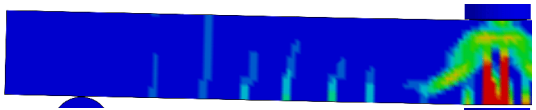
2 × 2 Gauss	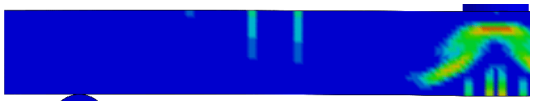	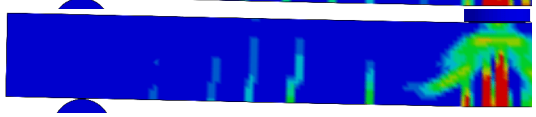
Truss element	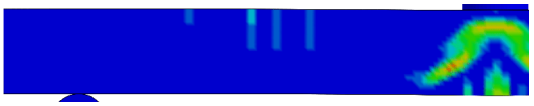	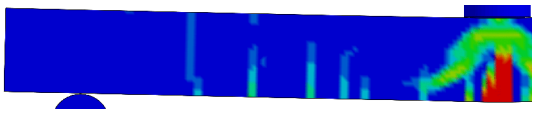
IP	**t = 4.0 ms**	**t = 9.2 ms**
1 × 1	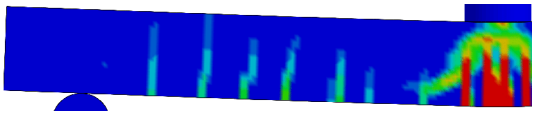	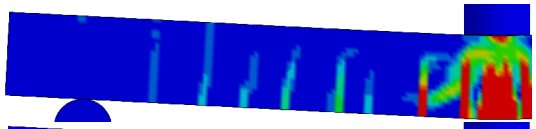
2 × 2 Gauss	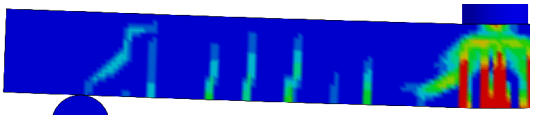	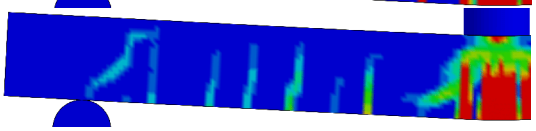
Truss element	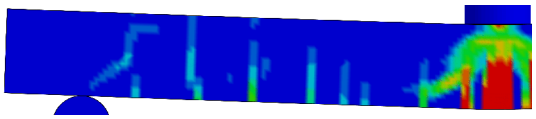	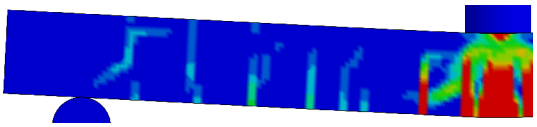
Principal strain [%]	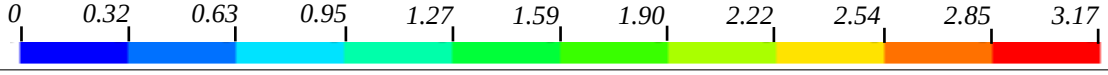	

The midpoint deflection over time for different element types is depicted in Figure 11.11 for the tetrahedron model. It was also observed that the model with truss elements produces virtually the same results as those of the model with one-integration point beam elements, although the truss-element model runs for a slightly longer time before reaching convergence problems. On the other hand, the analysis with 2×2 IP beam elements can be performed until termination (25 ms). Besides, the maximum deflection obtained with this model is about 5% smaller than the base model.

Since the tetrahedron model with 2×2 IP elements reaches no convergence issues, a comparison of the deflection over time relation after maximum deflection can be made with the experimental results for $h = 5.0$ m in Figure 11.11. Here, it is evident that the response of this model is stiffer since oscillations are found to occur at an earlier stage compared to the DIC results. Similar observations were found for the base model with drop-height of $h = 2.5$ m in Section 11.4.3 and may be a consequence of volumetric locking when tetrahedron elements are used.

More relevant differences can be observed on the cracking pattern, as shown in Table 11.16. While the three models exhibit a similar crack pattern during the first millisecond after impact, high values of strains are present along the reinforcement bars from $t = 2.0$ ms for the model with 2×2 IP. These results can be considered unrealistic, as such behavior was not observed in the laboratory tests.

To the extent of the modelling techniques and conditions studied here, modelling the reinforcement bars by using beam elements with one integration point or truss elements produces more reliable results in terms of deflection over time as well as in crack pattern representation.

Table 11.16 Strain field for the 5 mm tetrahedron LS-DYNA model for different modelling techniques of reinforcement bars.

IP	$t = 0.2$ ms	$t = 0.4$ ms
1×1		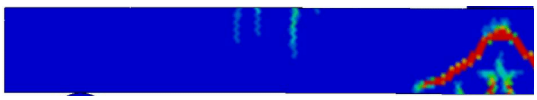
2×2 Gauss		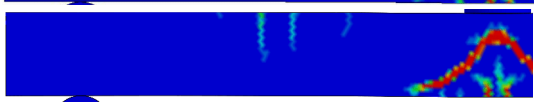
Truss element		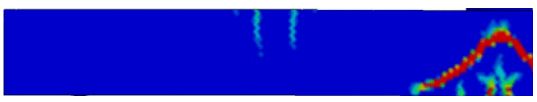

IP	$t = 0.8$ ms	$t = 2.0$ ms
1×1	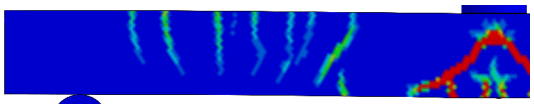	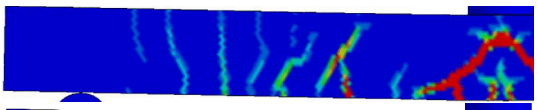
2×2 Gauss	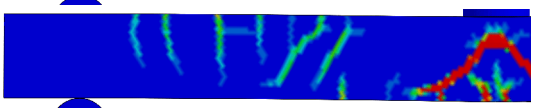	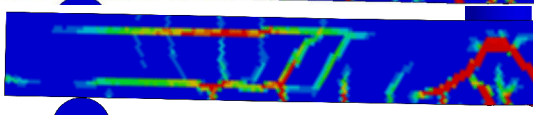
Truss element	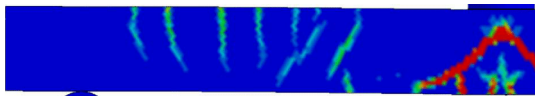	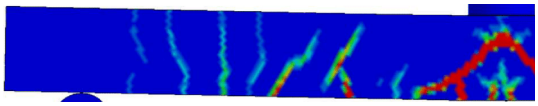

IP	$t = 4.0$ ms	$t = 7.4$ ms
1×1	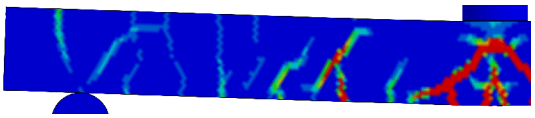	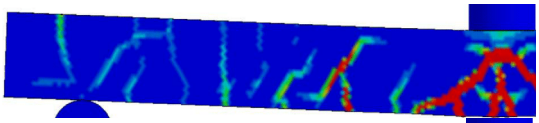
2×2 Gauss	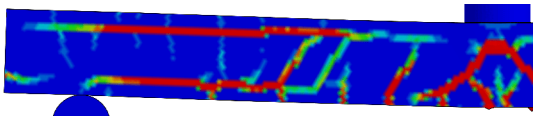	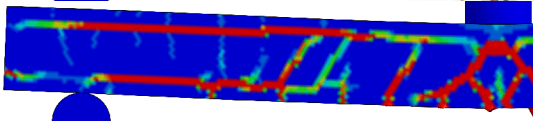
Truss element	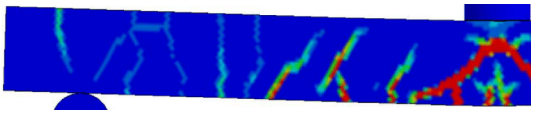	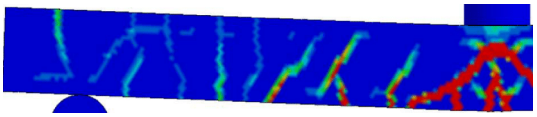
Principal strain [%]	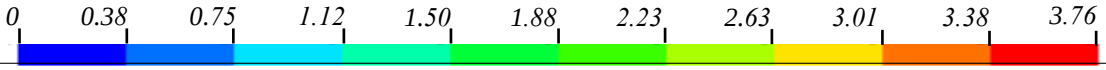	

11.6.5 Time step factor, TSSFAC

As explained in Section 10.8, the calculated critical time step is multiplied by a factor TSSFAC, equal to 0.9 by default. This time step proves to be small enough to perform the analysis for the hexahedron models for different drop-heights. However, in order to circumvent convergence problems with the tetrahedron models, TSSFAC needed to be reduced to 0.4 when performing FE analyses for $h = 5.0$ m. Similarly, static analyses for hexahedron model, detailed in Section 11.7, reached convergence problems for a load closed to peak load, and the scale factor was then reduced to 0.6 to avoid such problems.

This shows that changing the time step has an effect on the computations. Therefore, it was decided to perform several analyses for the hexahedron model for different values of time step factor. Figure 11.12 shows the deformation over time of the midpoint for all these different analyses. Only a minor difference can be observed regarding the midpoint deflection, and virtually no difference was detected between cracking patterns (not shown). This indicates that if the model is able to run until completion for a given time step size, then a smaller value of time step would not significantly influence the response.

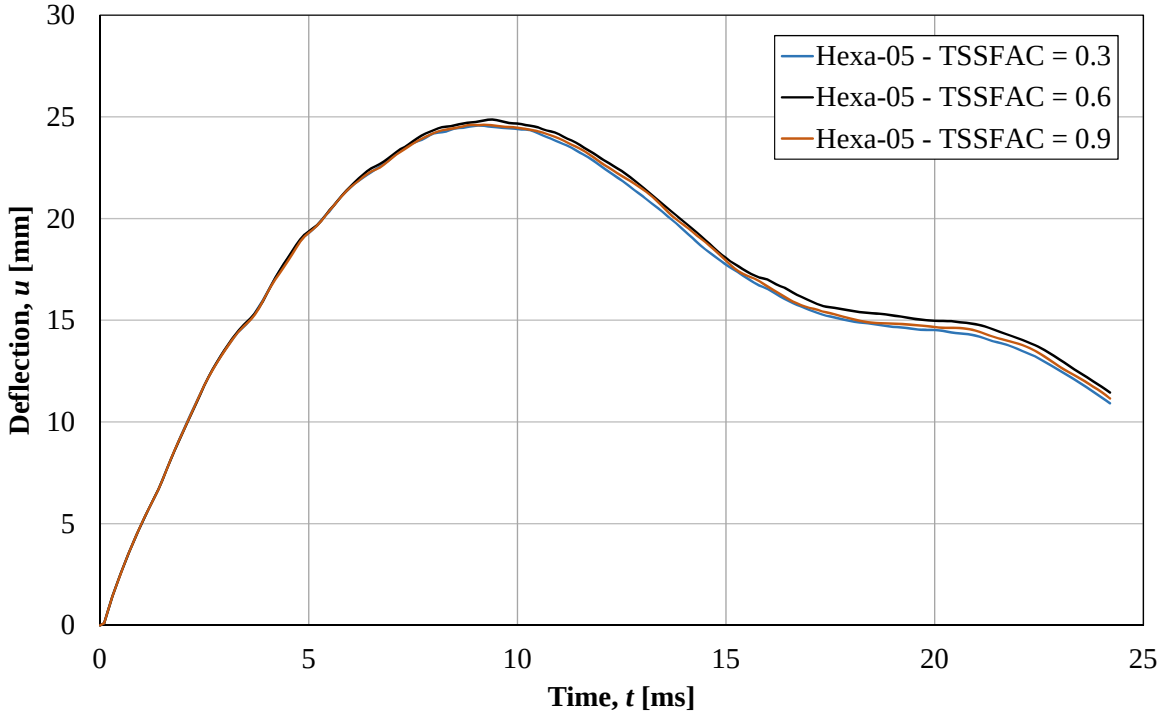

Figure 11.12 Midspan deflection over time for the model with 5 mm hexahedron elements for different values of time step factor, TSSFAC.

11.6.6 Conclusions

The hourglass coefficient used for one-integration point hexahedron elements was proved to have an important influence on the results of the FE analysis. Using QM = 0.01 overpredicted the midpoint deflection to a great extent, while the cracking pattern was found to be more concentrated than for the default value, QM = 0.1. On the other hand, using an increased value, QM = 1.0, resulted in a value of maximum deflection which closely corresponded to experimental results. However, the deflection-vs-

time relation indicates that the model exhibits a stiffer response compared with the experimental results; which, in conjunction with an unrealistic cracking pattern, leads to the conclusion that using QM = 1.0 would be inappropriate for this type of FE analysis. Finally, the model with the default value, QM = 0.1, produced the most reliable results in terms of deflection and cracking pattern.

When altering the compressive softening parameter for the hexahedron FE model from the default value of $\varepsilon_{fc} = 1 \cdot 10^{-4}$ to a more ductile response, little change in terms of cracking distribution was noticed. However, the deflection over time relationship showed a better correspondence to the experimental values, which indicates that a value $\varepsilon_{fc} = 1 \cdot 10^{-3}$ may be a more reliable choice when using hexahedron elements for the type of FE analysis described in this project.

Further studies were also conducted regarding reinforcement element types. The hexahedron FE model showed little sensitivity in terms of cracking pattern as well as in deflection over time for the three types studied. However, differences became more profound when performing the same study with tetrahedron elements. The investigation showed minor differences between truss elements and 1×1 integration points beam elements; however, significant differences were found for the tetrahedron model with 2×2 integration points in terms of midpoint deflection and cracking distribution, where large magnitude of strains where observed alongside reinforcement bars. In conclusion, the choice of element type to model the reinforcement bars might affect significantly the results if a tetrahedron mesh is used. This shows that the tetrahedron elements should be used carefully, and different trials are required to find the most suitable values for input parameters.

Finally, the study pertaining to the time step factor, TSSFAC, showed negligible differences regarding deflection and cracking pattern for different sizes of time step, provided that a suitable value of time step to reach completion of the analysis has been found. It was concluded that adjustments of TSSFAC could reliably be utilized with minor influence on results when attempting to circumvent convergence issues.

11.7 Static Analysis

11.7.1 General

As described in Section 10.7, an analysis simulating static tests was also performed on the LS-DYNA models. The loading was applied as a prescribed velocity on the nodes on the top of the beam at midspan. The velocity was increased gradually from 0 mm/ms to 0.07 mm/ms during the first 100 ms and kept constant thereafter until reaching the desired deformation.

However, in order to ensure that inertial effects under a specific loading rate are negligible, two other analysis with different loading rates were performed. This preliminary study was performed using a 20 mm mesh size due to computational costs, and was conducted using hexahedron elements. Table 11.17 shows the conditions for the different analyses.

The load-deformation relations for different loading rates are illustrated in Figure 11.13. It can be observed that there is good equivalence between all relations, particularly so until a deflection of 12 mm. From that point on, the structure exhibits a snap-through behavior. The results indicate that using the fastest studied loading rate, 0.07 mm/ms, is adequate to analyze the static behavior of the beam.

Table 11.17 Different loading rates to simulate static analysis in LS-DYNA.

Loading rate [mm/ms]	Final Deflection [mm]	Loading Time [ms]
0.070	31.5	500
0.033	31.4	1000
0.016	31.2	2000

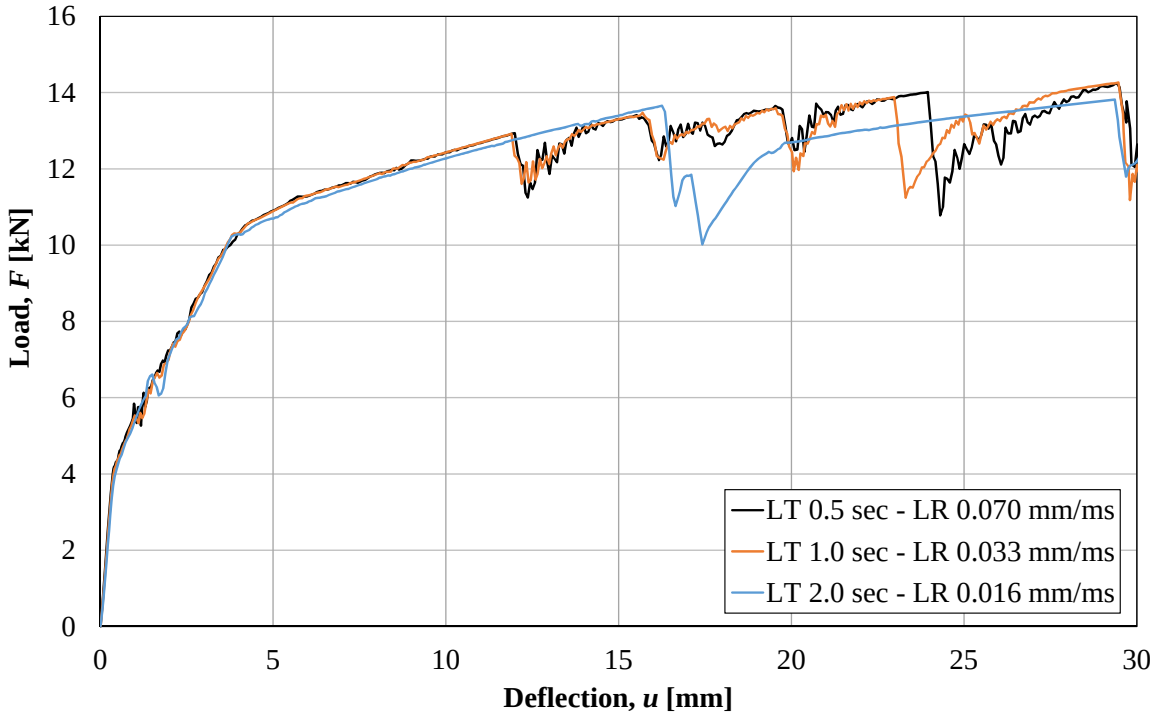

Figure 11.13 Static analysis for the model with 20 mm hexahedron elements for different loading rates. LT and LR stand for "loading time" and "loading rate", respectively.

After deciding on a reasonable loading rate, analyses were performed on the models with 5 mm elements. However, the static analysis using 5 mm tetrahedron elements could only be run until a deflection of 7.8 mm due to excessive computational costs since the number of elements for such model is close to $900 \cdot 10^6$. For this reason, the static analysis was also carried out on the model with 10 mm tetrahedron elements, in an attempt to capture the behavior of the beam up to and beyond peak load. Figure 11.14 shows the static load-deformation relationships for all models.

The 5 mm hexahedron model leads to a rather good prediction of the ultimate load capacity of the beam. Despite a slight underprediction, these results are closer to the mean experimental value of load capacity. However, the response up to the onset of yielding is stiffer in the FE analysis compared to experimental results.

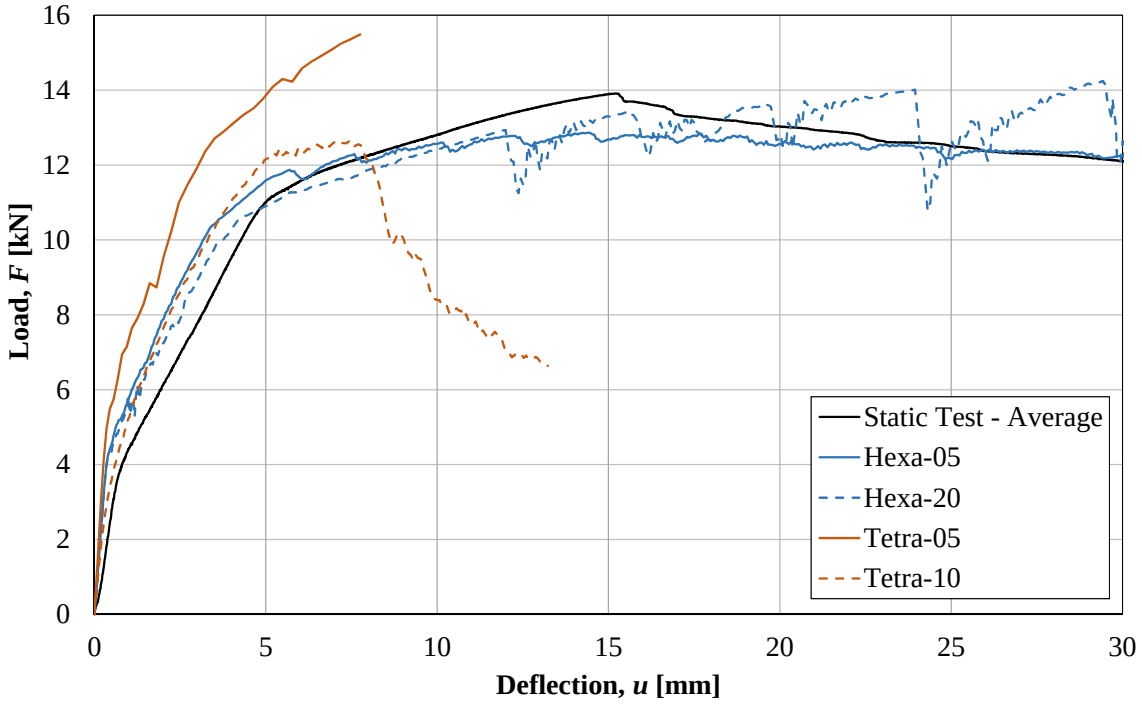

Figure 11.14 Static analysis for different models. LR = 0.070 mm/ms.

The results for the 5.0 mm tetrahedron model show a significant overprediction in terms of load capacity as well as stiffness. Recall that the analysis could only be simulated to a deflection of 7.8 mm due to computational costs and limitations in run-time; however, judging by the shape of the load-deflection relationship, the analysis should be run for a longer duration in order to reach the true load carrying capacity of the model, which indicates that the degree of overprediction for the 5.0 mm tetrahedron model is larger than documented.

As explained in Section 10.3, different meshing procedures can be adopted when creating a tetrahedron mesh in LS-DYNA. Initially, only the 10 mm tetrahedron model created using skin remesh was considered. However, the behavior appears to be unrealistic, as this beam fails due to shear mechanism, see Table 11.19. It was observed in the experiments that the undamaged beams of Series-3 should fail in a bending failure mechanism. In an attempt to reproduce this phenomenon, a new model with 10 mm tetrahedron elements was created where the optional procedure of skin remeshing was disregarded. This new model shows a considerable overprediction of the load capacity and a much stiffer response, although the dominant failure mode is bending, as shown in Figure 11.15.

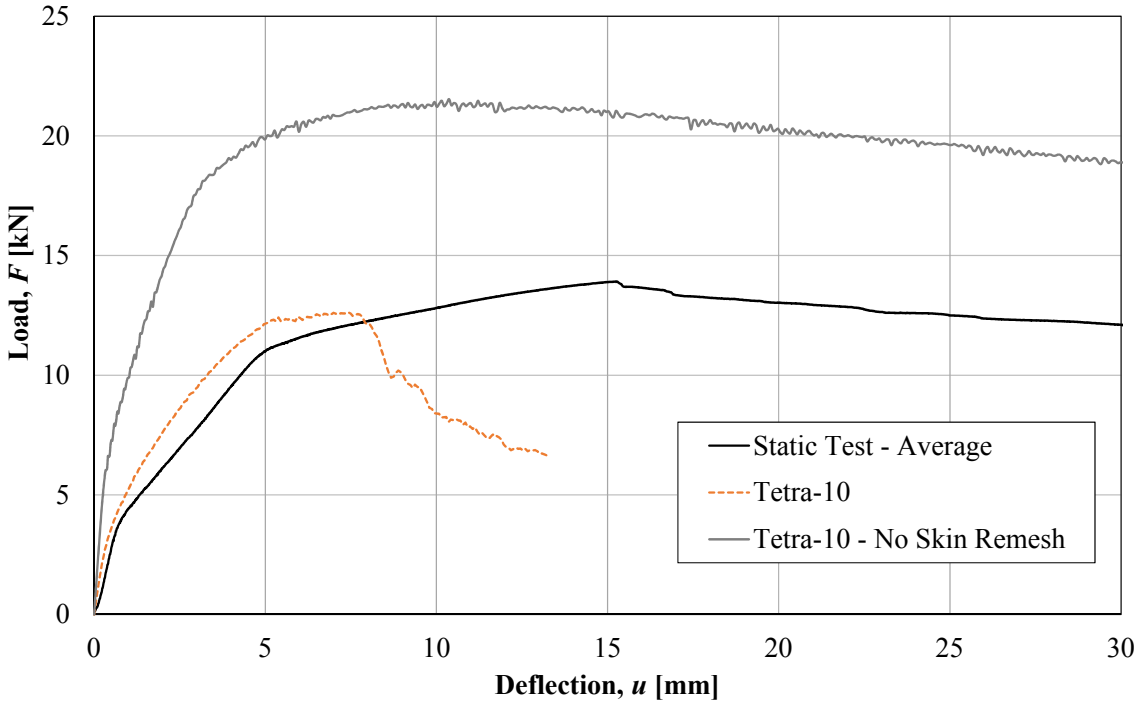

Figure 11.15 Static analysis for the model with 10 mm tetrahedron elements when using different meshing procedures.

Values of peak load for the analyses are summarized in Table 11.18. The strain distributions at peak load are shown in Table 11.19. Further information regarding cracking pattern at different times for all the models considered can be found in Appendix H.4. The tetrahedron models seem to overpredict the load capacity to a great extent, as long as the failure mode is bending; this effect also appears to be more pronounced for larger element sizes. The overprediction could be attributed to volumetric locking due to the geometry of the tetrahedron elements.

Table 11.18 Peak load for different static analysis.

Method	Peak Load [kN]
Hexa-05	13.0
Tetra-05	15.5
Tetra-10	12.6
Tetra-10 - no skin remesh	21.5
Static test - average	13.9

Table 11.19 Strain field at peak load for static analyses. Observe that the limits of the color-scale varies depending on the mesh size and element type, refer to Appendix H.4.

Deflection/ Load	Strain field at peak load
Hexa-05 $u = 25.0\,\text{mm}$ $F = 12.3\,\text{kN}$	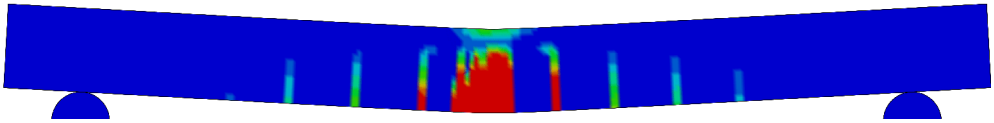
Tetra-05 $u = 7.5\,\text{mm}$ $F = 15.4\,\text{kN}$	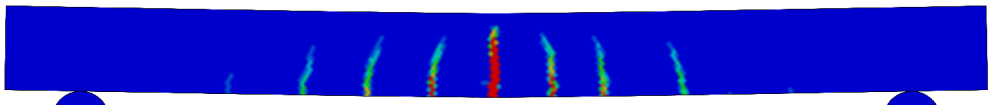
Tetra-10 $u = 9.4\,\text{mm}$ $F = 9.6\,\text{kN}$	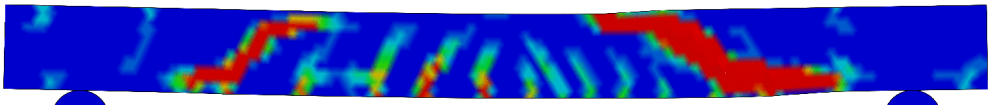
Tetra-10 (no remesh) $u = 15.0\,\text{mm}$ $F = 21.0\,\text{kN}$	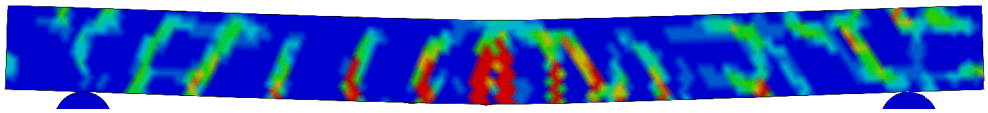

11.7.2 Sensitivity analysis

The influence of some modelling parameters of the material model CDPM2 on the results of the static analysis was also briefly verified, in order to gain further insight with respect to possible effects to the dynamic analysis.

Initially, the compressive softening parameter was evaluated and the results were compared against average experimental values and the predicted load-deflection relationship. The results are shown in Figure 11.16. The behavior in state I and II is virtually unaffected by this parameter. The difference commences to be noticeable for state III. The curve for $\varepsilon_{fc} = 1 \cdot 10^{-3}$ shows ascending behavior, while there is a small decrease for the curve for $\varepsilon_{fc} = 1 \cdot 10^{-4}$. However, the model with $\varepsilon_{fc} = 1 \cdot 10^{-4}$ presents convergence issues for a load level close to peak load. In order to circumvent this problem, the time step factor (originally set to the default value, 0.9), was reduced to 0.6. Ultimately, the influence of the compressive softening parameter does not appear to have a significant influence on the static analysis, and it is observed that the hexahedron model yields similar results in terms of load capacity to the results of the hand calculations.

Secondly, the hourglass coefficient, QM, was evaluated. The load-deformation relationship for different values of QM is shown in Figure 11.17. For an increased value of hourglass coefficient, QM = 1.0, a stiffer response and a larger load capacity was observed. This phenomenon is reflected on the behavior of the models for impact loading, shown in the sensitivity study performed in Section 11.6.2, where the maximum deflection due to impact loading has a smaller value for the model with QM = 1.0, and the oscillations of the structure begin at an earlier stage and exhibit a higher frequency.

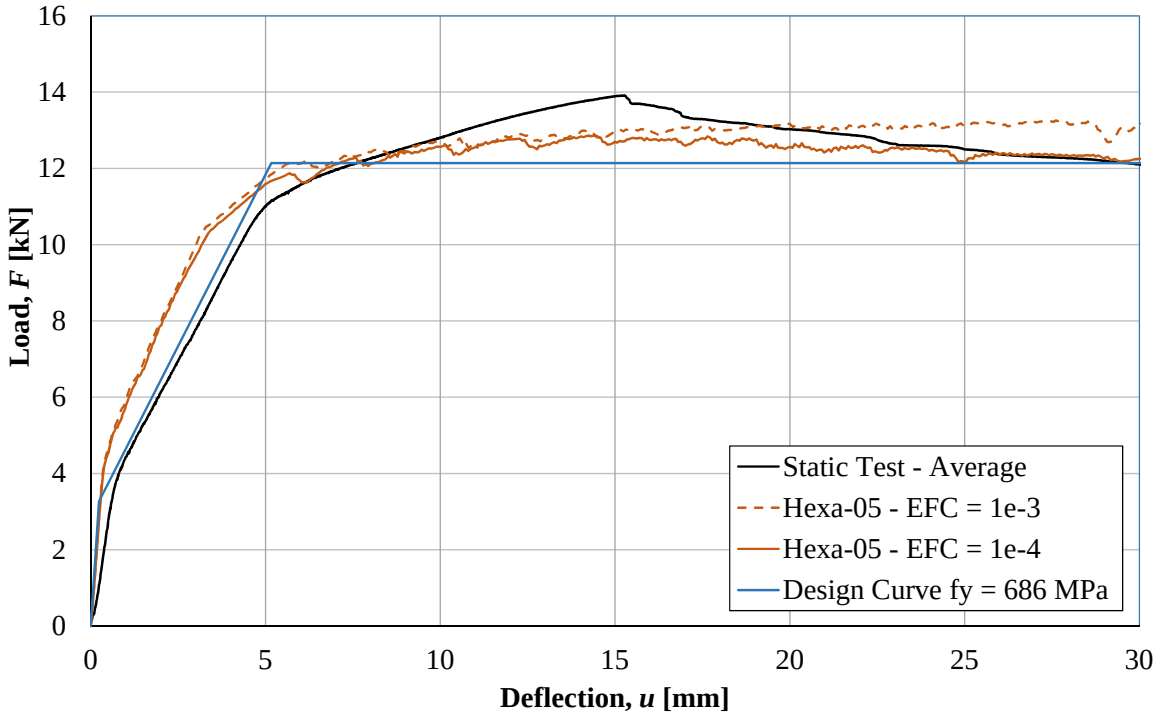

Figure 11.16 *Static analysis for model with 5 mm hexahedron elements for different values of softening parameters, EFC.*

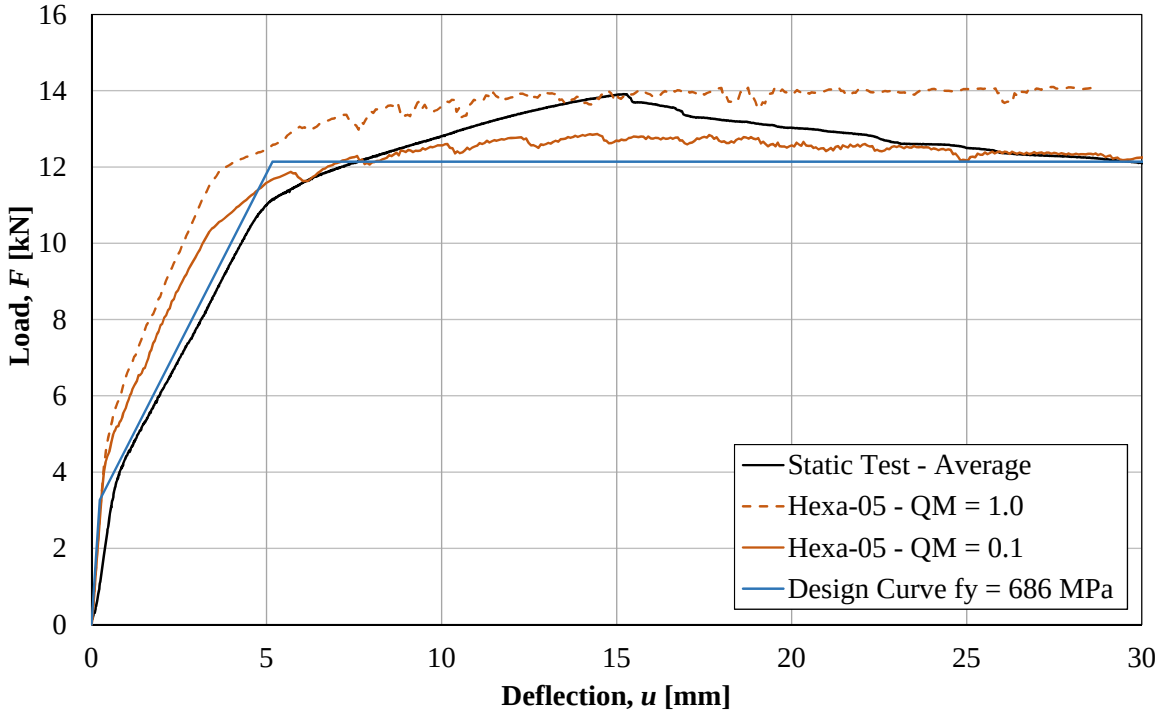

Figure 11.17 *Static analysis for model with 5 mm hexahedron elements for different values of hourglass coefficient, QM.*

11.7.3 Conclusions

Results from the static analyses show that the hexahedron base model with 5 mm elements is able to predict to a good extent the behavior of the beam specimens observed on the laboratory tests. The tetrahedron base model, on the other hand, overpredicts load-deflection relationships in terms of stiffness as well as load carrying capacity. This can be related to volumetric locking pertinent to tetrahedron elements, resulting in an overly stiff behavior of the structure. Such phenomenon is expected to influence the dynamic behavior during impact loading analysis, which was indeed observed in Section 11.4.4 and Section 11.6.6, and affects output parameters such as maximum deflection, time at which maximum deflection occurs, and frequency of oscillations.

Moreover, the distribution of tetrahedron elements and how the meshing procedure is performed was found to significantly influence the response of the model for the simulated static load. When following the meshing procedure used for the base model to create a 10 mm tetrahedron mesh, the structure failed in a shear failure. However, when disregarding the skin remesh option to generate a different 10 mm tetrahedron mesh, the predominant failure mode changed to flexural failure, with a significant increase of stiffness and load carrying capacity. These results point yet again to an attentive modelling procedure when using tetrahedron elements; since the element distribution seem to have a great effect on the response of the FE model.

Additionally, the results show that is possible to use a compressive softening parameter corresponding to $\varepsilon_{fc} = 1 \cdot 10^{-3}$ for both hexahedron and tetrahedron models. A small influence on the static analysis is noticed for hexahedron elements. On the other hand, the resultant maximum deflection in the dynamic response decreases with about 8 %, which is closer to the experimental results. This suggests that using the hexahedron model with $\varepsilon_{fc} = 1 \cdot 10^{-3}$ results in a more accurate representation of the real behavior of the structure.

Finally, it was concluded that increasing the value of the hourglass parameter results in a stiffer response as well as an increased load carrying capacity. This relationship was also observed in the sensitivity study for dynamic loading.

11.8 Parametric Studies

11.8.1 Overview

A parametric study was conducted for the hexahedron and tetrahedron base models. This was carried out in order to determine and assess how various loading scenarios would influence the dynamic response, and may serve as a basis for future experimental studies.

11.8.2 Position of the reinforcement bars

As mentioned in Section 9.6.2, the position of reinforcement bars were found to be displaced when the actual position was investigated by sawing the specimens. The mean adjusted position of the bars, shown in Figure 9.20, was introduced in the LS-DYNA models to test the effect on the response. Figure 11.18 shows how the midpoint deflection varies over time for different positions of the bars. It can be observed that the maximum deflection decreases for both models. This implies that the accuracy of the hexahedron model to predict the deflection improves slightly. On the other hand, since the deflection according to the tetrahedron model also decreases, the correspondence to experimental values diminishes.

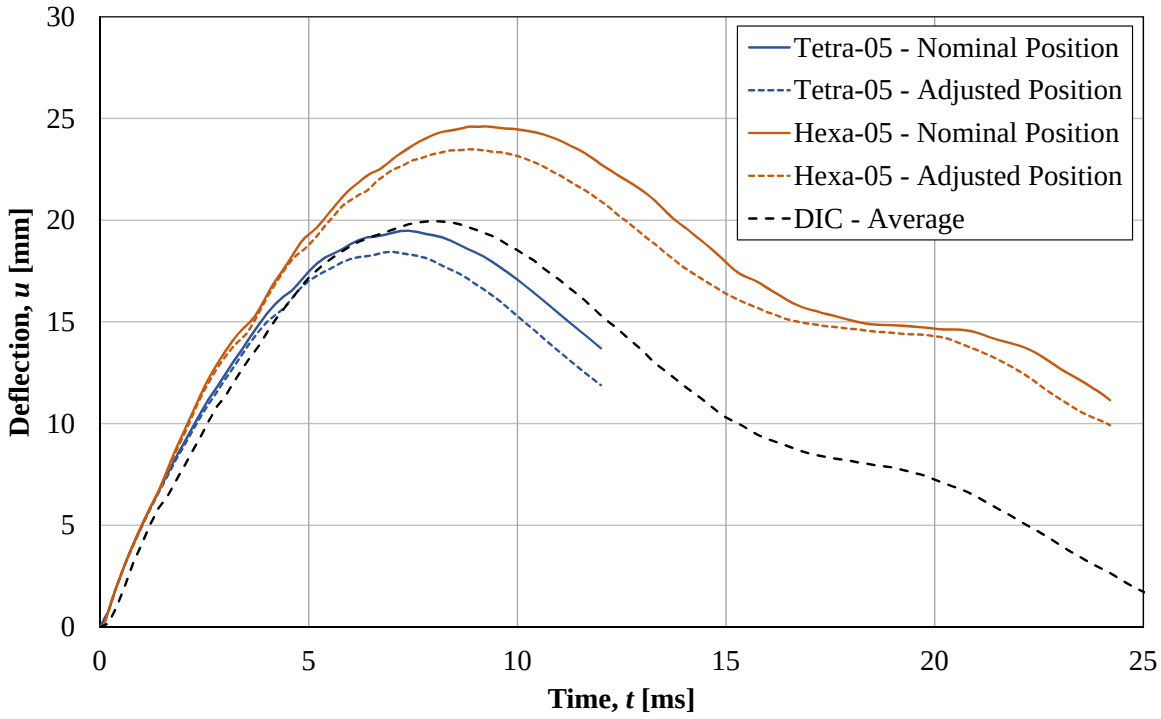

Figure 11.18 Midpoint deflection over time for models with 5 mm elements for different positions of the reinforcement bars.

The strain distribution for the hexahedron model (not shown) was not significantly affected by the change of position of the reinforcement. However, some differences were observed in the strain field obtained from the tetrahedron model, as seen in Table 11.20 for different times after impact. First, the magnitude and extension of the flexural cracks at the bottom edge at midspan are smaller for the model with adjusted position of the bars. Besides, a crack with a slight inclination which opens from the bottom edge can be observed close to the midspan region in the modified model. A similar crack can be noticed for the base model, but its magnitude and extension is much smaller. Finally, large values of strains can be noticed along the top bar close to the support region for the model with adjusted bar position from a time $t = 4$ ms. Even though such differences can be considered as minor, the results indicate that the tetrahedron model might be more sensitive to changes in the input parameters than the hexahedron model.

Table 11.20 Strain field for the 5 mm tetrahedron LS-DYNA model for different positions of the reinforcement bars.

Position	$t = 0.8$ ms	$t = 2.0$ ms
Nominal	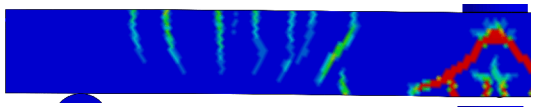	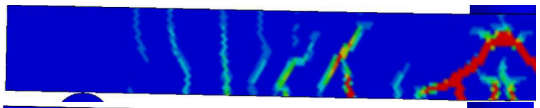
Adjusted	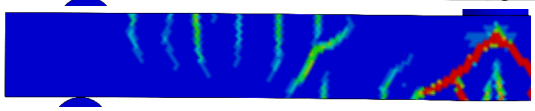	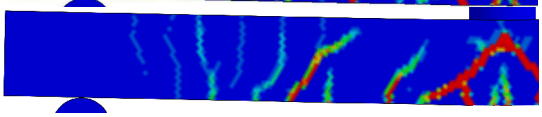
Position	**$t = 4.0$ ms**	**$t = 7.4$ ms**
Nominal	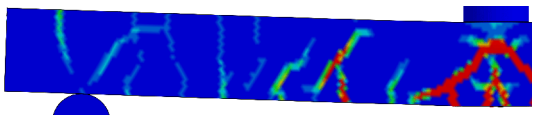	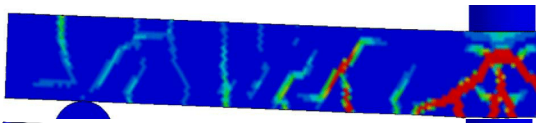
Adjusted	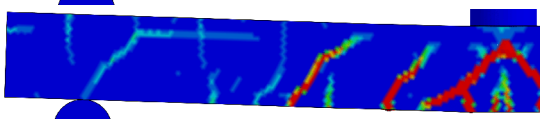	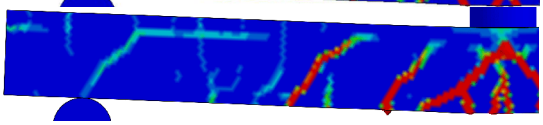
Principal strain [%]	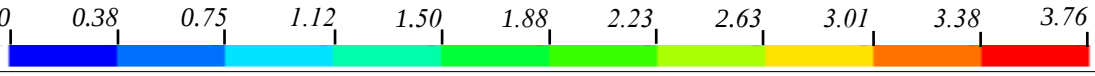	

11.8.3 Influence of drop-weight position

Another parametric study was conducted by dynamically loading the tetrahedron FE model asymmetrically with respect to a vertical axis crossing at midpoint of the reinforced concrete beam. The impact height was set to $h = 5.0$ m and the drop-weight was chosen to be displaced 50 mm towards the left support from the midpoint, see Figure 11.19. The study was performed with the purpose of gaining further insight of how the response might differ for a slightly asymmetric load case; an event which could happen unintentionally during experimental testing.

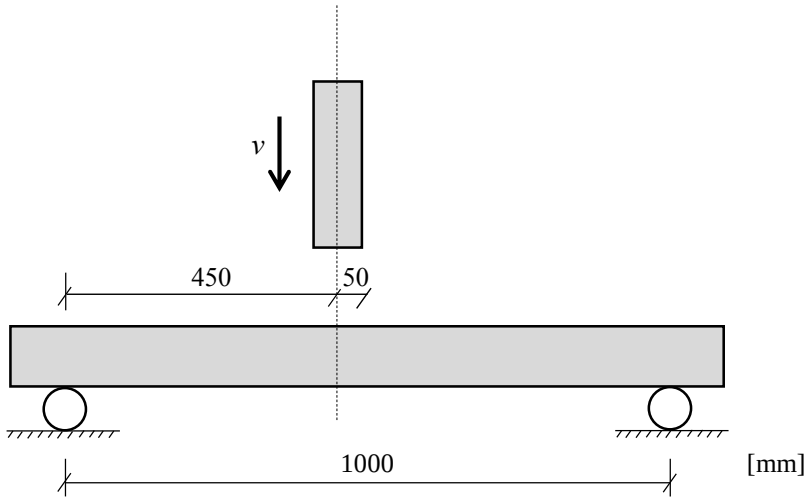

Figure 11.19 Loading condition for the asymmetric loading FE analysis.

The analysis was performed on the tetrahedron FE model since an accurate representation of the strain field due to the asymmetric loading was desired. Table 11.21 details the cracking distribution at given times and at the time of maximum deflection. A comparison with the base tetrahedron model for $h = 5.0$ m at the time of maximum deflection is also made.

Table 11.21 Strain field for the 5 mm tetrahedron LS-DYNA model for asymmetric impact loading.

Time	Strain field for impact loading
$t = 0.2$ ms	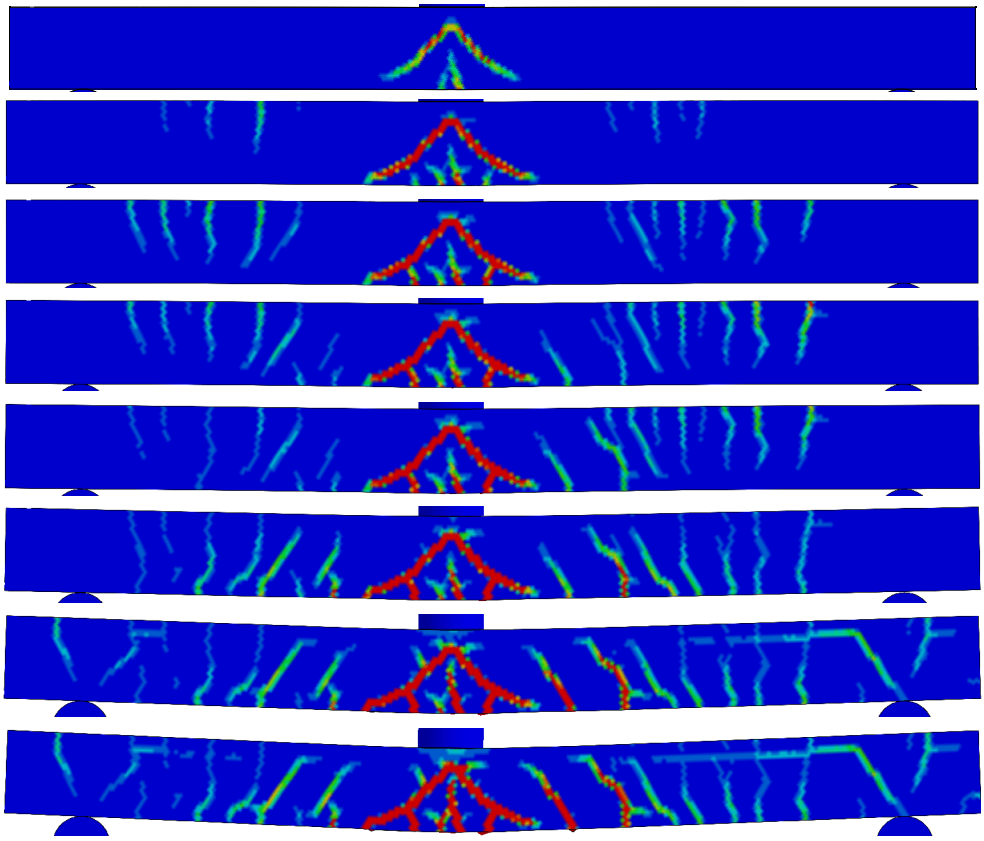
$t = 0.4$ ms	
$t = 0.6$ ms	
$t = 0.8$ ms	
$t = 1.0$ ms	
$t = 2.0$ ms	
$t = 4.0$ ms	
$t = 7.0$ ms [1]	
$t = 7.2$ m [2]	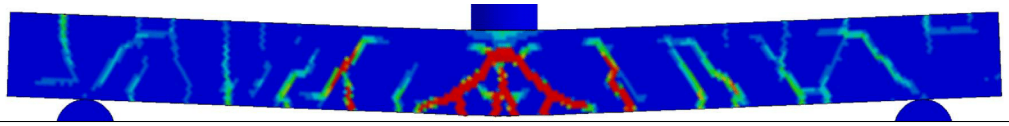
Principal Strain [%]	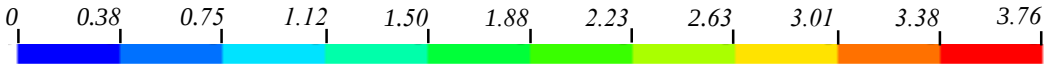

[1] Time at maximum deflection due to asymmetrical impact loading.
[2] Strain field at maximum deflection for the tetrahedron base FE model

From visual inspection it is noted that the overall strain field response is rather similar to what has been previously found for the base tetrahedron FE model. However, as a result of the asymmetric impact loading, the inclined flexural shear cracks appearing to the right of the impact location are more frequent. These cracks are also wider and thus propagate further than the cracks occurring to the left of the impacted area. The deformed shape over time is presented in Figure 11.20, where more distinct shifts in

curvature can be detected towards the right support, which reflect the cracks in Table 11.21.

Conclusively, an asymmetrical strain field response was indeed generated. While the cracked region underneath the impacted area appeared rather similar to the strain distribution of the base model, dissimilarities between the strain fields were found further away from the impacted area. For instance, indications of asymmetrical cracking over the supports can be noted for the asymmetrically loaded model, as more extensive cracking is observed over the right support. Besides, large values of strain along the top bar are noticed close to the right support.

Refer to Figure 11.20, where it can be noticed that the right end of the beam is lifted over the support to a higher extent than the left end. Furthermore, after the initial uplift, the left portion of the beam falls back on the support first, generating a reaction force of approximately 70 kN, see Figure 11.21. Eventually, the right end of the beam collides with its respective support as well, almost in conjunction with the second rebound of the left end. Presumably due to the higher uplift, a larger reaction force of 90 kN is registered on the right support. This occurrence could explain why more extended cracking is observed over the right support. Had the beam been loaded asymmetrically by a concentrated static load, a higher reaction force would have occurred at the support closest to the loading point. In that sense, the results of the asymmetrical impact loading differ from what would be expected from a static load case.

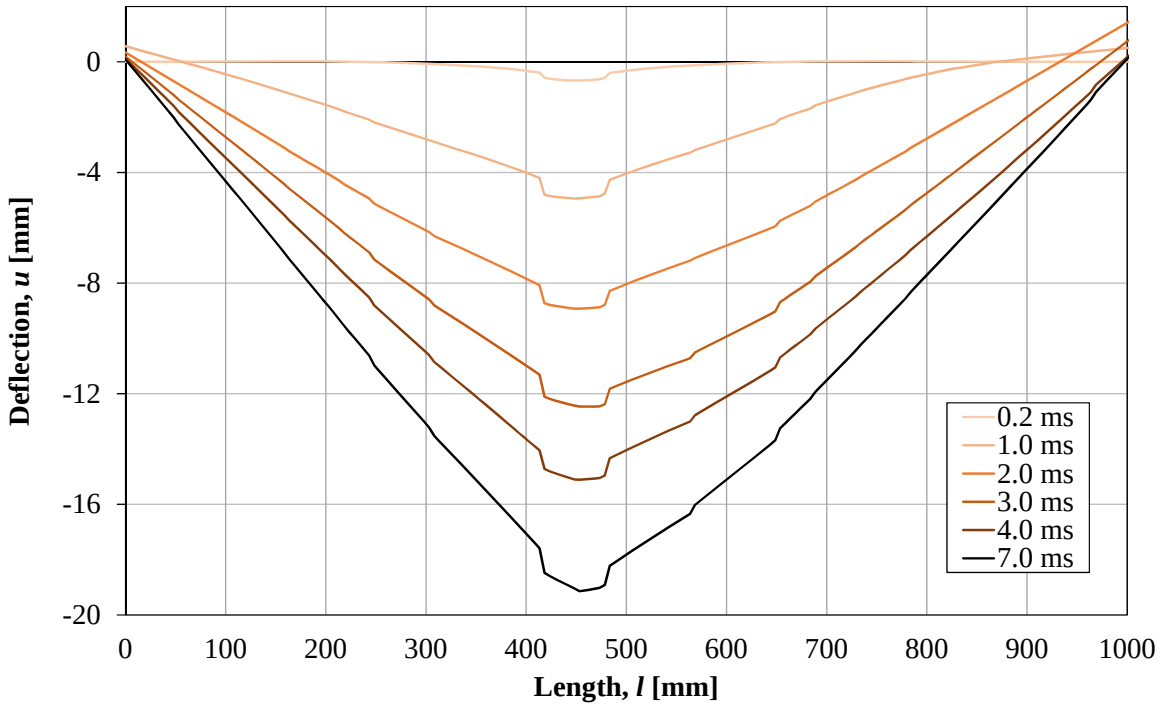

Figure 11.20 Deformed shape due to asymmetrical impact loading for the 5 mm tetrahedron LS-DYNA model. Maximum displacement occurred at $t = 7.0$ ms.

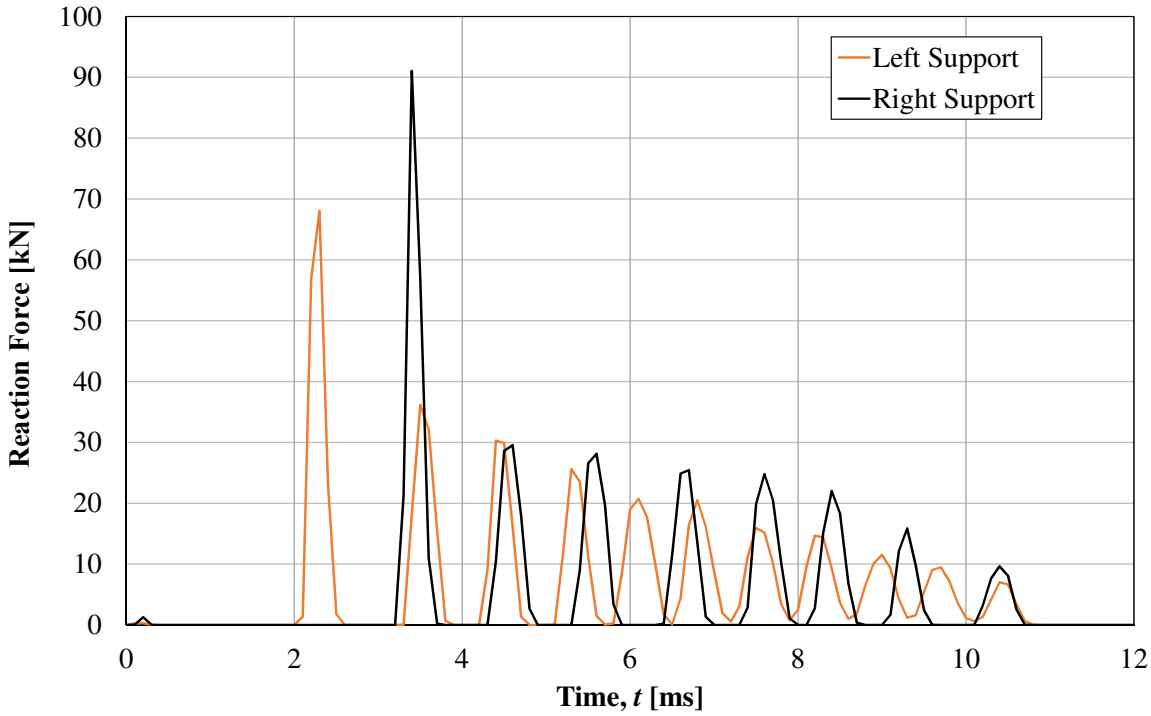

Figure 11.21 *Calculated reaction force for each support due to asymmetrical impact loading for the 5 mm tetrahedron LS-DYNA model. Note that the beam falls repeatedly on the left support with a higher frequency than on the right support.*

11.8.4 Influence of drop-height on the dynamic response

An investigation regarding effects of the drop-height on the dynamic response of the two base LS-DYNA models and the simplified 2DOF system was conducted. The additional studied drop-heights were set to $h = 1.0\,\text{m}$ and $h = 7.5\,\text{m}$. The results were compared to the response previously observed for drop-heights of $h = 2.5\,\text{m}$ and $h = 5.0\,\text{m}$. The deflection over time plots for the studied drop-heights are presented in Figure 11.22; relevant parameters gathered from the plots are shown in Figure 11.23.

Based on the dynamic response for various drop-heights, all three models seem to converge towards a similar response with decreasing drop-height, as can be seen in Figure 11.22. This is further strengthened by the key parameters gathered in Figure 11.23, where it can be seen that the differences between the three models decrease in terms of maximum deflection, u_{max}, and the time at which maximum deflection occurs, t_{max}, with lower drop-heights.

Further comparisons are made in terms of cracking distribution at maximum deflection for various drop-heights in Table 11.22. From visual inspection of the strain fields for the hexahedron model, no traces of inclined cracking if found in the impact region for $h = 1.0\,\text{m}$. However, with increased drop-height, the inclined crack region appears and is the most pronounced for the model with $h = 7.5\,\text{m}$, where the inclined cracks and the vertical cracks in fact merge to form a large cracked region at midspan. Furthermore, flexural cracks which form away from midspan for the model with $h = 1.0\,\text{m}$ are wider and more evenly spaced than in analyses conducted for larger drop-heights; such distribution resembles a typical crack distribution of a simply supported beam subjected to a static point load at midspan.

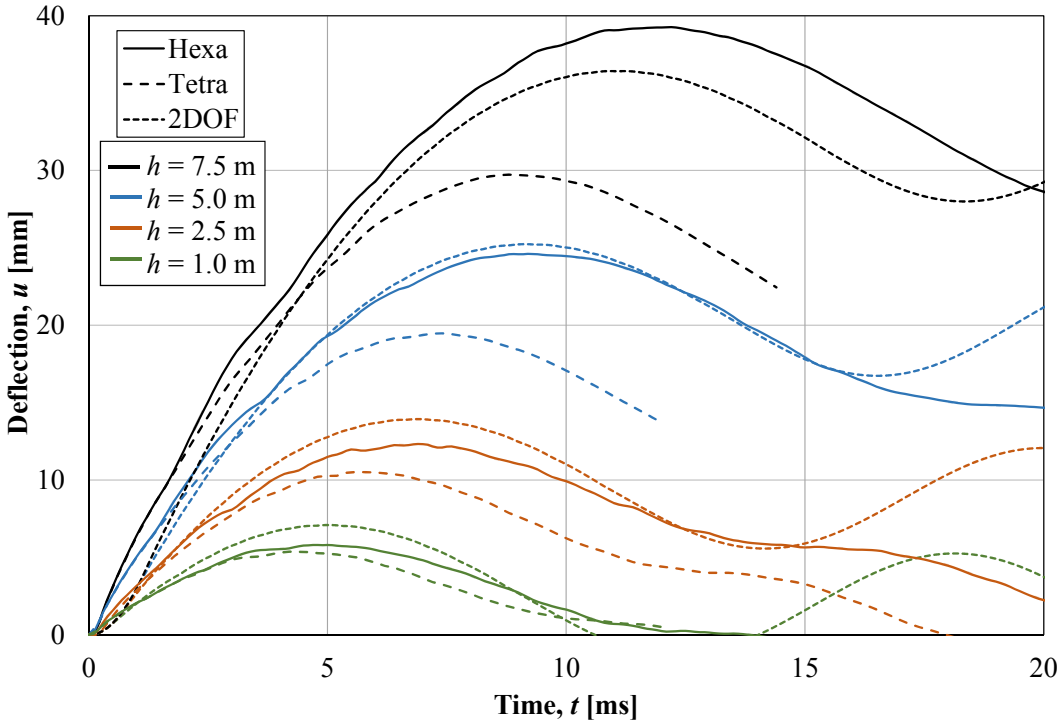

Figure 11.22 Deflection over time for different drop-heights for both LS-DYNA models and 2DOF system.

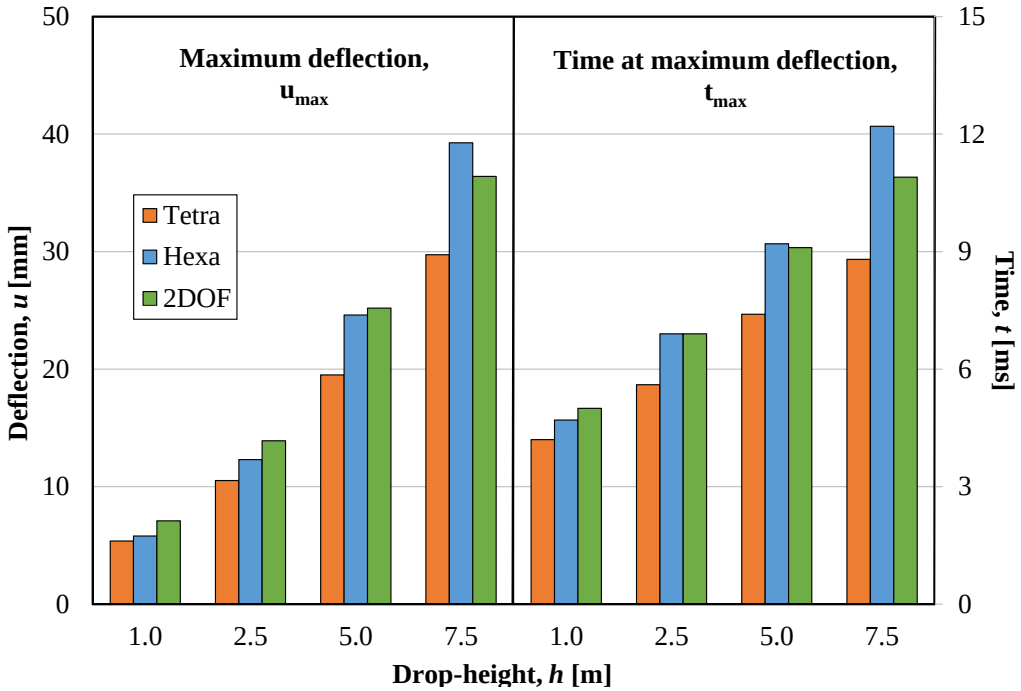

Figure 11.23 Maximum midpoint deflection, u_{max}, and time at maximum deflection, t_{max}, for different drop-heights for both LS-DYNA models and 2DOF system.

When studying the strain distribution of the tetrahedron model for different drop-heights, similar trends as observed for the hexahedron model are noticed. Namely, that the inclined cracks due to impact are less pronounced for lower drop-heights. Additionally, the inclined crack pattern underneath the impact region shows a relatively small propagation and a steeper inclination for $h = 1.0\,\text{m}$; these cracks extend further and become wider for increased drop-heights.

Table 11.22 Comparison of strain fields at t_{max} for the two LS-DYNA models for different drop-heights.

Drop-height	**Hexahedron FE model:** Strain field at time of maximum deflection
$h = 1.0\,\text{m}$ $h = 2.5\,\text{m}$ $h = 5.0\,\text{m}$ $h = 7.5\,\text{m}$	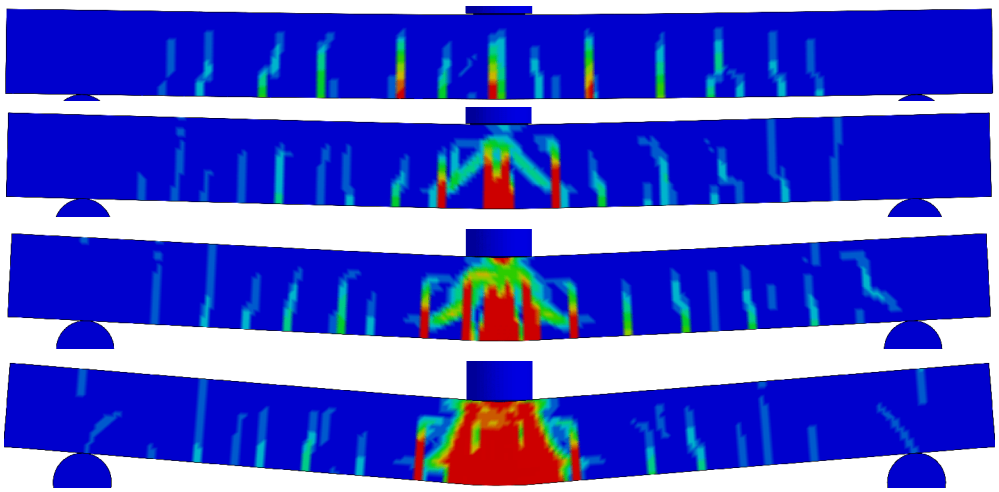
Principal Strain [%]	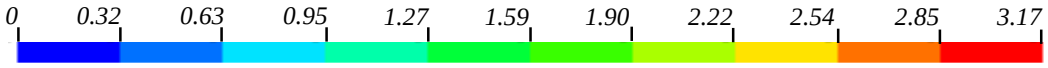
Drop-height	**Tetrahedron FE model:** Strain field at time of maximum deflection
$h = 1.0\,\text{m}$ $h = 2.5\,\text{m}$ $h = 5.0\,\text{m}$ $h = 7.5\,\text{m}$	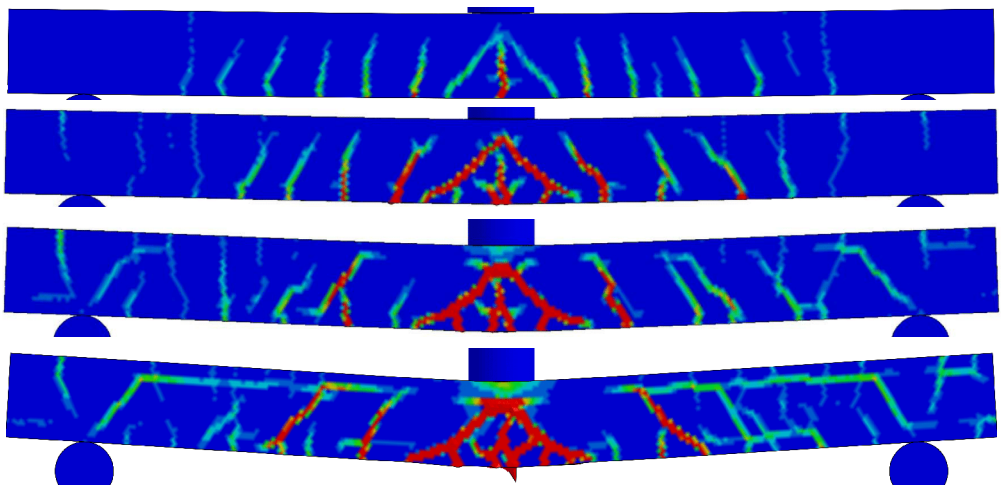
Principal Strain [%]	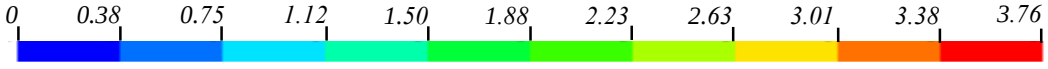

Furthermore, the strain distribution appears to be more symmetrical and cracks are more uniformly distributed along the span for lower drop-heights. In fact, cracks for $h = 1.0\,\text{m}$ propagate in almost a purely flexural form close to midspan, and exhibit a more noticeable inclination away from the midpoint as the effect of shear force becomes more relevant. Therefore, the crack pattern for $h = 1.0\,\text{m}$ strongly resembles that of a static loading case.

Moreover, with increasing drop-heights, cracking along the top reinforcement bars are found to be more pronounced. This behavior was also observed in the sensitivity study performed in Section 11.6.4 when using 2×2 IP beam elements to model the reinforcement bars, and could be an indication that some sort of anchorage failure is taking place or that there exist some compatibility issues when using material model CDPM2 in conjunction with tetrahedron elements for this type of analysis.

Conclusively, it can be stated that the capacity of the FE model to properly describe inclined cracking becomes less relevant with lower drop-heights. This can be due to the fact that the shear stresses generated by the impact event become relatively smaller with respect to bending stresses, as indicated by the strain distribution at t_{max} for $h = 1.0\,\text{m}$ for both models in Table 11.22. This could be an explanation as to why the two LS-DYNA models seem to converge towards a common response in terms of u_{max} and t_{max} with lower drop-heights, which can be noted in Figure 11.23.

11.8.5 Fracture energy

An investigation of the influence of the concrete fracture energy on the beam behavior was also carried out, as the parameter is intrinsically related to crack initiation and propagation. As described in Section 10.5, the fracture energy is used to determine the ultimate crack width, w_f, by using Equation (10.2). Then, the parameter w_f was changed accordingly to consider the variation of fracture energy. Apart from the base value determined experimentally, two other values of fracture energy were used on the FE models for a drop-height equal to $h = 5.0\,\text{m}$, namely: $0.5G_f = 66\,\text{N m/m}^2$ and $2.0G_f = 264\,\text{N m/m}^2$.

Figure 11.24 shows the deflection over time for both LS-DYNA models for different values of fracture energy. However, it was not possible to run an analysis with tetrahedron elements with $G_f = 66\,\text{N m/m}^2$ due to convergence issues.

It can be observed that the deflection increases for a reduced fracture energy. Conversely, the models with a larger fracture energy produce a smaller deflection. These results can be explained due to the fact that cracking occurs for higher stresses for larger values of fracture energy; and therefore the stiffness of the cross-section is larger.

Note that the ultimate crack width, w_f, for the models with tetrahedron elements is reduced by a factor of 0.56, as described in Section 10.5.1 according to recommendations in (Grassl, 2016). This implies that when using $G_f = 264\,\text{N m/m}^2$ for tetrahedron model, a similar response to a case when w_f is not reduced by a factor of 0.56 is obtained. The results show that using full fracture energy with tetrahedron elements yields an underprediction of the deflection and an overly stiff response.

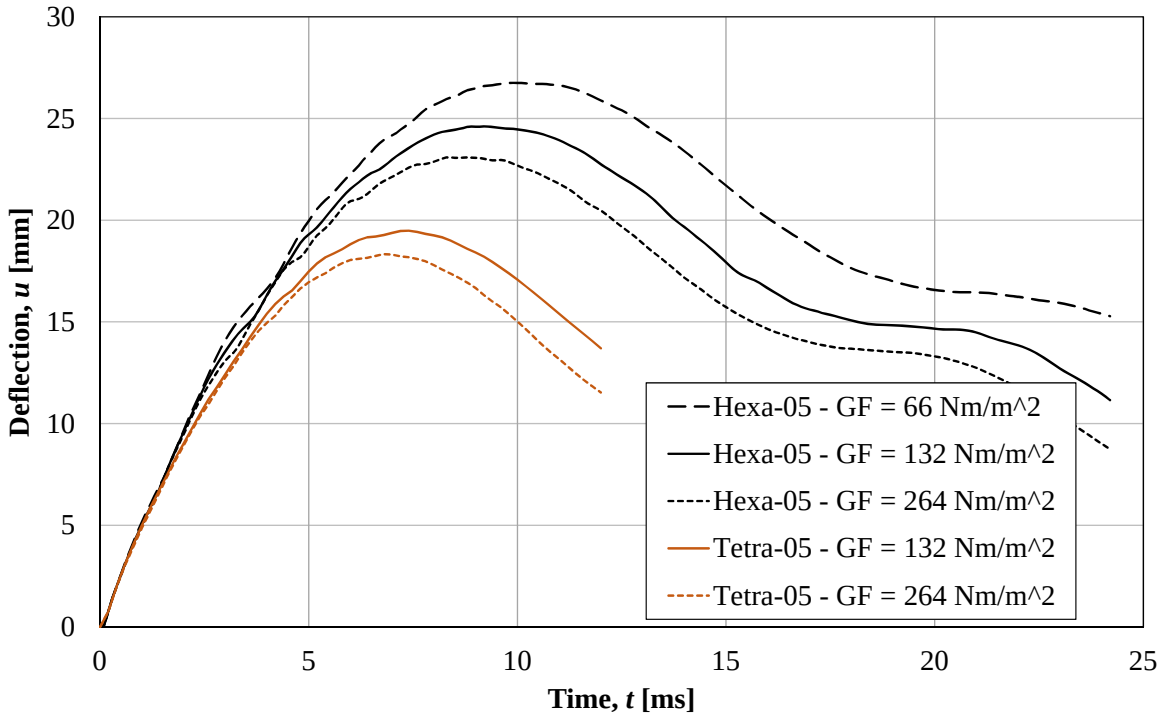

Figure 11.24 Deflection over time for both LS-DYNA models with drop-height h = 5.0 m for different values of fracture energy.

12 Discussion

12.1 General

A summary and discussion of relevant observations gathered during the development of the thesis is presented in this chapter. Initially, the observations from the experiments are treated. Subsequently, the results from the non-linear finite element analyses are discussed.

12.2 Experimental Results

12.2.1 Digital image correlation

Most experimental results were processed through digital image correlation (DIC) of photographs taken with a high-speed camera during the impact tests, and with a set of normal-speed cameras during the static tests. This tool has proven to be very useful throughout the work of this thesis, as it allowed to determine several resulting parameters from the experiments in order to gain further insight of the response of reinforced concrete structures subjected to different loading conditions.

There were some limitations regarding DIC as implemented in this thesis work, most of which were related to the equipment used. It was decided to record the entire length of the specimens, as opposed to the setup adopted in previous test-series in (Lovén and Svavarsdóttir, 2016), where only half the length was recorded. The decision of recording the entire length maintaining the same level of resolution as in (Lovén and Svavarsdóttir, 2016) resulted in a loss of detail regarding the location and size of individual cracks, particularly so for minor cracks, which may be misinterpreted as random background noise. Therefore, the DIC analysis of the impact event regarding cracking distribution was limited to identifying the presence of cracked regions instead of individual cracks.

However, interesting observations could still be made by recording the whole beam. For example, signs of asymmetric response could be captured in the strain field on the surface of some specimens through DIC post-processing. Such phenomenon might have been overlooked if only half of the beam had been recorded.

If determining the cracking distribution through DIC analysis is a relevant objective of a certain research, it is important to ensure that the experiments are recorded with satisfactory resolution. For the conditions of the equipment described in this project, recording only half of the beam with the same experimental setup is recommended. An alternative approach consists in using a similar camera on each half of the beam. Otherwise, when the deflection and velocity of the beam and the drop-weight are of interest, a lower level of resolution is acceptable.

12.2.2 Impact loading and static tests

The structural response of the beams during impact loading was noticed to be markedly different to the response usually observed on a concrete beam subjected to a static load. An important difference in the cracking distribution of concrete beams during impact loading compared to a static load case corresponds to the occurrence of inclined cracking in the impact area, which becomes more apparent for a higher impact energy. Moreover, it was noticed that the cracks generated during impact loading greatly influenced the cracking pattern of subsequent static tests. Only a minimum amount of new cracks

developed as static loading progressed on previously impact-damaged specimens; instead, previously initiated cracks due to impact loading were reopened during the static tests. As a result, as the presence of inclined cracking was more pronounced on beams subjected to a stronger impact, it was observed that the cracking distribution present in specimens of Series-2 (drop-height $h = 5.0\,\text{m}$) during static tests differed to a greater extent to that of the undamaged specimens than beams of Series-1 (drop-height $h = 2.5\,\text{m}$).

The static load-deflection relationship of specimens of Series-1 was observed to conform to the response of the undamaged beams; consequently, the beams of Series-1 exhibited similar characteristics in terms of stiffness, load capacity, as well as plastic rotational capacity, to those of the undamaged beams. Hence, it was concluded that the plastic rotational capacity of the damaged beams of Series-1 could be estimated by simply subtracting the permanent plastic rotation due to impact from the total rotational capacity of undamaged specimens.

On the other hand, it was found that the response during static loading of the beams of Series-2 differed significantly to that of Series-1 and Series-3, in terms of load capacity, stiffness and also overall behavior. As described in Section 9.4.2.2, it was found that the residual rotational capacity of Series-2 was higher than that of undamaged specimens for all load levels. This observation was attributed to the difference in cracking pattern. However, as explained in Section 9.4.3, comparisons of rotational capacity between testing series as performed in this project might not be fair since the calculated values of the ratio $W_{i,x\%}/\theta_{pl,x\%}$ for specimens of Series-2 indicate that the values of rotational capacity do not relate proportionally to the internal work.

A different procedure could be followed for a more fair assessment. Instead of calculating the rotational capacity of Series-2 for different load levels based on the load capacity of each individual beam, an average value of maximum load for undamaged specimens could be adopted as a basis for calculations of load levels. In that sense, $\theta_{pl,100\%}$ for Series-2 would correspond to a level lower than 100%, since the load capacity of specimens of series-2 was observed to decrease after impact loading. However, the procedure to determine the rotational capacity adopted in this project still holds true for specimens of Series-1, as the load capacity of such specimens did not decrease due to impact loading, and their load-deformation relationship conforms to that of the undamaged beams.

Furthermore, a tendency to develop shear failure was observed on some beams of Series-2. For instance, B-13 failed unexpectedly in a shear mechanism during static testing after impact loading. Additionally, signs of major shear cracking at the web were noticed in B-15 during residual static testing; however, the shear crack never became critical to the same extent as it did in B-13. These observations indicate that with a higher drop-height, members which are designed to fail in flexure under static load may instead exhibit a brittle shear failure mechanism when loaded dynamically or when subjected to a subsequent static load after impact loading.

12.2.3 Predictions according to hand calculations and 2DOF model

Predictions of static load carrying capacity resulted in underestimation compared to experimental values of the undamaged beams of Series-3. Attempts to improve the predictions were performed by considering the real position of the reinforcement bars (measured in the laboratory by sawing the beams after the static loading tests) and by assuming that the yield strength of the reinforcing steel is equal to the ultimate strength; however, underestimation of load carrying capacity up to 9 % was still found. Therefore, there

might exist some underlying effects which have not been accounted for in the calculations, or perhaps the procedure used may be too conservative in this regard.

The maximum deflection during impact load according to the 2DOF model was overestimated, which may be attributed to the underestimation of load carrying capacity and the omission of strain rate effects from the model. By including strain effects in terms of amplified values of stiffness and strength of the materials, an increase in correspondence between predictions by the 2DOF model and the experimental results could be obtained.

Additionally, it has been observed that the entire mass of the beam is not partaking in the initial stage of the dynamic response. To account for such effects, a variation over time of the beam mass could be adopted, similarly to what has been depicted in Figure 9.22 or to the work made in (Asplund and Steckmest, 2014), which may further improve the correspondence of the 2DOF predictions to experimental values.

12.3 Finite Element Analysis Results

12.3.1 Hexahedron FE model

The base 5 mm hexahedron FE model overpredicted the deflection over time for impact cases compared to experimental results, as much as 20 % for a drop-height $h = 5.0$ m. Furthermore, a crack propagation bias was noticed in that the cracks propagate following a vertical path, which could be attributed to the inherent element distribution of the hexahedron mesh. Thus, the FE analysis with hexahedron elements displayed a limitation at representing inclined cracking due to impact and static loads.

However, the shape of the deflection-time relationship was in phase with the experimental results, indicating that the general behavior of the structure was fairly well described by the hexahedron model. This was further emphasized by the static analyses conducted in Section 11.7, which showed good correspondence with average load-deflection relationships gathered from experimental results.

Sensitivity studies showed that the hourglass coefficient, QM, heavily influenced the overall response of the hexahedron model. Higher correspondence to experimental results in terms of maximum deflection was obtained by increasing the factor QM, and vice versa; although the increase of QM affected negatively the description of cracking distribution. These findings show that the effects of the hourglass control should be investigated carefully; however, they also prove that QM could be use for calibration of the hexahedron FE model, although the default value was found to be satisfactory.

A sensitivity analysis was also performed on the parameter ε_{fc}, which controls compressive damage softening of concrete in the material model CDPM2. When increasing from the default ($\varepsilon_{fc} = 1 \cdot 10^{-4}$) to $\varepsilon_{fc} = 1 \cdot 10^{-3}$, a higher correspondence to experimental results in terms of deflection over time was found. This change had no observable effect on the cracking pattern described by the model, and would seemingly be an appropriate value to adopt for this type of analyses.

Parametric studies conducted in Section 11.8.2 regarding the measure real position of the reinforcement bars resulted, in accordance to expectations, in a higher correspondence of the deflection-time relationship to experimental results. If an analysis were to be performed by considering the adjusted position of the reinforcement bars in conjunction with the adjusted value of $\varepsilon_{fc} = 1 \cdot 10^{-3}$, an improvement in terms of maximum deflection would most certainly be obtained; while hopefully, the overall shape of deflection-time relationship would still be in phase with experimental results. Perhaps, if needed, additional

adjustment could be performed by slightly modifying the hourglass control parameter, QM.

12.3.2 Tetrahedron FE model

At a first glance, the results of the analyses with the 5 mm tetrahedron model showed very satisfactory results in terms of maximum deflection compared to experimental results, and in terms of cracking pattern compared to the DIC results presented in (Lovén and Svavarsdóttir, 2016). However, as remarked in Sections 11.4.3 and 11.6.4, an overly stiff response was noticed for the model with tetrahedron elements. This issue was further highlighted by the static analyses performed in Section 11.7, where the base tetrahedron model significantly overpredicted the load carrying capacity and stiffness of the beam. Possible explanations have been attributed to volumetric locking inherent to tetrahedron solids. Therefore, the high correspondence in terms of maximum deflection is most likely a consequence of the stiffer behavior pertinent to the tetrahedron elements.

Further issues related to tetrahedron models include the fact that the meshing technique adopted, and more specifically the element distribution within the mesh of the FE model, has a significant influence on the results of the analyses conducted. As presented in Section 11.7, when adopting the skin remeshing procedure used for the base models, a shear failure mechanism was noticed in the static analysis of the base 10 mm tetrahedron model. Therefore, to investigate the influence of mesh distribution, an additional analysis was conducted where the optional remeshing procedure was omitted. Consequently, the failure mechanism of the loaded beam shifted from a shear failure to a flexural failure. However, a great overestimation in terms of load carrying capacity was also observed as a consequence of the different element distribution. It is apparent that the element distribution has a profound influence on the outcome of the results.

Additionally, models with tetrahedron elements proved to be more sensitive to changes of input parameters such as the compressive softening parameter, ε_{fc}, and the type of element used to model the reinforcement bars. Conclusively, findings from the conducted FE analyses using tetrahedron elements show that the modelling procedure and its influences should be studied more thoroughly. However, as shown in the parametric study in Section 11.8.2 when investigating the influence of drop-weight position, the ability of the tetrahedron model to accurately represent cracking pattern could be of great use. If a more reliable response in terms of deflection over time relationship could be simulated using tetrahedron elements, it may prove to be a powerful tool to predict the outcome of various impact scenarios.

13 Final Remarks

13.1 General Description

The general aim of this thesis was to deepen the understanding of the behavior of impact loaded simply supported concrete beams, where emphasis in studying plastic rotational capacity and how impact loading influences the rotational capacity of reinforced concrete structures was made. The work was divided into three main parts; namely, literature survey, experiments, and non-linear finite element analysis.

Two different loading conditions were considered during the experiments. Initially, some beams were subjected to drop-weight impact loading from two different heights. Subsequently, the impact-damaged beams were tested for deformation-controlled static loading. A group of undamaged beams were also tested for static loading. All experiments were recorded using a high-speed camera during the impact tests, and two normal-speed cameras during the static tests. The information recorded was post-processed using digital image correlation (DIC).

Concerning the FE analysis, two different solid elements were adopted to model the concrete beam; namely, hexahedron elements and tetrahedron elements. Both element types were implemented with one integration point. Based on a convergence study, it was decided to use an element size of 5 mm to construct the base models for both types of elements. Due to the geometry of the tetrahedron elements, the resulting amount of elements for this element type is much larger than the number of elements for a corresponding hexahedron model.

Preliminary predictions regarding load capacity, rotational capacity, and deflection of the beams during both impact and static loading could be validated based on the experimental results. Furthermore, results from FE analyses could also be compared with experimental results in order to assess the reliability of the FE models and how various input parameters could influence the behavior predicted by the FE models.

13.2 Conclusions

During the development of the thesis it was observed that the digital image correlation (DIC) analysis is a convenient tool for the study of the impact behavior of concrete beams. However, a good level of resolution is needed if the cracking pattern during the impact event is of interest. On the other hand, if information regarding deflection and velocity is needed, a lower resolution is acceptable.

Results gathered from impact tests showed that both the deformed shape and cracking distribution of the concrete beams a short time after impact differ considerably to those commonly observed in static loading tests. Significant differences in cracking pattern include temporary flexural cracking at the top edge of the beams and inclined cracking underneath the impact region.

During subsequent static experiments after impact loading, it was noted that the development of cracking depends to great extent on the cracks generated during the impact event. Furthermore, beams subjected to a weak impact exhibited a similar response in terms of load-deformation relationship to that of undamaged beams; therefore, the plastic rotation and load capacity for both cases were similar. Contrarily, the beams subjected to a strong impact showed a reduced load capacity and an increased rotational capacity

compared to undamaged beams. The increase in rotational capacity is likely a consequence of extensive cracking in the impacted region, which could allow for a larger amount of reinforcement to yield at ultimate limit state and beyond.

Regarding the non-linear FE analysis, it was observed that a rather good description of the impact behavior is achieved with both the hexahedron and tetrahedron model. However, the hexahedron model tended to overpredict the deflection of the beam and was shown to have difficulties at describing inclined cracking due to the rectangular direction of the mesh elements. On the other hand, the tetrahedron model predicted values of deflection closer to the experimental results, although an overstiff response was observed for this model. Additionally, the tetrahedron model could describe the cracking distribution, including secondary cracks, to a better extent than the hexahedron model. However, it was found that the tetrahedron model is significantly sensitive to changes in input parameters such as mesh size, element distribution on the mesh, and the element type used to model the reinforcement bars. In general terms, it can be concluded that the FE models based on both element types produced satisfactory results with respect to experimental results.

13.3 Future Studies

The experiments in this thesis work comprised impact loading tests followed by static testing of the impact-damaged beams. Future studies could assess the dynamic (and subsequent static) response of beams subjected to a second or more consecutive impact loads.

During the parametric studies presented in this document, the influence of variations in the loading and geometrical conditions on the dynamic response of the concrete beam was briefly studied using non-linear finite element analysis. It would be of interest to perform a similar parametric study through experiments in a laboratory. Important factors to be tested could include: drop-heights different to 2.5 or 5.0 m; longer span length or larger section height, different amount of reinforcement, inclusion of transverse reinforcement, and different location of the impact.

Regarding the post-processing of the experimental results, a relevant suggestion for future work is the implementation of a different procedure for the calculation of the experimental rotational capacity of impact-damaged beams. For instance, when the static load-deformation relationship of the impact-damaged beams meet the undamaged load-deformation curve after peak load; the rotational capacity could be determined based on the load capacity of undamaged beams, as opposed to the maximum load capacity of each damaged beam.

As shown in this project, a 2DOF model could be a powerful tool to describe the response of impact loaded concrete beams. However, some improvements could still be introduced to the model in future studies, including consideration of strain rate effects on the material and the variation of the mass transformation factor during the first milliseconds after impact.

Concerning the finite element modelling of the experiments, an interesting study would be the implementation of a static analysis after running the impact-loading analysis, so that the response of impact-damaged beams during static loading could be assessed further through finite element analysis. This type of analysis could facilitate the study and provide with further insight regarding the cracking distribution and the residual rotational capacity of damaged beams.

Furthermore, as described in this thesis, a model with tetrahedron elements is more suitable for describing cracking distribution than a model with hexahedron elements. However, the tetrahedron elements produce a stiffer response than what was observed in the experimental results as a consequence of volumetric locking. Additionally, the tetrahedron model was more sensitive to changes in the input data. Further studies regarding this type of element and its proper implementation is therefore deemed to be necessary. A suggestion for further investigation could be the use of tetrahedron elements with more integration points. A well implemented model could be of great use as it could, among others, accurately represent cracking pattern as well as deflection-time relationships.

Moreover, it should be stressed that both finite element models were created by disregarding strain rate effects and assuming full interaction between reinforcement bars and the surrounding concrete material. Therefore, strain rate effects and bond-slip relationship could be incorporated in the models in future studies with finite element analyses.

Finally, the response of the beams during impact loading, processed through DIC analysis, showed a certain degree of asymmetry regarding cracking distribution and deformation. This occurrence could indicate that the local properties of the material might vary from one section to the other. This phenomenon could be described in a finite element analysis in future studies if randomized material properties are assigned to the finite elements which form the concrete beam.

References

Adhikary, S. D., B. Li, and K. Fujikake (2012). “Dynamic Behavior of Reinforced Concrete Beams under Varying Rates of Concentrated Loading”. In: *International Journal of Impact Engineering* 47 (cit. on p. 63).

– (2015). “Residual Resistance of Impact-damaged Reinforced Concrete Beams”. In: *International Journal of Impact Engineering* 67 (cit. on pp. 63, 64).

Andersson, J. and J. Antonsson (2015). “Design with Regard to Collision Impact”. MSc Thesis. Chalmers University of Technology (cit. on p. 88).

Asplund, E. and D. Steckmest (2014). “Design with Regard to Collision Impact”. MSc Thesis. Chalmers University of Technology (cit. on p. 187).

Biggs, J. (1964). *Introduction to Structural Dynamics*. McGraw-Hill (cit. on pp. 25, 26).

Bosco, C. and P. Debernardi (1992). *Experimental Investigation on The Ultimate Rotational Capacity of RC Beams*. University of Turin (cit. on pp. 56, 60, 61).

Burström (2001). *Byggnadsmaterial (Building Materials)*. Studentlitteratur (cit. on p. 9).

Carpinteri, A., M. Corrado, G. Mancini, and M. Paggi (2009). “Size-Scale effects on Plastic Rotational Capacity of Reinforced Concrete Beams”. In: *ACI Structural Journal* 106 (cit. on p. 60).

CEB-FIP (1991). *CEB-FIP Model Code 1990*. Comité Euro-International du Béton (cit. on pp. 37, 40).

– (1998). *CEB Bulletin No. 242: Ductility of Reinforced Concrete Structures: Synthesis Report and Individual Contributions*. Comité Euro-International du Béton (cit. on pp. 37, 39, 55–59).

CEN (2004). *EN 1992-1-1 Eurocode 2: Design of concrete structures - Part 1-1: General rules and rules for buildings*. European Committee for Standardization (cit. on pp. 7, 8, 10, 11, 43, 45, 58, 128).

– (2009a). *EN 12390-3: Testing Hardened Concrete - Part 3: Compressive Strength of Test Specimens*. European Committee for Standardization (cit. on pp. 11, 71).

– (2009b). *EN 12390-6: Testing Hardened Concrete - Part 6: Tensile Splitting of Test Specimens*. European Committee for Standardization (cit. on pp. 12, 71).

Corley, W. (1966). “Rotational Capacity of Reinforced Concrete Beams”. In: *Journal of the Structural Division. ASCE* 92 (cit. on pp. 51, 52).

– (1967). “Discussion of "Rotational Capacity of Reinforced Concrete Beams" by Alan H. Mattock”. In: *Journal of the Structural Division. ASCE* 93 (cit. on p. 52).

Costovos, D., N. Stathopoulos, and C. Zeris (2010). “Behavior of RC Beams Subjected to High Rates of Concentrated Loading”. In: *Trends and Future Perspectives* 134 (cit. on p. 62).

Craig, R. and A. Kurdila (2006). *Fundamentals of Structural Dynamics*. Second. New York: John Wiley and Sons (cit. on p. 23).

Domone and Illston (2010). *Construction Materials – Their nature and behaviour*. Spon Press (cit. on p. 11).

Engström, B. (2001). *Design and Analysis of Reinforced Concrete Structures*. Chalmers University of Technology (cit. on pp. 7, 9).

Engström, B. (2015). *Design and Analysis of Continuous Beams and Columns*. Chalmers University of Technology (cit. on p. 13).

Erhart, T. ((2011). *Review of Solid Element Formulations in LS-DYNA: Properties, Limits, Advantages, Disadvantages*. URL: `https://www.dynamore.de/de/download/papers/forum11` (visited on 07/15/2017) (cit. on p. 134).

Fransson, H. (1997). *Rotation Capacity of Reinforced High Strength Concrete Beams*. Royal Institute of Technology (cit. on pp. 57, 60).

Fujikake, K., T. Senga, N. Ueda, T. Ohno, and M. Katagiri (2006). "Study on Impact Response of Reactive Powder Concrete Beam and its Analytical Model". In: *Journal of Advanced Concrete Technology* 4 (cit. on pp. 65, 66).

Grassl, P. (2016). *User manual for MAT_CDPM (MAT_273) in LS-DYNA*. URL: `http://petergrassl.com/Research/DamagePlasticity/CDPMLSDYNA/index.html` (visited on 03/31/2017) (cit. on pp. 136, 183).

Grassl, P. and M. Jirasek (2006). "Damage-plastic model for concrete failure". In: *International Journal of Solids and Structures* 43 (cit. on p. 135).

Grassl, P., D. Xenos, U. Nyström, R. Rempling, and K. Gylltoft (2013). "CDPM2: A damage-plasticity approach to modelling the failure of concrete". In: *International Journal of Solids and Structures* 50 (cit. on pp. 3, 135).

Johansson, M. (2000). "Structural Behaviour in Concrete Frame Corners of Civil Defence Shelters". PhD thesis. Chalmers University of Technology (cit. on pp. 22, 38).

Johansson, M. and L. Laine (2012). *Bebyggelsens motståndsförmåga mot extrem dynamisk belastning, Del 3 – Kapacitet hos byggnader*. Swedish Civil Contingencies Agency (cit. on pp. 13, 25–27, 32, 33, 43, 46, 48, 49).

Kheyroddin, A. and H. Naderpour (2007). "Plastic Hinge Rotation Capacity of Reinforced Concrete Beams". In: *International Journal of Civil Engineering* 5 (cit. on pp. 61, 62).

Ko, M., S. Kim, and J. Kim (2001). "Experimental Study on the Plastic Rotation Capacity of Reinforced High Strength Concrete Beams". In: *Materials and Structures* 34 (cit. on p. 61).

Langer, P. and R. Eligehausen (1987). *Rotation Capacity of Plastic Hinges and Allowable Degree of Moment Redistribution*. Universität Stuttgart (cit. on pp. 56, 59).

Latte, S. (1999). "Plastic Rotation Capacity of Reinforced Concrete Beams". MSc Thesis. Chalmers University of Technology (cit. on pp. 38, 43, 55, 58, 85).

Löfgren, I., J. F. Olesen, and M. Flansbjer (1981). *Application of WST-method for fracture testing of fibre-reinforced concrete*. Chalmers University of Technology (cit. on p. 71).

Lopez, S. and L. Bernardo (2003). "Plastic Rotation Capacity of High-strength Concrete Beams". In: *Materials and Structures* 36 (cit. on p. 58).

Lovén, J. and E. Svavarsdóttir (2016). "Concrete Beams Subjected to Drop Weight Impact". MSc Thesis. Chalmers University of Technology (cit. on pp. 1, 2, 9, 28, 29, 31, 74–76, 87, 96, 97, 101, 102, 134, 145, 155–159, 185, 188).

LSTC (2006). *LS-DYNA Theory Manual*. Livermore Software Technology Corporation (cit. on pp. 131, 134).

– (2015). *LS-DYNA Keyword User's Manual - Volume I*. Livermore Software Technology Corporation (cit. on pp. 131, 138).

Magnusson, J. (2007). *Structural Concrete Elements Subjected to Air Blast Loading*. Royal Institute of Technology (KTH) (cit. on pp. 57, 65–67).

Martin and Purkiss (2006). *Concrete Design to EN 1992*. Butterworth-Heinemann (cit. on p. 9).

Mattock, A. H. (1965). "Rotational Capacity of Hinging Regions in Reinforced Concrete Beams". In: *Special Publication. American Concrete Institute* 12 (cit. on p. 51).

Miyamoto, A., M. King, and M. Fuji (2008). "Non-Linear Dynamic Analysis and Design Concepts for RC Beams under Impulsive Loads". In: *Journal of Structural Engineering* 22 (cit. on pp. 62, 63).

Öberg, S. (1980). *Gränslastmetodens Användning för Armerade Betongbalkar på Oeftergivliga Stöd (Application of Lower Bound and Upper Bound Methods of Reinforced Concrete Beams on Rigid Supports)*. Chalmers Tekniska Högskola. Institutionen för Konstruktionsteknik Betongbyggnad (cit. on p. 46).

Park and Paulay (1975). *Reinforced Concrete Structures*. University of Canterbury (cit. on pp. 36, 37, 39, 41, 53).

Plem, E. (1981). *The Rotation Capacity of Plastic Hinges in Reinforced Concrete Beams*. Lund University (cit. on p. 58).

Yoo, D.-Y., N. Banthia, and Y.-S. Yoon (2017). "Impact Resistance of Reinforced Ultra-High-Performance Concrete Beams with Different Steel Fibers". In: *ACI Structural Journal* 114 (cit. on pp. 66, 67).

A Prediction of Equivalent Plastic Hinge Length

This section presents the original equations used to determine a value of equivalent plastic hinge length, l_p, and ultimate concrete strain, ε_{cu}, for reinforced concrete beams according to the models proposed by Mattock (1965) and Corley (1966).

The equations developed by Mattock (1965) in imperial units are given by

$$l_p = 0.5d + 0.5d\left(1.14\sqrt{\frac{l_0}{d}} - 1\right) \cdot \left(1 - \frac{\omega_s - \omega'_s}{\omega_b} \cdot \sqrt{\frac{d}{16.2}}\right) \tag{A.1}$$

$$\varepsilon_{cu} = 0.003 + \frac{0.5}{l_0} \tag{A.2}$$

Additionally, the original expressions presented by Corley (1966) were formulated as

$$l_p = 0.5d + 0.2\sqrt{d}\left(\frac{l_0}{d}\right) \tag{A.3}$$

$$\varepsilon_{cu} = 0.003 + 0.02\left(\frac{b}{l_0}\right) + \left(\frac{\rho'_w \cdot f_y}{20}\right)^2 \tag{A.4}$$

Here, the effective height of the cross-section, d, and the distance between the points of zero and maximum moments, l_0, are given in inches [in]; the steel yield strength, f_y, is given in kilopound per square inch [ksi].

B Material Properties Tests

B.1 Properties of Concrete

Table B.1 Results of compressive and tensile testing of concrete for different specimens, after 28 and 36 days. Specimen 10 was loaded on an incorrect face; therefore, results from that specimen are discarded.

Specimen	Batch	Days	b [mm]	l [mm]	h [mm]	Force at failure [N]	Compressive strength [MPa]	Splitting tensile strength [MPa]
1	1	28	150	150	150	1098	49	-
2	1	28	150	150	150	1095	49	-
3	1	28	150	147	150	126	-	5.7
						Average	**49**	**5.7**
4	2	28	150	151	150	1190	53	-
5	2	28	150	150	150	134	-	6.0
6	2	28	150	150	150	149	-	6.6
						Average	**53**	**6.3**
						Average all	**50**	**6.1**

Specimen	Batch	Days	b [mm]	l [mm]	h [mm]	Force at failure [N]	Compressive strength [MPa]	Splitting tensile strength [MPa]
7	1	36	150	149	150	1124	50	-
8	1	36	150	150	150	142	-	6.3
9	1	36	150	147	150	129	-	5.9
						Average	**50**	**6.1**
10	2	36	150	150	150	1048	-	-
11	2	36	150	150	150	1241	55	-
12	2	36	150	150	150	150	-	6.7
						Average	**55**	**6.7**
						Average all	**53**	**6.3**

B.2 Wedge-Splitting Test

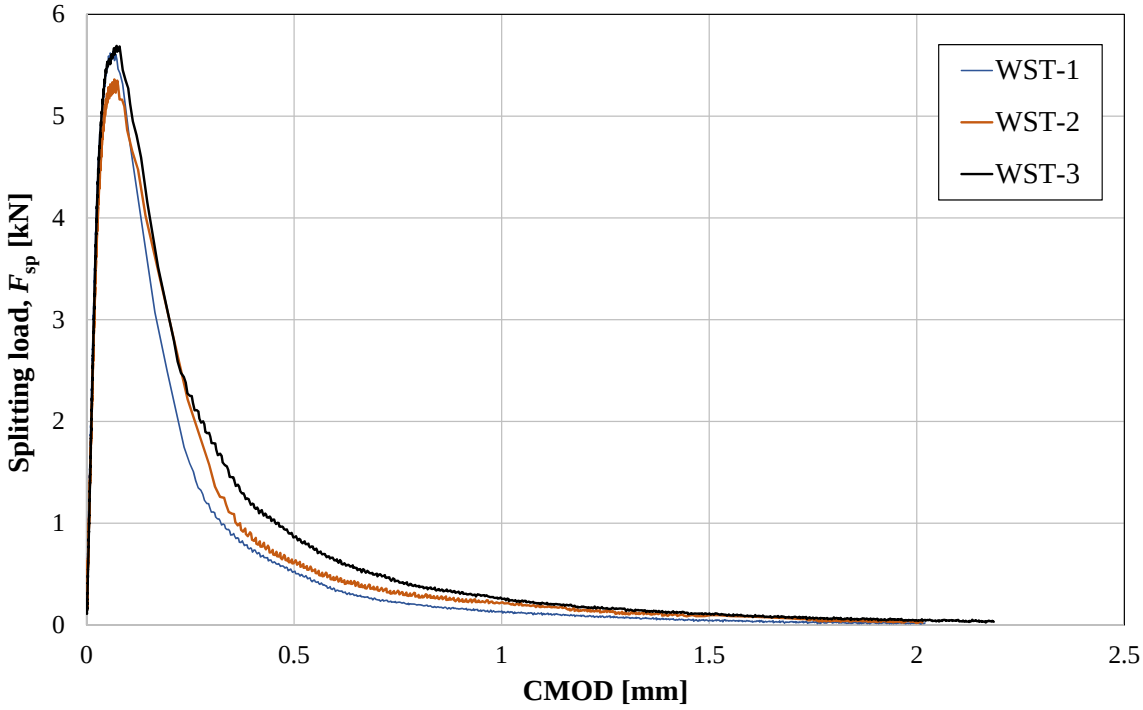

Figure B.1 Horizontal splitting load plotted against crack mouth opening displacement (CMOD). The fracture energy calculated for each specimen is given as the area under each graph.

Table B.2 Summary of WST results.

Specimen ID	Accumulated G_F [Nm/m^2]	$F_{sp,max}$ [kN]	CMOD at $F_{sp,max}$ [mm]	CMOD at fracture [mm]
WST-1	114	5.6	0.06	2.02
WST-2	133	5.4	0.07	2.01
WST-3	149	5.7	0.07	2.19

B.3 Properties of Reinforcing Steel

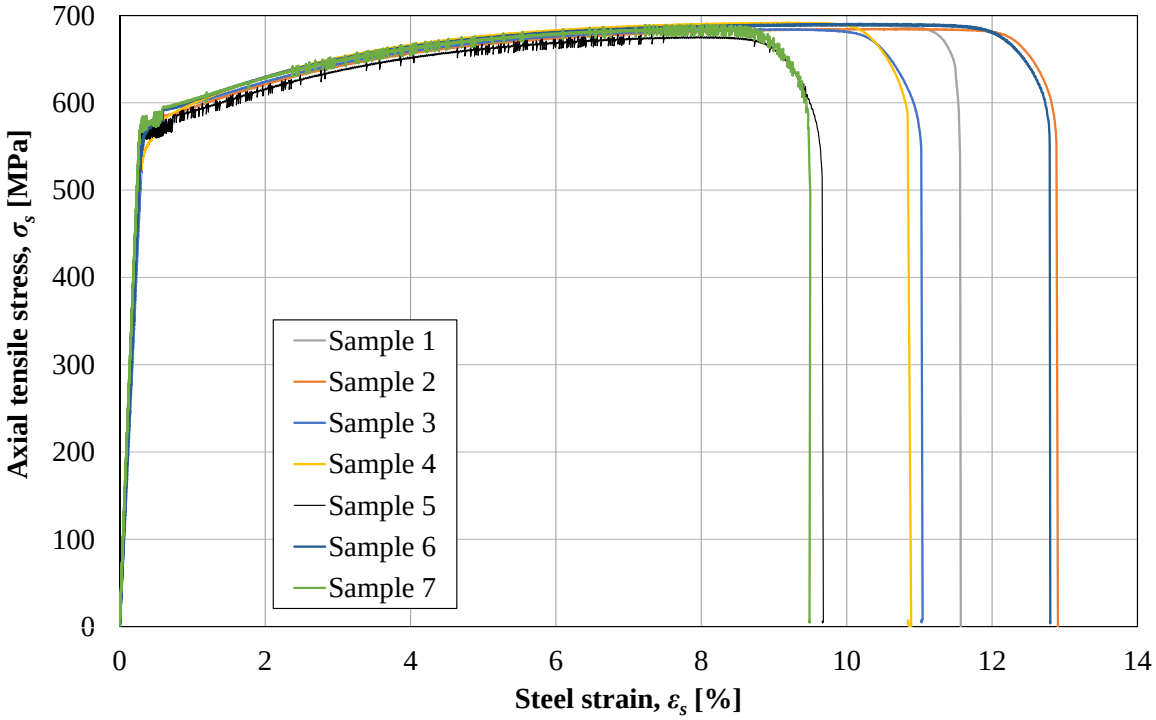

Figure B.2 Stress-strain curves of reinforcement bars samples used.

Table B.3 Results from tensile testing of reinforcing steel samples.

Sample	E_s [GPa]	F_{max} [kN]	ε_{su} [%]	$f_{0.2}$ [MPa]	f_t [MPa]
1	197	19.5	11.6	576	688
2	207	19.4	11.4	572	684
3	178	19.3	11.0	592	684
4	193	19.6	10.9	570	691
5	193	19.2	9.7	563	679
6	196	19.5	11.4	580	690
7	212	19.5	9.5	574	689
Average	**196**	**19.4**	**10.8**	**575**	**686**

C Measured Position of Reinforcement Bars

In this section, a summary of the real position of the reinforcement bars determined through sawing of the reinforced concrete beams is presented. Note that some specimens were severely damaged after static loading; therefore, such specimens were discarded.

The information presented in Table C.1 is supported by the notation described in Figure C.1.

Table C.1 Measured position of the reinforcement bars.

Specimen	d' [mm]	d [mm]
B-01	22	85
B-03	23	83
B-05	20	83
B-06	22	83
B-07	21	84
B-08	24	83
B-09	20	84
B-10	21	84
B-11	21	83
B-16	26	83
B-17	22	81
B-18	22	82
Average	22	83

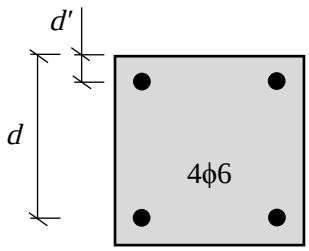

Figure C.1 Notation for the distance from the center of the bars to the concrete surface.

D Preliminary Static Test on an Impact-damaged Specimen

The results of a preliminary static three-point loading test on an impact-damaged specimen are presented in this section. The specimen had previously been impacted by the same drop-weight used in this thesis work, but from a height of 3.5 m, as described in (Lovén and Svavarsdóttir, 2016). The geometrical properties of such specimen, denoted RPC3 in (Lovén and Svavarsdóttir, 2016), are rather similar to the properties determined during this project; while the dimensions of the specimen are equal to the dimensions adopted for this thesis work.

The results of the static test on the impact-damaged beam are compared in Figure D.1 with the results for undamaged specimens of equal characteristics tested under static loading.

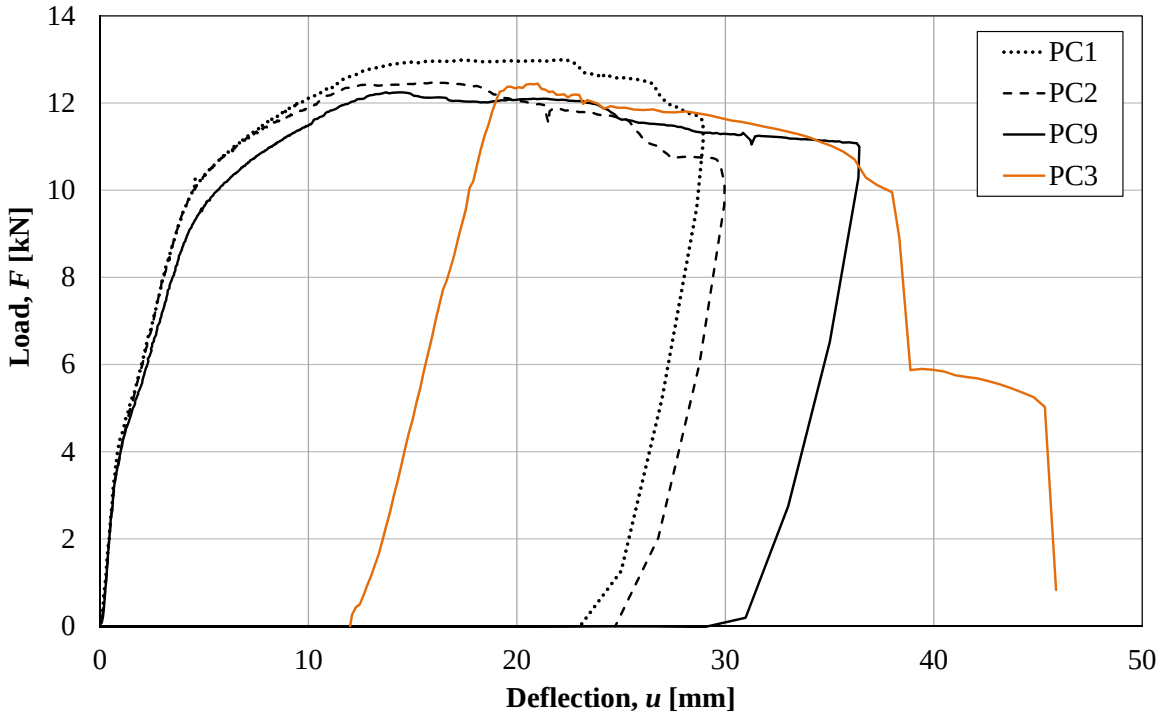

Figure D.1 Comparison of static response of a reinforced concrete specimen previously subjected to a 3.5 m drop-height impact to the response of undamaged specimens. Failure of specimen PC3 was due to steel rupture. Specimens PC1, PC2, and PC9 were completely undamaged before static testing.

E 2DOF System

Complementary results concerning the velocity of the drop-weight and the beam midpoint during the impact event according to the 2DOF model are presented in Figure E.1 and Figure E.2.

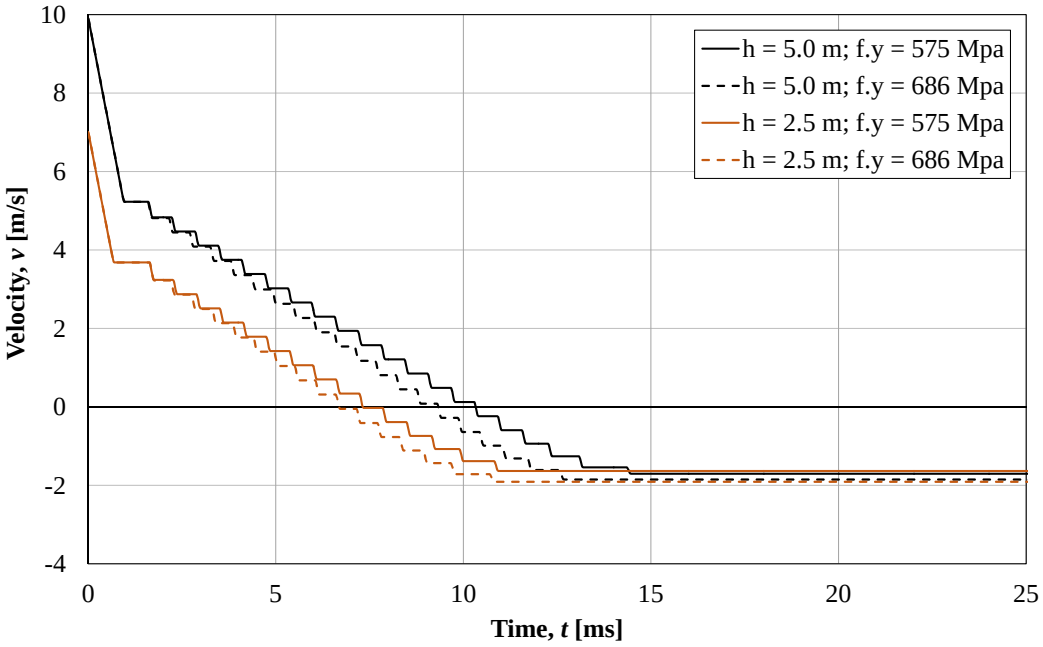

Figure E.1 Velocity of body 1 (which represents drop-weight) according to 2DOF model.

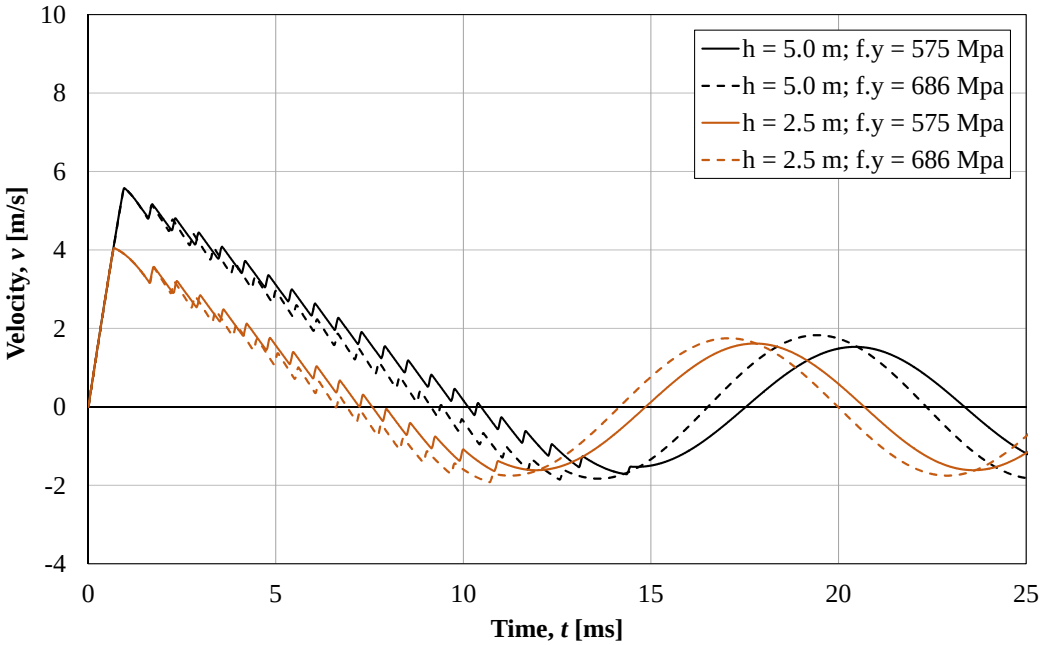

Figure E.2 Velocity of body 2 (which represents beam midpoint) according to 2DOF model.

F Experimental Results

F.1 Velocity and Support Displacement

F.1.1 Velocity of the beam midpoint

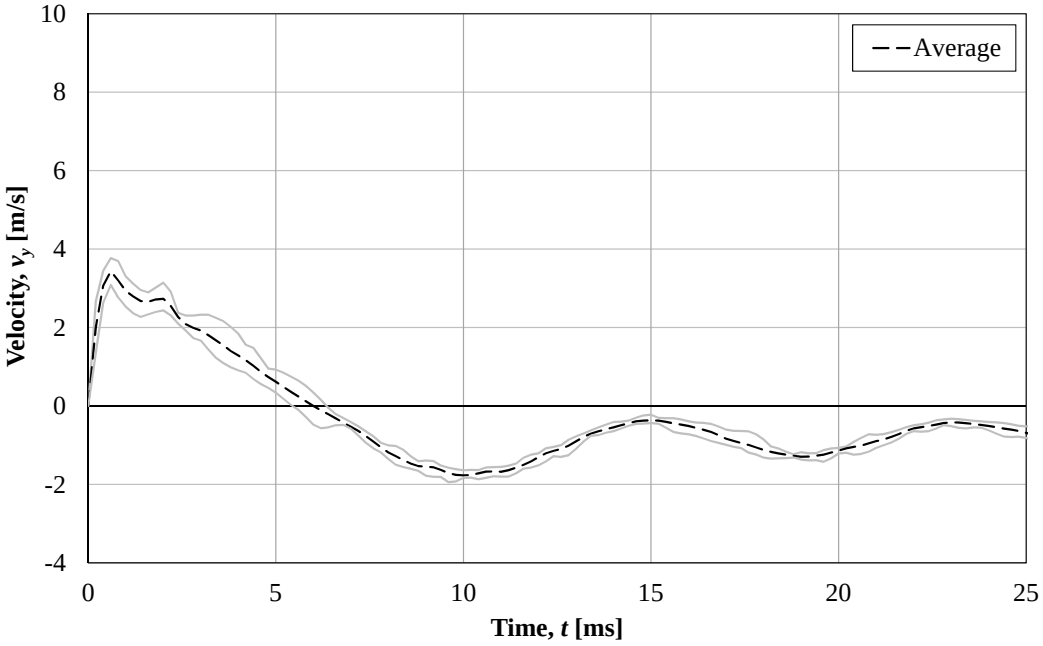

Figure F.1 Experimental values of velocity at beam midspan for a drop-height of 2.5 m.

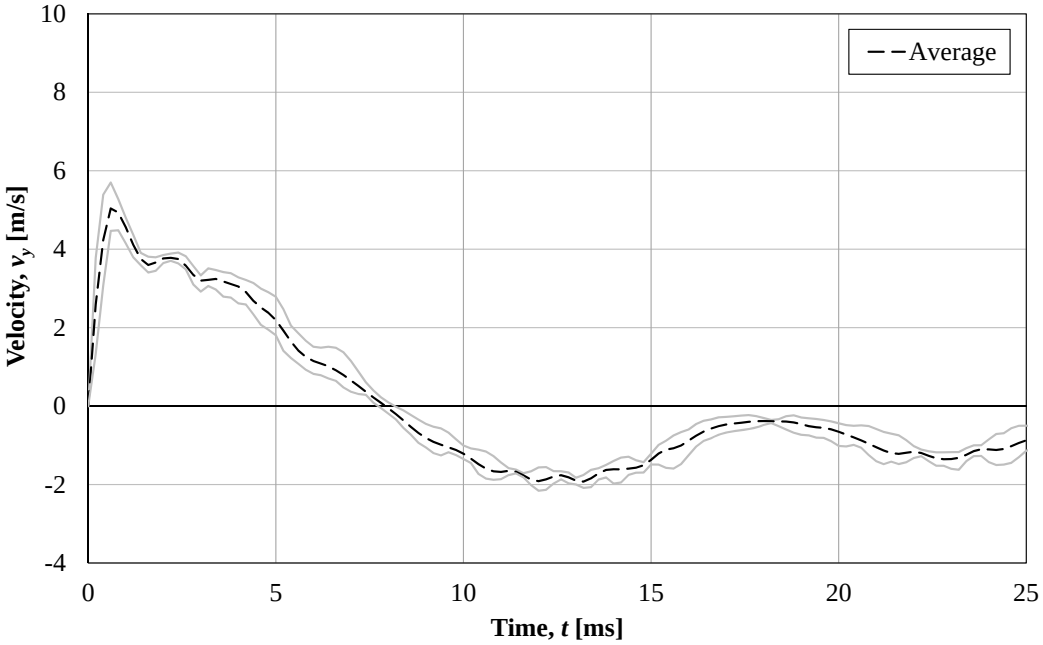

Figure F.2 Experimental values of velocity at beam midspan for a drop-height of 5.0 m.

F.1.2 Drop-weight velocity

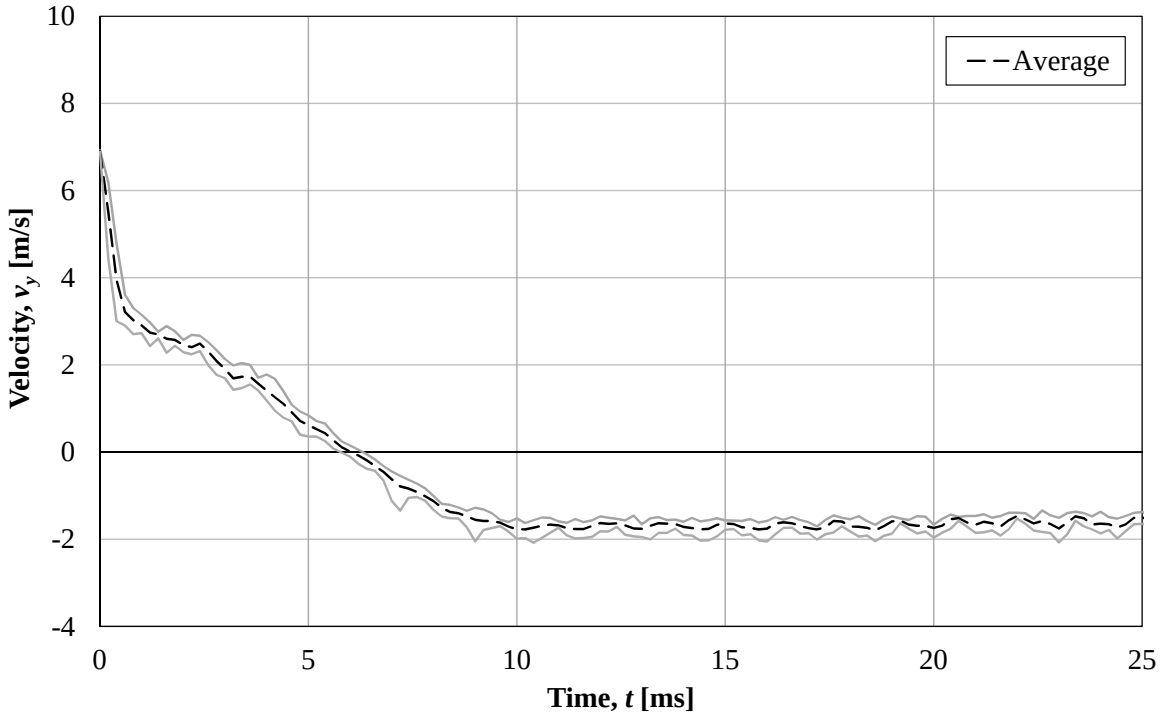

Figure F.3 Experimental values of velocity of the drop-weight for a drop-height of 2.5 m.

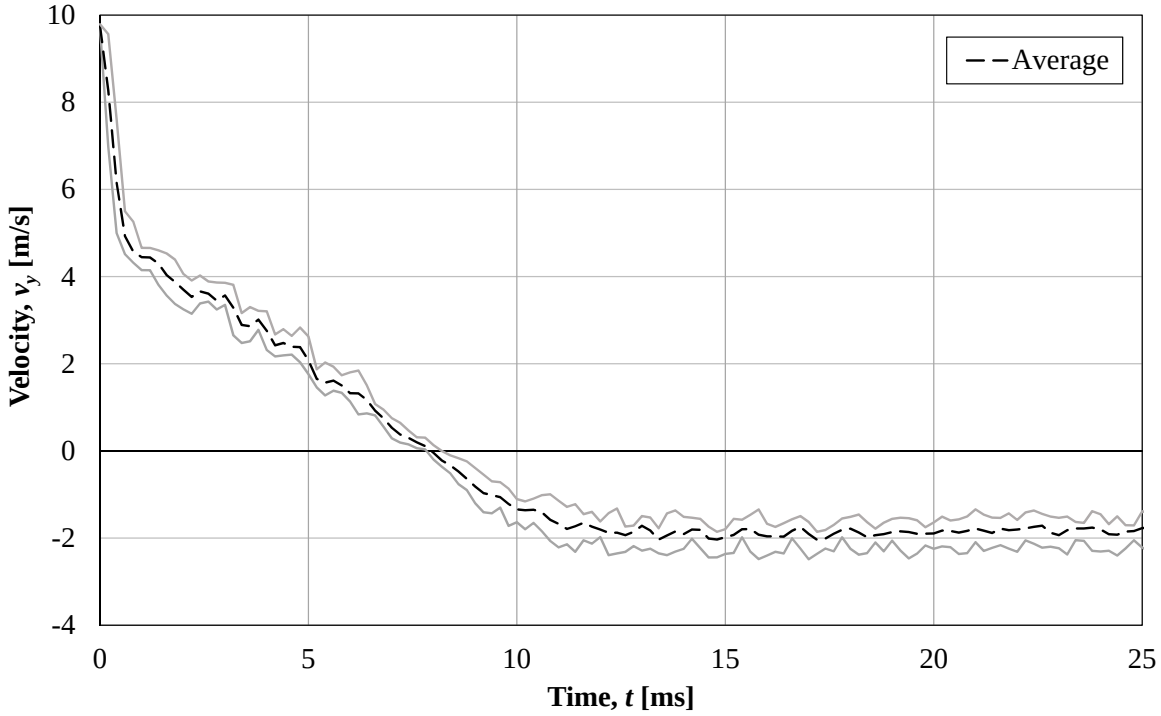

Figure F.4 Experimental values of velocity of the drop-weight for a drop-height of 5.0 m.

F.1.3 Displacement over the support

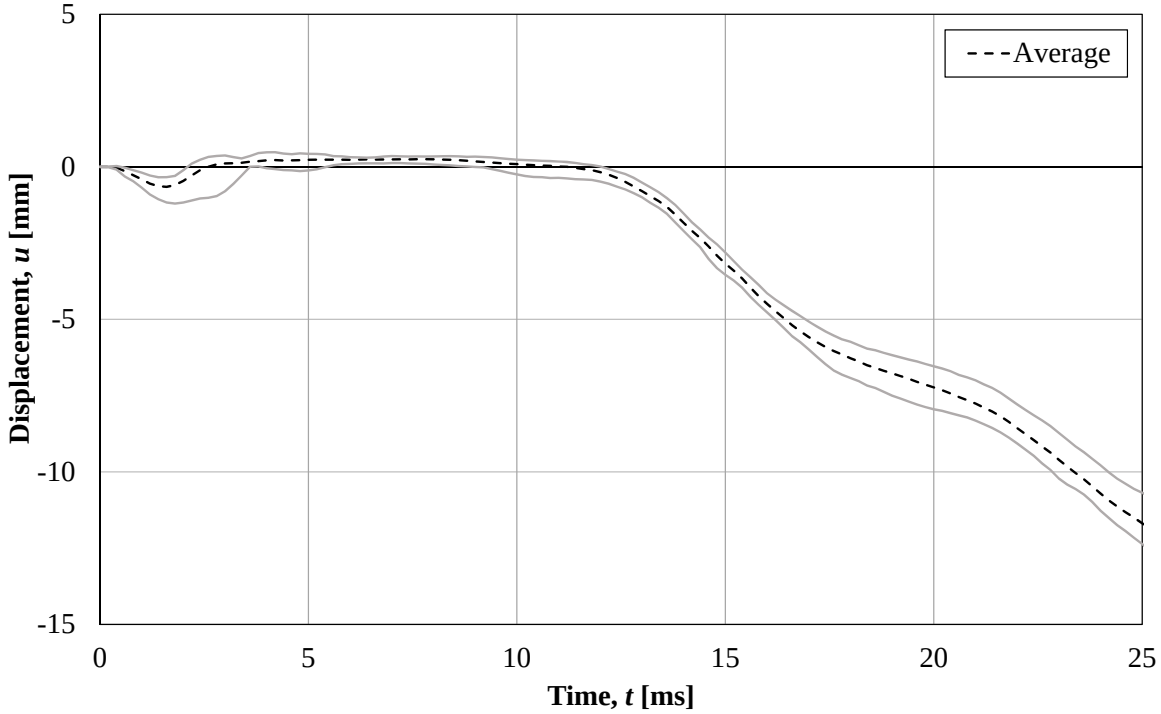

Figure F.5 Experimental values of displacement over the support for a drop height of 2.5 m.

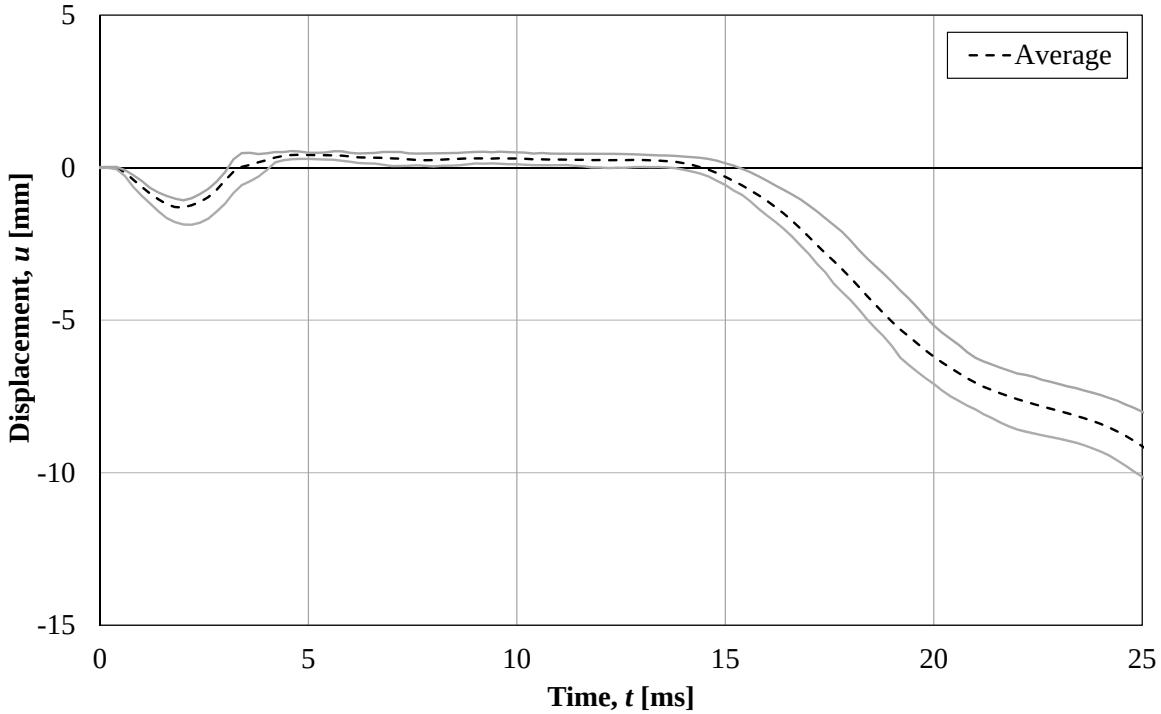

Figure F.6 Experimental values of displacement over the support for a drop-height of 5.0 m.

F.2 Deformed Shape of the Beam

F.2.1 Drop-height $h = 2.5$ m

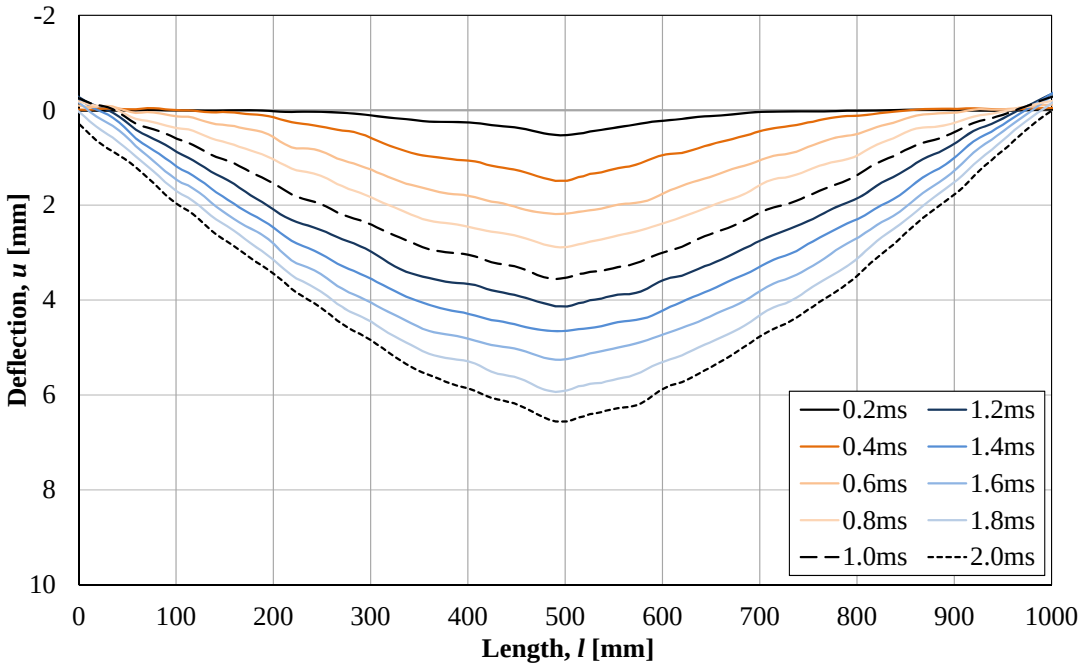

Figure F.7 Deformed shape of beam B-12 at different times after impact. B-12 is assumed to be representative of the behavior of beams subjected to 2.5 m drop.

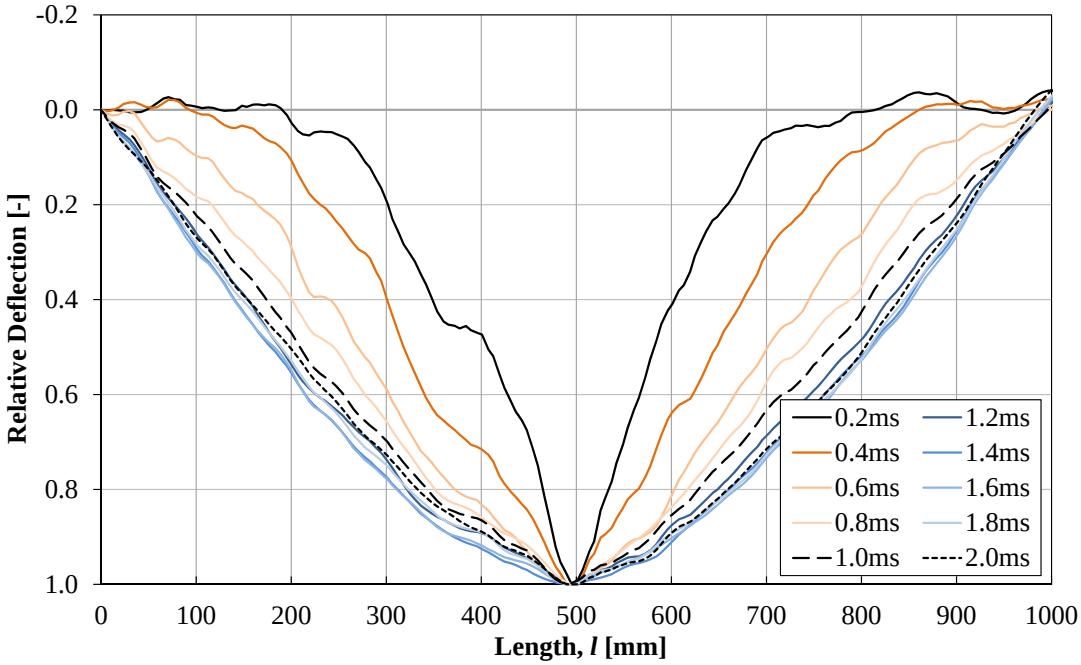

Figure F.8 Relative deformed shape of beam B-12 at different times after impact. B-12 is assumed to be representative of the behavior of beams subjected to 2.5 m drop.

F.2.2 Drop-height $h = 5.0\,\text{m}$

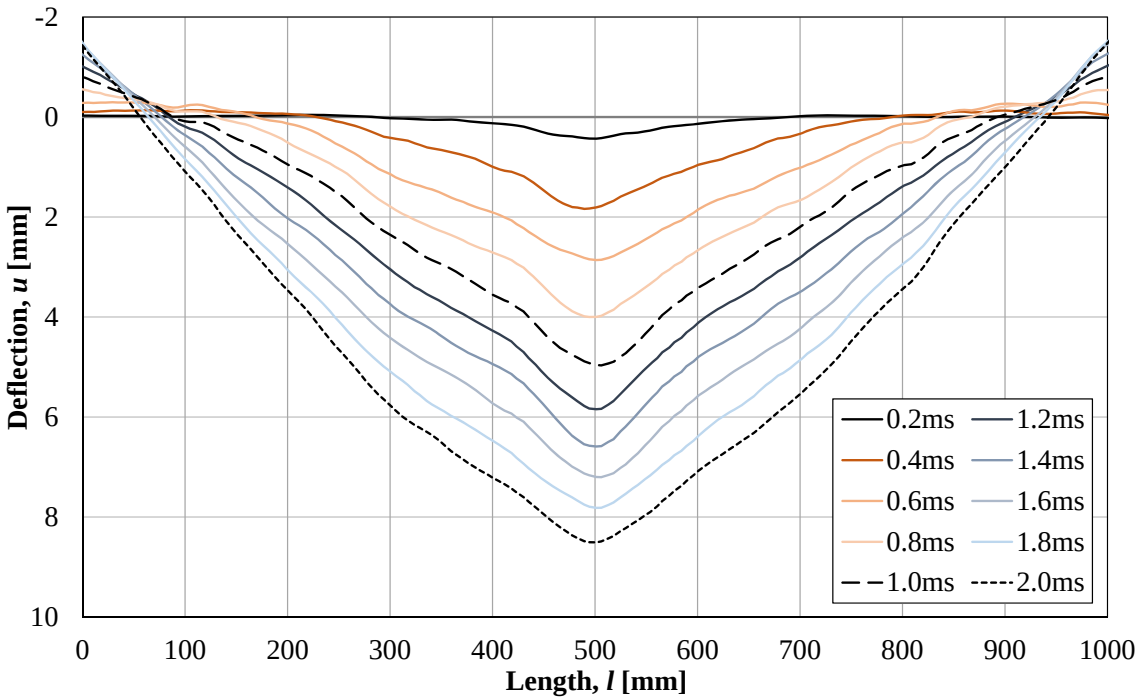

Figure F.9 Deformed shape of beam B-06 at different times after impact. B-06 is assumed to be representative of the behavior of beams subjected to 5.0 m drop.

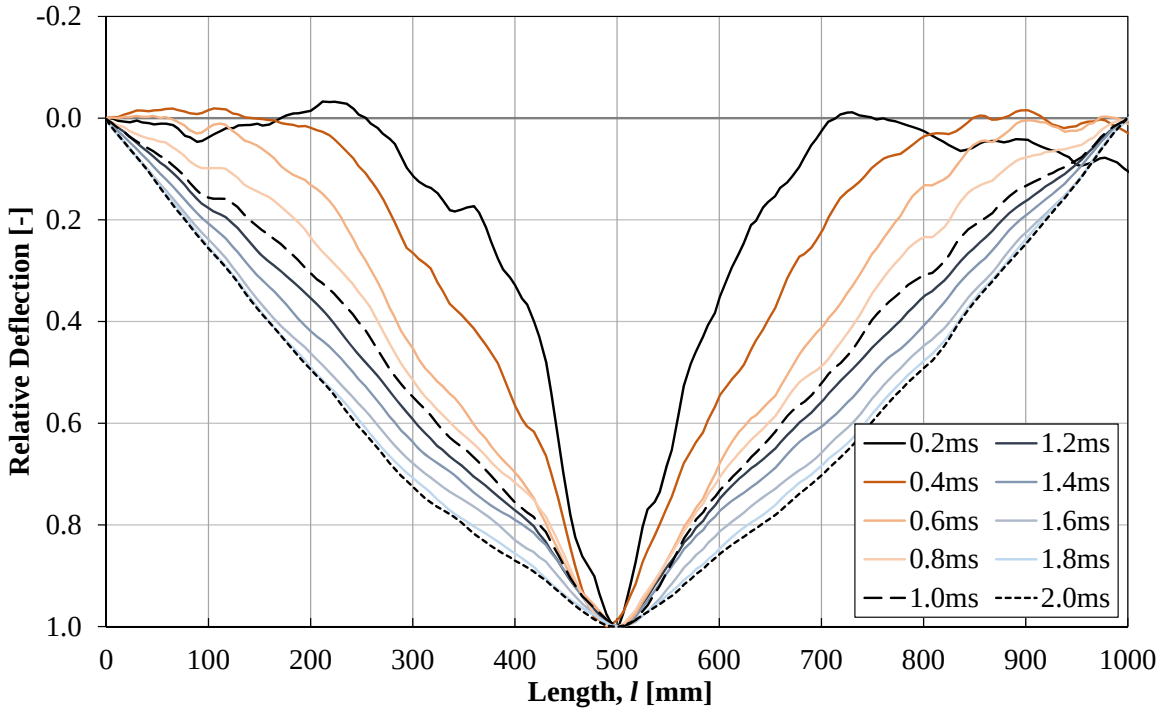

Figure F.10 Relative deformed shape of beam B-06 at different times after impact. B-06 is assumed to be representative of the behavior of beams subjected to 5.0 m drop.

F.3 Determination of Plastic Deformation

F.3.1 Permanent plastic deformation after impact

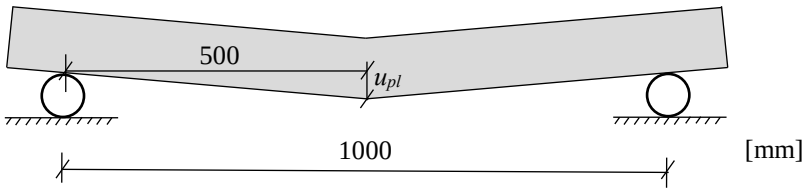

Figure F.11 Schematic illustration showing the procedure adopted when determining the resulting plastic deformation, u_{pl}, due to impact loading. The analysis was performed trough DIC of photographs from subsequent static tests. Note that u_{pl} was determined at the initial stage of the tests, meaning that no static loading had been applied yet.

F.3.2 Methodology adopted to determine plastic rotational capacity

Schematic overview on how plastic deflection at a given load level was determined. Equation (5.11) could then be used to calculate the resulting plastic rotation from the measured values of deflection.

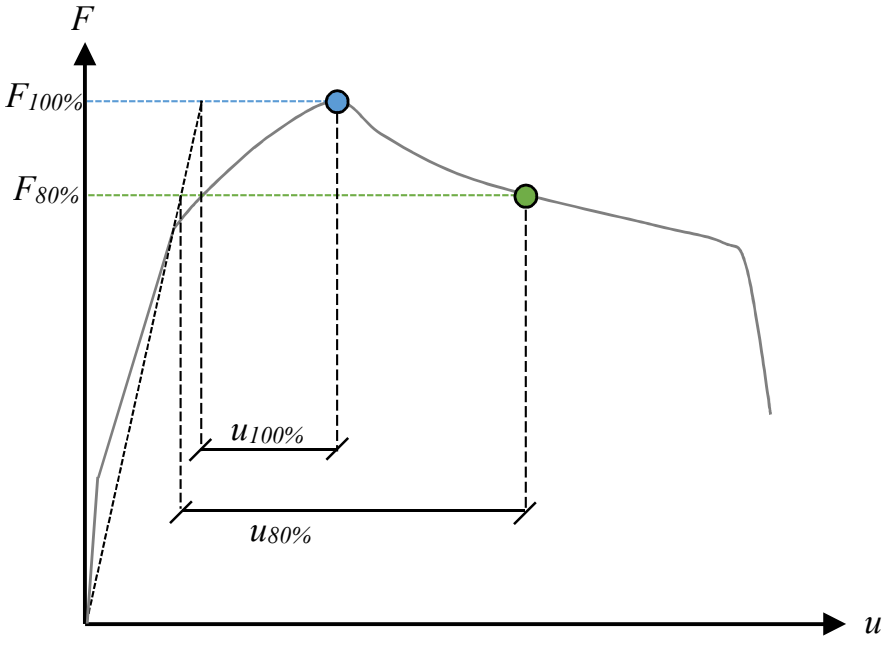

(a) Methodology used for Series-3 beams.

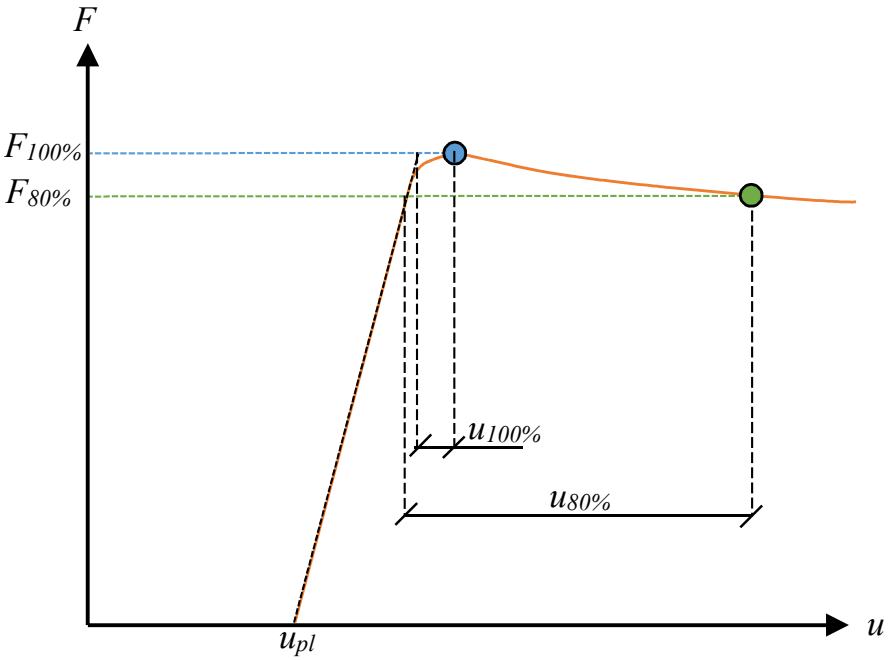

(b) Methodology used for Series-1 and Series-2 beams.

Figure F.12 Methodology adopted to determine plastic deformation and consequently plastic rotation.

F.4 Results from Static Tests

F.4.1 Key parameters: Series-1

Table F.1 Summary of key values for Series-1.

Beam-ID	B-01	B-02	B-03	B-10	B-11	B-12	Units
u_{pl}	8.5	7.0	8.0	7.5	10.0	9.5	[mm]
$u_{fail,s}$	43.1	-	36.9	39.0	47.0	40.2	[mm]
$u_{pl} + u_{fail,s}$	51.6	44.4	44.9	46.5	57.0	49.7	[mm]
k	2.1	2.1	2.3	2.2	1.9	2.2	[kN/mm]
$F_{100\%}$	13.5	14.1	14.7	14.0	13.3	14.0	[kN]
$u_{a,100\%}$	6.5	6.7	6.5	6.4	7.2	6.5	[mm]
$u_{b,100\%}$	10.6	16.5	12.9	12.4	17.6	10.9	[mm]
$\theta_{pl.100\%}$	**8.2**	**19.5**	**12.9**	**12.0**	**20.8**	**8.8**	[mrad]
$F_{95\%}$	12.9	13.4	13.9	13.3	12.7	13.3	[kN]
$u_{a,95\%}$	6.2	6.4	6.2	6.1	6.8	6.2	[mm]
$u_{b,95\%}$	18.8	20.9	13.8	16.6	20.3	14.7	[mm]
$\theta_{pl.95\%}$	**25.3**	**29.0**	**15.3**	**21.1**	**26.9**	**17.0**	[mrad]
$F_{90\%}$	12.2	12.7	13.2	12.6	12.0	12.6	[kN]
$u_{a,90\%}$	5.8	6.0	5.8	5.7	6.5	5.9	[mm]
$u_{b,90\%}$	25.5	27.1	18.8	27.8	23.5	15.8	[mm]
$\theta_{pl.90\%}$	**39.2**	**42.2**	**26.0**	**44.1**	**34.0**	**19.7**	[mrad]
$F_{80\%}$	-	11.3	-	-	10.7	11.2	[kN]
$u_{a,80\%}$	-	5.4	-	-	5.8	5.2	[mm]
$u_{b,80\%}$	-	35.2	-	-	45.9	35.2	[mm]
$\theta_{pl.80\%}$	**-**	**59.7**	**-**	**-**	**80.2**	**59.8**	[mrad]

F.4.2 Key parameters: Series-2

Table F.2 Summary of key values for Series-2. Rupture of reinforcement bars was obtained for all specimens, except for B-04.

Beam-ID	B-04	B-05	B-06	B-13[1]	B-14	B-15	Units
u_{pl}	17.0	19.0	16.0	20.0	16.0	18.0	[mm]
$u_{fail,s}$	-	50.0	49.3	12.9	56.6	52.3	[mm]
$u_{pl} + u_{fail,s}$	-	69.0	65.3	32.9	72.6	70.3	[mm]
k	1.6	1.5	1.8	1.4	1.8	1.7	[kN/mm]
$F_{100\%}$	12.3	12.0	13.1	8.5	13.5	13.2	[kN]
$u_{a,100\%}$	7.6	8.2	7.4	6.4	7.5	7.7	[mm]
$u_{b,100\%}$	18.7	16.1	13.0	6.7	12.1	13.7	[mm]
$\theta_{pl.100\%}$	**22.1**	**15.8**	**11.2**	**0.7**	**9.1**	**12.1**	[mrad]
$F_{95\%}$	11.7	11.4	12.4	8.1	12.9	12.5	[kN]
$u_{a,95\%}$	7.2	7.8	7.0	6.1	7.2	7.3	[mm]
$u_{b,95\%}$	26.0	40.5	29.4	9.6	20.4	29.6	[mm]
$\theta_{pl.95\%}$	**37.5**	**65.3**	**44.8**	**6.9**	**26.6**	**44.6**	[mrad]
$F_{90\%}$	11.1	10.8	11.8	7.6	12.2	11.9	[kN]
$u_{a,90\%}$	6.9	7.4	6.6	5.8	6.8	6.9	[mm]
$u_{b,90\%}$	47.4	47.2	47.5	9.6	36.1	32.0	[mm]
$\theta_{pl.90\%}$	**81.1**	**79.5**	**81.7**	**7.5**	**58.6**	**50.2**	[mrad]
$F_{80\%}$	9.9	-	-	6.8	10.8	10.6	[kN]
$u_{a,80\%}$	6.1	-	-	5.2	6.1	6.2	[mm]
$u_{b,80\%}$	57.4	-	-	9.5	55.8	45.9	[mm]
$\theta_{pl.80\%}$	**102.7**	**-**	**-**	**8.5**	**99.6**	**79.5**	[mrad]

[1] B-13 developed a shear failure mechanism.

F.4.3 Key parameters: Series-3

Table F.3 Summary of key values for Series-3. Beams were undamaged, hence $u_{pl} = 0$ mm. Rupture of reinforcement bars was obtained for all specimens, except for B-08.

Beam-ID	B-07	B-08	B-09	B-16	B-17	B-18	Units
u_{pl}	0.0	0.0	0.0	0.0	0.0	0.0	[mm]
$u_{fail,s}$	48.4	-	52.9	55.9	51.0	51.6	[mm]
k	2.0	2.2	2.4	2.2	2.4	2.2	[kN/mm]
$F_{100\%}$	13.7	13.9	14.1	14.5	13.8	14.1	[kN]
$u_{a,100\%}$	6.7	6.4	5.8	6.5	5.8	6.5	[mm]
$u_{b,100\%}$	16.9	16.5	16.9	15.6	15.2	25.6	[mm]
$\theta_{pl.100\%}$	**20.5**	**20.0**	**22.1**	**18.2**	**18.9**	**38.4**	[mrad]
$F_{95\%}$	13.0	13.2	13.4	13.8	13.1	13.4	[kN]
$u_{a,95\%}$	6.3	6.1	5.6	6.2	5.5	6.1	[mm]
$u_{b,95\%}$	23.4	19.0	22.8	16.8	15.4	31.1	[mm]
$\theta_{pl.95\%}$	**34.1**	**25.7**	**34.4**	**21.3**	**19.9**	**49.8**	[mrad]
$F_{90\%}$	12.3	12.5	12.7	13.1	12.4	12.7	[kN]
$u_{a,90\%}$	6.0	5.8	5.3	5.9	5.2	5.8	[mm]
$u_{b,90\%}$	26.2	24.7	29.4	20.9	15.5	33.9	[mm]
$\theta_{pl.90\%}$	**40.4**	**37.8**	**48.3**	**30.1**	**20.6**	**56.1**	[mrad]
$F_{80\%}$	11.0	11.1	11.3	11.6	11.0	11.3	[kN]
$u_{a,80\%}$	5.3	5.2	4.7	5.2	4.6	5.2	[mm]
$u_{b,80\%}$	43.9	44.1	50.7	23.1	47.1	48.5	[mm]
$\theta_{pl.80\%}$	**77.1**	**77.9**	**92.1**	**35.7**	**85.1**	**86.6**	[mrad]

F.5 Plastic rotational capacity

F.5.1 Rotational capacity of all beams

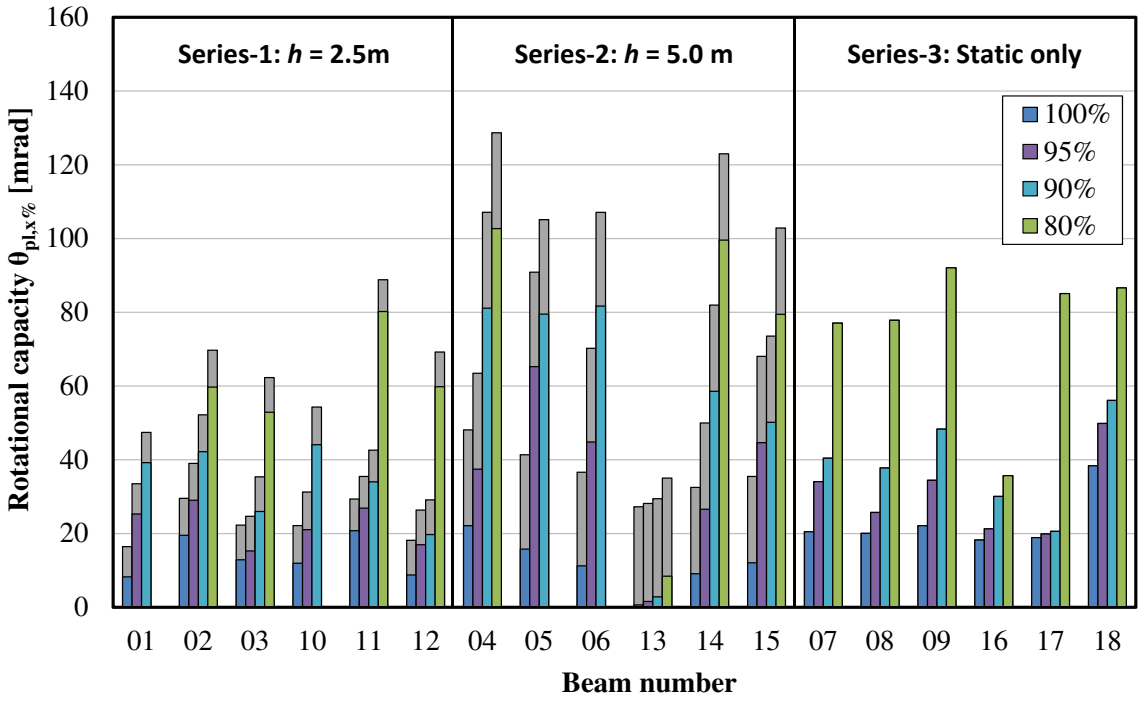

Figure F.13 Plastic rotational capacity with respect to a given load percentage of all beam specimens. B-13 developed a shear failure mechanism.

F.5.2 Internal Work

Table F.4 Comparison of internal work. $W_{i,tot}$ signifies total internal work, whereas $W_{i,x\%}$ denotes the accumulated internal work for a given load level on the descending branch. A comparison of the ratio of accumulated work to plastic rotational capacity for given load levels is also made.

			$W_{i,x\%}$ [J]				$W_{i,x\%}/\theta_{pl,x\%}$ [J/mrad]			
Series	Beam	$W_{i,tot}$ [J]	100%	95%	90%	80%	100%	95%	90%	80%
1	B-01	492	97	206	290	-	11.8	8.1	7.4	-
	B-02	426	180	240	323	419	9.2	8.3	7.6	7.0
	B-03	431	135	147	215	-	10.5	9.6	8.3	-
	B-10	456	125	182	325	-	10.4	8.6	7.4	-
	B-11	522	181	216	256	514	8.7	8.1	7.5	6.4
	B-12	447	103	154	168	398	11.7	9.1	8.5	6.7
Averages		**462**	**137**	**191**	**263**	**444**	**10.4**	**8.6**	**7.8**	**6.7**
2	B-4	-	176	263	508	613	7.9	7.0	6.3	6.0
	B-5	520	141	427	502	-	9.0	6.5	6.3	-
	B-6	566	120	330	551	-	10.6	7.4	6.7	-
	B-13[1]	67	27	29	32	48	42.2	18.3	11.1	5.6
	B-14	652	110	220	414	647	12.0	8.3	7.1	6.5
	B-15	571	126	329	358	509	10.5	7.4	7.1	6.4
Averages		**577**	**134**	**314**	**167**	**590**	**10.0**	**7.3**	**6.7**	**6.3**
3	B-7	538	180	265	302	507	8.8	7.8	7.5	6.6
	B-8	-	179	213	286	513	8.9	8.3	7.6	6.6
	B-9	630	191	271	358	611	8.6	7.9	7.4	6.6
	B-16	618	173	190	244	271	9.5	8.9	8.1	7.6
	B-17	565	167	170	171	529	8.8	8.6	8.3	6.2
	B-18	624	309	384	420	595	8.1	7.7	7.5	6.9
Averages		**595**	**200**	**249**	**297**	**504**	**8.8**	**8.2**	**7.7**	**6.7**

[1] B-13 developed a shear failure mechanism, it is not factored in average values.

F.6 Strain field for Dynamic and Static Tests

F.6.1 Specimen B-01

Table F.5 Strain field due to impact loading from DIC analysis for B-01, drop-height h = 2.5 m.

Deflection / Time	Strain field for impact loading: B-01
$u = 0$ mm $t = 0$ ms	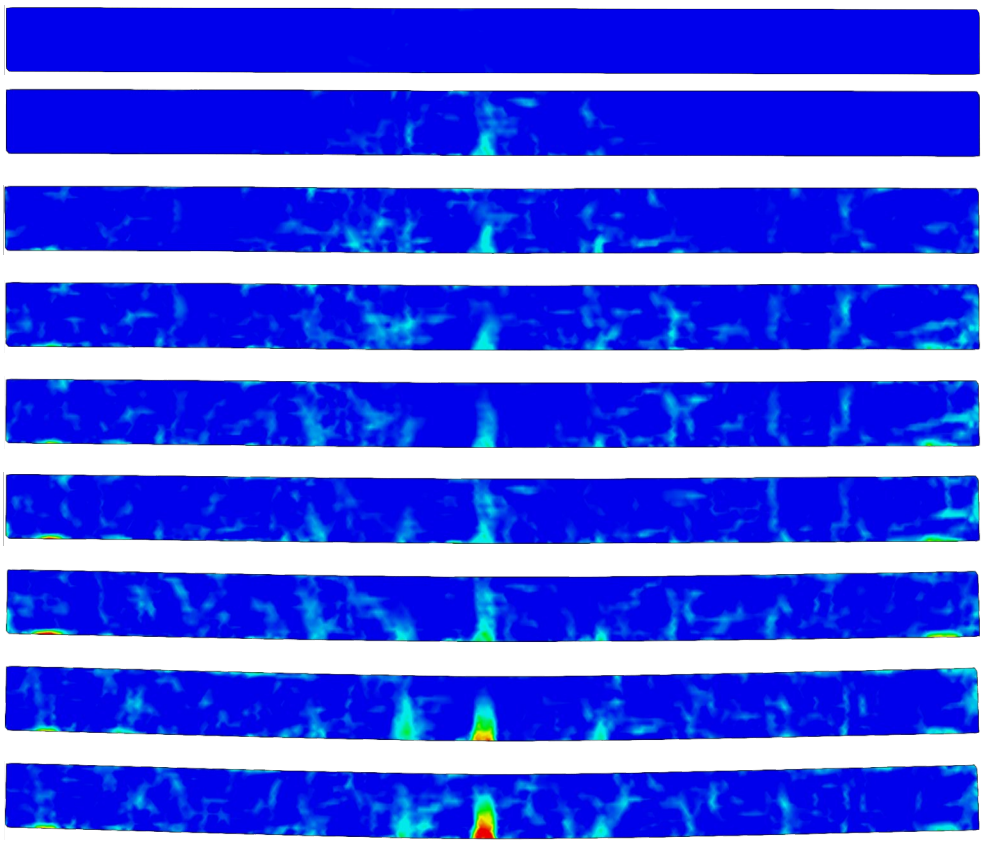
$u = 0.1$ mm $t = 0.2$ ms	
$u = 0.7$ mm $t = 0.4$ ms	
$u = 1.4$ mm $t = 0.6$ ms	
$u = 2.0$ mm $t = 0.8$ ms	
$u = 2.5$ mm $t = 1.0$ ms	
$u = 4.9$ mm $t = 2.0$ ms	
$u = 9.4$ mm $t = 4.0$ ms	
$u = 10.5$ mm [1] $t = 5.6$ ms	
Principal Strain [%]	

[1] Maximum deflection due to impact loading.

Table F.6 Strain field due to static loading from DIC analysis for B-01. Note that the strain field of the dynamic response has different limits in the colorscale (from 0.5 % to 5 %).

Deflection / Time	Strain field due to impact loading at maximum deflection: B-01
$u = 10.5\,\text{mm}$ $t = 5.6\,\text{ms}$	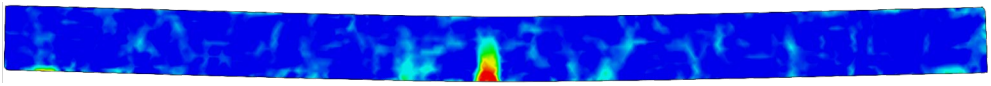
Deflection / Load	**Strain field due to static loading: B-01**
$u = 2.5\,\text{mm}$ $F = 5.1\,\text{kN}$ $u = 5.0\,\text{mm}$ $F = 10.4\,\text{kN}$ $u_{100\%} = 10.6\,\text{mm}$ $F_{100\%} = 13.5\,\text{kN}$ $u_{95\%} = 12.2\,\text{mm}$ $F_{95\%} = 12.9\,\text{kN}$ $u_{90\%} = 25.5\,\text{mm}$ $F_{90\%} = 12.2\,\text{kN}$	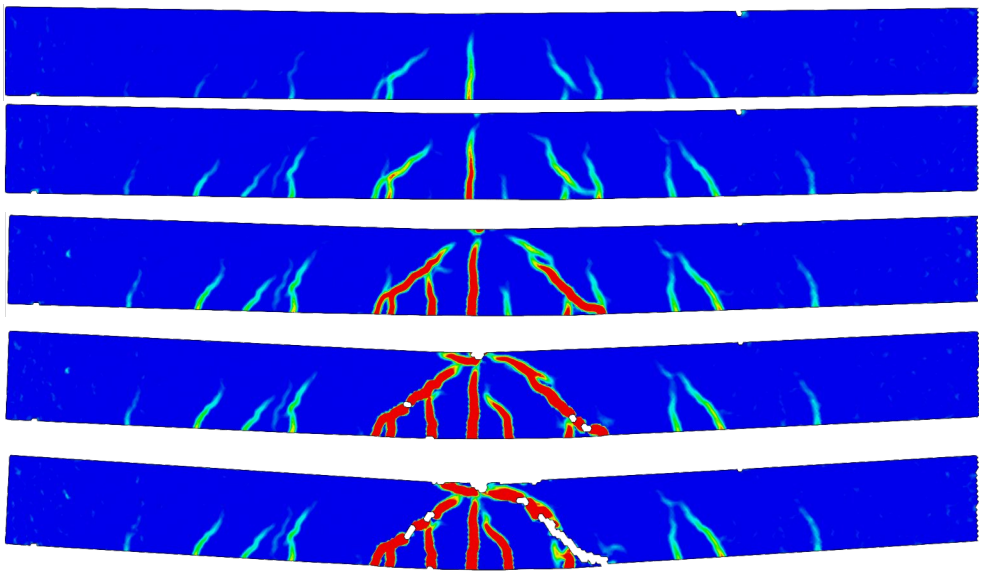
Principal strain [%]	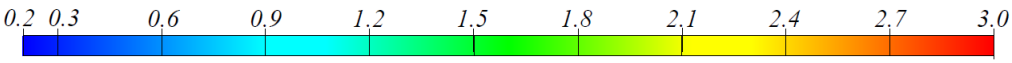

F.6.2 Specimen B-02

Table F.7 Strain field due to impact loading from DIC analysis for B-02, drop-height h = 2.5 m.

Deflection / Time	Strain field for impact loading: B-02
$u = 0$ mm $t = 0$ ms	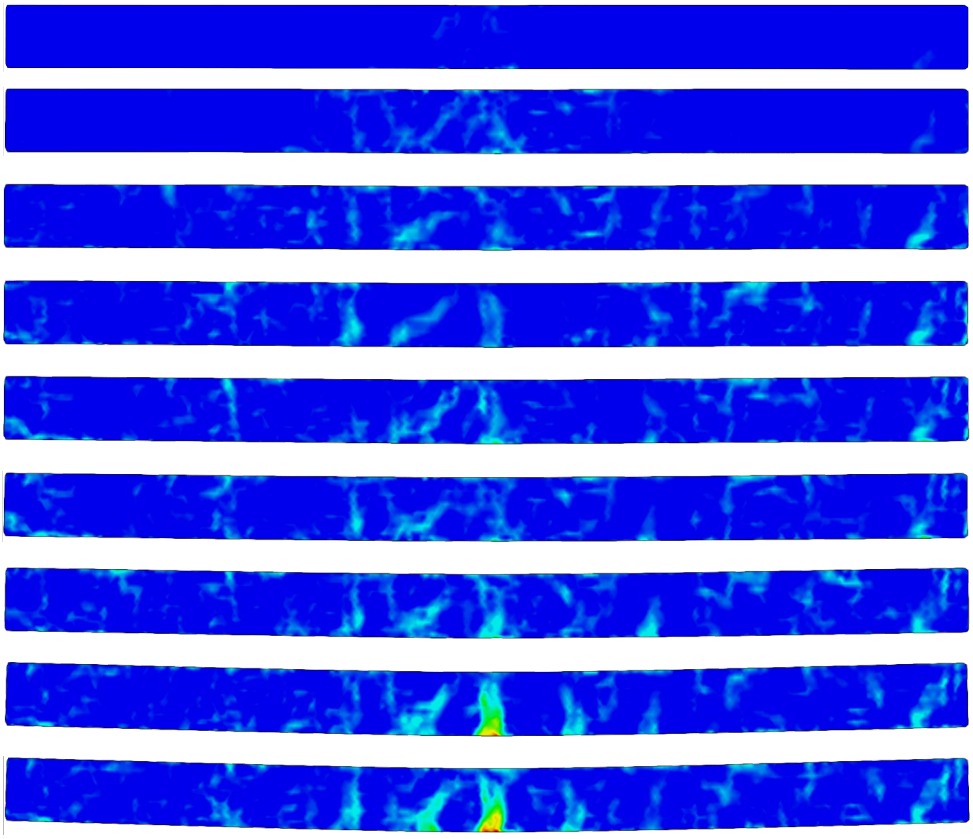
$u = 0.0$ mm $t = 0.2$ ms	
$u = 0.4$ mm $t = 0.4$ ms	
$u = 1.3$ mm $t = 0.6$ ms	
$u = 1.9$ mm $t = 0.8$ ms	
$u = 2.6$ mm $t = 1.0$ ms	
$u = 5.5$ mm $t = 2.0$ ms	
$u = 9.4$ mm $t = 4.0$ ms	
$u = 11.0$ mm [1] $t = 6.0$ ms	
Principal Strain [%]	

[1] Maximum deflection due to impact loading.

Table F.8 Strain field due to static loading from DIC analysis for B-02. Note that the strain field of the dynamic response has different limits in the colorscale (from 0.5 % to 5 %).

Deflection / Time	Strain field due to impact loading at maximum deflection: B-02
$u = 11.0\,\text{mm}$ $t = 6.0\,\text{ms}$	

Deflection / Load	Strain field due to static loading: B-02
$u = 2.5\,\text{mm}$ $F = 4.4\,\text{kN}$	
$u = 5.0\,\text{mm}$ $F = 9.8\,\text{kN}$	
$u_{100\%} = 16.5\,\text{mm}$ $F_{100\%} = 14.1\,\text{kN}$	
$u_{95\%} = 20.9\,\text{mm}$ $F_{95\%} = 13.4\,\text{kN}$	
$u_{90\%} = 12.7\,\text{mm}$ $F_{90\%} = 12.7\,\text{kN}$	
$u_{80\%} = 35.2\,\text{mm}$ $F_{80\%} = 11.3\,\text{kN}$	
Principal strain [%]	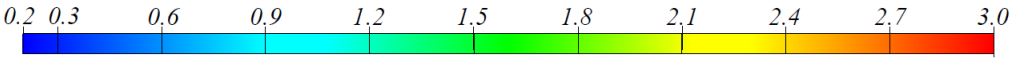

F.6.3 Specimen B-03

Table F.9 Strain field due to impact loading from DIC analysis for B-03, drop-height h = 2.5 m.

Deflection / Time	Strain field for impact loading: B-03
$u = 0$ mm $t = 0$ ms	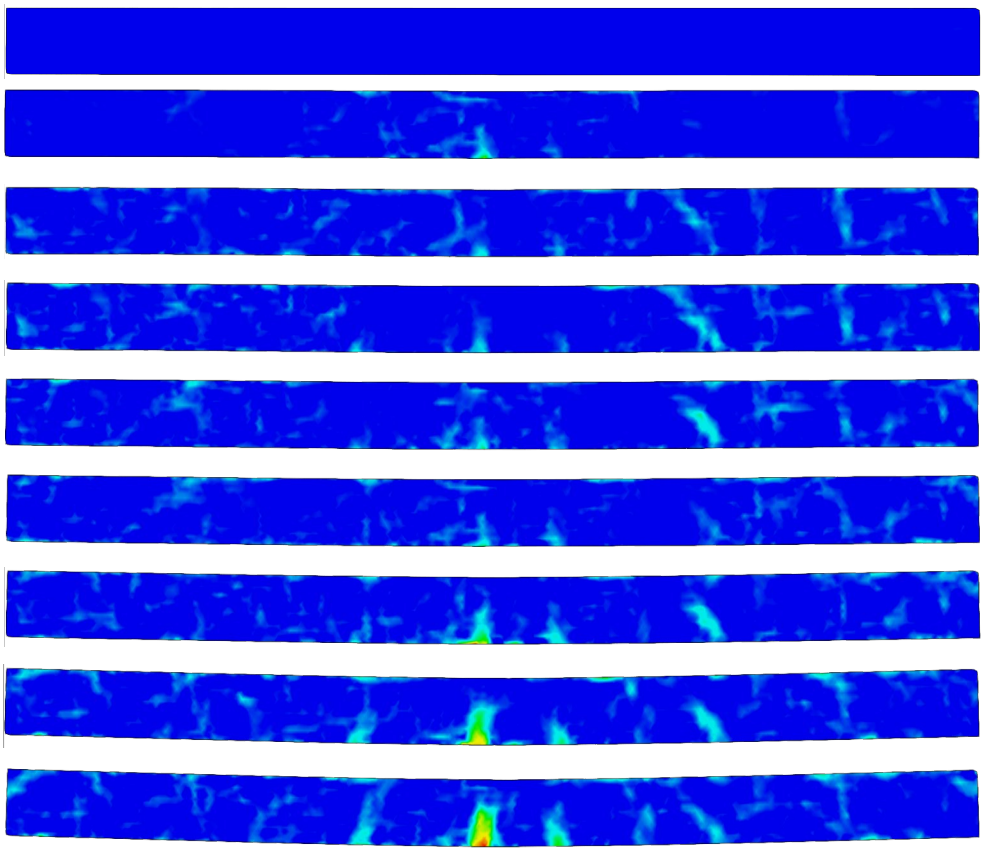
$u = 0.4$ mm $t = 0.2$ ms	
$u = 1.2$ mm $t = 0.4$ ms	
$u = 2.0$ mm $t = 0.6$ ms	
$u = 2.6$ mm $t = 0.8$ ms	
$u = 3.1$ mm $t = 1.0$ ms	
$u = 5.7$ mm $t = 2.0$ ms	
$u = 9.6$ mm $t = 4.0$ ms	
$u = 10.4$ mm [1] $t = 5.4$ ms	
Principal Strain [%]	

[1] Maximum deflection due to impact loading.

Table F.10 Strain field due to static loading from DIC analysis for B-03. Note that the strain field of the dynamic response has different limits in the colorscale (from 0.5 % to 5 %).

Deflection / Time	Strain field due to impact loading at maximum deflection: B-03
$u = 10.4\,\text{mm}$ $t = 5.4\,\text{ms}$	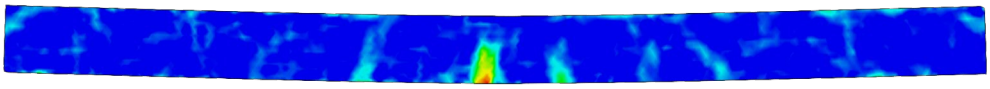

Deflection / Load	Strain field due to static loading: B-03
$u = 2.5\,\text{mm}$ $F = 5.4\,\text{kN}$	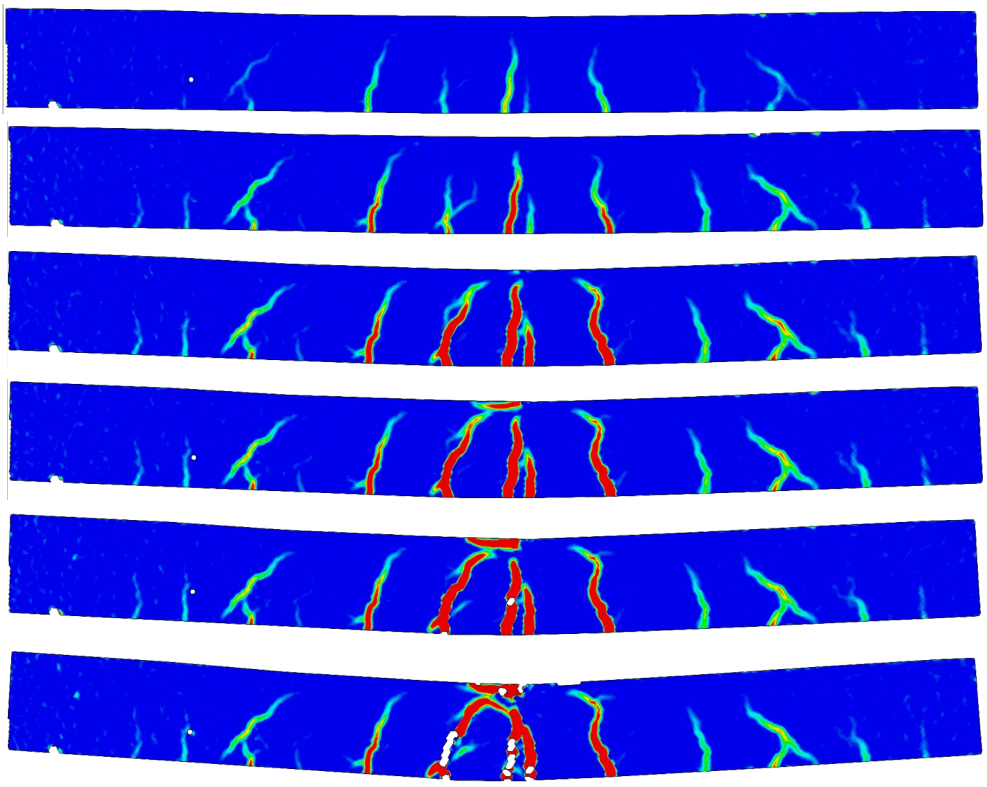
$u = 5.0\,\text{mm}$ $F = 10.8\,\text{kN}$	
$u_{100\%} = 12.9\,\text{mm}$ $F_{100\%} = 14.7\,\text{kN}$	
$u_{95\%} = 13.8\,\text{mm}$ $F_{95\%} = 13.9\,\text{kN}$	
$u_{90\%} = 18.8\,\text{mm}$ $F_{90\%} = 13.2\,\text{kN}$	
$u_{80\%} = 26.5\,\text{mm}$ $F_{80\%} = 11.7\,\text{kN}$	
Principal strain [%]	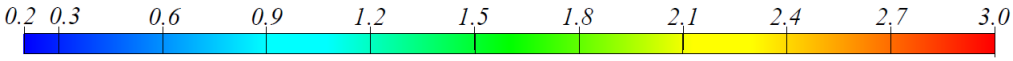

F.6.4 Specimen B-04

Table F.11 Strain field due to impact loading from DIC analysis for B-04, drop-height h = 5.0 m.

Deflection / Time	Strain field for impact loading: B-04
$u = 0$ mm $t = 0$ ms	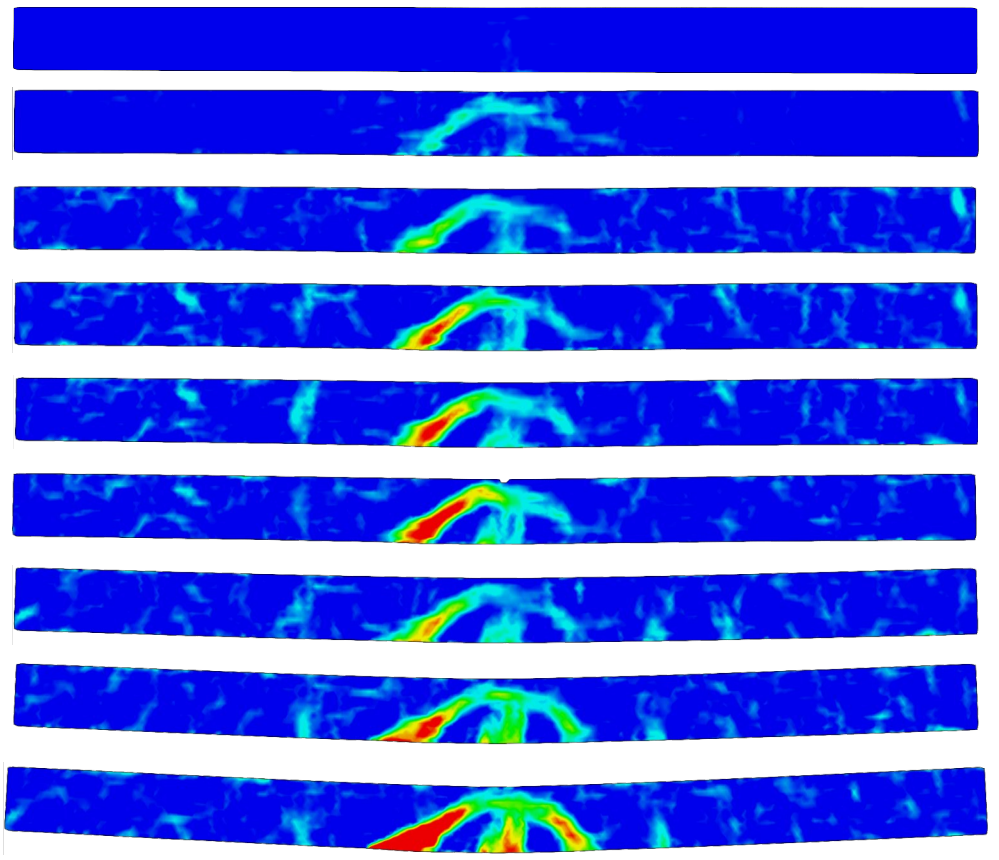
$u = 0.3$ mm $t = 0.2$ ms	
$u = 1.8$ mm $t = 0.4$ ms	
$u = 2.8$ mm $t = 0.6$ ms	
$u = 4.0$ mm $t = 0.8$ ms	
$u = 4.9$ mm $t = 1.0$ ms	
$u = 8.7$ mm $t = 2.0$ ms	
$u = 15.3$ mm $t = 4.0$ ms	
$u = 20.4$ mm [1] $t = 7.6$ ms	
Principal Strain [%]	

[1] Maximum deflection due to impact loading.

Table F.12 Strain field due to static loading from DIC analysis for B-04. Note that the strain field of the dynamic response has different limits in the colorscale (from 0.5 % to 5 %).

Deflection / Time	Strain field due to impact loading at maximum deflection: B-04
$u = 20.4\,\text{mm}$ $t = 7.6\,\text{ms}$	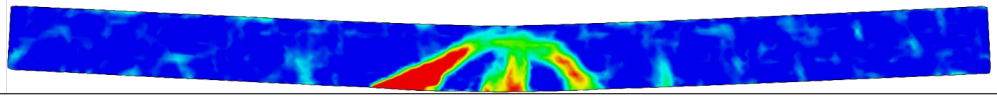
Deflection / Load	**Strain field due to static loading: B-04**
$u = 2.5\,\text{mm}$ $F = 3.7\,\text{kN}$	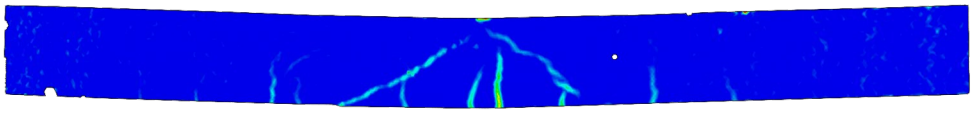
$u = 5.0\,\text{mm}$ $F = 7.8\,\text{kN}$	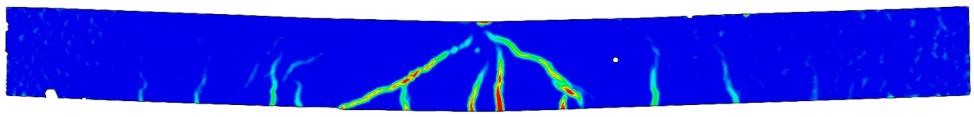
$u_{100\%} = 18.7\,\text{mm}$ $F_{100\%} = 12.3\,\text{kN}$	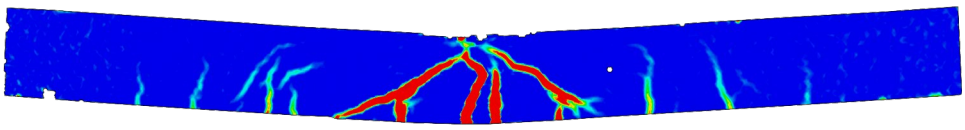
$u_{95\%} = 26.0\,\text{mm}$ $F_{95\%} = 11.7\,\text{kN}$	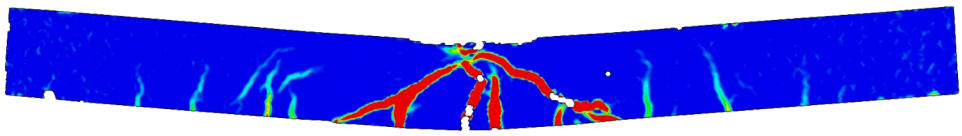
$u_{90\%} = 47.4\,\text{mm}$ $F_{90\%} = 11.1\,\text{kN}$	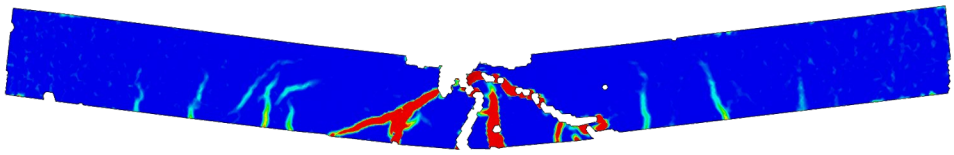
$u_{80\%} = 57.4\,\text{mm}$ $F_{80\%} = 9.9\,\text{kN}$	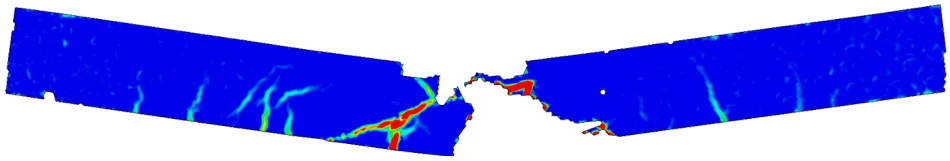
Principal strain [%]	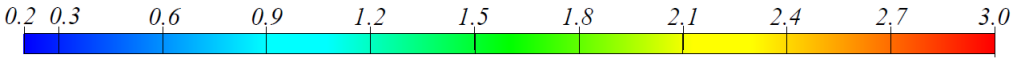

F.6.5 Specimen B-05

Table F.13 Strain field due to impact loading from DIC analysis for B-05, drop-height h = 5.0 m.

Deflection / Time	Strain field for impact loading: B-05
$u = 0$ mm $t = 0$ ms	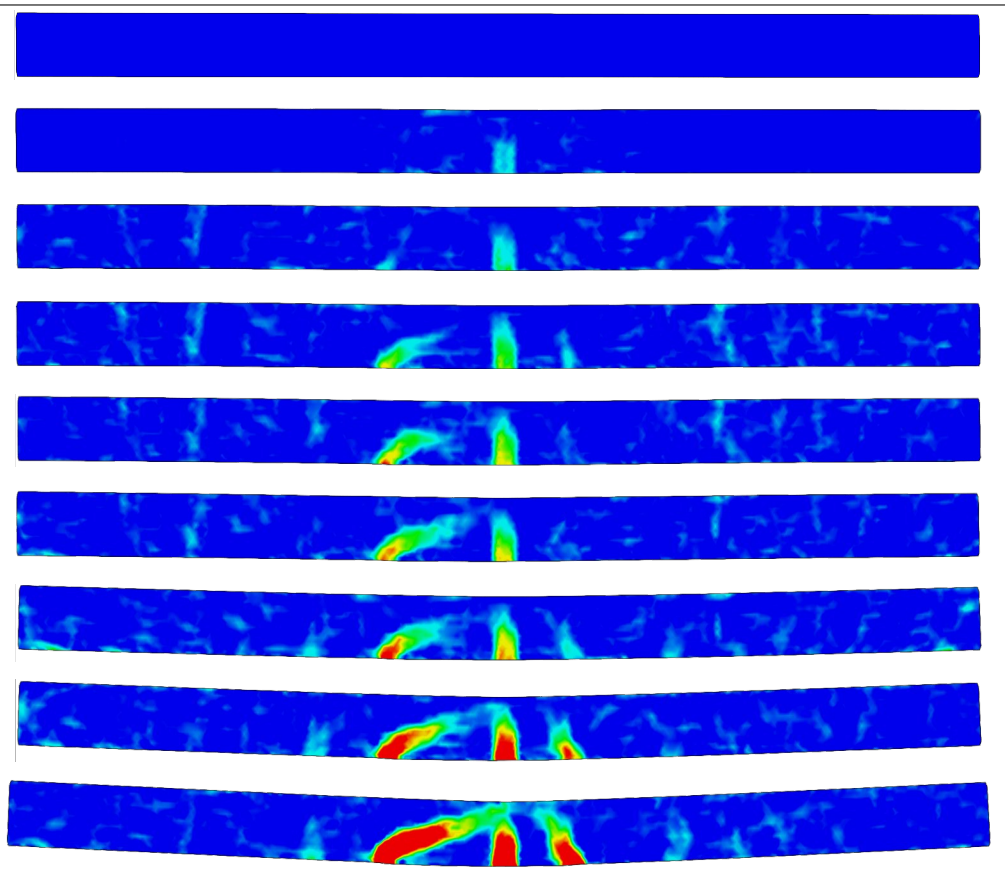
$u = 0.1$ mm $t = 0.2$ ms	
$u = 1.0$ mm $t = 0.4$ ms	
$u = 2.1$ mm $t = 0.6$ ms	
$u = 2.9$ mm $t = 0.8$ ms	
$u = 3.8$ mm $t = 1.0$ ms	
$u = 7.6$ mm $t = 2.0$ ms	
$u = 14.5$ mm $t = 4.0$ ms	
$u = 20.6$ mm[1] $t = 8.2$ ms	
Principal Strain [%]	

[1] Maximum deflection due to impact loading.

Table F.14 Strain field due to static loading from DIC analysis for B-05. Note that the strain field of the dynamic response has different limits in the colorscale (from 0.5 % to 5 %).

Deflection / Time	Strain field due to impact loading at maximum deflection: B-05
$u = 20.6\,\text{mm}$ $t = 8.2\,\text{ms}$	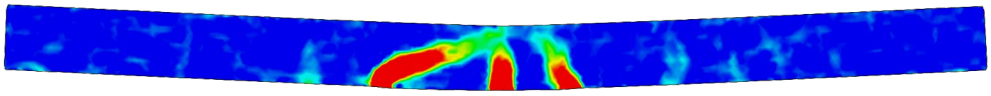
Deflection / Load	**Strain field due to static loading: B-05**
$u = 2.5\,\text{mm}$ $F = 3.5\,\text{kN}$ $u = 5.0\,\text{mm}$ $F = 7.3\,\text{kN}$ $u_{100\%} = 16.1\,\text{mm}$ $F_{100\%} = 12.0\,\text{kN}$ $u_{95\%} = 40.5\,\text{mm}$ $F_{95\%} = 11.4\,\text{kN}$ $u_{90\%} = 47.2\,\text{mm}$ $F_{90\%} = 10.8\,\text{kN}$	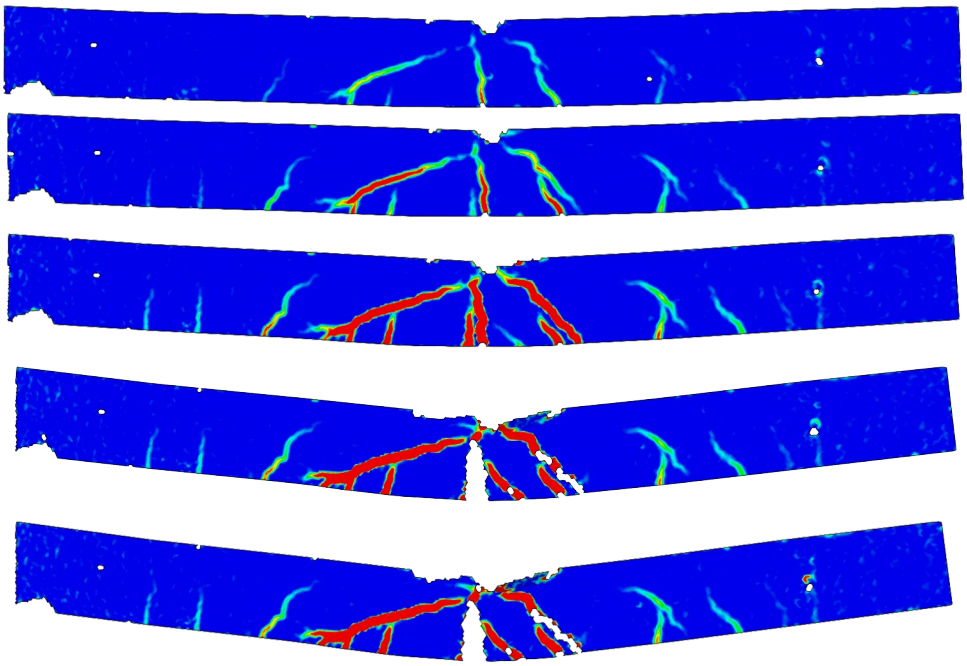
Principal strain [%]	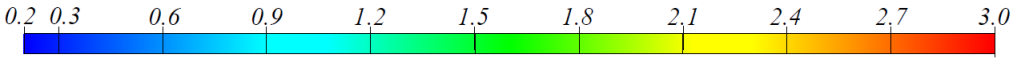

F.6.6 Specimen B-06

Table F.15 Strain field due to impact loading from DIC analysis for B-06, drop-height h = 5.0 m.

Deflection / Time	Strain field for impact loading: B-06
$u = 0$ mm $t = 0$ ms	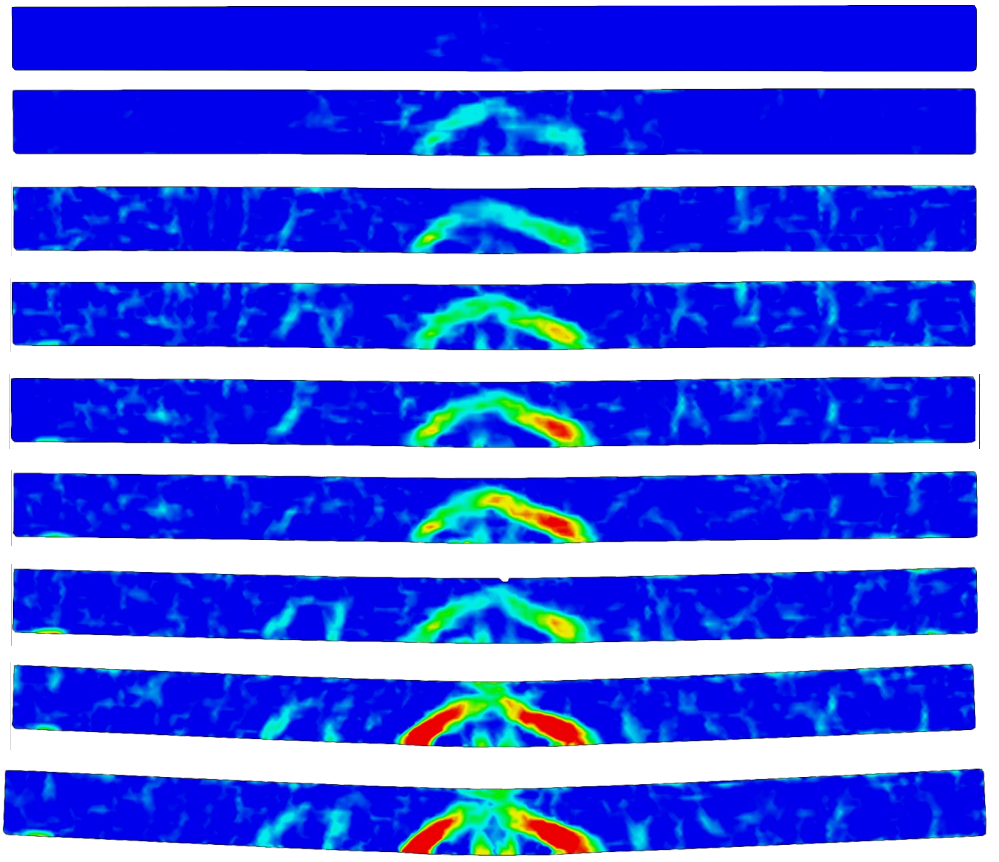
$u = 0.4$ mm $t = 0.2$ ms	
$u = 1.6$ mm $t = 0.4$ ms	
$u = 2.6$ mm $t = 0.6$ ms	
$u = 3.7$ mm $t = 0.8$ ms	
$u = 4.5$ mm $t = 1.0$ ms	
$u = 8.3$ mm $t = 2.0$ ms	
$u = 15.3$ mm $t = 4.0$ ms	
$u = 20.1$ mm [1] $t = 7.8$ ms	
Principal Strain [%]	

[1] Maximum deflection due to impact loading.

Table F.16 Strain field due to static loading from DIC analysis for B-06. Note that the strain field of the dynamic response has different limits in the colorscale (from 0.5 % to 5 %).

Deflection / Time	Strain field due to impact loading at maximum deflection: B-06
$u = 20.1$ mm $t = 7.8$ ms	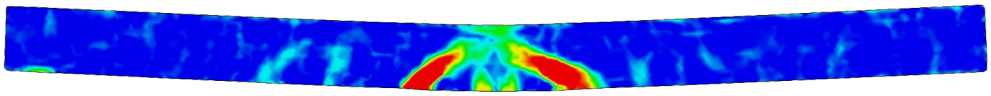
Deflection / Load	**Strain field due to static loading: B-06**
$u = 2.5$ mm $F = 4.1$ kN $u = 5.0$ mm $F = 8.9$ kN $u_{100\%} = 13.0$ mm $F_{100\%} = 13.1$ kN $u_{95\%} = 29.4$ mm $F_{95\%} = 12.4$ kN $u_{90\%} = 47.5$ mm $F_{90\%} = 11.8$ kN	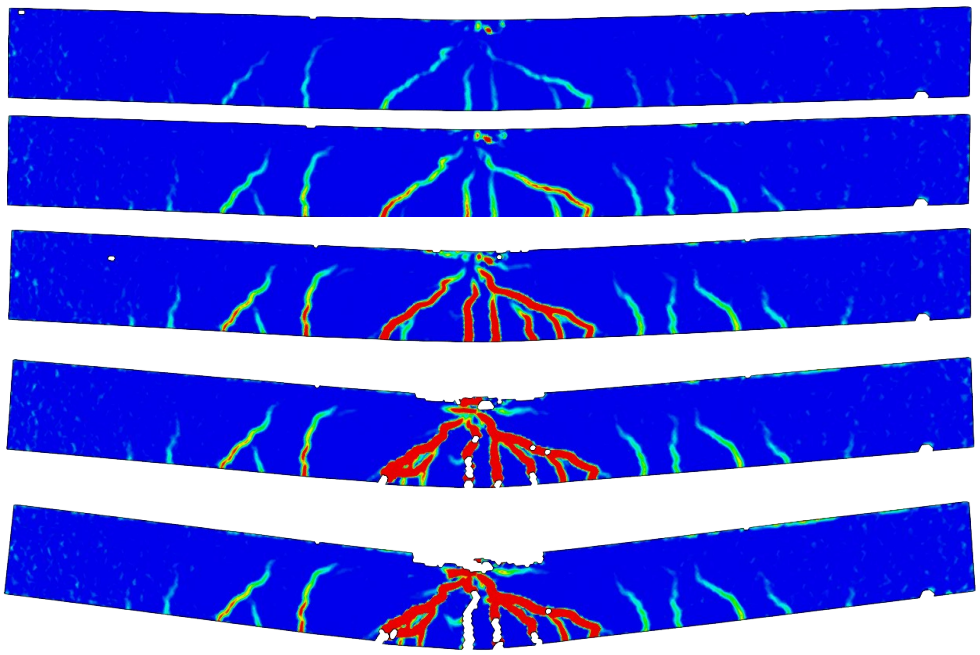
Principal strain [%]	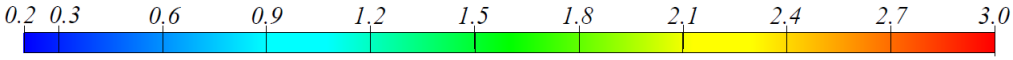

F.6.7 Specimen B-07

Table F.17 Strain field due to static loading from DIC analysis for B-07. Note that B-07 was tested only for static loading.

Deflection / Load	Strain field due to static loading: B-07
$u = 2.5\,\text{mm}$ $F = 5.8\,\text{kN}$	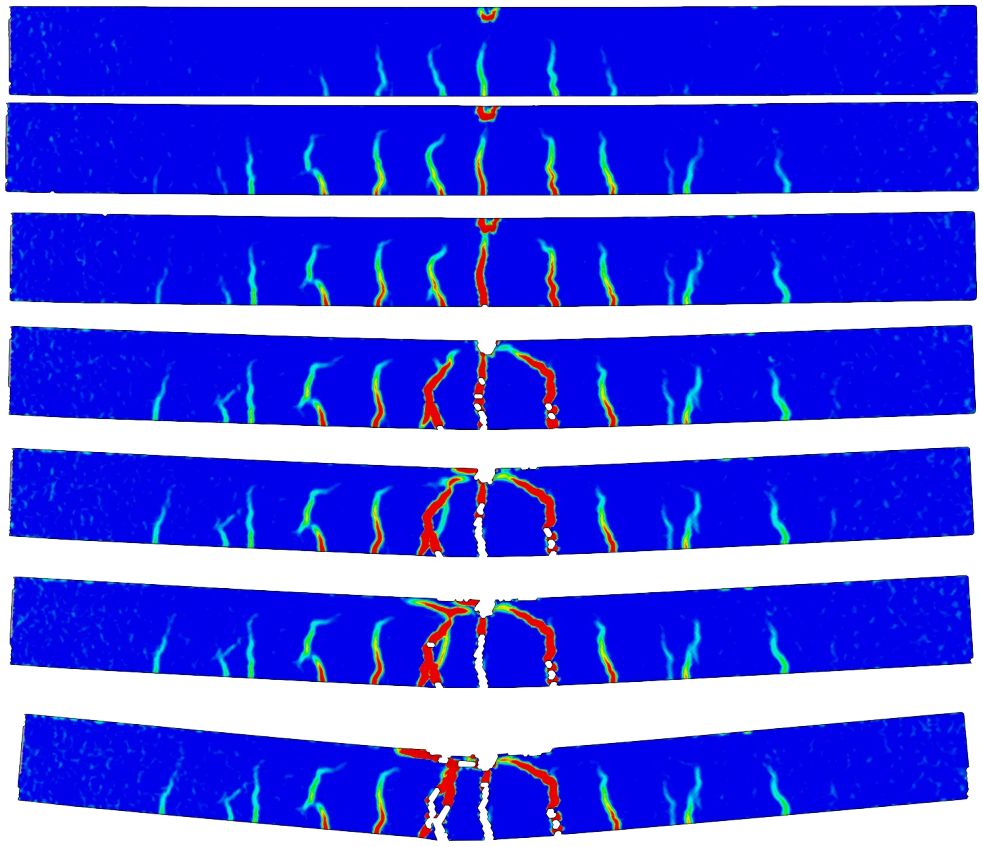
$u = 5.0\,\text{mm}$ $F = 10.4\,\text{kN}$	
$u = 7.5\,\text{mm}$ $F = 11.8\,\text{kN}$	
$u_{100\%} = 13.0\,\text{mm}$ $F_{100\%} = 13.1\,\text{kN}$	
$u_{95\%} = 29.4\,\text{mm}$ $F_{95\%} = 12.4\,\text{kN}$	
$u_{90\%} = 47.5\,\text{mm}$ $F_{90\%} = 11.8\,\text{kN}$	
$u_{80\%} = 47.5\,\text{mm}$ $F_{80\%} = 11.8\,\text{kN}$	
Principal strain [%]	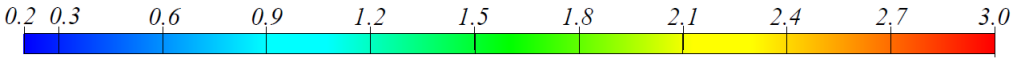

F.6.8 Specimen B-08

Table F.18 Strain field due to static loading from DIC analysis for B-08. Note that B-08 was tested only for static loading.

Deflection / Load	Strain field due to static loading: B-08
$u = 2.5$ mm $F = 6.3$ kN	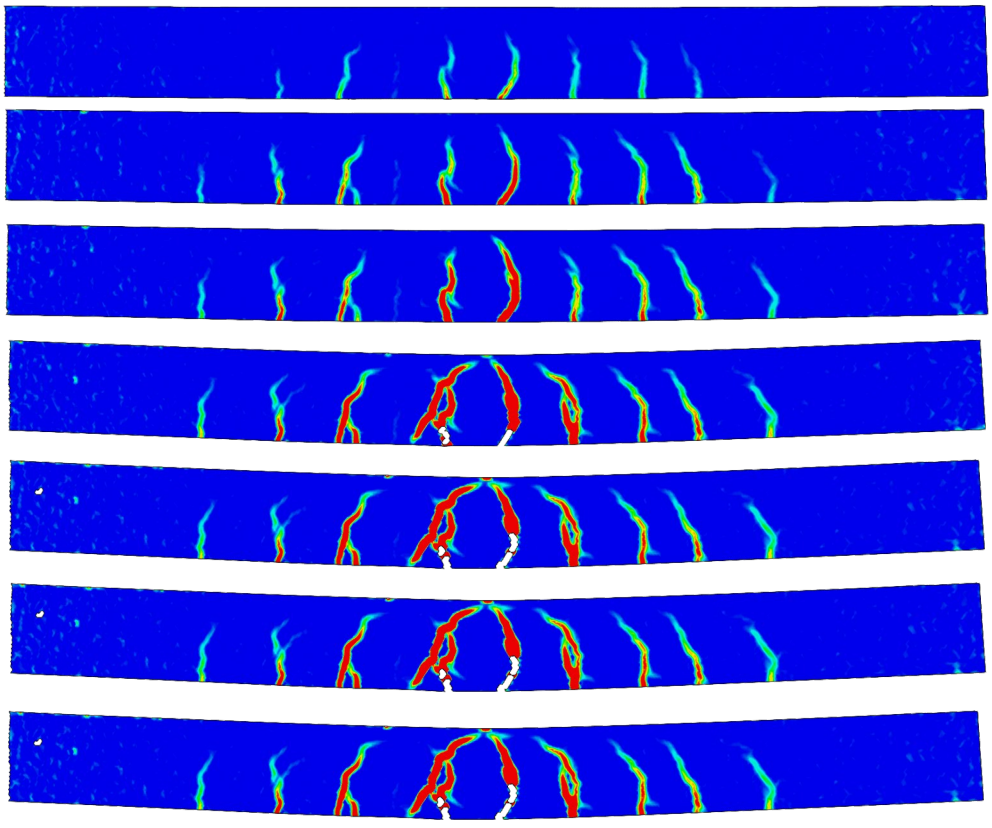
$u = 5.0$ mm $F = 10.1$ kN	
$u = 7.5$ mm $F = 11.7$ kN	
$u_{100\%} = 16.5$ mm $F_{100\%} = 13.9$ kN	
$u_{95\%} = 19.0$ mm $F_{95\%} = 13.2$ kN	
$u_{90\%} = 24.7$ mm $F_{90\%} = 12.5$ kN	
$u_{80\%} = 44.1$ mm $F_{80\%} = 11.1$ kN	
Principal strain [%]	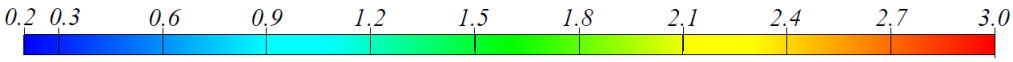

F.6.9 Specimen B-09

Table F.19 Strain field due to static loading from DIC analysis for B-09. Note that B-09 was tested only for static loading.

Deflection / Load	Strain field due to static loading: B-09
$u = 2.5\,\text{mm}$ $F = 7.6\,\text{kN}$	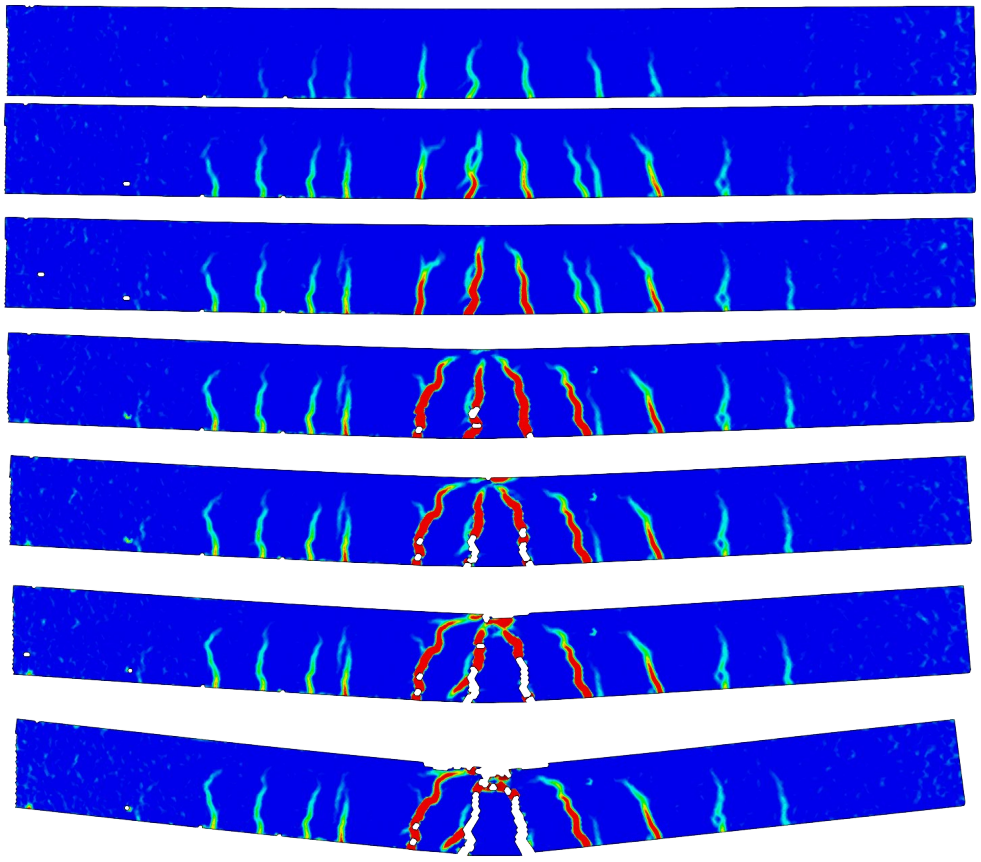
$u = 5.0\,\text{mm}$ $F = 11.3\,\text{kN}$	
$u = 7.5\,\text{mm}$ $F = 12.7\,\text{kN}$	
$u_{100\%} = 16.9\,\text{mm}$ $F_{100\%} = 14.1\,\text{kN}$	
$u_{95\%} = 22.8\,\text{mm}$ $F_{95\%} = 13.4\,\text{kN}$	
$u_{90\%} = 29.4\,\text{mm}$ $F_{90\%} = 12.7\,\text{kN}$	
$u_{80\%} = 50.7\,\text{mm}$ $F_{80\%} = 11.3\,\text{kN}$	
Principal strain [%]	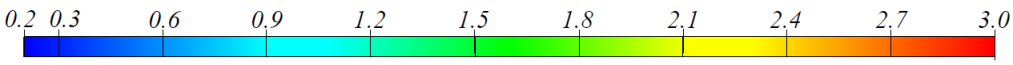

F.6.10 Specimen B-10

Table F.20 Strain field due to impact loading from DIC analysis for B-10, drop-height h = 2.5 m.

Deflection / Time	Strain field for impact loading: B-10
$u = 0$ mm $t = 0$ ms $u = 0.3$ mm $t = 0.2$ ms $u = 1.2$ mm $t = 0.4$ ms $u = 1.9$ mm $t = 0.6$ ms $u = 2.4$ mm $t = 0.8$ ms $u = 3.0$ mm $t = 1.0$ ms $u = 5.5$ mm $t = 2.0$ ms $u = 9.2$ mm $t = 4.0$ ms $u = 10.5$ mm [1] $t = 6.0$ ms	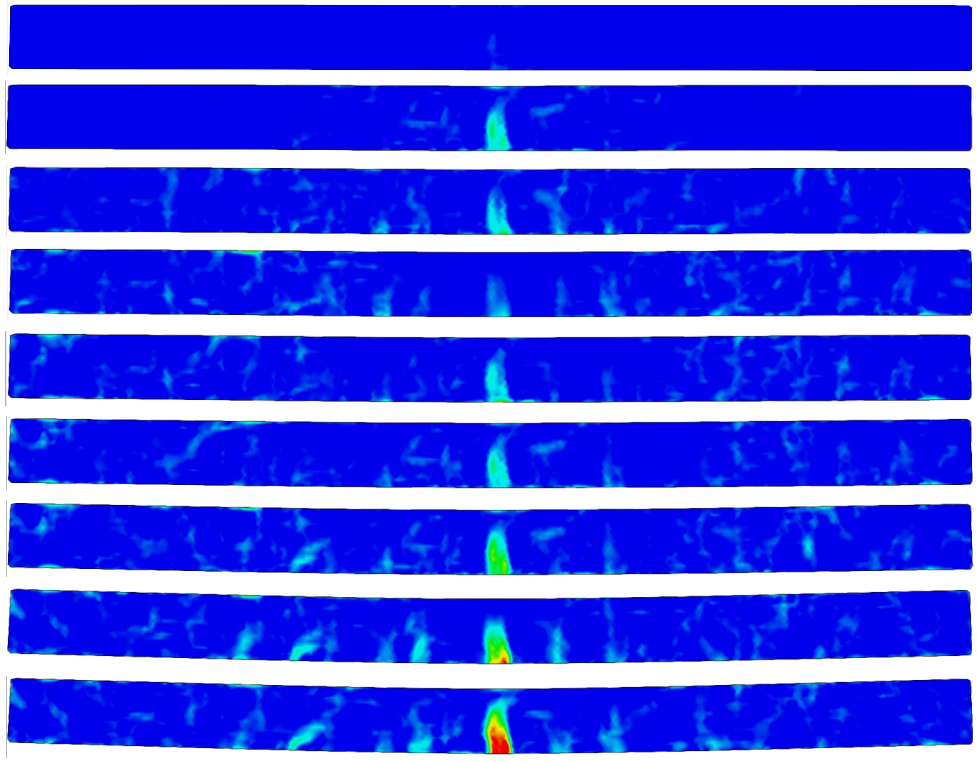
Principal Strain [%]	

[1] Maximum deflection due to impact loading.

Table F.21 Strain field due to static loading from DIC analysis for B-10. Note that the strain field of the dynamic response has different limits in the colorscale (from 0.5 % to 5 %).

Deflection / Time	Strain field due to impact loading at maximum deflection: B-10
$u = 10.5\,\text{mm}$ $t = 6.0\,\text{ms}$	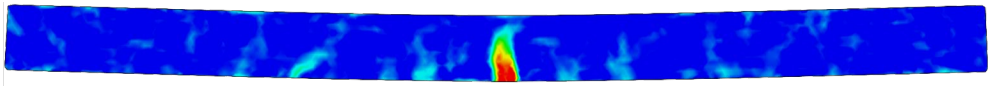
Deflection / Load	**Strain field due to static loading: B-10**
$u = 2.5\,\text{mm}$ $F = 5.5\,\text{kN}$	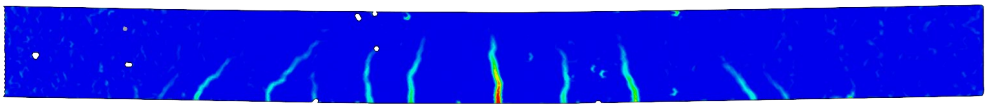
$u = 5.0\,\text{mm}$ $F = 11.0\,\text{kN}$	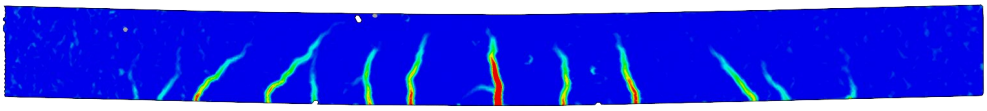
$u_{100\%} = 12.4\,\text{mm}$ $F_{100\%} = 14.0\,\text{kN}$	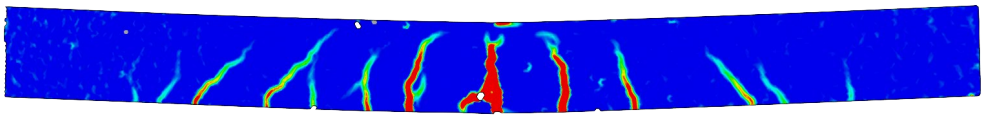
$u_{95\%} = 16.6\,\text{mm}$ $F_{95\%} = 13.3\,\text{kN}$	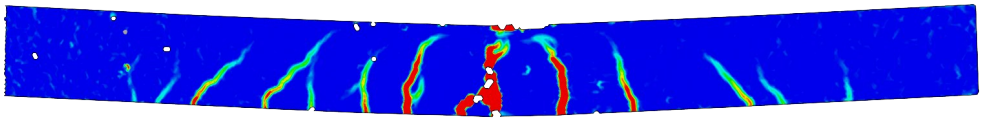
$u_{90\%} = 27.8\,\text{mm}$ $F_{90\%} = 12.6\,\text{kN}$	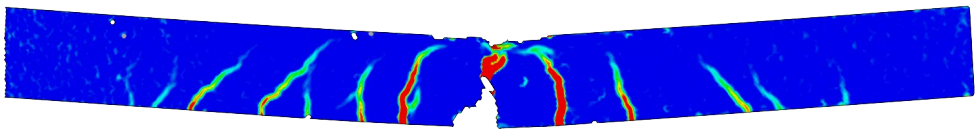
Principal strain [%]	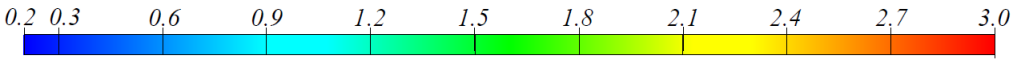

F.6.11 Specimen B-11

Table F.22 Strain field due to impact loading from DIC analysis for B-11, drop-height h = 2.5 m.

Deflection / Time	Strain field for impact loading: B-11
$u = 0$ mm $t = 0$ ms	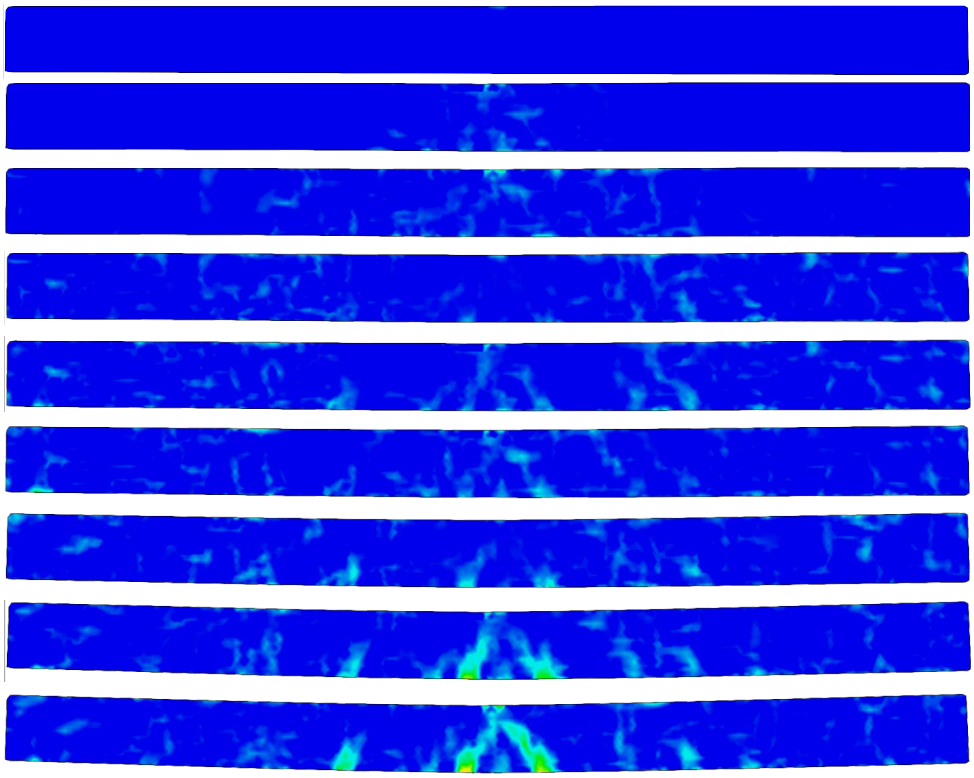
$u = 0.1$ mm $t = 0.2$ ms	
$u = 0.8$ mm $t = 0.4$ ms	
$u = 1.7$ mm $t = 0.6$ ms	
$u = 2.4$ mm $t = 0.8$ ms	
$u = 3.0$ mm $t = 1.0$ ms	
$u = 6.0$ mm $t = 2.0$ ms	
$u = 9.5$ mm $t = 4.0$ ms	
$u = 11.2$ mm [1] $t = 6.4$ ms	
Principal Strain [%]	

[1] Maximum deflection due to impact loading.

Table F.23 Strain field due to static loading from DIC analysis for B-11. Note that the strain field of the dynamic response has different limits in the colorscale (from 0.5 % to 5 %).

Deflection / Time	Strain field due to impact loading at maximum deflection: B-11
$u = 11.2\,\text{mm}$ $t = 6.4\,\text{ms}$	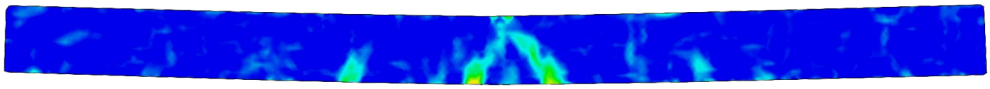
Deflection / Load	**Strain field due to static loading: B-11**
$u = 2.5\,\text{mm}$ $F = 4.2\,\text{kN}$ $u = 5.0\,\text{mm}$ $F = 9.2\,\text{kN}$ $u_{100\%} = 17.6\,\text{mm}$ $F_{100\%} = 13.3\,\text{kN}$ $u_{95\%} = 20.3\,\text{mm}$ $F_{95\%} = 12.7\,\text{kN}$ $u_{90\%} = 45.9\,\text{mm}$ $F_{90\%} = 10.7\,\text{kN}$	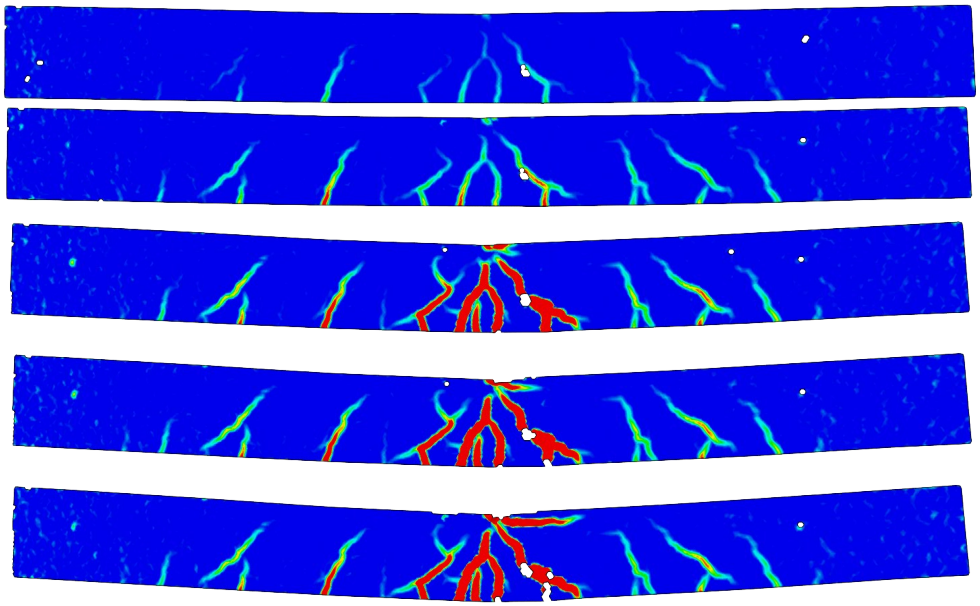
Principal strain [%]	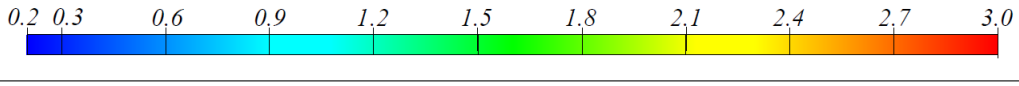

F.6.12 Specimen B-12

Table F.24 Strain field due to impact loading from DIC analysis for B-12, drop-height h = 2.5 m.

Deflection / Time	Strain field for impact loading: B-12
$u = 0$ mm $t = 0$ ms $u = 0.1$ mm $t = 0.2$ ms $u = 0.5$ mm $t = 0.4$ ms $u = 1.4$ mm $t = 0.6$ ms $u = 2.2$ mm $t = 0.8$ ms $u = 2.9$ mm $t = 1.0$ ms $u = 5.9$ mm $t = 2.0$ ms $u = 9.4$ mm $t = 4.0$ ms $u = 10.7$ mm [1] $t = 6.0$ ms	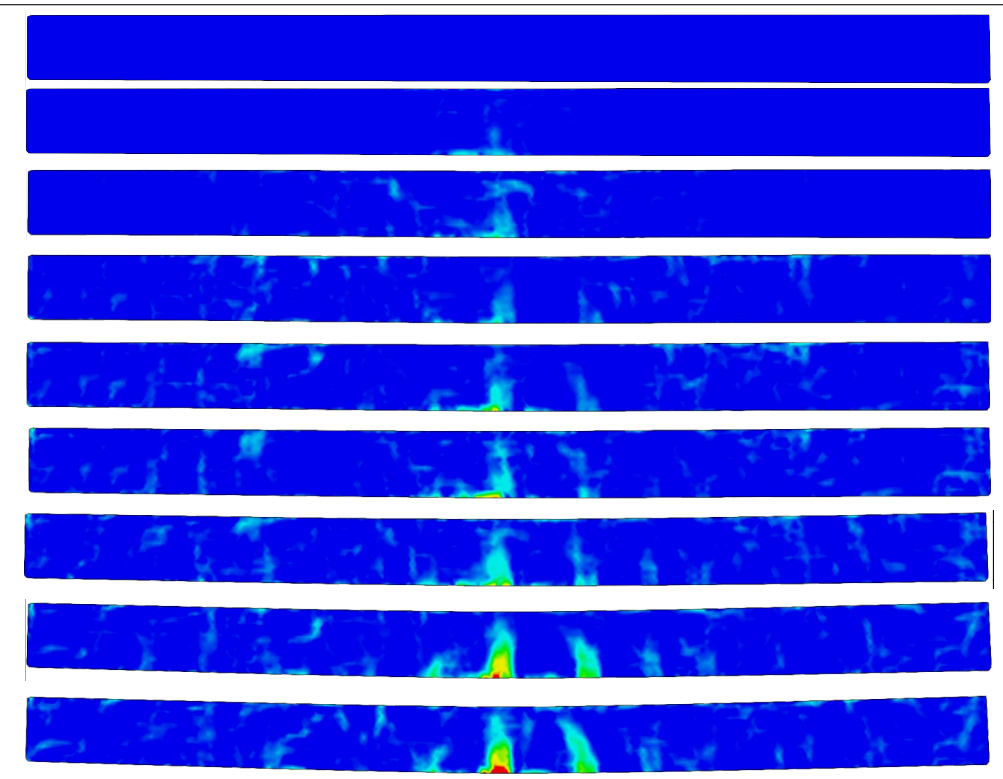
Principal Strain [%]	

[1] Maximum deflection due to impact loading.

Table F.25 Strain field due to static loading from DIC analysis for B-12. Note that the strain field of the dynamic response has different limits in the colorscale (from 0.5 % to 5 %).

Deflection / Time	Strain field due to impact loading at maximum deflection: B-12
$u = 10.7\,\text{mm}$ $t = 6.0\,\text{ms}$	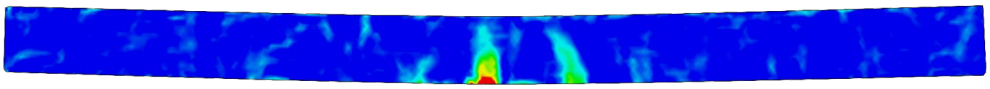
Deflection / Load	**Strain field due to static loading: B-12**
$u = 2.5\,\text{mm}$ $F = 5.1\,\text{kN}$ $u = 5.0\,\text{mm}$ $F = 10.8\,\text{kN}$ $u_{100\%} = 10.9\,\text{mm}$ $F_{100\%} = 14.0\,\text{kN}$ $u_{95\%} = 14.7\,\text{mm}$ $F_{95\%} = 13.3\,\text{kN}$ $u_{90\%} = 15.7\,\text{mm}$ $F_{90\%} = 12.6\,\text{kN}$ $u_{80\%} = 35.2\,\text{mm}$ $F_{80\%} = 11.2\,\text{kN}$	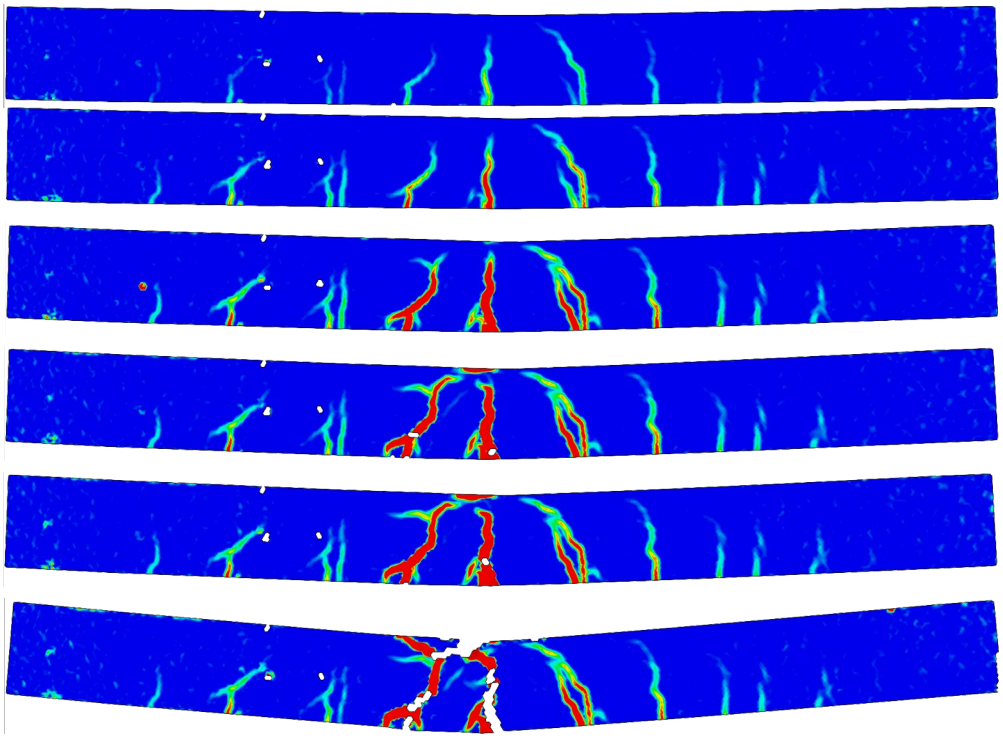
Principal strain [%]	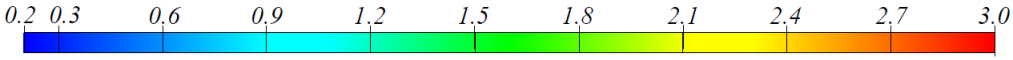

F.6.13 Specimen B-13

Table F.26 Strain field due to impact loading from DIC analysis for B-13, drop-height h = 5.0 m.

Deflection / Time	Strain field for impact loading: B-13
$u = 0$ mm $t = 0$ ms $u = 0.0$ mm $t = 0.2$ ms $u = 0.7$ mm $t = 0.4$ ms $u = 2.1$ mm $t = 0.6$ ms $u = 3.0$ mm $t = 0.8$ ms $u = 4.1$ mm $t = 1.0$ ms $u = 7.9$ mm $t = 2.0$ ms $u = 14.8$ mm $t = 4.0$ ms $u = 20.9$ mm [1] $t = 8.2$ ms	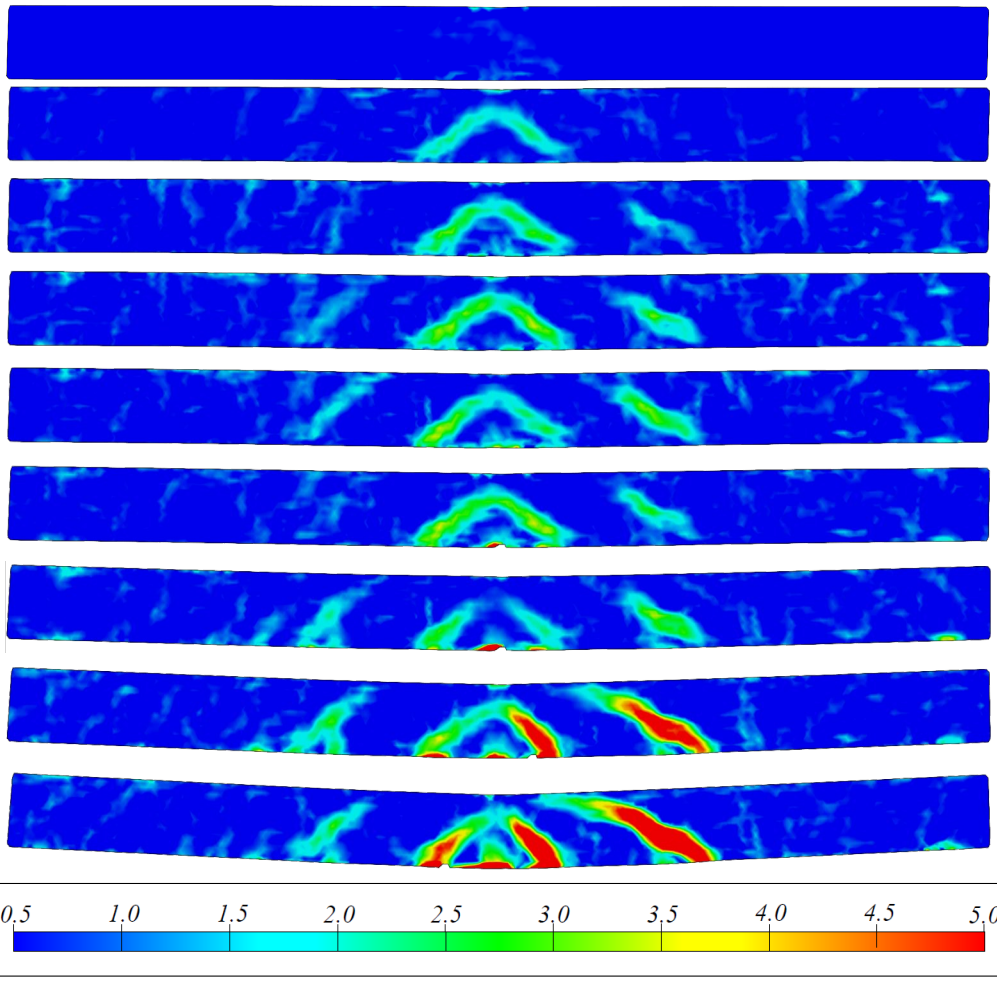
Principal Strain [%]	

[1] Maximum deflection due to impact loading.

Table F.27 Strain field due to static loading from DIC analysis for B-13. Note that the strain field of the dynamic response has different limits in the colorscale (from 0.5 % to 5 %).

Deflection / Time	Strain field due to impact loading at maximum deflection: B-13
$u = 20.9\,\text{mm}$ $t = 8.2\,\text{ms}$	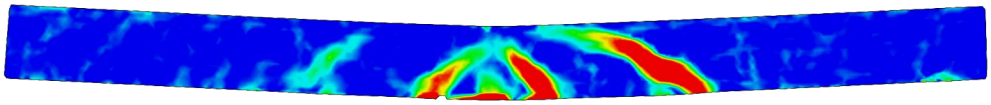
Deflection / Load	**Strain field due to static loading: B-13**
$u = 2.5\,\text{mm}$ $F = 2.7\,\text{kN}$	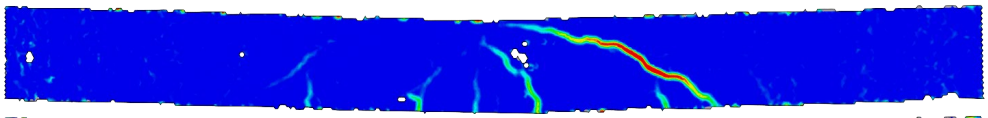
$u = 5.0\,\text{mm}$ $F = 4.0\,\text{kN}$	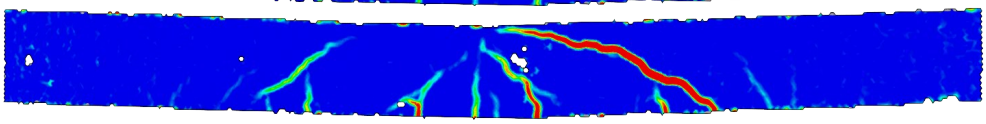
$u_{100\%} = 6.7\,\text{mm}$ $F_{100\%} = 8.5\,\text{kN}$	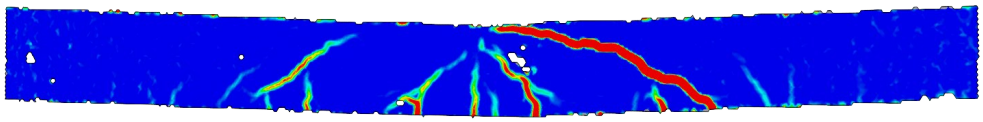
$u_{95\%} = 6.9\,\text{mm}$ $F_{95\%} = 8.1\,\text{kN}$	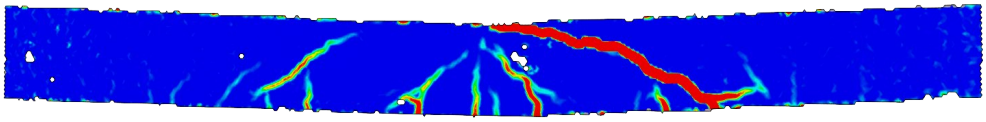
$u_{90\%} = 7.2\,\text{mm}$ $F_{90\%} = 7.6\,\text{kN}$	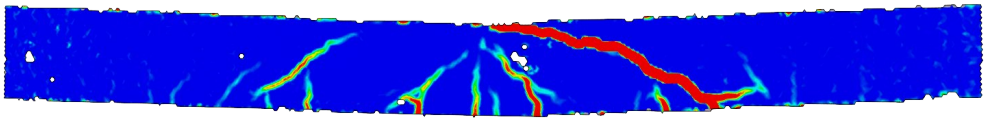
$u_{80\%} = 9.4\,\text{mm}$ $F_{80\%} = 6.8\,\text{kN}$	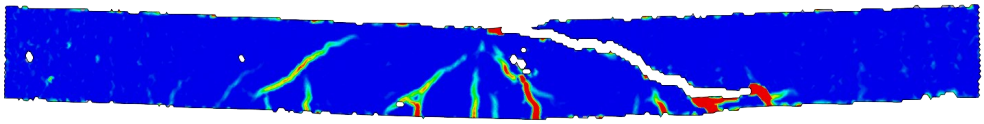
Principal strain [%]	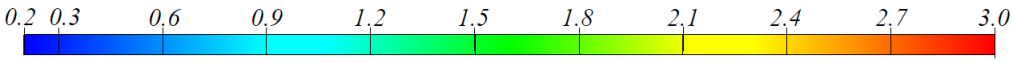

F.6.14 Specimen B-14

Table F.28 Strain field due to impact loading from DIC analysis for B-14, drop-height h = 5.0 m.

Deflection / Time	Strain field for impact loading: B-14
$u = 0$ mm $t = 0$ ms	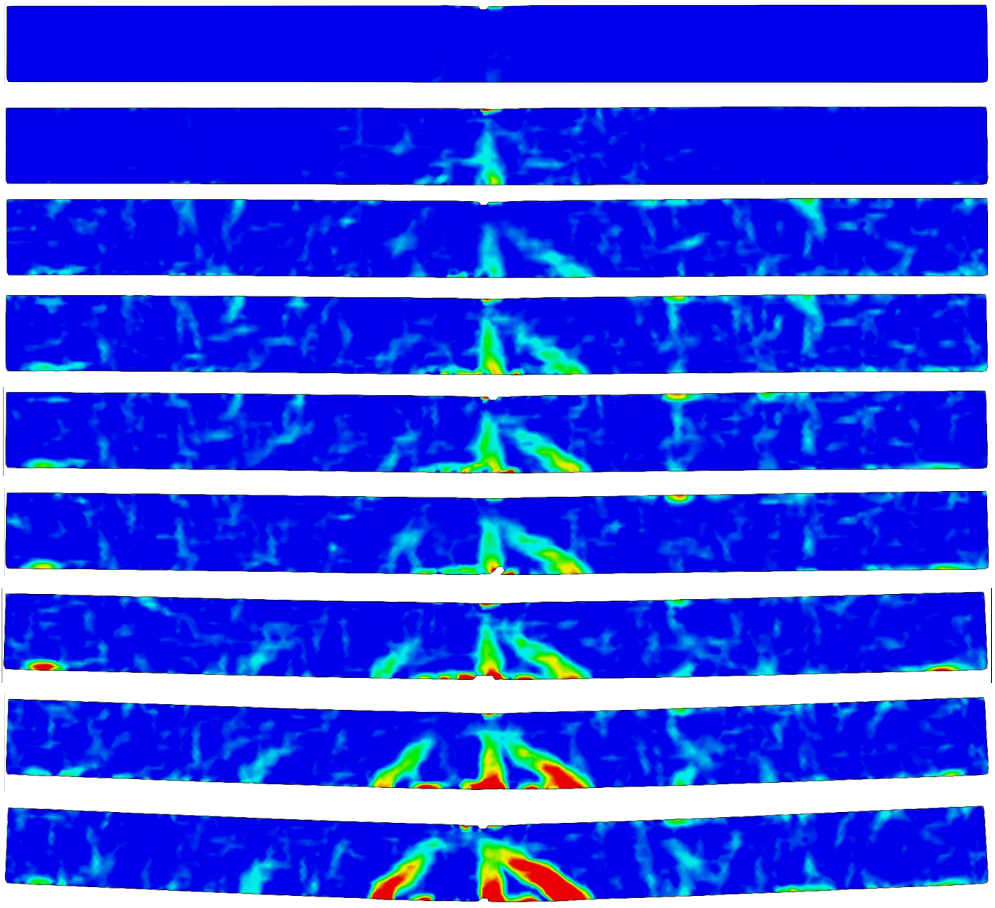
$u = 0.0$ mm $t = 0.2$ ms	
$u = 0.3$ mm $t = 0.4$ ms	
$u = 1.3$ mm $t = 0.6$ ms	
$u = 2.4$ mm $t = 0.8$ ms	
$u = 3.2$ mm $t = 1.0$ ms	
$u = 7.1$ mm $t = 2.0$ ms	
$u = 13.6$ mm $t = 4.0$ ms	
$u = 19.0$ mm [1] $t = 8.0$ ms	
Principal Strain [%]	0.5 1.0 1.5 2.0 2.5 3.0 3.5 4.0 4.5 5.0

[1] Maximum deflection due to impact loading.

Table F.29 Strain field due to static loading from DIC analysis for B-14. Note that the strain field of the dynamic response has different limits in the colorscale (from 0.5 % to 5 %).

Deflection / Time	Strain field due to impact loading at maximum deflection: B-14
$u = 19.0\,\text{mm}$ $t = 8.0\,\text{ms}$	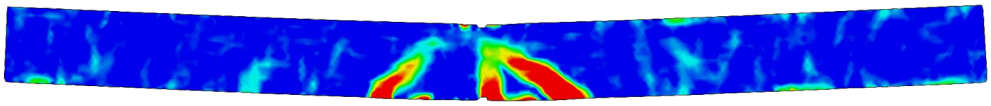
Deflection / Load	**Strain field due to static loading: B-14**
$u = 2.5\,\text{mm}$ $F = 4.3\,\text{kN}$	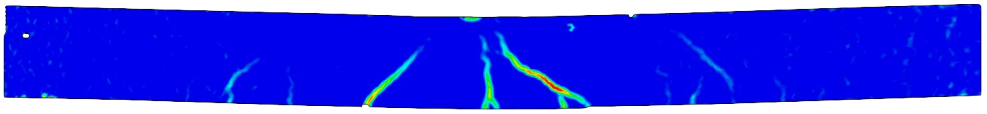
$u = 5.0\,\text{mm}$ $F = 9.1\,\text{kN}$	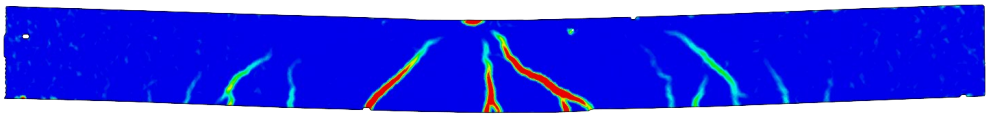
$u_{100\%} = 12.1\,\text{mm}$ $F_{100\%} = 13.5\,\text{kN}$	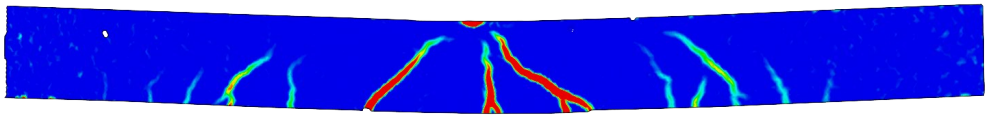
$u_{95\%} = 20.4\,\text{mm}$ $F_{95\%} = 12.9\,\text{kN}$	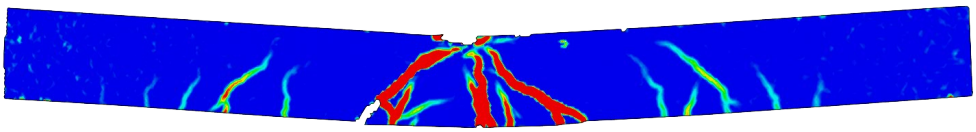
$u_{90\%} = 36.1\,\text{mm}$ $F_{90\%} = 12.2\,\text{kN}$	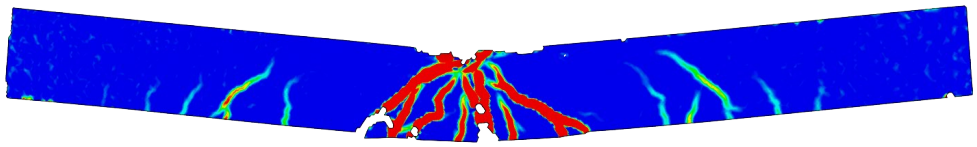
$u_{80\%} = 55.8\,\text{mm}$ $F_{80\%} = 10.8\,\text{kN}$	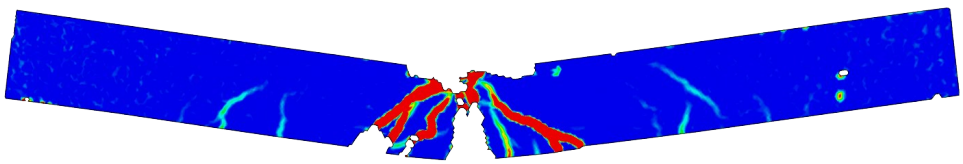
Principal strain [%]	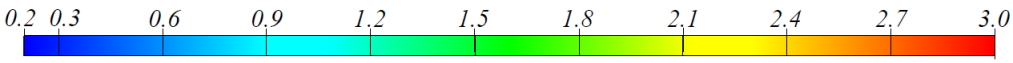

F.6.15 Specimen B-15

Table F.30 Strain field due to impact loading from DIC analysis for B-15, drop-height h = 5.0 m.

Deflection / Time	Strain field for impact loading: B-15
$u = 0$ mm $t = 0$ ms	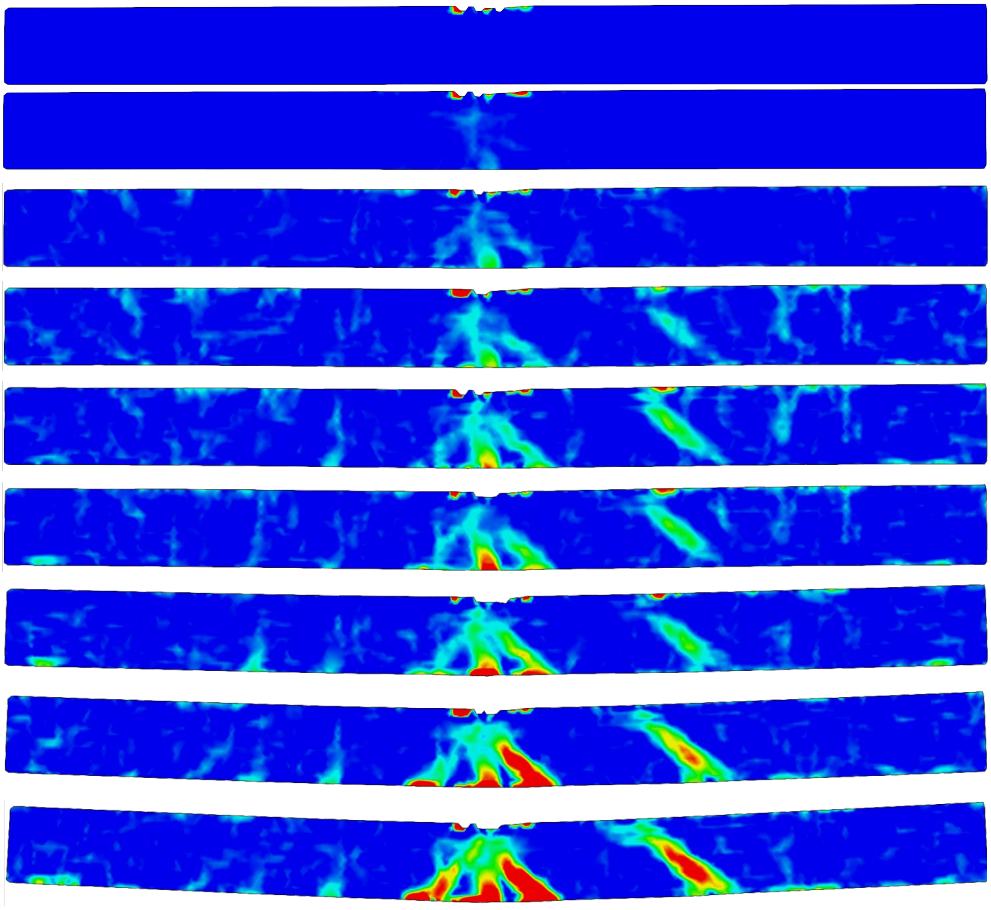
$u = 0.0$ mm $t = 0.2$ ms	
$u = 0.7$ mm $t = 0.4$ ms	
$u = 1.8$ mm $t = 0.6$ ms	
$u = 2.9$ mm $t = 0.8$ ms	
$u = 3.9$ mm $t = 1.0$ ms	
$u = 7.7$ mm $t = 2.0$ ms	
$u = 14.5$ mm $t = 4.0$ ms	
$u = 19.8$ mm [1] $t = 7.6$ ms	
Principal Strain [%]	0.5 1.0 1.5 2.0 2.5 3.0 3.5 4.0 4.5 5.0

[1] Maximum deflection due to impact loading.

Table F.31 Strain field due to static loading from DIC analysis for B-15. Note that the strain field of the dynamic response has different limits in the colorscale (from 0.5 % to 5 %).

Deflection / Time	Strain field due to impact loading at maximum deflection: B-15
$u = 19.8$ mm $t = 7.6$ ms	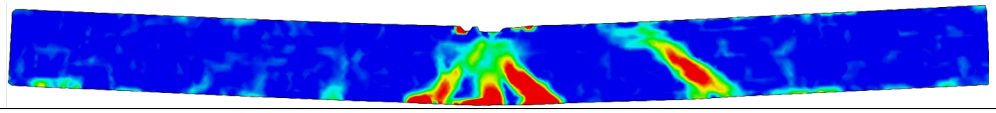
Deflection / Load	**Strain field due to static loading: B-15**
$u = 2.5$ mm $F = 4.2$ kN	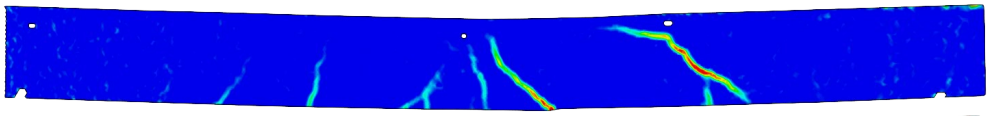
$u = 5.0$ mm $F = 8.9$ kN	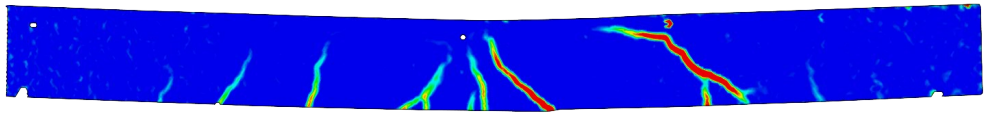
$u_{100\%} = 13.7$ mm $F_{100\%} = 13.2$ kN	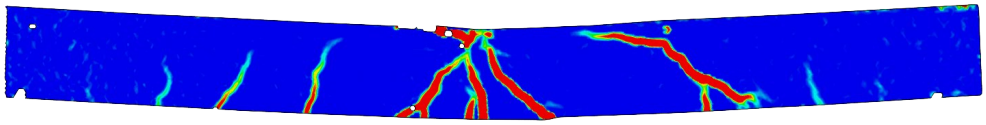
$u_{95\%} = 29.6$ mm $F_{95\%} = 12.5$ kN	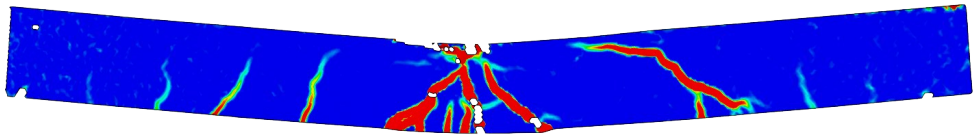
$u_{90\%} = 32.0$ mm $F_{90\%} = 11.9$ kN	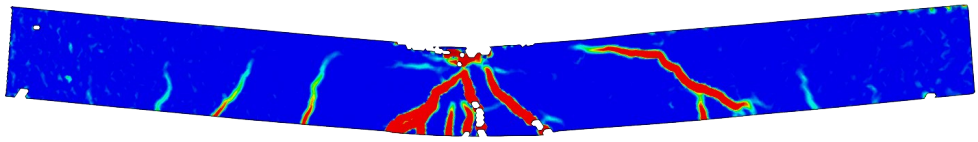
$u_{80\%} = 45.9$ mm $F_{80\%} = 10.6$ kN	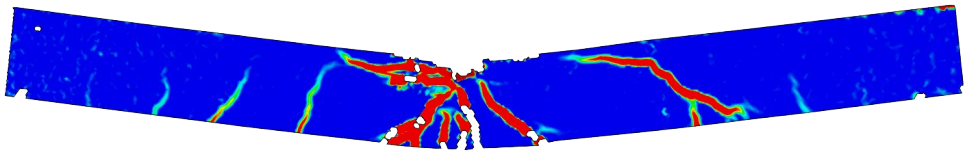
Principal strain [%]	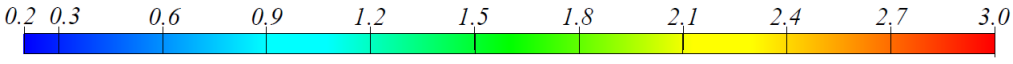

F.6.16 Specimen B-16

Table F.32 Strain field due to static loading from DIC analysis for B-16. Note that B-16 was tested only for static loading.

Deflection / Load	Strain field due to static loading: B-16
$u = 2.5\,\text{mm}$ $F = 6.7\,\text{kN}$	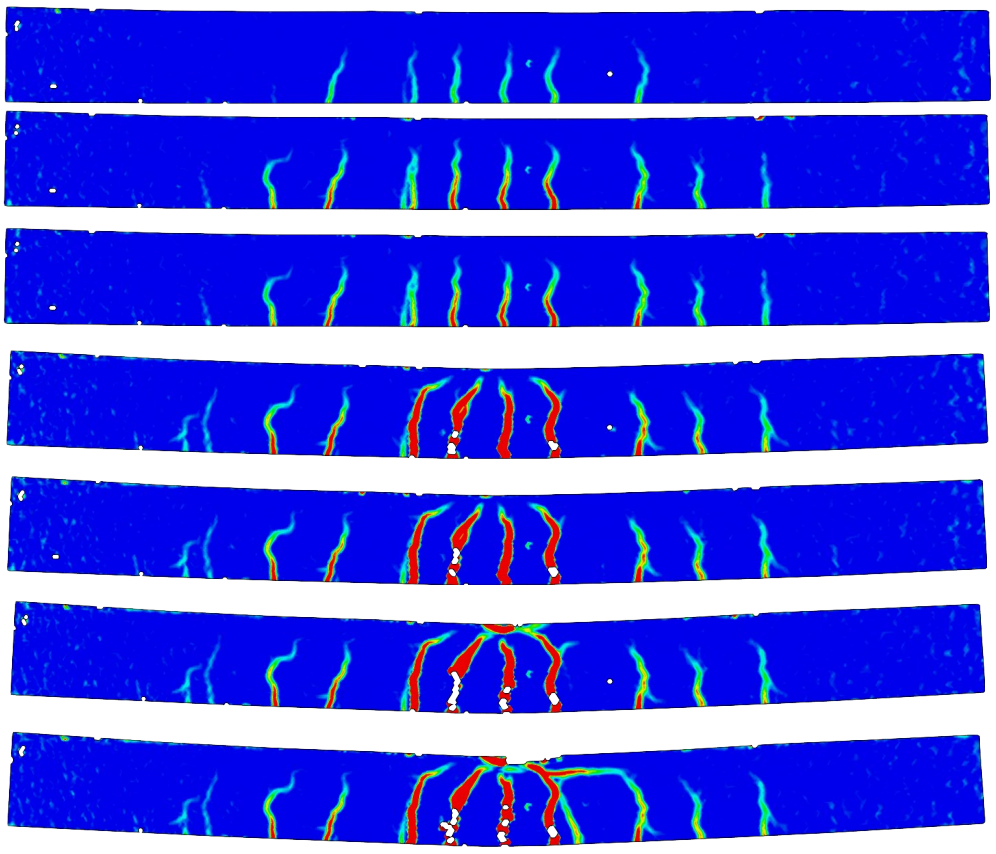
$u = 5.0\,\text{mm}$ $F = 11.0\,\text{kN}$	
$u = 7.5\,\text{mm}$ $F = 12.4\,\text{kN}$	
$u_{100\%} = 15.6\,\text{mm}$ $F_{100\%} = 14.5\,\text{kN}$	
$u_{95\%} = 16.8\,\text{mm}$ $F_{95\%} = 13.8\,\text{kN}$	
$u_{90\%} = 20.9\,\text{mm}$ $F_{90\%} = 13.1\,\text{kN}$	
$u_{80\%} = 23.1\,\text{mm}$ $F_{80\%} = 11.6\,\text{kN}$	
Principal strain [%]	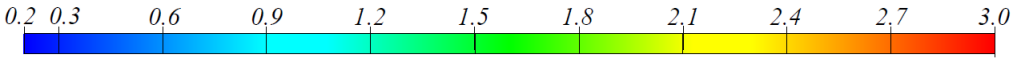

F.6.17 Specimen B-17

Table F.33 Strain field due to static loading from DIC analysis for B-17. Note that B-17 was tested only for static loading.

Deflection / Load	Strain field due to static loading: B-17
$u = 2.5$ mm $F = 6.1$ kN	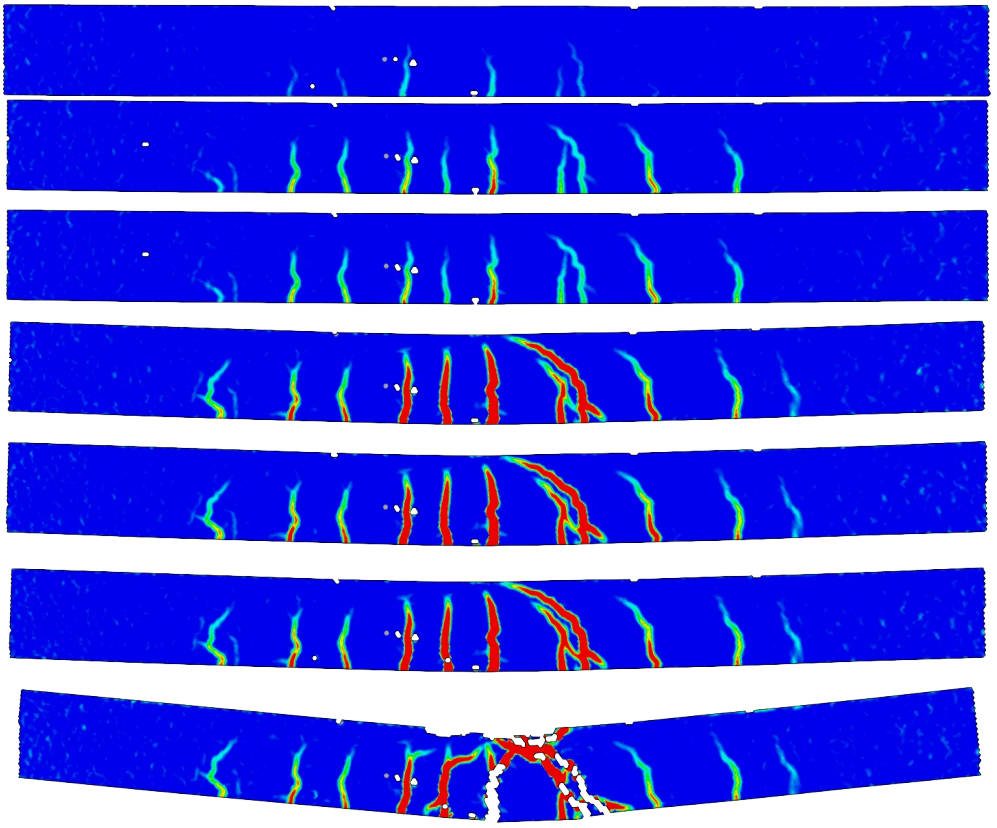
$u = 5.0$ mm $F = 10.9$ kN	
$u = 7.5$ mm $F = 12.1$ kN	
$u_{100\%} = 15.2$ mm $F_{100\%} = 13.8$ kN	
$u_{95\%} = 15.4$ mm $F_{95\%} = 13.1$ kN	
$u_{90\%} = 15.5$ mm $F_{90\%} = 12.4$ kN	
$u_{80\%} = 47.1$ mm $F_{80\%} = 11.0$ kN	
Principal strain [%]	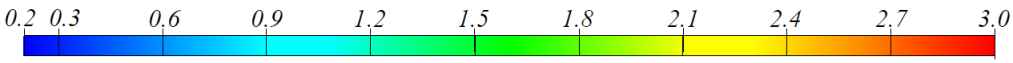

F.6.18 Specimen B-18

Table F.34 Strain field due to static loading from DIC analysis for B-18. Note that B-18 was tested only for static loading.

Deflection / Load	Strain field due to static loading: B-18
$u = 2.5$ mm $F = 7.3$ kN	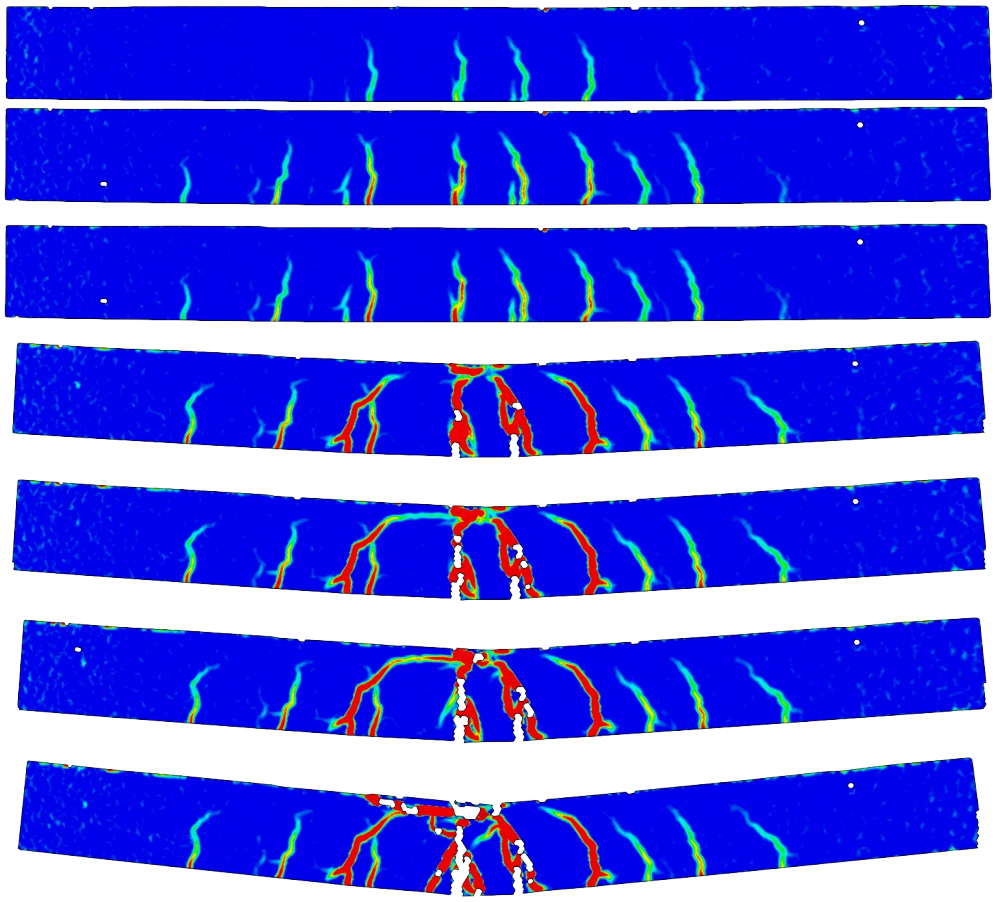
$u = 5.0$ mm $F = 11.2$ kN	
$u = 7.5$ mm $F = 12.7$ kN	
$u_{100\%} = 25.6$ mm $F_{100\%} = 14.1$ kN	
$u_{95\%} = 31.1$ mm $F_{95\%} = 13.4$ kN	
$u_{90\%} = 33.9$ mm $F_{90\%} = 12.7$ kN	
$u_{80\%} = 48.5$ mm $F_{80\%} = 11.3$ kN	
Principal strain [%]	

F.7 Cracking Response

F.7.1 Overview

Here, the structural response as well as the strain field of certain beams from all three series will be discussed in detail. The specimens investigated more thoroughly were selected in order to highlight differences between beam responses. The strain field is presented at midspan deflections $u = 2.5$ mm and $u = 5.0$ mm for all beams, for which the specimens show a linear-elastic response. Moreover, $u = 2.5$ mm and $u = 7.5$ mm are used to represent the cracking pattern when the undamaged beams exhibit a at state-II and state-III response, respectively.

The strain field at $u = 5.0$ mm for Series-3 happens to occur in close proximity to when a state-III response of the midspan cross-section is initiated.

Thereafter, the strain field at ultimate load $F_{100\%}$ are presented for all beams, and following that, the structural response is traced by presenting the strain fields at load levels of 95%, 90% and, if data is available, at 80%.

F.7.2 Series-3

F.7.2.1 Beam B-08

The structural response at midspan for beam B-08 is presented in Figure F.14 together with highlighted points; the strain field at given point of the structural response is presented in Table F.35. Beam B-08 exhibits values of $\theta_{pl,\%}$ similar to average gathered for beams in Series-3

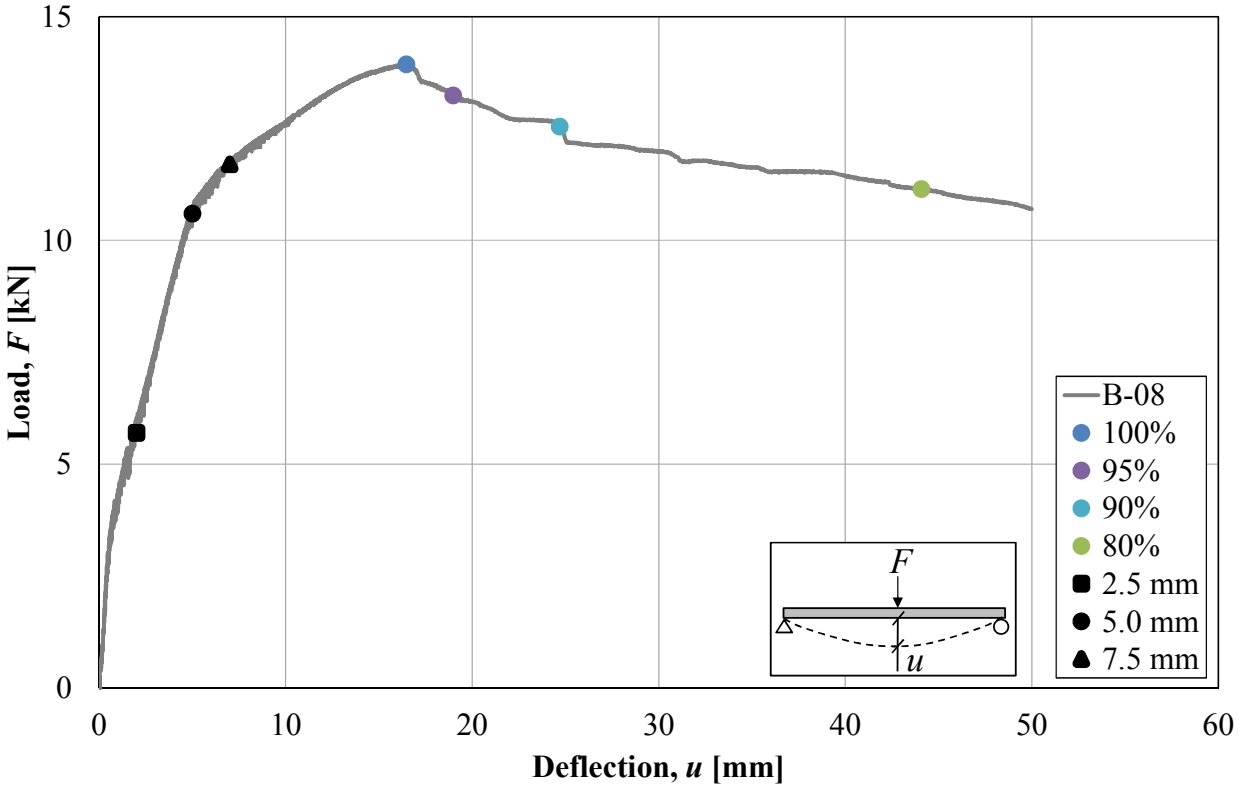

Figure F.14 Load-deflection curve of B-08 with highlighted points.

Table F.35 Strain field due to static loading from DIC analysis for B-08.

Deflection / Load	Strain field due to static loading: B-08
$u = 2.5$ mm $F = 6.3$ kN	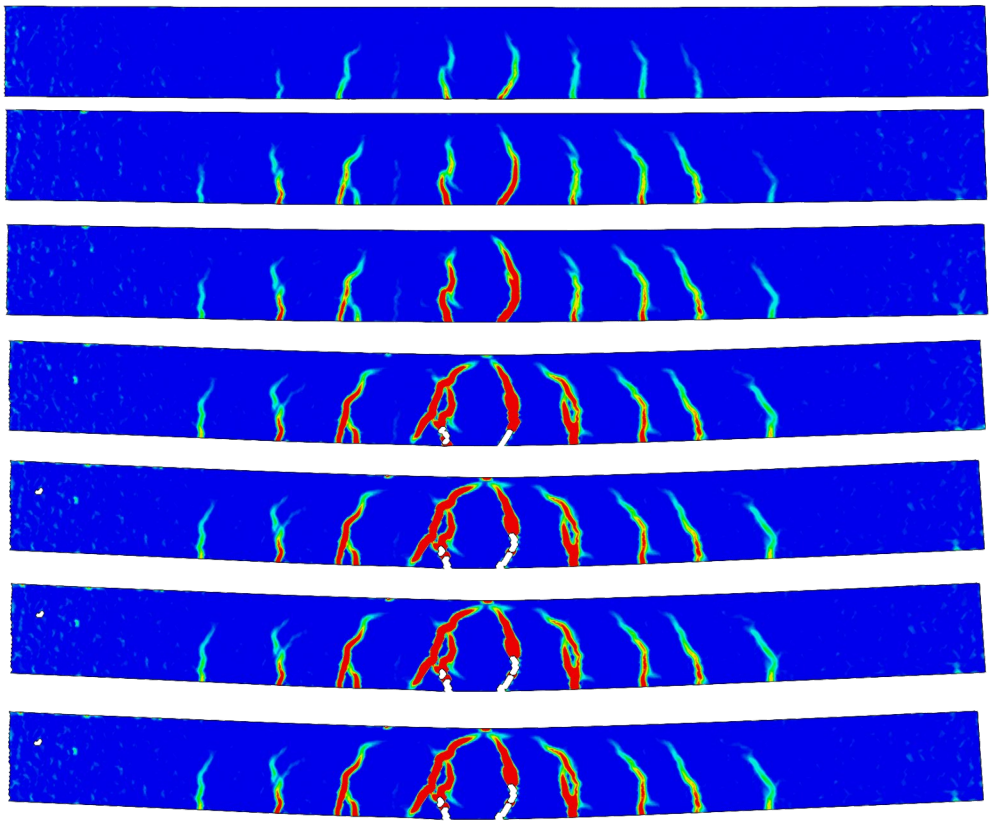
$u = 5.0$ mm $F = 10.1$ kN	
$u = 7.5$ mm $F = 11.7$ kN	
$u_{100\%} = 16.5$ mm $F_{100\%} = 13.9$ kN	
$u_{95\%} = 19.0$ mm $F_{95\%} = 13.2$ kN	
$u_{90\%} = 24.7$ mm $F_{90\%} = 12.5$ kN	
$u_{80\%} = 44.1$ mm $F_{80\%} = 11.1$ kN	
Principal strain [%]	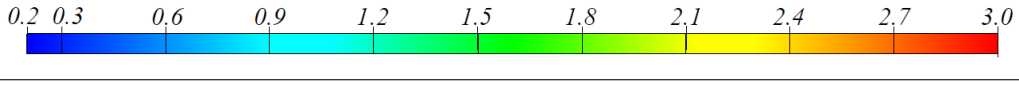

As can be seen in Figure F.14, a state-II response has been initiated at midspan for $u = 2.5$ mm. The cracking pattern at this point is heavily governed by flexural cracks, where a slight indication of inclined shear cracking is noted. A total of seven cracks can be outlined for $u = 2.5$ mm.

A state-III response has now been initiated for deflections at $u = 5.0$ mm and $u = 7.5$ mm. Furthermore, two additional cracks have been initiated to a total of nine, where previous cracks have further propagated and widened. However, the two cracks closest to midspan have developed more than cracks further away from midspan.

Further propagation of cracks is observed at ultimate load, where an additional crack close to midspan has been initiated and has propagated towards the load-application point. It is observed that the cracks closest to midspan are developing further for deformations beyond 100%, whereas the propagation of other cracks have stagnated. This would indicate that reinforcement steel in close proximity to the developing cracks at midspan would more than for reinforcement steel close to cracks further away from midspan. The deformation-controlled testing was aborted shortly after reaching deformations beyond a load level corresponding to 80%.

F.7.2.2 Beam B-16

The structural response at midspan for beam B-16 is presented in Figure F.15, with the strain field at highlighted points is shown in Table F.36. Similarly to beam B-08, the structural response of the midspan cross-section at $u = 2.5$ mm is governed by a state-II response, where the cracking is governed by flexural cracks to a total of six cracks. Four cracks at midspan are observed as mainly flexural, whereas the two outermost cracks propagate with a slight inclination.

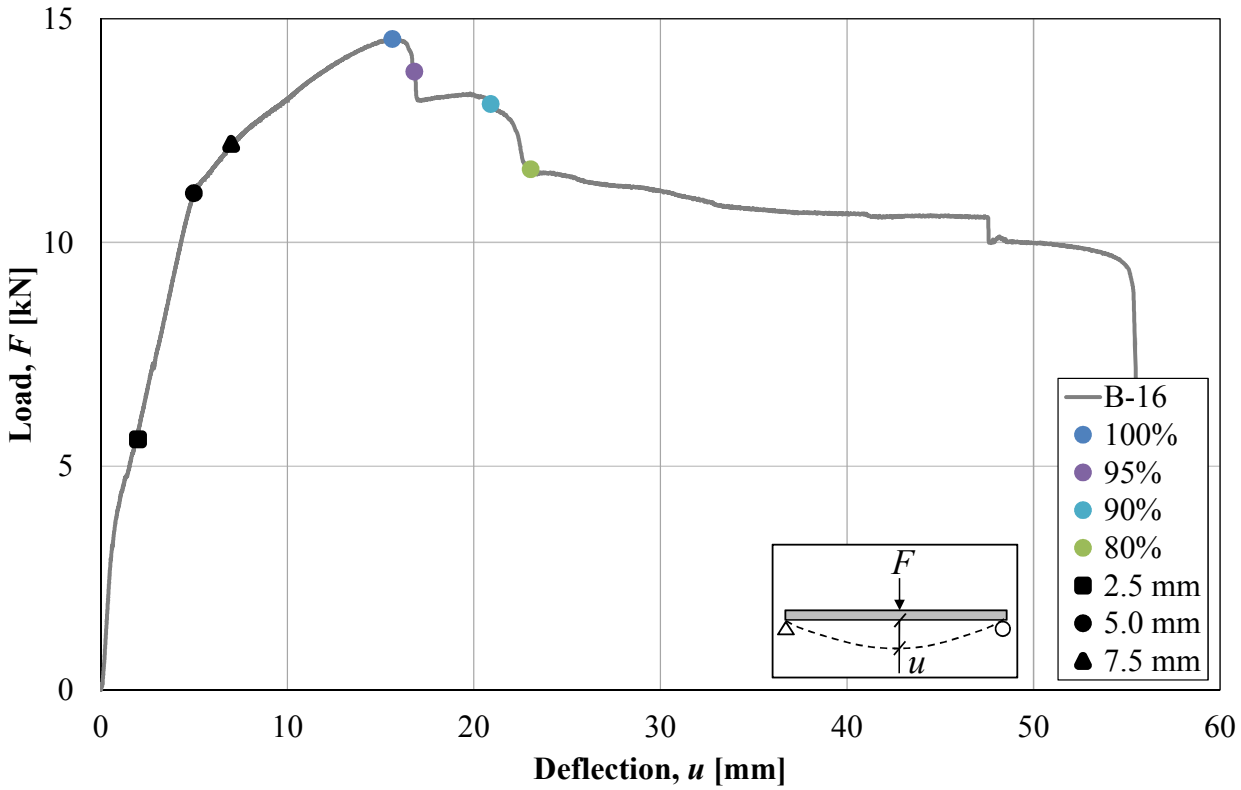

Figure F.15 Load-deflection curve of B-16 with highlighted points. Note the sudden drops after $u_{100\%}$, resulting in limited deformation before $u_{95\%}$ is reached.

A state-III response has been initiated for deformations at $u = 5.0$ mm as well as $u = 7.5$ mm, where two additional cracks has developed at the right hand side and one at the left hand side, to a total amount of nine cracks. An additional crack can be detected closest to the support at the left hand side, it is however regarded to be minor and therefore a limited influence on the response of the beam. The width and the height of cracks at this point are observed to be rather equal for all cracks.

At ultimate load and beyond, the four flexural cracks closest to midspan have markedly developed towards the load-application point, whereas minor propagation is noted for the other existing cracks. This again could serve as an indication that reinforcement steel in close proximity to the four flexural cracks in midspan would yield to a higher extent during non-linear behavior in state-III and at deformations surpassing $u_{100\%}$.

At deformations beyond $u_{100\%}$ a distinct reduction of load carrying capacity it noted in Table F.36, and is followed by a small plateau and a subsequent drop. The sharp reduction in load carrying capacity can be

attributed to extensive crushing of concrete, and as a consequence, relatively small values of $\theta_{pl,x\%}$ are measured for 95%, 90% and 80% respectively. It should however be noted that beam B-16 deforms well beyond measured values of $u_{80\%}$ with a limited reduction of load carrying capacity.

Table F.36 Strain field due to static loading from DIC analysis for B-16.

Deflection / Load	Strain field due to static loading: B-16
$u = 2.5\,\text{mm}$ $F = 6.7\,\text{kN}$	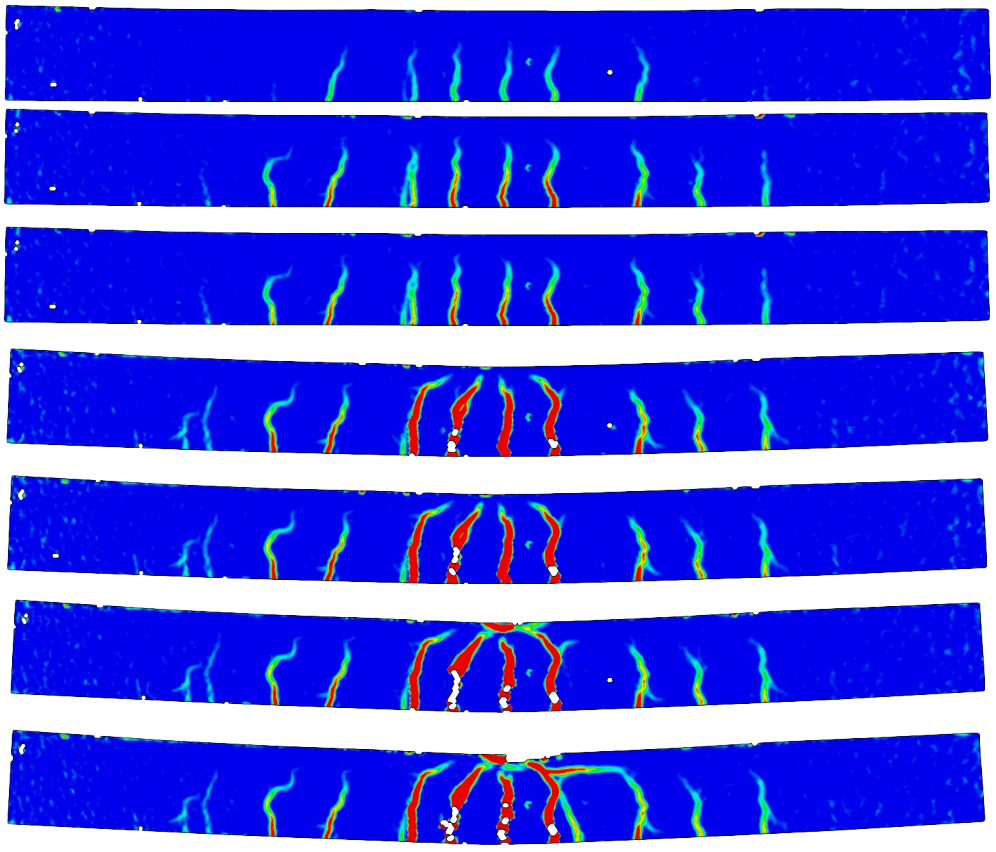
$u = 5.0\,\text{mm}$ $F = 11.0\,\text{kN}$	
$u = 7.5\,\text{mm}$ $F = 12.4\,\text{kN}$	
$u_{100\%} = 15.6\,\text{mm}$ $F_{100\%} = 14.5\,\text{kN}$	
$u_{95\%} = 16.8\,\text{mm}$ $F_{95\%} = 13.8\,\text{kN}$	
$u_{90\%} = 20.9\,\text{mm}$ $F_{90\%} = 13.1\,\text{kN}$	
$u_{80\%} = 23.1\,\text{mm}$ $F_{80\%} = 11.6\,\text{kN}$	
Principal strain [%]	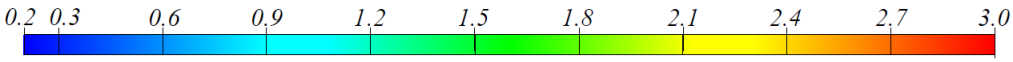

F.7.3 Series-1

F.7.3.1 Beam B-01

Figure F.16 shows the structural response for beam B-01 and Table F.37 presents the strain field at highlighted points as well as the strain field of the dynamic response at maximum deflection. Beam B-01 exhibits relatively small values of $\theta_{pl,100\%}$ and $\theta_{pl,95\%}$ compared to the remaining beams of Series-1. Rotation of $\theta_{pl,80\%}$ was not registered before failure of the test specimen was reached.

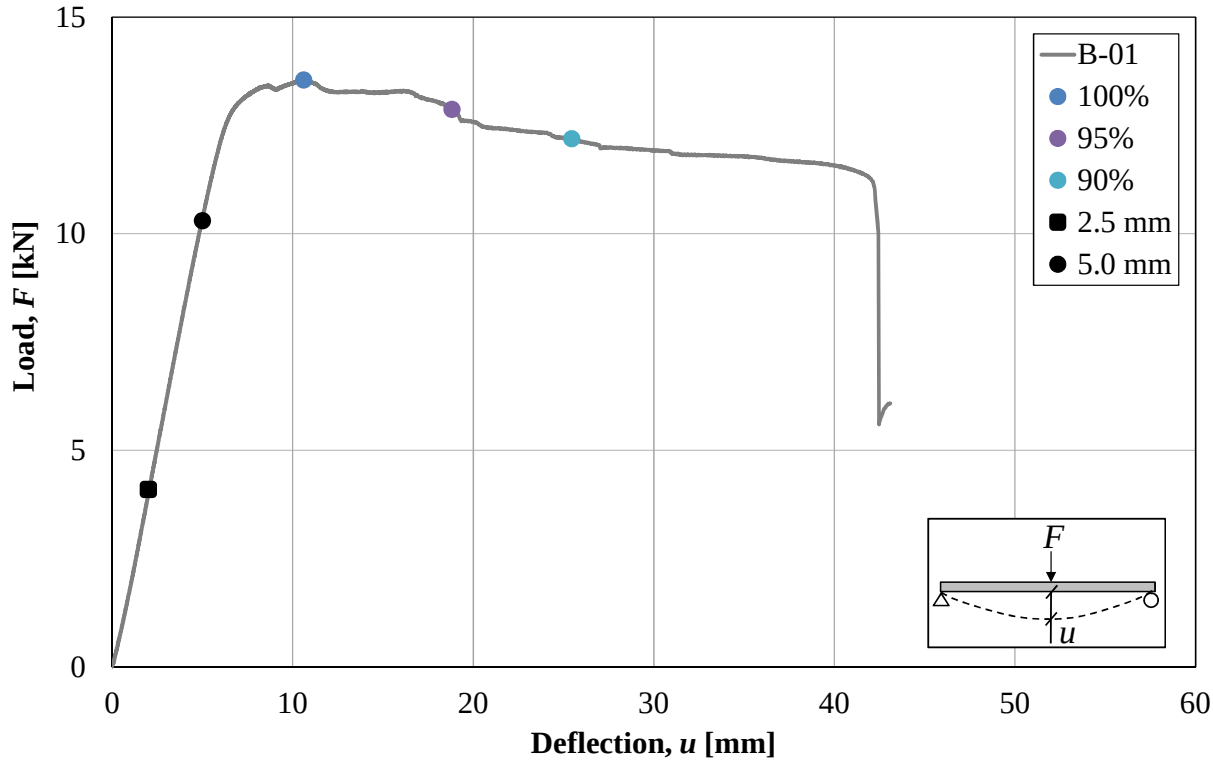

Figure F.16 Load-deflection curve of B-01 with highlighted points where the strain field is detailed in Table F.6.

The linear elastic response of the impact damaged beam is depicted by the strain field at deformations $u = 2.5$ mm and $u = 5.0$ mm. The strain field of the dynamic response gives a strong indication of the location of the main flexural crack, however the correspondence becomes significantly weaker for cracks further away. The crack formation compared to Series-3 is in general rather asymmetric with strong influences of inclined flexural shear cracks due to previous impact loading. No indications of new cracks being initiated due to static loading were found to be developed during the linear-elastic response, except for a flexural crack developing in close proximity to midspan.

It is observed that cracks in vicinity to midspan have developed considerably at ultimate load and are propagating towards the load-application point, where no new indications of cracks are observed. The crack propagation of main cracks develops in the same manner for deformations beyond $u_{100\%}$, whereas the propagation of cracks further away from midspan have halted. The cracks found around midspan are relatively evenly distributed together with a comparatively small spacing between cracks. The structural response show a comparatively small decrease in load capacity for deformations beyond $u_{100\%}$. The

reason why the reinforcement steel ruptures before any value for $\theta_{pl,80\%}$ is measured can be attributed to the gradual decrease of load carrying capacity, where it should be noted that the structure still deforms to large extents and therefore exhibits a ductile response.

Table F.37 Strain field due to static loading from DIC analysis for B-01. Note that the strain field of the dynamic response has different limits in the colorscale (from 0.5 % to 5 %).

Deflection / Time	Strain field due to impact loading at maximum deflection: B-01
$u = 10.5\,\text{mm}$ $t = 5.6\,\text{ms}$	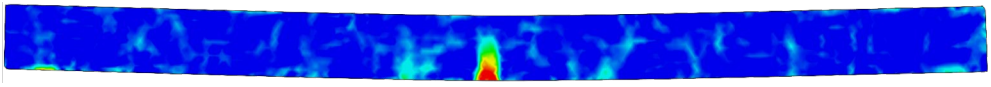
Deflection / Load	**Strain field due to static loading: B-01**
$u = 2.5\,\text{mm}$ $F = 5.1\,\text{kN}$ $u = 5.0\,\text{mm}$ $F = 10.4\,\text{kN}$ $u_{100\%} = 10.6\,\text{mm}$ $F_{100\%} = 13.5\,\text{kN}$ $u_{95\%} = 12.2\,\text{mm}$ $F_{95\%} = 12.9\,\text{kN}$ $u_{90\%} = 25.5\,\text{mm}$ $F_{90\%} = 12.2\,\text{kN}$	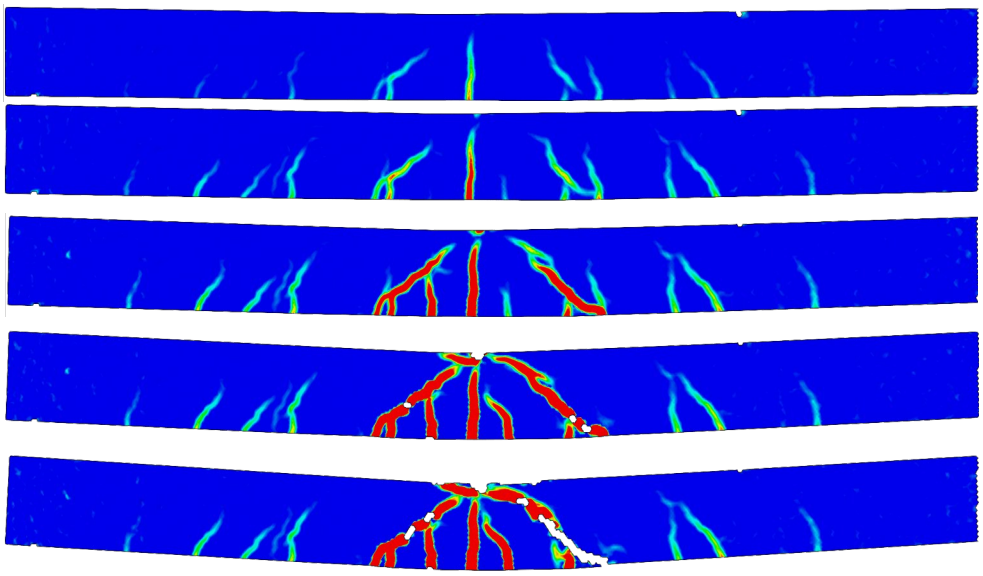
Principal strain [%]	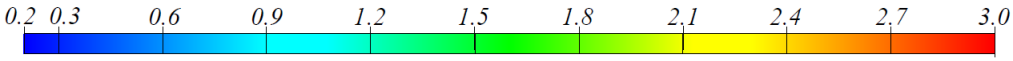

F.7.3.2 Beam B-12

The structural response for beam B-12 is shown in Figure F.17 and the strain field is detailed in Table F.38. Beam B-12 exhibits comparatively small values of $\theta_{pl,x\%}$ for 100% to 90%. It was also one of three beams that had registered values for 80% in Series-2.

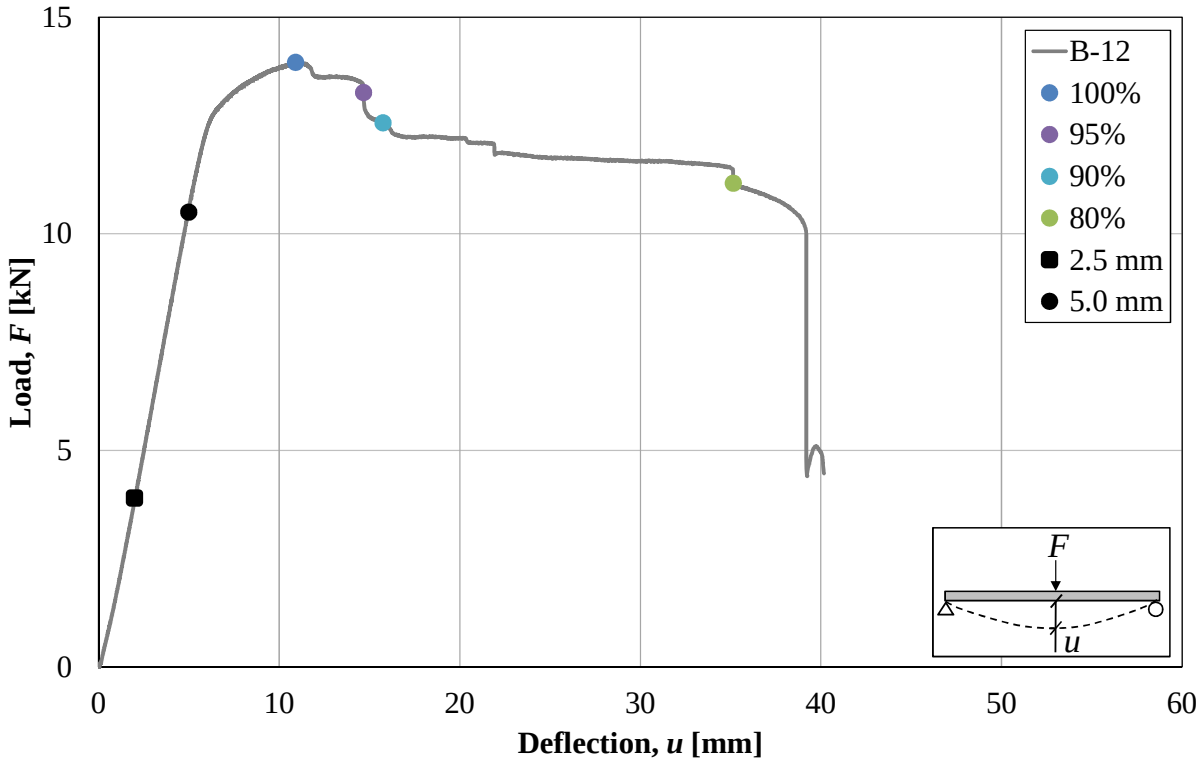

Figure F.17 Load-deflection curve of B-12 with highlighted points.

The linear-elastic response is presented in Table F.25 for deformations at $u = 2.5$ mm and at $u = 5.0$ mm, respectively. There is some correspondence to the crack pattern established in this range to the dynamic strain field at maximum deflection. Namely, the major flexural crack at midspan and the two cracks appearing rather symmetrically with respect to the main flexural crack. It is further noted that no new cracks are initiated in the linear-elastic response, instead the cracks formed have most likely been caused due to the impact loading.

The crack propagation in the linear elastic range to ultimate load show distinct development of the three main cracks in close proximity to midspan, especially so for deformations beyond $u_{100\%}$. The structural response shows distinct drops for deformations close to $u_{95\%}$, and thereafter a plateau is reached with very limited load reduction before $u_{80\%}$ is eventually reached. This results in a relatively large difference of measured values between $\theta_{pl,90\%}$ and $\theta_{pl,80\%}$. A failure mechanism seems to develop to the left of the midspan at load level of 80%, where it seems that the midspan crack and the one to its left have grown critical.

Table F.38 Strain field due to static loading from DIC analysis for B-12. Note that the strain field of the dynamic response has different limits in the colorscale (from 0.5 % to 5 %).

Deflection / Time	Strain field due to impact loading at maximum deflection: B-12
$u = 10.7\,\text{mm}$ $t = 6.0\,\text{ms}$	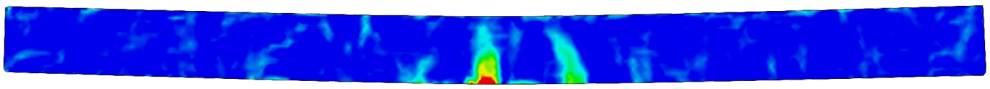

Deflection / Load	Strain field due to static loading: B-12
$u = 2.5\,\text{mm}$ $F = 5.1\,\text{kN}$	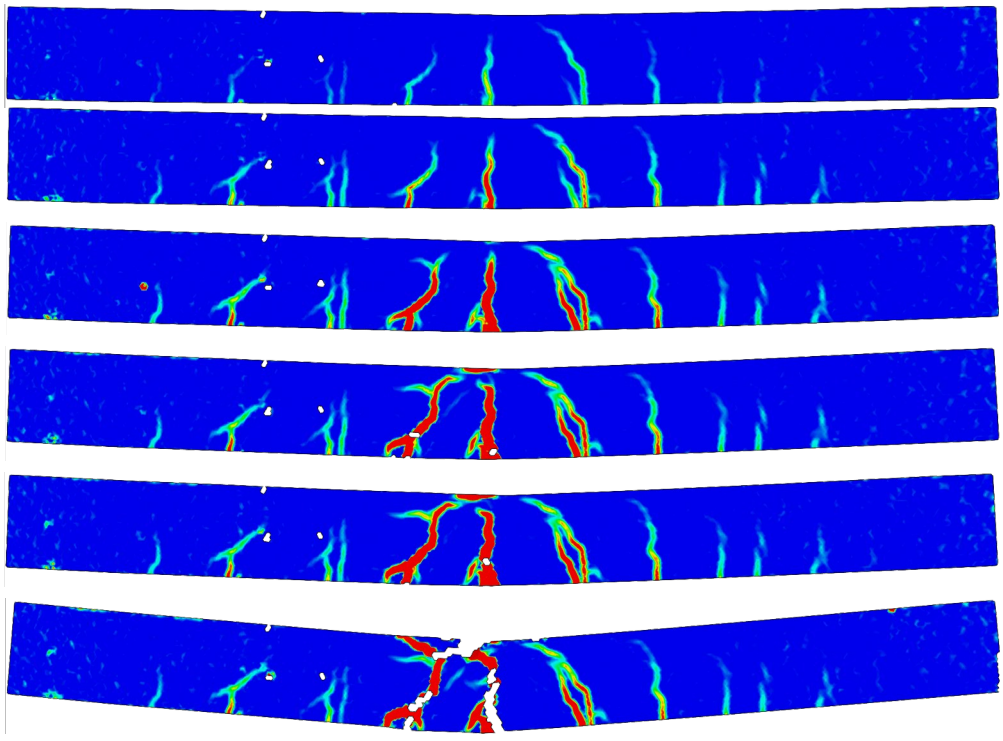
$u = 5.0\,\text{mm}$ $F = 10.8\,\text{kN}$	
$u_{100\%} = 10.9\,\text{mm}$ $F_{100\%} = 14.0\,\text{kN}$	
$u_{95\%} = 14.7\,\text{mm}$ $F_{95\%} = 13.3\,\text{kN}$	
$u_{90\%} = 15.7\,\text{mm}$ $F_{90\%} = 12.6\,\text{kN}$	
$u_{80\%} = 35.2\,\text{mm}$ $F_{80\%} = 11.2\,\text{kN}$	
Principal strain [%]	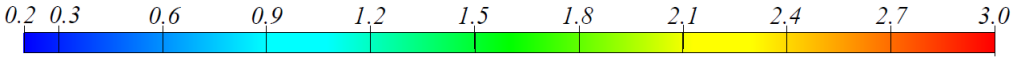

F.7.4 Series-2

F.7.4.1 Beam B-06

The structural response of beam B-06 is presented in Figure F.18 and the strain field at points of interest is detailed in Table F.39. Values of $\theta_{pl,80\%}$ were not registered for beam B-06, whereas remaining values for $\theta_{pl,x\%}$ are comparatively close to average values gathered for beams of Series-2.

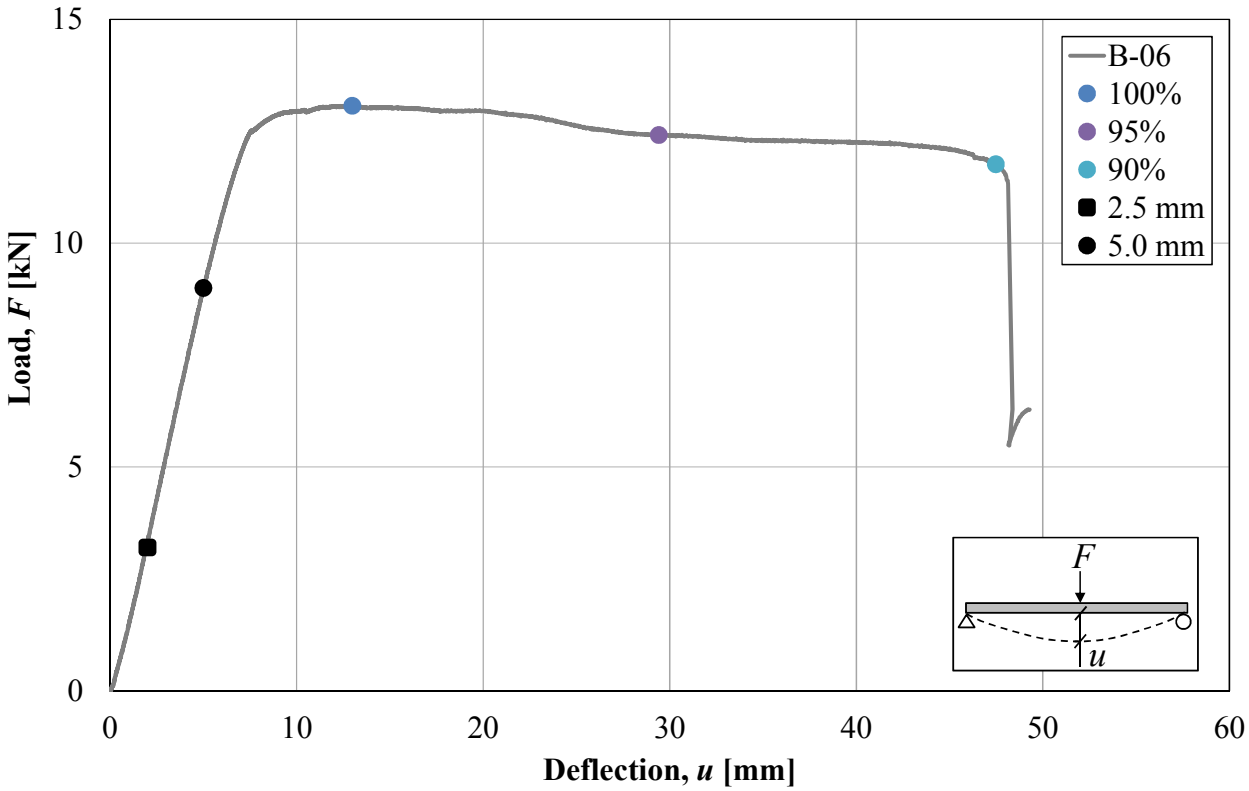

Figure F.18 Load-deflection curve of B-06 with highlighted points.

The linear-elastic range show a crack formation where major cracks can be outlined according to the strain field of the dynamic response at maximum deflection. Essentially no further cracking is initiated during the linear-elastic response, instead previous cracks caused by impact loading are reopened during the quasi-static loading. The crack pattern show a strong influence of inclined shear cracking due to impact, except for the two flexural cracks appearing close to midspan.

At ultimate load, further flexural cracking have been initiated at midspan. Crack development until this point is noted for all cracks, however more so for cracks at the vicinity of midspan. Furthermore, some of the flexural cracks at midspan merge together with the already present inclined flexural shear cracks.

As deformation progresses, further cracking at midspan can be observed together with widening of existing cracks. The crack distribution at midspan is rather even, with relatively small distances between cracks. These cracks have propagated towards a focal point located underneath the load-application point. The structural response is similar to an elasto-plastic response, where large deformations are measured without any significant decrease in load carrying capacity, and would also serve as an explanation as to

why values of $\theta_{pl,80\%}$ were not registered until rupture of reinforcement steel occurred.

Table F.39 Strain field due to static loading from DIC analysis for B-06. Note that the strain field of the dynamic response has different limits in the colorscale (from 0.5 % to 5 %).

Deflection / Time	Strain field due to impact loading at maximum deflection: B-06
$u = 20.1$ mm $t = 7.8$ ms	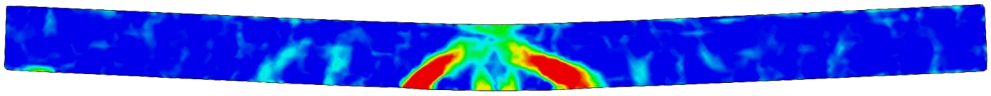
Deflection / Load	**Strain field due to static loading: B-06**
$u = 2.5$ mm $F = 4.1$ kN $u = 5.0$ mm $F = 8.9$ kN $u_{100\%} = 13.0$ mm $F_{100\%} = 13.1$ kN $u_{95\%} = 29.4$ mm $F_{95\%} = 12.4$ kN $u_{90\%} = 47.5$ mm $F_{90\%} = 11.8$ kN	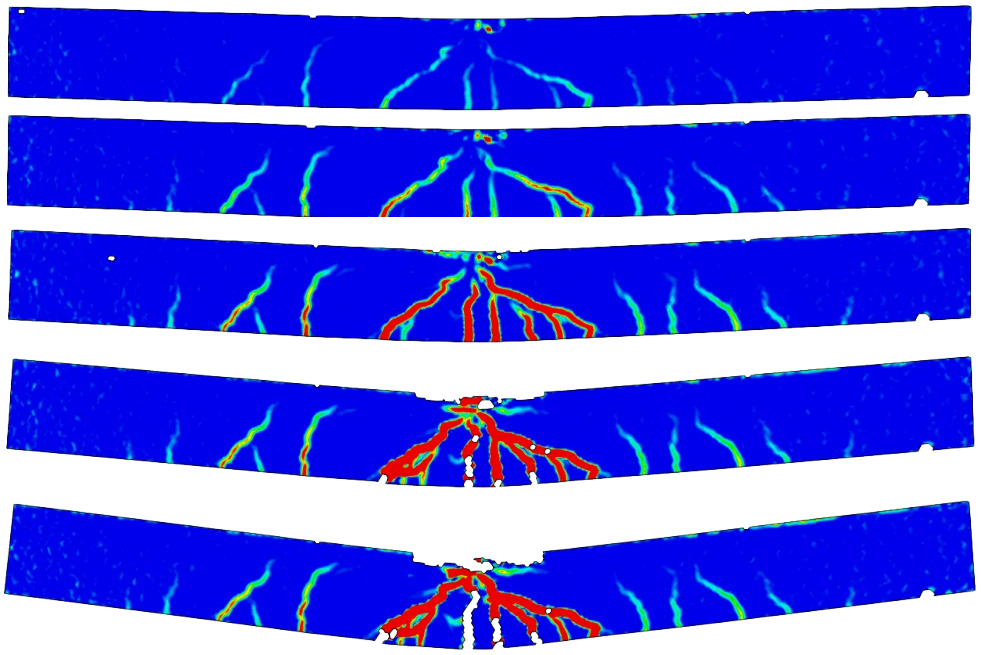
Principal strain [%]	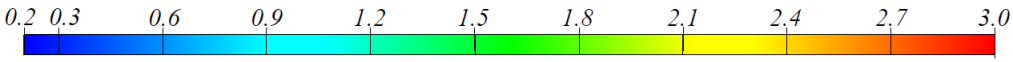

F.7.4.2 Beam B-13

The structural response for beam B-13 due to quasi-static loading is presented in Figure F.19, the strain field at highlighted points are detailed in Table F.40. A shear crack was noted to originate and develop in the web and therefore deformation at $u = 1.0$ mm is also presented in order to depict the propagation of said crack.

The dynamic strain field show a high correlation between cracked regions indicated at maximum deflection due to impact loading and the cracks developed due to static loading. This means that the crack development due to static loading is most likely a result of crack initiation caused by the earlier impact loading. A shear crack originating from the web and an additional flexural crack to the right of midspan can be distinguished at $u = 1.0$ mm. As loading progresses further cracks to the left and at midspan can be distinguished. However, most development is noted with said flexural crack and shear crack observed on the right hand side.

The shear crack does not grow critical when ultimate load is achieved. It is instead the flexural cracks situated close to midspan that propagate and connect with the point of load-application. The development of other cracks for deformations beyond $u_{100\%}$ have practically halted, whereas further cracking is observed to occur at midspan together with rather extensive concrete crushing.

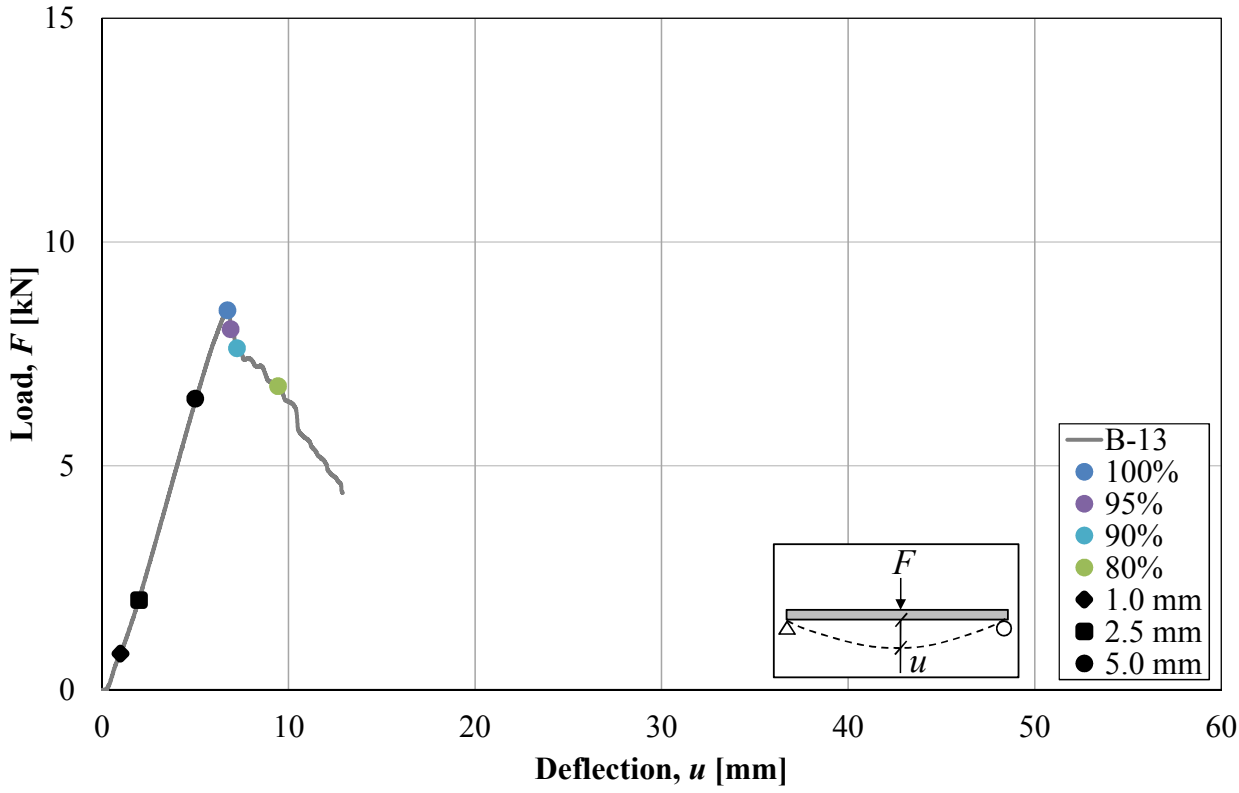

Figure F.19 Load-deflection curve of B-13 with highlighted points where the strain field is detailed in Table F.27.

Table F.40 Strain field due to static loading from DIC analysis for B-13. Note that the strain field of the dynamic response has different limits in the colorscale (from 0.5 % to 5 %).

Deflection / Time	Strain field due to impact loading at maximum deflection: B-13
$u = 20.9\,\text{mm}$ $t = 8.2\,\text{ms}$	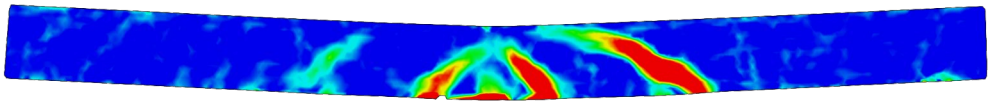
Deflection / Load	**Strain field due to static loading: B-13**
$u = 2.5\,\text{mm}$ $F = 2.7\,\text{kN}$	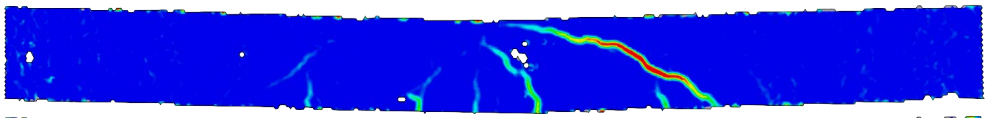
$u = 5.0\,\text{mm}$ $F = 4.0\,\text{kN}$	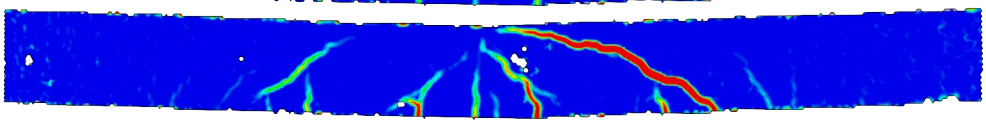
$u_{100\%} = 6.7\,\text{mm}$ $F_{100\%} = 8.5\,\text{kN}$	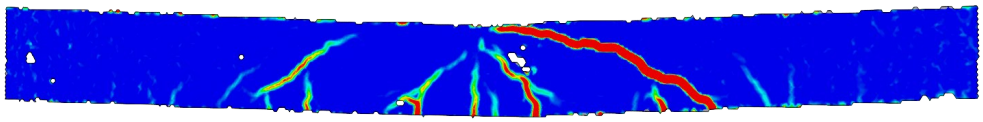
$u_{95\%} = 6.9\,\text{mm}$ $F_{95\%} = 8.1\,\text{kN}$	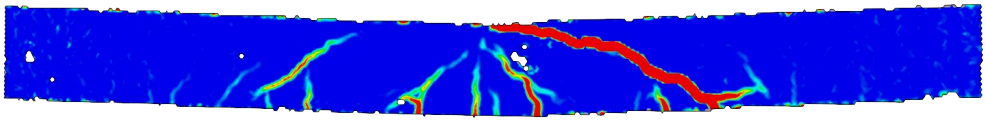
$u_{90\%} = 7.2\,\text{mm}$ $F_{90\%} = 7.6\,\text{kN}$	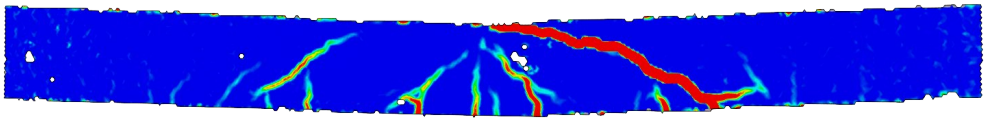
$u_{80\%} = 9.4\,\text{mm}$ $F_{80\%} = 6.8\,\text{kN}$	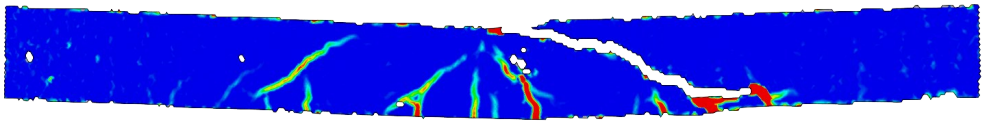
Principal strain [%]	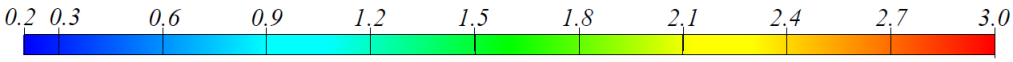

F.7.4.3 Beam B-15

Beam B-15 also exhibited a shear crack originating from the web due to dynamic loading. However, the beam did not fail in a brittle shear failure mechanism like beam B-13, instead it deformed and failed in a ductile response, as can be seen in Figure F.20. For beam B-15, the strain field in Table F.41 at $u = 1.0$ mm is also presented in order to detail the web shear crack propagation.

Indications of a web shear crack is noted in the dynamic response at the point of maximum deflection in Table F.41, unlike beam B-13, the web shear crack is initiated at one side of the midspan only. Further cracking such as flexural at midspan and inclined shear cracks are also noted, where a high correlation is found between cracks opening due in the linear-elastic response due to static loading and the indications of cracked regions of the dynamic response. It is noted that web shear crack is re-opened during the linear-elastic range. However, it does not become critical, it is instead the cracks close to midspan that becomes critical at peak load. For larger deformations beyond peak load, the propagation of the web-shear crack is halted, whereas cracking in close proximity to midspan continue to develop which eventually brings the beam to failure.

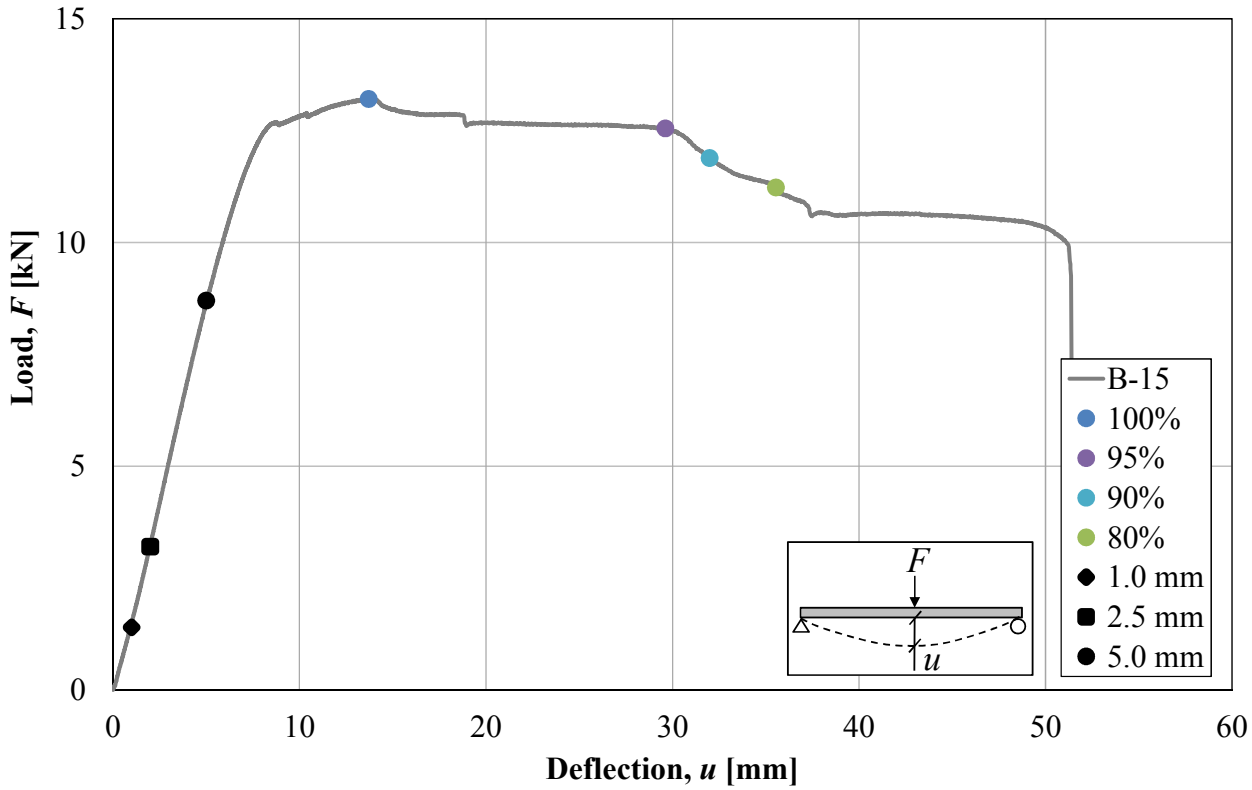

Figure F.20 Load-deflection curve of B-15 with highlighted points where the strain field is detailed in Table F.41.

Table F.41 Strain field due to static loading from DIC analysis for B-15. Note that the strain field of the dynamic response has different limits in the colorscale (from 0.5 % to 5 %).

Deflection / Time	Strain field due to impact loading at maximum deflection: B-15
$u = 19.8$ mm $t = 7.6$ ms	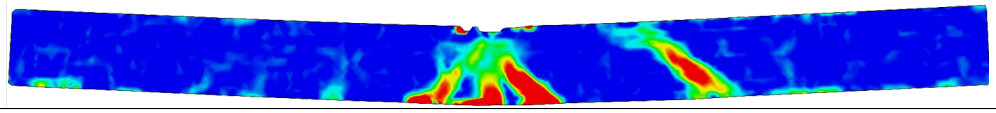
Deflection / Load	**Strain field due to static loading: B-15**
$u = 2.5$ mm $F = 4.2$ kN	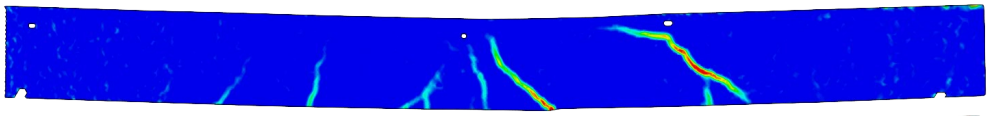
$u = 5.0$ mm $F = 8.9$ kN	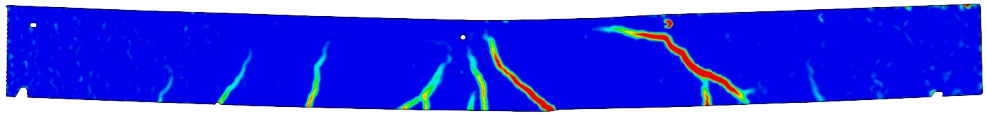
$u_{100\%} = 13.7$ mm $F_{100\%} = 13.2$ kN	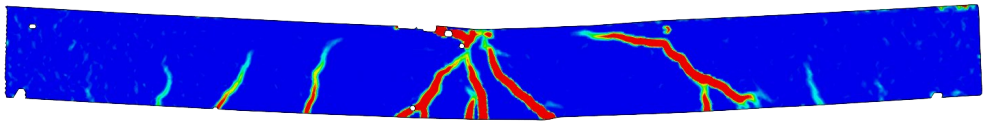
$u_{95\%} = 29.6$ mm $F_{95\%} = 12.5$ kN	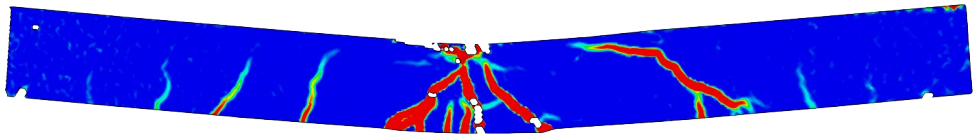
$u_{90\%} = 32.0$ mm $F_{90\%} = 11.9$ kN	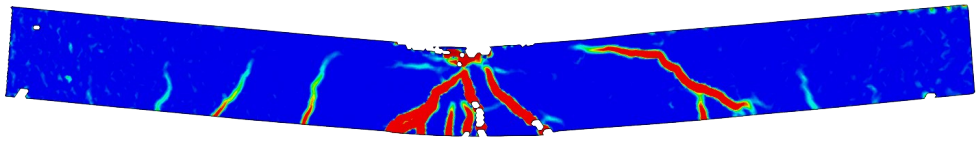
$u_{80\%} = 45.9$ mm $F_{80\%} = 10.6$ kN	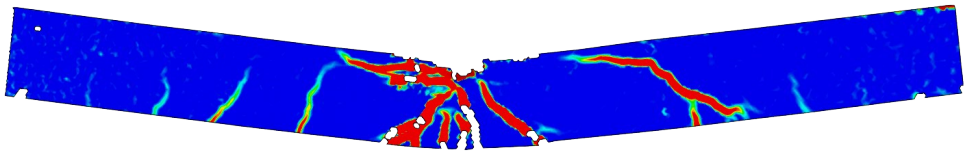
Principal strain [%]	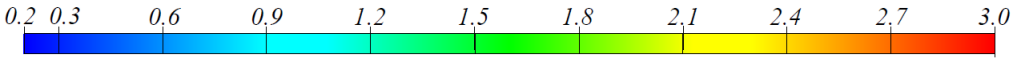

F.7.5 Adjusted colorscale

Table F.42 Strain field due to static loading from DIC analysis for beams of Series-3 at 95 % of the peak load.

Deflection/Load	Strain field due to static loading
B-07 $u_{95\%} = 29.4\,\text{mm}$ $F_{95\%} = 12.4\,\text{kN}$	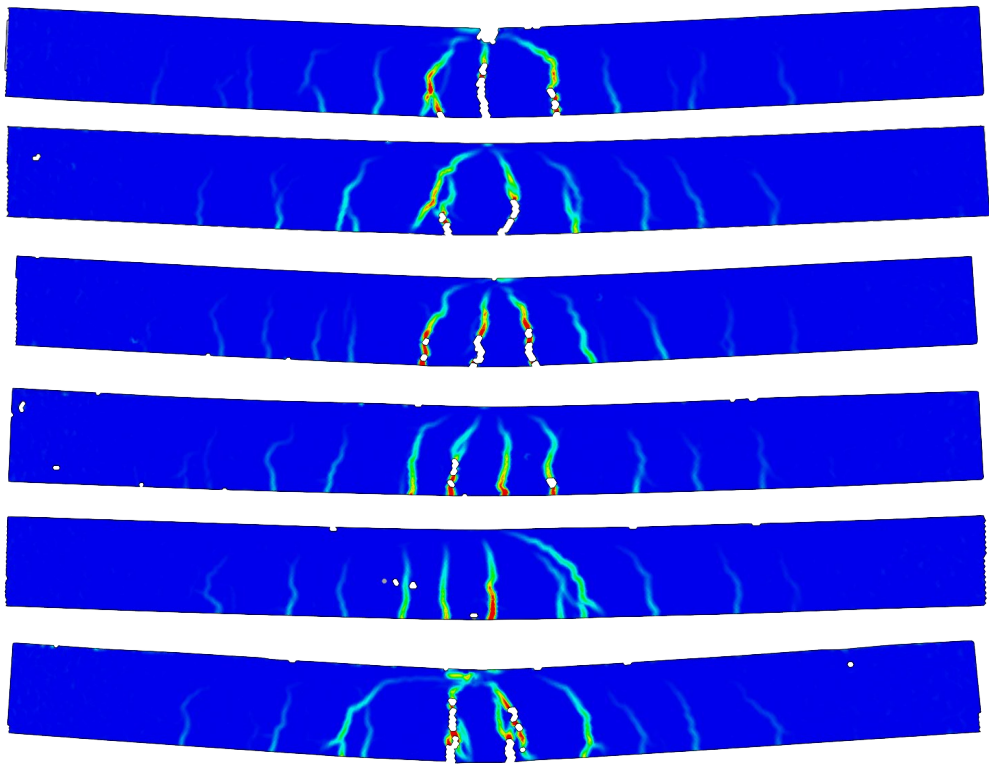
B-08 $u_{95\%} = 19.0\,\text{mm}$ $F_{95\%} = 13.2\,\text{kN}$	
B-09 $u_{95\%} = 22.8\,\text{mm}$ $F_{95\%} = 13.4\,\text{kN}$	
B-16 $u_{95\%} = 16.8\,\text{mm}$ $F_{95\%} = 13.8\,\text{kN}$	
B-17 $u_{95\%} = 15.4\,\text{mm}$ $F_{95\%} = 13.1\,\text{kN}$	
B-18 $u_{95\%} = 31.1\,\text{mm}$ $F_{95\%} = 13.4\,\text{kN}$	
Principal strain [%]	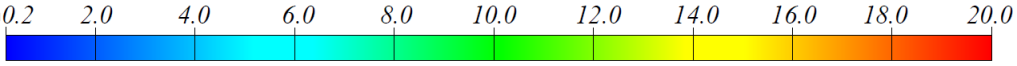

Table F.43 Strain field due to static loading from DIC analysis for beams of Series-1 at 95 % of the peak load.

Deflection/Load	Strain field due to static loading
B-01 $u_{95\%} = 12.2\,\text{mm}$ $F_{95\%} = 12.9\,\text{kN}$	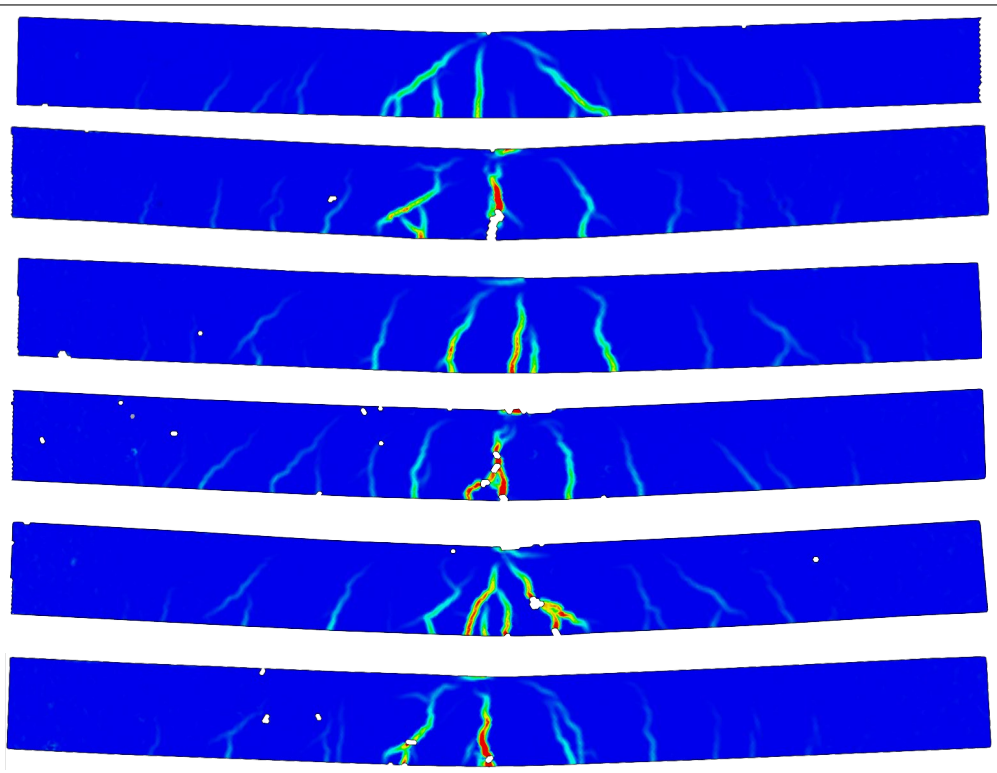
B-02 $u_{95\%} = 20.9\,\text{mm}$ $F_{95\%} = 13.4\,\text{kN}$	
B-03 $u_{95\%} = 13.8\,\text{mm}$ $F_{95\%} = 13.9\,\text{kN}$	
B-10 $u_{95\%} = 16.6\,\text{mm}$ $F_{95\%} = 13.3\,\text{kN}$	
B-11 $u_{95\%} = 20.3\,\text{mm}$ $F_{95\%} = 12.7\,\text{kN}$	
B-12 $u_{95\%} = 14.7\,\text{mm}$ $F_{95\%} = 13.3\,\text{kN}$	
Principal strain [%]	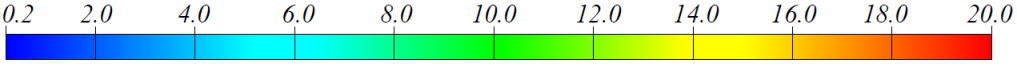

Table F.44 Strain field due to static loading from DIC analysis for beams of Series-2 at 95 % of the peak load.

Deflection/Load	Strain field due to static loading
B-04 $u_{95\%} = 26.0\,\text{mm}$ $F_{95\%} = 11.7\,\text{kN}$ B-05 $u_{95\%} = 40.5\,\text{mm}$ $F_{95\%} = 11.4\,\text{kN}$ B-06 $u_{95\%} = 29.4\,\text{mm}$ $F_{95\%} = 12.4\,\text{kN}$ B-13 $u_{95\%} = 6.9\,\text{mm}$ $F_{95\%} = 8.1\,\text{kN}$ B-14 $u_{95\%} = 20.4\,\text{mm}$ $F_{95\%} = 12.9\,\text{kN}$ B-15 $u_{95\%} = 29.6\,\text{mm}$ $F_{95\%} = 12.5\,\text{kN}$	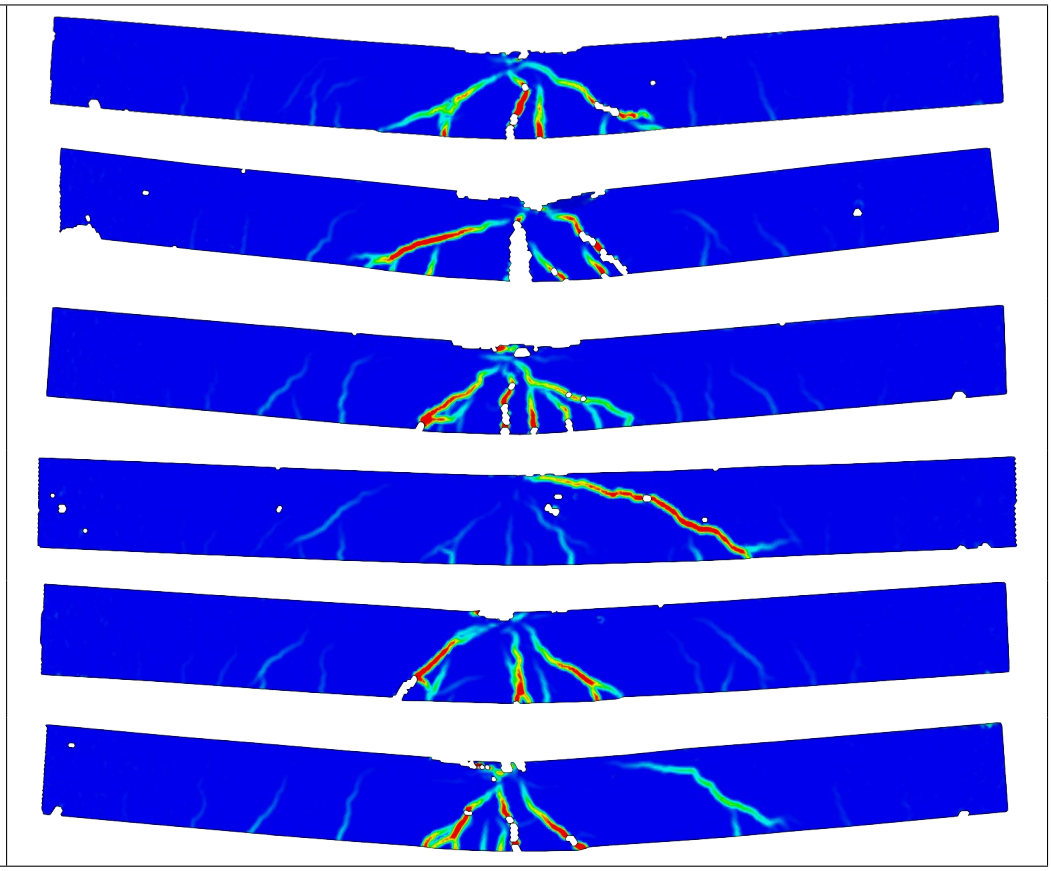
Principal strain [%]	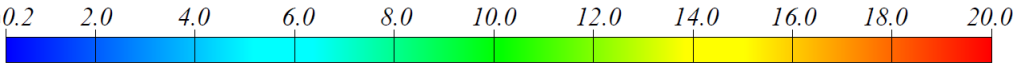

F.8 Photographs of Beams After Static Testing

Table F.45 Photographs of Series-3 beams after static testing.

Beam-ID	Series-3
B-07	
B-08	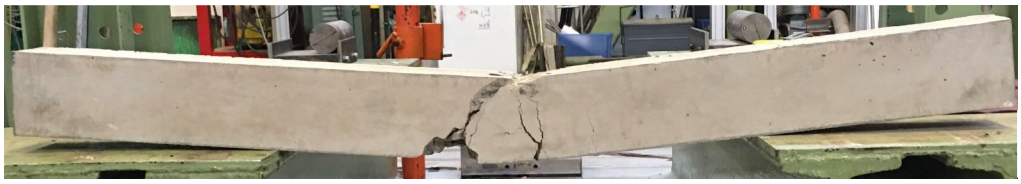
B-09	
B-16	
B-17	
B-18	

Table F.46 Photographs of Series-1 beams after static testing.

Beam-ID	Series-1
B-01	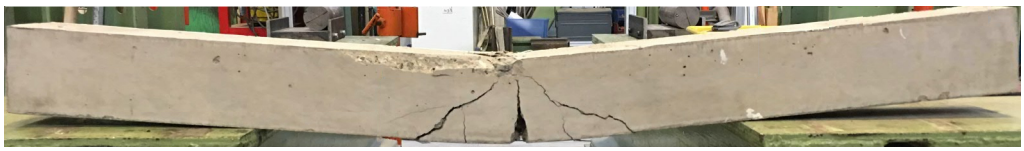
B-02	
B-03	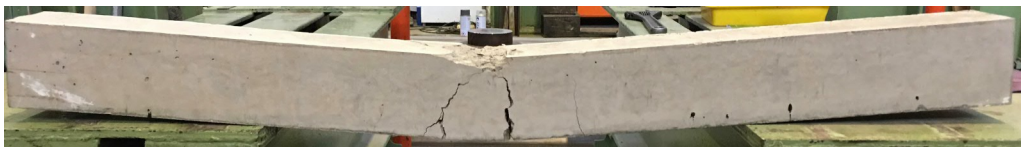
B-10	
B-11	
B-12	

Table F.47 Photographs of Series-2 beams after static testing.

Beam-ID	Series-2
B-04	
B-05	
B-06	
B-13	
B-14	
B-15	

G Finite Element Model - Different Meshes

Table G.1 Hexahedron mesh pattern. Part of the entire beam is presented as well as a zoomed-in pattern.

Mesh size	Hexahedron Mesh	Zoomed in mesh
20 mm	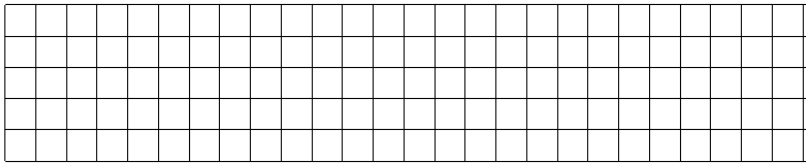	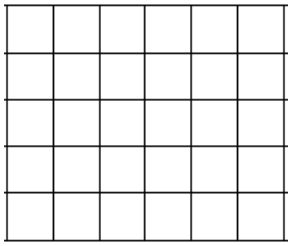
10 mm	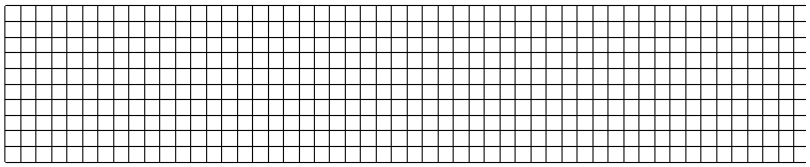	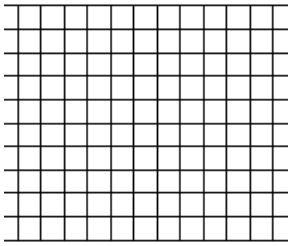
5 mm	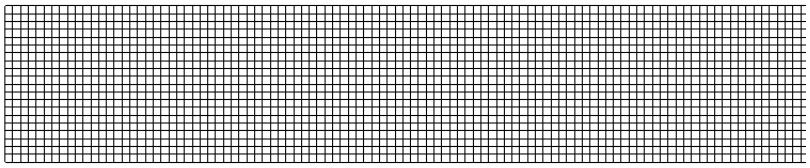	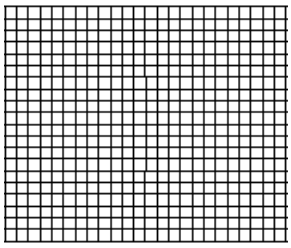

Table G.2 Tetrahedron mesh pattern. Part of the entire beam is presented as well as a zoomed-in pattern.

Mesh size	Tetrahedron mesh	Zoomed in mesh
20 mm	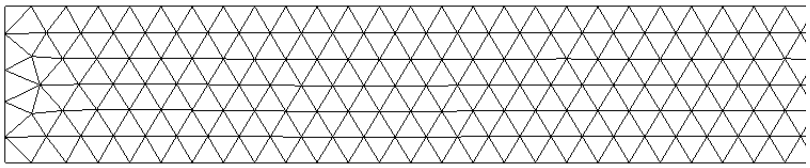	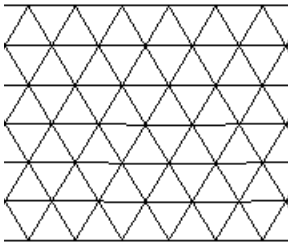
10 mm	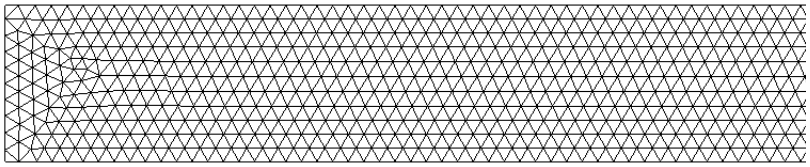	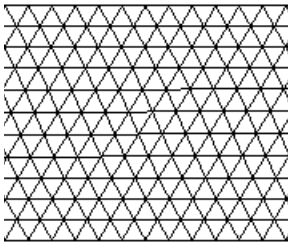
5 mm	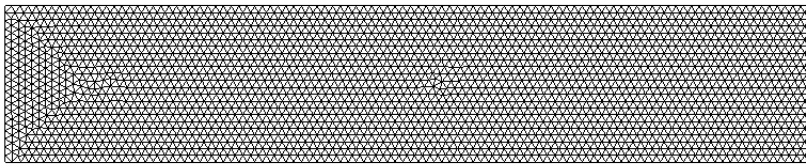	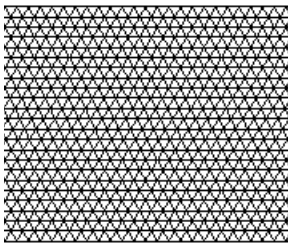

H Finite Element Model - Results

H.1 Velocity and Support Displacement

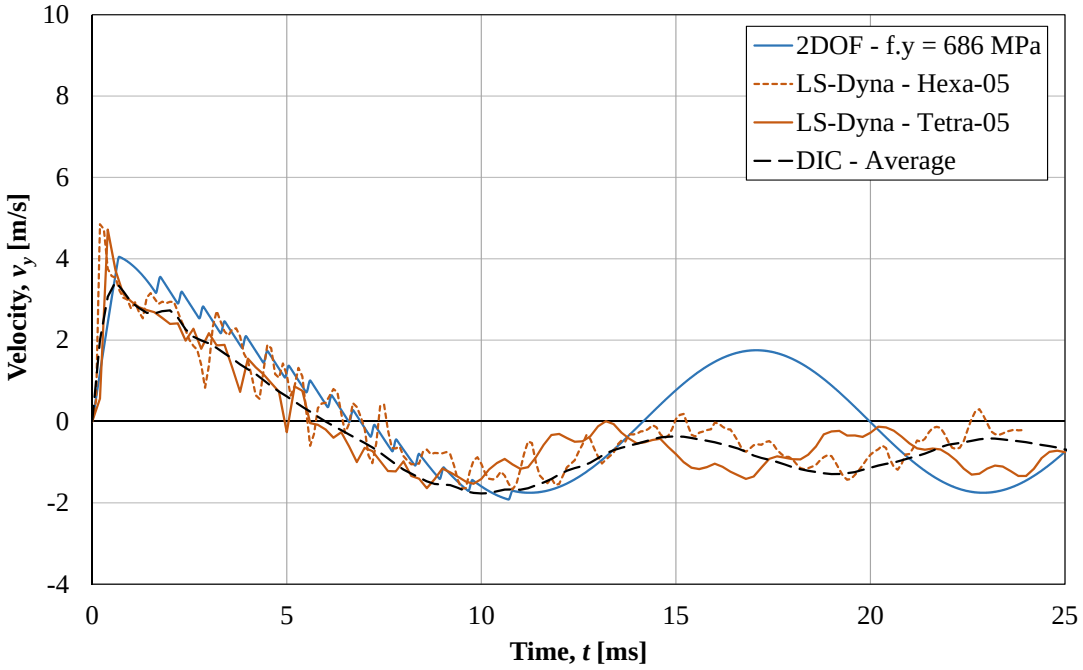

Figure H.1 Midspan velocity vs time for drop-height h = 2.5 m for all models.

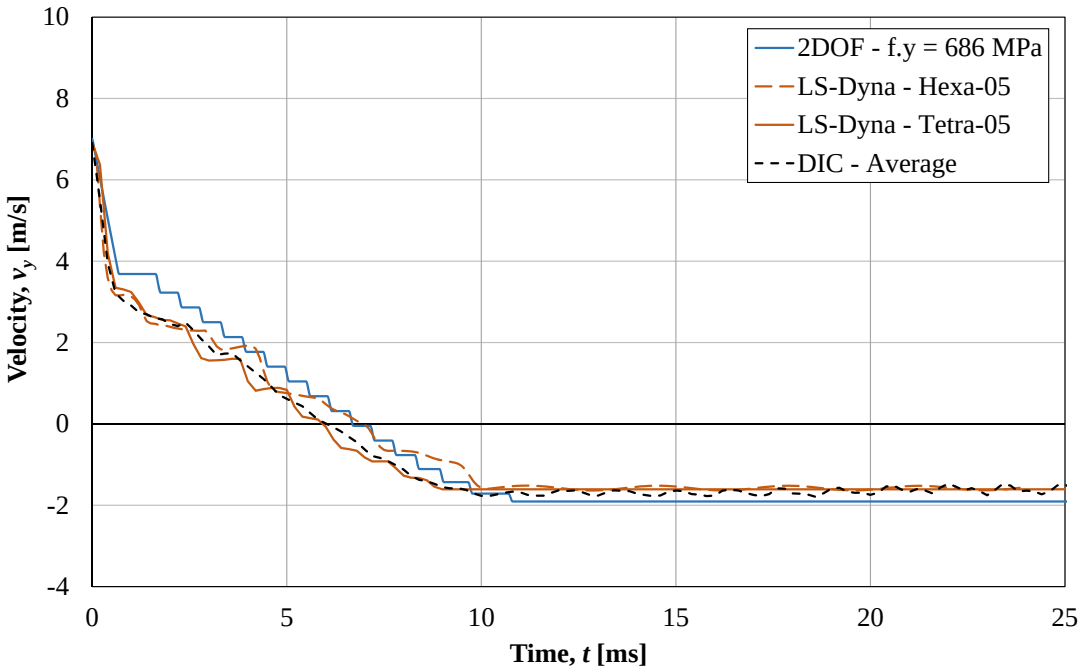

Figure H.2 Drop-weight velocity vs time for drop-height h = 2.5 m for all models.

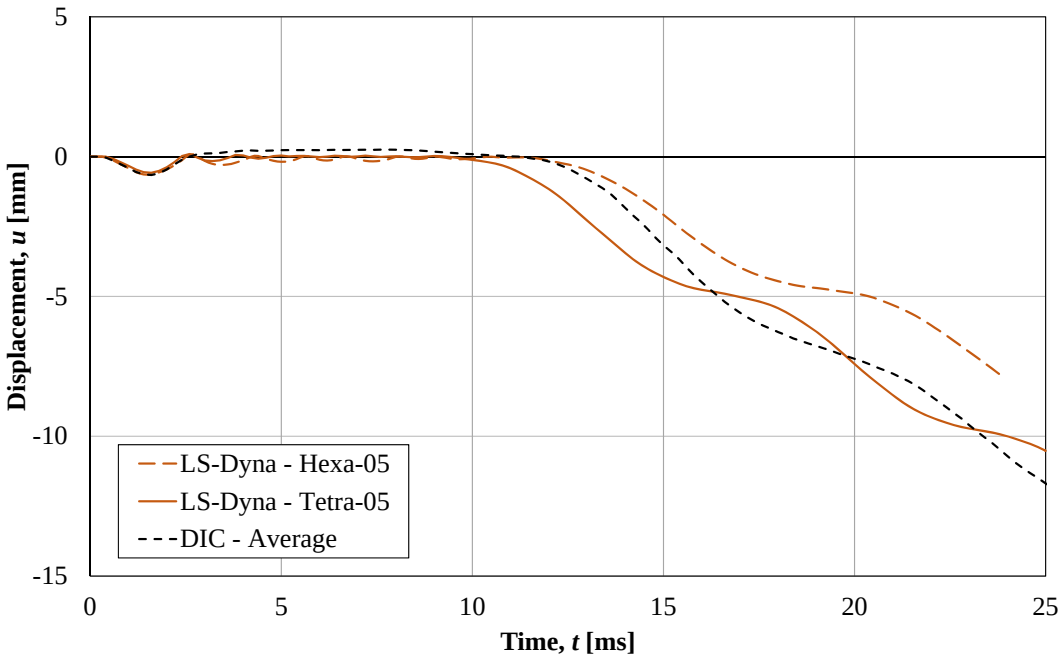

Figure H.3 Displacement over the support for a drop-height h = 2.5 m for the LS-DYNA models and DIC analysis.

H.2 Deformed Shape of the Beam

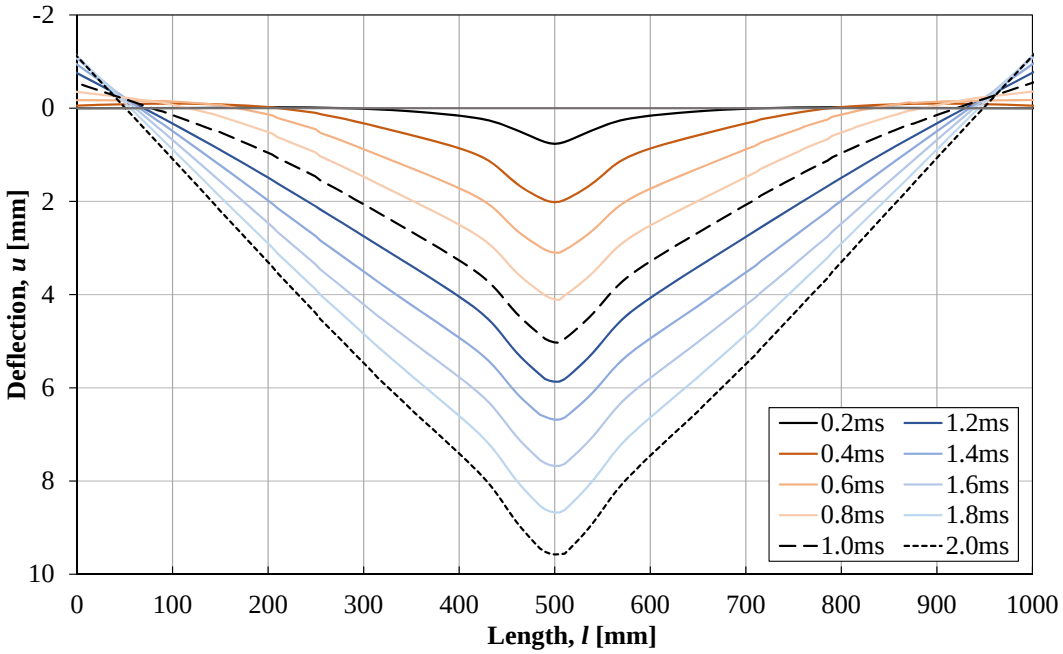

Figure H.4 Deformed shape of the beam according to the hexahedron LS-Dyna model at different times after impact for a drop-height of 5.0 m.

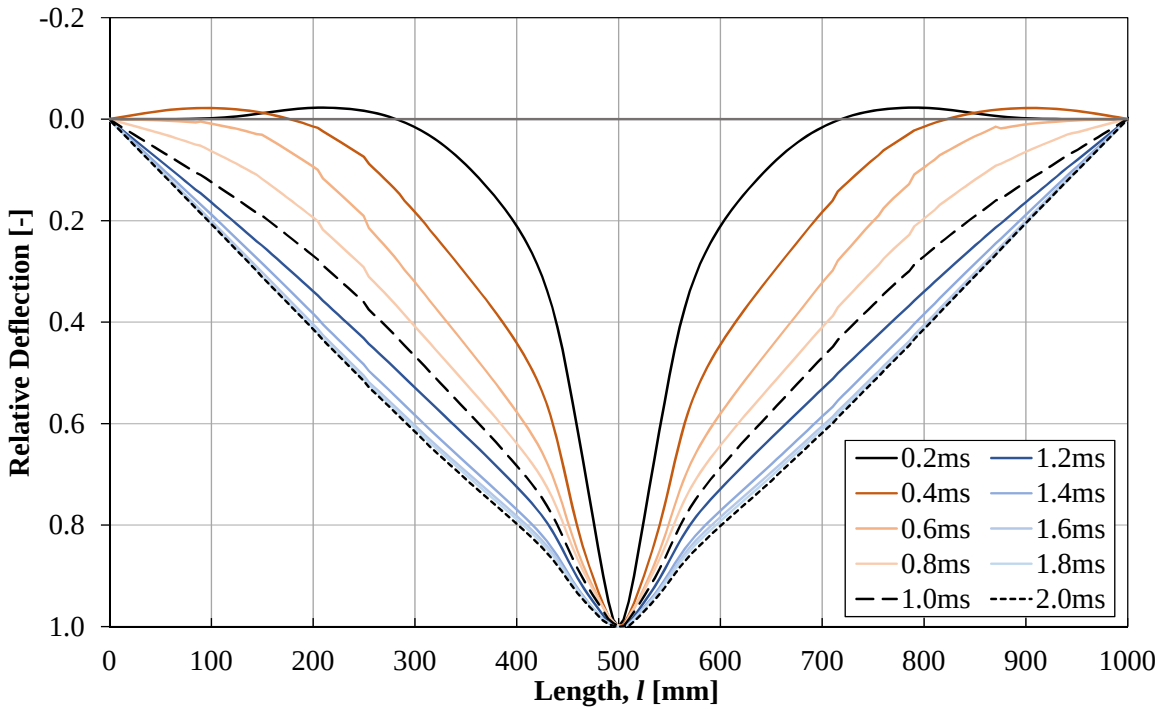

Figure H.5 Relative deformed shape of the beam according to the hexahedron LS-Dyna model at different times after impact for a drop-height of 5.0 m.

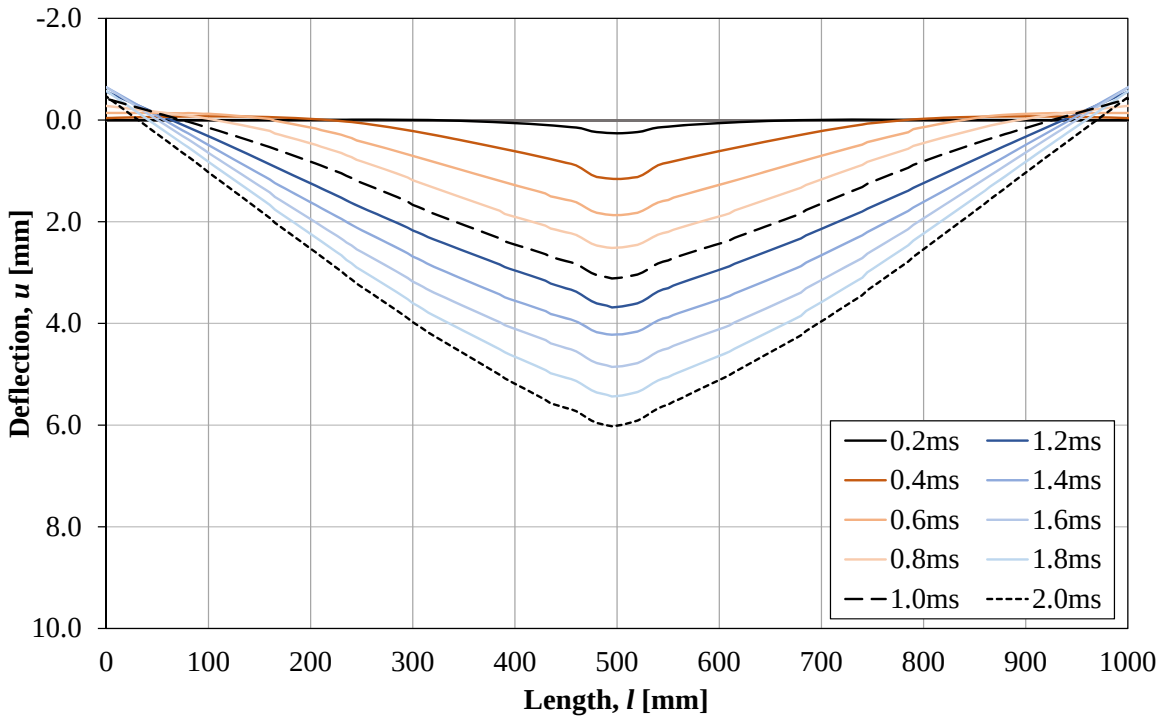

Figure H.6 Deformed shape of the beam according to the hexahedron LS-Dyna model at different times after impact for a drop-height of 2.5 m.

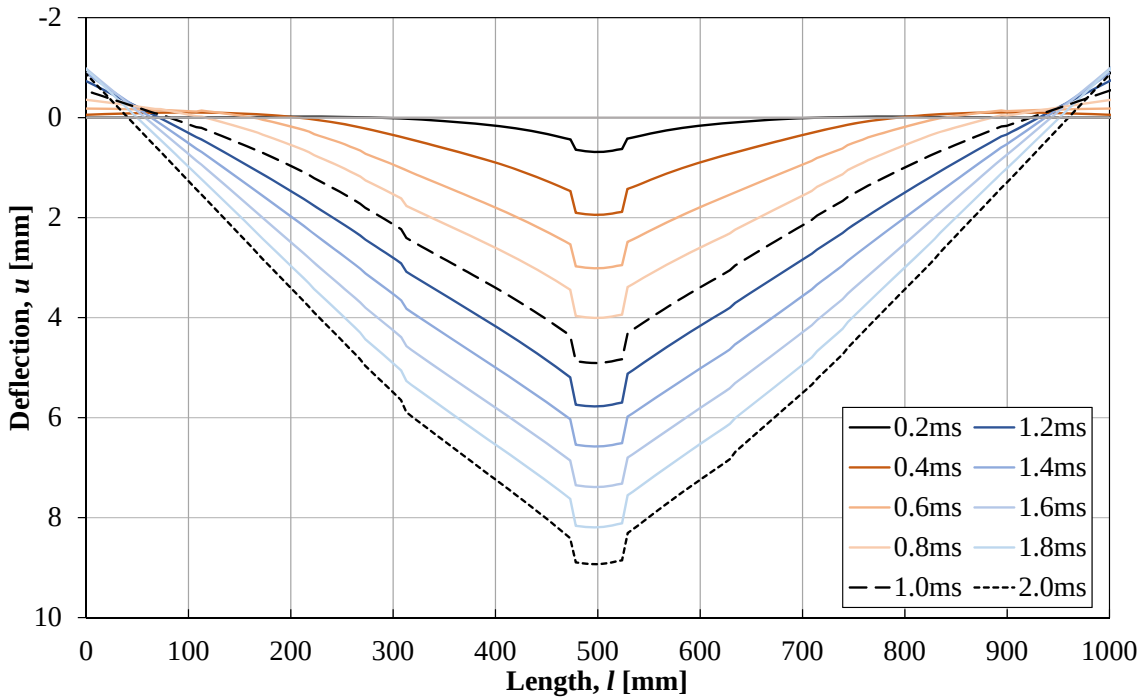

Figure H.7 Deformed shape of the beam according to the tetrahedron LS-Dyna model at different times after impact for a drop-height of 5.0 m.

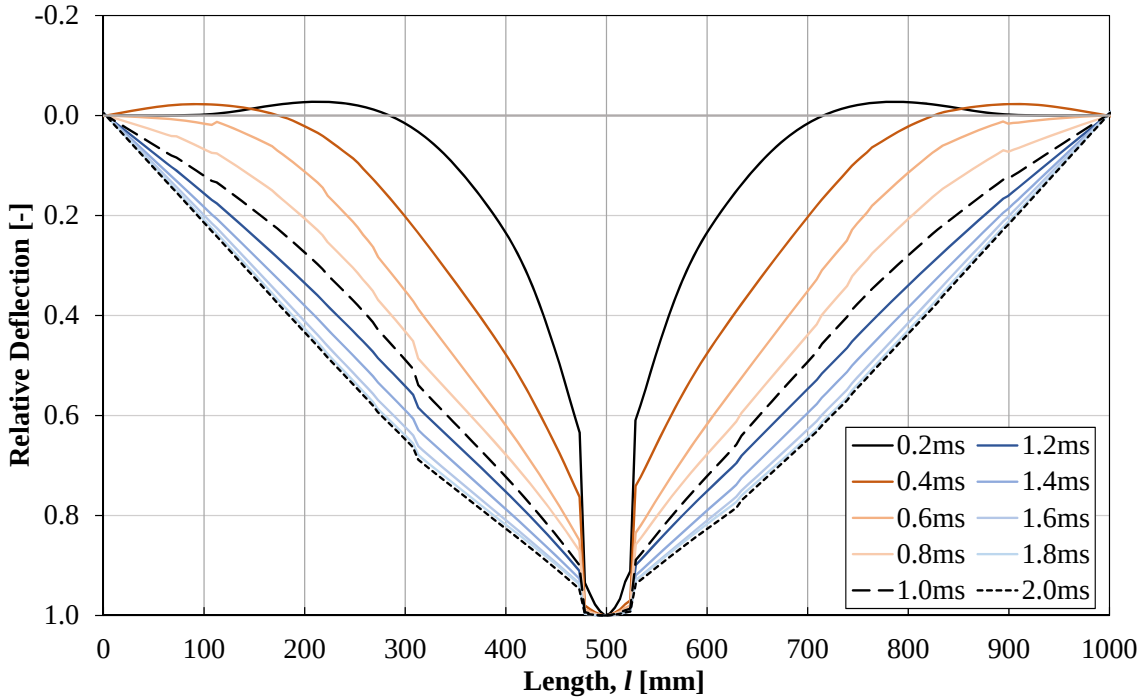

Figure H.8 Relative deformed shape of the beam according to the tetrahedron LS-Dyna model at different times after impact for a drop-height of 5.0 m.

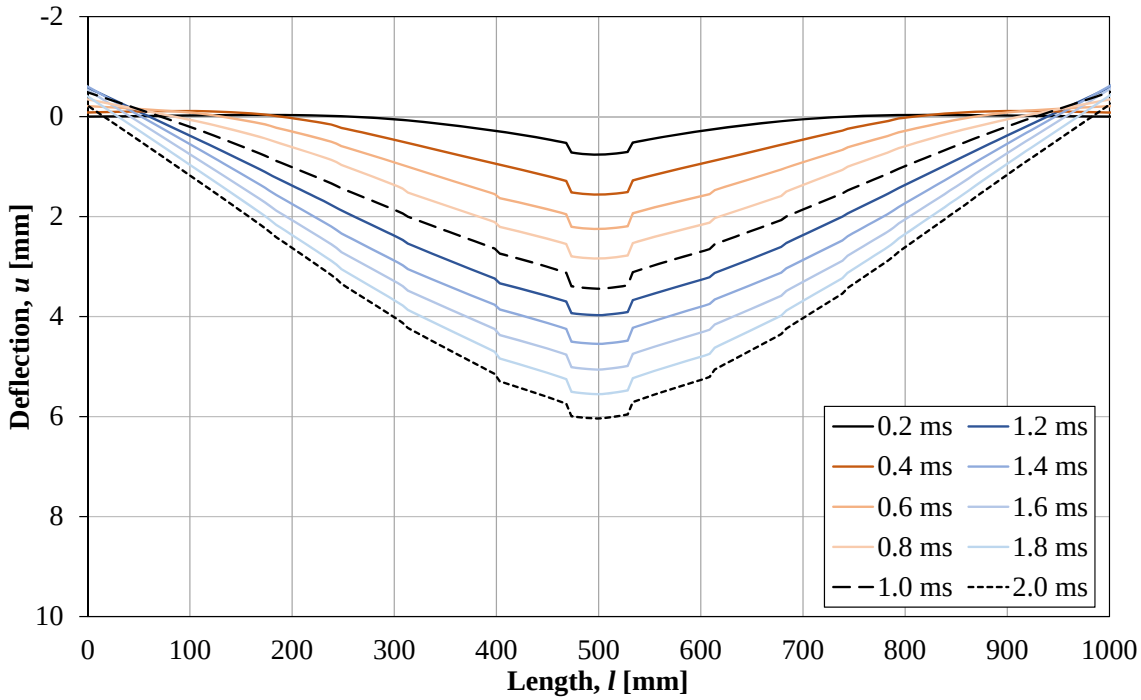

Figure H.9 Deformed shape of the beam according to the tetrahedron LS-Dyna model at different times after impact for a drop-height of 2.5 m.

H.3 Comparison with Experimental Results

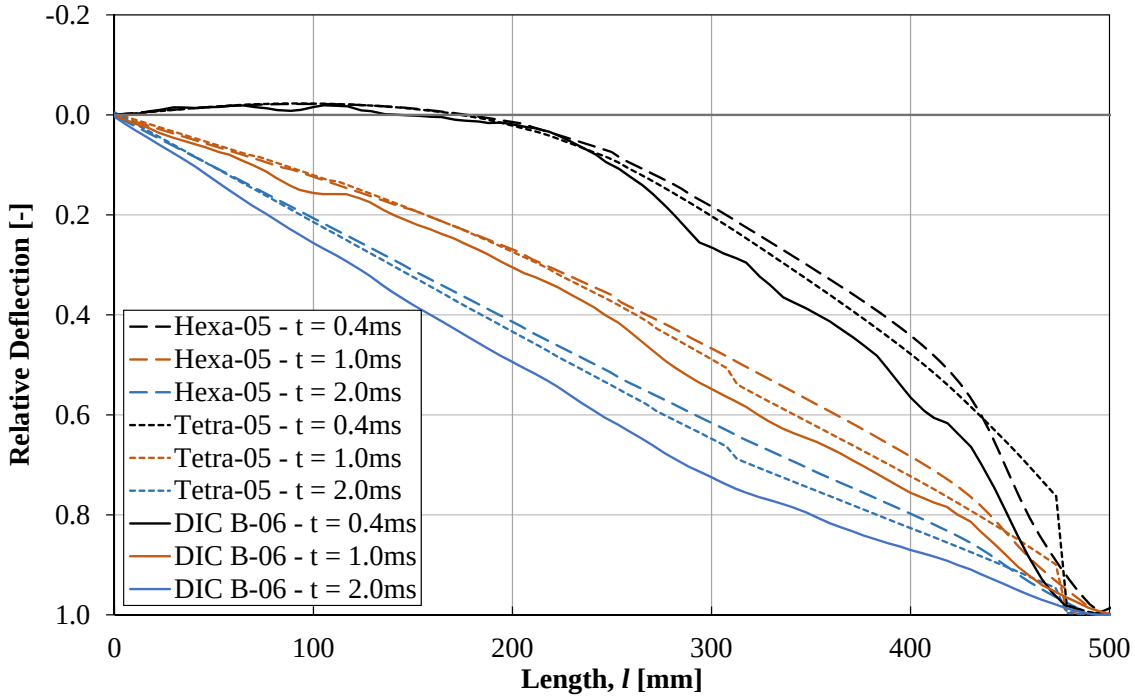

Figure H.10 Relative deformed shape at different times after impact for a drop-height of 5.0 m

H.4 Static FE Analysis

H.4.1 5 mm hexahedron model

Table H.1 Strain field for static analysis of the 5 mm hexahedron LS-DYNA model.

Deflection/ Load	Strain field for static loading
$u = 0.2$ mm $F = 3.4$ kN	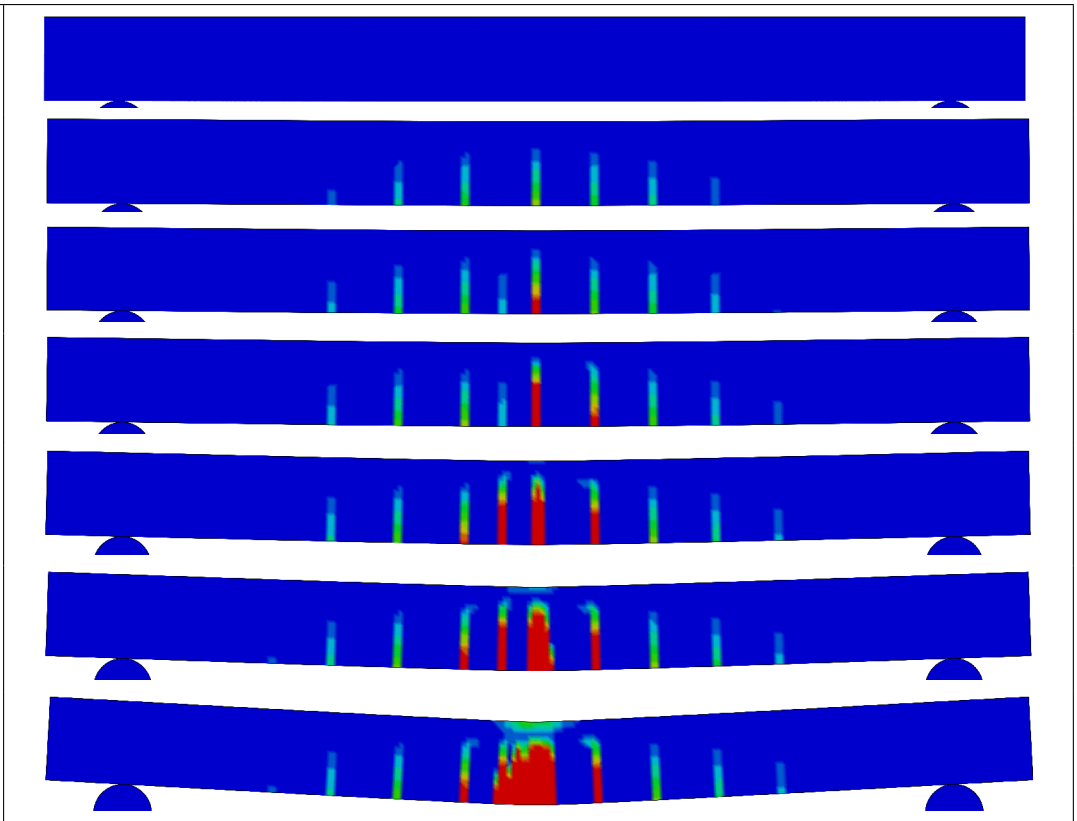
$u = 2.5$ mm $F = 9.1$ kN	
$u = 3.7$ mm $F = 10.7$ kN	
$u = 5.5$ mm $F = 11.8$ kN	
$u = 10.0$ mm $F = 12.6$ kN	
$u = 15.0$ mm $F = 12.5$ kN	
$u = 25.0$ mm $F = 12.3$ kN	
Principal Strain [%]	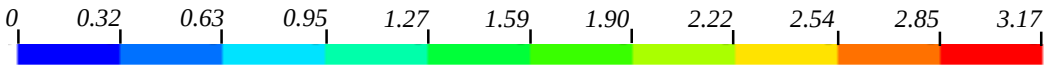

H.4.2 5 mm tetrahedron model

Table H.2 Strain field for static analysis of the 5 mm tetrahedron LS-DYNA model.

Deflection/ Load	Strain field for static loading
$u = 0.2$ mm $F = 3.1$ kN $u = 2.5$ mm $F = 11.0$ kN $u = 3.7$ mm $F = 12.9$ kN $u = 5.5$ mm $F = 14.3$ kN $u = 7.5$ mm $F = 15.4$ kN	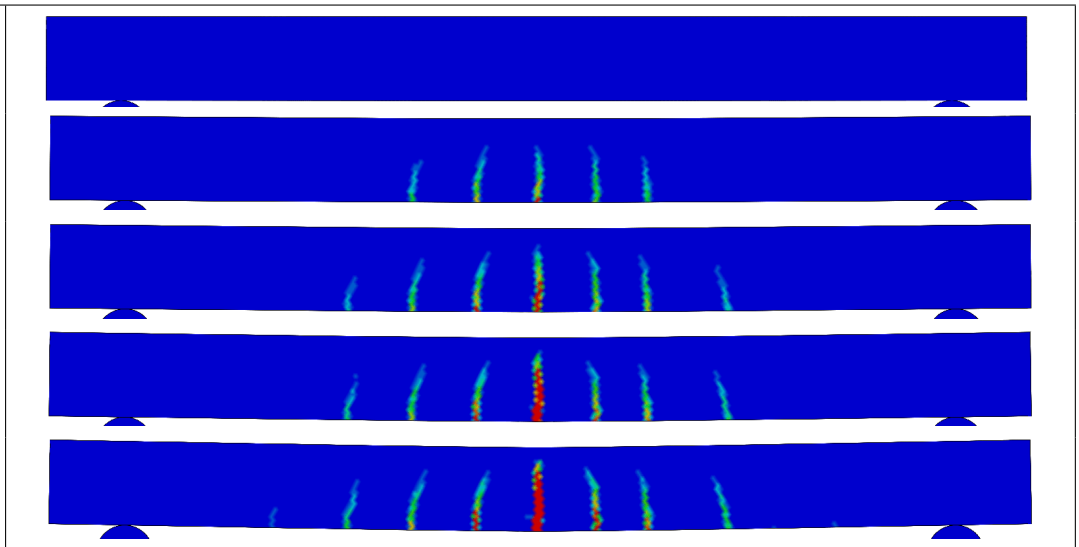
Principal Strain [%]	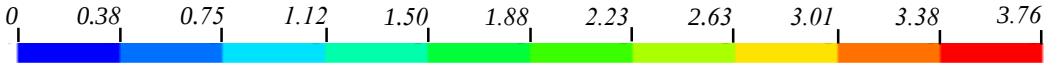

H.4.3 10 mm tetrahedron model

Table H.3 Strain field for static analysis of the 10 mm tetrahedron LS-DYNA model with skin remesh.

Deflection/ Load	Strain field for static loading
$u = 0.2$ mm $F = 2.3$ kN $u = 2.5$ mm $F = 8.6$ kN $u = 3.7$ mm $F = 10.6$ kN $u = 4.9$ mm $F = 12.0$ kN $u = 7.7$ mm $F = 12.6$ kN $u = 9.4$ mm $F = 9.6$ kN	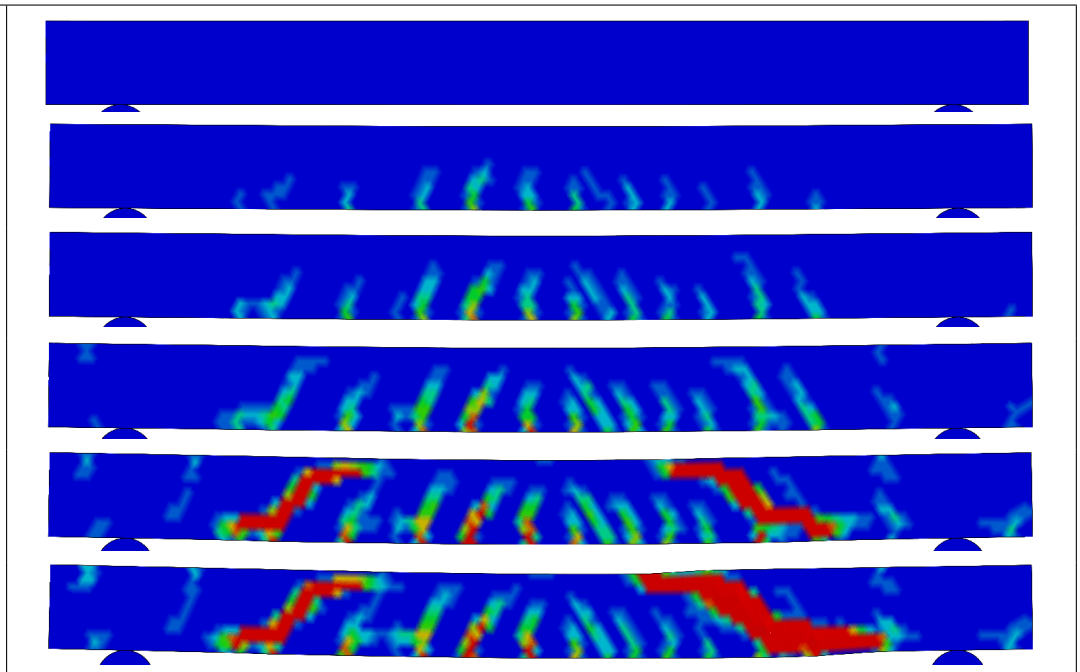
Principal Strain [%]	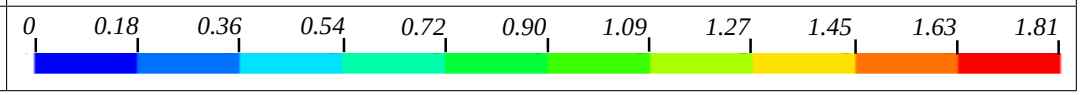

H.4.4 10 mm tetrahedron model without skin remesh

Table H.4 Strain field for static analysis of the 10 mm tetrahedron LS-DYNA model without skin remesh.

Deflection/ Load	Strain field for static loading
$u = 0.2$ mm $F = 4.9$ kN	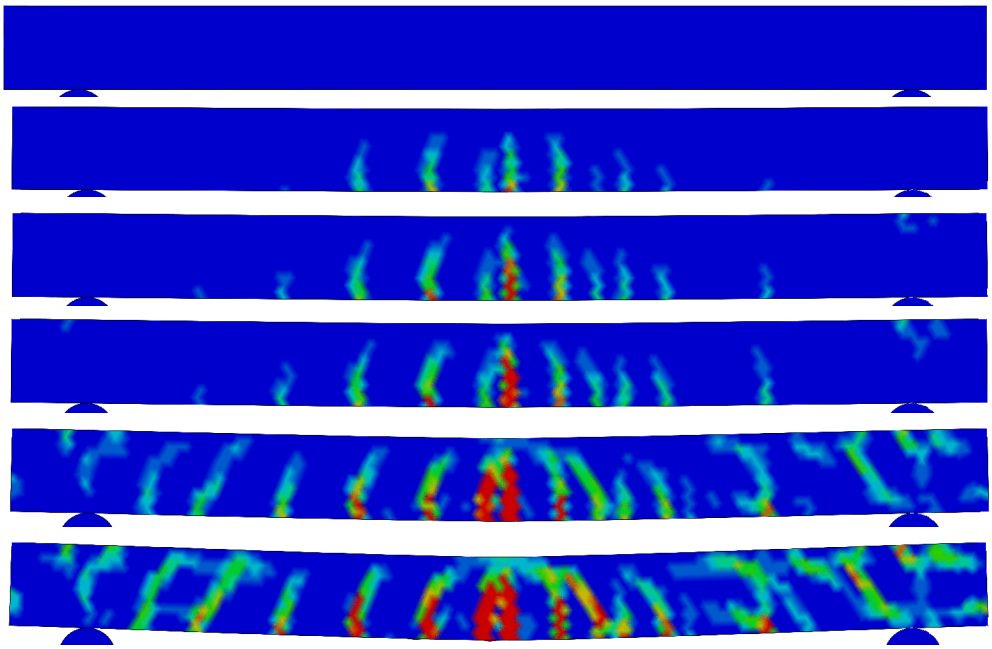
$u = 2.5$ mm $F = 16.2$ kN	
$u = 3.7$ mm $F = 18.7$ kN	
$u = 4.9$ mm $F = 19.9$ kN	
$u = 10.0$ mm $F = 21.2$ kN	
$u = 15.0$ mm $F = 21.0$ kN	
Principal Strain [%]	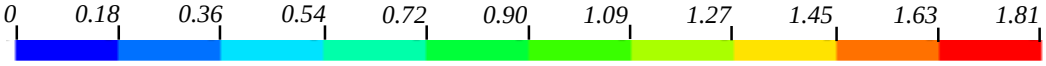

I Calculations

Load Capacity of Reinforced Concrete Beam

The load capacity of a reinforced concrete beam is determined for a given cross section.

$kN := N \cdot 10^3$ $MPa := Pa \cdot 10^6$

1. Input Data

1.1 Geometry

Beam height: $h := 0.1m$

Beam width: $b := 0.1m$

Effective span length: $L := 1m$

Nominal bar diameter: $\Phi := 6mm$

Area of reinforcement bar: $A_{bar} := \pi \cdot \frac{\Phi^2}{4} = 28.274 \cdot mm^2$

Stirrup dimension: $\Phi_s := 0mm$

Note: No stirrups

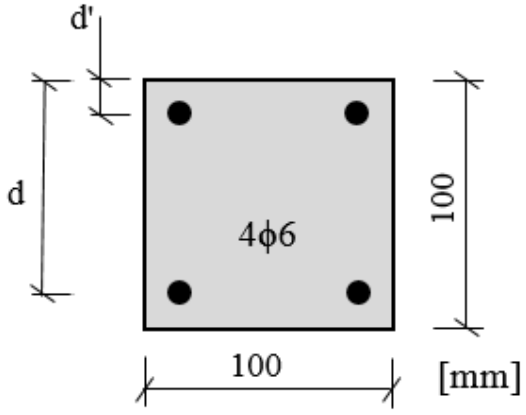

Number of bars in the top: $n' := 2$

Number of bars in the bottom: $n := 2$

Area of top reinforcement: $A_s := n \cdot A_{bar} = 56.549 \cdot mm^2$

Area of bottom reinforcement: $A'_s := n' \cdot A_{bar} = 56.549 \cdot mm^2$

Concrete cover: $c := 0.02m - \frac{\Phi}{2} = 0.017\,m$

Distance from top edge to bottom reinforcement:

Assuming nominal position of the bars: $d := h - \left(\frac{\Phi}{2} + c\right) = 80 \cdot mm$

Adopting the measured position of the bars: $d = h - \left(\frac{\Phi}{2} + 14mm\right)$

Distance from top edge to top reinforcement:

Assuming nominal position of the bars: $d' := \frac{\Phi}{2} + c = 20 \cdot mm$

Adopting the measured position of the bars: $d' = \frac{\Phi}{2} + 18.9mm$

1.2 Material properties

Concrete:	Mean compressive strength:	$f_{cm} := 42.2MPa$
	Mean tensile strength	$f_{ctm} := 3.7 \cdot MPa$
	Mean modulus of elasticity	$E_{cm} := 33.9GPa$
Reinforcing steel:	Mean yield strength:	$f_{ym} := 575MPa$
	Ultimate tensile stress:	$f_t := 686MPa$
	Mean modulus of elasticity:	$E_{sm} := 196 \cdot GPa$

2. Stress-strain Relationship of Concrete

2.1 Mathematic formulation

The parabola-rectangle stress-strain diagram for concrete under compression (according
EN 1992-1-1) is adopted.

Parameters for all concrete classes:

Concrete strain at maximum strength: $\varepsilon_{c2} := 2 \cdot 10^{-3}$

Ultimate concrete strain: $\varepsilon_{cu2} := 3.5 \cdot 10^{-3}$

Exponent: $n := 2$

Stress-strain relationship:

$$\sigma_c(\varepsilon_c) := \begin{cases} \left[1 - \left(1 - \frac{\varepsilon_c}{\varepsilon_{c2}}\right)^n\right] \cdot f_{cm} & \text{if } 0 \le \varepsilon_c \le \varepsilon_{c2} \\ f_{cm} & \text{if } \varepsilon_{c2} < \varepsilon_c \le \varepsilon_{cu2} \end{cases}$$

Create a vector with different values of strain: $\varepsilon_c := 0, 0.0001 .. \varepsilon_{cu2}$

Graphic representation of the stress-strain relationship:

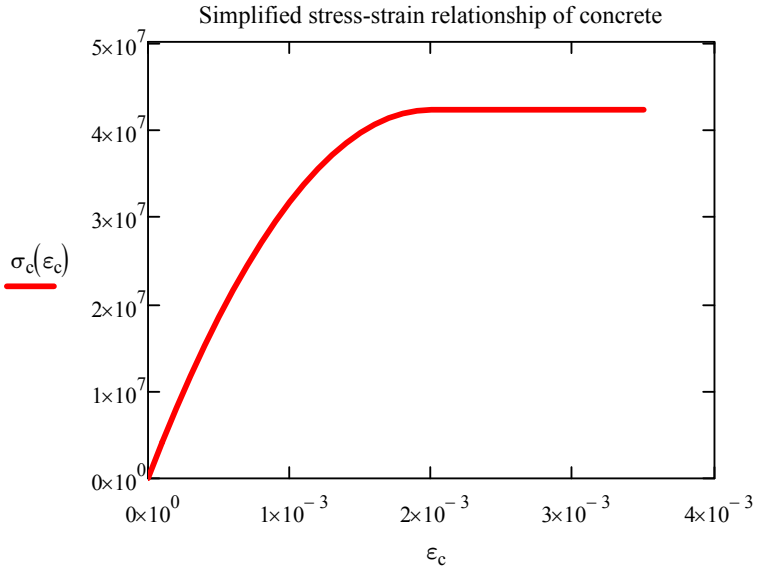

2.2 Determination of block factors

Area under the curve for a given value of strain:

$$\text{Area}(\varepsilon_c) := \int_0^{\varepsilon_c} \sigma_c(\varepsilon_c)\, d\varepsilon_c$$

Area under the curve multiplied by the distance from the origin to the center of gravity o
area:

$$\text{A\_}\varepsilon(\varepsilon_c) := \int_0^{\varepsilon_c} \sigma_c(\varepsilon_c)\cdot\varepsilon_c\, d\varepsilon_c$$

Determination of factors $\alpha_{R.S}$ and $\beta_{R.S}$

$$\alpha_{R.S}(\varepsilon_c) := \frac{\text{Area}(\varepsilon_c)}{f_{cm}\cdot\varepsilon_c} \qquad \alpha_{R.S}(\varepsilon_{cu2}) = 0.81$$

$$\beta_{R.S}(\varepsilon_c) := \frac{\varepsilon_c - \frac{\text{A\_}\varepsilon(\varepsilon_c)}{\text{Area}(\varepsilon_c)}}{\varepsilon_c} \qquad \beta_{R.S}(\varepsilon_{cu2}) = 0.416$$

3. Stress-strain Relationship of Reinforcing Steel

3.1 Mathematic formulation

Ultimate steel strain: $\varepsilon_{su} := 0.108$

Yield strain: $\varepsilon_{sy} := \frac{f_{ym}}{E_{sm}}$ $\varepsilon_{sy} = 2.934 \times 10^{-3}$

Relationship parameters: $p_1(\varepsilon_s) := \frac{\varepsilon_s - \varepsilon_{sy}}{\varepsilon_{su} - \varepsilon_{sy}}$

Stress-strain relationship:

$$\sigma_s(\varepsilon_s) := \begin{cases} (E_{sm} \cdot \varepsilon_s) & \text{if } \varepsilon_s \le \varepsilon_{sy} \\ f_{ym} + p_1(\varepsilon_s) \cdot (f_t - f_{ym}) & \text{if } \varepsilon_s > \varepsilon_{sy} \end{cases}$$

$\varepsilon_s := 0, 0.001 .. \varepsilon_{su}$

Graphic representation of the stress-strain relationship for reinforcing steel:

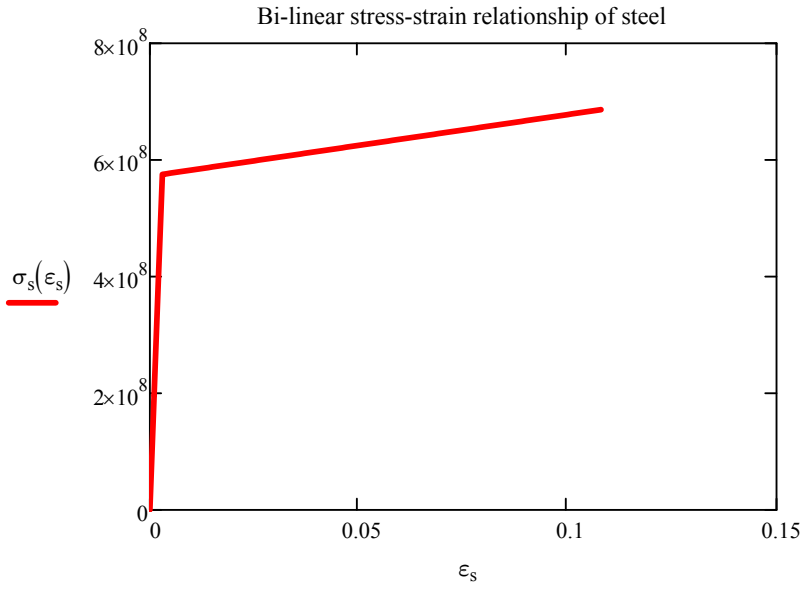

4. Design Strength Values

4.1 Concrete

Partial factor: $\gamma_C := 1.0$

Design compressive strength: $f_{cd} := \frac{f_{cm}}{\gamma_C}$ $f_{cd} = 42.2 \cdot MPa$

Concrete ultimate strain: $\varepsilon_{cu} := 0.0035$

Stress block factors: $\alpha_R := \alpha_{R.S}(\varepsilon_{cu}) = 0.81$

$\beta_R := \beta_{R.S}(\varepsilon_{cu2}) = 0.416$

5%-fractile tensile strength: $f_{ctk0.05} := 0.7 \cdot f_{ctm} = 2.59 \cdot MPa$

Flexural tensile strength: $\kappa := 0.6 + \frac{0.4}{\sqrt[4]{\frac{h}{m}}} = 1.311$

$f_{ct.fl} := \kappa \cdot f_{ctm} = 4.852 \cdot MPa$

4.2 Reinforcing steel

Partial factor: $\gamma_S := 1.0$

Design yield stress: $f_{yd} := \frac{f_{ym}}{\gamma_S}$ $f_{yd} = 575 \cdot MPa$

5. Load Capacity in Ultimate Limit State

5.1 Analysis of field section without top reinforcement

Number of bars in the top: $n' := 0$

Number of bars in the bottom: $n = 2$

Assume yielding: $\varepsilon_{s.1} > \varepsilon_{sy}$ $\varepsilon_{s.1} = \frac{d - x_1}{x_1}\varepsilon_{cu}$

Position of neutral axis:

Initial guess: $x_{u.1} := 20mm$

Calculated value: $x_{u.1} := root\left(\alpha_R \cdot f_{cd} \cdot b \cdot x_{u.1} - \sigma_s\left(\frac{d - x_{u.1}}{x_{u.1}}\varepsilon_{cu}\right) \cdot n \cdot A_{bar}, x_{u.1}\right)$

$x_{u.1} = 9.9 \cdot mm$

Check the strain in the reinforcement bars:

$\varepsilon_{s.1} := \frac{d - x_{u.1}}{x_{u.1}}\varepsilon_{cu} = 0.025$ $\varepsilon_{sy} = 2.934 \times 10^{-3}$ $\varepsilon_{s.1} > \varepsilon_{sy} = 1$

Calculation of load capacity:

$M_{u.1} := \alpha_R \cdot f_{cd} \cdot b \cdot x_{u.1} \cdot (d - \beta_R \cdot x_{u.1})$ $M_{u.1} = 2.566 \cdot kN \cdot m$

$F_{u.1} := \frac{4 \cdot M_{u.1}}{L}$ $F_{u.1} = 10.266 \cdot kN$

Calculation of stress in the steel bars:

$\sigma_{s.1} := \sigma_s(\varepsilon_{s.1})$ $\sigma_{s.1} = 598.083 \cdot MPa$

Calculation of curvature at failure:

$\varepsilon_{s.1} = 0.025$ $\varphi_{u.1} := \frac{\varepsilon_{s.1}}{d - x_{u.1}} = 0.354\,m^{-1}$

5.2 Analysis of field section including top reinforcement

Number of bars in the top: $n' := 2$

Number of bars in the bottom: $n = 2$

Assume tension in top and bottom and that the neutral axis is located above the top reinforcerment.

Strain in bottom reinforcement: $\varepsilon_{s.2} = \frac{d - x_{u.2}}{x_{u.2}}\varepsilon_{cu}$

Strain in top reinforcement: $\varepsilon'_{s.2} = \frac{d' - x_{u.2}}{x_{u.2}}\varepsilon_{cu}$

Position of neutral axis:

Initial guess: $x_{u.2} := 20mm$

Calculated value:

$$x_{u.2} := \text{root}\left(\alpha_R \cdot f_{cd} \cdot b \cdot x_{u.2} - \sigma_s\left(\frac{d' - x_{u.2}}{x_{u.2}}\varepsilon_{cu}\right)\cdot A'_s - \sigma_s\left(\frac{d - x_{u.2}}{x_{u.2}}\varepsilon_{cu}\right)\cdot A_s, x_{u.2}\right)$$

$x_{u.2} = 14.288 \cdot mm$

Note: The neutral axis is indeed located above the top reinforcement. Top bars are subjected to tensile stress.

Check the strain in the reinforcement bars:

$\varepsilon_{s.2} := \frac{d - x_{u.2}}{x_{u.2}}\varepsilon_{cu} = 0.016$ $\quad \varepsilon_{sy} = 2.934 \times 10^{-3}$ $\quad \varepsilon_{s.2} > \varepsilon_{sy} = 1$

$\varepsilon'_{s.2} := \frac{d' - x_{u.2}}{x_{u.2}}\varepsilon_{cu} = 1.399 \times 10^{-3}$ $\quad \varepsilon'_{s.2} > \varepsilon_{sy} = 0$

Calculation of moment capacity:

$M_{u.2} := \alpha_R \cdot f_{cd} \cdot b \cdot x_{u.2} \cdot \left(d - \beta_R \cdot x_{u.2}\right) - \sigma_s\left(\frac{d' - x_{u.2}}{x_{u.2}}\varepsilon_{cu}\right)\cdot A'_s \cdot (d - d')$ $\quad M_{u.2} = 2.684 \cdot kN \cdot m$

$F_{u.2} := \frac{4 \cdot M_{u.2}}{L}$ $\quad F_{u.2} = 10.737 \cdot kN$

Calculation of stress in the steel bars:

$\sigma'_{s.2} := \sigma_s\left(\varepsilon'_{s.2}\right)$ $\quad \sigma'_{s.2} = 274.25 \cdot MPa$

$\sigma_{s.2} := \sigma_s\left(\varepsilon_{s.2}\right)$ $\quad \sigma_{s.2} = 588.907 \cdot MPa$

Calculation of curvature at failure:

$\varepsilon_{s.2} = 0.016$ $\quad \varphi_{u.2} := \frac{\varepsilon_{s.2}}{d - x_{u.2}} = 0.245\ m^{-1}$

6. Moment and Curvature at Onset of Yielding

6.1 Analysis of field section without top reinforcement

Yielding strain: $\varepsilon_{sy} = 2.934 \times 10^{-3}$

Definition of strain in the compressed edge:

$$\varepsilon_{cc.y.1} = \frac{x_{y.1}}{d - x_{y.1}} \cdot \varepsilon_{sy}$$

Tensile force in the bottom reinforcement:

$$F_{sy} := f_{yd} \cdot n \cdot A_{bar} = 32.515 \cdot kN$$

Equivalent compressive force in concrete

$$F_{C.y.1} = \alpha_{R.y} \cdot f_{cd} \cdot b \cdot x_{y.1} \qquad \alpha_{R.y} = \alpha_{R.S}\left(\varepsilon_{cc.y.1}\right)$$

Horizontal equilibrium condition:

$$F_{sy} = F_{C.y}$$

Assume $x_{y.1} := 19.425mm$

Total tensile force: $F_{sy} = 32.515 \cdot kN$

Total compressive force: $F_{C.y.1} := \alpha_{R.S}\left(\frac{x_{y.1}}{d - x_{y.1}} \cdot \varepsilon_{sy}\right) \cdot f_{cd} \cdot b \cdot x_{y.1} = 32.513 \cdot kN$

$\Delta F := F_{C.y.1} - F_{sy} = -2.503 \times 10^{-3} \cdot kN$

Note: Check that $\Delta F \approx 0$

Calculation of strains

$$\varepsilon_{cc.y.1} := \frac{x_{y.1}}{d - x_{y.1}} \cdot \varepsilon_{sy} = 9.408 \times 10^{-4} \qquad \varepsilon_{cc.y.1} < \varepsilon_{c2} = 1$$

Calculation of moment at yielding:

$\alpha_{R.y} := \alpha_{R.S}\left(\varepsilon_{cc.y.1}\right) = 0.397$ $\beta_{R.y} := \beta_{R.S}\left(\varepsilon_{cc.y.1}\right) = 0.349$

$M_{y.1} := \alpha_{R.y} \cdot f_{cd} \cdot b \cdot x_{y.1} \cdot \left(d - \beta_{R.y} \cdot x_{y.1}\right)$ $M_{y.1} = 2.381 \cdot kN \cdot m$ $F_{y.1} := \frac{4 \cdot M_{y.1}}{L} = 9.523 \cdot kN$

Determination of stresses in the reinforcement bars:

$\sigma_{s.y.1} := \sigma_s(\varepsilon_{sy})$ $\sigma_{s.y.1} = 575 \cdot MPa$

Curvature at yielding

$\varepsilon_{sy} = 2.934 \times 10^{-3}$ $\varphi_{y.1} := \frac{\varepsilon_{sy}}{d - x_{y.1}} = 0.048\,m^{-1}$

6.2 Analysis of field section including top reinforcement

Assume tension in the top reinforcement bars

Yielding strain: $\varepsilon_{sy} = 2.934 \times 10^{-3}$

Definition of strain in the compressed edge and top reinforcement:

$$\varepsilon_{cc.y.2} = \frac{x_{y.2}}{d - x_{y.2}} \cdot \varepsilon_{sy} \qquad \varepsilon'_{s.y.2} = \frac{d' - x_{y.2}}{d - x_{y.2}} \cdot \varepsilon_{sy}$$

Tensile force in the reinforcement:

Top reinforcement: $F'_{sy.2} = \sigma_s(\varepsilon'_{s.y.2}) \cdot A'_s$

Bottom reinforcement: $F_{sy} := f_{yd} \cdot A_s = 32.515 \cdot kN$

Equivalent compressive force in concrete

$F_{C.y.2} = \alpha_{R.y} \cdot f_{cd} \cdot b \cdot x_{y.2}$ $\alpha_{R.y} = \alpha_{R.S}(\varepsilon_{cc.y.2})$

Horizontal equilibrium condition:

$F'_{sy.2} + F_{sy} = F_{C.y.2}$

Assume $x_{y.2} := 19.505mm$

Total tensile force: $F_{T.y.2} := F_{sy} + \sigma_s\left(\frac{d' - x_{y.2}}{d - x_{y.2}} \cdot \varepsilon_{sy}\right) \cdot A'_s = 32.782 \cdot kN$

Total compressive force: $F_{C.y.2} := \alpha_{R.S}\left(\frac{x_{y.2}}{d - x_{y.2}} \cdot \varepsilon_{sy}\right) \cdot f_{cd} \cdot b \cdot x_{y.2} = 32.791 \cdot kN$

$\Delta F := F_{C.y.2} - F_{T.y.2} = 9.902 \times 10^{-3} \cdot kN$

Note: Check that $\Delta F \approx 0$

Calculation of strains

$$\varepsilon_{cc.y.2} := \frac{x_{y.2}}{d - x_{y.2}} \cdot \varepsilon_{sy} = 9.459 \times 10^{-4} \qquad \varepsilon_{cc.y.2} < \varepsilon_{c2} = 1$$

$$\varepsilon'_{s.y.2} := \frac{d' - x_{y.2}}{x_{y.2}} \cdot \varepsilon_{cc.y.2} = 2.4 \times 10^{-5}$$

Calculation of moment at yielding:

$$\alpha_{R.y} := \alpha_{R.S}(\varepsilon_{cc.y.2}) = 0.398 \qquad \beta_{R.y} := \beta_{R.S}(\varepsilon_{cc.y.2}) = 0.349$$

$$M_{y.2} := \alpha_{R.y} \cdot f_{cd} \cdot b \cdot x_{y.2} \cdot (d - \beta_{R.y} \cdot x_{y.2}) - \sigma_s\left(\frac{d' - x_{y.2}}{x_{y.2}} \varepsilon_{cc.y.2}\right) \cdot A'_s \cdot (d - d')$$

$$M_{y.2} = 2.384 \cdot kN \cdot m \qquad F_{y.2} := \frac{4 \cdot M_{y.2}}{L} = 9.537 \cdot kN$$

Determination of stresses in the reinforcement bars:

Top reinforcement: $\sigma'_{s.y.2} := \sigma_s(\varepsilon'_{s.y.2})$ $\sigma'_{s.y.2} = 4.705 \cdot MPa$

Bottom reinforcement: $\sigma_{s.y.2} := \sigma_s(\varepsilon_{sy})$ $\sigma_{s.y.2} = 575 \cdot MPa$

Curvature at yielding

$$\varepsilon_{sy} = 2.934 \times 10^{-3} \qquad \varphi_{y.2} := \frac{\varepsilon_{sy}}{d - x_{y.2}} = 0.048\ m^{-1}$$

7. Shear Capacity of Reinforced Concrete Beam

Theoretical shear capacity:

$V_c = b \cdot d \cdot f_v$

$f_v = \tau_{Rd} \cdot \kappa_V \cdot (1.2 + 40 \cdot \rho_1)$

Tensile strength: $f_{ctm} = 3.7 \cdot MPa$

5%-fractile tensile strength: $f_{ctk0.05} = 2.59 \cdot MPa$

Factor: $\kappa_V := 1$

Partial design factor: $\gamma_c := 1$

$$\tau_{Rd} := 0.25 \cdot \frac{f_{ctk0.05}}{\gamma_c} = 0.647 \cdot MPa$$

Area of tensile reinforcement: $A_s = 56.549 \cdot mm^2$

Tensile reinforcement ratio: $\rho_1 := \frac{A_s}{b \cdot d} = 7.069 \times 10^{-3}$

Design Shear Strength: $f_v := \tau_{Rd} \cdot \kappa_V \cdot (1.2 + 40 \cdot \rho_1) = 0.96 \cdot MPa$

Desing Shear Capacity: $V_c := b \cdot d \cdot f_v = 7.681 \cdot kN$

Ultimate External Load: $F_{V.c} := 2 \cdot V_c = 15.361 \cdot kN$

8. Summary

8.1 Moment and curvature at yielding without consideration of top reinforcement

$M_{y.1} = 2.381 \cdot kN \cdot m$ $x_{y.1} = 19.425 \cdot mm$

$F_{y.1} = 9.523 \cdot kN$ $\varphi_{y.1} = 0.048\ m^{-1}$

8.2 Moment and curvature at yielding considering both top and bottom reinforcement

$M_{y.2} = 2.384 \cdot kN \cdot m$ $x_{y.2} = 19.505 \cdot mm$

$F_{y.2} = 9.537 \cdot kN$ $\varphi_{y.2} = 0.048\ m^{-1}$

8.3 Load Capacity at Ultimate State without consideration of top reinforcement

$M_{u.1} = 2.566 \cdot kN \cdot m$ $x_{u.1} = 9.9 \cdot mm$

$F_{u.1} = 10.266 \cdot kN$ $\varphi_{u.1} = 0.354\ m^{-1}$

8.4 Load Capacity at Ultimate State considering both top and bottom reinforcement

$M_{u.2} = 2.684 \cdot kN \cdot m$ $x_{u.2} = 14.288 \cdot mm$

$F_{u.2} = 10.737 \cdot kN$ $\varphi_{u.2} = 0.245\ m^{-1}$

Increase in load capacity if top reinforcement is considered: $\frac{F_{u.2} - F_{u.1}}{F_{u.1}} = 4.592 \cdot \%$

8.5 Shear Capacity

$V_c = 7.681 \cdot kN$

$F_{V.c} = 15.361 \cdot kN$

$F_{V.c} > F_{u.2} = 1$ **Note:** The dominant failure mode corresponds to bending failure

Theoretical Load vs Deformation Relationship

1. Determination of Cracking Moment and Cracking Curvature:

Modular ratio: $\alpha_s := \frac{E_{sm}}{E_{cm}} = 5.782$

Moment of inertia in State I: $I_I := \frac{b \cdot h^3}{12} + (\alpha_s - 1) 2n \cdot A_{bar} \cdot \left(d - \frac{h}{2}\right)^2 = 8.82 \times 10^6 \cdot mm^4$

Cracking stress: $f_{ct.fl} = \frac{M_{cr} \cdot \left(\frac{h}{2}\right)}{I_I}$

Cracking moment: $M_{cr} := \frac{f_{ct.fl} \cdot I_I}{\frac{h}{2}} = 0.856 \cdot kN \cdot m$

Cracking force: $F_{cr} := \frac{4 \cdot M_{cr}}{L} = 3.423 \cdot kN$

2. Determination of Moment of Inertia in State II

Calculation of position of neutral axis:

Number of bars in the top: $n' = 2$

Number of bars in the bottom: $n = 2$

Consider first moment of area around the neutral axis:

$$\frac{b \cdot x_{II}^2}{2} + (\alpha_s - 1) \cdot A'_s \cdot (x_{II} - d') = \alpha_s \cdot A_s \cdot (d - x_{II})$$

Initial guess:

$x_{II} := 50mm$

Calculated value:

$$x_{II} := root\left[\frac{b \cdot x_{II}^2}{2} - (\alpha_s) \cdot A'_s \cdot (d' - x_{II}) - \alpha_s \cdot A_s \cdot (d - x_{II}), x_{II}\right]$$

$x_{II} = 19.855 \cdot mm$

Moment of inertia:

$$I_{II} := \frac{b \cdot x_{II}^{3}}{3} + (\alpha_s) \cdot A'_s \cdot (d' - x_{II})^2 + \alpha_s \cdot A_s \cdot (d - x_{II})^2$$

$$I_{II} = 1.444 \times 10^{-6}\, m^4$$

3. Load-Deformation plot

3.1 Determination of equivalent stiffness

Stiffness in State I:

$$K_I := \frac{48 \cdot E_{cm} \cdot I_I}{L^3} = 14.352 \cdot \frac{kN}{mm}$$

Stiffness in State II:

$$K_{II} := \frac{48 \cdot E_{cm} \cdot I_{II}}{L^3} = 2.349 \cdot \frac{kN}{mm}$$

3.2 Deformation considering only State II until ultimate load

Peak load:

$$F_{u.2} = 10.737 \cdot kN$$

Deflection at peak load:

$$u_{II} := \frac{F_{u.2}}{K_{II}} = 4.571 \cdot mm$$

Load as a function of displacement:

$$Force_2(u) := \begin{cases} u \cdot K_{II} & \text{if } u < u_{II} \\ F_{u.2} & \text{if } u > u_{II} \end{cases}$$

3.3 Deformation considering State I and State II

Cracking load:

$$F_{cr} = 3.423 \cdot kN$$

Deflection when cracking occurs:

$$u_{cr} := \frac{F_{cr}}{K_I} = 0.239 \cdot mm$$

Peak load:

$$F_{u.2} = 10.737 \cdot kN$$

Deflection at peak load:

$$u_{II} = 4.571 \cdot mm$$

Stiffness between cracking and yielding:

$$K_{cy} := \frac{F_{u.2} - F_{cr}}{u_{II} - u_{cr}} = 1.688 \cdot \frac{kN}{mm}$$

Load as a function of displacement:

$$\text{Force}(u) := \begin{cases} (K_I \cdot u) & \text{if } u \le u_{cr} \\ \left[F_{cr} + (u - u_{cr}) \cdot K_{cy}\right] & \text{if } u > u_{cr} \\ F_{u.2} & \text{if } u > u_{II} \end{cases}$$

$u := 0\text{mm}, 0.01\text{mm} .. 30\text{mm}$

3.4 Load-deformation curves

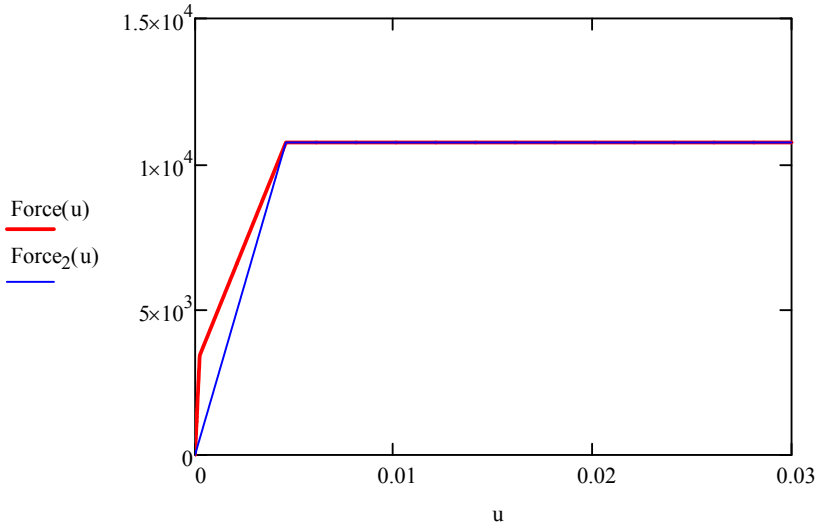

Prediction of Plastic Rotational Capacity

The plastic rotational capacity of a simply-supported reinforced concrete beam is to be determine according to different equations.

1. Input Data

1.1 Geometry

Beam height: $h = 0.1\,m$

Beam width: $b = 0.1\,m$

Effective span length: $L = 1\,m$

Distance to critical section from support: $l_0 := \frac{L}{2} = 500 \cdot mm$

Effective height: $d = 0.08\,m$

2. Rotation Capacity According to Eurocode 2

Determine allowable rotation for reference beam ($\lambda = 3$):

$x_u := x_{u.1} = 9.9 \cdot mm$ **Note:** Position of neutral axis considering only bottom reinforcement.

$\frac{x_u}{d} = 0.124$

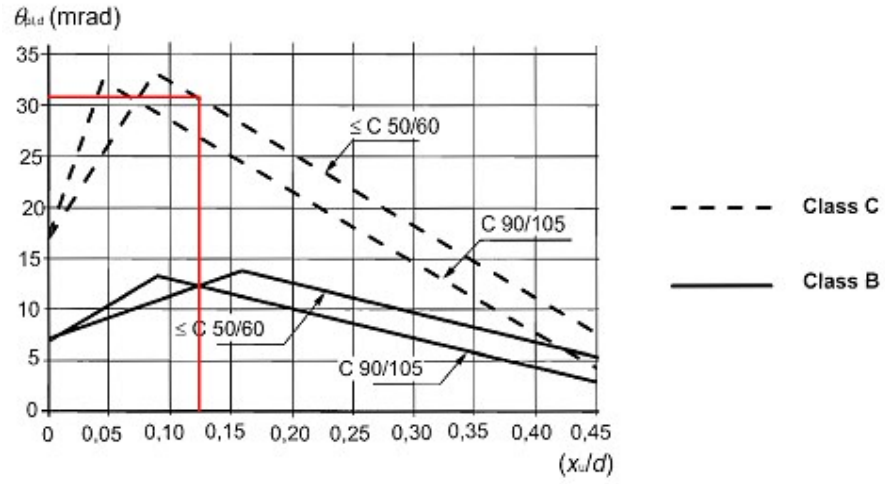

Rotation capacity from the chart:

$\Theta_{total.Eur.R} := 0.031$

Correction for different values of shear slenderness:

$$\lambda := \frac{l_0}{d} = 6.25 \qquad \kappa_\lambda := \sqrt{\frac{\lambda}{3}} = 1.443$$

$$\Theta_{total.Eur} := \kappa_\lambda \cdot \Theta_{total.Eur.R} = 0.045$$

Consider:

$$\Theta_{total.Eur} = 2 \cdot \theta_{pl.Eur}$$

Rotational capacity according to Eurocode 2:

$$\theta_{pl.Eur} := \frac{\Theta_{total.Eur}}{2} = 0.022$$

$$u_{pl.Eur} := \frac{\theta_{pl.Eur} \cdot L}{2} = 11.186 \cdot mm$$

3. Rotation Capacity According to Betonghandbok-Konstruktion (ABC Method)

Mathematic expression:

$$\theta_{pl.ABC.95} = A \cdot B \cdot C \cdot 10^{-3}$$

When measured values of material strength are used in calculation, then:

$$A = 1 + 1.3 \cdot \omega_v + 3 \cdot \omega'_s - 5 \cdot \omega_s$$

Area of tensile reinforcement: $A_s = 56.549 \cdot mm^2$

$$\omega_s := \frac{A_s}{b \cdot d} \cdot \frac{f_{ym}}{f_{cm}} = 0.096$$

Since no stirrups were included, the contribution of the top bars can be disregarded

Area of compression reinforcement: $A_c := 0$ **Note:** the top reinforcement has been proved to be subjected to tensile stress.

$$\omega'_s := \frac{A_c}{b \cdot d} \cdot \frac{f_{ym}}{f_{cm}} = 0$$

Shear reinforcement $A_v := 0$

$\omega_v := 0$

Calculation of factor *A:*

$A := 1 - 5 \cdot \omega_s = 0.518$ $A > 0.05 = 1$

$A < 2.3 = 1$

Parameter *B* depends on the steel type:

$B := 1.0$

Parameter *C* takes into account the position of the plastic hinge.

$C := 7 \cdot \frac{l_0}{d} = 43.75$

Determination of plastic rotational capacity:

$\theta_{pl.95.ABC} := A \cdot B \cdot C \cdot 10^{-3} = 0.023$

$u_{pl.95.ABC} := \frac{\theta_{pl.95.ABC} \cdot L}{2} = 11.341 \cdot mm$

4 Rotation Capacity According to Bk 25

Empirical expression:

$l_{p.Bk25.f} = 0.5 \cdot d + 0.15L$ Plastic hinge on the field

$l_{p.Bk25.s} = 0.5d + 0.1l_0$ Plastic hinge over the support

Plastic hinge length:

$l_{p.Bk25.f} := 0.5 \cdot d + 0.15L = 190 \cdot mm$

$l_{p.Bk25.s} := 0.5 \cdot d + 0.1l_0 = 90 \cdot mm$

Dominant failure mode:

$\omega_{s.crit} := \frac{0.8 \cdot \varepsilon_{cu}}{\varepsilon_{cu} + \varepsilon_{su}} = 0.025$ $\omega_s = 0.096$

$\omega_s > \omega_{s.crit} = 1$ **Note:** The dominant failure mode is concrete crushing

Determination of plastic rotation capacity:

$$\theta_{pl.Bk25.f} := \frac{0.4\cdot\varepsilon_{cu}}{\omega_s}\left(1 + 0.3\cdot\frac{L}{d}\right) = 0.069 \qquad u_{pl.Bk25.f} := \frac{\theta_{pl.Bk25.f}\cdot L}{2} = 34.523\cdot mm$$

$$\theta_{pl.Bk25.s} := \frac{0.4\cdot\varepsilon_{cu}}{\omega_s}\left(1 + 0.2\cdot\frac{l_0}{d}\right) = 0.033 \qquad u_{pl.Bk25.s} := \frac{\theta_{pl.Bk25.s}\cdot L}{2} = 16.353\cdot mm$$

5. Empirical Methods Based on Equivalent Plastic Hinge Length

5.1 Plastic curvature

Curvature at yielding: $\varphi_y := \varphi_{y.1}$

Curvature at failure: $\varphi_u := \varphi_{u.1}$

Plastic curvature: $\varphi_{pl} := \varphi_{u.1} - \varphi_y = 0.305\ m^{-1}$

5.2 Determination of equivalent plastic hinge length and rotational capacity

The plastic rotational capacity is determined according to: $\theta_{pl} = \varphi_{pl}\cdot l_p$

$M_u := M_{u.1}$ $M_y := M_{y.1}$

Mattock

Empirical expression:

$$l_{p.Mattock} = 0.5\cdot d + 0.5d\cdot\left(1.14\cdot\sqrt{\frac{l_0}{d}} - 1\right)\cdot\left[1 - \left(\frac{\omega_s - \omega'_s}{\omega_b}\right)\cdot\sqrt{\frac{d}{411.48mm}}\right]$$

Mechanical tensile reinforcement ratio: $\omega_s = 0.096$

Mechanical compressive reinforcement ratio: $\omega'_s = 0$

Balanced mechanical reinforcement ratio: $\omega_b := \frac{0.8\cdot\varepsilon_{cu}}{\varepsilon_{cu} + \varepsilon_{sy}} = 0.435$

Determination of plastic hinge length:

$$l_{p.Mattock} := 0.5 \cdot d + 0.5d \cdot \left(1.14 \cdot \sqrt{\frac{l_0}{d}} - 1 \right) \cdot \left[1 - \left(\frac{\omega_s - \omega'_s}{\omega_b} \right) \cdot \sqrt{\frac{d}{411.48mm}} \right] = 106.779 \cdot mm$$

Rotational capacity:

$$\theta_{pl.Mattock} := \left(\varphi_{u.1} - \varphi_y \cdot \frac{M_u}{M_y} \right) \cdot l_{p.Mattock} = 0.032$$

Corley

Empirical expression:

$$l_{p.Corley} = 0.5 \cdot d + 1.008 \sqrt{d} \cdot \left(\frac{l_0}{d} \right)$$

Determination of plastic hinge length:

$$l_{p.Corley} := 0.5 \cdot d + 1.008 \sqrt{d \cdot mm^{-1}} \cdot \left(\frac{l_0}{d} \right) \cdot mm = 96.349 \cdot mm$$

Rotational capacity:

$$\theta_{pl.Corley} := \left(\varphi_u - \varphi_y \cdot \frac{M_u}{M_y} \right) \cdot l_{p.Corley} = 0.029$$

Mattock's discussion on Corley's work

Empirical expression:

$$l_{p.Corley.Mattock} = 0.5 \cdot d + 0.05 \cdot l_0$$

Determination of plastic hinge length:

$$l_{p.Corley.Mattock} := 0.5 \cdot d + 0.05 \cdot l_0 = 65 \cdot mm$$

Rotational capacity:

$$\theta_{pl.Corley.Mattock} := \left(\varphi_u - \varphi_y \cdot \frac{M_u}{M_y} \right) \cdot l_{p.Corley.Mattock} = 0.02$$

Sawyer

Empirical expression:

$l_{p.Sawyer} = 0.25 \cdot d + 0.075 \cdot l_0$

Determination of plastic hinge length:

$l_{p.Sawyer} := 0.25 \cdot d + 0.075 \cdot l_0 = 57.5 \cdot mm$

Rotational capacity:

$\theta_{pl.Sawyerr} := \varphi_{pl} \cdot l_{p.Sawyer} = 0.018$

6. Summary

Eurocode 2:	$\theta_{pl.Eur} = 0.022 \cdot rad$
Bk25 method:	$\theta_{pl.Bk25.s} = 0.033 \cdot rad$
ABC method :	$\theta_{pl.95.ABC} = 0.023 \cdot rad$
Mattock:	$\theta_{pl.Mattock} = 0.032 \cdot rad$
Corley:	$\theta_{pl.Corley} = 0.029 \cdot rad$
Mattock's discussion on Corley's:	$\theta_{pl.Corley.Mattock} = 0.02 \cdot rad$
Sawyer:	$\theta_{pl.Sawyerr} = 0.018 \cdot rad$

J MATLAB Script

```
%%%%%%%%%%%%%%%%%%%%%%%%%%%%%%%%%%%%%%%%%%%%%%%%%%%%%%%%%%%%%%%%%%%%%%%%%%%%%%%%
%%%%%%%%%%%%                                                          %%%%%%%%%%%%
%%%%%%%%%%%%    Plastic Deformation Capacity of Concrete Beams        %%%%%%%%%%%%
%%%%%%%%%%%%           Subjected to Impact Loading                    %%%%%%%%%%%%
%%%%%%%%%%%%                                                          %%%%%%%%%%%%
%%%%%%%%%%%%              Simplified 2DOF System                      %%%%%%%%%%%%
%%%%%%%%%%%%                                                          %%%%%%%%%%%%
%%%%%%%%%%%%                                                          %%%%%%%%%%%%
%%%%%%%%%%%%               Fabio Lozano Mendoza                       %%%%%%%%%%%%
%%%%%%%%%%%%               Josef Makdesi Aphram                       %%%%%%%%%%%%
%%%%%%%%%%%%                                                          %%%%%%%%%%%%
%%%%%%%%%%%%         Chalmers University of Technology                %%%%%%%%%%%%
%%%%%%%%%%%%                                                          %%%%%%%%%%%%
%%%%%%%%%%%%               03 - April - 2017                          %%%%%%%%%%%%
%%%%%%%%%%%%                                                          %%%%%%%%%%%%
%%%%%%%%%%%%%%%%%%%%%%%%%%%%%%%%%%%%%%%%%%%%%%%%%%%%%%%%%%%%%%%%%%%%%%%%%%%%%%%%
clear all
close all
clc

%% MATERIAL PROPERTIES

% Concrete
r_c = 2425;          % [kg/m^3] Mass density
E_c = 33.9e9;        % [Pa] Modulus of elasticity

% Steel
r_s = 7800;          % [kg/m^3] Mass density
E_s = 200e9;         % [Pa] Modulus of elasticity


%% GEOMETRY

A_1 = 5027e-6;       % [m^2] Area dropweight
A_2 = 0.1*0.1;       % [m^2] Area beam

L_b = 1;             % [m] Length Beam
L_d = 0.258;         % [m] Length Drop-weight


%% TRANSFORMATION FACTORS

% Transformation factors for the beam

k_b_m_el = 0.486;    % Elastic mass transformation factor
k_b_m_pl = 0.333;    % Plastic mass transformation factor

k_b_F_el = 1;        % Elastic load transformation factor
k_b_F_pl = 1;        % Plastic load transformation factor
```

```
k_b_K_el = 1;       % Elastic stiffness transformation factor
k_b_K_pl = 1;       % Plastic stiffness transformation factor

% Trasnformation factors for the drop-weight

k_d_m = 1;          % Plastic mass transformation factor
k_d_F = 1;          % Plastic load transformation factor
k_d_K = 1;          % Plastic stiffness transformation factor


%% MASS PROPERTIES

m_1 = 10.093;       %[kg] mass of the drop-weight
m_2 = r_c*A_2*L_b;  %[kg] mass of the beam

% Mass matrix

M = [m_1*k_d_m 0; 0 m_2*k_b_m_pl];


%% STIFFNESS PROPERTIES

% I_b_ii = 1.565e-6;   % [m^4] Second moment of inertia of the beam
%                      %       corresponding to the stiffness in state II.
%                      %       Calculated beforehand for adjusted position of
%                      %       reinforcement bars.

I_b_ii = 1.444e-6;   % [m^4] Second moment of inertia of the beam
                     %       corresponding to the stiffness in state II.
                     %       Calculated beforehand for nominal position of
                     %       reinforcement bars



K_el_1 = A_1*E_s/L_d;          % [N/m] Elastic stiffness of the drop-weight
K_el_2 = 48*E_c*I_b_ii/L_b^3;  % [N/m] Elastic stiffness of the beam


% Initial stiffness matrix

K_el = [K_el_1 -K_el_1;
        -K_el_1 K_el_1+K_el_2];


%% MATERIAL RESPONSE

% Drop-weight

R_1 = 50000;                % [N] Plastic resistance
u_el_1 = R_1/K_el_1;        % [m] Limit of elastic deformation
u_rd_1 = 50;                % [m] Limit of plastic deformation
```

```
% Beam

R_2_sw = r_c*9.81*A_2*L_b/2; % [N] Reduction of plastic resistance
                             %    due to self-weight

R_2 = 12.138e3 - R_2_sw;     % [N] Plastic resistance.
                             %     Nominal position of the rebars.
                             %     f.y = 686 MPa

R_2 = 10.737e3 - R_2_sw;     % [N] Plastic resistance.
                             %     Nominal position of the rebars.
                             %     f.y = 575 MPa
%
% R_2 = 12.787e3 - R_2_sw;     % [N] Plastic resistance.
%                              %     Adjusted position of the rebars.
%                              %     f.y = 686 MPa
%
% R_2 = 11.344e3 - R_2_sw;     % [N] Plastic resistance.
%                              %     Adjusted position of the rebars.
%                              %     f.y = 575 MPa


u_el_2 = R_2/K_el_2;         % [m] Limit of elastic deformation
u_rd_2 = 50;                 % [m] Limit of plastic deformation


%% DETERMINATION OF EIGENFREQUENCIES

[L,X] = eig(K_el, M);        % "L" is a matrix containing the eigenvectors
                             % "X" is a matrix containing the eigenvalues

% Maximum eigenfrequency

w_max = sqrt(max(max(X)));


%% CRITICAL TIME STEP

h_crit = 2/w_max;                    % [s] Maximum admissible value
h = 0.1e-4;                          % [s] Chosen time step

t_end = 40e-3;                       % [s] End of sequence
t = linspace(0,t_end,t_end/h);       % Time vector

if h >= h_crit
    disp('ERROR, chosen time step too large')
end

%% INITIAL CONDITIONS

% Empty matrices
dofs = 2;                        % Number of degree of freedom
```

```
u = zeros(dofs, length(t));      % Empty matrix storing displacement vectors
v = zeros(dofs, length(t)-1);    % Velocity vectors
a = zeros(dofs, length(t)-1);    % Acceleration vectors

% Assigning initial values

u(:,1) = [0;0];                  % Initial Displacement

height = 5.0;                      % [m] Drop height
v_d = 9.76;                      % [m/s] Initial velocity of drop-weight
                                 % [measured value]
% v_d = sqrt(2*9.81*height);       % [m/s] Initial velocity of drop-weight
%                                  % [theoretical value]
v(:,1) = [v_d; 0];               % Velocities at time t = 0

a_0 = inv(M)*(-K_el*u(:,1));     % Initial acceleration vector
a(:,1) = a_0;                    % Initial acceleration as calculated before

u_b0 = u(:,1)-h*v(:,1)+h^2/2*a(:,1);    % Displacement at time step n-1

% Initial plastic deformation

u_pl_1 = 0;         % Plastic deformation of rod
u_pl_2_pos = 0;     % Plastic deformation of beam in compression
u_pl_2_neg = 0;     % Plastic deformation of beam in tension

 %% CENTRAL DIFFERENTIAL METHOD
m_b(1) = m_2*Kappa_mass(0);

for i =2:length(t)

   du = u(1,i-1)-u(2,i-1);       % [m] Relative displacement bewteen beam
                                 %     and drop-weight

   u2 = u(2,i-1);                % [m] Downwards beam displacement
   % Determining resistance and stiffness of ficticious spring between
   % drop-weight and beam

   % If du = 0, set stiffness equal to elastic stiffness
   if du == 0;
           K_1 = K_el_1;
   % If spring is in tension, set stiffness to 0
   elseif du < u_pl_1;
           K_1 = 0;
   % If spring is in elastic range
   elseif du > u_pl_1 && du <= u_pl_1+u_el_1;
           R = K_el_1*(du-u_pl_1);
           K_1 = R/du;
   % If spring is in plastic range
   elseif du > u_pl_1+u_el_1
           K_1 = R_1/du;
           u_pl_1 = du-u_el_1;
   end
```

```
    % Determining resistance and stiffness of beam spring

    % If u2 = 0, set stiffness equal to elastic stiffness
    if u2 == 0;
        K_2 = K_el_2;
    % If spring is in elastic tension/compression
    elseif u2 > u_pl_2_pos - u_el_2 && u2 <= u_pl_2_pos + u_el_2
            R = K_el_2*(u2-u_pl_2_pos);
            K_2 = R/u2;
    % If spring is in plastic compression
    elseif u2 > u_pl_2_pos + u_el_2;
            K_2 = R_2/u2;
            u_pl_2_pos = u2-u_el_2;
    % If spring is in plastic tension
    elseif u2 <= u_pl_2_pos - u_el_2
            K_2 = -R_2/u2;
            u_pl_2_neg = abs(u2+u_el_2-u_pl_2_pos);
            u_pl_2_pos = u_pl_2_pos - u_pl_2_neg;
    end


    % Storing values of resistance for all time steps
    Res(1,i-1) = K_1*du;
    Res(2,i-1) = K_2*u2;

    % Computing stiffness matrix
    K = [(K_1) -(K_1); -(K_1) (K_1)+(K_2)];

    % Calculation of displacement, velocity and acceleration
    if i==2
        u(:,i) = inv(M/h^2)*(-(K-2*M/h^2)*u(:,i-1)-(M/h^2)*u_b0);
    else
        u(:,i) = inv(M/h^2)*(-(K-2*M/h^2)*u(:,i-1)-(M/h^2)*u(:,i-2));
        v(:,i-1) = (u(:,i)-u(:,i-2))/(2*h);
        a(:,i-1) = (u(:,i)-2*u(:,i-1)+u(:,i-2))/h^2;
    end

end

%% CALCULATION OF ENERGY

% External Work of Beam

DeltaWe(1) = 0;
We(1) = 0;
for i = 2:(length(t)-1)
    DeltaWe(i) = 0.5*(Res(1,i-1)+Res(1,i))*(u(2,i)-u(2,i-1));
    We(i) = We(i-1)+DeltaWe(i);
end

% Internal Work of Beam
DeltaWi(1) = 0;
Wi(1) = 0;
```

```
for i = 2:(length(t)-1)
    DeltaWi(i) = 0.5*(Res(2,i-1)+Res(2,i))*(u(2,i)-u(2,i-1));
    Wi(i) = Wi(i-1)+DeltaWi(i);
end

% Kinetic Energy
Wk(1)=0;
for i = 2:(length(t)-1)
    Wk(i) = m_2*k_b_m_pl*0.5*v(2,i-1)^2;
end

% Total Energy
Wt(1)=0;
for i = 2:(length(t)-1)
    Wt(i) = Wi(i)+Wk(i);
end


%% CREATING PLOTS

% Displacement vs Time plots

figure(1)
plot(t*1000,u(1,:)*1000,'LineWidth',3);
set(gca,'fontsize',16)
title('Displacement of mass 1', 'FontSize', 30)
xlabel('Time [ms]'); ylabel('Displacement [mm]');

figure(2)
plot(t*1000,u(2,:)*1000,'LineWidth',3);
set(gca,'fontsize',16)
title('Displacement of mass 2', 'FontSize', 30)
xlabel('Time [ms]'); ylabel('Displacement [mm]');

% Resistance vs Displacement

figure(3)
plot(u(2,1:length(u)-1)*1000,Res(2,:)/1000,'LineWidth',3);
set(gca,'fontsize',16)
title('Internal Resistance vs Displacement - Body 2', 'FontSize', 30)
xlabel('Displacement [mm]'); ylabel('Resistance [kN]');

figure(4)
plot(u(1,1:1500)*1000-u(2,1:1500)*1000,Res(1,1:1500)/1000,'LineWidth',3);
set(gca,'fontsize',16)
title('Internal Resistance vs Displacement - Body 1', 'FontSize', 30)
xlabel('Displacement [mm]'); ylabel('Resistance [kN]');
```

```
% Resistance vs Time

figure(5)
plot(t(1:length(t)-1)*1000,Res(2,:)/1000,'LineWidth',3);
set(gca,'fontsize',16)
title('Internal Resistance vs Time - Body 2', 'FontSize', 30)
xlabel('Time [ms]'); ylabel('Resistance [kN]');

figure(6)
plot(t(1:1500)*1000,Res(1,1:1500)/1000,'LineWidth',3);
set(gca,'fontsize',16)
title('Internal Resistance vs Time - Body 1', 'FontSize', 30)
xlabel('Time [ms]'); ylabel('Resistance [kN]');

% Velocity vs Time

figure(7)
plot(t(1:(length(t)-1))*1000,v(1,:),'LineWidth',3);
set(gca,'fontsize',16)
title('Velocity of Body 1', 'FontSize', 30)
xlabel('Time [ms]'); ylabel('Velocity [m/s]');

figure(8)
plot(t(1:(length(t)-1))*1000,v(2,:),'LineWidth',3);
set(gca,'fontsize',16)
title('Velocity of Body 2', 'FontSize', 30)
xlabel('Time [ms]'); ylabel('Velocity [m/s]');

% Work vs Time

figure(9)
plot(t(1:(length(t)-1))*1000,We(:),'LineWidth',3);
hold on
plot(t(1:(length(t)-1))*1000,Wi(:),'LineWidth',3);
hold on
plot(t(1:(length(t)-1))*1000,Wk(:),'LineWidth',3);
hold on
plot(t(1:(length(t)-1))*1000,Wt(:),'LineWidth',3);
set(gca,'fontsize',16)
title('External Work of Body 2', 'FontSize', 30)
xlabel('Time [ms]'); ylabel('Velocity [m/s]');



height;
v_init = v(1,2);
maxdisp = max(max(u(2,:)));
u_pl = maxdisp - u_el_2;


[height v_init maxdisp u_pl]
```